Abstract

MULLING, JAMES FREDERICK. Design and Use of Pre-Stressed Unimorphs for High-Displacement, High-Load Applications. (Under the direction of Angus I. Kingon, Chair, and Edward Grant, Co-Chair)

The purpose of this research was threefold: to characterize pre-stressed unimorph actuators fabricated by different routes, to investigate 3-D orientation of the polarization vector through the piezoceramic thickness using piezoresponse force microscopy (PFM), and to design a motor to use the strengths of a compliant actuator. Applications such as robotics need high-force, high displacement actuators with potential for scaling. Pre-stressed unimorphs, typified by THUNDER^{TM} actuators by Face International Corporation, provide larger displacement than traditional unimorph or bimorph actuators because pre-stress introduced during fabrication enhances piezoelectric strain. The fact that these are compliant actuators has important implications for use.

This research showed that bond material and thickness, as well as end conditions all affect actuator performance. Substrate material and thickness relative to that of the ceramic element were shown to have more subtle effects than previously reported. The likely signature of performance enhanced by pre-stress was found in load-displacement test data, which showed that the effect appears to be modified as displacement under load interacts with the original actuator curvature due to pre-stress.

The novel application of PFM showed that orientation of the polarization vector did indeed vary through the actuator thickness. Internal stress bias has a dominant role in determining orientation of the polarization vector, so much so that effects of initial poling were not seen except at a location likely to be a neutral surface. With overall domain orientation generally out of alignment with the poling direction, piezoelectric strain augmented by a large extrinsic contribution can be expected when electric field is applied in the poling direction.

Performance of a linear motor using an inchworm cycle was found to be limited by clamp slip. The passive (unpowered) clamps otherwise had the advantage of simplifying operation. A rotary motor of novel design was tested using several configurations of

actuators and other parts. Its chief advantage was that resonant behavior was little affected by load, since actuators and load were indirectly coupled. Characterization yielded a range of torque and speed data, with best performance generally provided by the simplest drive signals and configurations of parts. Design principles allow the motor to generate high torque. Experimental results, although promising, imply that ample opportunity exists to identify and ameliorate performance-limiting factors.

DESIGN AND USE OF PRE-STRESSED UNIMORPHS FOR HIGH-DISPLACEMENT, HIGH-LOAD APPLICATIONS

by

JAMES F. MULLING

A Thesis submitted to the Graduate Faculty of
North Carolina State University
in partial fulfillment of the requirements for the Degree of Master of Science

MATERIALS SCIENCE AND ENGINEERING

Raleigh

2004

APPROVED BY:

Ronald O. Scattergood

Co-Chair of Advisory Committee

Edward Grant

Chair of Advisory Committee

Angus I. Kingon

Dedication

To my parents and all who made my success in graduate school possible.

Biography

James Frederick Mulling was born James Frederick Mulling II (after his grandfather) on November 1, 1956 in Gainesville, Florida. He graduated from Seaford Senior High School, Seaford, Delaware, in the Class of 1974. During this time, he achieved the rank of Eagle in Scouting. Based on work involving high-temperature decomposition of organic compounds, he was selected to attend the 1973 National Junior Science and Humanities Symposium in West Point, New York, the 1973 National Youth Conference on Science and the Environment in Chicago, Illinois, and received the Bausch & Lomb Science Award Medal. He displayed considerable talent as an artist, and has been a distance runner from high school until the present day.

James was accepted into the Open Curriculum Program at Wake Forest University in Winston-Salem, North Carolina, and was awarded a Carle C. Conway Scholarship (sponsored by Continental Can Company, where his grandmother was employed). He received a Bachelor of Arts degree in English in 1978. He worked in a number of trades in Winston-Salem, including new construction and renovation. He met Kay S. Davis, and the two were married in 1988.

James worked as a Research Technician at Hoechst Celanese Corporation, Separation Products Division, in Charlotte, North Carolina, where he played a key role in the production of a new, fluorinated, microporous membrane. He obtained a new position as Q.A. Laboratory Supervisor during a period where quality emphasis was upgraded and ISO certification was considered.

James was accepted at North Carolina State University and earned his Bachelor of Science degree in Materials Science and Engineering in 1998. He entered a graduate program at N.C. State University and received a Master of Science degree in Materials Science and Engineering in 2004. Most of his research was conducted through interdisciplinary association with the Center for Robotics and Intelligent Machines in the Department of Electrical Engineering.

Acknowledgements

My project was unusually long-running. Many people provided invaluable assistance in ways large and small. If I have forgotten anyone, please excuse my lack of memory. Whoever you are, whatever you did for me: I appreciate it.

Thanks to Larisa Oktyabrsky, Linda Legnasky, Jan Jackson, and other current and former members of the administrative staff in the Department of Materials Science and Engineering, and to Michele Joyner in the Department of Electrical Engineering. Thanks to Dan Leonard for answering many questions, and for helping me find or store things on many occasions.

Special thanks to Edna Deas, whose knowledge, organization, energy, patience, and friendliness are amazing.

I appreciate the exceptional efforts extended by my committee members to help me bring my program to completion. Thanks to all three professors for cheerfully dealing with massive amounts of material provided with short lead times before my defense. Thanks to Dr. Eddie Grant for providing friendliness, encouragement and a home in the robotics lab for many years, and to Dr. Angus Kingon for patience, insightful guidance and critiques, and allowing me the latitude to follow an unconventional path.

My role in “the robotics group” (one in a succession of robotics groups) was assisted by some very knowledgeable people, notably Dr. Tim Usher and Dr. Alexei Gruverman, who helped me acquire and use research equipment. Dr. Charles Parker also provided ongoing assistance with lab instruments and facilities. Thanks to Brenda Bradley, in collaboration with Darin Thomas, for using their expertise to boost several aspects of the early program into technical reality. The high-quality, deadline-sensitive fabrication by JMC Tool and Machine Co. was an asset both to collaborative efforts within the robotics group and to my individual experiments. Thanks also to Chris Kennedy (think PEAK, Inc.) for consultation regarding ANSYS modeling. Gratitude is extended to Brian Dessent and Jeremy Palmer for their assistance and worthwhile collaboration, and to Jian Xu, Stacey Rhody, Tim Slusser, and John Galeotti, for assistance in various forms. The robotics group

appreciates support provided by DARPA (Defense Advanced Research Projects Agency, Department of Defense).

In addition, appreciation is extended to various people who provided assistance with my individual research. Thanks to Dr. Robert Schwartz for willingness to answer questions. Thanks to Dr. Reg Cook of Opto-Acoustic Sensors, Inc. for numerous meetings and consultations to help me use his instrument correctly and understand its principles of operation. Thanks to Kyle Luthy and Carey Merritt, next wave graduate students who were very helpful with some of my final activities. Thanks to Khalid Alhammadi for extended assistance in developing a special purpose data acquisition capability, to Leonardo Mattos for substantial help with an important circuit design, and to Indradeep Sen (Rozgonyi Group) for taking time to find out if his equipment could polish my actuator cross sections.

Special thanks to Dr. Brian Rodriguez for collaboration with the experiment to investigate polarization orientation using PFM. This required meetings, e-mail discussions, sharing various information and software, and of course, instrumental analysis to obtain original data. The expertise of Dr. Alexei Gruverman was also an important factor in this experiment.

Special thanks to Ray Cornwell, Technical Engineer for SIA Adhesives (Akron, OH), who managed to locate small samples of two of their epoxy adhesive films and to ship them overnight on ice in spite of the fact that SIA Adhesives typically sells only large quantities. This speaks highly for the company, its technical support, and relationship with customers and potential customers. Although actuators made with these epoxy films did not perform as well as those reported on in this thesis (possibly due to my fabrication methods), they provided an important first step in dispelling the mystique of bonding only with polyimide adhesive.

Finally, I extend my enormous gratitude and appreciation to Kay Davis, my wife, who went along with my venture to acquire additional higher education and shared its consequences for many years. For every one of her photographs included in this thesis, she shot 50 others to capture the necessary visual documentation. In addition, her repeated proofreading of many sections of this document will benefit anyone who reads it.

Table of Contents

List of Tables

List of Figures

(Appendix 1 contains 226 plots in “gallery” format; that is, not identified separately. Figures for Appendix 2, listed as follows.)

1. Introduction

1.1 Piezoelectric Actuators in Context—Principles and Applications

The advantages of piezoelectric actuators and sensors are compelling. They have no internal backlash or threshold voltage. If voltage is applied along a continuum, dimensional change likewise follows a continuum, with sub-nanometer resolution. Displacement response to a cycled drive signal is inherently hysteretic. However, closed-loop operation yields highly linear and predictable movement. Constrained monoliths can generate large forces, on the order of 10^3 to 10^4 N. Maintaining a static displacement may require applied voltage, but consumes virtually no power, except to offset a very small leakage current. As solid state devices, there is no internal sliding or contact friction, which dispenses with the need for lubricants. In addition, modern piezoelectric ceramics do not tend to wear or shed particles, making them ideal for vacuum and cleanroom applications. They do not generate magnetic fields, and can operate under a wide range of temperatures and pressures. [1]

Nominal displacement can be achieved in approximately one-third the period of an actuator's resonant frequency, which implies response on the order of microseconds, and high potential accelerations. [1] The same device can operate both as a sensor and actuator simply by making driving and sensing circuit connections to separate electroded areas. Likewise, traveling elastic waves can be generated by applying an appropriate signal to a series of isolated electrodes.

Applications for piezoelectric actuators would be more extensive except for the fact that achieving high force and high displacement in the same actuator has thus far eluded investigators. Although piezoelectric actuators can generate considerable force and provide fast response and high bandwidth of operation, displacements in the sub-micron to micron range are small enough to make engineering applications difficult. Total displacement increases in proportion to the length of the actuator. Given typical piezoelectric strains on the order of 0.1%, displacement in the millimeter range would imply improbably large actuators and operating voltages. A number of strategies for dealing with this drawback

will be described below. Let us first consider applications for which piezoelectric actuators are already well-suited and which could benefit from improved performance, which almost always means better displacement relative to actuator size.

There are some applications for which piezoelectric actuators are already ideal candidates. Vibration suppression is one such application because the weight of equipment or structure does not have to be directly supported or moved by the actuator. [2] The actuator only needs to transmit small scale movements through the object to cancel the small scale movements arising from other sources. Applications include sensitive equipment, space structures, and vehicles. [2- 9] (Conversely, acoustic waves can be generated for speakers, buzzers, and underwater acoustics, which leads to a body of literature too extensive to mention.) Since piezoelectric actuators are space-efficient, lightweight, and can be easily bonded to or embedded in a variety of surfaces, they are well-suited to shape control [17], to minimizing drag or turbulence in submarines, correcting for small surface errors in reflective antennas on communications satellites [10] or large telescope mirrors.

Piezoelectric actuators are also well-suited to micro-positioning or micro-dispensing, as in ink-jet printing cartridges, VCR head tracking actuators, precision translation stages, machine tool cutting error correction, alignment in laser systems and interferometers. [3, 11, 12] Finally, they are ideal candidates for integration into micro-electro-mechanical systems (MEMS) which require actuation of microscopic cantilevers, diaphragms, and sensors. [13-19]

Applications which could benefit from improved piezoelectric actuator performance would include most items already mentioned because the need for close tolerances, and precision machining and manufacturing would be relaxed somewhat, lowering costs and improving reliability. In addition, the field of small-scale robotics, would gain new design options.

A number of military and scientific missions would be well-served by redirecting robotic development away from large, expensive robots actuated by electromagnetic motors, pneumatics, or hydraulics toward insect-sized, disposably cheap, mobile sensor

and actuator platforms linked by wireless communications. Such “swarms” would embody distributed sensor data acquisition, intelligence and control. [20, 21] The work of this thesis was originally motivated by collaboration with a group seeking to develop jumping locomotion in a small (less than 5 cm linear dimension) package, under the sponsorship of the Department of Defense. [22]

The reason why piezoelectric and other solid state actuator types have a strong opportunity to supplant mature electromagnetic (EM) motor technology is that EM motors encounter fundamental physical limitations when reduced to millimeter scale, which would offer serious obstacles to further reduction is size. [23] Torque-per-mass density is limited by magnetic flux density across the rotor / stator gap. Electromagnetic coils provide magnetic flux on the rotor side, and can be used on the stator side with permanent magnets or induced currents as alternatives. [24, 25] It is difficult to reduce the size of electromagnetic coils because their magnetic fields depend on electrical current which leads to resistance losses due to ohmic heating. Furthermore, smaller wires have inherently higher resistance, and conductor resistance generally increases with temperature.

In smaller motors, stator-side coils can be replaced with modern rare-earth magnets, which are not easily demagnetized and can provide magnetic flux densities at the rotor / stator gap at the magnetic saturation limit of electrical steel. [26] This implies that the motor will be limited by temperature rather than magnetism. [24]

The other issue is motor torque. Continuous torque is temperature-limited, and so is peak torque at stall. Peak torque at stall is also limited by motor design and voltage that the power supply can provide. [24] To provide high torque at low speed, large coils and motor mass are necessary. As motors are reduced in size, output power can be maintained by operating at higher speeds, with gear reduction transforming high speed at low torque to more useful speed at higher torque. Of course, this necessity adds both the mass and mechanical complexity of the gear system.

The advent of high-performance ultrasonic piezoelectric motors offered a significant alternative to EM motors. The work of many capable researchers has been devoted to achieving the present state of the art [27-43]. However, only the operating

principles of the two types of ultrasonic motors will be described only in passing because the scope of this thesis will be limited to bending actuators and motors which incorporate bending actuators into continuous-stroke linear or rotary motors. (There is some cross-over: see [44].) More particularly, a newer type of bending actuator which achieves improved performance due to permanent internal stress bias will be the chief subject of experiments, as will be discussed in greater detail.

An ultrasonic motor generates movement through the interaction of a vibrator and a reaction surface, which can be a rail or a surface connected to an axle. Based on mode of vibration, ultrasonic motors can be categorized as using standing waves, or propagating waves. A necessary principle for the generation of propagating waves is the superposition of two standing waves which are out-of-phase by 90º in both time and space domains (phase difference and offset). A point worth noting is that a standing wave (including the propagating superposition of two standing waves) is the only type of wave that can be confined to a finite surface or volume and yet remain stable. [3]

Standing wave motors employ various rod or bar-shaped components assembled with a piezoelectric driver to provide a resonant system. With appropriate design, the tip of the driven bar or rod traces an elliptical path resulting from the combination of out-of-phase orthogonal components in the waveform. Generally, it is the repeated impacts, as in a pneumatic hammer, that propel the driven surface (which Uchino terms “woodpecker-type” operation). However, if the surfaces remain in contact for a brief moment while vibrator translates parallel to the surface, a pushing action could be obtained which might lead to reduced wear. This type of ultrasonic motor requires one vibration source, can be made cheaply, and has the potential for high efficiency.

The vibrator in a propagating wave motor achieves the same elliptical path of displacement at every point along a surface, which can be an annular ring or linear plate. (Most readers will have seen an elementary physics demonstration of wave motion in which a floating ball in the water traces a circular path as it rises and falls on a train of water waves passing by.) When pressed against a reaction surface, the parallel component of elliptical surface displacement moves the driven surface. This type of ultrasonic motor

requires two vibration sources, which reduces theoretical efficiency to 50%, but achieves bi-directional motion, better control, and excellent holding torque. [3]

Returning to the subject of compensating for the inconveniently small displacements typical of piezoelectric actuation: the first step on the road to higher displacement is to break the link between operating voltage scaling as the thickness of ceramic across which the voltage is applied. Where size is not an issue, a larger actuator yields larger displacement, since strain multiplied by original length determines displacement. However, piezoelectric strain is proportional to electric field strength, defined as potential difference divided by distance between levels of electrical potential (voltage). A longer monolithic piezoceramic requires proportionally higher applied voltage to maintain equivalent electric field strength, which soon becomes problematic.

Layered "stack" actuators were developed to overcome this problem. The tape-casting method, developed for manufacturing ultra-capacitors, involves the lamination and co-firing of ceramic green sheets with printed electrodes. Diffusion bonded multilayers with integral electrodes allow operation at lower voltage. A typical low voltage design incorporates 20 to 100 layers 0.1 to 0.2 mm thick, requiring about 100 V for maximum displacement. High voltage actuators are constructed from 0.2 to 1.0 mm thick layers and require about 1000 V for maximum displacement. This design involves bonding or clamping a stack of cut and polished ceramic disks interleaved with metal foil electrodes. [1, 9]

Figure 1.1 illustrates the concept of how inter-digital electrodes establish equivalent electric field (**E**) strength with alternating polarity. The implication is that the direction of polarization must also alternate, remaining parallel to the electric field vector. (Polarization is signified by the vector quantity **P**.) Sign conventions have been defined for the electric field vector, for the polarization vector, and for piezoelectric strain constants based on polarization, so that this stack actuator will expand axially and contract laterally (by half as much in terms of strain) when all quantities are directed as shown.

Strategies for improving displacement performance of piezoelectric actuators fall into three categories: improved materials, mechanical amplification, or multi-step

actuators, which exchange “the speed of the material for infinite stroke,” an option which Niezrecki and co-authors term “frequency-leveraged actuators.” [4] Advances in material science and engineering have come in the form of single crystal and single crystal relaxor ferroelectrics which can achieve strains on the order of one percent. [45-47]

Various means for mechanical amplification have been devised, involving external hinged levers or integral structures which deflect as beams [48, 49, 50, 51]. Devices known as Moonies and Cymbals transform lateral contraction of piezoceramic into outward flexure of hollowed or shaped plates bonded to the perimeter of the ceramic. [52-57] Figure 1—2 shows schematic representations of a Moonie and a Cymbal actuator. Unimorphs and bimorphs are composite structures which exhibit beam deflection. They are made by bonding thin piezoceramic sheets to one or both sides of a thin but stiff substrate (ususally metal). [58- 65] Actuators that bend in response to in-plane strain possess integral amplification resulting from the mechanics of beams and plates. Consequently, flexural or bending strain is used to achieve deflection rather than extensional strain. However, in all cases amplification achieves higher displacement at a

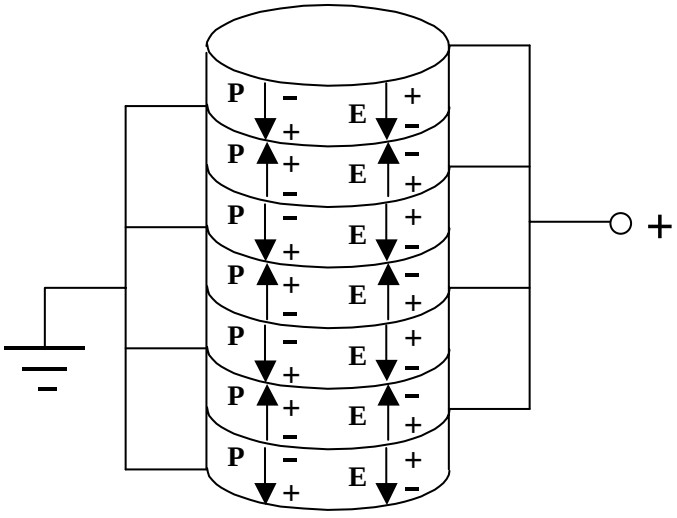

Figure 1—1. Illustration of equivalent electric field strength of alternating polarity established by interdigital electrodes in stack actuators

cost of reduced force. [66] This tradeoff will necessarily remain incontrovertible, except for gains afforded by developing new materials with enhanced strain response.

Finally, the actuator itself can enhance material properties through the effects of internal stress. [67- 69] A new generation of actuators with built-in pre-stress achieve higher displacement than traditional unimorphs and bimorphs of comparable dimensions and stiffness. They are composite structures manufactured by a means which leaves finished structures in a deformed shape that necessarily incorporates a permanent, internal, non-uniform stress.

In 1994, Haertling [70- 81] introduced a new type of transducer / actuator, which he called RAINBOW (Reduced And Internally Biased Oxide Wafer). The actuator is formed by reducing one side of a PLZT (lead lanthanum zirconate titanate) disk at high temperature, thereby transforming a surface layer from ceramic to nearly metallic

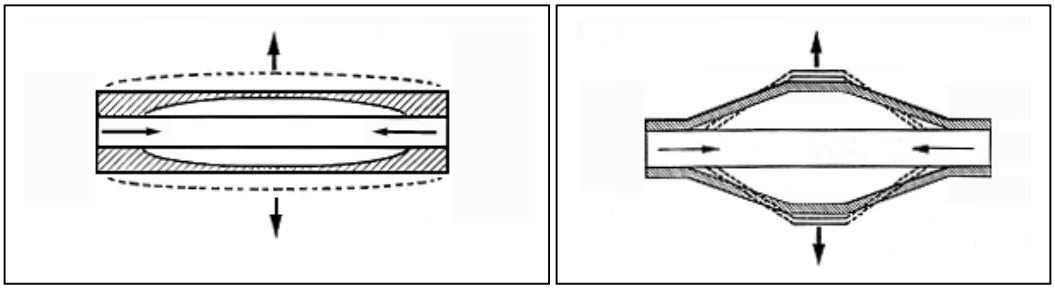

Figure 1—2. Schematic depiction of Moonie and Cymbal “flextensional” actuators

composition. Upon cooling, the disk deforms to a characteristic, shallow dome shape due to a difference in coefficients of expansion between the reduced layer and the bulk of the ceramic. Actuator fabrication is completed by poling perpendicular to the piezoelectric / metallic interface. These actuators produced flexural strains of 0.5%. Flexural strain is defined as the flexural displacement divided by the active length (i.e., covered by piezoceramic) of the composite beam. For disk actuators, the active diameter is substituted for beam length.

The THUNDER™ (Thin-layer composite unimorph ferroelectric driver and sensor) actuator [82- 86], developed under grants from NASA, achieves deformation and pre-stress by a different route. A PZT (lead zirconate titanate) ceramic thin sheet is bonded under hydrostatic pressure to a metal substrate *while at* elevated temperature. Upon cooling, the laminate develops curvature and consequent internal stresses due to differences in the coefficients of expansion between the metal layer and ceramic layer. As with RAINBOWs, actuator fabrication is completed by poling perpendicular to the piezoelectric / metal interface.

When compared, the RAINBOW and THUNDER actuators show many similarities. The fabrication methods, however, are very different. Reported free displacements were 10-25% higher for RAINBOW actuators [87]. However, the THUNDER actuators are very rugged, and standard commercial manufacturing techniques have been developed. No such manufacturing techniques have been developed for RAINBOW actuators, according to available literature, and they are somewhat fragile. [4]

The aspect of stiffness is crucially important in using these and all flexural actuators because they are compliant structures. By contrast, extensional actuators (monoliths and stacks) are essentially uncompliant. A stiffer actuator can apply greater forces and displace greater loads, as long as it is provided with an equally stiff support and the load itself is not too compliant. [67, 88] However, it is all too easy to lose most or all of their miniscule displacement though imperfect surface contact, actuator-load misalignment, localized plastic deformation, and so forth. The advantages of boosting displacement by an order of magnitude are substantial, since losses do not necessarily increase, but using a less stiff actuator affects design problems substantially. The implications for use of compliant actuators will be discussed at length in this thesis.

1.2 Statement of goals

The most general goal is to achieve incremental advances in both the displacement of THUNDER-type actuators (to be called “pre-stressed unimorphs” hereafter) and their load-bearing capability. Also, determine if alternative fabrication methods using different adhesives yield notably different actuator performance.

Key metrics are blocked force and free displacement. Free displacement, of course, is displacement in the absence of an applied load (no-load condition) as determined at a typical load-bearing location on an actuator (center). Blocked force is essentially the load which prevents displacement. Free displacement and blocked force will be used as indicators of what works and what does not.

Additional goals of this work can be further divided into the following categories:

1. Conduct experiments that might expand upon or yield insight into the underlying mechanism of enhanced performance due to internal stress bias.
2. Investigate the implications of compliance and end conditions on actuator performance.
3. Investigate the design of motors or other work-producing applications that might utilize the performance properties of pre-stressed unimorph actuators.

1.3 Overview of Thesis

Two general themes have been adopted. The first is a juxtaposition of fabrication and application considerations: how the actuators are made; how they are used. The second is that characterization includes both low and high load regimes.

The topics which have received greatest emphasis are (1) comparison of actuator characterization results to fabrication technique, (2) use of a novel approach (piezoresponse force microscopy, or PFM) to determine change in net polarization through

the cross-sectional thickness of an actuator, and (3) design and characterization of linear and rotary motors powered by pre-stressed unimorphs.

It is very important to mention that a large fraction of the figures in this thesis include **color**. Often, the use of color was the only way to visually organize complicated juxtapositions of graphic elements which needed to be distinguished from one another. Figures including color have the parenthetical insertion , “(color)”, after the figure number. If your copy of this thesis does not include color, please seek another source.

This notation will typically not be made, however, for figures which include a small amount of color, such as a single dark blue line on a plot which would be perfectly intelligible in a photocopy.

1.4 References

[1] http://www.physikinstrumente.com/tutorial/
PI (Physik Instrumente) L.P. (Auburn, MA and Tustin, CA), is the U.S. operation of Physik Instrumente (PI) GmbH & Co. KG in Germany.

[2] E.L Colla, E.S. Thiele, D. Damjanovic, N. Setter. New high performance—low cost monolithic bimorph piezoelectric actuators for applications requiring large displacements with significant forces. IEEE International Symposium on Applications of Ferroelectrics, 1, 317-320 (2000).

[3] K. Uchino. *Piezoelectric Actuators and Ultrasonic Motors*. (Kluwer Academic Publishers, 1997).

[4] C. Niezrecki, D. Brei, S. Balakrishnan, and A. Moskalik. Piezoelectric actuation: state of the art. The Shock and Vibration Digest, 33, 269-280 (2001).

[5] C. D. Near. Piezoelectric actuator technology. Proceedings of SPIE - The International Society for Optical Engineering, 2717, 246-258 (1996).

[6] U. Kumar, B. Rawal, and A. P. Ritter. Multilayer actuators for surface mount applications. IEEE International Symposium on Applications of Ferroelectrics, 1, 301-304 (1996).

[7] J. Garcia-Bonito, M.J. Brennan, S.J. Elliott, A. David and R.J. Pinnington. A novel high-displacement piezoelectric actuator for active vibration control. Smart Materials and Structures, 7, 31-42 (1998).

[8] S.M. Yang and Y.J. Lee. Modal analysis of stepped beams with piezoelectric materials. Journal of Sound and Vibration, 176, 289-300 (1994).

[9] S. Yoshikawa, M. Farrell, D. Wakentin, R. Jacques, and E. Saarma. Monolithic piezoelectric actuators and vibration dampers with interdigital electrodes. Proceedings of SPIE - The International Society for Optical Engineering, 3668, 578-585 (1999).

[10] B. N. Agrawal and K. E. Treanor. Shape control of a beam using piezoelectric actuators. Smart Materials and Structures, 8, 729-740 (1999).

[11] K. Yen, C. Yang, and G. Roig. Linear piezoelectric step motors. (Session 1C1) Conference Proceedings - IEEE SOUTHEASTCON. 1, 21-29 (1990).

[12] J. W. Judy, D. L. Polla, and W. P. Robbins. A linear piezoelectric stepper motor with submicrometer step size and centimeter travel range. IEEE Transactions on Ultrasonics, Ferroelectrics, and Frequency Control, 37, 428-437 (1990).

[13] K.J. Gabriel, J. M. McMichael. Realizing systems with MEMS. Proceedings of the ASME (American Society of Mechanical Engineers), Aerospace Division, AD-52, 733-741 (1996).

[14] M. Tabib-Azar. *Microactuators: Electrical, Magnetic, Thermal, Optical, Mechanical, Chemical & Smart Sstructures*. (Kluwer Academic Publishers, 1998).

[15] Ph. Luginbuhl, G.-A. Racine, Ph. Lerch, B. Romanowicz, K.G. Brooks, and N.F. de Rooij. Piezoelectric cantilever beams actuated by PZT sol-gel thin film. Sensors and Actuators A, 54, 530-535 (1996).

[16] C.K. Lee, S.H. Chang, and P.-Z. Chang. Miniature piezoelectric actuators: design concept, fabrication and performance evaluation. Smart Materials and Structures, 7, 312-326 (1998).

[17] S. J. Kim and J. D. Jones. Quasi-static control of natural frequencies of composite beams using embedded piezoelectric actuators. Smart Materials and Structures, 4, 106-112 (1995).

[18] G. Horner and B. Taleghani. Single axis piezoelectric gimbal. Proceedings of SPIE - The International Society for Optical Engineering, 3674, 371-378 (1999).

[19] G.-A. Racine, P. Muralt and M.-A Dubois. Flexural-standing-wave elastic force motor using ZnO and PZT thin film on micromachined silicon membranes for wristwatch applications. Smart Materials and Structures, 7, 404-416 (1998).

[20] J.G. Smits. Design considerations of a piezoelectric-on-silicon microrobot. Sensors and Actuators A, 35, 129-135 (1992).

[21] A.M. Flynn, L.S. Tavrow, S.F. Bart, R.A. Brooks, D.J. Ehrlich, K.R.Udayakumar, and L.E. Cross. Piezoelectric micromotors for microrobots. Journal of Microelectromechanical Systems, 1, 44-51 (1992).

[22] Support provided by DARPA (Defense Advanced Research Projects Agency, Department of Defense), contract number N3998-98-C3536.

[23] K. Matsuzaki, T. Matsuo, and Y. Mikuriya. Comparison of electrostatic and electromagnetic motors based on fabrication and performance criteria. Proceedings of the International Symposium on Micromechatronics and Human Science. 77-81 (1994).

[24] J.M. Hollerbach, I.W. Hunter, J. Ballantyne. A comparative analysis of actuator technologies for robotics, Part V in *The Robotics Review 2* (O. Khatib, J.J. Craig, and T. Lozano-Pérez, eds. The MIT Press, 1992).

[25] R. Rabinovici. Scaling of switched reluctance motors. IEE Proceedings: Electric Power Applications, 142, 1-4 (1995).

[26] K. J. Binns and D. W. Shimmin. The relationship between performance characteristics and size of permanent magnet motors. “Electrical Machines and Drives”, IEE Conference Publication No. 412, 423-427 (1995).

[27] K. Uchino. Piezoelectric ultrasonic motors: overview. Smart Materials and Structures, 7, 273-285 (1998).

[28] A. M. Flynn. Performance of ultrasonic mini-motors using design of experiments, Smart Materials and Structures, 7, 286-294 (1998).

[29] M. Kuribayashi, Kurosawa, M. Chiba, and T. Higuchi. Evaluation of a surface acoustic wave motor with a multi-contact-point slider. Smart Materials and Structures, 7, 305-311 (1998).

[30] S-W. Ricky Lee and H. L. Li. Development and characterization of a rotary motor driven by anisotropic piezoelectric composite laminate. Smart Materials and Structures, 7, 327-336 (1998).

[31] J.-F. Manceau, S. Biwersi and F. Bastien. On the generation and identification of traveling waves in non-circular structures—applications to innovative piezoelectric motors. Smart Materials and Structures, 7, 337-344 (1998).

[32] J. Tsujino. Ultrasonic motor using a one-dimensional longitudinal-torsional vibration converter with diagonal slits. Smart Materials and Structures, 7, 345-351 (1998).

[33] P. Hagedorn, T. Sattel, D. Speziari, J. Schmidt, and G. Diana. The importance of rotor flexibility in ultrasonic traveling wave motors. Smart Materials and Structures, 7, 352-368 (1998).

[34] J. Wallaschek. Contact mechanics of piezoelectric ultrasonic motors. Smart Materials and Structures, 7, 369-381 (1998).

[35] S.-F. Ling, H. Du, and T. Jiang. Analytical and experimental study on a piezoelectric linear motor. Smart Materials and Structures, 7, 282-388 (1998).

[36] S. Dong, S. Wang, W. Shen, and L. Li. A miniature piezoelectric ultrasonic motor based on circular bending vibration mode. IEEE/ASME Transactions on Mechatronics, 5, 325-330 (2000).

[37] K. Nakamura and S. Ueha. Performance of a hybrid transducer-type ultrasonic motor as a function of size. IEEE Ultrasonics Symposium, 557-560 (1994).

[38] M. Aoyagi and Y. Tomikawa. New control method of contact force between rotor and stator on rod-type ultrasonic motor. IEEE Ultrasonics Symposium, 1, 695-698 (1998).

[39] T. S. Glenn and N. W. Hagood. Development of a two-sided piezoelectric rotary ultrasonic motor for high torque. Proceedings of SPIE - The International Society for Optical Engineering, 3041, 326-338 (1997).

[40] T. Takano, Y. Tomikawa, M. Yagimuma, T. Ogasawara. A linearly moving ultrasonic motor using a longitudinal and bending multi-mode vibrator. IEEE 7th International Symposium on the Applications of Ferroelectrics. (1992) 521-524.

[41] T. Takano, Y. Tomikawa, M. Aoyagi, T. Ogasawara, A. Yabuki. Ultrasonic linear motors for application to driving a light pick-up element. IEEE Ultrasonics Symposium, 1, 445-448 (1993).

[42] K. Mori, T. Kumagae, and H. Hirai. Ultrasonic linear motor for a high precision X-Y stage. IEEE Ultrasonics Symposium, 657-660 (1989).

[43] K. Nakamura, M. Kurosawa, H. Kurebayashi, and S. Ueha. IEEE Transactions on Ultrasonics, Ferroelectrics and Frequency Control, 38, 481-485 (1991).

[44] T. Hemsel, J. Wallaschek. Survey of the present state of the art of piezoelectric linear motors. Ultrasonics, 38, 37-40 (2000).

[45] S.E. Park and T.R. Shrout. Ultrahigh strain and piezoelectric behavior in relaxor based ferroelectric single crystals. Journal of Applied Physics, 82, 1804-1811 (1997).

[46] S.-E. Park, V. Vedula, M.-J. Pan, W. S. Hackenberger, P. Pertsch and T. R. Shrout. Relaxor based ferroelectric single crystals for electromechanical actuators. Proceedings of the SPIE—The International Society for Optical Engineering, 3324, 136-144 (1998).

[47] S.-Eek Park, S. Wada, P. W. Rehrig, S.-F. Liu, L. E. Cross, and T. Shrout. Crystallographic engineering in high-performance piezoelectric crystals. Proceedings of the SPIE—The International Society for Optical Engineering, 3675, 2-9 (1999).

[48] B. J. Pokines and E. Garcia. A smart material microamplification mechanism fabricated using LIGA. Smart Materials and Structures, 7, 105-112 (1998).

[49] Z. Zhu and B. Zhang. A linear piezomotor integrated by a monolithic flexural frame. Transactions of the ASME, 119, 414-417 (1997).

[50] K. Duong and E. Garcia. Design and performance of a rotary motor driven by piezoelectric stack actuators. Japanese Journal of Applied Physics, Part 1: Regular Papers & Short Notes & Review Papers, 35 [12A], 6334-6341 (1996).

[51] K. Duong and E. Garcia. Development of a rotary inchworm piezoelectric motor. Proceedings of the SPIE—The International Society for Optical Engineering, 2443, 782-788 (1995).

[52] Y. Sugawara, K. Onitsuka, S. Yoshikawa, Q. Xu, R. Newnham, and K. Uchino. Metal-ceramic composite actuators. Journal of the American Ceramic Society, 75, 996-98 (1992).

[53] A. Dogan, Q. Xu, K. Onitsuka, S. Yoshikawa, K. Uchino, and R. E. Newnham. High displacement ceramic metal composite actuators (moonies). Ferroelectrics, 156, 1-6 (1994).

[54] K. Onitsuka, A. Dogan, J.F. Tressler,Q. Xu, S. Yoshikawa, and R. Newnham. Metal-ceramic composite transducer, the Moonie. Journal of Intelligent Material Systems and Structures, 6, 447-455 (1995).

[55] A. Dogan, J.F. Fernandez, K. Uchino, and R. E. Newnham. The Cymbal electromechanical actuator. IEEE International Symposium on Applications of Ferroelectrics, 1, 213-216 (1996).

[56] A. Dogan, K. Uchino, and Newnham, R.E. Composite piezoelectric transducer with truncated conical endcaps “Cymbal”. IEEE Transactions on Ultrasonics, Ferroelectrics, and Frequency Control, 44, 597-605 (1997).

[57] W. Y. Shih, W.-H. Shih, and I. A. Aksay. Scaling analysis for the axial displacement and pressure of flextensional transducers. Journal of the American Ceramic Society, 80, 1073-1078 (1997).

[58] M.R. Steel, F. Harrison, and P.G. Harper. The piezoelectric bimorph: an experimental and theoretical study of its quasistatic response. Journal of Physics D: Applied Physics, 11, 979-989 (1978).

[59] J. G. Smits, S. I. Dalke and T. K. Cooney. The constituent equations of piezoelectric bimorphs. Sensors and Actuators A, 28, 41-61 (1991).

[60] J. G. Smits and W.-S. Choi. The constituent equations of piezoelectric heterogenous bimorphs. IEEE Transactions on Ultrasonics, Ferroelectrics and Frequency Control, 38, 256-270 (1991).

[61] J. G. Smits and T. K Cooney. The effectiveness of a piezoelectric bimorph actuator to perform mechanical work under various constant loading conditions. Ferroelectrics, 119, 89-105 (1991).

[62] Q.-M. Wang and L. E. Cross. Performance analysis of piezoelectric cantilever bending actuators. Ferroelectrics, 215, 187-213 (1998).

[63] Q.-M. Wang, X.-H. Du, B. Xu, and L. E. Cross. Electromechanical coupling and output efficiency of piezoelectric bending actuators. IEEE Transactions on Ultrasonics, Ferroelectrics and Frequency Control, 46, 638-646 (1999).

[64] X. Li, W. Y. Shih, I. A. Aksay, and W.-H. Shih. Electromechanical Behavior of PZT-brass unimorphs. Journal of the American Ceramic Society, 82, 1733-1740 (1999).

[65] Q.M. Wang and L.E. Cross. Tip deflection and blocking force of soft PZT-based cantilever Rainbow actuators. Journal of the American Ceramic Society. 82 (1999) 103-10.

[66] V. Giurgiutiu, Z. Chaudhry, C. A. Rogers. Stiffness issues in the design of ISA displacement amplification devices: case study of a hydraulic displacement amplifier. Proceedings of the SPIE—The International Society for Optical Engineering, 2443, 105-119 (1995).

[67] G. H. Haertling. Stress-induced effects in PLZT ceramics. IEEE International Symposium on Applications of Ferroelectrics, 1, 65-68 (1996).

[68] R. W. Schwartz, L. E. Cross, and Q.-M. Wang. Estimation of the effective d31 coefficients of the piezoelectric layer in Rainbow actuators. Journal of the American Ceramic Society, 84, 2563-2569 (2001).

[69] R.W. Schwartz, M. P. Laoratanakul, W. D. Nothwang, J. Ballato, Y. Moon, and A. Jackson. Understanding mechanics and stress effects in Rainbow and Thunder stress-biased actuators. Proceedings of SPIE - The International Society for Optical Engineering, 3992, 363-375 (2000).

[70] G.H. Haertling. Rainbow actuators and sensors: a new smart technology. Proceedings of the SPIE—The International Society for Optical Engineering, 3040, 81-92 (1997).

[71] C. Elissalde and L.E. Cross. Dynamic characteristics of Rainbow ceramics. Journal of the American Ceramic Society, 78, 2233-2236 (1995).

[72] G.H. Haertling. Rainbow ceramic—a new type of ultra-high displacement actuator. Bulletin of the American Ceramic Society, 73, 93-96 (1994).

[73] C. Elissalde, L. E. Cross, and C. A. Randall. Structure-property relations in a reduced and internally biased oxide wafer (Rainbow) actuator material. Journal of the American Ceramic Society, 79, 2041-2048 (1996).

[74] G. Li, E. Furman and G.H. Haertling. Composition and microstructure of chemically reduced PLZT ceramics. Ferroelectrics, 182, 69-76 (1996).

[75] G. Li and G. H. Haertling. Stress-sensing characteristics of PLZT-based Rainbow ceramics. Smart Materials and Structures, 6, 425-431 (1997).

[76] S. Chandran, V.D. Kugel and L. E. Cross. Characterization of the linear and non-linear dynamic performance of Rainbow actuator. IEEE International Symposium on Applications of Ferroelectrics, 2, 743-746 (1996).

[77] S. Sherrit, H.D. Wiederick B.K. Mukherjee, and G.H. Heartling. The dielectric, piezoelectric and hydrostatic properties of PLZT based Rainbow ceramics. IEEE International Symposium on Applications of Ferroelectrics, 390-393 (1995).

[78] G. Li, E. Furman, and G.H. Haertling. Fabrication and properties of PSLT antiferroelectric Rainbow actuators. Ferroelectrics, 188, 223-236 (1996).

[79] G. H. Haertling. Chemically reduced PLZT ceramics for ultra-high displacement actuators. Ferroelectrics, 154, 101-106 (1994).

[80] E. Furman, G. Li, and G.H. Haertling. Electromechanical properties of Rainbow devices. IEEE International Symposium on Applications of Ferroelectrics, 146-149 (1994).

[81] G. Li, E. Furman and G. H. Haertling. Finite element analysis of Rainbow ceramics. Journal of Intelligent Systems and Structures, 8, 434-443 (1997).

[82] K. M. Mossi, G. V. Selby, R. G. Bryant. Thin-layer composite unimorph ferroelectric driver and sensor properties. Materials Letters, 35, 39-49 (1998).

[83] K.M. Mossi, R.P. Bishop, R.C. Smith and H.T. Banks. Evaluation criteria for Thunder actuators. Proceedings of the SPIE—The International Society for Optical Engineering, 3667, 738-743 (1999).

[84] K.M. Mossi, R.P. Bishop. Characterization of different types of high performance Thunder actuators. Proceedings of the SPIE—The International Society for Optical Engineering, 3675, 43-52 (1999).

[85] C. Shakeri, C. M. Bordonaro, M. N. Noori, and R. Champagne. Experimental study of Thunder: a new generation of piezoelectric actuators. Proceedings of the SPIE—The International Society for Optical Engineering, 3675, 63-71 (1999).

[86] J.-K. Song and G. Washington. Thunder modeling and control with classical and fuzzy control algorithm. Proceedings of the SPIE—The International Society for Optical Engineering, 3668, 866-877 (1999).

[87] S. Wise. Displacement properties of Rainbow and Thunder piezoelectric actuators. Sensors and Actuators A, 69, 33-38 (1998).

[88] V. Giurgiutiu, C.A. Rogers, Z. Chaudhry. Design of displacement-amplified induced-strain actuators for maximum energy output. Journal of Mechanical Design, 119, 511-516 (1997).

2. Review of Literature and Theory

2.1 Brief Overview of Piezoelectric Theory and Materials

Although matter is composed of charged particles, the internal electrical state of most materials is neutral and remains so under the influence of mechanical stress or heat. However, certain solid materials—primarily inorganic, crystalline solids—either respond to mechanical stress or heat by developing internal polarization, or in some cases possess permanent polarization at the atomic level (or at the molecular level in the case of certain organic polymers). Electrical polarization results, of course, when centers of positive and negative charge within some repeated subunit of material structure do not coincide. These materials present the possibility of charge displacement by both electrical fields, mechanical stress, or simple temperature change, and hence have coupled electromechanical or electrothermal properties. The phenomena of electrostriction, piezoelectricity, pyroelectricity, and ferroelectricity depend on a state of internal polarization. [1] (Electrostriction occurs in all dielectric materials, even non-solids, and will not be discussed at this point.)

Of the 32 crystal classes, 11 are centrosymmetric and cannot become polarized. Of the 21 non-centrosymmetric crystal classes, 20 are piezoelectric. (Crystal class 432 has a combination of symmetry elements that excludes it from having coupled properties.) They have one or more polar, crystallographic axis or axes. Mechanical stress causes an asymmetric shift in internal charge (direct piezoelectric effect), which results in charge accumulation on external surfaces to maintain overall electrical neutrality. Conversely, an electric charge presented to appropriate surfaces induces mechanical strain (indirect or converse piezoelectric effect). [2]

Ten of the twenty piezoelectric classes have a unique polar, crystallographic axis. This additional *a*symmetry allows polarization change even with the uniform strain of thermal expansion, and thus these are known as pyroelectric materials. (Uniform strain would create canceling charge shifts in materials without a unique polar axis.)

A subset of pyroelectric materials have a permanent, reorientable polarization, and are termed ferroelectric. There is no means of predicting with certainty whether a particular pyroelectric is ferroelectric. Membership in this set of materials must be established by experiment. Figure 2.1—1 illustrates that these material properties formed nested subsets. Therefore, all piezoelectrics are dielectrics, but not the converse. All pyroelectrics are also piezoelectric and dielectric, but not the converse, and likewise for ferroelectrics. [3]

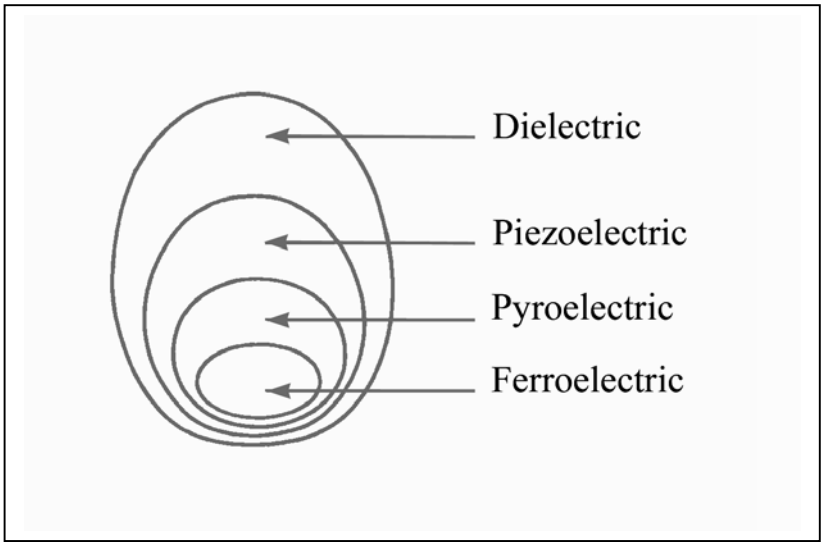

Figure 2.1—1. The hierarchy of electromechanical and electrothermal material properties related to internal polarization. (after [3])

The PZT system offers some of the highest piezoelectric strain capabilities occurring in all available materials, and so is generally the piezoceramic of choice in fabricating actuators. Its properties can be tailored by the addition of up to a few percent of dopants to the composition, which is nearly always done. PZT, or lead zirconate titanate, is a solid solution of lead zirconate, $PbZrO_3$, and lead titanate, $PbTiO_3$, represented by the schematic phase diagram in Figure 2.1—2. Each compound is a member of the perovskite family, named after the mineral form of calcium titanate, which has the generalized formula ABO_3 , where A represents a cation of valence 2+, B represents a cation of

valence 4+, and the oxygen anion has a valence of 2–. (Compounds having the perovskite structure can also have A^{1+} B^{5+} or A^{3+} B^{3+} cations, but no ferroelectrics have been discovered among the latter. [4])

A typical representation of the unit cell of the PZT crystal structure would be that shown for the diagram for the paraelectric cubic phase overlaid onto the high temperature region of the phase diagram, where "paraelectric" signifies a symmetric, non-polarized phase of the material. As a particular composition is cooled below its Curie temperature (T_C) a structural phase transformation occurs in which the cubic paraelectric phase adopts a lower-symmetry rhombohedral form for zirconium-rich compositions or a tetragonal form for titanium-rich compositions. Spontaneous polarization appears with the development of the elongated low-temperature unit cells which have a unique, polar, crystallographic axis.

Except for a non-piezoelectric phase that forms when the titanate component falls below about 7%, compositions up to Pb $Zr_{0.53}$ $Ti_{0.47}$ O_3 (47% titantate) adopt a rhombohedral structure. At higher titanate fractions, a tetragonal structure is assumed. The arrow marked P_S beside the diagrams for the rhombohedral and tetragonal structures indicates a spontaneous polarization vector caused by the displacement of the Ti^{4+} cation away from the geometric center of the unit cell. Note that the Ti^{4+} cation displaces toward a vertex or corner of the rhombohedral cell, and there are eight such equivalent directions. The Ti^{4+} cation displaces toward a face of the tetragonal cell, and there are six such equivalent directions.

The nearly vertical line marked "MPB" is known as the morphotropic phase boundary. It is a narrow region where both phases are present in equal amounts [7], and morphotropic compositions yield the highest piezoelectric strains of all possible compositions. It is believed that the maximum performance occurs at this composition because the combination of eight equivalent orientations for P_S in rhombohedral cells and six equivalent directions for P_S in tetragonal cells increases the probability that a large fraction of polarization dipoles are oriented nearly in parallel with applied electric field, where their combined interaction will have a higher response to its influence.

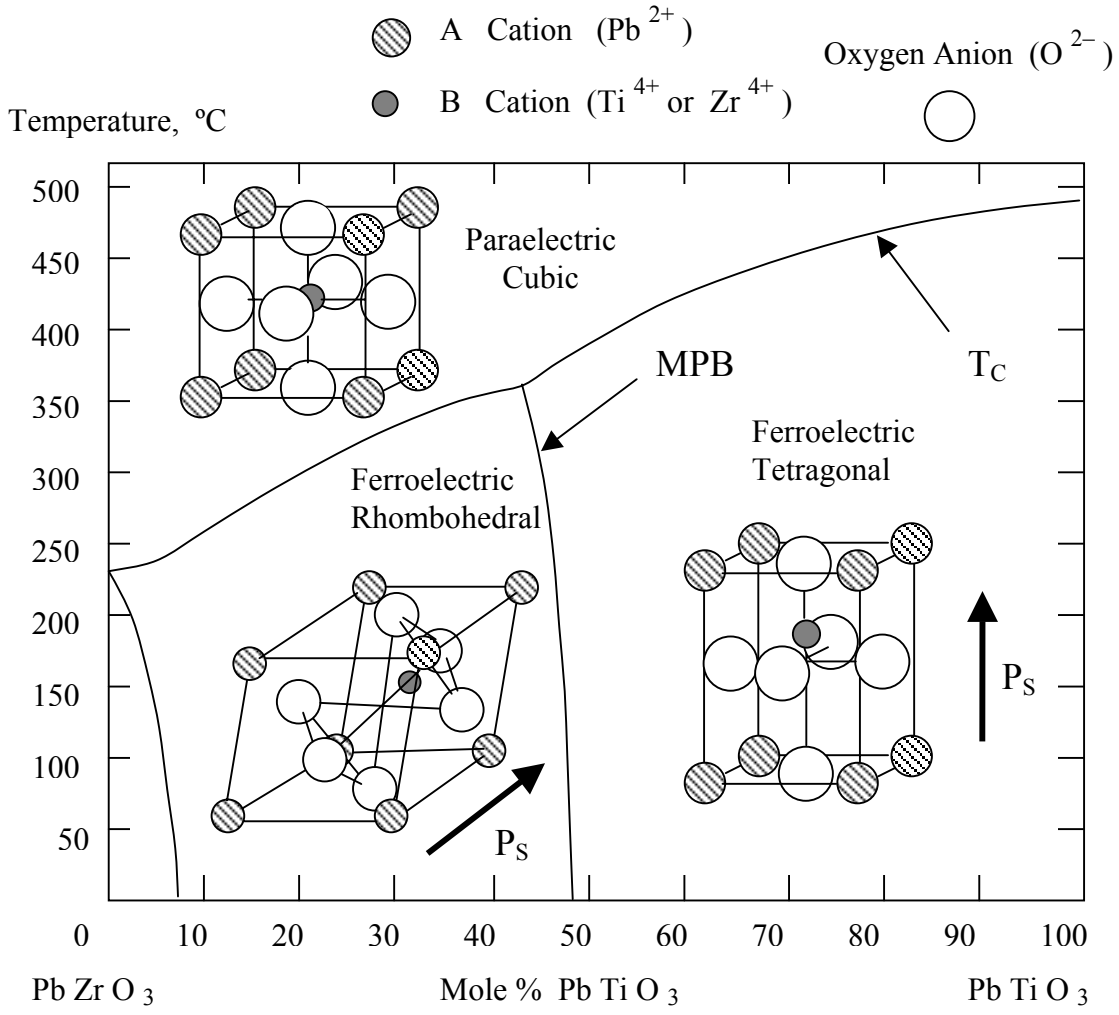

Figure 2.1—2. A schematic depiction of the Pb Zr_X $Ti_{(1-X)}$ O_3 phase diagram with overlaid crystal structures for high and low temperature phases (after [5] and [6])

To better explain the previous statements, the subject of polarization domains must be mentioned. As the reader may know, as spontaneous polarization appears upon transition to lower temperature phases, large numbers of dipoles develop an aggregate parallel orientation in volumes of material, known as domains, on approximately the same scale as ceramic grain structure. However, research indicates that volumes associated with

polarization domains typically do not coincide with specific grains. In virgin piezoceramic, the domain structure is oriented randomly, and response to an applied electric field is generally self-canceling.

By applying a voltage across the ceramic above the coercive field, E_C, typically equal to 20 kV per centimeter of its thickness (50 V /mil) for PZT-based devices, for a duration of a minute to some fraction of an hour, any component of the randomly oriented polarization vectors that can align with the applied field will do so. [8] The duration of poling is approximate because the alignment occurs rapidly at first, then continues at a diminishing rate. Some researchers pole piezoceramics at modest temperature, say 100-200ºC, to facilitate dipole realignment and assist any accompanying strain to dissipate. [6]

The boundaries between ferroelectric domains are known as domain walls, and have specific characteristics which minimize total crystal energy. In one type of domain wall (180º), the polarizations are oriented anti-parallel to one another, which leaves no polarization component normal to the wall. A discontinuity in the normal components of polarization must be compensated for by surface charge. The resulting free charge would increase crystal energy. In tetragonal materials, the only other orientation that would be energetically favored would be one in which the polarization vectors on either side of a wall are oriented at 90º to one another, leaving the wall in an approximately 45º orientation relative to the direction of polarization on either side. Thus, polarization components normal to the wall either approximately cancel or are approximately continuous. [9]

An important consequence of this scenario is that 90º domains allow what is termed extrinsic contribution to piezoelectric strain. Intrinsic piezoelectric strain arises from the additional distortion in spontaneous polarization dipoles due to applied electric field. It happens that 180º domain walls contribute only to the dielectric properties of ferroelectrics, not to piezoelectric strain. The movement of non-180º walls has both ferroelectric and ferroelastic consequences, and is believed to be the primary contributor to extrinsic strain. [10-12] It is reported that more than 60% of the room temperature dielectric and piezoelectric response is from domain wall motion, with both 180º and non-180º domain walls active in soft PZT. [13, 11]

The phenomenological theory of piezoelectricity and other polarization-based phenomena, as the accepted theory is known, is based on thermodynamics. The internal energy of a polarizable, deformable crystal in equilibrium is the summation of all appropriate state (path independent) variables, which include electric field, E, polarization, P, mechanical stress, T, mechanical strain, S, temperature θ, entropy, σ, where the first member of a conjugate pair is the extensive variable, the second is the intensive variable (e.g., stress does not depend on how much material is present, representing a potential "field", while strain depends on original dimensions). Partial derivatives of a selected thermodynamic potential, such as the Gibbs free energy, yield relationships between conjugate pairs in terms of internal energy.

A derivative expression, such as that taken for a thermodynamic energy function can be alternatively expressed as a Taylor series expansion, which is strictly true only for the infinite series. However, lowest order terms provide useful relations for scientific and engineering purposes.

Since the quantities involved are vectors or tensors (e.g., electric field, mechanical strain), they are related by tensors of third rank or higher, depending on which quantities are related. By applying tensor symmetries deduced both from the logical constraints of accommodating known material properties and the symmetries derived from crystallographic considerations, the number of independent components is greatly reduced. Further simplification can then be achieved by using a so-called "reduced notation" (also known as matrix notation or Voigt notation), although the rules of tensor manipulation cannot be directly applied to matrices in reduced notation.

The resulting expressions, familiar to consumers of theoretically-established results, are the constitutive relations for the direct piezoelectric effect, given by (2.1—1) and the indirect piezoelectric effect (2.1—2) which relate the coupled properties of mechanical strain and polarization. The top lines in each equation give the complete tensor notation, the middle lines give reduced notation, and the last lines drop tensor notation altogether. Tensor relationships are necessary to mathematically describe the effect of a vector quantity, such as electric field, in an anisotropic medium, such as a crystal, where

components of the induced effect, such as polarization, appear not only in parallel with the field direction, but in other coordinate directions as well. (Normally, tensor subscripts are written in lower case. However, in the interest of seeing them more clearly as subscripts, upper case will be used throughout this discussion.)

(2.1—1) $$-\left(\frac{\partial G}{\partial T}\right)_E = S_{IJ} = s^E_{IJKL}\, T_{KL} + d_{MIJ}\, E_M$$

$$= S_K = s^E_{KL}\, T_L + d_{MK}\, E_M$$

$$= S = s^E\, T + d\, E$$

(2.1—2) $$-\left(\frac{\partial G}{\partial E}\right)_P = P_M = d_{MIJ}\, T_{IJ} + \kappa^T_{MN}\, E_N$$

$$= P_M = d_{MK}\, T_K + \kappa^T_{MN}\, E_N$$

$$= P = d\, T + \kappa^T\, E$$, where G is Gibbs free energy, d is one of several piezoelectric constants which have tensor representations, κ is dielectric susceptibility (polarization per unit of applied electric field, a dimensionless constant applicable to linear dielectrics), s is the compliance tensor, and T, S, E, P retain their previously given meanings.

Since the thermodynamic potential is a function of several variables, the expressions which provide the constitutive relations are derived from the exact differential of the thermodynamic potential by holding one or more variables constant. Thus, various factors or constants in constitutive relations and other expressions have superscripts, as seen in (2.1—1) and (2.1—1), to indicate that the non-conjugate property is held constant (such as the effect of electric field on the relation between strain and stress). To aid in applying the theory to an experimental setting where the quantities might be measured, the following conventions for holding mechanical or electrical boundary conditions constant at zero have been adopted, as shown in Table 2.1—1.

Table 2.1—1. Boundary conditions signified by superscripted variables

T = Constant (Zero) Stress ≡ Mechanically Free
E = Constant (Zero) Electric Field ≡ Short Circuit
D = Constant (Zero) Electrical Displacement ≡ Open Circuit
S = Constant (Zero) Strain ≡ Mechanically Clamped

Table 2.1—2 presents a standard set of piezoelectric constitutive relations with parent thermodynamic potentials, adapted from Ikeda [14]. Note that Gibbs free energy is defined as G = F – TS – EP, where F = U – TS is Helmholtz free energy, given all contributions to internal energy. Two variants, the elastic Gibbs energy, $G_1 = F - TS$ (mentioned also in introductory material in [15]), and electric Gibbs energy, $G_2 = F - EP$, are state functions appropriate to the ferroelectric system. Note also that electrical displacement, $D = \varepsilon_0 E + P$ (where ε_0 is the permittivity of a vacuum, $8.854(10)^{12}$ F/m), is the combined charge displacement due to applied electric field and non-field dependent spontaneous polarization arising from crystallographic order.

It is also important to mention that the choice of symbols for various constants such as permittivity of a vacuum just mentioned (symbolized by κ_0 in [16]) vary widely among authors. In particular, the symbol, χ, is used to represent both direct dielectric susceptibility ($\partial P / \partial E$) and inverse dielectric susceptibility ($\partial E / \partial P$). This presentation will use χ for inverse susceptibility and κ for direct susceptibility, in keeping with Ikeda [14] and Jona and Shirane [5]. It is helpful to compare the constitutive relations given by a particular source to determine which version the author is using, if not clear from the text. Note that a relation giving polarization will contain electric field multiplied by direct susceptibility, $(\partial P / \partial E)\, E$, in a manner analogous to an algebraic rather than differential

expressions. A relation giving electric field will contain indirect susceptibility multiplied by polarization, $(\partial E / \partial P)P$.

Table 2.1—2. Piezoelectric constitutive relations and source thermodynamic potentials

Piezoelectric Relations	Independent Variables	Thermodynamic Potential
$T = c^D S - a P$ $E = -a S + \chi^S P$	S, P	Helmholtz free energy
$S = s^E T + d E$ $P = d T + \kappa^T E$	T, E	Gibbs free energy, G
$S = s^D T + b P$ $E = -b T + \chi^T P$	T, P	Elastic Gibbs energy, G_1
$T = c^E S + e E$ $D = -e S + \kappa^S E$	S, E	Electric Gibbs energy, G_2

The two equations in the second row of Table 2.1—2 are essential to the description of piezoelectric devices used as actuators and sensors. In the case of strain as a function of stress and applied field, a voltage applied to actuator electrodes will produce an electric field, E, which would be the quotient of applied voltage divided by thickness of the piezoelectric material, in volts per meter (V / m). Since strain is a unitless fraction, the piezoelectric d-coefficient must have units of [m / V]. However, the relationship giving polarization as a function of field and applied stress also uses the piezoelectric d-coefficient. Spontaneous polarization can be expressed as dipole moment per unit volume integrated over volume. [15] Since dipole moment has units of [C · m], the

volume integration produces units of [C / m^2], although [C / cm^2] would be more typical in practice.

However, in the case of a change in polarization induced by mechanical strain (the result of applied stress), we want to know how much charge in Coulombs will appear on electroded surfaces to maintain electrical neutrality when the internal charge state of the material has been changed by mechanical strain. In this case, the d-coefficient is multiplied by stress in [N / m^2] and must yield generated charge in [C / m^2], implying simplified units of [C / N]. Equation (2.1—3) demonstrates that the units are equivalent, which implies both versions of the d-coefficient have the same numerical value.

$$(2.1\text{—}3) \qquad [V] = \left[\frac{J}{C}\right] = \left[\frac{N\ m}{C}\right] \Rightarrow \left[\frac{m}{V}\right] = \frac{m}{\frac{N\ m}{C}} = \left[\frac{C}{N}\right] = \left[\frac{\frac{C}{m^2}}{\frac{N}{m^2}}\right]$$

It must be remembered, however, that the piezoelectric d-coefficient is actually a third rank tensor with 27 independent components in the absence of any simplifying considerations due to symmetry or deductive assessments. One such consideration is that stress and strain tensors are known to be symmetric with respect to the principal diagonal (i.e., $T_{I\,J} = T_{J\,I}$ and $S_{I\,J} = S_{J\,I}$) because in the absence of body torques, a shear stress of the form T_{IJ} cannot be applied without applying a shear of the form T_{JI}. [16] Further, for a component of a tensor property to have a non-zero value, an n-fold rotational transformation of tensor components must be compatible with the symmetry of the crystal point group (e.g., 4-fold rotation for the class 4mm, to which tetragonal PZT belongs, or 3-fold rotation for rhombohedral PZT). As a result, it can be shown that the only way for various symmetry conditions to hold is for some components to either equal zero or take on mutually dependent values such as being equal to one another, or equal in magnitude but opposite in sign. [7]

The symmetry of a poled perovskite ceramic has been established as ($\infty \cdot m$), that is, an ∞-fold rotation axis and an infinite number of mirror planes parallel to the axis, but none perpendicular to it (described as ∞ mm in [17]). If the x_3 axis of a tensor coordinate system is taken as the ∞-fold rotation axis, then the piezoelectric tensor for this material system can be ultimately simplified to that given in (2.1—4). [5]

(2.1—4)
$$\begin{bmatrix} 0 & 0 & 0 & 0 & d_{15} & 0 \\ 0 & 0 & 0 & d_{15} & 0 & 0 \\ d_{31} & d_{31} & d_{33} & 0 & 0 & 0 \end{bmatrix}$$

Consequently, piezoelectric coefficients typically included in research and commercial literature for PZT and related ceramics are as follows (after [17]).

d_{33} (strain coefficient): strain developed in parallel with electric field applied in the 3-direction (which we assume is the direction of poling)

d_{33} (charge coefficient): internal charge separation occurring in the 3-direction—resulting in counter-charge density on electrode surfaces perpendicular to the 3-axis—when stress is applied in the 3-direction, normal to the surfaces

d_{31} (strain coefficient): strain in the 1-direction when electric field is applied in the 3-direction (electrodes perpendicular to the 3-axis). Thus, for a thin plate poled in the thickness direction, the d_{31} coefficient would give lateral or in-plane strain perpendicular to the poling direction. This is an indication of the cross-coupling of tensor properties. Lateral strain is about – ½ the strain associated with the d_{33} coefficient. [18]

d_{31} (charge coefficient): charge density accumulated in a direction lateral to the direction of poling and applied electric field (would be difficult to discern on a thin plate without electrodes on lateral surfaces)

d_{15} coefficient: shear strain that develops when electric field is applied in a direction perpendicular to the poling direction. For example if a block of piezoceramic were poled in the 3-direction and afterwards the electrodes normal to the 3- direction were removed and redeposited on faces normal to the 1-direction, then voltage applied across the new electrodes would induce a sideways shear. Likewise, an applied shear about the 2-axis would accumulate charge on the new electrodes in this example.

In summary, the d-coefficient is the constant of proportionality between charge displacement and stress, or strain and electric field, as shown in 2.1—5 (after [17, 19]).

(2.1—5) $$d = \frac{P}{T} = \frac{S}{E}$$

There is both a small-signal and large-signal aspect to these relationships. Across short excursions of a few volts or a few tens of volts, the proportionality would be approximately constant, creating a linear relationship. However, if applied electric field ranges from zero to a high positive level then returns through zero to a large field of negative polarity, a plot of polarization as a function of applied field traces a hysteresis loop. (Polarization is determined from the voltage measured across a large, integrating capacitor placed in series with the ferrorelectric specimen [19], or nowadays from an operational amplifier circuit which mimics the series capacitance.) If associated strains in parallel and transverse directions are also plotted against applied electric field, so-called butterfly (strain-displacement) loops result. These plots, shown in schematic form in Figure 2.1—3, are strongly identified as familiar manifestations of the electromechanical properties of ferroelectrics. The slope of the butterfly loops is essentially a large-signal d-coefficient, but one which is a derivative function rather than a constant.

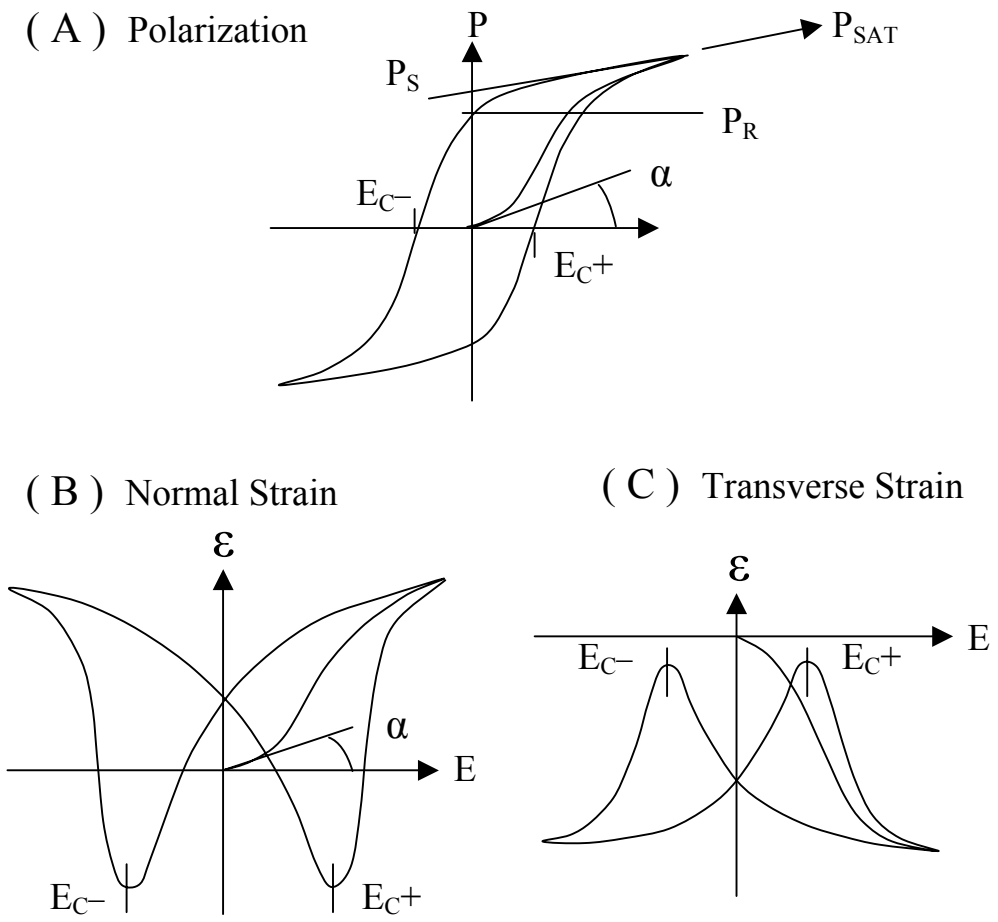

Figure 2.1—3. (A) P-E hysteresis loop, (B) Butterfly loop for strain in 3-direction, (C) Butterfly loop for strain in 1-direction (Electric field in 3-direction in all cases)

Various features of the loops have been indicated in Figure 2.1—3. Polarization is the net alignment of all dipoles in the volume of material, which includes both intrinsic and extrinsic contributions. In unpoled ceramic, the vector sum of individual dipoles is approximately zero due to random orientation. At low field strengths in unpolarized (virgin) material, polarization is initially reversible and linearly proportional to electric field. The slope of the response to this small signal perturbation gives the initial dielectric

constant, k_I', according to (2.1—6), which will be similar to the dielectric constant of the paraelectric phase. [20]

(2.1—6) $$\tan \alpha = \frac{P}{E} = \left(k'_I - 1 \right) \varepsilon_0$$

As electric field strength increases, domains switch orientation to align with the field. Also, domain walls move if energetically favored under the electric field stress. At some high field strength, every dipole component which can align with the field has done so. This is the asymptotic saturation polarization, P_{SAT}, approached by the pointed saturation edges shown in Figure 2.1—3A. With field strength reversed to zero, a fraction of dipole alignment is lost, but polarization retained at zero field is termed remanent polarization, shown as P_R, in Figure 2.1—3A. A measure of spontaneous polarization, P_S , is given by extrapolation to zero of a line tangent to the high-field end of the hysteresis loop. P_S is slightly higher than P_R in ceramics, but the two values are nearly equivalent in single crystals. [19]

A negative "coercive field" of strength E_C– is required to negate positive remanent polarization and to induce increasing alignment in the opposite direction. This field strength corresponds to "switching points" at the bottom tips of the normal strain butterfly loop and the top tips of the transverse strain butterfly loop. The directions of strain associated with the field direction reverse, and the piezoceramic expands in directions that were contracting and *vice versa*. (If the direction of strain response did not switch while electric field direction remained the same, then the strain-displacement loops would have the same general shape as the P-E loop.) A negative saturation level is achieved, then the sequence of events reverses by reducing and eventually reversing electric field direction. The tangent of the initial trace of the butterfly, shown at an angle α in Figure 2.1—3B, is often taken as the piezoelectric d-coefficient.

Quantities known as piezoelectric coupling factors (e.g., k_{33} , k_{31} , k_T , k_P) provide a dimensionless measure of the capacity of a piezoceramic to convert electrical or

mechanical work into its counterpart. In general, they are defined as the square root of either the ratio of mechanical energy available to total electrical energy input, or the ratio of electrical energy available to total mechanical energy input. (So, the squared coupling factor is the ratio.) Although the coupling factors describe the incompleteness of conversion, they do not represent efficiency in the sense of a thermodynamic cycle. That is, the storage of energy in one form and retrieval in another, if conducted quasi-statically, are both lossless processes. [19, 7]

A short discussion of how coupling factors for piezoceramic elements having common geometries and boundary conditions is provided in [17], which presents expressions for calculating the coupling factors in terms of resonant and anti-resonant peaks determined by electrical impedance analysis. A discussion in [19] defines various coupling factors in terms of factors appearing in piezoelectric equations of state, such as compliances or d-coefficients with appropriate boundary conditions. A precise but accessible explanation of the meaning of the coupling coefficients, illustrated by a graphic example based on a thought experiment, is given in the 1987 IEEE Standard on Piezoelectricity. [21] The Standard provides examples of how the ratio of work available in output form to work done in input form (as the sum of available and unavailable portions) can be translated into expressions involving factors appearing in piezoelectric equations of state. Giurgiutiu and Rogers derive expressions which allow calculation of effective electromechanical coupling coefficients based on commercial vendor data. [22] However, values determined by their method ranged between 0.45 and 1.038, departing from the typical value of 0.7 normally quoted for PZT ceramic.

The final topic to be included in this section concerns property-altering dopants or additives which are nearly always used when fabricating PZT components. Cationic substituents having larger positive valences than Pb^{2+} or (Zr^{4+}, Ti^{4+}) create lead vacancies and yield so-called “soft” PZT modifications. A lead vacancy is generated for every two La^{3+} cations on an A-site (Pb^{2+}), for every two Nb^{5+} or Ta^{5+} cations or one W^{6+} cation on a B-site (Zr^{4+}, Ti^{4+}). Lead vacancies are believed to enable domain wall motion under the

influence of smaller electric fields and mechanical stresses than would otherwise be the case.

Cationic substituents having smaller positive valences than Pb^{2+} (or Zr^{4+}, Ti^{4+}) create oxygen vacancies and yield so-called "hard" PZT modifications. A K^{1+} cation on an A-site (Pb^{2+}), or an Mg^{2+} , Sc^{3+} ,or Fe^{3+} cation on a B-site (Zr^{4+}, Ti^{4+}) tends to create oxygen vacancies that gradually distort the framework of oxygen octahedra in perovskite lattices. The distortion probably impairs domain wall motion and generally creates opposing effects to high-valence substituents. In addition, isovalent additives are often used as modifiers to achieve property alterations such as enhanced electromechanical coupling factors.

For actuator purposes, soft PZT compositions are generally selected because of easier poling, increased elastic compliance and higher piezoelectric coupling factors. However, a hard PZT might be more desirable for ultrasonic motor applications due to small hysteretic loss and a large mechanical quality factor with a small, high-frequency electric field. [23] The numbered series of commercially available PZT ceramics originated with the Clevite Corporation in the 1950's. PZT compositions modified with Nb, Cr, La, or Fe were numbered PZT-5, PZT-6, PZT-7, and PZT-8, respectively. A variant of PZT-5 is used exclusively for actuators fabricated in this project. A detailed assemblage of information is available in [19]. Nickles created an excellent summary of it. [7] Uchino includes a short but useful section. [12]

2.2 Brief Overview of Non-Piezoelectric Actuator Principles

As mentioned in Chapter 1, robotics applications provide an excellent testing ground for technologies which currently have limited usefulness in the design of equipment requiring force and movement. Macro-motion devices traditionally include electromagnetic, hydraulic, and pneumatic actuators and motors. As a benchmark, their performance will be discussed first, with emphasis on new directions. In facing the demands of mobility and scaling, the emphasis with traditional technologies is to

reexamine design concepts that fell into disfavor or were never well-developed, or to fully address issues, such as the possibility of hydraulic fluid leaks, that have discouraged selection for new applications. Although miniaturization has been named as a driving force in the selection of non-traditional actuator technologies, this discussion will not include actuator types which are only viable at small scale, such as electrostatic drives. Polymer gel actuators will also be omitted although their development is promising.

Modern electromagnetic (EM) motors are close to the limits of torque per mass set by non-superconducting electromagnetics. It was noted previously that magnetic coils are current-dependent devices and are temperature-limited. Equipping an EM motor to provide high-torque implies large coils, maintaining high torque at small scale by increasing motor speed implies gear reduction, and scaling coils beyond the millimeter scale is beset by competing physical limitations. Based on a survey of motor specifications, Hollerbach, Hunter, and Ballantyne determine a state-of-the-art torque per mass of 6 N·m/kg, for which little improvement is likely. [24] Design concepts being re-examined include brushless motors and reluctance motors.

Hydraulic and pneumatic actuators have the intrinsic problem of equipment overhead needed to provide fluid pressure. Hydraulic actuators are faster than pneumatic actuators because the fluid is nearly incompressible. Aside from equipment overhead, torque is a highly non-linear function of actuator size. A small increase in size can dramatically increase torque and complicate comparisons with other actuator types. [24] As a benchmark, torque per mass for the multiple rotary hydraulic actuators used by the Sarcos Dextrous Arm averaged about 120 N·m/kg, with power per mass at 600 W/kg. [25] Modern hydraulic actuator design involves a vast array of complex design principles and component assemblages, and their development continues.

Pneumatic actuator components and operating principles resemble their hydraulic counterparts, but differences in design and operation result from the substantially lower viscosity and higher compressibility of air relative to hydraulic fluid. Also, air does not provide lubrication. Practical consequences are the need for tighter tolerances and faster valves. Sophisticated development continues. A sophisticated robotics application is

reported in [26]. A re-emerging trend involving pneumatic actuators is the use of inflatable tubes surrounded by braided mesh designed to shorten with inflation. The McKibben muscle, which has existed for decades, is an archetype. [27]

Shape memory alloys (SMA) have been extensively investigated as an intermediate scale technology. Shape memory effects have been known for decades. However, the discovery of a nickel titanium alloy generated serious inquiry into underlying causes. [28, 29] The NiTi alloy is popular because of its favorable material properties, nontoxicity, and reasonable cost. [24] Well over a dozen alloy systems are known to exhibit the shape memory effect, but other than NiTi, only Cu-Zn-Al and Cu-Al-Ni currently have any commercial importance. [30]

The NiTi alloy has a high temperature austenitic phase with a cubic structure, which undergoes a hysteretic phase transformation across a region of temperature upon cooling, forming a twinned martensitic phase with a rhombic (monoclinic) structure alternating in orientation due to the twinning. (The hysteresis involves transition temperature: the austenite to martensite transformation occurs within a lower temperature range than the martensite to austenite recovery transformation.) Upon re-heating, the diffusionless martensitic transformation is crystallographically reversible. Self-accomodated martensitic plates undergo a “backwards shear” which precisely reverses the forward process, thereby exhibiting a form of structural memory. (Self-accommodation means that habit plane variants sympathetically group together so that net distortion from the martensite transformation it zero.) [30]

The martensitic yield stress is about 10% that of the parent phase. [30] Deformation at room temperature induces de-twinning, a reorientation which requires little stress and which places atoms into a sheared version of their relative locations in the original austenitic structure. There is also a two-way shape memory effect in which the metal not only returns to a high temperature shape upon heating, but also to a low temperature shape upon cooling. [28, 30]

A typical process for creating actuation is to form a shape memory wire into a spring at high temperature. At low temperature, the spring will be easily deformed into a

state of complete compression by a load. If, while under load, the spring is heated (to about 500ºC, usually by electrical current), the recovered austenitic phase will have a much higher elastic modulus, lifting the load to the level of strain it would have generated if the spring had never left the parent phase. Another strategy, which would apply to a robotic leg, would involve a return stroke requiring little force applied by the robot itself in the low temperature phase. Upon heating, the leg would recover its extended shape and propel the robot one step. Material strains of 8% due to recovery are typical, although springs can achieve higher displacement. Repeated deformation without resetting the high temperature shape results in degraded recovery strains. [28]

The appeal of NiTi actuators is that large force per wire cross-section is created by shape recovery, which can exceed 200 MN/m^2, with power per mass of 50 kW/kg. [24] Increasing wire cross-section increases the force. The disadvantages of SMA actuators are low efficiency (2-3%) and low-frequency, since not only must the heat associated with high temperature be removed, but the heat of transformation as well. Recovery times are measured in seconds, but modified wires and improved cooling have achieved twitches as short as 400 ms. [31] Hirose *et al* developed a rotary actuator for which they report a maximum torque of 1.1 N·m, a speed of 2.7 rpm, torque per mass of 1.2 N·m / kg, 6.32 W output power at an efficiency of 5.7%. [32]

The phenomenon of magnetostriction resembles piezoelectricity in that certain alloys, primarily Terfenol-D (alloy of terbium, dysprosium, and iron) display the property of giant magnetostriction and can achieve strains as high as 0.2% [24, 33], but more typically 0.07% [34]. Thus, displacement is proportional to the size of the actuator, and strain under load decreases linearly. An energy density of 14 to 25 kJ / m^3 is achieved by Terfenol-D, compared with 0.7 to 1.3 kJ / m^3 for PZT. Magnetostrictive actuators can achieve displacement frequency above 2000 Hz.

However, to achieve 0.2% magnetostrictive strains, large magnetic fields (0.5 T) are required, generated by water-cooled electromagnets, indicating an intrinsic problem of equipment overhead. Induction in nearby metal can also be a problem. Also, Terfenol-D is brittle, difficult to machine, and expensive. [24] Since it has low tensile stress,

magnetostrictive actuators must be operated under compressive pre-load, typically 8 to 20 MPa. [33, 34]

Two phenomena that are closely associated with piezoelectricity have not been included elsewhere and will be discussed here because they represent useful actuator principles. The first is the phenomenon of electrostriction, which actually cannot be eliminated from piezoelectric strain itself, since piezoelectric strain and electrostrictive strain are first order (linear) and second order (quadratic) terms of the Taylor series expansion of thermodynamic energy functions essential to the phenomenological theory of polarization-based phenomena. The linear term represents the dominant effect at low electric fields and mechanical stresses, and the contribution of higher order terms can be neglected. At higher fields and stresses, a second order term must be included to account for the effect of electrostriction, represented by **Q**, a fourth order tensor.

In simplified form, the relationship between strain and electric field is given by $S= M E^2$ for electrostriction (compared with the piezoelectric relationship, $S = d E$). The electrostrictive coefficient, $M = Q \varepsilon_0^2 \varepsilon^2$, is derived from expressions based on the series expansion of the elastic Gibbs energy, G_1. The same treatment yields the important equation, $d = 2 \varepsilon_0 \varepsilon Q P_S$, which implies (in the words of Uchino) than piezoelectricity is equivalent to the electrostrictive phenomenon biased by the spontaneous polarization. [12] A consequence of the squaring of electric field in terms representing electrostriction, is that strain does not change sign as electric field changes sign. Thus, expansions remain expansions; contractions remain contractions. By applying arguments based on crystal symmetry, it can be shown that all dielectric materials, even liquids and gases, display electrostriction. [7] Ceramic materials having structures represented by centrosymmetric point groups will develop only electrostrictive strain with applied electric field.

So-called Relaxor ferroelectrics have been developed such as $Pb(Mg_{1/3} Nb_{2/3})O_3$, or PMN, which display especially large electrostrictive strains. Designed materials such as an alloy of PMN and PT (lead titanate), which are often doped as well, display strains comparable to piezoceramics (about 0.1%). Electrostrictive actuators are capable of generating about the same forces as piezoelectric actuators—about 35 to 40 MPa. Features

include near absence of hysteresis in strain-electric field loops, no need for poling and better stability under conditions that lead to de-poling such as high loads or temperatures. On the other hand, piezoelectric properties are less temperature-dependent, and piezoelectric strain is faster than electrostrictive strain. [12]

The second phenomenon closely associated with piezoelectricity concerns a promising application of Maxwell stress. Electrical actuators were made from dielectric elastomer films which yielded strains in the neighborhood of 30 to 40%. Pre-stretching the polymer films, either uniaxially or biaxially, was shown to increase actuated strains to 117% for silicone elastomers, and as high as 215% for acrylic elastomers. [35] In 1994, actuation strains of about 3-4% were demonstrated using polyurethanes with gold surface electrodes 20 nm thick. [36] Investigating researchers concluded that the dominant effect was Maxwell stress with accompanying electrostriction. [37]

When exposed to an electric field, all dielectric polymers contract in the field direction and expand laterally. The stress compressing the polymer film thickness in the field direction is given by $T = \varepsilon_0 \varepsilon E^2$. [35] This expression, which resembles the expression for electrostrictive strain, is the stress applied by capacitor electrodes on a dielectric layer. The effect is called Maxwell stress and has often been regarded as a nuisance. In making actuators, the researchers needed highly compliant electrodes and used a dispersion of carbon particles in elastomer matrix.

During development, a fortuitous discovery was made that pre-stretching the polymer films increased the dielectric breakdown voltage by a factor of about 100, and improved actuation strains by a similar amount. It is believed that pre-stretching causes molecular alignment, increasing stiffness in the stretching direction. Consequently, a tubular actuator might be made by stretching elastomer film around a compressed spring, so that the wrapping stretches in the circumferential direction and the blocked spring stretches in the orthogonal, axial direction. Such actuators have generated 30 N of force, achieved a stroke of about two centimeters, and operation frequency of 50 Hz. They operate on 1 to 5 kV at low current. [38]

The foregoing synopsis is not meant to imply that actual piezoelectric polymers do not exist. Certain polyamides (nylons), in which molecules arrange themselves in hydrogen-bonded sheets, adopt hydrogen-bond arrangements that do not allow polar moments to cancel, as they do in other nylon types, and exhibit piezoelectric strain. Polyvinylidene fluoride (PVDF or PVF_2) adopts phases which have been shown to meet the demanding requirements of classification as ferroelectric materials—reorientable polarization, Curie transition, and hysteresis loops—as demonstrated by x-ray and infrared techniques. [39]

The electroactive polymers (EAPs) described represent a type of EAP known as the electronic EAPs, a category which includes piezoelectric polymers, electrets, dielectric elastomers and electrostrictive graft elastomers. The other type is known as the ionic EAPs, and includes ionic polymer gels, conductive polymers, and polymer-metal composites. Ionic EAPs operate by mechanisms based on the mobility or diffusion of ions, and require small actuation voltages. However, actuation rates are considerably slower, the actuators must be kept wet in sealed containers, and do not hold a position well because continuing ionic migration can damage the materials. By contrast, electronic EAPs are faster, do not need a sealed environment, and can hold a position while drawing virtually no current. [38]

2.3 Bending Piezoelectric Actuators

2.3.1 History, Design and Operation, Reported Performance

2.3.1.1 The Development of Actuators for Flexure

Although the force capabilities of stack piezoelectric actuators are impressive (order of 10^3 N), their overall usefulness is limited by their small strains (order of 0.1%). Much ingenuity has been expended in attempting to overcome this limitation. A number of mechanical amplification mechanisms have been developed despite the fact that amplification always exchanges higher displacement for reduced force. Mechanical amplifiers typically employ either a hinged moment arm lever or flexural device. In a

sense, flexural devices are also levers—angular levers rather than moment arm levers.

Moment arm levers rely on the principle of an applied moment to a rigid body, which couples a smaller force acting at a longer moment arm to larger force acting at a shorter moment arm. Displacements are proportional to the lengths of the moment arms. High amplification (force or distance) implies either a long moment arm with the disadvantages of size and unavoidable compliance, or a tiny moment arm which must compete with hinges and external connections for space.

An angular lever relies on the fact that orthogonal displacements coupled through a rotating radial line change in a highly nonlinear way. Large amplifications occur during very small deviations from flatness (rotation = 0º), which favors amplifying the miniscule displacements of a macroscopic device with another macroscopic device. In the three-hinged angular lever in Figure 2.3.1.1—1A, the ratio of the change in vertical displacement of the top hinge to the change in horizontal displacement of the bottom hinges is d(sin θ) / d(2 cos θ), which is – ½ cot θ. The cotangent function is infinite at 0º, falling to a value of 57 at θ = 1º, and a value of one at θ = 45º. Flexural beam displacement is analogous to a continuously hinged or jointed elaboration of the three-hinged lever as shown in Figure 2.3.1.1—1B.

In flexural displacement, a beam becomes a distributed hinge and difficulties of incorporating hinges as discrete mechanisms are eliminated. The analogy between hinged, angular levers and continuous beams is of course simplified: beam deflection is due to the accumulation of continuous angular deflection across a structure having a long dimension. The similarity is nonetheless shown by the fact that beam theory assumes that the slightly diminished in-plane span (due to curvature) that accompanies a small transverse deflection is *so much smaller* than the transverse deflection that it can usually be disregarded. More important, however, is that *internal* strains accompanying beam deflection are considerably amplified through the long dimension of the structure, which can allow the structure to function as its own amplifier for internally *induced* strains.

Actuator designs which can provide amplified transverse deflection in response to small internal strains have the advantage of integral amplification—that is, the output of

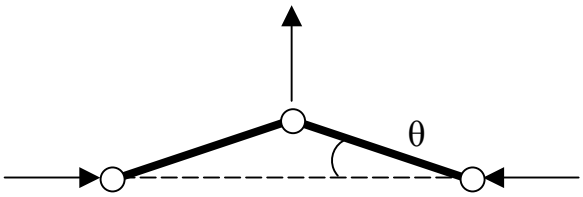

Figure 2.3.1.1—1A. Three-hinged angular lever

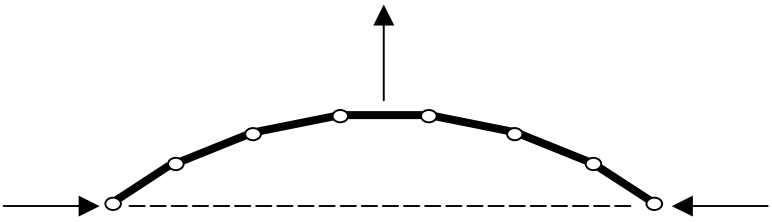

Figure 2.3.1.1—1B. Multi-hinged angular lever approximating continuous beam (Interior angles are constrained to approximate equality.)

the actuator does not need to be amplified by an external device. The present work will limit its scope to actuators with integral strain amplification. An excellent survey of available methods of fabricating piezoelectric actuators with amplified strain output is provided by [40]. A number of externally-amplified or compounded designs are discussed (in addition to discussion of internally leveraged actuators), and several ingenious examples of external angular levers are shown.

It can be shown that for a given longitudinal strain within a beam, displacement of the elastic curve is a quadratic function of length. Since a beam actuator used to amplify in-plane strain of some integral piezoelectric plate or rod element is able to deflect without an externally applied load or moment, a demonstration would proceed as follows. Using familiar equations of beam mechanics, where σ and ε are uniaxial stress and strain related by Young's modulus, E; where I is the area moment of inertia of the beam cross-section,

M is a bending moment, and ν is transverse deflection as a function of distance x across the beam, and y is an unspecified but fixed distance from the neutral surface at which the internal strain is ε, we have the following.

(2.3.1.1—1) $$\sigma = -\frac{M\ y}{I}, \quad \sigma = E\ \varepsilon \quad \rightarrow \quad \varepsilon = -\frac{M\ y}{E\ I} \quad \rightarrow \quad M = -\frac{E\ I\ \varepsilon}{y}$$

(2.3.1.1—2) $$E\ I\ \nu'' = M = -\frac{E\ I\ \varepsilon}{y} \quad \rightarrow \quad \nu'' = -\frac{\varepsilon}{y}$$

(2.3.1.1—3) $$\nu = -\iint \frac{\varepsilon}{y}\, dx\, dx = -\frac{1}{2}\frac{\varepsilon}{y} x^2 + C_1 x + C_2$$

The constants C_1 and C_2 would be determined for boundary conditions such as where ν(x) = 0 or ν'(x) = 0. For x = L (total length of the beam) in the case of a cantilever beam or x = ½ L for a beam simply supported at both ends, one could determine maximum displacement. Nonetheless, (2.3.1.1—3) indicates that an internal strain, ε, at a distance y from the neutral surface will be magnified as the square of beam length.

The idea of using "principle of opposition" bonded piezoelectric plates to produce mechanical amplification by bending was developed by C.B Sawyer [41] and patented in 1931 [42], but Smits and Choi note that the double strip (bilamé) idea can be traced to P. and J. Curie. [43] Germano notes that Sawyer compared his device to a bimetallic thermostat. [44] The term "unimorph," signifying an active piezoelectric layer bonded to a non-piezoelectric layer, apparently had nebulous beginnings, and terms such as "heterogenous bimorph" have been used with the implication that a unimorph is a specialized instance of a bimorph. However, the term bimorph, signifying a bilayer device with both layers serving elastic and piezoelectric functions, was registered as a trademark to the Vernitron Corporation. It was often called a bender Bimorph because early work at Brush Laboratories, where Sawyer worked, involved twisting devices made of bonded Rochelle salt shear plates. [44]

Today the term bimorph and bender are nearly synonymous, and the bonded plates are typically polycrystalline ceramic such as piezoelectric lead zirconate titanate (PZT) or electrostrictive lead magnesium niobate (PMN). A bimorph can include a metal shim central layer, which maintains structural integrity if the ceramic cracks, or the interface can be only adhesive and / or conductive material without significant mechanical rigidity. A comprehensive history of notable, reported work on bimorphs and their applications is given in [45, 43].

As discussed in [45], bimorphs are manufactured in one of several designs. The series bimorphs depicted in Figures 2.3.1.1—2A and 2.3.1.1—2B have no electrode between top and bottom plates. An applied electric field crosses the double thickness of both layers and hence has only half the value of the electric field present in the parallel design depicted by Figure 2.3.1.1—2C and 2.3.1.1—2D, which have intermediate electrodes. Consequently, the designs A and B are referred to as series bimorphs because the voltage source must first establish a field across the thickness of one layer, then the thickness of the other in series. The designs C and D are referred to as parallel because the voltage source simultaneously establishes an electric field across both layers referenced to the central electrode. The electrical connections shown in 2.3.1.1—2D have the advantage of allowing external electrodes to be kept at zero volts, allowing safer operation. [46] Figure 2.3.1.1—2E depicts a unimorph, characterized by an electrically inactive layer. It is understood that some mechanical support is provided in every instance, although no support is shown in the Figures 2.3.1.1—2. Often benders are mounted as cantilevers to obtain maximum displacement at their tips, in which case the end mount would both support and block rotation of the embedded end of the actuator.

Polarization is normal to the surface in all cases shown, directed as indicated. In cases A, B, C, and D (bimorphs), at least one layer experiences an applied electric field opposite the direction of poling. At high field, de-poling could occur. Since electric field strength is inversely proportional to distance between voltage levels, the parallel bimorph can be driven at half the voltage as series bimorphs and produce the same displacement, or

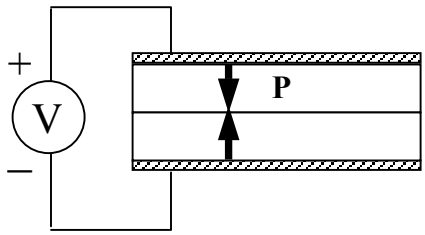

Figure 2.3.1.1—2A. Inward series bimorph

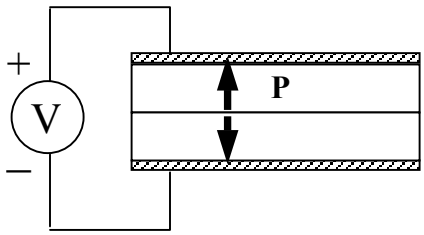

Figure 2.3.1.1—2B. Outward series bimorph

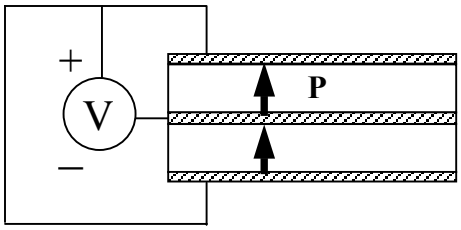

Figure 2.3.1.1—2C. Parallel bimorph

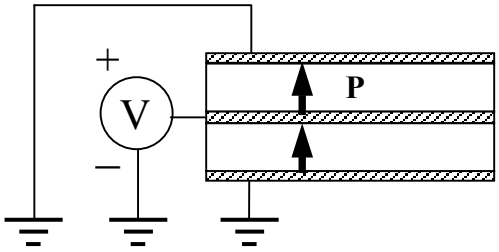

Figure 2.3.1.1—2D. Parallel bimorph

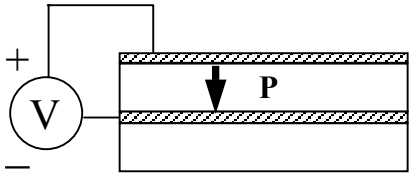

Figure 2.3.1.1—2E. Unimorph

be driven at the same voltage as series bimorphs and produce twice the displacement. However, dielectric capacitance of the parallel bimorph is four times that of the series bimorph (capacitance, $C = (\varepsilon\ \varepsilon_0\ A) / t$: electrode area, A, is doubled and dielectric thickness, t, is halved); thus, power consumption, $P = C\ V^2$, is identical in both series bimorphs driven at voltage V and parallel bimorphs driven at voltage ½V. [47]

For many years, the premier application of bimorph devices was for stereo phonograph cartridges in addition to microphone and headphone cartridges, for which they

are still used. [44] Bimorph and unimorph resonators are common in fire alarms and other such devices. New applications include video tracking control [12], microelectro-mechanical systems (MEMS) components [48, 49], helicopter flap control and aerodynamic and machine vibration control applications [40].

Design refinements enabling specialized applications are discussed in [12, 40]. These include a tapered bimorph (both as a triangular "plan view" and / or taper of plate thickness) to increase response frequency or to more efficiently utilize the material in bending. A configuration involving upper and lower parallel bimorphs with flexible spring tip connection allows the actuator tip to move up and down without transmitting the end rotation that accompanies beam curvature to the tip element. Other novel configurations include an S-shaped complex bimorph, ring bimorph, and shim extensions—embedded in a restraining mount—formed as U-section hinges to allow less hindered deflection. Carbon fiber-reinforced polymeric shim layers with anisotropic elasticity have been shown to boost displacement by a factor of 1.5, presumably in comparison with metal shim. [12]

A useful feature in many bimorphs and unimophs is the electrical isolation of a small portion of surface electrode from the bulk of the electroded surface which receives a driving signal for mechanical actuation. The isolated electrode can serve as a sensing element, since induced strain (converse piezoelectric effect) will produce an electrical response (surface charge) from the direct piezoelectric effect accompanying induced mechanical strain. Charge variation can be detected as current by control circuitry to create a feedback loop. [12, 51]

A useful modification of the flat bimorph was developed by Moskalik and Brei. [52] C-blocks, as they call their device, are benders with a semi-circular cross-section. They are fabricated from semi-cylindrical piezoelectric polyvinylidene fluoride (PVDF) polymer sheets bonded to electrically inactive substrates of the same shape, where the curvature is not maintained by internal stress. The procedure and figures provided in [53] suggest that epoxy adhesive between two PVDF sheets is itself the substrate, with the curved shape created by allowing the epoxy to cure while the layered assembly is wrapped around a cylindrical mold. The two piezoelectric layers allow the finished actuator to bend

in or out (smaller or larger radius of curvature) depending on polarity of applied voltage. Maximum free deflection along the bisecting plane of the semi-cylindrical shapes was about 0.9 mm, while blocking force was slightly larger than 3.5 mN.

As the name implies, C-blocks were also designed with the intent of combining building block units into series and / or parallel arrays to vary aggregate stiffness and displacement. A two-block series (contiguous substrate) is shown in Figure 2.2.1.1—3. A motivation for this innovation was to develop an actuator which had intermediate stiffness, force, and deflection in comparison with piezoelectric stacks and compliant, flat bimorphs.

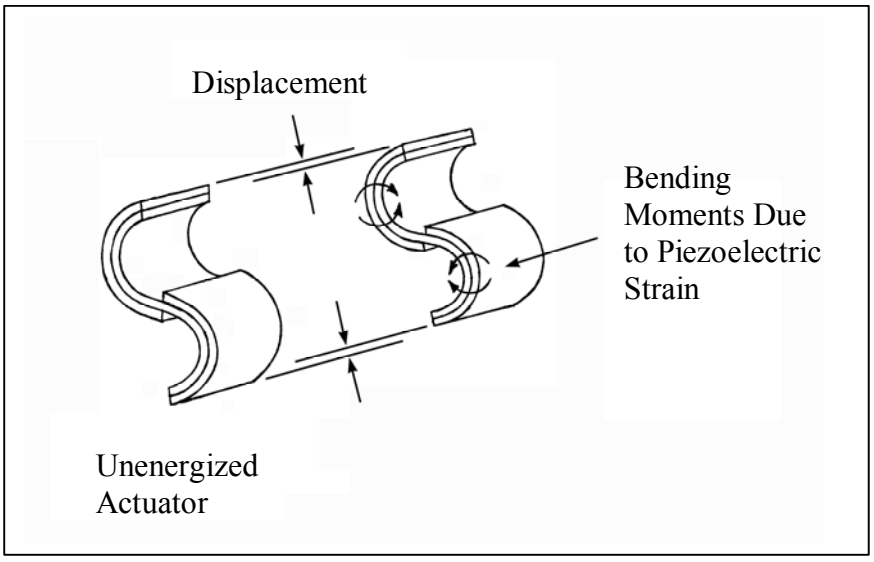

Figure 2.3.1.1—3. Schematic depiction of two-block series of C-Blocks (Design variant: single piezoceramic layer and substrate)

In [52], additional work was reported involving C-blocks with one piezoceramic layer bonded to the outer surface (the larger of the radii about cylindrical axis) of a substrate layer. This configuration allows the actuators to be energized with an applied voltage that causes in-plane expansion, placing the ceramic layer in compression, protecting it from tensile failure. Consequently, the energized actuator would deflect by

developing a smaller radius of curvature. Using strain energy analysis, thickness and other layer properties were chosen to cause the neutral plane of bending (for a beam with unstressed curvature) to fall between layers. The curved shape allowed an 8% higher work output than would be available from a flat bender. [54] Maximum free deflection along the bisecting plane of the semi-cylindrical shapes was about 50 μm, while blocking force was about 2 N. [52] An investigation into producing co-extruded, co-fired actuators with a range of cross-sectional shapes, including the corrugated C-block shape, at small scale (features as small as 5 μm), was reported in [55].

Another useful modification of the conventional bimorph is the diskbender (circular bimorph), which maintains the advantage of flatness when vertical space is limited, but which utilizes the geometrical effect of a circular shape on deflection and stiffness. When energized, a diskbender deforms into a shallow dome shape, where the height of the dome apex relative to its perimeter represents usable deflection. A dome shape has greater inherent stiffness than a bent strip, based on having curvature in more than one direction. Circular actuators can exert larger forces than strip bimorphs at the expense of somewhat diminished displacement.

A notable example of a refined technique for diskbender fabrication was described in [46]. Colla and coauthors state that a motivation for their innovation was to develop an actuator with intermediate stiffness, force, and deflection in comparison with piezoelectric stacks and compliant, flat bimorphs (a reason also given by the C-block developers). The conventional method for diskbender fabrication requires that thin piezoelectric disks be cut from cylindrical stock, lapped, then electroded and / or bonded with conductive adhesive. The refined method utilizes the same techniques used to manufacture multi-layer cantilever bimorphs, thereby reducing cost. Essentially, hard PZT (high Curie temperature) layers were electroded with sputtered gold, co-fired to produce a platinum central electrode of effectively zero thickness. Two prototypes were fabricated, one having 50 mm diameter, 0.9 mm thickness, weighing 13.5 g, the other having 36 mm diameter, 0.6 mm thickness, weighing 4.7 g. The devices were operated at 200 V and 150 V, respectively. A central

hole was drilled through the larger actuator, permitting access to the central electrode layer.

Their intended application was vibration suppression in tables supporting small, precision instruments such as microscopes or interferometers. Since the actuators were not capable of directly supporting a table and instruments, the envisioned system called for static weight to be supported by sufficiently stiff springs of some kind, with the actuators mechanically coupled in parallel. The actuators would then respond only to cancel incoming vibrations.

Results based on finite element modeling of a circular bimorph with a central electrode thickness from zero to 0.4 mm indicated that free displacement decreases linearly while blocking force increases linearly with increasing central electrode thickness. Both factors taken together indicate that increasing the thickness of a central shim increases actuator stiffness. The model also indicated that an ideal mount for the diskbender would have very high stiffness in the vertical (or axial) direction but offer minimal resistance to radial components of flexure at the perimeter. The actuator model assumed a radius of 50 mm, thickness of 0.9 mm, and predicted 206 μm free displacement, 18 N blocking force. The prototype of the same dimensions yielded 275 μm free displacement, 31 N blocking force. The authors think the difference is probably due to nonlinearity of the piezoelectric strain coefficient at high electric field strength, which evidently was not incorporated into the model.

2.3.1.2 Pre-Stressed, Asymmetric Devices

In 1994, Haertling reported having developed a new type of unimorph with internal stress bias or pre-stress, known by the acronym RAINBOW^{TM} (Reduced And Internally Biased Oxide Wafer). [56-60] The internal stress state of RAINBOWs and other types of pre-stressed actuators give them a permanent curvature which introduces asymmetry into their deflection characteristics. The stress bias is superimposed on internal stress due to induced piezoelectric strain or load induced strain, so that unlike bimorph actuators,

flexure in one direction is not equivalent to flexure in the other. Haertling and others have investigated the performance of RAINBOWs [51, 60-64], which produce flexural strains on the order of 1%, and have claimed among other things that the stress bias leads to enhanced performance, in part due to altering the strain capability of the piezoceramic in a favorable way. [65, 66] (Flexural strain is defined as the flexural displacement divided by the length of the ceramic element.)

The RAINBOW transducer / actuator is fabricated by reducing one side of a PLZT (lead lanthanum zirconate titanate) disk at high temperature, thereby transforming a surface layer from ceramic to a nearly metallic composition. Upon cooling, the disk deforms to a characteristic, shallow dome shape due to a difference in coefficients of expansion between the reduced layer and the bulk of the ceramic. The circular actuator is finished by poling perpendicular to the piezoceramic / metallic interface.

The CERAMBOW [67] and Crescent [68, 69] actuators are made by methods similar to RAINBOW fabrication, although the chemical reduction aspect is unique to RAINBOWs. Metal and piezoceramic thin plates are bonded at elevated temperature using either epoxy or solder. A stress-biased, curved shape results upon cooling, which can be poled for use as a unimorph actuator.

A final pre-stressed unimorph to be discussed is the THUNDER^{TM} actuator, developed at the NASA Langley Research Center also in the mid 1990s. [70-72] Fabrication involves bonding a PZT thin plate to a metal substrate under hydrostatic pressure at elevated temperature using polyimide adhesive film. Upon cooling, the laminate develops internal stress and consequent curvature due to differences in coefficients of expansion between the metal layer and ceramic layer. Circular bonded layers develop a shallow dome shape, while rectangular strip components develop a shallow arc, although the precise shapes actually involve double curvature and depend on area to thickness ratio for circular actuators and on length to width ratio for rectangular actuators. As discussed by Hyer and Jilani, more than one equilibrium shape might be stable at room temperature. [73] Actuator fabrication is finished by poling the ceramic perpendicular to the ceramic-metal interface.

THUNDER development might have involved a conscious attempt to improve on the RAINBOW design. The U.S. patent [74] granted to Helbaum *et al* (1997) for THUNDER actuator design and manufacture stated that goals of the invention had been to create a ferroelectric actuator with improved durability, to avoid release of lead vapor during manufacture, and to accomplish these goals in a simple manner. Reduction of PLZT at 975ºC [60, 57] in fabricating a RAINBOW actuator could be expected to release traces of lead vapor, and the finished product has the disadvantage of fragility. No commercially manufactured RAINBOW actuators are currently available, although they were previously produced by Aura Ceramics, Inc. THUNDER actuators, by comparison, are especially robust, able to withstand high electric fields and severe deformation under load or when driven at resonant conditions. They are currently manufactured by Face International Corporation (Norfolk, VA). Studies have shown, however, that RAINBOW actuators yield 10% to 25% higher displacement than THUNDER actuators of comparable design. [8, 69] It should be noted that RAINBOW devices can serve as efficient sensors even if the market demand is not supporting their use as actuators. [51]

2.3.1.3 Characterization of Pre-Stressed, Asymmetric Devices

RAINBOW and THUNDER actuators have been characterized in similar ways. Key metrics of actuator performance are no-load displacement and displacement under increasingly greater loads. Both actuator types are typically poled so that positive voltage applied to the top surface causes downward flexural deflection (so-called indirect actuation, discussed in Section 2.3.2, following). Typically, the curved actuators are placed on a hard, planar surface with concave side downward and convex side upward, and operated with supporting edges as little constrained as possible—that is, the edge is free to rotate or horizontally translate during deflection (simply supported). [75, 70] Alternatively, a beam-shaped THUNDER actuator or cut section of a circular actuator can be mounted as a cantilever with one end embedded in a clamping fixture, preferably with rounded edges where the actuator extends outward from in between clamping faces. [60, 63, 76]

Mossi *et al* mention clamping the four corners of a rectangular THUNDER actuator with modeling clay during testing, presumably to fix its location without strong constraints. [72] Shakeri *et al* depict another soft clamp. [71] Mossi and Bishop show the schematic design of a measurement fixture for testing circular actuators which has tubular Nylon sleeves on posts pressing the actuator edge by spring force at three points. In addition, they present a schematic design for a fixture which clamps THUNDER actuator end tabs in axles. [75] In [71], the point is made that an experimental plan would probably specify affixing a clamp or holding mechanism a certain, short distance from the "active" parts of the actuator (i.e., away from the bonded piezoceramic patch). Clamping across the piezoceramic area will produce different results (and may lead to device failure) than clamping the metal tab or skirt extension. In general, where and how the actuator is held establishes boundary conditions for its movement.

Displacement has been measured by linear differential variable transformer (LVDT, discussed in Chapter 3) or dial indicator [51, 56, 66, 59, 71, 77], or Angstrom Resolver fiber-optic gauge [70, 71, 72, 75], or other non-contact system. Non-contact displacement measurement is particularly desirable during dynamic displacement (cyclic displacement resulting from AC driving signals) because contact systems produce inertial and mass loading. Mossi *et al* describe a low-spring-constant metal or polymer foil bellows apparatus for maintaining constant force during deflection with low inertial loading as well. [71] They also describe a fixture for applying a mass load to an actuator via a stepped shaft and linear bearing assembly, which would seem more practical. The loading shaft can attach to an LVDT core, allowing load control and displacement measurement from an integral mechanism. Typically, a curved, pre-stressed actuator would be loaded in a direction normal to its apex, and displacement measured by the displacement of the apex point. However, Schwartz and Narayanan discuss applying spring loads in the transverse direction of a THUNDER actuator (as a chord subtending an arc) in combination with mass loads in the normal direction to augment its elastic properties. The elastic elements allow the modified actuator to store mechanical energy, resist passive deformation under applied mass loads, and alter its resonant response to AC drive signals. [116]

In addition to frequency response, the electrical properties and coupled electromechanical properties of pre-stressed actuators have also been characterized. Haertling has studied temperature-dependent dielectric properties of PLZT RAINBOW wafers. [60] Elissalde *et al* conducted extensive electromechanical characterization, involving temperature-dependent dielectric measurements using a multi-frequency inductance-capacitance-resistance (LCR) meter. Electromechanical resonant behavior was measured using an impedance / gain phase analyzer, and transverse and longitudinal sound velocities were measured with an acoustic microscope. [62] Among other things, these researchers were able to determine that a reduction in stiffness of the reduced layer of a RAINBOW actuator—relative to the unreduced ceramic—occurs due to an interconnected pore structure and the compliance of metallic lead.

Li and Haertling characterized RAINBOW actuators as sensors by measuring charge induced by point loads and uniform pressure load applied to one side of an actuator sealed in a fixture using an electrometer. [51] While measuring displacement by optical fiber sensor, Chandran *et al*, investigated the response of RAINBOW cantilevers to sinusoidal signals of varying amplitude and frequency. Both the voltage drop across a series resistor (for determining current drawn by actuator) and output signal from the fiber-optic gauge were measured using a lock-in amplifier. The frequency spectrum of impedance at low electric field strength was measured using an impedance / gain phase analyzer. [63]

Strain-displacement loops are an important characterization tool for all piezoelectric actuators, but also reveal an important feature in the behavior of stress-biased unimorphs. It was mentioned previously that stress bias introduces asymmetry into their operation—that is, flexural displacement that flattens the pre-stress induced curvature is not the same as displacement that augments the curvature. The strain-displacement loop reveals the electromechanical imprint of stress bias.

Large signal strain-displacement loops, known as butterfly loops because of their shape, indicate ferroelectric switching at sufficiently large electric fields. Since stress directly affects polarization, both load stress and stress bias should affect the shape of the

butterfly loop. In [8], Wise presents asymmetric butterfly loops for both RAINBOW and THUNDER actuators, but does not comment on the asymmetry.

The idealized shape of a butterfly loop is shown in Figure 2.3.1.3—1, along with an asymmetric butterfly loop drawn according to actual strain-electric field data for a THUNDER model 8R actuator. The arrows in boxes indicate the polarization state for each lobe of the butterfly loop. Typically, a Thunder-type pre-stressed unimorph would be poled "downward" (to be explained in Section 2.3.2) and either operated under positive electric

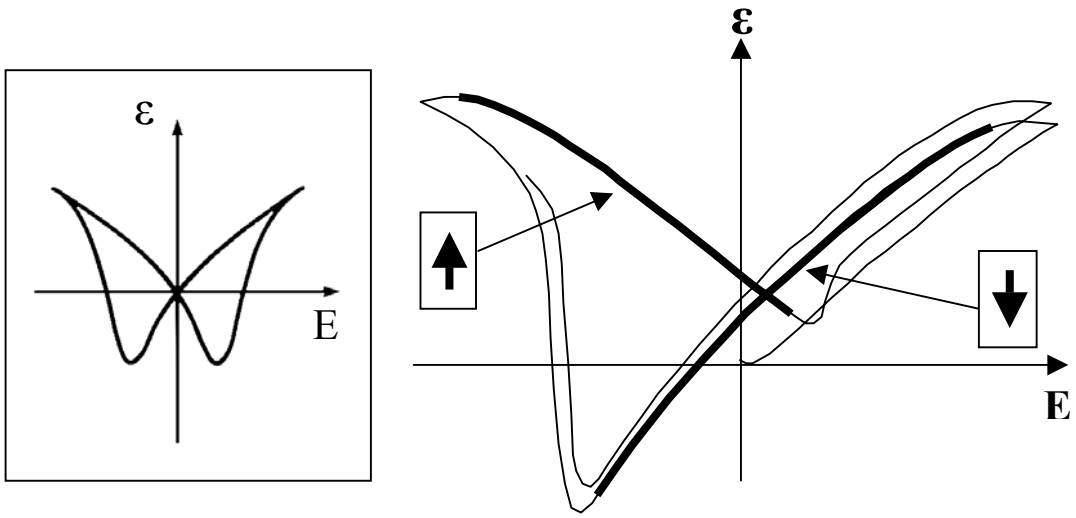

Figure 2.3.1.3—1. Assymmetric strain-field loop showing different performance depending on polarization state and applied field direction, compared with an idealized strain-field loop at left

field (established when positive voltage is applied to the top of the actuator) or under bi-directional field range shifted by positive bias. This causes the actuator to flatten, reducing pre-stress induced curvature and shifting the stress state in the upper part of the actuator in a compressive direction.

If an applied negative field reaches the magnitude marked by the lower tip of the left lobe of the butterfly loop (the negative coercive field strength), then net polarization

switches “upward.” After switching, a negative voltage applied to the top of the actuator (establishing a negative electric field) causes the actuator to flatten, reducing pre-stress induced curvature and shifting the stress state in the upper part of the actuator in a compressive direction. (Before switching, this was the effect of a positive voltage applied to the top of the actuator.)

However, given the mechanical stress bias set during actuator fabrication, there is a difference in its performance in a state of downward polarization versus upward polarization, as indicated by the thickened line segments on each lobe of the butterfly loop. If a downward-poled actuator were driven between ends of the positively-sloped, thickened line segment, it would clearly cover a greater interval of flexural strain than if an upward-poled actuator were driven between ends of the negatively-sloped, thickened line. Not only can the downward-poled actuator be driven across a larger interval of applied field without switching, but the slope of its thickened line segment is steeper, indicating a greater increment of flexural strain per increment of applied field. The slope of the butterfly loop is proportional to the d_{31} piezoelectric strain coefficient of the actuator ceramic, indicating enhanced strain in one direction relative to the other.

2.3.1.4 Adhesive Bonding for Actuators: A Demanding Application

The bond provided by the polyimide adhesive variant known as LaRC-SI (named after NASA Langley Research Center) was a key component in THUNDER actuator design. [79] Epoxy adhesives and solders remain viable candidates for making a pre-stressed unimorph, but thermoplastic polyimides are a class of polymers used in a variety of high performance / high temperature applications. According to the claims given in the patent to Bryant (1998) [80], prior polyimide compositions were soluble only in highly toxic, usually halogenated solvents, which made the use of solvent–recovery systems necessary during processing. Consequently, forming or application techniques typically involved solutions of polyamic acid precursor in “milder” nitrogenous solvents. Subsequent cyclodehydration caused reactive functional groups to form the aromatic ring

structure which gives polyimides their impressive mechanical properties and stability at high temperature. However, polyamic acid intermediates are unstable, susceptible to hydrolysis and release water upon imidization.

Bryant's modification created a fully imidized polymer which could be dissolved in nitrogenous, industrial solvents. The polyimide chains were terminated with mono-functional reactive ends. The inclusion of a lesser amount of unpolymerized polyamic acid solution allowed the precursor polyimide to achieve high molecular weight at high temperature with minimal release of water during forming or application operations or subsequent heat treatment.

A research report on LaRC-SI polyimide [114] provided a comprehensive study of mechanical properties as a function of polymer molecular weight and temperature, in addition to fractography analysis. Figure 2.3.1.4—1 plots the average of five Young's modulus values as a function of temperature for five different molecular weights of the polymeric material: $\overline{M}_w$ = 15880, 21180, 24290, 41100, 51070 g / mol. The extrapolation was based on a parabolic least squares fit to the last three data points on each set. The "errors bars," showing not error but the range of tabulated values at each temperature for specimens having five different molecular weights, indicate that the elastic moduli of this polymer adhesive are not very sensitive to molecular weight.

The uncured LaRC-SI adhesive used in experimental fabrication in the present work, as described in Chapter 3, had a 3% offset, which sets the expected molecular weight of the cured adhesive at $\overline{M}_w$ = 24290 g / mol, according to [114]. Offset is a slight molar deficit of one reactant relative to the other which determines the final molecular weight of the polymerized material. [129]

Based on the plotted values, one can see that heated polymer experiences a rapid loss of mechanical stiffness above about 220º C. Models of the effects of fabrication conditions on final actuator curvature and pre-stress, should therefore assume that the adhesive layer provides negligible resistance to differential contraction above this temperature.

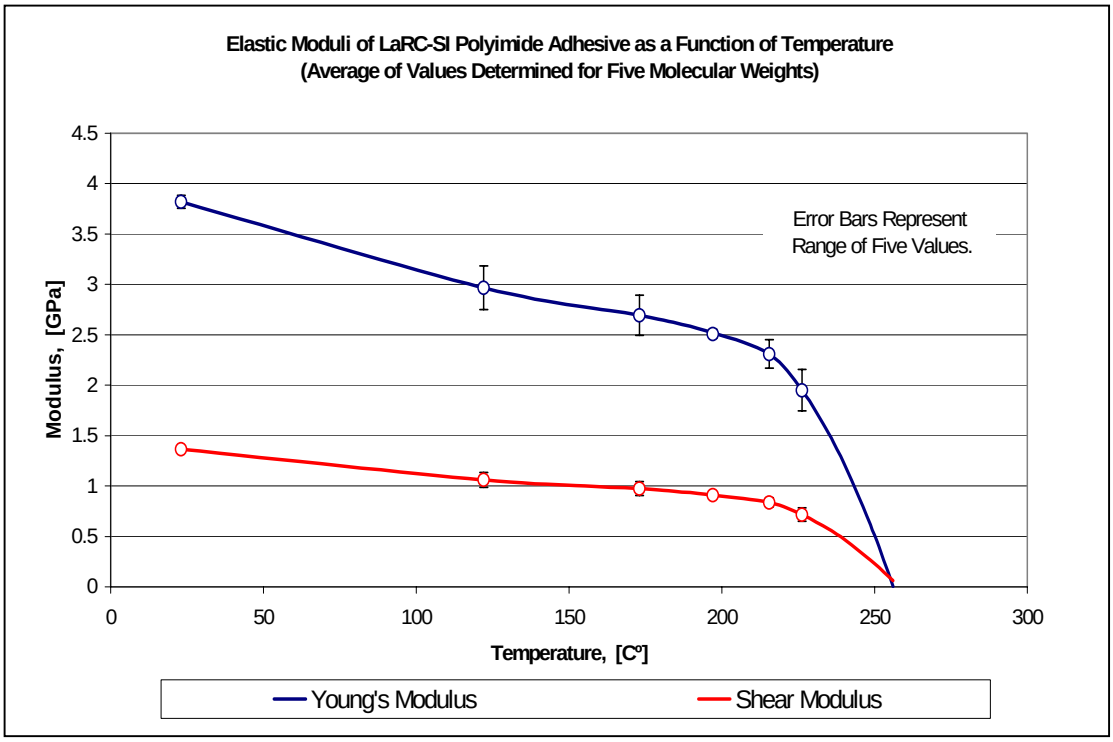

Figure 2.3.1.4—1 (color). Young's modulus and shear modulus of LaRC-SI polyimide as a function of temperature

Investigation in the literature after adhesive bonds between piezoceramic and metal parts in an experimental motor failed repeatedly led to the short paper posted in 1995 at [81] by Friend and Stutts. The authors condensed some of the extensive information provided in [82], and provided recommendations pertinent to bonding piezoceramic to metal. Surface cleaning was of paramount importance. In general, they recommended as many of the following techniques (in order of severity) as needed: solvent cleaning, mechanical cleaning, or chemical treatment. In addition, priming is an option that may be useful.

Solvent cleaning can include wiping, immersion, or spraying, and can be combined with solvent cleaning in an ultrasonic bath followed by solvent rinse. Vapor degreasing or ultrasonic vapor degreasing (where hot solvent vapor condenses on the surface and contaminants are flushed away in the flow of a thin solvent film) enhances solvent power

by the effect of temperature. Ultrasound also adds the scrubbing provided by cavitation of bubbles on the surface.

Mechanical surface preparation can include grit blasting, wire brushing, sanding, and abrasive scrubbing. Chemical treatment can include detergent cleaning or acid or alkaline etching (which removes surface oxide films and produces microscopic surface roughening). Solvent cleaning should be performed before chemical treatment, and priming may be necessary immediately after. For example, stainless steel owes its corrosion resistance to a thin, tightly-bonded, oxidized surface film. If removed by chemical treatment, the film reforms almost immediately upon exposure to air unless sealed from contact. [83]

Priming is the process of applying a dilute solution of adhesive in a compatible solvent to achieve a dried film thickness on the order of 5-15 μm. The film protects the surface from oxidation, improves wetting, and reduces adhesive peeling.

After evaluating metal-adhesive and non-metal-adhesive compatibility charts, Friend and Stutts conclude that epoxy adhesives comprise the only category fully compatible with both stainless steel and ceramic. Adhesive alloys, such as epoxy-polysulfone or epoxy-phenolic (both thermosets) are also candidates.

A phenomenon mentioned by Messler [82] and Sirohi and Chopra [84] is the shear lag effect which should be accounted for by actuator models attempting to model the effect of an adhesive bond of finite thickness. Shear lag effects influence shape after differential contraction or deformation under load, and phase effects with dynamic operation. Essentially, if the adherends (materials bonded by the adhesive) are non-rigid materials or are experiencing strain (e.g., thermal or piezoelectric strain) parallel to the bond layer, the adhesive material deforms in shear, or in differential shear near boundaries. Shear-lag analysis was first examined by Volkerson in 1938, who assumed that adherends deformed only in tension while the adhesive bond deformed only in shear. Readers can consult Volkerson's original work in German or the following references provided by Messler. [85-88]

2.3.2 The Compliance Issue

Free deflection (δ_{MAX}) is an actuator's maximum displacement in the absence of external load or resistance (for a specific driving voltage). However, in the absence of resistance, no force is generated. On the other hand, force generation is always accompanied by reduction in displacement. The maximum force (blocked force, F_{MAX}) an actuator can generate depends not only on its own stiffness, but on the stiffness of the restraint as well. Given perfect contact with an infinitely rigid restraint (load *and* support), maximum force will be generated; displacement will be zero. Blocked force created by a constant load (e.g., supported weight) compresses an actuator by an amount equal to its free deflection. Figure 2.3.2—1 shows the interaction of the schematic actuator force-deflection curve with the schematic load force-deflection curve.

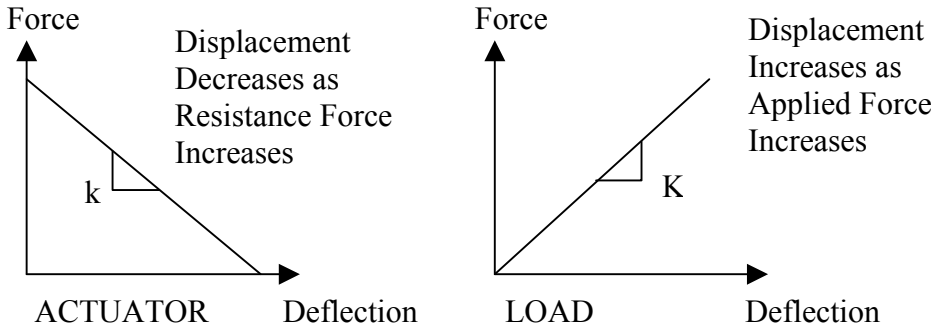

Figure 2.3.2—1. Force-deflection components of actuator-load system

Figure 2.3.2—2 depicts a generalized force-deflection performance curve for a piezoelectric actuator by superimposing the two force-deflection curves in Figure 2.3.2—1.

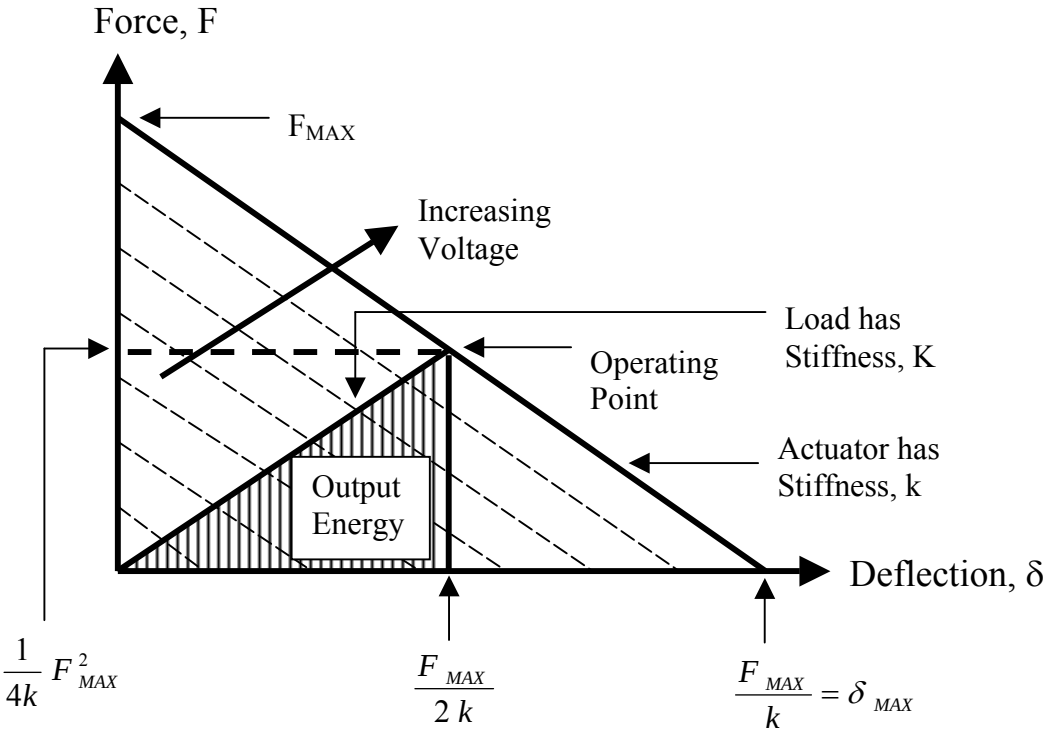

Figure 2.3.2—2. Superimposed force-deflection components of actuator-load system. (Specific values derive from optimization discussed in text.)

Maximum work is transferred from actuator to load when deflection is constrained to one-half the free deflection, allowing one-half the blocked force to develop. It can be shown, as follows, that this occurs when the stiffness of the external load matches that of the actuator. The set of rectangular areas (work) corresponding to twice the triangular area labeled "energy" in Figure 2.3.2—2 for all possible operating points is given by (2.3.2—1).

(2.3.2—1) $\text{Area} = (- k \delta + F_{MAX})(\delta) = - k \delta^2 + F_{MAX} \delta$

The maximum such area is found by setting the derivative of (2.3.2—1) equal to zero.

(2.3.2—2) $d\text{Area} / d\delta = - 2k\delta + F_{MAX} = 0 \quad \text{if} \quad \delta = F_{MAX} / 2k$

Then, determine $F = -k\,\delta^2 + F_{MAX}\,\delta$ for $\delta = F_{MAX} / 2k$:

(2.3.2—3) $$F = -k\left(\frac{F_{MAX}^2}{4k^2}\right) + F_{MAX}\left(\frac{F_{MAX}}{2k}\right) = \left(\frac{1}{2k} - \frac{1}{4k}\right)F_{MAX}^2 = \frac{1}{4k}F_{MAX}^2$$

Equations (2.3.2—2) and (2.3.2—3) give the intersection of the load stiffness line with the actuator stiffness line as the diagonal of the rectangular area associated with the operating point of maximum energy output. Since the load stiffness line crosses the origin of the axes, its slope, K, is given by (2.3.2—4).

(2.3.2—4) $$\frac{\frac{1}{4k}F_{MAX}^2}{\frac{1}{2k}F_{MAX}} = \frac{1}{2}F_{MAX} = K$$

This slope can be related to the actuator stiffness, k, by determining the negative slope of the line segment between the operating point and the x-intercept, δ_{MAX} , where $F = -k\,\delta^2 + F_{MAX}\,\delta = 0$ for $\delta = \delta_{MAX} = F_{MAX} / k$. The slope is found in (2.3.2—5).

(2.3.2—5) $$\frac{\frac{1}{4k}F_{MAX}^2 - 0}{\frac{1}{2k}F_{MAX} - \frac{1}{k}F_{MAX}} = -\frac{1}{2}F_{MAX} = k \;\rightarrow\; \therefore |k| = |K|$$

Although this particular demonstration was not found in the literature, the general appearance of Figure 2.3.2—2 was given in [52] and the well-known conclusion that maximum work output is achieved when actuator and load stiffnesses are equal has been discussed in [89].

In [89], Giurgiutiu *et al* present a comprehensive analysis of stiffness issues, accounting not only for the intrinsic stiffness of an induced strain actuator (ISA) and that

of its load, but also for the stiffness of the actuator support, and the implications of stiffness when displacement amplification is provided. Their analysis examined both displacement and energy considerations. They define a stiffness ratio, r , which is the ratio of the stiffness provided by external resistance (k_e) to the internal stiffness of the actuator itself (k_i), and show that the ratio of output displacement (u_e) to free displacement (u_{ISA}) is given by $1 / (1+ r)$. Furthermore, an analogous output energy coefficient, $E_e' = r / (1+ r)^2$, gives the ratio of output energy (E_e) to a reference energy (E_{ref}), which is the energy of the ISA producing free deflection against only its internal resistance. In the stiffness-matched condition, the energy output of an ISA represents only 25% of the reference energy. Unfortunately, that is the maximum. Figure 2.3.2—3, after a plot in [89], illustrates the form of the displacement and energy functions of the stiffness ratio for this fundamental case. Note that for a load slightly less stiff that the actuator, say one-half to one-fifth, the displacement improves markedly, while energy transfer is not greatly diminished.

By extending their model to include the elastic energy stored in the structure supporting the actuator, Giurgiutiu *et al* also derive the result that the stiffness of the support must ideally be as much as 10 times the actuator stiffness for the ratios shown in Figure 2.3.2—3 to approach the maximum values achievable when stiffness of actuator and load are well matched and support is unyielding. Furthermore, when a displacement amplifying device is used with the actuator, the maximum in the ratio of output to reference energy will occur for stiffness ratios less than one (less than equal stiffness). As amplifier gain increases, the bell-shaped energy transfer curve is shifted to lower and lower orders of magnitude. In other words, a displacement amplifier increases the mechanical advantage of load resistance force. Hence, a proportionately less stiff load is required.

One implication of these results concerns piezoceramic actuators incorporating pre-load or compressive bias (to prevent potentially damaging tensile stress from developing during dynamic operation). The stiffness of the pre-load spring should be limited to one-tenth the stiffness of the actuator. [115]

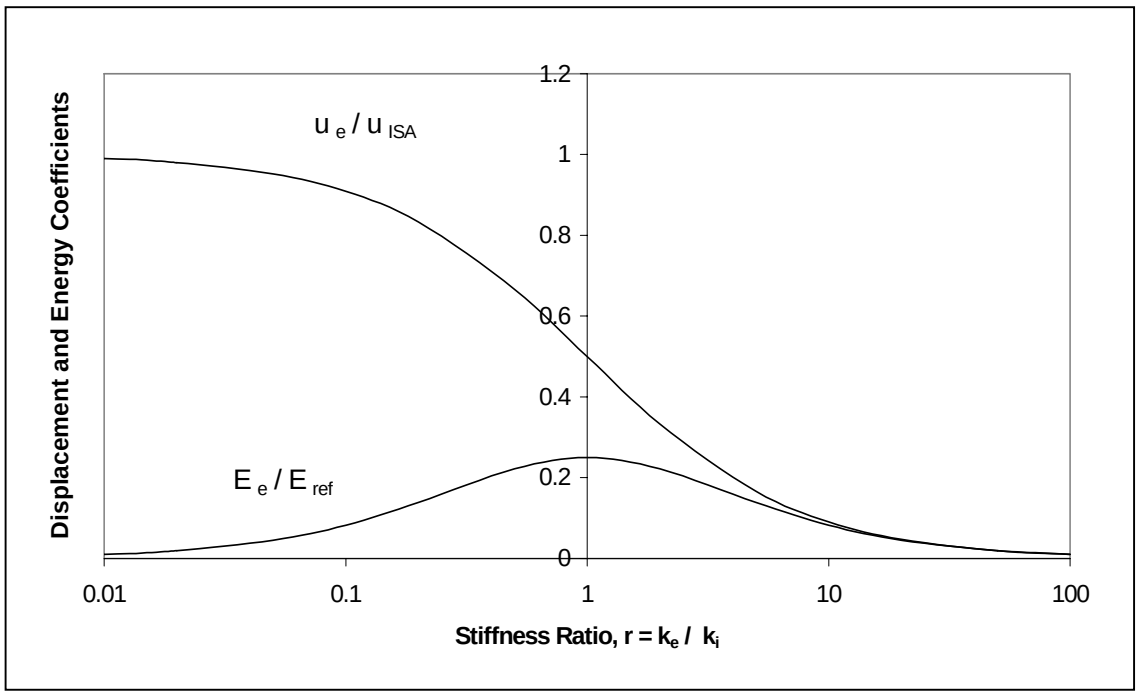

Figure 2.3.2—3. Variation in ratios of output displacement to free displacement and output energy to reference energy with changing stiffness ratio (after [52])

Another important aspect of stiffness matching arises with dynamic operation at higher frequencies where output energy travels as vibration coupled into a medium. By analogy with electrical impedance, which includes DC resistance as a special case, acoustic or mechanical impedance matching is necessary for efficient transfer of energy from actuator to load. Uchino [12] explains that without acoustic impedance-matching layers fabricated onto the piezoceramic element of a sonar transducer, most of the acoustic energy generated would be reflected at the interface with water. Although frequency introduces its own effects, the fact still stands that energy or work output depends on both force and displacement. Without stiffness, water cannot provide adequate resistance to allow an actuator to exert force. The converse situation would occur if the piezoelectric polymer PVDF were coupled directly to a load through a steel plate. (Force might be high, but the steel coupling would experience only miniscule displacements because the actuator

stiffness is so much less than that of the load.) The formula (2.3.2—6), adapted from Uchino indicates that the product of material density, ρ, and elastic stiffness, c , must be adjusted to match mechanical impedance.

(2.3.2—6) $\sqrt{\rho_{ISA}\, c_{ISA}} = \sqrt{\rho_{LOAD}\, c_{LOAD}}$, where ISA refers to "induced strain actuator," following the terminology of Giurgiutiu. [89]

All the preceding could apply equally well to stack actuators as to flexural actuators, but the following discussion focuses on flexural actuators, which are inherently compliant. All actuators have finite compliance, but a pre-stressed unimorph is exceptionally compliant even among flexural actuators. As in the art of *Judo*, compliance is not necessarily a liability, but it has significant implications in designing for the use of such actuators. One consequence is that pre-stressed unimorphs are almost without exception used in an indirect mode of operation, that is, in a situation where the induced strain of the piezoceramic acts in parallel with the load to create a larger strain than is appropriate for load deflection alone. The additional elastic energy stored in a PSU substrate is recovered as work performed against the load when induced (piezoelectric) strain is released. This means that the non-piezoelectric material in a composite structure actuator plays as significant a role in actuator performance as the piezoelectric material. An illustration of the difference between direct and indirect actuation is given in Figure 2.3.2—4A and Figure 2.3.2—4B in cartoon form where dimensions, of course, are not to scale.

In both figures, the piezoceramic top layer in each schematic cross-section is poled "downward." That is, the net polarization is oriented such that when positive voltage is applied to the top surface, resulting in electric field directed in parallel with the polarization vector (Figure —4A), the piezoelectric material expands in the d_{33} direction (thickness direction) and contracts in the d_{31} direction (in-plane or transverse direction). With the positive electric field vector direction defined as oriented from positive to negative, the positive polarization vector direction (the aggregate effect of oriented dipoles

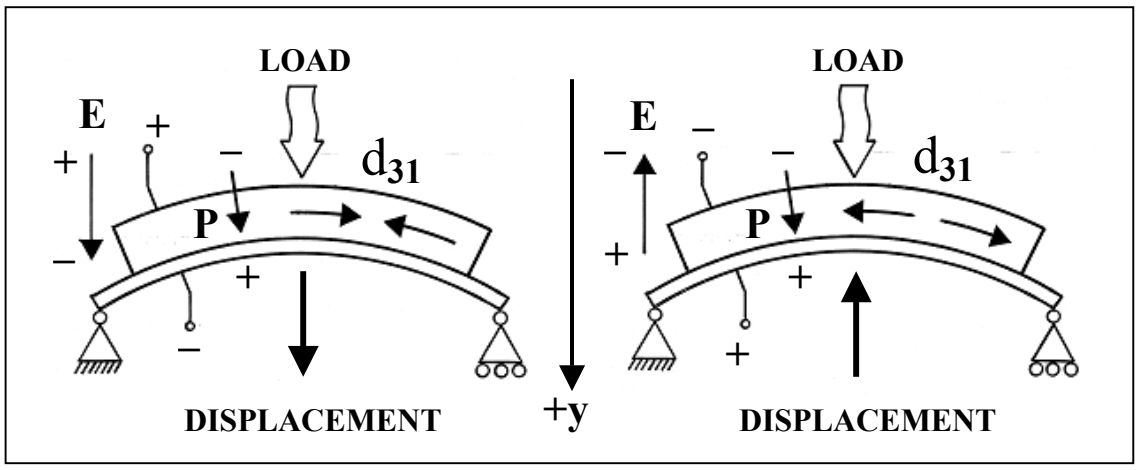

Figure 2.3.2—4A. Indirect actuation

Figure 2.3.2—4B. Direct actuation

in a dielectric material) is oriented from negative to positive. This reflects the fact that if material dipoles are free to move (e.g., as in water), they align themselves such that their aggregate electric field opposes the externally applied electric field. [90] However, since the piezoceramic element of the actuator would typically be ferroelectric, polarization remains downwardly oriented in Figure 2.3.2—4B unless the oppositely oriented electric field vector were to exceed the coercive field strength for the particular ceramic.

Upon contraction or expansion of the piezoceramic, opposition stresses develop in both ceramic layer and the bottom substrate layer (typically metal), which create an internal moment in the composite beam, causing transverse deflection just as would a moment-inducing external load. The direct and indirect modes of operation depend on whether the piezoelectric strain-induced deflection opposes load deflection or aids it.

Indirect actuation involves the following sequence of events. First, apply a load to the top of the actuator, which causes the actuator deflect downward to an equilibrium level. Apply electric field in the polarization direction and the actuator displaces further downward. Remove applied field and the actuator returns to the equilibrium level. Note that it is actually the mechanical restitution (elastic rebound) that performs work against the load, not piezoelectric strain.

Direct actuation proceeds as follows. Again, apply a load to the top of the actuator and the actuator deflects downward to an equilibrium level. Negative voltage applied to the top surface results in electric field directed opposite the polarization direction, and the actuator displaces upward against the load. Remove the applied field and the actuator returns to the equilibrium level. In this case, elastic strain in the actuator is not directly involved in actuation.

It would also be possible to create direct actuation by flipping the actuator over so that ceramic side faced downward, applying a load to the substrate side, and an electric field in the polarization direction, causing upward (previously downward) deflection against the load. This inverted configuration would be unfavorable both from a structural and a materials point of view. A "pre-sagged" beam would have about the same resistance to a transverse force as a buckled column. In fact, as curvature increases, support reactions (for a simply supported beam) develop an axial component, facilitating collapse. Furthermore, downward beam deflection places material below the neutral surface in tension, and high tensile stress facilitates brittle failure in ceramics.

The direct actuation configuration depicted in Figure 2.3.2—4B is feasible by comparison, but has disadvantages. By driving the piezoceramic against its polarization, there is a risk of de-poling it. There is also a higher failure potential because increasing curvature tends to shift internal stress in the positive (tensile) direction in material above the neutral surface, especially in dynamic operation.

Indirect actuation, however, tends to shift stress within the ceramic in the compressive direction, which reduces failure potential. Indirect actuation is especially advantageous during dynamic displacement where peak displacements are more likely to generate high transient stresses. The indirect actuator is a "smart spring" which has a stiffness modulated by piezoelectric strain. Displacement shifts to a level appropriate to its current stiffness. From the viewpoint of the load, an energized actuator appears more compliant, but that is only because the actuator is able to augment internal strain beyond that induced by the load, so that a smaller load is able to accomplish a larger deflection than the inactive structure would experience.

An actuator structure—especially the metal substrate— storing more elastic strain energy is capable of performing more work in the rebound phase of indirect actuation. Total energy stored increases as the square of strain ($U = \frac{1}{2} \sigma \varepsilon = \frac{1}{2} E \varepsilon^2$). There is an energetic advantage to augmenting load-induced deflection with piezoelectric strain. An additional deflection added to an existing deflection stores a larger strain energy in the already strained material than if the same amount of deflection were induced in unstrained material. This is why an archer's bow is bent considerably when strung. When bent further on drawing the arrow, much more energy is available to propel the arrow than if the bow were simply a curved piece of wood. A stress-strain diagram makes the principle obvious, as shown in Figure 2.3.2—5. [91]

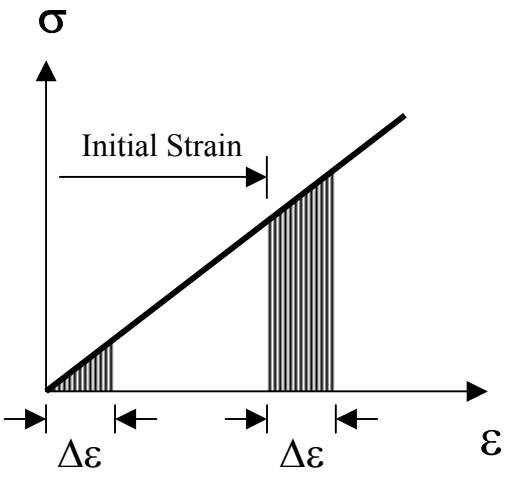

Figure 2.3.2—5. Energy (represented by shaded areas) associated with increments of strain (after [91])

The concept of blocked force becomes more subtle when a compliant actuator is used in the indirect mode. Note that downward deflection was defined as positive (+ y) in Figure 2.3.2—2. Figure 2.3.2—6 shows a schematic plot of actuator position (i.e., of the center point or apex of the pre-stressed shape) as a function of load (force), with initial, unloaded position taken as zero. Thus, the slopes of the position lines represent

compliance, the inverse of stiffness. The line marked "V = 0" represents downward deflection of the unenergized actuator, the elastic behavior of a passive, composite beam. The line marked "$V = V_{MAX}$" represents the additional downward deflection from electrically-induced strain at the maximum rated voltage for the actuator.

As shown in Figure 2.3.2—6, the two lines tend to converge under increasing load. The zero voltage line indicates passive deflection under increasing load, while the maximum voltage line indicates that the loaded actuator becomes proportionately less

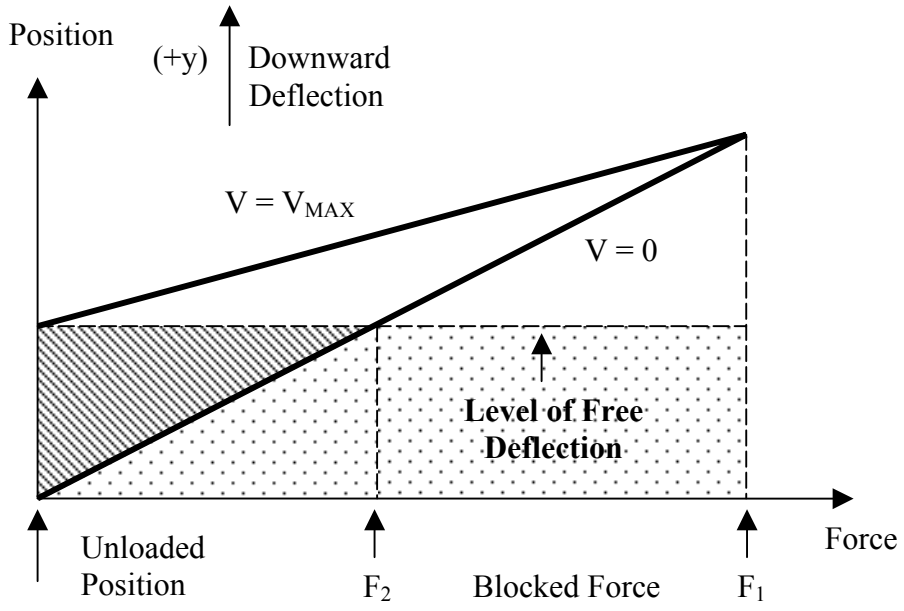

Figure 2.3.2—6 Alternative definition of blocked force for characterizing performance of compliant pre-stressed unimorphs

capable of deflecting farther downward with the addition of piezoelectric strain. Consequently, elastic rebound becomes more limited and ultimately deflection in the indirect mode has been blocked by the force labeled F_1. By applying a load of F_1 to the unenergized actuator, considerable deflection results. On applying electric field in the polarization direction, nothing happens: the actuator displaces neither downward nor

subsequently upward after the field is removed. (One might hear a click as the stress wave due to applied electric field propagates through the piezoceramic.)

The motivation for examining the situation in greater depth arises from the fact that F_1 tends to be much larger than a load associated with any useful deflection. It does not adequately characterize the actuator for design purposes. Since a PSU actuator is typically mounted in a fixture and tested against the weight of a mass, the following idea considers the level of free deflection as a benchmark level on a scale of gravitational potential. (The idea was originally conceived by Brian Dessent, graduate student in Electrical Engineering, NC State University.) In other words, elastic recovery from this level is the work the actuator does upon itself, although the work is not actually performed until the electric field is turned off.

In quasi-static operation, a PSU really cannot move a load higher than the unenergized level of load deflection. A certain acceleration probably results from the speed with which piezoceramics respond to applied electric field, but mostly this results in "ringing" around the equilibrium level. In dynamic operation, the exchange between kinetic energy and elastic strain energy can generate deflections exceeding the envelope, particularly at resonance, but then the overshoot and undershoot are approximately equivalent. (In other words, dynamic operation creates a means of storing energy.)

Once any load is applied to the actuator, additional unenergized deflection imposes a deflection penalty that makes it not only more difficult to return to the original unloaded, unenergized position, but ultimately even to rebound as high as the level of electric field-induced free deflection, the downward limit of the free-displacement interval. In motor applications, it becomes very likely that, beyond this point, the actuator does little useful work on the load. It creates internal movement, but not forward movement, primarily due to the additional penalty imposed by clamp or latch losses.

The triangular area in Figure 2.3.2—5 (shaded with parallel lines) indicates the region where a PSU actuator can recover to a level above the energized lower level of the free-displacement interval. The maximum load at the right tip of the triangle can easily be

determined from experimental data and is designated as F_2, an alternative blocked force rating for a PSU actuator.

2.3.3 Bending Actuator Models

Various aspects of bending actuator performance have been modeled by researchers whose interactions can be traced in the literature. Traditional bimorphs and unimorphs were initially modeled. [92-95, 43, 45] Surface or embedded actuators for smart structures were also modeled. [117-120] Pre-stressed RAINBOW and THUNDER actuators were considered later. [47, 96] Some impressive mathematical models have been developed for predicting the shape, deformation, and even material characteristics of pre-stressed unimorphs. [121-125]

Finite element models have been especially plentiful, especially for characterization of dynamic performance. A number of researchers have determined by various means the optimal ratio of piezoelectric layer thickness to non-piezoelectric layer thickness in various types of bending actuators. [8, 76, 94, 97]

Reported work most closely allied to this project involves analytical models based on solid mechanics predicting bending actuator outputs such as displacement, based on likely inputs, such as applied electric field, force or moment loads. A definitive foundation was developed by Smits and collaborators [43, 45], who acknowledged the previous contribution of Steel *et al* [92]. Further developments were introduced by Wang and Cross and collaborators [96, 98, 99]. Wang and Cross later collaborated with Schwartz to use bimorph models to better explain the performance of RAINBOW actuators and indicate the effect of pre-stress. [76]

In [45], Smits and co-authors derived an expression for the total energy in a bimorph beam by combining piezoelectric constituent relations with beam theory equations, notably, $E I y'' = M$. They derived all necessary quantities for substitution in equations for the energy density of the upper and lower layers. Integration over the volumes of each element gave a total energy function, one for free displacement, one for

applied internal force and applied external load. In the manner of derivations from the phenomenological theory of polarized materials, partial derivatives of the energy function relative to one property in a conjugate pair yielded expressions for the other property in terms of known parameters, e.g., maximum deflection as the conjugate of applied force. Ultimately a summation of results was expressed in matrix form of various input and output parameters, in which a general relation combined input and output quantities through linear superposition. [43]

In an article building upon these results, Smits and Cooney examine the effectiveness with which a bimorph actuator performs work against different types of constant loads, including constant force, constant moment, and distributed constant force. They use the linear superposition matrix from the article by Smits, Dalke and Cooney [45] (although a symposium proceedings paper by Smits and Dalke was actually cited) that describes an anti-parallel or outward series bimorph as a starting point. [93]

In [94], Wang and Cross cited the one-dimensional strain models of Steele and Smits, and subsequent results from Japanese manufacturers and researchers, including analytical expressions assuming two-dimensional deformation that describe characteristics of piezoelectric vibrators. However, they contended that three characteristic parameters of primary concern in practical actuator design—resonant frequency, tip deflection, and generative force—had not been systematically derived and presented in the literature.

Using the method of transformed sections (transformed *to* the modulus of the piezocermic), the authors derive the equivalent flexural rigidity, $E_P I_C$ (subscript p for piezoceramic, subscript c for composite structure) of a bimorph and a unimorph. Equivalent flexural rigidity is then used to develop expressions for natural bending resonance frequency and fundamental bending resonance.

A factor which involved ratios of Young's moduli (called A), layer thicknesses (called B), and densities of piezoceramic relative to substrate (called C), was devised to illustrate the effect of metal / ceramic thickness ratio and Young's modulus of metal shim on bending resonance. Four illustrative substrate materials were considered: steel, brass, aluminum, and acrylic polymer. Depending on the specific property ratios, a high modulus

or a low density substrate material can lead to high resonance frequency. A similar approach was taken to derive bending resonance, tip deflection, blocking force and equivalent moment for a unimorph actuator.

Some key features of their derivations are summarized as follows. Since curvature is defined as the second derivative of ν, the vertical displacement of the midplane, extensional strain, S, is given by (2.3.3—1)

(2.3.3—1) $$S = \frac{(R + y)\theta - R\theta}{R\theta} = \frac{y}{R} = \kappa\, y$$

Extensional strain can be converted to axial stress and a term for stress due to piezoelectric strain included for a piezoceramic layer, as shown in (2.3.3—2).

(2.3.3—2) $$T = E_P\,(\kappa\, y) \pm E_P\, d_{31}\, E_3$$

A differential force would be given as dF = T dA = T w dA, where w is the width of the actuator. A differential moment would be given as dM = y dF = y T dA = y T w dy. The sum of integrated contributions to extensional force due to curvature and bending moment due to curvature were combined into two expressions giving total extensional force and bending moment, each in terms of extensional strain and curvature. The expressions were solved for curvature. Deflection was then obtained as $\nu(x) = \frac{1}{2}\,\kappa\, x^2$.

The thickness ratio of ceramic to metal corresponding to maximum tip deflection in a unimorph actuator was determined and is given in (2.3.3—3).

(2.3.3—3) $$B_{MAX} = \frac{t_M}{t_P} = \sqrt{\frac{1}{A}} = \sqrt{\frac{E_P}{E_M}}$$, where E is Young's modulus of a layer of

thickness, t, and subscript m refers to (metal) substrate, subscript p refers to piezoceramic. Considering the elastic moduli of commercial PZT ceramic and type 302 stainless steel,

typical materials used in experiments for the current work, as 66 GPa and 200 GPa, respectively, equation (2.3.3—3) indicates that a unimorph actuator would have maximum tip deflection for layer thicknesses in the ratio of 0.574. That is, substrate thickness would be about half that of the piezoceramic thickness or 36.5% of the total thickness—a little more than one-third.

In [99], Wang and Cross revisited the constitutive relations derived by Smits and Choi [43] to formulate expressions for electromechanical coupling in bimorph and unimorph actuators. Their intent was to determine design parameters for maximum mechanical output energy by incorporating the constitutive relations into expressions for fraction of mechanical work available from bimorphs and unimorphs under specific loading conditions.

During vibration, a piezoelectric actuator stores part of electrical input energy in the electric field between electrodes, since it is a capacitor. The other part is stored in the actuator structure as mechanical energy (strain or kinetic energy). The square of the electromechanical coupling factor, k, of a material or actuator is defined as the ratio of stored mechanical energy to input electrical energy, given piezoelectric motor function. (If the material or transducer were serving as a piezoelectric generator, the words, "mechanical" and "electrical," would have to be switched.)

There are cases where the actuator stores mechanical energy, but little work is actually done by the actuator on a load—that is, either during mostly free deflection involving little force or during mostly blocked conditions involving little displacement. It can be more useful to consider the energy transmission coefficient, λ , defined as the ratio of output (rather than stored) mechanical energy to input electrical energy to evaluate the actual work done by piezoelectric devices. [12] Wang and Cross show, among other things, that maximum output mechanical energy can be obtained when the external load is half the maximum generative force for the actuator.

In 1999, Wang and Cross derived a model for the tip deflection, blocking force, and equivalent moment of a cantilever sliced from a RAINBOW actuator. [96] Since this actuator involved stress-bias from differential thermal contraction (DTC) during

fabrication, the effect of DTC was necessarily incorporated into the model. In a model of this sort, the behavior of piezoelectric strain and thermal strain are identical. Anywhere a thermal strain term is included, a piezoelectric strain term can also be included. Mechanics of a bimetallic strip were applicable, which include the conditions that all internal forces and moments must be in equilibrium. (Let quantities related to the piezoelectric layer be denoted by subscript "P" and quantities related to the reduced layer, which would correspond to a unimorph substrate, be denoted by "R".) Thus, $F_P = F_R = F$, and ½ F(t_P + t_R) = $M_P + M_R$, where t signifies thickness of a layer. Using the relation that M = EI / R, where E is Young's modulus, I is the area moment of inertia, and R is the radius of curvature, one gets the expression in (2.3.3—4), which can be solved for force.

(2.3.3—4) $$\frac{F\left(t_P + t_R\right)}{2} = \frac{E_P I_P}{R} + \frac{E_R I_R}{R} \quad \rightarrow \quad F = \frac{1}{R}\,\frac{2\left(E_P I_P + E_R I_R\right)}{H}$$, where H is the

sum of the layer thicknesses, t_P and t_R. Since (2.3.3—4) has two unknowns, another equation relating F and R is needed. This can be obtained if a perfect bond between the layers is assumed. At the interface, then, the total strain in the piezoelectric layer equals the total strain in the reduced layer in the same direction, yielding (2.3.3—5), where w is the width of the beam actuator.

(2.3.3—5) $$\alpha_P \Delta T + d_{31} E_3 - \frac{F}{E_P t_P w} - \frac{t_P}{2R} = \alpha_R \Delta T + \frac{F}{E_R t_R w} + \frac{t_R}{2R}$$

Equation (2.3.3—5) can be rearranged as shown in (2.3.3—6)

(2.3.3—6) $$\left(\alpha_P - \alpha_R\right)\Delta T + d_{31} E_3 = F\left(\frac{1}{E_P t_P w} + \frac{1}{E_R t_R w}\right) + \frac{t_P + t_R}{2R}$$

Substituting for F, from (2.3.3—4), gives (2.3.3—7).

(2.3.3—7) $$(\alpha_P - \alpha_R)\Delta T + d_{31} E_3 = \frac{2}{R}\frac{(E_P I_P + E_R I_R)}{H}\left(\frac{1}{E_P t_P w} + \frac{1}{E_R t_R w}\right) + \frac{H}{2R}$$

Note that $H = t_P + t_R$, has been substituted into the last term in (2.3.3—7). This expression can be solved for inverse radius, yielding (2.3.3—8).

(2.3.3—8) $$\frac{1}{R} = \frac{(\alpha_P - \alpha_R)\Delta T + d_{31} E_3}{\frac{H}{2} + \frac{2(E_P I_P + E_R I_R)}{H}\left(\frac{1}{E_P t_P\ w} + \frac{1}{E_R t_P w}\right)}$$

On the other hand, Wang and Cross obtain the following equation, (2.3.3—9), after the preliminaries in (2.3.3—4) and (2.3.3—5).

(2.3.3—9) $$\frac{t_P + t_R}{2R} = (\alpha_P - \alpha_R)\Delta T + d_{31} E_3 - \frac{2}{R}\left(\frac{E_P + E_R}{t_P + t_R}\right)\left(\frac{1}{E_P I_P w} + \frac{1}{E_R I_R w}\right)$$

Rearranging terms gives (2.3.3—10), where H is substituted for $t_P + t_R$, and then equation (2.3.3—11).

(2.3.3—10) $$(\alpha_P - \alpha_R)\Delta T + d_{31} E_3 = \frac{2}{R}\left(\frac{E_P + E_R}{H}\right)\left(\frac{1}{E_P I_P w} + \frac{1}{E_R I_R w}\right) + \frac{H}{2R} \quad \rightarrow$$

(2.3.3—11) $$\frac{1}{R} = \frac{(\alpha_P - \alpha_R)\Delta T + d_{31} E_3}{\frac{H}{2} + \frac{2(E_P + E_R)}{H}\left(\frac{1}{E_P I_P w} + \frac{1}{E_R I_R w}\right)}$$

After several attempts to reconcile (2.3.3—8) and (2.3.3—11) by algebraic manipulation, it appears that they are not algebraically equivalent. It would seem that equation (2.3.3—8) was correctly derived nonetheless, as shown here. The reason for pointing this out is that Section 5.2 in this thesis contains a model based on the same

assumptions and derivational process. It was important to compare with models in the literature to establish how my model might differ from other reported models. If there were differences, it was important to make comparisons between models.

In [76], Schwartz, Cross, and Wang attempted to fit performance data for an unloaded RAINBOW cantilever to an existing [99] non-stress-biased unimorph model. (Although RAINBOW actuators are typically fabricated as a circular shape, Haertling [60] and others [63] mention that they can be cut into smaller elements of different shapes.) The reduced layer of a RAINBOW device corresponds to the substrate of a conventional unimorph actuator. The hypothesis, already advanced in a number of articles, was that the extrinsic (domain switching) contribution to electromechanical response was altered by internal stress bias, resulting in enhanced d_{31} coefficients.

It was noted that calculated tip deflection described the shape, but not the magnitude, of measured deflection for a RAINBOW cantilever actuator. According to a comparison in [96] (the article containing the derivation which was re-worked, above), measured values exceeded predicted values and the discrepancy increased with increasing electric field strength. Rather than supposing that standard d_{31} values applied to the strain characteristics of the piezoelectric component of a RAINBOW actuator and that the unimorph model failed to describe the mechanics, Schwartz, Cross, and Wang proceeded on the assumption that unimorph theory was perfectly valid and that large deflections corresponded to "effective" d_{31} values modified by internal stress. [76] Given deflection data for an unloaded cantilever ($F = 0$), the expression, $\delta = a F + b V$, reduces to $\delta = b V$, which can be rearranged to solve for the b coefficient in terms of measured tip deflection and applied voltage: $b = \delta / V$. From (2.3.3—6), the expression for b can be rearranged to provide effective d_{31} corresponding to the deflection data and actuator dimensions and properties.

For the PZT 5H polycrystalline ceramic used to fabricate the RAINBOW actuators studied, a standard value of –329 pm / V had been reported. The effective d_{31} values resulting from the analysis of Schwartz *et al* varied between approximately –300 pm / V to –600 pm / V, with the variation related to both electric field strength and to thickness of

the reduced layer relative to total device thickness. In general, higher field strength resulted in approximately linear increases, and maximum effective values peaked for a reduced layer thickness about one-third the total thickness.

A body of work with relevance to a discussion of bending actuator models was motivated by a need to design intelligent structures with intrinsic vibration and shape control, especially for applications in outer space. Founding work by Crawley and de Luis involved a two-dimensional analytical treatment of discrete piezoelectric actuator patches symmetrically bonded to the top and bottom surfaces of a beam substructure. [117] This model accounted for an elastic bonding layer of finite thickness.

Crawley and de Luis made the following assumptions. (1) The adhesive layer experiences only shear stress, which is constant through its thickness, but varying along its length. (2) The piezoelectric layer is subject only to axial stress, constant through its thickness, but varying along the length of each actuator segment. (3) The beam itself develops the linear stress profile consistent with Bernoulli-Euler beam theory when subjected only to external forces causing pure bending and actuation strain—applied with equal magnitude and opposite sign to the top and bottom surfaces of the beam substructure.

The authors concluded that both actuation strain and added passive stiffness of the actuator segments bonded to the beam surface contribute to shear stress transmitted through the adhesive layer. Shear stress in the adhesive layer varies from zero at the center of an actuator segment to maximum magnitude at its ends (edges). As adhesive thickness decreases, shear stress concentrates toward the ends. Increasing the stiffness of actuator material induces greater strain in the underlying beam, given constant adhesive layer properties and actuation voltage.

An investigation of dynamic behavior was conducted by adapting the derived expression for shear stress in the adhesive layer to serve as a forcing function. This approach allowed the added stiffness of the piezoelectric segments, but not their added mass, to influence beam vibration. The authors concluded that their model accurately predicted tip displacement of a beam cantilever driven by a sinusoidal signal at the beam's fundamental resonance frequency.

Im and Atluri [118] extended the static model of Crawley and de Luis to allow unsymmetric actuation strain and externally applied axial and shear forces in addition to the externally applied bending moment allowed by the earlier model. Im and Atluri concluded that axial and shear forces externally applied to a beam by surface-bonded actuators significantly affects the shear stress transmitted through adhesive bond layers, again with stress effects concentrated toward the ends of the actuators.

Crawley and Anderson reported work in 1990 continuing the theme of highly-distributed induced strain actuators for intelligent structures having intrinsic vibration and shape control capabilities. The authors established that an analytical model in which actuator segments experienced the same Bernoulli-Euler strain profile as the underlying deflected beam was more consistent with both a finite element model and experimental results than was an analytical model in which the actuator segments experienced only uniform contraction or expansion parallel to the beam surface. They also investigated the extent to which the nonlinear and hysteretic strain behavior at high electric field strengths rendered linear model predictions increasingly approximate.

A shear lag parameter, Γ , was introduced, which characterized the effective stiffness of an adhesive bond, based on an expression involving the ratio of bond layer shear modulus to actuator Young's modulus, as well as the ratio of bond layer thickness to actuator thickness, a stiffness parameter for the ratio of beam substructure stiffness to actuator stiffness, and a geometric factor. Larger values of Γ indicate that predicted strains approach those expected for a perfect bond (which has infinitesimal thickness and experiences negligible shear strain). Shorter actuator segments and less stiff bonding layers resulted in greater departure from perfect bond behavior. The authors concluded that for a Γ value greater than 20 and actuator length-to-thickness ratio greater than 100, the shear effects of a bond of finite thickness and stiffness could be ignored and a Bernoulli-Euler model would suffice to predict behavior.

Robbins and Reddy [120] developed finite element formulations to apply the generalized laminate plate theory previously proposed by Reddy to the problem of a piezoelectrically actuated beam. Four variant models were compared, based on applying

them to the problem of predicting modal amplitudes and vibration modes for an unsymmetric laminate of piezoceramic bonded to an aluminum beam. The comparison allowed the authors to determine the level of complexity needed in such a modeling procedure to obtain consistent results. (Their article also provides an excellent summary of the articles by Crawley and de Luis and by Crawley and Anderson.)

Although Crawley and de Luis investigated dynamic response extrapolated from a model derived under static conditions, Pan *et al* formulated a model with explicit dynamic coupling between surface actuators and beam substructure that included a free stress boundary condition applied at actuator edges. The scenario for their model was a simply supported elastic beam (considerably longer than attached actuators) with a pair of piezoelectric actuators glued to upper and lower beam surfaces at equal distances from one end of the beam. Perfect bonding was assumed. [122]

A system of fourth order homogenous differential equations was obtained, which was solved numerically. Results from this model, in the form of beam surface strain at any location along the beam, agreed well with the static coupling-based model at locations far from the actuators. At locations close to the actuators, results of dynamic analysis demonstrated that previous static analyses were unable to accurately model beam surface strain near actuator edges, especially at driving frequencies other than the natural beam resonance. Reasonably good agreement with experimental data was shown, but the authors acknowledged that additional experimental verification was needed.

An elegant paper by Yang and Lee, with emphasis on vibration control, [123] also modeled a beam with surface-bonded actuator patches. A stepped beam model was developed to include the stiffness and inertia of the piezoelectric material and bonding layer. Shear deformation and rotary inertia of the beam were also considered. The authors determine that by judicious selection of relative dimensions, the first natural frequency of the composite structure can be shifted by as much as 5% relative to predictions from a non-stepped beam model—depending on the placement of piezoelectric actuators. Numerous conclusions were drawn and verified by experiments.

Kim and Jones [124] developed a quasi-static control strategy using embedded actuators to modify the vibration spectrum of a composite beam-actuator model. Non-linear equations of motion were incorporated, including in-plane loads developed by actuation of the piezoelectric layers. Particular emphasis was given to electric field strengths necessary to create buckling deflections. This model also showed that natural frequencies of a simply-supported composite beam can be modified by actuation of the piezoelectric layers. The model was evaluated using material parameters for PZT (lead zirconate titanate) ceramic, PVDF (polyvinylidene fluoride) polymer and a PVDF copolymer.

Agrawal and Treanor [125] developed another model to determine optimal placement of piezoelectric actuators for shape control of composite beams. Their motivation was to find a means of maintaining the considerable accuracy in surface contour needed for satellite antenna reflectors during service. In their paper, the objective was to minimize error between target and actual shapes of the structure, given inputs consisting of actuator location and excitation voltage. This resulted in an optimization program involving fifth order polynomials representing optimal actuator placement and second order polynomials representing optimal actuator input voltages, which was solved using embedded Nader and Mead simplex algorithms to separately optimize each variable. A convergent solution was obtained for various initial conditions, given small-signal voltage input. However, discrepancies between predicted behavior and experimental results arose from nonlinearities and hysteretic effects created by large-signal drive conditions.

This section will conclude with a short discussion of models which have been developed for predicting the fabricated shape, deflection, and even material characteristics of pre-stressed unimorphs. Such problems represent exercises in applied mathematics based on materials science.

Previous work by M.W. Hyer to explain the behavior of unsymmetric cross-ply laminates was adapted by Hyer and Jilani to the problem of predicting the room-temperature shapes of rectangular constructions, THUNDER actuators in particular, which

are fabricated at elevated temperature, then cooled and operated at room temperature. [121] The problem is predicated on the shape transition of a laminate which is flat at an elevated curing temperature, deforming into a cylindrical shape upon cooling. The model allows curvature in more than one direction.

The curved shaped that develops for any combination of temperature or electric field is that which minimizes the total potential energy of the laminate. Exact solutions to the problem were considered unlikely, so the authors used displacement fields according to the Rayleigh-Ritz approach and variational methods to determine shapes associated with minimum potential energy. Geometric nonlinearities were included in the model, allowing prediction of multiple shapes.

The authors' results predicted, among other things, that laminates can change from one stable shape to another by simple snap-through action, or may achieve only one stable shape, depending on relationship to a critical sidelength-to-thickness ratio. The snap-through action can be verified by manipulation of a large, rectangular THUNDER actuator (e.g., Face Corporation model 6R), but Hyer and Jilani discuss how the same transition could also be achieved by applied electric field.

A number of papers related to piezoelectric actuators and materials has been published by various members of the mathematics department at North Carolina State University in collaboration with scholars at other universities and at the NASA Langley Research Center. A representative paper reports the development of a partial differential equation model for the displacements of a THUNDER actuator in response to generalized load and boundary conditions. [126]

The effects of applied electric field and load were applied to a core model of actuator shape resulting from the fabrication process, which began by balancing forces and moments to obtain static differential equations. Linear piezoelectric and stress-strain relations were assumed. Mechanical contributions from the adhesive bond layer were typically omitted in the model formulation, but the authors referred to techniques for including them. Although the authors essentially derived an analytical model with defined boundary and external load conditions, numerical techniques were used to obtain solutions.

Predicted curvature resulting from fabrication and response to load and boundary conditions were shown to be in agreement with experimental data.

Another paper by Smith and Ounaies, a subset of the authors of the previous paper, develops a domain wall model to address hysteresis and nonlinear constitutive relations in piezoelectric material when driven above the small-signal level. [127] Based on a model for hysteresis in general ferroelectric materials, an ordinary differential equation model based on five parameters was obtained. An iterative algorithm and an algorithm based on the method of least squares were given for determining parameter values in conjunction with measured or approximate values related to the polarization response of piezoelectric materials to electric field. Predicted polarization-electric field loops were shown to be in agreement with experimentally determined loops for three common types of PZT (lead zirconate titanate) ceramics.

2.3.4 Enhanced Performance Due to Pre-Stress

In explaining the performance in RAINBOW actuators, the hypothesis that enhanced extrinsic electromechanical response results from internal stress bias has been advanced by a few researchers who have gathered a body of evidence in support. In 1994, not long after inventing RAINBOWs, Haertling devised a finite element model of curvature developed during fabrication and electric field induced displacement. Upon finding that measured induced displacement substantially exceeded predictions by the model, he speculated on probable materials explanations for the phenomenon. [58]

A key development of the idea that internal stress profile interacts with domain structure to augment induced strain capability and actuator displacement was presented in [66]. Evidence was advanced by constructing a two-dimensional axisymmetric finite element model (3 x 20 rectangular mesh) and by conducting x-ray diffraction (XRD) across the top surface of actuators with different thickness ratios (ratio of reduced layer thickness to total thickness) both in the presence and absence of applied electric field. (Hereafter, let R represent thickness ratio, which was experimentally determined by

examining actuator cross-sections under a microscope.) Maximum displacements were found to correspond with actuators having R values near 0.3. The following observations can be made based on output of the FEA model, then the XRD experiment, as described or illustrated in schematic form.

Variation of stress across thickness for **R = 1/3**

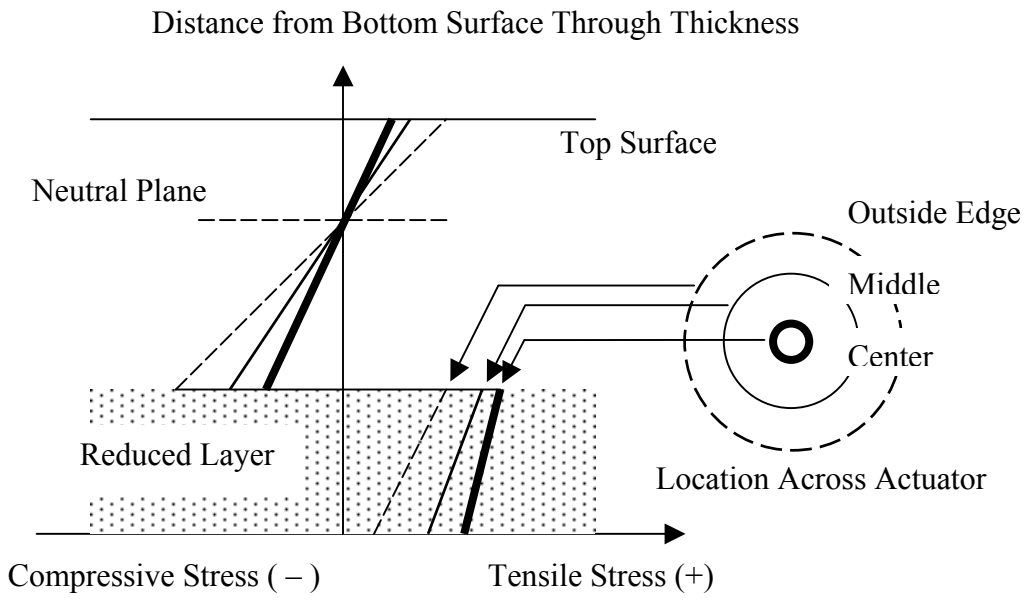

Figure 2.3.4—1. Variation of stress across thickness for **R = 1/3**

Variation in stress from center to edge as a function of thickness ratio, R:

For small thickness ratio (R = 0.3), the whole surface is in tension and the magnitude of the tensile stress increases toward the center. For large thickness ratio (0.8), the surface is in a compressive state. With intermediate value (R=0.6), the RAINBOW surface is in compression at the center but in tension at the edge.

Domain orientation determined by XRD at center of sample on unreduced ceramic:

Under the conditions of the model, polarization domain structure will have tetragonal order. An "a-domain," associated with (200) XRD peak, can be symbolized by a rectangle lying horizontally on its long side. A "c-domain," associated with (002) XRD peak, can be symbolized by a rectangle standing vertically on its short side. The intensities of the (200) and (002) XRD peaks are contributed by a-domains and c-domains, respectively.

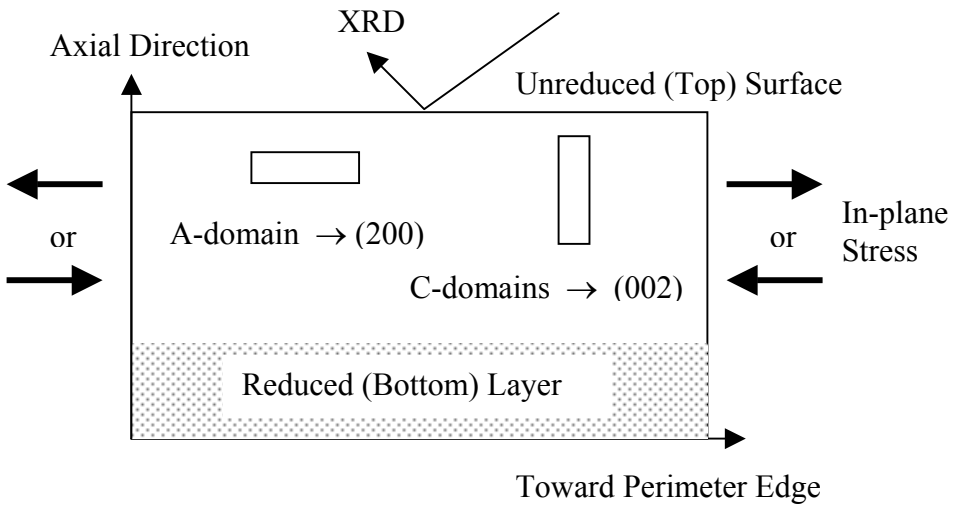

Figure 2.3.4—2. Schematic portion of RAINBOW actuator cross-section showing a- or c-domain orientation relative to surfaces

Theoretically, the ratio of the (200) to (002) peak intensities is equal to two for a virgin, stress-free sample, because of random domain orientations. In other words, there are two a-axes (a_1 and a_2) for each c-axis. Intensity ratio greater than two indicates tension; a ratio less than two indicates compression. In other words, the most energetically favored (+ / –) pair of polarization directions is one which allows the long side of a tetragonal unit cell to align with tensile stress or become unaligned with compressive stress.

Intensity ratio as a function of thickness ratio:

Thickness ratios below approximately R = 0.45 correlate with intensity ratio greater than two, implying tensile stress on the surface. Above R = 0.45, I(200) / I(002) < 2 implies compressive surface stress. Agrees with FEA results.

Stress distribution across unreduced surface determined by XRD as a function of normalized radius for thickness ratios 0.36, 0.45, 0.64:

The entire surface was in tension for the lower thickness ratio, entirely in compression for the large thickness ratio, and in tension at the edge but nearly unstressed for the middle ratio. Consistent with FEA results.

Axial displacement under 16 kV/cm (40.6 V/mil) unipolar electric field as a function of thickness ratio:

Although FEA suggested maximum displacement corresponding to a thickness ratio of 0.6, actual displacement maxima were skewed strongly toward thickness ratios around 0.3. In addition, the displacement maxima (near R=0.3) were two to three times greater than the maximum displacement predicted by FEA (near R = 0.6). Modeled displacement was based on virgin dome curvature. Poling could reduce pre-stress and dome height, and a shallower dome would have a lower stiffness. FEA models based on lower stiffness would predict higher displacements. The difference would not be sufficient to account for amount by which the experimental displacements exceeded predicted displacements.

The case for stress-enhanced domain reorientation:

Various I(200) / I(002) ratios were measured by XRD while applying an electric field (cycled at low frequency between 0 and 16 kV/cm across 0.432 mm thickness) to five

RAINBOW samples having different thickness ratios. Measurement of intensity ratio vs. applied field for a ceramic sample without stress bias was included for comparison. The non-stress-biased sample was a flat unimorph of the same dimensions as the RAINBOW actuators, made by adhesive bonding an unreduced ceramic disk to a completely reduced wafer.

Hysteretic loops arising for stress-biased samples specified as having surfaces in tension exhibited larger shifts in determined intensity ratio, resulting in steeper inclination of their loops than loops corresponding to a sample without tensile surface stress or to the non-stressed unimorph of identical dimensions. (However, the scale on the vertical axis was marked in a way—I(200) / I(002) between 0.25 and 0.6—that did not seem to follow from previous discussion.)

Nonetheless, for RAINBOWs having planar tensile stress in their unreduced layers, the results can be attributed to reorientation of 90º domains initially parallel to the surface into alignment with the direction of an applied field perpendicular to the surface. At reduced electric field strength, 90º domains return to alignment with the tensile stress field, thereby making an additional extrinsic contribution to the piezoelectric effect that would not be obtained without internal stress.

Considering the stress profile through the entire cross-section, however, tensile surface stress decreases linearly, transforming to compressive stress within the unreduced ceramic. In the compressive region the piezoelectric effect is expected to be lower than in stress-free ceramic, due to the constraints of compressive stress on domain wall motion.

By assuming that d_{31} at the internal neutral plane of the ceramic corresponded to a standard, unstressed value and scaling this value using the fraction of a-domains transforming to c-domains as indicated by XRD, Li *et al* calculated d_{31} values for surface ceramic (in the range of about –300 to –500 pC / N) and used a cross-section of interpolated values as inputs to the FEA model to calculate displacement. Measured displacements were uniformly larger than those produced by the model.

The modeling experiment also showed, however, that both the presence of tensile stress in the unreduced layer and the non-uniform distribution of internal stress through its

thickness are necessary to achieve high displacement. The model had also previously shown that the effect of a d_{31} gradient is even more pronounced for a domed actuator, perhaps because it helps to reduce the dome curvature.

The domains observed by the XRD experiment were on the surface of a sample, including only those alignments for which the c-axis was either parallel or perpendicular to the sample surface. Effects of the internal stress may be different on surface domains than on bulk domains. However, it should not be assumed that bulk domains with orientation similarly parallel or perpendicular to the surface behave in the same way as the average of all domains with various orientations. Note also that internal stress should also influence the intrinsic d_{31} contribution.

2.4 Motors Using Flexural Actuators

The quest for a solid state motor driven by piezoelectric actuators has engaged the efforts and ingenuity of many researchers. The subset of motors designed to use bimorph and unimorph actuators is smaller, and the nested subset of reported designs for motors using pre-stressed unimorphs (PSUs, e.g., THUNDER actuators) is also comparatively small.

Although the spectrum of motor designs using unimorphs is limited, applications as actuators, or single-stroke devices, have been extensive. A motor, however, is seen as a device which operates in a cycle to output continuous motion or other work. An essential feature of such a system is the incorporation of a device to convert the oscillatory motion characteristic of actuator dynamic displacement to one-way output motion. Devising such a "mechanical diode" that does not limit device performance can be a substantial challenge in motor design.

Bryant *et al* , working at NASA Langley Research Center, fabricated a set of "high displacement actuators," (HDAs) using the polyimide film adhesive used by PAR Technologies, PZT-5A plates and aluminum and stainless steel substrates. [100] The

actuators were characterized and incorporated into a linear motor prototype for a satellite instrumentation drive system.

The motor does not appear to cycle because no mention of stepping or latches to block or allow motion between steps was made. It consists of four pairs of actuators, where each pair is mounted in a "clamshell configuration," depicted in Figure 2.4—1. However, the series of connected actuators was guided by a rod, which would have allowed the system to operate as a motor if front and rear clamps had been added.

The researchers decided that maximum extension could be obtained only if the actuators were compliantly mounted, meaning that actuator ends were fastened by plastic hinges with metal pins, and outward-facing centers of pairs of actuators were clamped with plastic clamps contacting each actuator by rubber pads. The motor was initially tested with an applied voltage range from –130 to +550 V. Displacement provided by four pairs of actuators exceeded design requirements, allowing the configuration to be operated under reduced voltage. Total displacement was not indicated , but characterization of individual actuators gave approximately 1.0 to 1.2 mm for actuators with aluminum substrates, and approximately one millimeter for an actuator with stainless steel substrate, under an applied voltage of about 500 V. (Displacements at higher voltages were also plotted.)

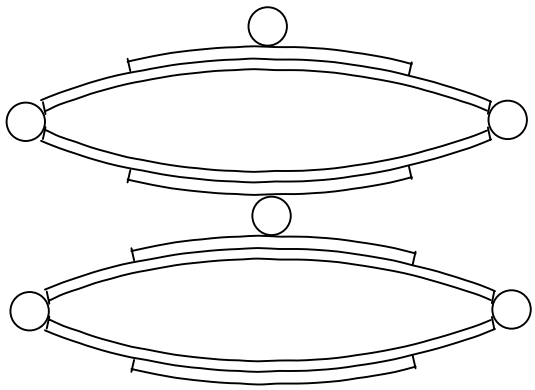

Figure 2.4—1. Two pairs of pre-stressed unimorphs in "clamshell configuration"

A motor does not necessarily need to displace itself on a track, or turn a shaft. THUNDER actuators (or similar actuators not falling under the trademarked name) have been used in thrust-producing propulsive devices. In a report on work prior to the linear device mentioned above, Bryant *et al* discuss a synthetic jet application. [101] Another jet propulsion application for special-purpose underwater vehicles was investigated by Niezrecki *et al*. The authors' motivations were to avoid the potential problems of seals, shafts and bearings in deep sea exploration vehicles by creating a sealed, displacive chamber, and to study the possibility of using THUNDER actuators with resonant (capacitive-inductive) drive electronics for propelling autonomous underwater vehicles (AUVs) at high efficiency to minimize power consumption. [102]

A pair of actuators in a clamshell configuration was immersed in water, with a linear variable differential transformer (LVDT) displacement transducer used to measure displacement of the actuators. The connected ends of the actuators were bonded with flexible adhesive to provide unrestrained end conditions. The researchers were able to show that a significant amount of water was displaced at a resonant operating frequency, but left the matter of channeling water in a single direction during intake and expulsion portions of the displacement cycle for future work. Channeling the water in a single direction is an important topic, because it has to do with the conversion of oscillatory to one-way motion that is at the heart of designing motors using bending actuators. The measured average and RMS power consumption for the paired actuators was 8 and 12 Watts, respectively. [102]

An example of a genuine multi-step motor design using THUNDER actuators was reported by Hyder *et al*, although no movement was obtained with a prototype. [103] Their concept, called a "linear traveling wave motor," was based on the inchworm motor cycle. They note that the first inchworm motor, and the name "inchworm", were patented in 1975 by Burleigh Instruments, a leader in the field of micropositioning and other applications often involving piezoelectric actuation.

In fact, the inchworm cycle is a fundamental aspect of virtually any linear motor design using extensional or bending actuators. Analogous steps can even be discerned in

some rotary motor designs (e.g., the "walking" motor of Bexell *et al*, discussed below). The inchworm cycle can be illustrated in Figures 2.4—2A through 2.4—2F using the flexural actuator "wave" configuration of the linear traveling wave motor just discussed, configured with three end-linked flexural actuators on each side of some unspecified guide mechanism.

The set of figures is intended to illustrate the inchworm cycle more that the operation of the linear traveling wave motor designed by Hyder, Horner, and Clark, and may not represent exactly what they intended. Readers should consult their article for details of their design. [103] (In the following figures, horizontal extension and horizontal movement are not shown, but are implied by arrows and sequence of events.)

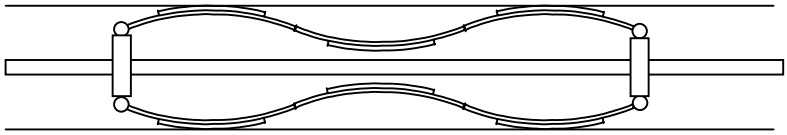

Figure 2.4—2A. Initial state

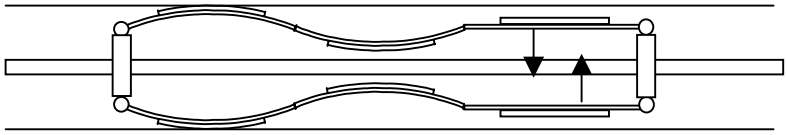

Figure 2.4—2B. Front clamp disengages

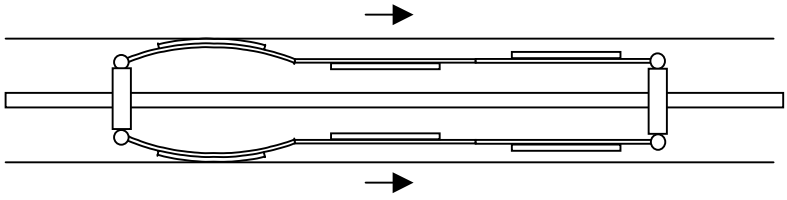

Figure 2.4—2C. Horizontal extension advances front end of device

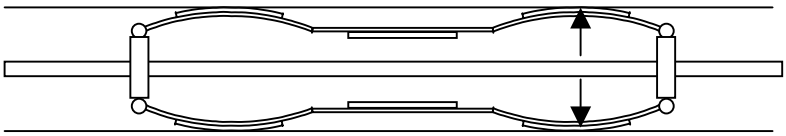

Figure 2.4—2D. Front clamp engages while extension is maintained

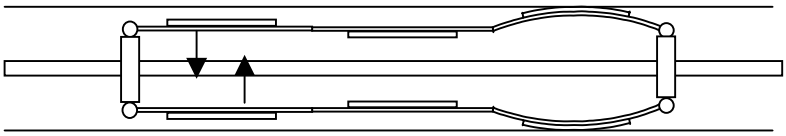

Figure 2.4—2E. Back clamp disengages while extension is maintained

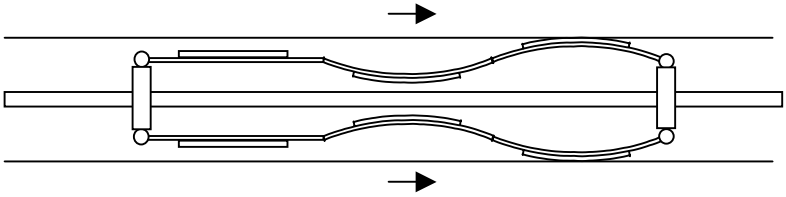

Figure 2.4—2F. Horizontal contraction advances back end of device

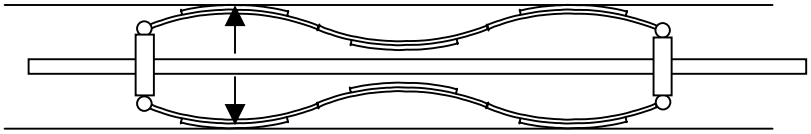

Figure 2.4—2G. Back clamp engages—one step has been accomplished

Obviously, there will be horizontal extensions and contractions associated with engaging and disengaging clamps if a flexural actuator is envisioned as means of clamping, but they have been disregarded. The principle and steps of the inchworm cycle have been illustrated nonetheless. An important feature is that the front and back clamps are never disengaged at the same time. This would be especially important if the traveling device were opposed by a load. Although the stroke of one step is miniscule, it is expected that the speed of piezoelectric actuation would allow many steps per second.

Bexell *et al* developed a motor in which four bimorph elements turn a central rotor with pairs of actuators operating sequentially. They elongate and grip the rotor surface by pressure contact, turn in the manner of a walking leg, contract and release, and return. Each pair must make contact before the opposite pair releases. That process creates the clamping mechanism which effectively creates an inchworm cycle. Lengthwise elongation and contraction for gripping and ungripping are accomplished by adding an additional bias field to the opposed fields in the drive signal that cause bending.

Their prototype used bimorphs 45 mm long, but they intended to produce a micromotor using bimorphs 500μm long. [104] They acknowledge that Smits has devised a similar mechanism. [105, 106] The opposing actuators were to be arranged radially around a central axle so that actuator ends would "walk" on the curved side of a cylindrical axle. In [107], they report having fabricated a motor 4 mm in diameter. The miniature motor was redesigned so that an array of six bimorphs in parallel alignment with an axle "walk" on a flat, disk-shaped platen or stator forming an extension of the axle radius, perpendicular to its axis.

2.5 The Essential Mechanical Diode

In many ways, the clamping or latching mechanism is the most important part of step-cycle motor design. It may seem trivial to design a fast, efficient means of holding the position of some part of a motor anywhere along a continuous range of positions without

slippage, but in practice the problem is difficult, especially during fast, dynamic operation and when substantial force opposes the motor.

Almost any clamping or latching mechanism exhibits some backlash, which is unintended movement or loss of position during the brief moment between the start of clamping and when the mechanism becomes fully engaged. The phenomenon is aggravated by intermittently-applied force or changing direction. (Threaded rods experience backlash *specifically* when direction of travel is reversed.)

Given the small displacements achieved even by amplified piezoelectric strain, the scale of backlash is typically close enough to the same scale of actuator displacement that small actuator displacements may be mostly consumed by small losses. One could specify large, powerful brakes and wait for inertial forces to dissipate before clamping and unclamping, but that would defeat the purpose of piezoelectric devices, which is to attain high energy density in small packages and overcome small displacements by fast operation.

One means of limiting backlash is to use a mechanism that latches in discrete steps. However, the stroke of actuators must be able to reach the next step (or an integral number of steps), even under load, which implies many small steps. This approach was taken by Zhu *et al*, who note that the force an inchworm cycle motor is able to apply is not limited by the force that piezoelectric stack actuators are able to apply, but rather by friction between clamping surfaces.

They proposed repeatedly engaging and disengaging sets of etched silicon micro-ridges 10 μm high and 10 μm apart as discrete step clamps. Initial results described in the paper consisted of developing a process for micromachining the microridges on a silicon surface, using MEMs techniques. The silicon was oxidized, patterned by photolithography, etched to expose sections of the silicon surface, then subjected to anisotropic etching to create grooves with vertical walls. [108]

More often than not, clamps use friction to achieve a continuum of latched positions. However, binding clamps are preferable to brakes using surface friction imposed by normal forces. Binding clamps are designed so that the forces blocked by the clamp

cause the mechanism to tighten its hold on the clamped surface. Sections 7.1.1 and 7.2.1 discuss clamping devices based on this principle. Binding clamp principles are not new, and commercial devices are available. [109, 110]

Comprehensive investigations on the subject of incorporating such devices into linear and rotary piezoelectric motors were undertaken by a research group lead by Frank, Mockensturm, and Lesieutre. They built a sequence of devices with wedge-based clamps that exploited the concept of a "self-locking taper." [111] In other devices, spherical or cylindrical bearings blocked movement in one direction by becoming wedged into the tapered cavities, but allowed movement in the other by shifting slightly toward the divergent direction of the taper. Backlash was minimized by using light springs to maintain the bearings permanently on the verge of binding. [111, 112] The concept of "rectification of a small cyclic displacement of the active element using a mechanical diode," [111] goes to the heart of the problem of designing motors with oscillatory driving elements.

It has been mentioned a number of times in this thesis that part of the promise of piezoelectric actuation lies in the potential to make small (sub-millimeter) devices. An illuminating article by Astumian [128] discusses how molecular mechanisms used by biological cells convert directionless fluctuations into the directed movements of protein motors and switches, ion transport channels, structural assembly and disassembly, and so forth. Any deterministic motion at the molecular scale is beset by an incessant tempest of thermal and other physical vibrations at fairly large amplitudes relative to the objects composing the medium. The key to ordered activity is to rectify the noise, filtering out components that are inconsistent with the directed movement.

In such an environment, motive power is freely available in the form of vibrations, but the net sum of movement in all directions is zero. The energy input into molecular machinery is consumed by the rectification or filtering processes, thereby allowing thermodynamic laws extract their toll as always. A concept sometimes termed the Brownian ratchet principle emerges. Astumian illustrates the principle with the scenario of a car parked at the foot of a hill while being pummeled by hailstones striking from every direction. A protein molecule and water molecules would have about the same relative

masses as the car and hailstones, but billions of impacts would occur every second. If billions of hailstones per second were striking an imaginary car, one could imagine the car shifting and lurching back and forth. If an intelligent occupant applied a brake only as needed to keep the car from rolling or shifting backwards, the car might climb the hill. Alternatively a ratchet and pawl mechanism could be installed on the car axles which would allow forward motion but block backward motion. Then, the car would climb the hill without intelligence. The author discusses additional refinements and considerations regarding such a process, and provides various examples of natural or man-made functional arrangements that have been shown to make use of it.

Finally, a novel latching concept for rectification of vibration is included as a illustration of what is possible. It was developed by the New Focus company (San Jose, CA), who produce devices for use with optics and optical networks. A motor consists of a piezoelectric transducer sandwiched between two angled mounts as represented in Figure 2.5—1. The parallel opposite arms of the angles embrace an 80-pitch screw so that they alternately slide back and forth against the screw in opposite directions. By some means (perhaps isolated drive pulses) the relative motion of the arms is fast in one direction and slow on the recovery. Since dynamic friction is lower than static friction, the screw turns against the surfaces when they move slowly, while fast-moving surfaces slip without turning it. This creates rectification of oscillatory motion by turning the screw in one direction. Rotation of the screw in its threads creates rectified linear motion with good holding capability. It is an example of how the supply of novel mechanical diode designs can remain unexhausted as long as sufficient ingenuity is applied to the problem. [113]

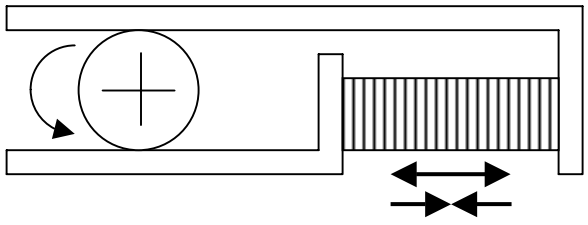

Figure 2.5—1. Illustration of the Picomotor^{TM} operating principle

2.6 References

[1] A. von Hippel. *Dielectrics and Waves* (Boston, London: Artech House, 1995).

[2] G.H. Haertling. Ferroelectric ceramics: History and technology. Journal of the American Ceramic Society, 82, 797-818 (1999).

[3] H. Yanagida, K. Koumoto, M. Miyayama. *The Chemistry of Ceramics* (John Wiley & Sons / Tokyo: Maruzen Co., Ltd, 1996).

[4] Y. Xu. *Ferroelectric Materials and Their Applications* (North-Holland / Elsevier Science Publishers, 1991).

[5] F. Jona and G. Shirane. *Ferroelectric Crystals* (New York: Dover Publications, 1993).

[6] L.E. Cross and K.H. Härdtl. Ferroelectrics, in *Piezoelectricity* (C.V. Rose, B.V. Hiremath and R. Newnham, eds. New York: American Institute of Physics, 1992).

[7] A.S. Nickles. 1998. *The Development of Lead Zirconate Titanate Thin Films for Piezoelectric Microactuators*. PhD Dissertation, University of California, Berkeley, CA.

[8] S. Wise. Displacement properties of Rainbow and Thunder piezoelectric actuators. Sensors and Actuators A, 69, 33-38 (1998).

[9] B.J. Rodriguez. 2003. *Nanoscale Investigation of the Piezoelectric Properties of Perovskite Ferroelectrics and III-Nitrides*. PhD Dissertation, North Carolina State University, Raleigh, NC.

[10] L.E. Cross. *Ferroelectric Ceramics* (N. Setter and E.L.Colla, eds. Berlin: Birhäuser, 1993).

[11] D.-J. Kim. 2001. *Piezoelectric and Ferroelectric Properties of Lead Zirxonate Titatnate Thin films*. PhD Dissertation, North Carolina State University, Raleigh, NC.

[12] K. Uchino. *Piezoelectric Actuators and Ultrasonic Motors* (Kluwer Academic Publishers, 1997).

[13] Q.M. Zhang, H. Wang, N. Kim and L.E. Cross. Direct evaluation of domain-wall and intrinsic contributions to the dielectric and piezoelectric response and their temperature dependence on lead zirconate-titanate ceramics. Journal of Applied Physics, 75, 454-459 (1994).

[14] T. Ikeda. *Fundamentals of Piezoelectricity* (Oxford Science Publications, 1996).

[15] Y. Xu. *Ferroelectric Materials and Their Applications* (North-Holland / Elsevier Science Publishers, 1991).

[16] J.F. Nye. *Physical Properties of Crystals: Their Representation by Tensors and Matrices* (Oxford University Press, 1960).

[17] G.H. Haertling. Piezoelectric and electrooptic ceramics, in *Ceramic Materials for Electronics: Processing, Properties and Applications* (R. C. Buchanan, ed. 2nd ed.; Marcel Dekker, 1991).

[18] C. S. Lynch. Electro-mechanical coupling in 8/65/35 PLZT. IEEE International Symposium on Applications of Ferroelectrics, 357-360 (1994).

[19] B. Jaffe, W.R. Cook, and H. Jaffe. *Piezoelectric Ceramics* (Academic Press Limited, 1971).

[20] L.L. Hench and J.K. West. *Principles of Electronic Ceramics* (John Wiley and Sons, 1990).

[21] Standards Committee of the IEEE Ultrasonics, Ferroelectrics and Frequency Control Society. IEEE Standard on piezoelectricity (*ANSI / IEEE Standard 176-1987, 1988*), in *Piezoelectricity* (C.V. Rose, B.V. Hiremath and R. Newnham, eds. New York: American Institute of Physics, 1992).

[22] V. Giurgiutiu and C. A. Rogers. Comparison of solid-state actuators based on power and energy criteria. Proceedings of the SPIE—The International Society for Optical Engineering, 2717, 287-300 (1996).

[23] K. Uchino. Materials issues in design and performance of piezoelectric actuators: an overview. Acta Materialia, 46, 3745-3753 (1998).

[24] J.M. Hollerbach, I.W. Hunter, J. Ballantyne. A comparative analysis of actuator technologies for robotics, Part V in *The Robotics Review 2* (O. Khatib, J.J. Craig, and T. Lozano-Pérez, eds. The MIT Press, 1992).

[25] S.C. Jacobsen, F.M. Smith, and E.K. Iversen, D.K. Backman. High performance, high dexterity, force reflective teleoperator. Proceedings of the Conference on Remote Systems Technology, 2, 180-185 (1990).

[26] S.C. Jacobsen, J.E. Wood, D.F. Knutti, and K.B. Biggers. The Utah / MIT dextrous hand: work in progress. International Journal of Robotics Research, 3, 21-50 (1984).

[27] Bertrand Tondu and Pierre Lopez. Modeling and Control of McKibben Artificial Muscle Robot Actuators. IEEE Control Systems Magazine, 15-38 (2000).

[28] T.C. Waram. *Actuator Design Using Shape Memory Alloys*. (Published by T.C. Waram, 1993, Available through Mondotronics, Inc., San Raphael, CA).

[29] L.M. Schetky. Shape memory alloys, Scientific American, 241, 74-82 (1979).

[30] C.M. Wayman. Shape memory alloys. MRS Bulletin, 18, 49-56 (1993).

[31] I. W. Hunter, S. Lafontaine, J.M. Hollerbach, and P.J. Hunter. Fast reversible NiTi fibers for use in microrobotics. Proceedings of the IEEE workshop on Micro Electro Mechanical Systems, 166-170 (1991).

[32] S. Hirose, K. Ikuta, and K. Sato. Development of a shape memory alloy actuator. Improvement of output performance by the introduction of an s-mechanism. Advanced Robotics, 3, 89-108 (1989).

[33] K. B. Hathaway and A. E. Clark. Magnetostrictive materials. MRS Bulletin, 18, 34-41 (1993).

[34] A.P. Dorey and J.H. Moore. *Advances in Actuators* (Bristol and Philadelphia: Institute of Physics Publishing, 1995).

[35] R. Pelrine, R. Kornbluh, Q. Pei, J. Joseph. High-speed electrically actuated elastomers with strain greater than 100%. Science, 287, 836-839 (2000).

[36] M. Zhenyi, J.I. Scheinbeim, J.W. Lee, B.A. Newman. High field electrostrictive response of polymers. Journal of Polymer Science B: Polymer Physics, 32, 2721-2731 (1994).

[37] H. Wang, M. Zhang, L.E. Cross, R. Ting, C. Coughlin, and K. Rittenmyer. The origins of electromechanical response in polyurethane elastomers. IEEE International Symposium on Applications of Ferroelectrics, 182-185 (1994).

[38] S. Ashley. Artificial muscles. Scientific American, 289, 52-59 (2003).

[39] A.J. Lovinger. Ferroelectric Polymers. Science, 220, 1115-1121 (1983).

[40] C. Niezecki and S. Balakrishnan . Power characterization of Thunder actuators as underwater propulsors. Proceedings of the SPIE—The International Society for Optical Engineering, 4327, 88-98 (2001).

[41] C.B. Sawyer. The use of rochelle salt crystals for electrical reproducers and microphones. Proceedings of the Institute of Radio Engineering, 19, 2020-2029 (1931).

[42] U.S. Pat. No. 1,802,782 to C.B. Sawyer. Piezoelectric device (April, 1931).

[43] J. G. Smits and W.-S. Choi. The constituent equations of piezoelectric heterogenous bimorphs. IEEE Transactions on Ultrasonics, Ferroelectrics and Frequency Control, 38, 256-270 (1991).

[44] C. P. Germano. Flexure mode piezoelectric transducers. IEEE Transactions on Audio and Electroacoustics, AU-19, 6-12 (1971).

[45] J. G. Smits, S. I. Dalke and T. K. Cooney. The constituent equations of piezoelectric bimorphs. Sensors and Actuators A, 28, 41-61 (1991).

[46] E.L. Colla, E.S. Thiele, E.S., D. Damjanovic, N. Setter. New high performance—low cost monolithic bimorph piezoelectric actuators for applications requiring large displacements with significant forces. IEEE International Symposium on Applications of Ferroelectrics, 1, 317-320 (2000).

[47] Q.-M. Wang, X.-H. Du, B. Xu, and L. E. Cross. Theoretical analysis of the sensor effect of cantilever piezoelectric benders. Journal of Applied Physics, 85, 1702-1712 (1999).

[48] D. L. Polla, L. F. Francis. Processing and characterization of piezoelectric materials and integration into micorelectromechanical systems. Annual Review of Materials Science, 28, 563-597 (1998).

[49] D. E. Glumac, T. G. Cooney, L.F. Francis, and W.P. Robbins. “A theoretical examination of MEMS microactuator responses with emphasis on materials and fabrication,” Materials Research Symposium - Proceedings, 360, 407-412 (1995).

[50] T. Kitamura, Y. Kodera, K. Miyahara, and H. Tamura. A piezoelectric ceramic material and a bimorph for auto-tracking in VTR. Japanese Journal of Applied Physics, Supplemental 20-4, 97-100 (1981).

[51] G. Li and G. H. Haertling. Stress-sensing characteristics of PLZT-based Rainbow ceramics. Smart Materials and Structures, 6, 425-431 (1997).

[52] A. J. Moskalik and D. Brei. Force-deflection behavior of individual unimorph piezoceramic C-block actuators., Proceedings of the ASME Aerospace Division. ASME, AD-52, 679-687 (1996).

[53] D. Brei. Force-Deflection Behavior for C-Block Piezoelectric Actuator Architectures. Proceedings of the SPIE—The International Society for Optical Engineering, 2443, 362-373 (1995).

[54] A.J. Moskalik, D. Brei. "Quasi-static behavior or individual C-block piezoelectric actuators." Journal of Intelligent Material Systems and Structures, 8, 571-587 (1997).

[55] J. D. Ervin, D. Brei, C. A. Van Hoy, J. R. Mawdsley, and J. W. Holloran. New fabrication process for active, micro-sized metal/ceramic devices. Proceedings of the ASME (American Society of Mechanical Engineers), Aerospace Division, AD-52, 695-701 (1996).

[56] G.H. Haertling. Rainbow ceramic—a new type of ultra-high displacement actuator. Bulletin of the American Ceramic Society, 73, 93-96 (1994).

[57] G. H. Haertling. Chemically reduced PLZT ceramics for ultra-high displacement actuators. Ferroelectrics, 154, 101-106 (1994).

[58] E. Furman, G. Li, and G.H. Haertling. Electromechanical properties of Rainbow devices. IEEE International Symposium on Applications of Ferroelectrics, 146-149 (1994).

[59] U.S. Patent 5,471,721 to Gene H. Haertling. Method for making monolithic prestressed ceramic devices (Dec. 5, 1995).

[60] G.H. Haertling. Rainbow actuators and sensors: a new smart technology. Proceedings of the SPIE—The International Society for Optical Engineering, 3040, 81-92 (1997).

[61] C. Elissalde and L.E. Cross. Dynamic characteristics of Rainbow ceramics. Journal of the American Ceramic Society, 78, 2233-2236 (1995).

[62] Catherine Elissalde, L. Eric Cross, and Clive A. Randall. Structure—property relations in a reduced and internally biased oxide wafer (Rainbow) actuator material. Journal of the American Ceramic Society, 79, 2041-2048 (1996).

[63] S. Chandran, V.D. Kugel and L.E. Cross. Characterization of the linear and non-linear dynamic performance of Rainbow actuator. IEEE International Symposium on Applications of Ferroelectrics, 2, 743-746 (1996).

[64] M.W. Hooker. Properties and Performance of Rainbow Piezoelectric Actuator Stacks. Proceedings of the SPIE—The International Society for Optical Engineering, 3044, 413-420 (1997).

[65] Guang Li, Eugene Furman and Gene H. Haertling. Finite element analysis of Rainbow ceramics. Journal of Intelligent Systems and Structures, 8, 434-443 (1997).

[66] Guang Li, Eugene Furman, and Gene Haertling. Stress-enhanced displacements in PZLT Rainbow Actuators. Journal of the American Ceramic Society, 80, 1382-1388 (1977).

[67] B.W. Barron, G. Li, and G.H. Haertling. Temperature Dependent Characteristics of Cerambow Actuators. IEEE International Symposium on Applications of Ferroelectrics, 1, 305-308 (1996).

[68] S. Chandran, V.D. Kugel, and L.E. Cross. Crescent: A Novel Piezoelectric Bending Actuator. Proceedings of the SPIE—The International Society for Optical Engineering, 3041, 461-469 (1997).

[69] V.D. Kugel, S. Chandran, and L.E. Cross. A Comparative Analysis of Piezoelectric Bending–Mode Actuators. Proceedings of the SPIE—The International Society for Optical Engineering, 3040, 70-80 (1997).

[70] Karla M. Mossi, Gregory V. Selby, Robert G. Bryant. Thin-layer composite unimorph ferroelectric driver and sensor properties. Materials Letters, 35, 39-49 (1998).

[71] K.M. Mossi, R.P. Bishop, R.C. Smith and H.T. Banks. Evaluation criteria for Thunder actuators. Proceedings of the SPIE—The International Society for Optical Engineering, 3667, 738-743 (1999).

[72] Cirrus Shakeri, Christine M. Bordonaro, Mohammed N. Noori, Raymond Champagne. Experimental study of Thunder: a new generation of piezoelectric actuators. Proceedings of the SPIE—The International Society for Optical Engineering, 3675, 63-71 (1999).

[73] M.W. Hyer and A Jilani. Predicting the deformation characteristics of rectangular unsymmetrically laminated piezoelectric materials. Smart Materials and Structures, 7, 784-791 (1998).

[74] U.S. Patent 5,632,841 to R. F. Helbaum, R. G. Bryant, R. L. Fox. Thin layer composite unimorph ferroelectric driver and sensor (May 27, 1997).

[75] K.M. Mossi, R.P. Bishop. Characterization of different types of high performance Thunder actuators. Proceedings of the SPIE—The International Society for Optical Engineering, 3675, 43-52 (1999).

[76] R. W. Schwartz, L. E. Cross, and Q. M. Wang. Estimation of the effective d31 coefficients of the piezoelectric layer in Rainbow actuators. Journal of the American Ceramic Society, 84, 2563-2569 (2001).

[77] G. Li, E. Furman and G.H. Haertling. Fabrication and properties of PSLT antiferroelectric Rainbow actuators. Ferroelectrics, 188, 223-236 (1996).

[78] Y. Sugawara, K. Onitsuka, S. Yoshikawa, Q. Xu, R. Newnham, and K. Uchino. Metal-ceramic composite actuators. Journal of the American Ceramic Society, 75, 996-998 (1992).

[79] R.G. Bryant. LaRC-SI: A soluble aromatic polyimide. High Performance Polymers, 8, 607-615 (1996).

[80] U.S. Patent 5,741,883 to Robert G. Bryant. Tough, soluble, aromatic thermoplastic copolyimides (April 21, 1998).

[81] J. Friend and D. Stutts. Bonding suggestions for the piezoelectric motor system. http://www..umr.edu/~piezo/MotorAnalysis/BondingNote/BondingNote..html, 6/7/99.

[82] R.W. Messler, Jr. *Joining of Advanced Materials* (Butterworth-Heinemann, 1993).

[83] F.A. Lowenheim. *Electroplating* (McGraw-Hill, 1978).

[84] J. Sirohi and I. Chopra. A fundamental understanding of piezoelectric strain sensors. Proceedings of the SPIE Conference on Smart Structures and Integrated Systems, 3668, 528-542 (1999).

[85] R.D. Adams. Theoretical Stress Analysis of Adhesively Bonded Joints, in *Joining Technologies for the 1990's: welding, brazing, soldering, mechanical, explosive, solid-state, adhesive.* (John D. Buckley and Bland A. Stein, eds. Park Ridge, N.J.: Noyes Data Corp., 1986).

[86] R.D. Adams. Theoretical Stress Analysis of Adhesively Bonded Joints, in *Joining Fibre-Reinforced Plastics* (F.L. Matthews, ed. London: Elsevier, 1987).

[87] R.D. Adams. *Structural Adhesive Joints in Engineering* (New York: Elsevier, 1984).

[88] H.A. Perry. How to Calculate Stresses in Adhesive Joints. Product Engineering, 64-67 (1958).

[89] V. Giurgiutiu, Z. Chaudhry, C. A. Rogers. Stiffness issues in the design of ISA displacement amplification devices: Case study of a hydraulic displacement amplifier. Proceedings of the SPIE—The International Society for Optical Engineering, 2443, 105-119 (1995).

[90] D. Halliday, R. Resnick, J. Walker. *Fundamentals of Physics* (4^{th} ed.; John Wiley and Sons, 1993).

[91] D. Roylance. *Mechanics of Materials* (John Wiley and Sons, 1996).

[92] M.R. Steele, F. Harrison, P.G. Harper. The piezoelectric bimorph: an experimental and theoretical study of its quasistatic response. Journal of Physics D: Applied Physics, 11, 979-989 (1978).

[93] J. G. Smits and T. K Cooney. The effectiveness of a piezoelectric bimorph actuator to perform mechanical work under various constant loading conditions. Ferroelectrics, 119, 89-105 (1991).

[94] Q.-M. Wang and L. E. Cross. Performance analysis of piezoelectric cantilever bending actuators. Ferroelectrics, 215, 187-213 (1998).

[95] X. Li, W. Y. Shih, I. A. Aksay, and W.-H. Shih. Electromechanical Behavior of PZT-brass unimorphs. Journal of the American Ceramic Society, 82, 1733-1740 (1999).

[96] Q.M. Wang and L.E. Cross. Tip deflection and blocking force of soft PZT-based cantilever Rainbow actuators. Journal of the American Ceramic Society, 82, 103-110 (1999).

[97] Z. Ounaies, K. Mossi, R. Smith, J. Bernd. Low-field and high-field characterization of Thunder actuators. ICASE Report No. 2001-9, NASA/CR-2001-210859, April 2001.
or see:
Proceedings of SPIE - The International Society for Optical Engineering, 4333, 399-407 (2001).

[98] T. Hikada, T. Maruyama, M. Saitoh, N. Mikoshiba, M Shimizu, T. Shiosaki, L.A. Wills, R. Hiskes, S.A.Dicarolis, J. Amano. Formation and observation of 50 nm polarized domains in PbZr1-xTixO3 thin film using scanning probe microscope. Applied Physics Letters, 68, 2358-2359 (1996).

[99] Q.-M. Wang, X.-H. Du, B. Xu, and L. E. Cross. Electromechanical coupling and output efficiency of piezoelectric bending actuators. IEEE Transactions on Ultrasonics, Ferroelectrics and Frequency Control, 46, 638-646 (1999).

[100] R.G. Bryant, S.A. Evans, E.R. Long Jr., and R.L. Fox. Thermal and Mechanical Characterization of NASA High Displacement Actuators for Satellite Instrumentation. Proceedings of the SPIE—The International Society for Optical Engineering, 3991, 195-201 (2000).

[101] R.G. Bryant, R.L. Fox, J.T. Lachowicz, and F-J.Chen. Piezoelectric synthetic jets for aircraft control surfaces. Proceedings of the SPIE Smart Structures and Materials Symposium: Industrial and Commercial Applications of Smart Structures Technologies, 3674, 220-227 (1999).

[102] C. Niezecki and S. Balakrishnan . Power characterization of Thunder actuators as underwater propulsors. Proceedings of the SPIE—The International Society for Optical Engineering, 4327, 88-98 (2001).

[103] C. Hyder, G. C. Horner, W. W. Clark. Linear traveling wave motor. Proceedings of the SPIE—The International Society for Optical Engineering, 3674, 205-211 (1999).

[104] M. Bexell, A.-L. Tiensu, J.-Å. Schweitz, J. Söderkvist and S. Johansson. Characterization of an inchworm prototype motor. Sensors and Actuators A, 43, 322-329 (1994).

[105] J.G. Smits. Design considerations of a piezoelectric-on-silicon microrobot. Sensors and Actuators A, 35, 129-135 (1992).

[106] U.S. Patent No. 5,049,775 to J.G. Smits. Integrated micromechanical piezoelectric motor (Sept. 17, 1991).

[107] M. Bexell, S. Johansson. Fabrication and evaluation of a piezoelectric miniature motor. Sensors and Actuators A, 75, 8-16 (1999).

[108] J. Zhu, D. Wang, C-J. Kim, and G.P. Carman. Development of mesoscale actuation device. Proceedings of the ASME (American Society of Mechanical Engineers), Aerospace Division, AD-52, 649-654 (1996).

[109] U.S. Patent Number 4,874,155 to A.S. Goul. Fast Clamp (1989).

[110] Fact Sheet: Drawn Cup Roller Clutches. TheTorrington Company, Division of Ingersoll-Rand (Torrington, CT), 1996.

[111] J. Frank, E. M. Mockensturm, W. Chen, G. H. Koopman, G. A. Lesieutre. Roller-wedgeworm: a piezoelectrically-driven rotary motor. 10th International Conference on Adaptive Structures and Technologies, 1-11 (1999).

[112] E. M. Mockensturm, J. Frank, G. H. Koopmann, G. A, Lesieutre. Modeling and simulation of a resonant bimorph actuator drive. Proceedings of the SPIE: Smart Structures and Materials: Smart Structures and Integrated Systems, 4327, 472-480 (2001).

[113] Applicaton Note 6: Applications of the Picomotor in the semiconductor industry. New Focus Inc., San Jose, CA, 2001.

[114] L.M. Nicholson, K.S. Whitley, T.S. Gates, and J.A. Hinkley. Influence of Molecular Weight on the Mechanical Performance of a Thermoplastic Glassy Polyimide, NASA/TM-1999-209720 (Technical Memorandum by NASA Langley Research Center, November, 1999).
or see:
L.M. Nicholson, K.S. Whitley, T.S. Gates. The role of molecular weight and temperature on the elastic and viscoelastic properties of a glassy thermoplastic polyimide. International Journal of Fatigue, 24, 185-195 (2002).

[115] http://www.physikinstrumente.com/tutorial/
PI (Physik Instrumente) L.P. (Auburn, MA and Tustin, CA), is the U.S. operation of Physik Instrumente (PI) GmbH & Co. KG.

[116] R.W. Schwartz and M. Narayanan. Development of high performance stress-biased actuators through the incorporation of mechanical pre-loads. Sensors and Actuators A: Physical, 101, 322-331 (2002).

[117] E.F. Crawley and J. de Luis. Use of piezoelectric actuators as elements of intelligent structures. AIAA Journal (American Institute of Aeronautics and Astronautics), 25, 1373-1385 (1987).

[118] S. Im and S.N. Atluri. Effects of a piezo-actuator on a finitely deformed beam subjected to general loading. AIAA Journal (American Institute of Aeronautics and Astronautics), 27, 1801 (1989).

[119] E.F. Crawley and E.H. Anderson. Detailed models of piezoelectric actuation in beams. Journal of Intelligent Materials, Systems, and Structures, 1, 4-25 (1990).

[120] D.H. Robbins and J.N. Reddy. Analysis of piezoelectrically actuated beams using a layer-wise displacement theory. Computers and Structures, 41, 265-279 (1991).

[121] M.W. Hyer and A. Jilani. Predicting the deformation characteristics of rectangular unsymmetrically laminated piezoelectric materials. Smart Materials and Structures, 7, 784-791 (1998).

[122] J. Pan, C.H. Hansen, S.D. Snyder. A study of the response of a simply supported beam to excitation by a piezoelectric actuator. Journal of Intelligent Materials, Systems, and Structures, 3, 3-16 (1992).

[123] S.M. Yang and Y.J. Lee. Modal analysis of stepped beams with piezoelectric materials. Journal of sound and vibration, 176, 289-300 (1994).

[124] S.J. Kim and J.D Jones. Quasi-static control of natural frequencies of composite beams using embedded piezoelectric actuators. Smart Materials and Structures, 4, 106-112 (1995).

[125] B.N. Agrawal and K.E. Treanor. Shape control of a beam using piezoelectric actuators. Smart Materials and Structures, 8, 729-740 (1999).

[126] R. Wieman, R.C. Smith, T. Kackley, Z. Ounaies, J. Bernd. Displacement models for Thunder actuators having general loads and boundary conditions. Proceedings of SPIE - The International Society for Optical Engineering, 4326, 252-263 (2001).

[127] R.C. Smith, Z. Ounaies. Domain wall model for hysteresis in piezoelectric materials. Journal of Intelligent Material Systems and Structures, 11, 62-79 (2000).

[128] R. Dean Astumian. Making molecules into motors. Scientific American, 285, 57-64 (2001).

[129] Imitec, Inc. (Schenectady, NY), private communication.

Chapter 3. Experimental Methods

3.1 Pre-Stressed Unimorph Fabrication and Characterization

3.1.1 Fabrication Procedures

3.1.1.1 Actuators Bonded with Polyimide Adhesive

The essential process of fabricating a polyimide-bonded, pre-stressed unimorph (PSU) involves five steps: (1) abrasion of metal surface and solvent cleaning of ceramic and metal surfaces prior to applying adhesive, (2) coating surfaces to be bonded with adhesive solution and subsequent drying, (3) assembly of a vacuum bag or envelope with supporting plate and outlet port to enclose stacked actuator elements, (4) pre-bonding, and (5) final bonding with applied heat and pressure treatments in an autoclave.

Typical actuator components include a thin plate of piezoceramic, usually PZT (lead zirconate titanate). The ceramic is bonded to a piece of metal shim (substrate) with tabs on ends of rectangular strips, or rim around circular shapes, where metal extends beyond the perimeter of the ceramic to enable mounting in a device or fixture in either case. The substrate is typically stainless steel, aluminum or brass [1- 3], but could be other materials, especially a composite material. The bond is typically formed using an adhesive which not only resists high-temperature, but sets at high temperature, notably polyimide. However, other adhesives such as an epoxy, or bonding agent such as solder are possible.

A number of characteristic features typical of the fabrication process have been discussed in existing literature. An example application given in the patent for the polyimide composition which came to be known as LaRC-SI mentions applying a 10% polyimide solution in N-methyl pyrrolidinone (NMP) with an airbrush as a means of producing a sprayable dielectric coating / adhesive on various materials, including ceramic and metal. [4] The patent for Thin Layer Composite Unimorph Ferroelectric Driver and Sensor [5], from which the acronym THUNDER™ was derived, describes a stacked assembly of electroded ferroelectric wafer, adhesive film, and metal underlayer subjected to curing / bonding at 300º C while encased in a vacuum bag of Kapton™ polyimide film sealed with high temperature tape. It also mentions the use of a curved molding surface

below stacked actuator components to enhance the curvature which would also develop from differential thermal contraction.

This element of the procedure must have resulted in a high failure rate because a subsequent patent was awarded for incorporating a pre-curved ceramic element into the assembly of metal and adhesive, " to avoid breaking the brittle ceramic layer during the manufacture of THUNDER actuators." [6] Reports of work accomplished soon thereafter by Mossi in association with original patentholders do not mention a curved molding surface, but rather a supporting metal plate covered with fiberglass cloth and Kapton polyimide film coated with a mold release agent. [7, 2]

The original procedure used to manufacture pre-stressed unimorphs is detailed in the following outline. It approximately follows the key points given in [2]. Minor modifications introduced in our research are noted within the outline; others will be noted afterwards.

Fabrication of Pre-Stressed Unimorphs Similar to THUNDER Actuators

1. Preparation of actuator components (assumes parts are already cut to shape)
    A. Roughen bonding surface of metal shim substrate with silicon carbide paper. (Used 240 grit)
    B. Clean substrate, ceramic thin plate and aluminum foil with alcohol. (Reagent grade acetone, a better degreasing agent, was used, dispensed from wash bottle.)
2. Application and drying of adhesive
    A. Apply two coats of polyimide adhesive in solution to bonding surfaces of both metal and ceramic by spraying solution with an airbrush.
    B. Dry coated pieces in oven for two hours at 70º C.
3. Assembly of actuator components and vacuum envelope
    A. Assemble each set of actuator components as shown in Figure 3.1.1.1—1.
    B. Assemble vacuum envelope as shown in Figure 3.1.1.1—2, enclosing positioned, stacked actuator components. Note that the surfaces of the Kapton

polyimide sheets facing actuator parts have been wiped with mold release agent and allowed to dry.

4. Pre-bonding

A. Connect vacuum source and evacuate envelope.

B. Insert into oven / autoclave and raise temperature to 325º C at 5º C per minute. Leave at temperature for one hour.

C. Lower temperature to 180º C, then release vacuum. Allow to cool to room temperature.

5. Final bonding

A. Connect vacuum source and evacuate envelope.

B. Insert in autoclave and raise temperature to 320º C at 5º C per minute.

C. After reaching 320º C, pressurize autoclave to 30 psi (207 kPa) for 30 minutes.

D. Release pressure and lower temperature to 200º C.

E. Release vacuum and allow system to cool to room temperature.

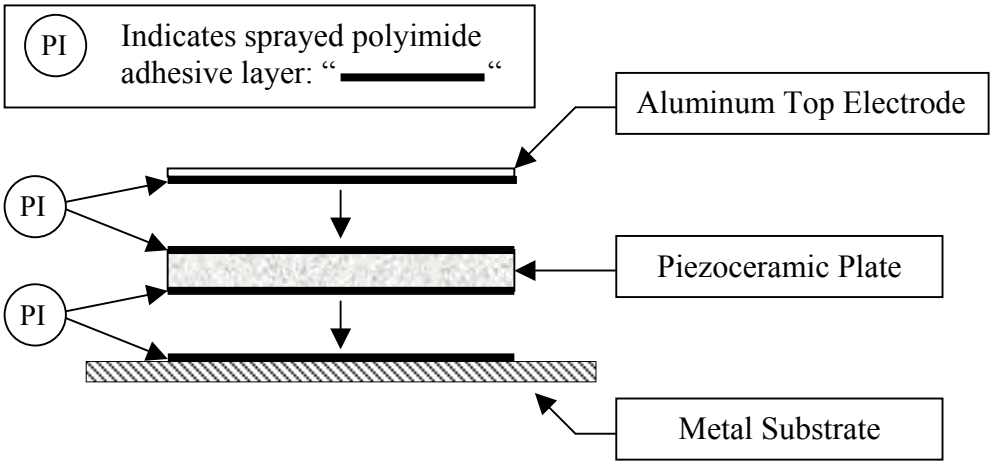

Figure 3.1.1.1—1. Assembly of actuator components

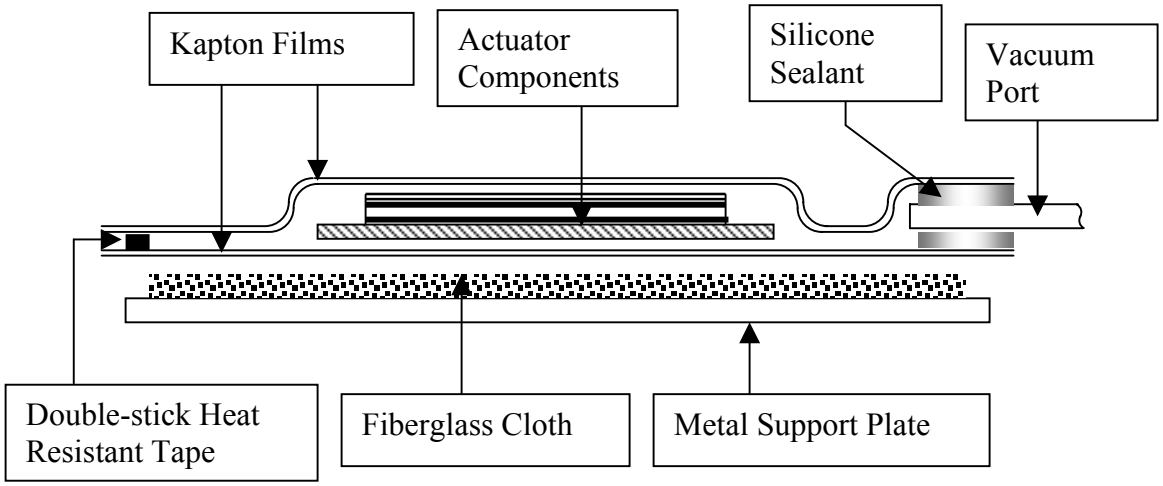

Figure 3.1.1.1—2. Construction of vacuum envelope (Note: inner surfaces of both Kapton films have been wiped with Frekote release agent and allowed to dry completely.)

Table 3.1.1.1—1 Materials

Metal shim substrates, typically type 302 stainless steel, 11H18 full-hard aluminum, 4-mil and 8-mil thickness, each type (1 mil = 0.001 inch)
PZT-5A thin plates: used PSI-5A4E from Piezo Systems, Inc. (Cambridge, MA) , 1.5" x 1.49" x 0.0075" (thickness = 190.5 μm)
LaRC-SI^{TM} polyimide precursor from Imitec, Inc. (Schenectady, NY), 10% solids, 3% offset, dissolved in N-methyl pyrrolidinone (NMP)
0.25 mil aluminum foil (Fisher Scientific)
Kapton® polyimide film (DuPont Company), 5-mil thickness
4321 / D-C Kapton polyimide tape, 0.25" width, with pressure sensitive silicone adhesive on both sides from The Great Tape Company (So. Hampton, NH)
Frekote 44-NC mold release agent from Dexter Corporation (Seabrook, NH)
Fiberglass cloth, rolled strip, 2 inches wide, approximately 1/8 inch thick
HPLC-grade acetone, Fisher Scientific Company
240 grit silicon carbide emery paper
N-methyl pyrrolinidone, Fisher Scientific
HPLC grade tetrahydrofuran, Fisher Scientific (Use of this additional solvent discussed in Section 3.1.1.3.)

Table 3.1.1.1—2 Equipment

Lindberg Blue HTF55000 Series Hinged Tube Furnace adapted for autoclave capability using 3-inch diameter inconel tube with type 304 SS female straight “sanitary coupling” adapters, clamps, Teflon gaskets, and endcaps (McMaster-Carr Supply Co.) drilled and tapped for vacuum, pressure and thermocouple access fittings
Cole-Parmer instrument Corp. “Air Cadet” vacuum pump, model no. 7530-40
Omega Engineering model DPI8 temperature / process monitor
Type K thermocouple probe, 18 inches long
Dry grade nitrogen, 300 cu. ft. cylinder at 2600 psig (for pressurizing autoclave)
Paasche model VL air brush with Thomas model 600-13 low-pressure compressor
aluminum plate, 2” x 12” x 0.125”

3.1.1.2 General Procedure Notes

Applying adhesive precursor by airbrush has advantages but allows opportunities for variability and mishap. Therefore, it was important to establish an appropriate technique for obtaining a thin, uniform coating of actuator parts.

Instead of spraying two coats of NMP-based solution, the procedure was modified to include four or five light coats of sprayed adhesive solution on each surface to be bonded. This gave an opportunity to correct for non-uniformly sprayed areas. This change was aided by using the more volatile solvent blend described in Section 3.1.3.

The airbrush quickly clogged if not cleaned after every spray coat. The easiest way to clean it was to have on hand two of the reservoir bottles that attached to the body of the airbrush. One contained polymer solution, the other pure solvents. After each spray, the airbrush body was detached from the polymer solution bottle, transferred to the pure solvent bottle, sprayed for several seconds. Residual solvent in the airbrush was blown out with air before spraying another round of polymer solution. All spraying was conducted under a fume hood.

Immobilizing light and thin sheets in the spray from an airbrush is a challenge. Metal and ceramic pieces were mounted for spraying on a paper-covered box by inserting four model-building pins around each piece. The slightly protruding shafts prevented lateral movement, while the heads blocked vertical movement. Each fastened piece did not rest on the paper but was supported upon the heads of an additional four pins inserted through the box top under each location. The slight separation prevented overspray from sticking the pieces to the underlying paper. The ceramic, in particular, was so fragile that removing such a stuck piece from underlying paper would probably have broken it. Parts were removed with forceps, usually after slightly rotating the heads of fastening pins to break adhesion.

Aluminum foil used for top electrodes was typically mounted for spraying by lightly pressing part of a long edge of each piece onto a low-stick adhesive strip already fastened to the box surface. (The adhesive strips of Post-It™ note papers worked better than low-stick, double-sided plastic tape. They were tacked to the box with the writing surface downward by spots of some other adhesive.)

Unlike most uncured adhesives, dried polyimide precursor has no tack. Consequently, positioning and alignment of actuator parts was difficult to maintain while sealing them in a vacuum envelope. The remedy was to stack the parts for each actuator perfectly, then dab the smallest possible droplets of viscous polyimide precursor solution at several points across the edges of the layers using a needle. The droplets were allowed to dry.

Area dimensions of ceramic thin plates and metal substrates used in this project are shown in Figure 3.1.1.2—1. Typical thicknesses are given in Table 3.1.1.1—1. This design, adapted from the Face International Corp. THUNDER model 8R, was a constant factor in all experiments. Experiments were performed on circular THUNDER actuators, including a set custom manufactured by Face International Corp., but none were fabricated in my work.

The ceramic pieces were custom cut by the vendor from stock sheets, 2.85 inches square, to the dimensions given in Figure 3.1.1.2—1. Some substrates were cut by water

jet. The edges were left somewhat roughened and required sanding, but were generally acceptable. Others were cut by automatic milling machines or by high-power laser. Milled substrates are flawless, but expensive to produce. Laser-cut substrates resembled water-cut substrates in that the edges had to be de-fritted. Also, localized high temperature probably alters the material properties of the shim stock. For later experiments, cutting rectangular blanks on a heavy-duty paper cutter worked well (as long as the tendency to the shearing blade to pull the metal sheet was compensated for). Cutouts in the end tabs were made using a combination of Dremel™ tool with pointed grinding tip and metal shears. (Drilling thin sheet metal often leaves ragged edges even with special holding techniques—hence the grinding approach.)

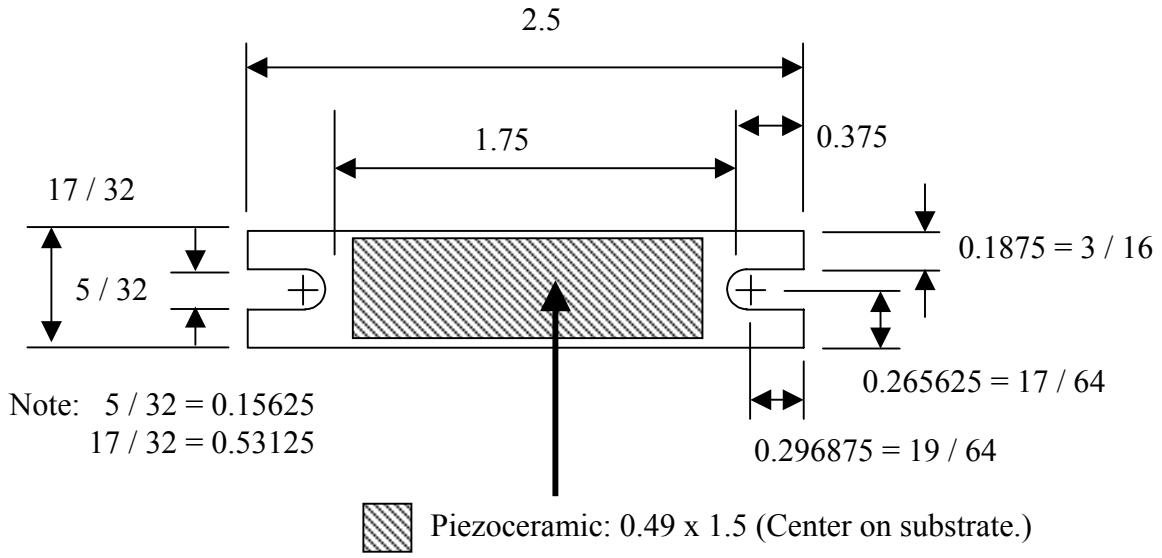

Figure 3.1.1.2—1. Top View: Nominal dimensions of substrate and ceramic layers of fabricated actuators. (All dimensions in inches.)

Actuators were re-poled before use since piezoceramic elements were subjected to temperatures close to their rated Curie temperature (350º C) during fabrication. Jaffe, Cook, and Jaffe [8] recommend applying 20-40 kV/cm for several seconds to 30 minutes or longer depending on specimen variation. Wise reported poling THUNDER actuators at

20 kV/cm for 30-60 s at room temperature. [1] (20 kV/cm is equivalent to about 50 V/mil, where 1 mil = 0.001 inch.) Given a ceramic thickness of 7.5 mils (0.019 cm), voltage between 375-750 V applied across in-house actuators would be appropriate. Since THUNDER 8R actuators (Face International Corp.) are rated at a maximum of 480 V during actuation, our actuators were poled at 500-520 V for at least 5 minutes.

3.1.1.3 Procedure Modifications

In [2], Mossi *et al* provide details of a manufacturing process for THUNDER devices. They mentioned using LaRC-SI™ polyimide adhesive in both spray and film form, obtained from Imitec, Inc. (Schenectady, NY). In discussing the purchase of LaRC-SI adhesive in solution form, a representative of Imitec said he did not want to sell the dry film because production was not commercially worthwhile. It involved producing pelletized polymer which was then sintered / calendered at 360˚C using equipment rented on a per run basis. The alternative, he noted, would be solution casting, which is difficult. When Wise summarized THUNDER actuator fabrication procedure in [1], no mention was made of LaRC-SI polyimide adhesive in film form, only spray-coating each surface with adhesive solution. This was the route chosen for all fabrications in the present project.

As received, LaRC-SI polyimide precursor solution is quite viscous. NMP serves as both solvent and thinner. Initially, adding 3 parts NMP to 1 part polyimide solution was found to yield a sprayable liquid which contained 2.5% solids. In spraying the two recommended coats, however, coverage was often not uniform, and drying time was inconveniently long, since NMP has a boiling point of 202º C.

Prior experience using NMP as a polymer solvent showed that a lower boiling solvent, tetrahydrofuran (THF, b.p. 67º C), is remarkably similar to NMP in regard to what polymers will dissolve in it and how well. THF alone, however, usually does not perform quite as well as a solvent mixture containing 10-25% NMP. The resulting polymer solutions have the useful property that cast or sprayed films lose much of their volume quickly, leaving a viscous layer which dries in less time overall than if NMP alone were

used, but with much less tendency to coalesce into spots than solutions based on low-boiling solvent alone.

Therefore, LaRC-SI precursor solution was blended directly in a 40 : 60 weight ratio of polyimide concentrate to THF. Approximate composition of thinned polyimide precursor solution: 4% polyamic acid ("solids"), 36% NMP, 60% THF. On adding THF, polymer often started to come out of solution, but re-dissolved suddenly after continued stirring. If a transparent orange solution did not develop, a small additional amount of NMP helped re-dissolve precipitated polymer.

Item 2B in the procedure outline was modified. Instead of drying coated pieces in an oven for two hours at 70º C, they were left in a fume hood overnight still mounted on the spraying holder. The reason was that the slight additional compliance of the air-dried adhesive films seemed to facilitate melding the two free surfaces while becoming set at high temperature. Adhesive films on oven-dried pieces were very hardened, making it more difficult for surface incompatibilities to flow and merge during curing.

The top aluminum foil electrodes were omitted after an initial phase of fabrication. As received from the manufacturer, the PZT sheets are electroded on both sides with a reduced, conductive layer of nickel glass. To achieve optimal electric field-induced strain, piezoceramics require an intimate connection at the material level to a conductive surface, which the co-fired nickel electrodes provided. Adding an additional foil electrode added mechanical encumbrance without notable advantages.

A few actuators were initially autoclaved in a 2.5 inch-diameter alumina tube, 3 feet long. Results were completely acceptable: however, one has qualms about pressurizing a long, thermally-cycled, ceramic tube. After converting to the Inconel tube (autoclave) described in Table 3.1.1-2, it became apparent that its thermal mass was large and that it would not be possible to achieve the temperature ramp rates stated in the fabrication outline given in Section 3.1.1, adapted from [2]. An attempt was made to move the sensor for the furnace heat controller to the inside of the autoclave. However, temperature response from inside the tube was on such a longer time scale than the controller programs

were designed to handle that error conditions developed and the furnace became overheated.

It was decided not to optimize the PID controller for the large thermal mass of the autoclave, mostly for safety reasons. The heat controller probe was returned to its as-manufactured location outside the autoclave and heating schedules were developed by trial and error that achieved approximately the prescribed conditions inside of the autoclave. The thermocouple probe mounted through the autoclave endcap was essential in developing the modified programs. For example, Figure 3.1.3-1A shows the intended heating schedule for pre-bonding. Because of the thermal mass inertia of the autoclave tube, the actual heat controller program required to get the intended internal process conditions might look more like the schedule shown in Figure 3.1.3-1B. The challenge was

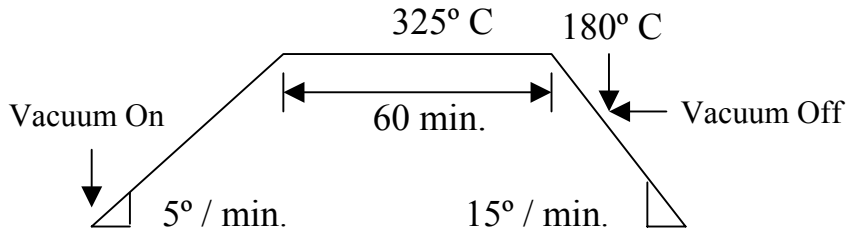

Figure 3.1.1.3—1A. Pre-bonding target heating schedule

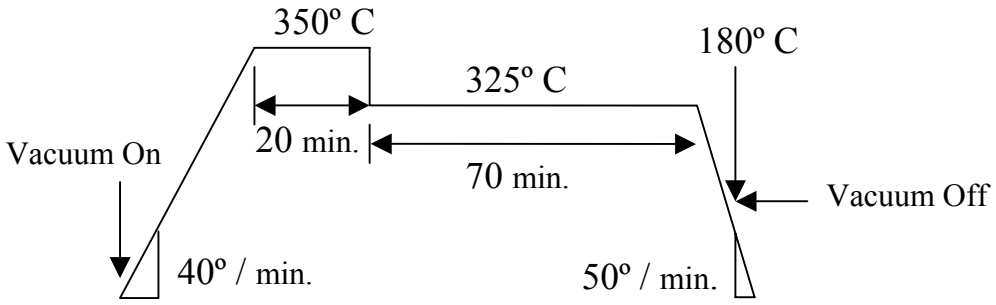

Figure 3.1.1.3—1B. Controller program to approximately meet target

to minimize temperature overshoot by stepping down from the excessively high target before autoclave internal temperature reached the intended target.

After an initial set of actuators was fabricated, the Kapton film vacuum envelope was no longer fastened to a 1/8" aluminum plate with fiberglass cloth in between. Since the lower Kapton film had not been sealed against the aluminum plate and air trapped in the fiberglass evacuated, external pressure was actually bearing against the lower Kapton film. Omitting the plate and fiberglass created a compliant, layered container allowing hydrostatic compression, as before, of actuator parts during heat treatment.

With or without the plate and fiberglass, it was difficult to assemble this envelope configuration so that minor leaks did not develop. Small gaps where pieces of double-sided tape met at corners sometimes leaked. Although silicone sealant was adequate for creating a vacuum-tight seal around the vacuum port, it became quite soft at actuator-bond-curing temperatures and could be sucked into the tubing. The plug of silicone sealant had to be kept well away from the end of the port while it cured during vacuum envelope assembly, which was at odds with pressing the Kapton films to achieve good contact with the sealant and double-sided tape.

Later in the project, a stainless steel vacuum plate fixture was designed and fabricated as an improved means of confining actuator parts between Kapton films during heat treatment. Figure 3.1.1.3—2 provides an overview of the appearance of the fixture from the side and the process of assembly. Figures 3.1.1.3—3A and 3.1.1.3—3B show additional views and details of the design.

As with previous fabrication procedures, inner surfaces of two pieces of Kapton polyimide film were wiped with Frekote release agent and allowed to dry completely. The bottom piece was then placed on the vacuum plate base and several slits cut with a razor blade where the film covered the milled channel which allowed distributed access to vacuum.

From Figure 3.1.1.3—3A, one can see that the Kapton film pieces would measure a little less than 1.75 x 9.75 inches to fit beneath the retaining ring without being too large for clearance within the ring of machine screws. The ideal size was difficult to judge,

especially since confined actuator parts distorted the top Kapton film slightly. A sheet metal template was used to cut the sheets to optimal dimensions. An improved vacuum fixture design would allow an additional 1/16 inch on the inside of the retaining ring.

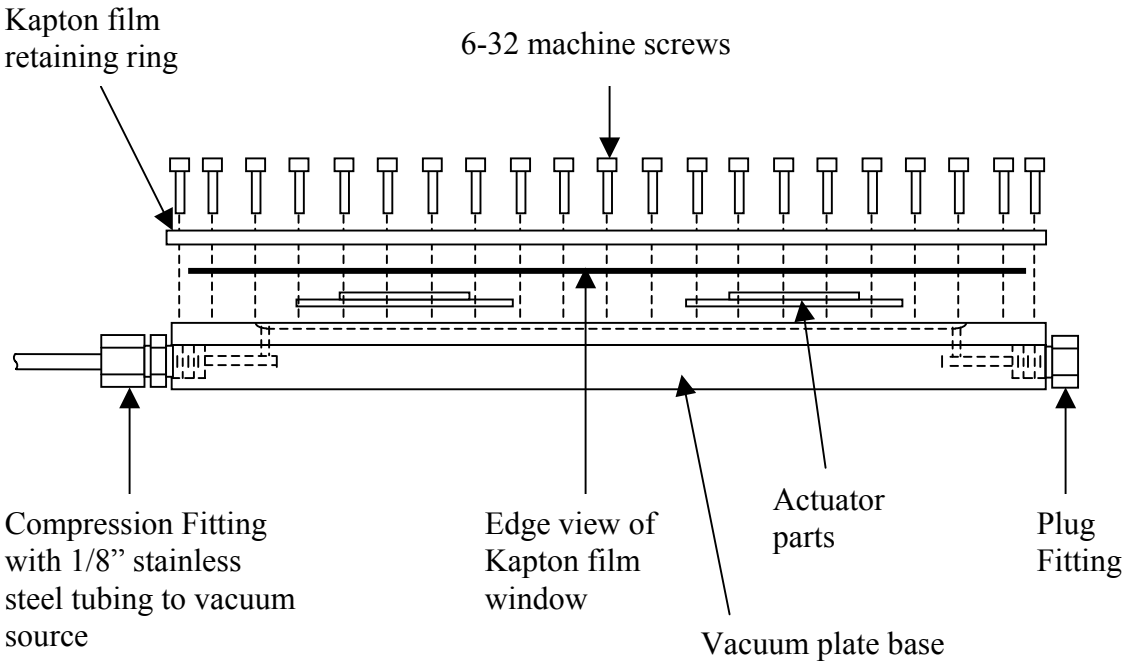

Figure 3.1.1.3—2. Exploded view: assembly of actuator parts and vacuum plate components. (Not shown: a lower layer of Kapton film beneath actuator parts which has slits to allow access to vacuum channel)

The vacuum plate fixture proved useful, although an additional consideration should be noted. As designed and fabricated, the ring of holes in the vacuum plate base were threaded for directly fastening with the machine screws. After exposure to high temperature, a number of screws seized and broke upon attempted removal. Consequently, the threaded holes were drilled out and longer screws were used with nuts.

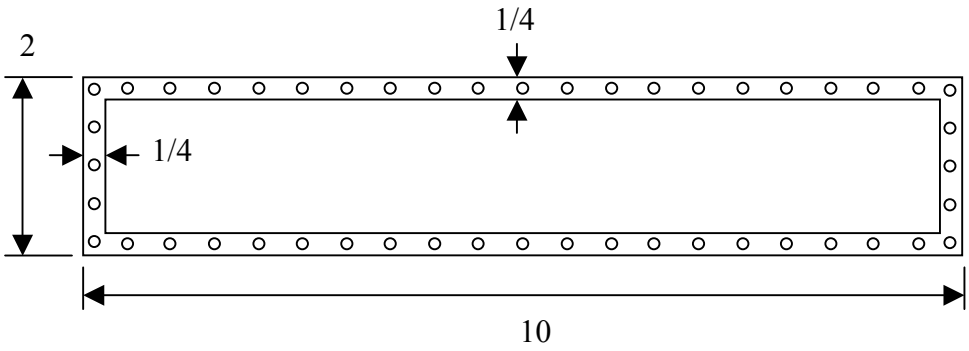

Figure 3.1.1.3—3A. TOP VIEW: Kapton film window retaining ring, 1/8" thick. (All dimensions in inches.)

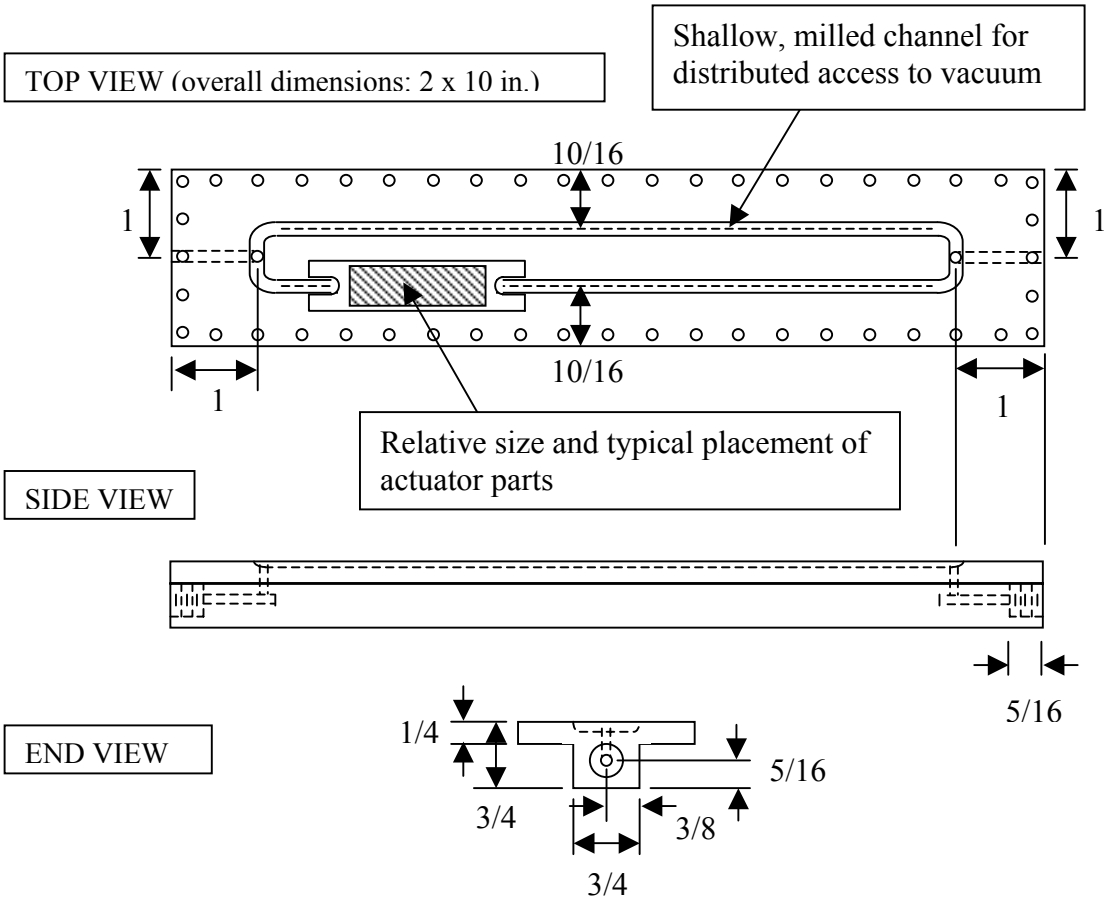

Figure 3.1.1.3—3B. Vacuum plate base. (All dimensions in inches.)

3.1.1.4 Fabrication with Alternative Adhesives

Some experiments had been conducted which indicated that pre-stress unimorph actuators fabricated at lower temperatures than required for LaRC-SI polyimide often provided comparable performance. To explore this, unimorphs were fabricated with epoxy adhesives—one (M-Bond 610) cured at lower temperature than LaRC-SI polyimide, the other (J.B. Weld) set at room temperature.

As noted in a short paper posted at [44], which summarized information from [45] deemed most pertinent to the problem of bonding of piezoceramics to metals, the only adhesive category judged compatible with both stainless steel and ceramics is epoxy. Epoxy alloys, such as epoxy-phenolic or epoxy-polysulfone are also candidates, and may offer superior peel resistance.

3.1.1.4.1 M-Bond Epoxy Adhesive System

Micro-Measurements (Raleigh, NC) M-Bond 610 is a two-component epoxy system sold in kit form for bonding strain gages and special purpose sensors. (Micro-Measurements Division is part of Vishay Measurements Group.) The components are each substantially diluted in tetrahydrofuran solvent with the intent of forming a very thin glue-line when the combined system is applied. The components are combined before use and stored in a brush cap bottle. Directions for use call for surface preparation identical to the method used to prepare for bonding with polyimide adhesive—metal surface roughening and solvent rinse for all surfaces.

After surface preparation, bonding with M-Bond epoxy adhesive is accomplished by the following general procedure.

1. Apply solvent-thinned adhesive. Allow solvent to evaporate for 5 to 30 minutes at 24ºC and 50% relative humidity, adjusted to longer times for lower temperature and / or higher humidity. Ten minutes was considered sufficient.

2. Position surfaces and press gently together. During the curing cycle, apply pressure from 10 to 70 psi for general work and 40 to 50 psi for transducers. A pressure of 40 psi was selected.
3. Following a time versus temperature graph in supplier's directions, a curing temperature of 175ºC was selected and applied for one hour, followed by post-curing at 210ºC (30º to 40ºC above maximum curing temperature) for two hours. (Start with cold autoclave to allow residual volatiles time to escape as temperature builds—rather than placing assembled materials in a pre-heated autoclave.)
4. Decrease temperature and release pressure.

One exception to the recommended procedure was implemented. Manufacturers of the M-Bond kit intended the solvent-thinned mixture to be brushed onto bonding surfaces. Brushed coats became viscous and gum-like in seconds. Touching up uneven areas often made things worse. The modified procedure was to spray M-Bond solution by airbrush. Immediately after each spray, a reservoir of pure THF was attached and sprayed through the airbrush for cleaning. This allowed considerably thinner and more uniform coats to be applied to the actuator parts than did application by brush. Three spray coats were typically applied because of the much thinner layer resulting from each spray. In one experiment, a set of actuators was made in which the bond thickness was varied by spraying one, two, or three coats on three different pairs of parts.

Unlike dried polyimide adhesive films, which had no tack, parts sprayed with M-Bond adhesive were sticky. If misaligned when pressed together, they could not be re-positioned. A simple technique helped to get perfect alignment on the first try. Ceramic pieces were held by the low-stick ends of strips cut from Post-It notes, positioned at right angles to the ceramic. Attached on their other surfaces to the spray box, they immobilized the ceramic pieces during spraying, but could be cut free and used as handles to turn each piece over and position it above a coated metal substrate before making contact. It was also helpful to use low-stick adhesive paper to mask the end tabs of substrates from spray.

Since curing temperature was well below the Curie point of the ceramic parts, the polarity of piezoceramic pieces remained essentially as poled by the supplier. Therefore, it was helpful to mark the surfaces identified as positive with pencil before cleaning, since solvent removed all inks.

3.1.1.4.2 Actuators Fabricated Using J.B. Weld Epoxy

J.B. Weld epoxy is a two-component epoxy system sold as a consumer product in hardware stores. Other high-perfomance consumer epoxies are available, but often have the viscosity of putty. Squeezed from metal tubes, J.B. Weld components yielded a mixture with the approximate viscosity of uncured silicone rubber sealant. The mixture remained workable for about five minutes, after which time viscosity had noticeably increased. Micrographs later taken of actuator cross-sections appeared to show that the resin is moderately filled with metal particles. Filled polymers are more rigid than unfilled polymers, although a high filler content, as in conductive epoxies, tends to lower adhesion. The product package advertised good adhesion to a wide range of materials in addition to strength and rigidity suitable for such jobs as repairing farm equipment.

Actuator fabrication with J.B. Weld epoxy began with the same roughening and cleaning techniques used in bonding with other adhesives. Dabs of blended components were applied to bonding surfaces with a large needle. The objective at this stage was to cover all surfaces quickly and with approximate uniformity. Then a razor blade was drawn across each layer with light pressure to remove all but a thin, uniform layer of the epoxy and was wiped with lab tissue in between each draw. Using either needle-pointed forceps or a low-stick adhesive paper method, the ceramic pieces were turned over and positioned on the similarly coated substrates.

Using the forceps for light tapping, pressing, or wiggling, the ceramic was aligned, leveled, and any entrapped air was forced out from in between the layers. The assembled pieces were placed at equidistant locations on an aluminum block which had guide pins protruding through its corners, perpendicular to its surface. Another matching aluminum

block with holes for the guide pins was placed in a smooth motion on top of the positioned sets of assembled pieces. Ideally, it would rest in a position perfectly parallel to the base block.

The pieces were moved to a level place where they would not be disturbed for 24 hours (if not already located there) and a 0.5 kg mass gently placed at the center of the top aluminum block. No part of this assembly was shifted, moved, or re-positioned until after 24 hours had elapsed. Some epoxy adhesive was invariably forced from in between the metal and ceramic by the weight on top. Consequently, it was important that both aluminum blocks had been wiped with a generous amount of Frekote mold release agent and allowed to dry before positioning and compressing the actuator parts. Otherwise, it would not have been possible to remove the cured actuators. After cure and removal from the block fixture, epoxy flashing was removed with sandpaper.

A range of cold-bonded actuators was made. Relatively thin bonds were achieved by wiping away most of the epoxy coating with the razor blade; thicker bonds were achieved by drawing lightly, using the blade mostly to level the coatings on each surface. (In this case, the stack of actuator parts sandwiched between aluminum blocks was compressed by a 200 g mass rather than a 500 g mass. Some actuators were made with thin wires of known diameter embedded in the uncured epoxy to achieve a specific bond thickness. However, in all cases, the bonding layers in actuators made with J.B. Weld adhesive were substantially thicker than the bonding layers in actuators made with the other adhesives described previously. An important observation is that the J.B. Weld epoxy layers in actuators functioned not only as adhesive, but also functioned mechanically as part of a composite substrate.

3.1.2 PSU Actuators Bonded at Room Temperature Under Load

Observations indicated that carefully loaded PZT sheets used in actuator fabrication (190 μm thick) could withstand deflection similar to that obtained by differential thermal contraction in bonded actuators. A fixture with two bolted Nylon sleeves 1.25 inches apart

was used to support 1.5-inch-long PZT plates, allowing 0.125 inch of ceramic to extend beyond the lines of support on either side. A three-point bending test determined a 1.74 mm deflection at failure, under a load of 56.6 g. Using equations from linear beam theory (3.1.2—1), this information gave a calculated Young's modulus of 30 GPa, which was lower than expected, compared with a modulus of 66 GPa in supplier data. Nonetheless, many finished PSU actuators have maximum deflections between 1—3 mm resulting from differential thermal contraction. The experiment described suggested that the brittle ceramic plate could withstand mechanical bending of a comparable magnitude.

(3.1.2—1) For a simply supported beam, single concentrated load at center,

$$\delta_{MAX} = \frac{P\,L^3}{48\,E\,I}, \quad I = \frac{b\,h^3}{12} \quad \rightarrow \quad E = \frac{P\,L^3}{4\,b\,h^3\,\delta_{MAX}}$$, where δ_{MAX} is deflection at center, P is applied load in Newtons, L is beam length, E is Young's modulus in Pascals, I is moment of inertia of a rectangular beam section of width b and height h (all lengths in meters).

To evaluate the effect of pre-stress in a unimorph actuator induced by a means other than differential thermal contraction, eight pairs of actuators were fabricated using J.B. Weld epoxy as an adhesive. Pre-stress was developed by loading the stacked actuator parts while the adhesive was uncured. After cure, the load was removed, but the rigid adhesive prevented a full recovery of the deflected substrate and ceramic layers.

Loading was accomplished in two ways. Figure 3.1.2—1 shows the first method: a mass placed at the center of upside-down actuator parts subjected them to three-point bending. Figure 3.1.2—2 shows an arrangement for sandwiching actuator parts within a highly compliant, two-layer beam which was loaded and supported so that the section containing actuator parts bent under pure applied moment. The pure moment approach was devised after observing that the deflected curvature of the actuators made under direct load was visibly larger at their centers, where the circular mass contacted the stacked parts. This could have resulted from localized deformation in the metal substrate, which could not transmit shear through the uncured adhesive and was effectively supported by the ceramic

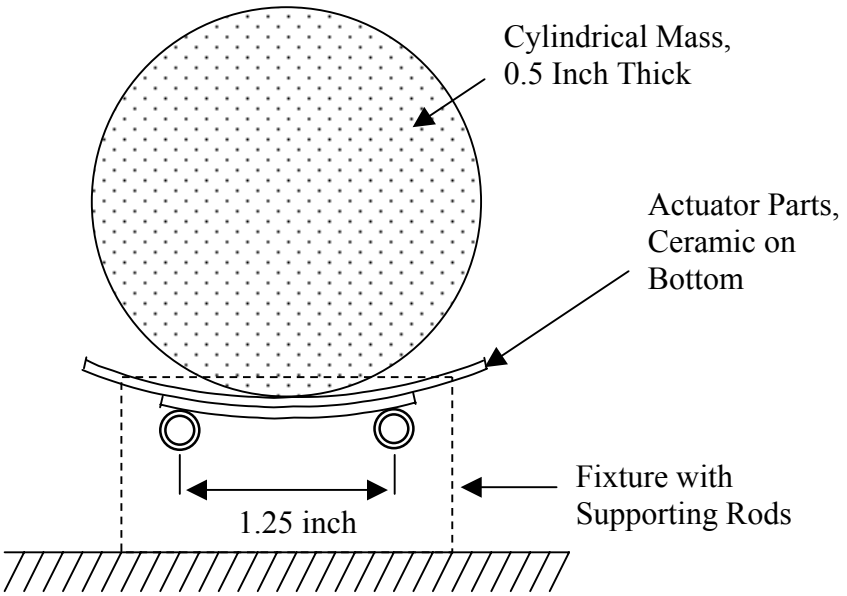

Figure 3.1.2—1 Upside-down actuator parts bonded under three-point bending load.

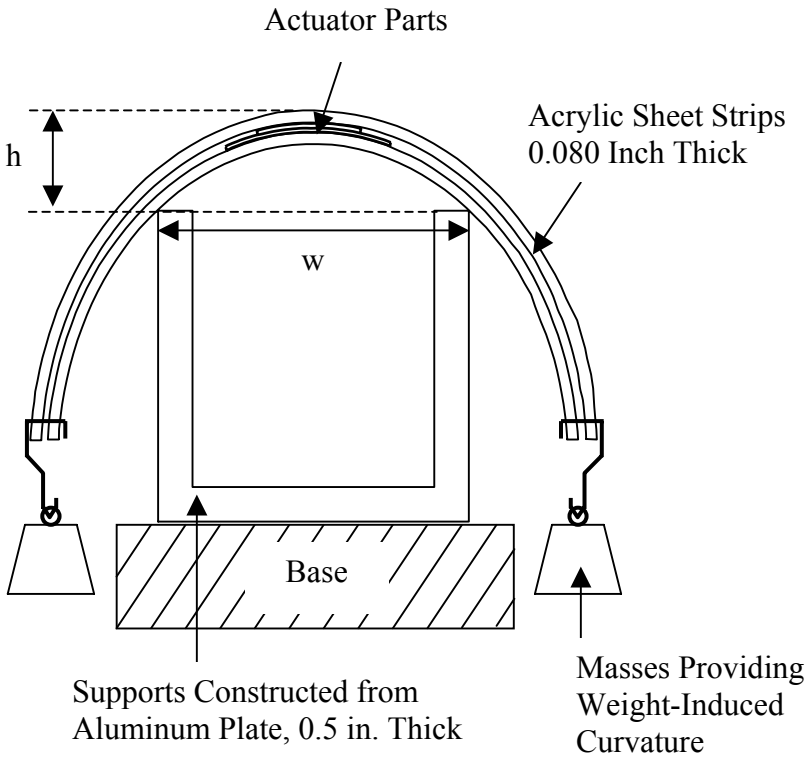

Figure 3.1.2—2. Bending by pure applied moment between supports

directly under the load. It seemed preferable to find a way to induce more uniform bending in both layers. What appears to be a single piece supported by a U-shaped piece of aluminum in Figure 3.1.2—2 was actually two L-shaped pieces which could be set at a variable distance, w, apart. The horizontal part of each support would have faced outward to allow this.

Eight pairs of "ASUL" actuators ("Actuators Set Under Load") were made. Table 3.1.2—1 lists the names and distinguishing characteristics. Certain actuators did not survive fabrication, namely ASUL031703B and LastASUL-B (not included in Table 3.1.2—1). When the series of actuators pre-stressed by applied moment was created, the plan was to increase curvature (decrease radius of curvature) as new pairs were fabricated until an appreciable number had been fabricated or further decrease was not possible.

Table 3.1.2—1 ASUL actuators (All dimensions in inches.)

Actuator Name	Distinguishing Characteristic	w (see Fig. 3.1.2—2), If Applicable	h (see Fig. 3.1.2—2), If Applicable
ASUL021513A,B	8-mil Substrate, Proof of Concept, 300 g Load		
ASUL022803A,B	Flat		
ASUL030703A,B	3-Point Bending, 100 g Load		
ASUL031203A,B	Moment Bending	6.75	0.5625
ASUL031703A	Moment Bending	4.25	0.5625
ASUL032103A,B	Moment Bending	5.25	1.0625
ASUL032603X,Y	Moment Bending,	4.3125	0.21875

3.1.3 Actuator Cross-Sections

Upon completion of PSU actuator fabrication and characterization, a selection of 90 actuators representing a cross-section of design variants and commercial actuators was embedded in clear, metallographic sample prep epoxy (Epoxy Set Resin and Hardener, Allied High Tech Products, Rancho Dominguez, CA). The purpose was to determine bond layer thickness by cutting cross-sections for examination under magnification as well as to determine overall curvature in the actuator long dimension under low magnification.

The actuators were inserted into five-slide, polyethylene transporter boxes (Fisher Scientific) with cardboard tabs glued onto each end because the actuators were a little less than 2.5 inches long whereas the boxes were designed to carry microscope slides three inches long. Once actuators were inserted, the slide boxes were filled with weighed, blended epoxy components, which cured in 24 hours.

The embedding resin appeared to be an excellent product, but it should be noted that the curing reaction is exothermic and temperature-accelerated. Too large a volume of curing resin created a runaway process: the resin bubbled and darkened. This was discovered by setting some filled boxes too close to one another to allow adequate heat dissipation, perhaps less than one-half inch. The samples were rescued for analysis by prompt immersion in cold water. However, a set of large-diameter round actuators were later embedded while the container used for a mold was immersed in ice.

The blocks containing embedded actuators were rough cut with a high-quality hacksaw. One rough cut goal was to produce a block that left the actuator piezoceramic plate surrounded by about 2 mm of resin on all six sides, which implies that most of the metal shim end tabs were cut off. The other rough cut goal was to produce cuts such that block faces were parallel to each other and with top, bottom, and each pair of edges of the actuator. Due to the slight actuator curvature, the top and bottom cuts were parallel to an imaginary chord subtending the arc of the actuator. Considerable care was taken to mark, store, and otherwise track the identity of each embedded actuator.

A lengthwise cross-section was cut using a diamond saw (Buehler Isomet low speed diamond saw, Buehler, Ltd.). Cutting the 90 specimens took about two weeks; polishing the cross-sections would have taken as long as three months, which could not be accommodated. Therefore, each sawed edge was lapped sequentially with 400, 600, 800, 1200 grit silicon carbide metallographic paper disks, which was still faster than polishing. Resulting specimens were mounted on glass slides in modeling clay using a sample press to set cut edges parallel to the glass slide. Each cut face was examined at several locations under a microscope equipped with Nomarski prism contrast and video camera frame capture capability. Each half of a cut specimen was examined. Resulting graphic file images were measured with Photoshop graphic editor. The relationship in pixel dimensions between adhesive bond layer thickness and scale bars superimposed by the microscope, allowed bond thickness determination.

3.1.4 Load-Displacement Test Equipment and Methods

Characterization of both commercial actuators and actuators fabricated in-house was central to this investigation. To obtain quasi-static voltage-displacement-load data, vertical displacement was measured using a linear variable differential transformer (LVDT) mounted in an apparatus shown in Figure 3.1.4—1. The actuator under test could be loaded by placing slotted weights on an enlarged section on the shaft connected to the LVDT core. Figure 3.1.4—1 also shows a mounting fixture for beam actuators which provides controlled end conditions. Each end of an actuator was clamped into an axle, which was free to rotate unless pinned by a bolt (not shown—on top of axle mounts). One axle is mounted in a socket slightly elongated in the horizontal direction, allowing translation during actuator flexure unless blocked by a bearing-tipped machine screw. (Allowing translation in both axles is redundant.)

In general, characterization assumed unrestrained rotation and translation of ends (“free” end conditions). However, based on the capability for selectively blocking end translation or blocking one or both end rotations, an experiment was conducted to

determine the effect of selectively constrained or unconstrained end conditions on actuator performance.

A linear variable differential transformer (LVDT) is a type of inductance transducer which can resolve very small displacements, producing a proportional voltage output signal. An LVDT shell contains a primary winding and two secondary windings. An oscillating excitation voltage is applied to the primary winding, inducing a voltage signal in the secondary windings. The secondary windings are connected in phase opposition, so that the amplitude of their combined voltage signal varies as the difference between the

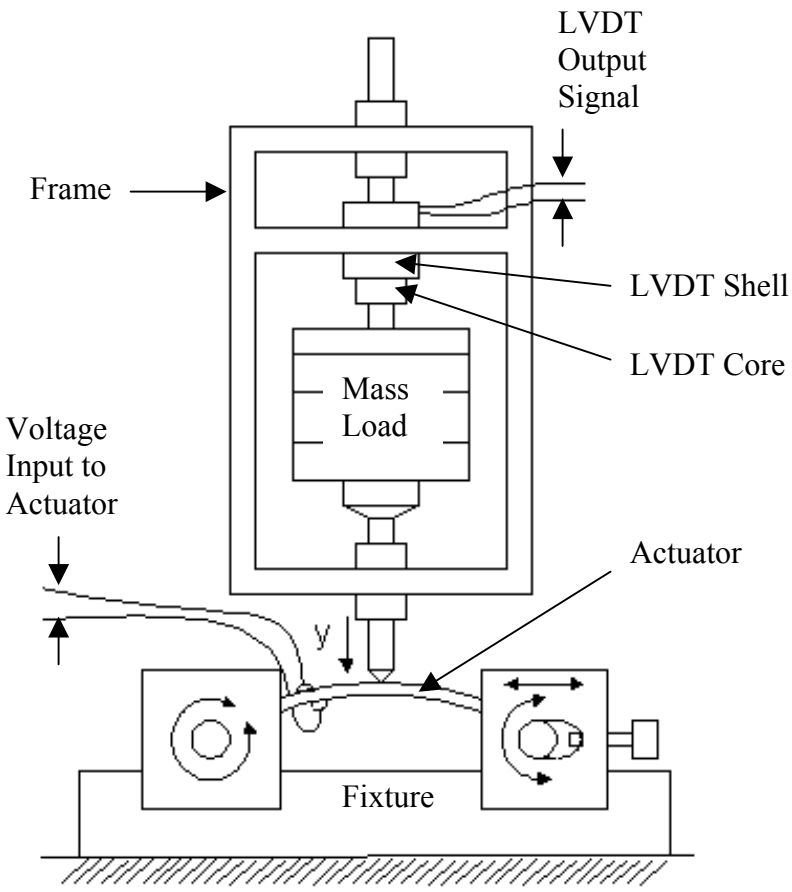

Figure 3.1.4—1. Apparatus for voltage-displacement-load characterization of actuators

voltages induced in each. A ferromagnetic core concentrates the magnetic field and has a null position, where equal voltages are induced in both secondary coils for a net output of zero.

Displacement from the null position in either direction changes the ratio of mutual inductance and outputs a positive signal which has a linear range typically limited by the width of the primary core. Signal conditioners can provide a bipolar output voltage so that direction of travel can be determined. A rotary variable differential transformer (RVDT) operates by the same principles, but has a rotating magnetic core for measurement of angular displacements. [9]

An LVDT has limited usefulness in measuring dynamic displacement, and is not well-suited for measurements at greater than 10% of the excitation frequency. In addition, the mass of the core creates some inertial load. [9] An Omega Engineering, Inc. transducer, model LD100-20, was used in the apparatus described, in conjunction with a model SP200A signal conditioner / processor. It uses an excitation signal of 5 kHz, and has a range of 0.5 inch, which yields an output signal from –10 V to +10 V. Measurements of dynamic displacements measured by LVDT were limited to less than 200 Hz.

Equally important for actuator characterization was a set of LabVIEW^{TM} programs (National Instruments Corp.) which provided instrument control and data acquisition. LabView provides a graphical environment for program development without directly using a programming language. In combination with NI-DAQ I/O channel management and signal conditioning software, LabView facilitates creation of a computer interface to control and / or acquire measurements from external equipment. This is displayed to the user as a "VI" or "virtual instrument," that is, a computer window depicting a stereotypical instrument face with buttons and sub-windows for input values, processed output values, or plotted curves. The characterization system used LabView 5.0 with NI-DAQ 6.1.0 operating through an ATE series DAQ multifunction I/O board, AT-MIO-16DE-10, all produced by National Instruments.

The project used three VI programs. Two of the programs were modifications of a foundation program which will be referred to as "TP.vi". TP.vi was originally created by

Brian Dessent, graduate student in Electrical Engineering, NC State University. The program conducted a test routine which involved two nested loops. The inner loop applied a series of voltages to an actuator by sending discrete voltage outputs scaled by the gain of a Matsusada model HEOPT-0.6B100 high-voltage amplifier for input (Matsusada Precision, Inc.). The specific voltages derived from maximum and minimum voltages entered in the VI front panel divided by "number of voltage levels" also in a front panel window. The outer loop asked the user to configure the test fixture for a series of 17 load levels which were hard-coded into the LabView program and paused execution until input was entered. When ready, the user selected either "continue" or "skip" from a pop-up dialog box. Assuming skip options were not selected, the inner loop repeated automatically at each load level, and LVDT response at each load-voltage condition was acquired by LabView, which compiled the data into a table (array) and wrote them to a csv-format text file at the end of program execution. Figure 3.1.4—2 depicts the operation of TP.vi in flowchart form.

The organization and features of this program proved remarkably useful, particularly for work flow. For example, a sub-window in the VI front panel was labeled, "output data file: filename.csv". After the first data at zero load were acquired, the program searched its folder in the computer directory to determine if "filename.csv" already existed. If not, a new file was created; if yes, new data was appended to the existing file. Furthermore, by allowing "continue" and "skip" options at each load level, the user could skip to a level in the middle of the sequence, say 800 g, take data for that load, then skip to the end of the program. (By pressing the "Enter" key to continue and the "Esc" key to skip, such a process could be done quickly.) A user could write to different output data files between such partial executions. By not allowing new data to replace existing data, data previously taken was not lost simply because the user forgot to rename an existing file.

In Figure 3.1.4—2, the process steps labeled "determine input channel measurement range" and "acquire and average 20,000 data points," refer to important functions conducted by the program. Stepping to discrete voltages caused mechanical ringing in the test actuator. Sampling for changes in variability ("determine input

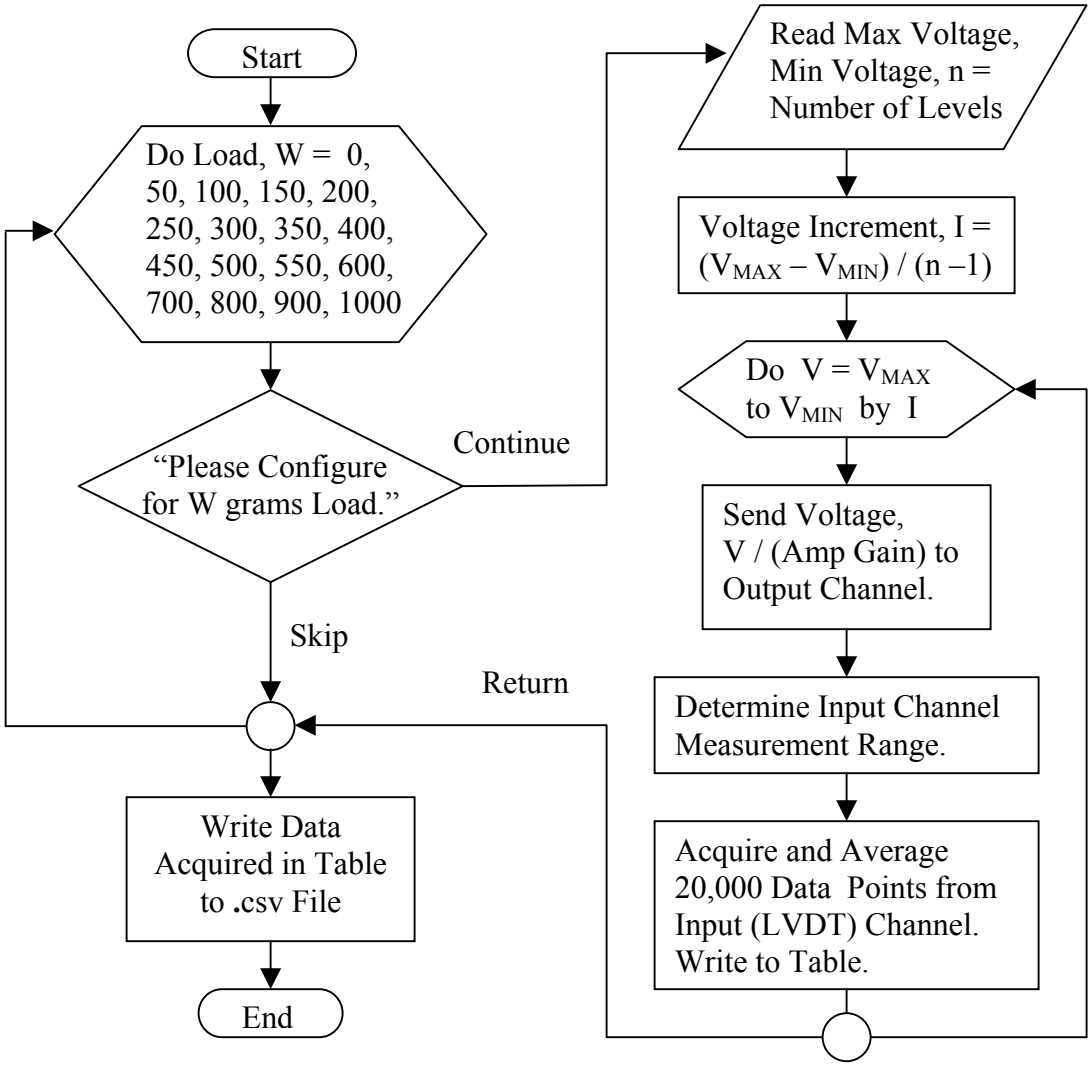

Figure 3.1.4—2. Conceptual flowchart of TP.vi program execution

channel measurement range") established when the actuator had stabilized. However, LVDT signals sampled at a relatively fast data acquisition rate will continue to show a baseline variability after transients have dissipated. The resulting jitter is clearly visible in plotted form. (See, for example, "typical displacement performance" figures in [1].) By averaging two seconds of data taken at 10,000 data points per second, the central tendency at each test condition was resolved and smooth curves could be plotted.

The two modifications of TP.vi were called butterfly_3.vi and nestedloops_3.vi. My first modified program was developed to measure large-signal displacement-voltage loops (aka butterfly loops because of their shapes) by stepping from zero voltage to a positive maximum, back to zero, then to a negative maximum, and back to zero. The other program, nestedloops_3.vi, was a single-polarity version of butterfly_3.vi. It was designed to cycle in stepwise fashion from zero voltage to a positive maximum, then back to zero. Although the resulting plot should not be confused with polarization-electric field loops, commonly known as hysteresis loops, the single-polarity displacement-voltage loops also display a hysteretic effect (because of the coupled electrical and mechanical effects).

The single-polarity loops were especially useful as an alternative to constant (DC) high-voltage for poling or re-poling an actuator because their so-called saturation edges gave an indication whether the net polarization had approached the effective maximum achievable (because the slopes would appear asymptotic to an undetermined horizontal value). Since butterfly loops switch actuator polarization, experiments were planned so that nestedloops_3.vi would be run before subsequently measuring voltage-displacement-load performance on the same actuator if a butterfly loop had previously been measured.

Some additional LabView functions were introduced into the organization of TP.vi to create the modified programs. The butterfly_3.vi program used the "number of voltage levels" value, n (renamed "number of data points"), entered on the VI front panel to divide 2π into angular increments of $2\pi / n$ which were input to a sine function with an amplitude of V_{MAX}, as in equation (3.1.4—1). A result of using this approach to cycle between negative and positive extreme voltages was that voltage levels applied to an actuator were not equally spaced.

(3.1.4—1) $V_i = V_{MAX} \sin \theta_i : \ \theta_i \leftarrow \theta_{i-1} + \frac{2\pi}{n}, \quad i = 1 \ to \ (n-1)$, where θ was initialized to zero.

To further modify the TP.vi program to get nestedloops_3.vi , a vertical shift was introduced into the function for discrete voltages based on angular increments. Adding $+V_{MAX}$ to the function given in (3.1.4—1) caused it to range between zero and $+2V_{MAX}$. The better choice, then, was to reduce both the amplitude of the sine function and the vertical shift to ½ V_{MAX} . A vertically shifted sine function no longer starts at zero, so a phase shift was also necessary. The necessary function is developed in (3.1.4—2).

(3.1.4—2) $0 = 0.5\ V_{MAX}\ (1 + \sin \theta_0\ ) \rightarrow\ \sin \theta_0 = -1\ \rightarrow \theta_0 = -\ \frac{\pi}{2}$

However, $V = 0.5\ V_{MAX}\ (1 + \sin\ (\ \theta - \frac{\pi}{2}\ )) = 0.5\ V_{MAX}\ (1 -\ \cos \theta\ )$,

since $\sin\ (\frac{\pi}{2} - \theta\ ) = \cos \theta$ and $\sin\ (-\ \theta\ ) = -\ \sin \theta$.

Thus, $V_i = 0.5\ V_{MAX}\ (\ 1 -\ \cos\ (\ \theta_i\ ))$ was substituted for the function in (3.1.4—1) to create nestedloops_3.vi from butterfly_3.vi .

To calibrate the relationship between LVDT signal and actuator position, a scaling factor (in μm/V) was determined. Originally this was done by stacking a number of thickness gauges and measuring the resulting incremental voltage shift in the LVDT signal. Later calibrations were conducted by resting the bottom tip of the shaft in the displacement-load apparatus (Figure 3.1.4—1) on a vertically mounted, micrometer-driven translation stage. The LVDT core was raised or lowered in 5-mil (0.005 inch) increments by micrometer while acquiring the response voltage with the TP.vi LabView program, in which the amplifier input signal was disconnected, the number of voltages set to two, and the load values served only as markers in the data file. Restarting the program as often as necessary appended additional data. Using LabView was not only convenient for data collection, but also gave the benefit of generating averages of the sampled LVDT signal. Figure 3.1.4—3 shows a typical full-range calibration curve, which is nearly linear, especially in mid-range.

A particular LVDT core, shell, and signal conditioning box formed a matched set to which a specific calibration curve applied. A slightly different calibration factor was obtained if the core entered the shell from the top or from the bottom. Steps were taken to keep matched instrument components together and use applicable calibration factors. As a reality check, note that the full-scale output signal divided by the total range of the LVDT yields the value in (3.1.4—3), similar to the value shown in Figure (3.1.4—3).

(3.1.4—3) $$\frac{\left(25400\ \frac{\mu m}{inch}\right)\left(0.5\ inch\right)}{20\ V} = 635\ \frac{\mu m}{V}$$

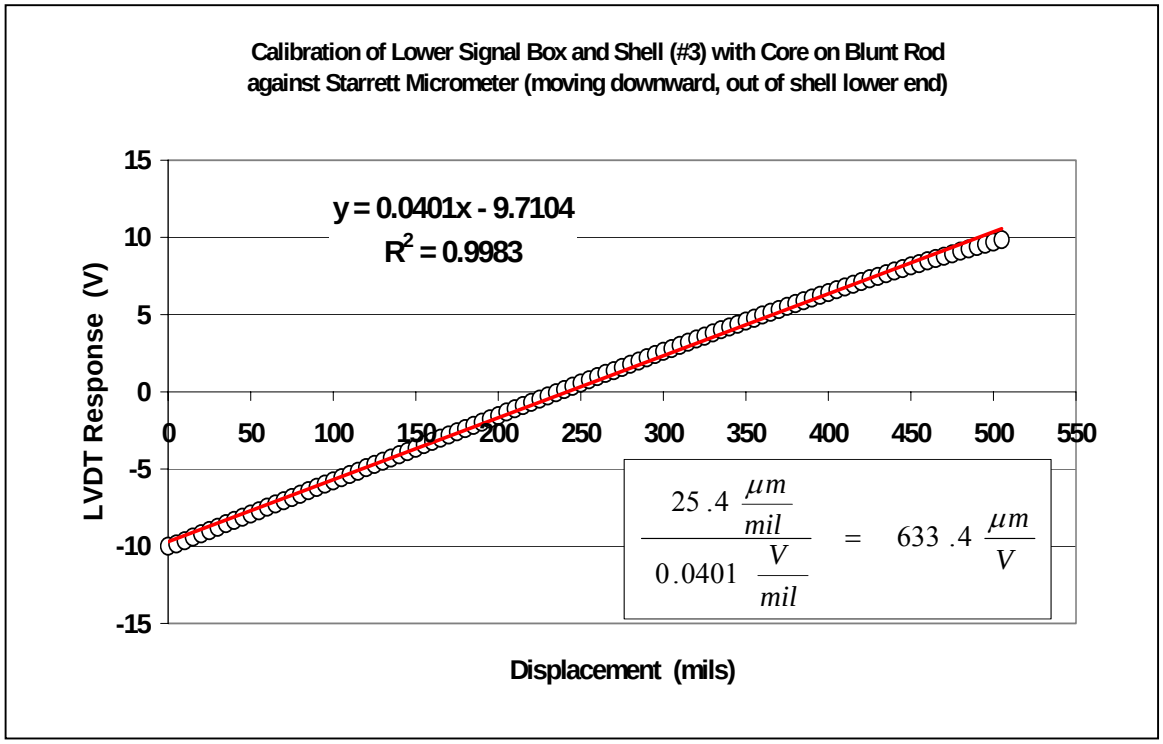

Figure 3.1.4—3. Typical LVDT calibration curve by micrometer method

3.2 Using the Angstrom Resolver® Non-Contact Displacement Gauge

3.2.1 General Principles and Recommendations

Whether characterizing an actuator (especially a compliant one) in quasi-static or dynamic operation, any measurement technique that makes physical contact introduces some change in its position and displacement. If an experiment involves resonant behavior, then weight and inertia of contacting mass will shift the resonant frequencies. Clearly, a non-contact gauging method would be desirable. The Angstrom Resolver® non-contact displacement gauge is not the only non-contact gauging instrument available, but is used in many laboratories, as in ours. Background and operating principles of this instrument will be explained in detail.

The term *optic lever* refers to a class of non-interferometric techniques for using the modulated radiant power of a reflected beam of light to measure dynamic displacement of a surface, based on knowing the proportionality of reflected power with displacement. By then converting reflected radiant power to a proportional electrical signal via photosensor, a non-contact displacement transducer is available. [10]

Two patents were granted in 1966, 1967 for the nearly simultaneous realization by two researchers that the reflection of the diverging annular cone of light emitted by step-index optical fibers provided the means for a sensitive optic lever. [11, 12] A principal feature of such an instrument is a fiber optic bundle in which a central illumination fiber is packed within a concentric ring of reflection-receiving fibers, all terminated by perpendicularly cut and polished ends in a probe tip. A basic seven-fiber arrangement is depicted in schematic form in Figure 3.2.1—1. A high-power illumination source connects

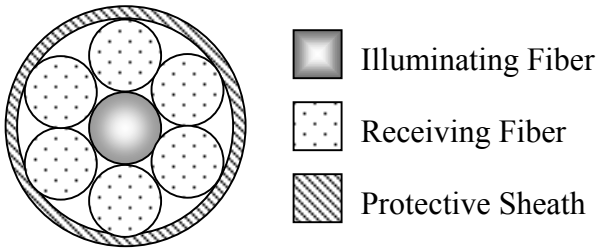

Figure 3.2.1—1. Schematic cross-section of fiber optic lever probe tip

with the illuminating fiber; receiving fibers connect with a photosensor. A stable fixture holds the probe at a fixed standoff distance from a reflective target, ideally at a perpendicular orientation to its surface.

The particular instrument used in this research was an Angstrom Resolver® model 201R two-channel fiber-optic gauge with 300 μm tip probes, 2 m long, manufactured by Opto Acoustic Sensors, Inc. (Raleigh, NC). The illumination source was an 860 nm LED (near infrared, approximately 5% visible). A standard calibration method at specified instrument settings is detailed in the Technical Manual. [13] The standard optical target surface was aluminized reflective tape sold in camera stores (used to mark off photographic negatives). A reference calibration under standard conditions was provided with the instrument. For many applications, especially if complex vibration spectra or low signal-to-noise ratio were involved, the instrument output would ideally be sent to a spectrum analyzer. However, the output signal can be displayed on an oscilloscope. (In this project, a Tektronix TDA 3014 four channel color digital phosphor oscilloscope, 100 MHz bandwidth, was used.)

The fiber optic gauge photodiode inputs to an operational amplifier (op amp) configured as a current to voltage converter operating in the inverting mode. Consequently, the DC output (and any modulated DC response signal) of the photosensor has negative polarity. However, all measurements taken for this project are presented as absolute magnitudes without reference to the negative polarity. The op amp provides sensor amplification from –10 to 50 dB, selectable on the front instrument panel. Since "sensor gain" in dB equals 20 $\log_{10}$ (V_{OUT} / V_{IN}), the gain ratios would be 1, 3.162, 10, or 31.62 V/V, for settings of 0, 10, 20, or 30 dB. Further discussion of sensor gain and introduction of signal gain, both of which must be accounted for in converting the amplitude of the instrument response voltage to actual target displacement amplitude, are discussed below.

The instrument back panel provides three different outputs for each fiber optic probe channel (A and B). The sensor gain setting determines a primary level of amplification by the photosensor for all three outputs. Also, the reading shown on a front panel DC display used for calibration reflects the sensor gain setting in the sense that the

gain from the photosensor op amp has created an analog muliplication of what its output would be with sensor gain set to zero. The digitized value of the amplified signal is shown on the front panel display.

The photosensor-amplified output is conducted without further processing to a pair of outputs on the back panel called “A AC/DC” and “B AC/DC”. A branch also conducts photosensor-amplified output through a high-pass filter intended to attenuate the effects of low-frequency building vibrations. The high-pass-filtered, photosensor-amplified signal is conducted without further processing to a pair of back panel outputs called “A1”, “B1”. A second branch also conducts the high-pass-filtered, photosensor-amplified output to a signal amplifier intended to boost low amplitude AC over the equipment noise floor. One can adjust signal gain from the front panel for higher-voltage instrument output in response to very small target displacements. The doubly amplified and filtered signal is sent to a pair of outputs on the back panel called “A2”, “B2”. The signal gain settings are simply gain ratios: 1, 10, 100, and 500 V/V.

Deviations from standard reflectivity, from flatness or smoothness of the target surface, or perpendicularity of probe orientation relative to the target surface all affect the usefulness of reference calibrations under standard conditions which are provided with the instrument. *In situ* calibration is prescribed in such circumstances. This requires a calibrated fixture (e.g., micrometer translation stage), which allows a calibration curve to be generated under the specific physical conditions of a given experiment. Based on previous experiences using another group’s identical instrument without a micrometer-driven probe holder, we decided to purchase micrometer translation stages (J.A. Noll Co., Monroeville, PA, model NTS 213 with Starrett model 283 micrometer) with probe holders and mounted them on a stable structure. With this capability at hand, it was also decided that taking *in situ* calibrations at the start of each experiment would become standard procedure.

Calibration curves were acquired by stepping through one mil increments from near contact with the target surface to whatever distance was appropriate *while the target surface was <u>not</u> moving*. Typically, during experiments with unimorph-driven motors, one

calibration curve was generated by translating from far away (e.g., 4 mm) to near contact (approx. 10μm—when measured values "bottom out" near zero volts), then a second curve taken after reversing micrometer direction to move the instrument probe far away from the target. The two curves were slightly shifted due to backlash upon reversing micrometer direction. If position as well as displacement was important in an experiment, then position relative to the second curve was used.

Once instrument output voltage as a function of displacement has been determined under specific experimental conditions, *then AC and DC response are the same*. [13] This key principle has been tested to MHz frequencies. [14] The calibration or response curve always has a shape similar to that depicted in Figure 3.2.1—2.

The peak of the curve is a key feature. Its location is determined by observing instrument response first increasing then starting to decrease when probe movement is continued without changing direction. Usually, it is not necessary to determine an entire calibration curve, just the portion of interest—front or back slope—relative to the peak. Based on the set of all complete calibration curves taken (about 45), the peak was located at 24 or 25 mils from the target surface about 75% of the time, with the full range from 22 to 28 mils.

Generally, the instrument has been manufactured with the expectation that users will position a fiber optic probe at a standoff distance which causes the V_{DC} levels shown in Figure 3.2.1—2 to fall into an approximately linear range of either the front slope or back slope of the response curve. The V_{DC} level corresponding to the standoff distance is often called the operating point—the DC bias around which an AC response signal fluctuates.

Since the front slope is steeper and thus indicates larger instrument response to any physical vibration amplitude, it would be preferable to choose the front linear range, unless target displacement is so large that instrument response spills out of the linear portion of the front slope, or even so large that response spills out of the entire front slope range by crossing the peak. In such a case, one uses the back slope, which is less steep and thus indicates smaller instrument response to any physical vibration amplitude.

Note also that when using the front slope, absolute magnitude of instrument response increases when the target moves away from the probe; when using the back slope, absolute magnitude of instrument response decreases when the target moves away from the probe. Therefore, the two localized responses are 180º out of phase. The term absolute magnitude was used, of course, because the displacement gauge output has negative polarity. The calibration curve could be plotted "upside-down" if we wanted to faithfully reflect this fact.

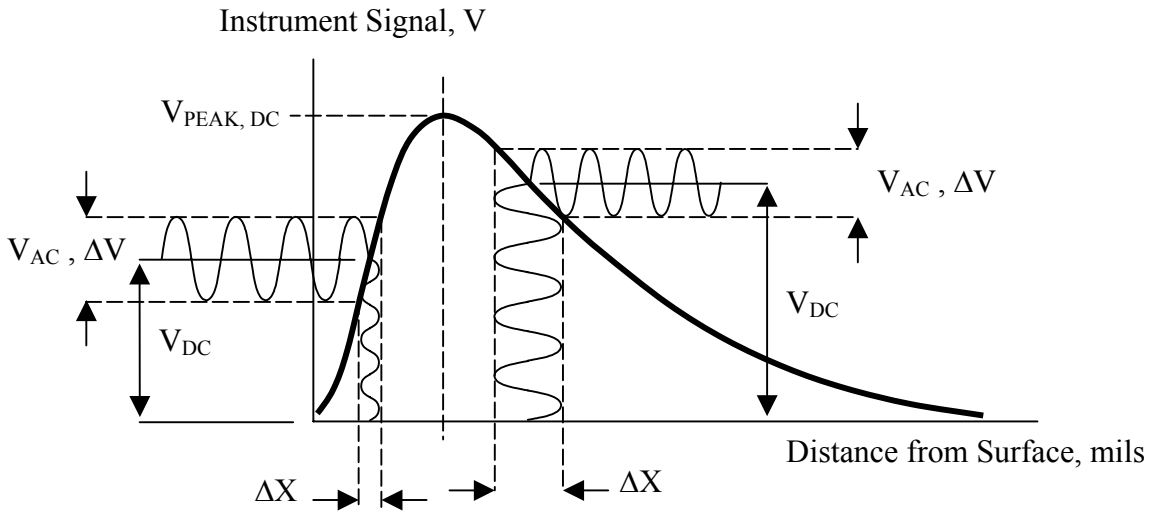

Two Different Dynamic Displacements of Target Surface
as Measured on Front Slope (Left of Peak) or Back Slope (Right of Peak)

Figure 3.2.1—2. Generic shape of an Angstrom Resolver displacement gauge calibration curve showing transducer response in front slope linear range and in back slope linear range

The advantage of taking measurements around an operating point, V_{DC} , set within linear regions is that the inverse calculation for obtaining average target displacement, ΔX, from instrument V_{AC} amplitude (referred to as ΔV, hereafter) is greatly simplified. Only the slope of the linear region, ΔV/ΔX [V / mil], is needed. Its inverse is simply ΔX/ΔV [mil / V], and the operating point can be disregarded. The distance unit "mil" (1 mil =

0.001 inch) is used because the instrument manufacturer uses it and most micrometers made in the U.S. are scaled in thousandths of an inch. We converted to microns by calculation (1 mil = 25.4 μm exactly), and of course, one could directly generate a calibration curve using a micrometer scaled in microns.

Recalling that the sensor gain affects all instrument outputs, including the front panel display used to compile the calibration curve, and that signal gain affects the A2,B2 outputs, a preliminary "calibration factor" equation for determining ΔX from ΔV taken from A2,B2 outputs is given by (3.2.1—1).

$$\Delta X\ [\mu m] = \frac{25.4\left[\frac{\mu m}{mil}\right]}{\frac{\left(\frac{\Delta V}{\Delta X}\right)_{SLOPE}\left[\frac{V}{mil}\right]}{G_{SENSOR}}} * \frac{\Delta V\ \ [V]}{(G_{SENSOR})(G_{SIGNAL})} \quad \text{(3.2.1—1)}$$

, where G_{SENSOR} and G_{SIGNAL} are sensor gain and signal gain, respectively, in [V/V], and the notation $(\Delta V/\Delta X)_{SLOPE}$ is used to indicate that it is a pre-determined constant—the measured slope of a linear region of the calibration curve. To determine G_{SENSOR} in [V/V] from the front panel setting in dB, one would have to calculate the exponential quantity, $10^{(\text{PANEL SENSOR GAIN} / 20)}$. However, as is apparent from (3.2.1—1), sensor gain cancels from the expression and does not have to be included. The values shown by the front panel display have experienced analog multiplication by the sensor gain. One could divide all front panel indicated values by the sensor gain and also divide all ΔV measurements by the sensor gain, but that would be pointless. Thus, a simplified version of (3.2.1—1) is given by (3.2.1—2). Note, however, that once a calibration curve has been created under a particular sensor gain setting, all subsequent measurements should be made *without changing the sensor gain setting* for as long as the particular calibration curve is expected to apply. If using back panel outputs A AC/DC, B AC/DC or A1,B1, signal gain (G_{SIGNAL}) will not apply and can be dropped from equations (3.2.1—1) and (3.2.1—2).

(3.2.1—2) $$\Delta X\ [\mu m] = \frac{25.4}{(SLOPE)(G_{SIGNAL})}\left[\frac{\mu m}{V}\right] * \Delta V\ [V]$$

In some of our first experiments that used the Angstrom Resolver Displacement Gauge, we faithfully applied (3.2.1—2) to measured ΔV (same as V_{AC}) values taken from A2,B2 outputs, but noticed that the resulting dynamic displacements seemed unexpectedly small. After a test experiment and consultation with the manufacturer, it was concluded that the high pass filter affecting both A1,B1 and A2,B2 outputs was attenuating the output signal. More often than not, our unimorph actuators were operated at less than 100 Hz, rarely above 400 Hz. Building vibrations are typically less than 50 Hz, and the high pass filter is designed to attenuate only lower frequencies. (The manufacturer can install a filter with even lower frequency exclusion.)

Nonetheless, the filter rolloff appeared sufficiently gradual that measured ΔV at almost any frequency under 1 kHz appeared diminished. (The instrument is particularly well-suited for measuring vibrations at ultrasonic frequencies—greater than 20 kHz.) As a result, in nearly all experiments with the displacement gauge, it was decided to use the A AC/DC, B AC/DC outputs as a signal source. In this case, signal gain does not apply and can be dropped from equations (3.2.1—1) and (3.2.1—2). Note also that when displaying the AC/DC output on an oscilloscope, the oscilloscope must be set for AC coupling, that is, nullifying DC bias. The V_{DC} component is typically so much larger than the V_{AC} component that failing to do this will produce problematic results.

The Angstrom Resolver displacement gauge was used in an experiment with the purpose of mapping the general dynamic behavior of a THUNDER actuator as a function of both frequency and load. The shaft of the apparatus depicted in Figure 3.1.3—1 was capped with an aluminum reflector (disk with threaded socket) covered with aluminized tape (the standard target surface). The displacement gauge probe was mounted in a micrometer-driven translation stage clamped to a sturdy ring stand.

Endnote: Explanation for the Shape of the Calibration Curve

Two physical factors contribute to the shape of the curve. Figure 3.2.1—3 illustrates the origin of these factors. On the one hand, in moving from close surface proximity to greater standoff distances, (A) the receiving fibers initially intercept only a few low-angle (relative to surface) reflections falling across part of their receiving ends while a substantial portion of light is reflected back into the illuminating fiber. Then (B), light reflected through a range of angles is captured through a maximum cross-sectional area. Then (C), only a few high-angle reflections are captured while most of the reflected light entirely misses the outer perimeter of the probe tip.

On the other hand, reflected light power increases or decreases (inversely) depending on how large an area of target surface is illuminated by the annular ring of light emitted by the illuminating fiber. If the probe is closer, a smaller area is illuminated; reflected power is greater. If the standoff distance is increased, a larger target area is illuminated; reflected power weakens. This is depicted in Figure 3.2.1—3 by showing the annular illumination spot becoming lighter gray and less well-defined as its size increases.

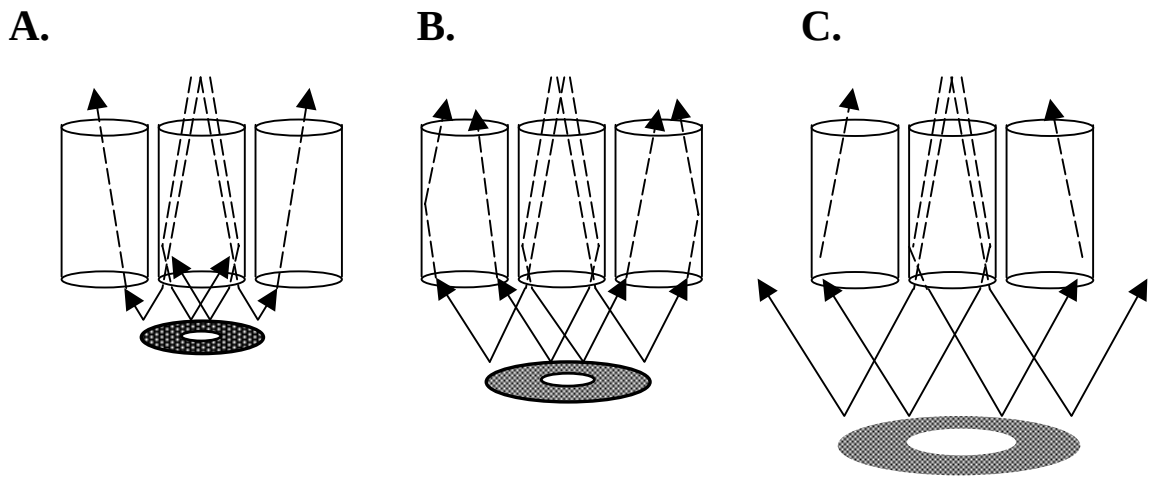

Figure 3.2.1—3. Schematic illustration of interaction between capture angle of receiving fibers and reflected radiant power based on area of illumination. Middle cylinder represents illuminating fiber; outside cylinders represent receiving fibers. (See text for discussion of cases A, B, and C.)

As the probe moves away from the surface, the received power builds rapidly due to the intensity of light reflected from a small area. A peak output is obtained when reflected light is mostly captured by the receiving fibers *and* reflected power from a moderately enlarged illuminated area is still relatively high. As standoff distance is further increased, a substantial amount of light is reflected at such a large angle that it entirely misses the receiving fibers *and* a larger illuminated area reflects light at lower power.

While this provides a satisfying qualitative explanation, constructing a theoretical model which gave even an approximately correct prediction of the specific calibration curve arising from specific conditions would be extraordinarily difficult. [17] For example, a typical optical model would assume a single mode transmission. In reality, a non-collimated light source is used, multi-modal light transmission occurs, some light is reflected back into the illuminating fiber, some falls onto the spaces between receiving fibers, some is lost outside the probe. From zero degrees relative to the illumination fiber axis to the largest transmission angle the fiber will support, one would have to know the radiant power at each angle, perhaps by sweeping a pinhole sensor through the angular range. Then, however, the target is imperfect. One cannot know what returns through receiving fibers unless one knows the power at each angle reflected from the target. The return through each of the six receiving fibers is probably not identical, so a summation of unknown parts is involved, whereas a model would have to assume an average reflection return. Theory has been advanced to explain or critique simplified aspects of the full process, but in general, empirical models of the response curve are entirely justified.

3.2.2. Measuring Large Amplitude Displacements

Experiments to measure PSU actuator displacements at resonance—particularly those devoted to characterization of a motor discussed elsewhere, which used cantilever-mounted THUNDER actuators—often resulted in millimeter-scale displacements. However, using the Angstrom Resolver displacement gauge was necessary to avoid physical contact. Internal or external electronic means of diminishing the signals could have been attempted,

but it would have been necessary to generate calibration curves under the same conditions, which was not considered the best option. The large-signal measurements often extended beyond the linear range of either front slope or back slope of the response curve. Therefore, it was decided to explore techniques for non-linear inverse determination of target dynamic displacement from measured amplitude of the instrument voltage signal.

The first choice, in dealing with large displacements, would be to use the back slope linear range. For signals extending beyond the back slope linear range, one could try using a low-order polynomial fitted to the entire back slope data. A second or possibly third-order polynomial fit was needed because determining ΔX from ΔV involved taking the inverse function. Accomplishing this by mathematics other than closed-form analytical expressions would have been too involved. Figure 3.2.2—1 shows that a third order polynomial least squares fit matched the data very closely, giving at least 60 mils or 1500 μm of measurement range across the calibration curve back slope. Goodness of fit to this degree or better for cubic polynomials was typical of many measured calibration curves. Simple inspection revealed that second order polynomials of best fit were not adequate. A system of formulas for solving cubic equations can be implemented in a spreadsheet—one solution per row. An excellent modern explanation of the cubic solution method is given in [15].

Eventually, it became necessary to model the functional form of the entire curve. The motivation came mostly from a need to extrapolate the tail of the curve (to the right). In some experiments, it became apparent that the high end of a ΔV amplitude interval was crossing the peak. To avoid this, the setpoint was changed on the fly (which can be done if one is not concerned about staying within a linear region) by moving the probe farther from the target. Given the large amplitudes involved, this sometimes caused the low end of a ΔV amplitude interval to reach beyond the rightmost measured value in the calibration curve (which was not realized until data workup after the experiment had been completed). Extrapolation from a very good model was needed because the small slope of the curve in the tail meant that small variations in ΔV corresponded to large variations in ΔX. Thus, small errors in ΔV corresponded to large errors in ΔX.

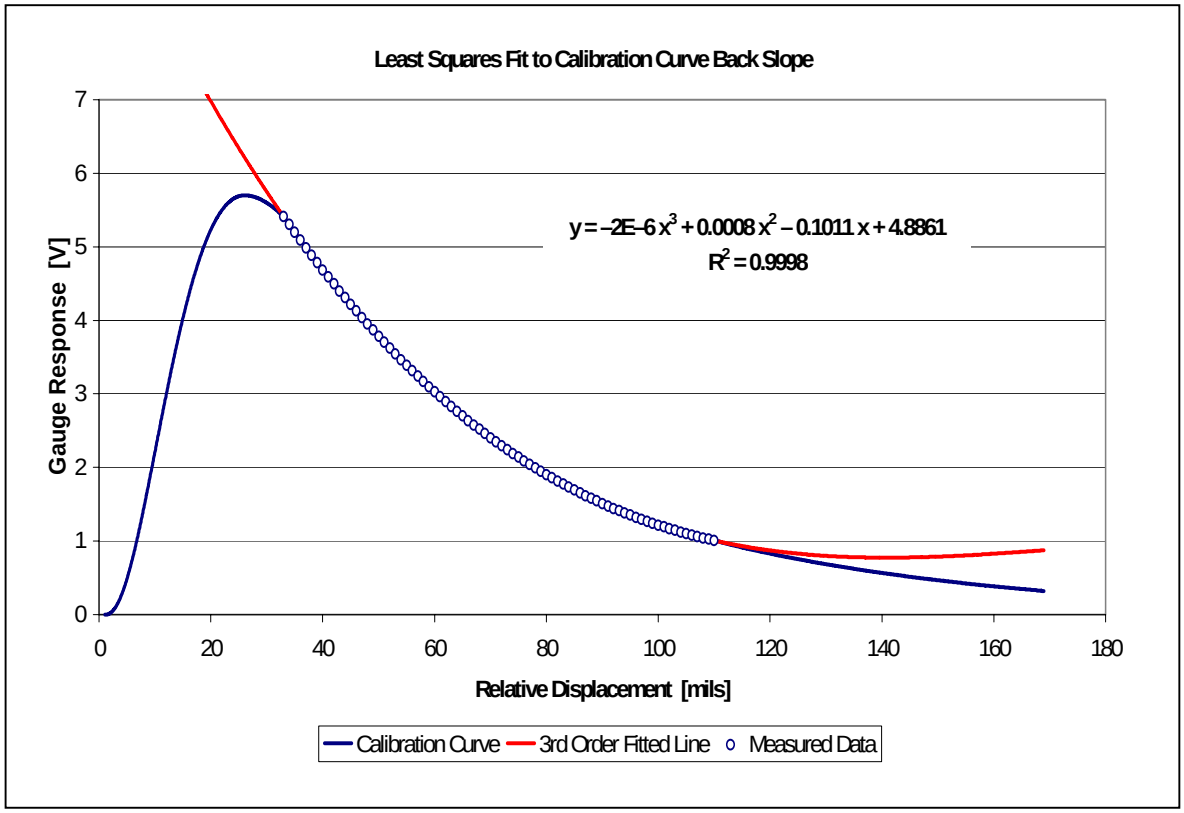

Figure 3.2.2—1. (color) Example of cubic polynomial fitted to back slope calibration data

A simple model good enough for presentation purposes was developed by taking the natural logarithms of independent and dependent data values. A plot yielded a curve resembling a shallow parabola. A polynomial fit to the curve was determined, then an exponential function was applied. A point of caution in using this approach: input values to the polynomial of best fit are the *logarithmic* values—squared, cubed, etc. The input to the exponential is the output of the entire polynomial which was fitted to the logarithmic values. The accuracy of the curve resulting from this model was undependable near the peak, but very convincing for extrapolating the tail of the curve. It became apparent that this type of model was not adequate when instances occurred where some very low endpoints of ΔV values yielded calculated ΔX values too large for credibility. A local

minimum followed by an upturn, as seen in figure 3.2.2—1, is typical of cubic fits to the calibration curve back slope. The logarithmic / exponential model follows the same trend on an extenuated scale. The actual calibration curve decays faster than such an approximation, and does not rebound.

The shape of the Angstrom Resolver gauge response curve resembles a number of skewed "bell-curve" functions. Its shape resembles that of a gamma probability distribution for a random variable X, a series which includes the negative-exponential function, $f(X) = ae^{-aX}$, as an initial, special case (b = 1). [15] Laplace transform solutions of LCR circuits yield such candidates as $f(x) = e^{-x} - e^{-2x}$ and $x\, e^{-2x}$. [16]

Consider the function $f(x) = Ax^n e^{-Bx}$, where A = 0. 1, B = 0.1, n = 2. A plot clearly resembles the response function of the displacement gauge over its typical domain. We would like to fit a function of this form to measured data from the response curve for the displacement gauge only by visual overlay and by knowing specified values for peak height and horizontal offset of the peak.

The x-value corresponding to the peak for $f(x) = Ax^n e^{-Bx}$, is found by setting the derivative function equal to zero, as in (3.2.2—1).

(3.2.2—1) $$f'(x) = nAx^{n-1}e^{-Bx} + Ax^n\left(-Be^{-Bx}\right) = \left(nx^{n-1} - Bx^n\right)Ae^{-Bx}$$

$$f'(x) = 0 \quad iff \quad nx^{n-1} - Bx^n = 0 \quad \rightarrow \quad n - Bx = 0, \quad x = \frac{n}{B}$$

Therefore, $f\left(\frac{n}{B}\right)$ gives the peak value of the function. For a measured peak value C, the function in (3.2.2—2) has a peak value C at $x = \frac{n}{B}$.

(3.2.2—2) $$f(x) = \frac{C}{f\left(\frac{n}{B}\right)} x^n e^{-Bx}$$

Including an additional coefficient A is superfluous because the pre-factor containing f (n / B) simply adjusts to cancel its effect.

The exponent, n, for a given B value, controls skewness, in the sense that the function to the left of the peak increases more steeply with increasing n and with increasing B than the function to the right of the peak. (This use of the term, "skewness," does not correspond to its precise statistical definition.) However, both values (n and B) must be adjusted to match the shape of measured data, which introduces added difficulty and subjectivity into the fitting process. (The most challenging aspect of the process is that the peak shifts location relative to the x-axis as either value is adjusted.)

This interdependence can be removed by setting $n = Bx$, based on $x = n / B$ from (3.2.2—1). With this modification, one sets a constant x where the peak value is located. Then the peak location remains fixed while B is adjusted to get the desired fit. The observed result is that decreasing the value of B produces a more outwardly bulging curve, while increasing B gives a more inwardly contracted curve. The value of n adjusts itself depending on adjustments made to B, given the fixed location of the peak. It ranges between one and two. The fixed location of the peak must be renamed because in defining the exponent, it has a constant value, whereas the full function still returns a value for each value of the variable x: $x > 0$. Therefore, let $x = L$ be the location of the peak.

Note that $f(n / B)$, in the (3.2.2—2) pre-factor, becomes simply $f(x = L)$, given $n = Bx = BL$. The function as developed to this point was also shifted horizontally to the right by one unit by substituting $(x - 1)$ for x. In compiling calibration data, this first data point was numbered one, not zero, whereas the theoretical calibration curve falls to zero at $x = 0$, not $x = 1$. An expression to reflect the modifications introduced thus far is given by (3.2.2—3), which will be referred to as the core model. Two additional modifications were made, one for the front slope, one for the back slope.

(3.2.2—3) $$f(x) = \frac{C}{L^{BL}\, e^{-BL}} (x-1)^{BL}\, e^{-B(x-1)}$$

The core model yielded insufficient curvature to fit front slope data. In other words, the modeled front slope was too linear, rather than having the elongated S-shape as initial

positive curvature shifted to negative curvature. A makeshift solution was to square the value of the entire function (only for x < L) and adjust the peak height input as mentioned below. Then it was realized that the fit became optimal if instead of squaring the values of the entire function across the front slope, the values were raised to the power n = BL. As a consequence of taking the entire core function to a power, however, the value of C in (3.2.2—3) must be replaced by C to the root n.

On the back slope, the core model decayed to approximately zero over a much shorter interval than did the calibration curve. The divergence appeared to begin at the back slope inflection point, where its curvature switched from negative to positive. The reader can verify by solving the second derivative of $f(x) = Ax^n e^{-Bx}$ set equal to zero, that this occurs at $x = \frac{n \pm \sqrt{n}}{B}$, where the numerator sum determines the back slope inflection point; the numerator difference determines the front slope inflection point. The differences between measured data and the model back slope were plotted, and it was found that the shape of the plot resembled the shape of the core model at reduced scale.

A correction function of the same form as (3.2.2—3) was devised using the same exponent value, n, as used by the core function. The location of its peak was the exponent value divided by its own B coefficient (call it b), which was adjusted to fit the plotted differences, once the height of its peak had been set to the data. To provide an adjustable height, the correction function also contained a pre-factor which was again the ratio of desired height (call it c) to the value of the function at the peak location—its L, so to speak, which we can call m. The correction function also contained a horizontal offset, i.e., substitute (x – k) for x, since the function would otherwise have started at x = 0. Although the optimal offset value was always approximately equal to the inflection point, better fit could be obtained by adjusting offset along with b and c. The back slope correction function was added to the core function for all values, x > k. Figure 3.2.2—2 shows a back slope correction function fitted to a curve of differences resulting from discrepancies between the data shown in Figure 3.2.2—3 and a fitted core model. The core

model curve is plotted in Figure 3.2.2—3 to show the effect of both front slope correction and back slope correction.

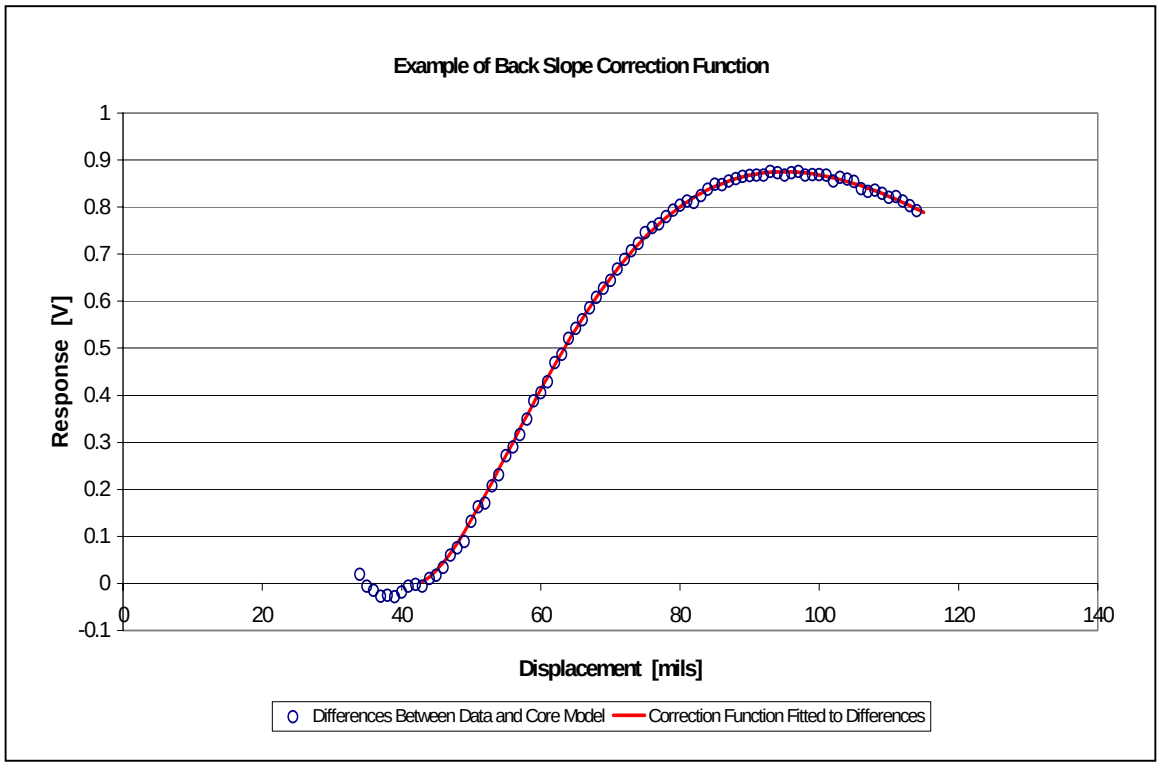

Figure 3.2.2—2. (color) Back slope correction fitted to curve of differences between data and core model (Data values and core model curve both plotted in Figure 3.2.2—**3**)

While this empirical model, which can be called the composite curve model, provided an excellent fit to displacement gauge calibration curves, obtaining a direct solution for the inverse function was not possible. This situation had already been dealt with, however, because a previous decision had been made to develop a finely-incremented lookup table which spreadsheets could search automatically. Unless the original data showed atypically high variability or had shifted during collection, measured data points were directly used by two layers of interpolation to return inverse values for specific high and low voltages defining a ΔV interval. The tail of the calibration curve was always

extrapolated, providing additional input points for interpolation. If flaws such as were just mentioned had occurred for a specific calibration, points from the fitted curve could be substituted for measured data where necessary and received the same interpolation treatment.

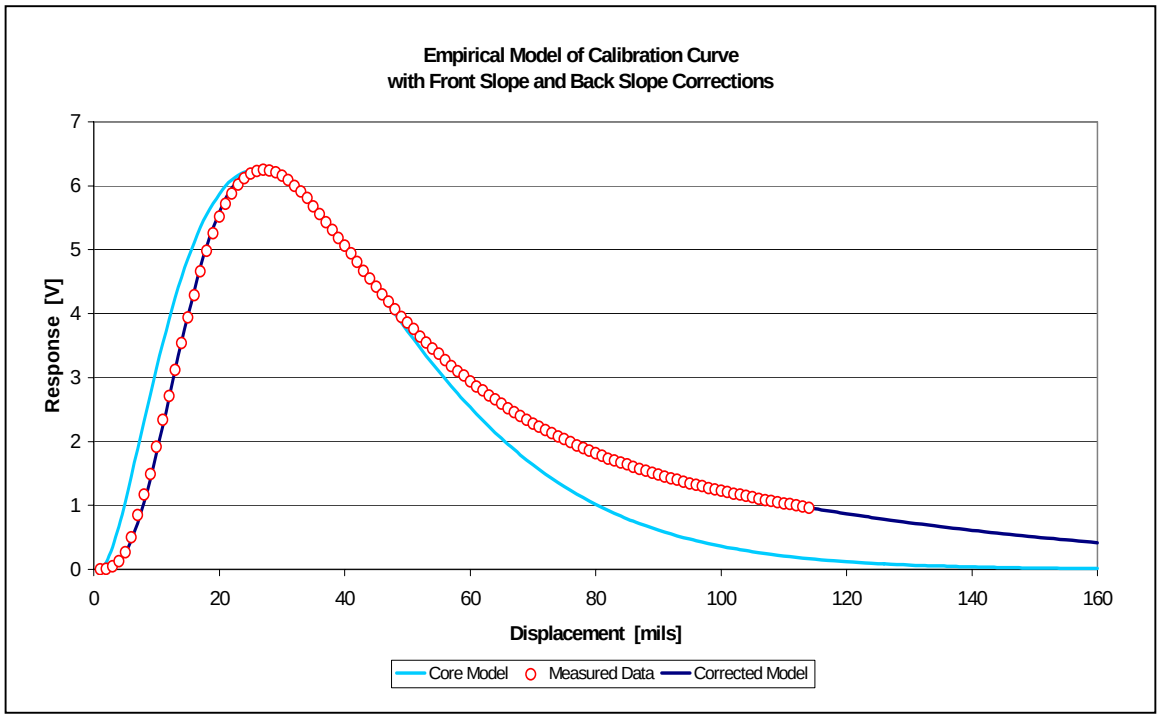

Figure 3.2.2—3. (color) Empirical (composite / corrected) model of calibration curve compared with source data and plot of uncorrected core model

The interpolation / lookup table process, conducted by blocks of template formulas in Excel spreadsheets, operated as follows. Three columns of formulas for determining the coefficients of second order (parabolic) least squares fit applied themselves in a rolling fashion to each successive set of three data points. Calibration points were always taken at one mil intervals, so the first interpolation layer created points at 0.05 mil increments. Since each data point was the initial point for one set of least-squares coefficients, the middle point for another, or the last point for the other, and since some parabolic curves

might match the calibration curve better than others, a two-out-of-three selection process was applied. The average of each set of three interpolations was taken and used to calculate a standard score of scatter relative to the average. Equation 3.2.2—4 gives the formula, where n = 3. Logic formulas evaluated to one if a standard score was less than or equal to one; zero if the score was greater than one. It appeared that this scheme almost always

(3.2.2—4) standard score = $\sqrt{\frac{(x_1 - \bar{x})^2 + (x_2 - \bar{x})^2 + (x_3 - \bar{x})^2}{n - 1}}$

returned two ones and one zero. Another column averaged the three interpolations with the logic formula values as weights. Thus, interpolations yielding standard scores greater than one were excluded. The first interpolation layer, then, created twenty well-determined intervals (nineteen additional values) for each original interval.

The automatic lookup process involved a small block of cells that was cut and pasted wherever needed like a special-purpose calculator in associated workbook sheets which handled experimental data other than the calibration curve. Half of the calculator was dedicated to the front slope, half to the back slope. A target value entered into the appropriate half was echoed to automatic lookup / secondary interpolation blocks of template formulas in the particular sheet dedicated to the calibration curve.

A column of absolute differences between the target value and each measured or interpolated voltage value on the curve updated itself. The minimum difference across the entire column was determined by a MIN(column range) formula. A column of logic formulas referring to the MIN() formula displayed “” (null string) unless the adjacent cell happened to contain the unique minimum value, in which case the minimum difference as a signed quantity was displayed by the particular logic formula that found it.

Only for the cell displaying a non-null value, two additional columns determined whether the target value fell into the interval formed by the cell containing the minimum and its predecessor or the interval formed by the cell containing the minimum and its

successor, based on the sign of the minimum difference. A linear interpolation formula was applied as illustrated by Figure 3.2.2—4.

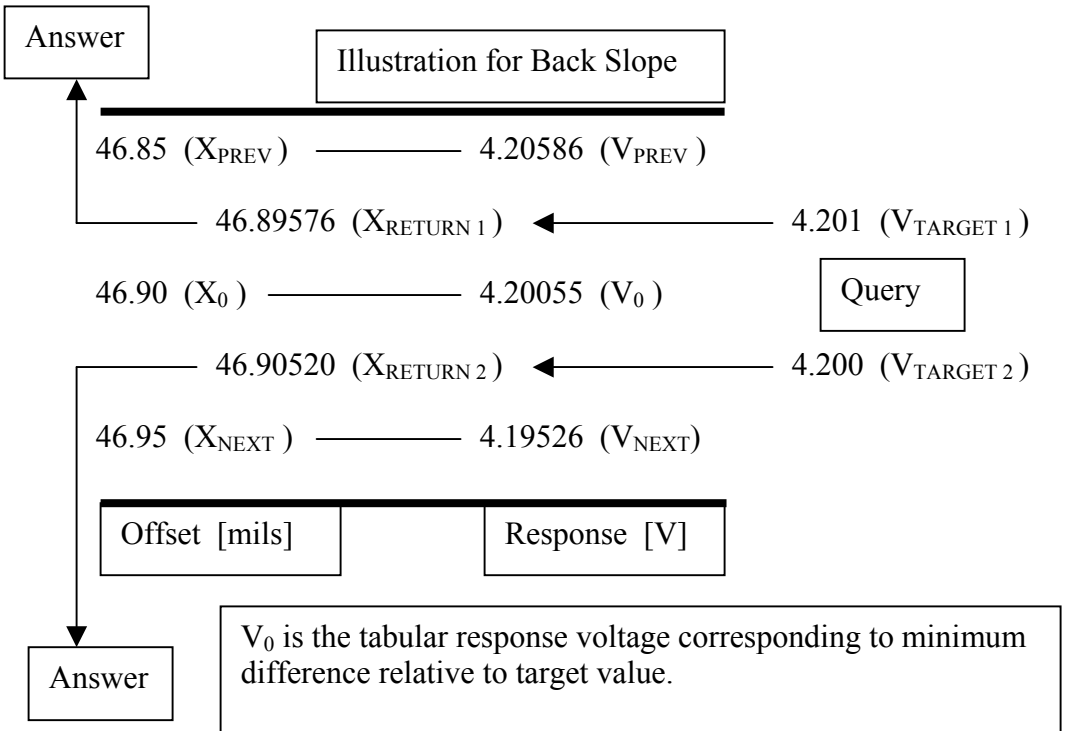

V_0 is the tabular response voltage corresponding to minimum difference relative to target value.

Let $D = V_0 - V_{TARGET}$ → $D < 0$ if $V_{TARGET} > V_0$
$D > 0$ if $V_{TARGET} < V_0$

If $D > 0$, take V_{NEXT} (Back Slope), or V_{PREV} (Front Slope)
If $D < 0$, take V_{PREV} (Back Slope), or V_{NEXT} (Front Slope)

$$X_{RETURN} = X_0 \pm \left(\frac{D}{|V_0 - (V_{PREV} \text{ or } V_{NEXT})|} \right) * 0.05$$

(X_0 +) for Back Slope, (X_0 –) for Front Slope

Figure 3.2.2—4. Scheme for automatic lookup and linear interpolation used with displacement gauge calibration curve

Finally, a formula summed the entire column containing only one non-null value from the lookup and secondary interpolation process (another formula counted to make sure there was only one). This was echoed back to the block of cells serving as a special purpose calculator, providing a nearly instantaneous result.

Although it has not been explicitly noted, two pieces of information were necessary to determine the dynamic displacement, ΔX, of the target surface if the instrument response signal, ΔV, spanned a non-linear section of the calibration curve. Not only was ΔV (measured by oscilloscope) needed, but also the operating point, or DC bias around which ΔV varied. V_{DC} was necessary to locate ΔV at some absolute position on the front slope or back slope. (The assumption was that the experimenter was aware whether measurements were coming from the front or back slope, which was not difficult to follow.) To determine ΔX, high and low voltages were calculated as $V_{DC} \pm 0.5\ \Delta V$. The high and low voltages were entered into the calibration curve automatic lookup table calculator, and ΔX was taken as the difference between the two resulting offsets from the target surface.

If a voltage interval was measured too close to the peak to remain on the back slope, then $V_{DC} + 0.5\ \Delta V$ would give a high voltage greater than the voltage level of the peak. In this case, the formula $V_{FRONT} = 2\ V_{PEAK} - (V_{DC} + (\Delta V / 2))$ gave a voltage reflected through the peak which could be entered into the automatic lookup table calculator for the front slope. Once again, ΔX could be taken as the difference between the resulting offset from the back slope less the offset from the front slope. Figure 3.2.2—5 demonstrates why the formula is correct. (If not convinced, imagine that the front slope of the bottom curve and the back slope of the inverted, top curve are invisible.)

The DC bias or operating point was taken from the same display (DC voltage LCD display) on the Angstrom Resolver gauge front panel as was used for calibrations. Since the oscilloscope was set for AC coupling, this seemed like the logical choice, but the assumption was that the front panel display indicated an average position during dynamic displacement of the target. The display was intended by the manufacturer to serve only for

indication of DC level. A low-pass RC network damps oscillations in the signal received by the meter at 6 dB per octave. However, if the vibration source caused a DC shift, one would see an indication in the meter provided the shift were relatively close to DC in terms of rate of change. [17]

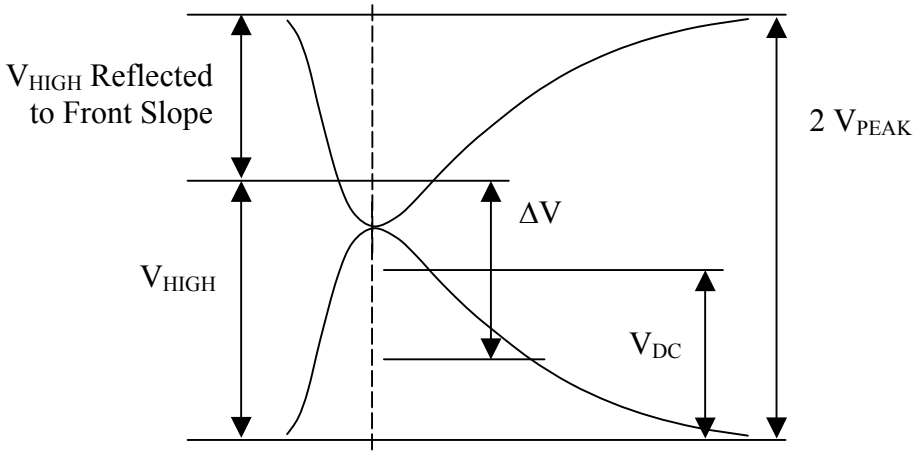

Figure 3.2.2—5. Schematic explanation of the formula, $V_{FRONT} = 2\ V_{PEAK} - (V_{DC} + (\Delta V / 2))$

Even if the shift were sudden (e.g., when first applying power to the actuator), the meter would eventually indicate a sustained, shifted magnitude even if voltage transients were excluded, provided the average position during vibration stabilized and did not fluctuate rapidly. General observations have indicated that the average position of a vibrating actuator is not the same as its static position, but that the dynamic average position is stable unless input voltage, frequency, load, or end conditions are changed. Even if one of these quantities is changed, the actuator stabilizes at a new average position, unless the operating conditions continue changing.

3.2.3 Using the Fiber Optic Gauge as a Tachometer

Chapter 8 discusses the performance of different motors driven by THUNDER

actuators. One of the motors discussed was a low-speed rotary motor. (The other two were linear motors.) Commercial tachometers can be expensive. One that was bought for another project gave wildly fluctuating values at low speed (less than 50 rpm). Therefore, rather than searching for another commercial tachometer with acceptable price and performance, an analog optical tachometer was designed which used the second probe of the Angstrom Resolver Fiber Optic Gauge. (The first probe was used for measuring vibration amplitude.) The Tektronix TDS 3014 oscilloscope served as a clock.

An optically modulating wheel was designed and built from art-grade cardboard. The central disk (outside diameter = 3.581 inches) was cut with an X-acto blade compass (U.S. Pat. No. 3,537,181). A black-and-white striped pattern was created using Microsoft Word and printed. The paper was bonded to cardboard with spray adhesive. The 0.5 x 11.25 inch rectangle was cut by razor blade, bent and glued to the central disk. Figure 3.2.3—1 shows a photo of the assembled wheel mounted on the motor. The pattern on the

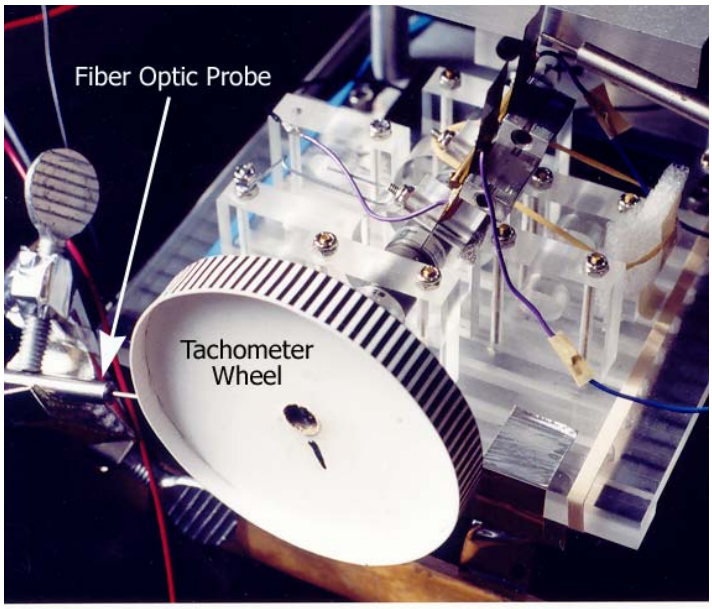

Figure 3.2.3—1. (color) Optically modulating tachometer wheel with probe to fiber optic gauge for measuring motor speed (Photograph by Kay S. Davis)

wheel rim was composed of 90 black-and-white-stripe pairs, each 0.125 inch wide, for a total circumference of 11.25 inches. In actuality, the seam was not perfect, adding an additional 0.0079 inches to the circumference. Thus, the actual wheel circumference was 11.2579 inches. Also, the black stripes were 0.070 inches wide while the white stripes were 0.055 inches wide due to differences in the printed pattern which were not apparent during composition. Nonetheless, the period of the pattern (the repeat distance) was 0.125 inch. From this information, a conversion factor between the repeat distance in time (as measured by the oscilloscope displaying the fiber optic gauge response to the spatial pattern) and motor speed was determined.

Given that the 0.125 inch spatial period equals 0.3175 cm, that the 11.2579 inch perimeter equals 28.5951 cm, and an average measured time period t (in milliseconds), the conversion factor is determined in (3.2.3—1). The distance-time relationship is illustrated by Figure 3.2.3—2.

(3.2.3—1) $$\text{Rotational Speed} = \frac{\frac{0.3175\ cm\ \ per\ period}{t\ \ ms}}{28.5951\ \frac{cm}{rev}} * 60000\ \frac{ms}{\text{min}} = \frac{666.2}{t}\ \frac{rev}{\text{min}}$$

The procedure was to stop the oscilloscope scan to capture a screen sample. The oscilloscope vertical measurement bars (v-bars) were alternately placed on identical, distinctive locations on each peak and trough combination to measure time intervals across the sampled wave train. The time intervals were averaged to determine an average period of the tachometer signal in milliseconds. If the modulated signal appeared uniform, then 20 to 30 periods were measured and recorded. If the wheel speed appeared to be fluctuating, several periods from two or three captured screens or from faster (narrower periods) and slower (wider periods) sections of the wave train were measured. A data collection spreadsheet averaged each set of results and converted average periods in milliseconds to motor speeds expressed as rpm.

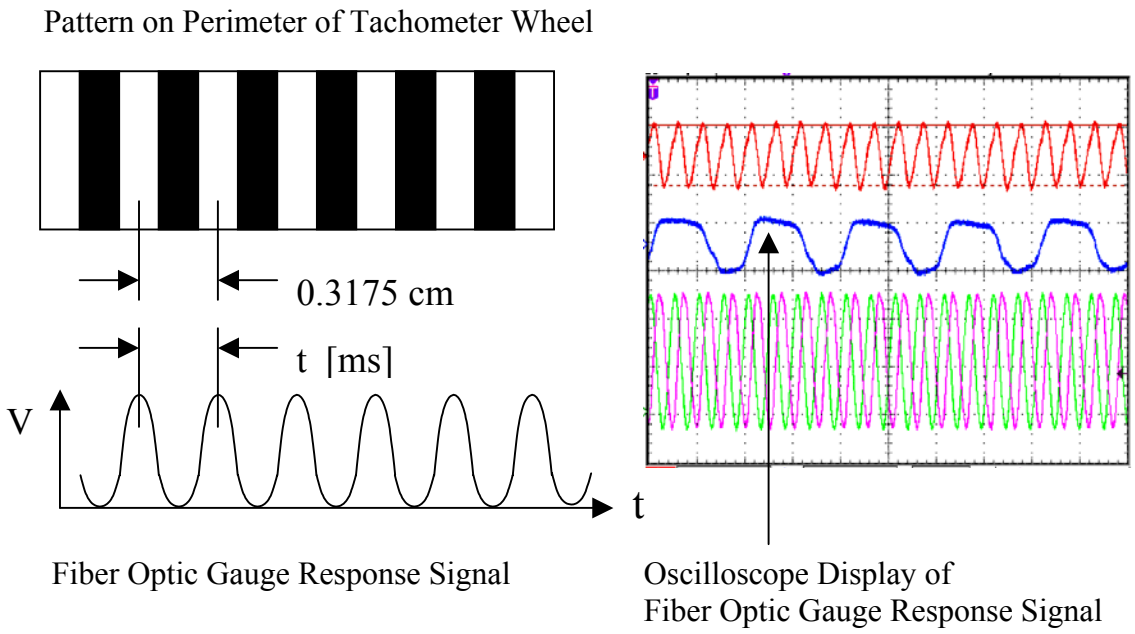

Figure 3.2.3—2. (color) Illustration of relationship between tachometer wheel pattern and optically modulated signal from fiber optic gauge

3.3 Providing High-Voltage, Out-of-Phase Drive Signals to the Motor

The rotary motor mentioned in Section 3.2.3 was designed to use two actuators, although single actuator configurations were also tested. An experimental objective was to compare motor performance when two actuators were driven in-phase with performance when actuators were driven out-of-phase, specifically 180º out-of-phase.

The Matsusada HEOPT-0.6B100 high-voltage amplifier (amp) with DC offset is suitable for driving two actuators with in-phase signals, but after considering options it was decided that using two amplifiers receiving input from the same function generator was the best approach for driving the actuators out-of-phase. Clearly, a circuit element would be required to split the original source signal into two out-of-phase signals. Unfortunately, the other high-voltage amplifier available, a TREK Model 609D-6, did not have internal DC bias capability, so yet another circuit element would be needed to provide DC bias to the

TREK amplifier. Also, the two amplifiers had very different gains, so the voltage of each part of the split, out-of-phase input signal would have to be adjusted to get equivalent outputs from each amp.

Full-wave rectifiers often use center-tapped transformers to generate two signals with 180º phase difference. By making the center tap the return or ground connection, each secondary half-winding has an opposite magnetic orientation to the primary winding, given the polarity of their connections to the secondary circuit. This produces the 180º phase difference. [18] A dual split bobbin transformer was used to generate the out-of-phase signals. The secondary winding was used as the primary, so the transformer was used to step up voltage at the expense of drawing more current from the signal generator. The split windings on the input side were connected, while the split windings on the output side were joined to a center tap connection. Figure 3.3—1 shows the entire circuit used to drive two actuators out-of-phase. Table 3.3—1 lists commercial and electronic information for the components.

The output of each amplifier, (1) and (2), at the right edge of the diagram in Figure 3.3—1, provided the driving signal for an actuator. The signal from the function generator, (3), approximately 20 V maximum, was split into two signals with a phase difference of 180º, as discussed, by the transformer (5). Precision wire-wound potentiometers, (7) and (8), acted as voltage dividers to control the inputs of the amplifiers which had different gain. The Matsusada amp had a gain of 60, while the Trek amp had a gain of 1000. The function generator had a DC offset, which can serve as input bias to an amplifier, but DC levels cannot pass through a transformer. The DC power supply, (4), provided DC bias for the Trek amp, but transferred its voltage offset through the variable resistor, (6), because a DC power supply generally has an internal capacitor across its inputs to protect its circuitry from any incoming AC signals. If the Trek amp were connected directly to the DC source, the power supply internal filter capacitor would act as a short to ground for all AC signal components. The capacitor, (9), likewise protected the rest of the circuit in Figure 3.3—1 from the output of the DC power supply by blocking DC bias.

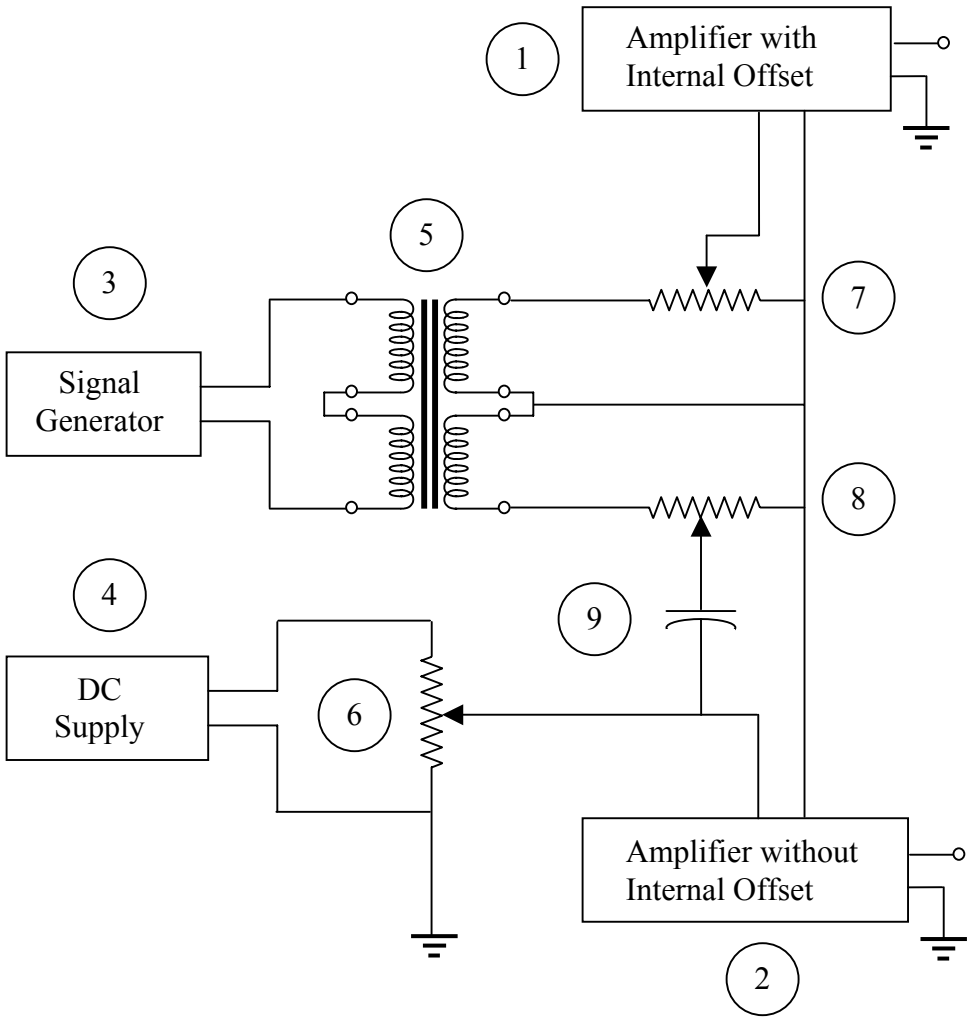

Figure 3.3—1. Equipment and circuit for providing high-voltage, out-of-phase drive signals to dual-actuator rotary motor

Table 3.3—1. Equipment and components in the circuit shown in Figure 3.3—1.

1. (High voltage amplifier with internal DC offset) Matsusada HEOPT-0.6B100
2. (High voltage amplifier without internal DC offset) TREK Model 609D-6
3. (Signal source) Tektronix CFG250, 2 MHz function generator (or) Leader LFG-1300S function generator, 20V output (sine waveform used)
4. (DC power supply) Manufacturer and model not recorded
5. Thordarson Meissner 20 VA MIM 721 Mini-iso-mite transformer (primary 115 / 230 VAC, secondary 5 / 10 VAC)
6. Colvern Ltd. Romford Wire Wound variable resistor CLR 4001/15 100,000 Ω
7. Spectra Precision Potentiometer, model 860-9734, 30 k Ω ± 3%, Linearity ± 0.1%
8. Spectra Precision Potentiometer, model 860-9734, 30 k Ω ± 3%, Linearity ± 0.1%
9. 0.12 μF capacitor, rated for 100 VDC

It happens that the two out-of-phase signals generated by the circuit shown in Figure 3.3—1 can be seen as the bottom channel displayed in the oscilloscope screen shot included in Figure 3.2.3—2, which was meant to illustrate fiber optic gauge response to the optically-modulating wheel described in Section 3.2.3. The end result was that the two driving signals were not offset by 180º, but by approximately 130º. This offset was reasonably constant (1º—3º variation) across the frequency range used. The suspected explanation is that by incorporating three large, precision wire-wound resistors as voltage dividers, the circuit also incorporated a large, unintended inductance which also influenced the phase of the output signals.

3.4 Motor Output Torque Determination

In Chapter 8, the design of a rotary motor driven by THUNDER actuators and characterization results will be presented. The equivalent of the blocking force of an actuator or linear motor is the blocking torque of a rotary motor. A mechanical load

receiving work through the rotation of a motor axle, and providing increasing resistance (counter-torque), will slow and eventually stop the rotation. Unloaded rotational speed, reduced speed as a function of increasing load, and blocking torque define the energy output of the motor under a range of operating conditions.

In this project, a brake stand served as a passive load by providing increasing levels of contact friction against the moving surface of the motor axle. The brake stand, pictured in Figure 3.4—1 supported a vertical shaft in linear bearings, upon which slotted weights could be stacked. The shaft had a hollowed end matching the curvature of the motor axle to provide good contact between both surfaces. Weight acting through the shaft applied a force normal to the horizontal axis of the motor axle, which, according to fundamental physics, resulted in a proportional force of friction acting tangentially to the moving surface of the axle in an opposing direction. The proportionality is the coefficient of friction (dynamic friction, in this case), which is generally a constant, given clean, relatively smooth surfaces of two homogeneous materials in good contact across an area.

As detailed in Appendix 2, the contact friction was tested at several levels of weight-induced-force normal to the motor axle. Plotted results, shown in Figure 3.4—2, indicate that coefficient of friction for this particular arrangement of materials is an inverse function of normal force which appears to be approaching a constant value. Why would the coefficient of friction be a decreasing function in this system rather than a constant value?

The best explanation available is illustrated by the view in Figure 3.4—1. Notice that there are approximately two centimeters between where the vertical brake force is applied to the axle and where the axle is supported by the vertical block and underlying structure. This creates a moment arm allowing the brake force to exert a torque on the body of the motor which probably tilts the motor slightly in the counter-clockwise direction (relative to the photograph) as brake load increases. Therefore, contact between brake shaft and motor axle would change with increasing brake load from surface contact to edge contact. Although friction is supposed to depend entirely on normal force and not area of contact in textbook discussions, we know that in practice surface area does have some influence, especially for very small areas of contact. Large force applied to an edge would

likely cause wear, surface contamination, and deformation, which would change the proportion of normal force appearing as tangential friction.

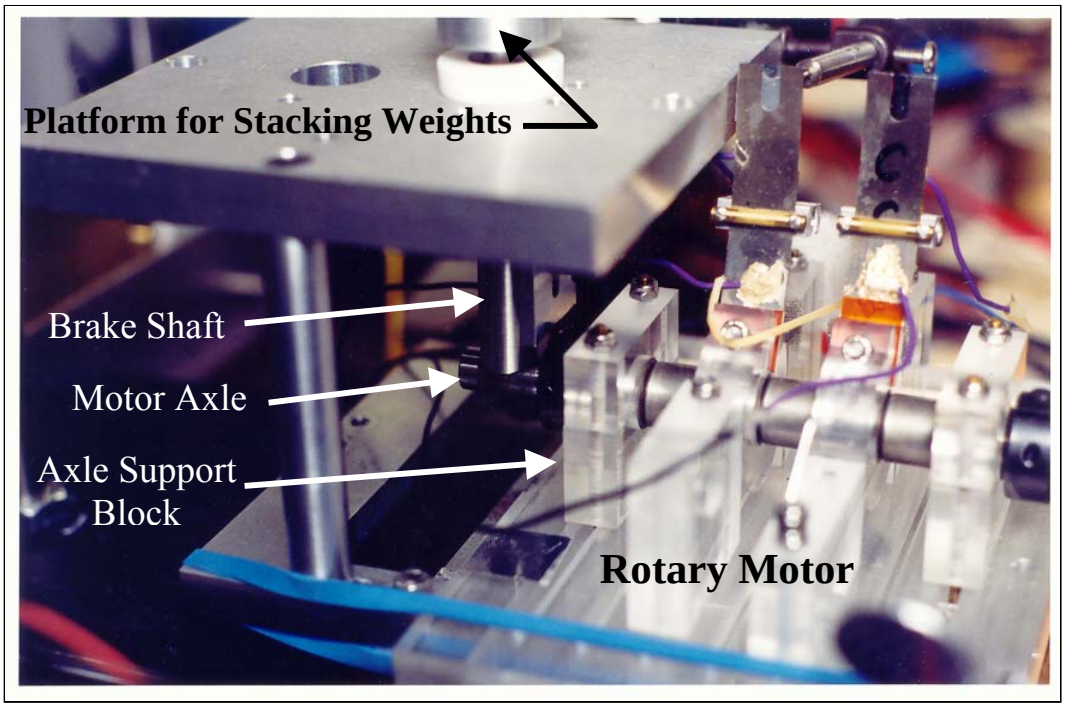

Figure 3.4—1. (color) Rotary motor in torque test stand showing contact between vertical brake shaft and motor axle (Photograph by Kay S. Davis)

The motor was fastened in the test stand and clamped on a corner of its base plate, but additional clamping hampered performance, probably by slightly warping the plastic base plate, thereby creating misalignment among other parts. So it would have been possible for the motor to tilt slightly because it was not a very rigid or tightly clamped structure. The original motivation for testing the actual proportion of resistance torque to normal brake force was that the motor axle accumulated narrow bands of surface contamination. It was thought that a reference book value might not accurately apply.

As notated on Figure 3.4—2, the curve fitted to measured data requires a piecewise function. The quadratic equation determined by least-squares method contains a minimum

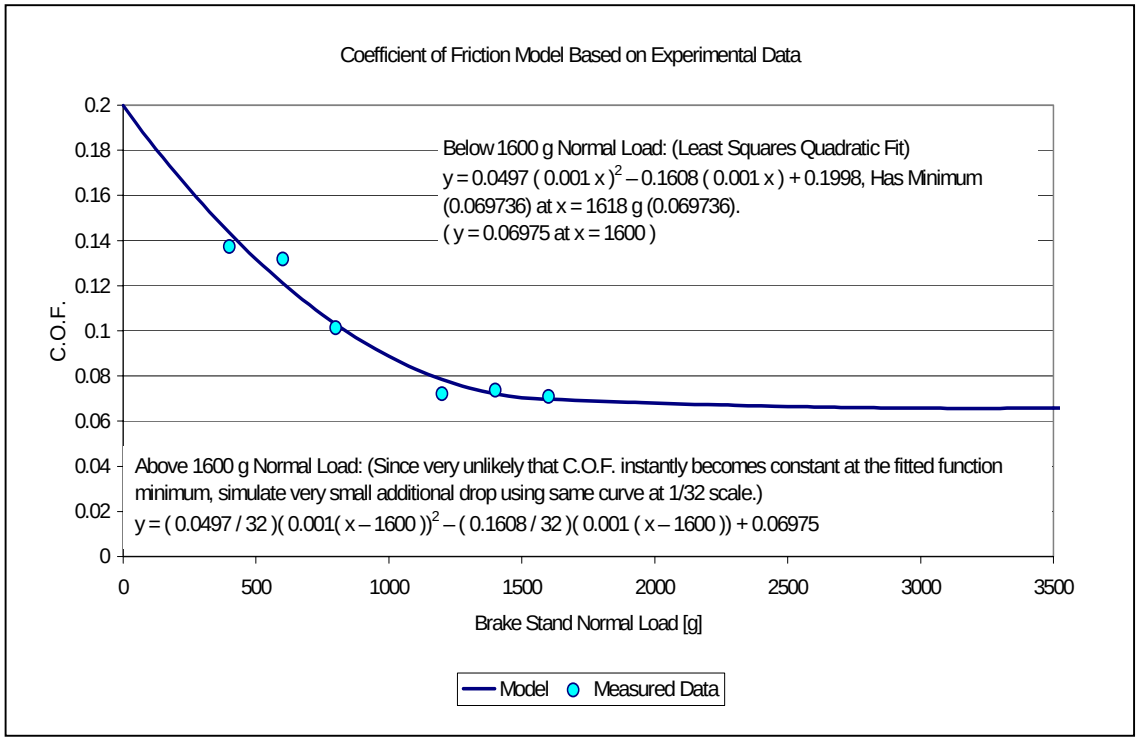

Figure 3.4—2. (color) Plot of measured friction coefficients between brake shaft and motor axle shown with fitted curve and notations about the functions that generate the curve

near 1600 g, after which it becomes an increasing function tracing a mirror image to the decreasing half shown. So the coefficient of friction values determined at highest brake loads were converging toward a constant value, as implied by proximity to the minimum in the fitted equation. Rather than simply assuming that the actual brake shaft / motor axle friction became immediately constant with increasing load, a second function (a compressed version of the original function) was adjoined to the first, allowing for a very slight additional decrease. Thus, the functional model to be applied in determining motor blocking torque is given by (3.4—1). The scaling factor 1/32 was chosen by visual judgment.

(3.4—1)

$$\text{Coefficient of Friction, } F(x = \text{Load}) = \begin{cases} 0.0497\,(0.001\,x)^2 - 0.1608\,(0.001\,x) + 0.1998, & \text{if } x \le 1600 \\ \frac{1}{32}\left[\,(0.0497)(0.001(x - 1600))^2 - (0.1608)(0.001\,(x - 1600))\,\right] + 0.06975, & \text{if } x > 1600 \end{cases}$$

Note that both functions have a value of 0.06975 at $x = 1600$. The reason for pre-multiplying input values by 0.001 is that the x-values and y-values differ by four orders of magnitude. The simultaneous solution of the system of equations underlying the least squares method is prone to ill-conditioning and may yield excessively approximate solutions when the numbers differ by so many orders of magnitude. [19, 20] The approach taken to remedy this is the same as determining least squares fit to input values expressed in kilograms, but plotting the resulting curve against the values expressed in grams.

Since tangential friction acts at an axle radius of 0.1875 inch or $4.7625(10)^{-3}$ m, resistance torque provided by friction for the test stand / motor system would be given by (3.4—2), where F(x) = F(Load in grams), as given in (3.4—1).

(3.4—2)

$$\text{Counter-Torque [Nm]} = (4.7625(10)^{-3}\ [\text{m}]) \left(9.8\,\frac{m}{s^2}\right)\left(x\,[g]\,\frac{0.001\,[kg]}{[g]}\right) F(x)\left[\frac{g}{g}\right]$$

3.5 Polarization Orientation through Cross-section Investigated by PFM

This experiment determined trends in distribution of effective d-coefficient values by vertical PFM (VPFM) [21-34] and lateral PFM (LPFM) imaging [35-42], which are useful tools for detecting out-of-plane and in-plane polarization components. The purpose was to reconstruct three-dimensional polarization orientation mapped at the sub-grain level

as a function of position between top and bottom edges of the piezoceramic element in an actuator cross-section.

A THUNDER pre-stressed unimorph actuator was embedded in clear metallographic sample prep epoxy. A transverse cross-section (approximately 4.7 mm thick) was cut using a low speed diamond saw, pre-polished using 320, then 600, then 1200 grit sanding disks. Faces to be imaged by PFM were subjected to a final polish using a Solid State Measurements Autopolisher boxing ring L/P machine with 0.3 μm alumina slurry for approximately 10 hours. The sample was rinsed in an ultrasonic bath with acetone to remove moisture and stored in a desiccant-filled container. Fine wires were attached to the cross-sections of top and bottom electrodes with conductive epoxy applied under magnification.

Imaging across the polished PZT section was accomplished using a Park Scientific Instruments M5 AFM, a tip-scanning system, with a maximum scan size of 100 μm. The scanning tip cantilever was platinum-coated silicon with a rectangular cross-section, having a force constant of 5.0 N/m . A 10 kHz excitation signal for PFM was applied through the top and bottom electrodes of the embedded, sectioned sample through attached wires. (An excitation signal at 10 kHz avoids interference with natural resonant frequency of the AFM cantilever or scanning frequency during image acquisition.) The signal amplitude was 1.5 V_{RMS}. Electrostatic interaction between tip and sample, a potential source of error, was minimized. This was verified by observing that if the tip was at the same potential as a sample electrode, resulting images were unchanged.

In some PFM experiments, the AFM tip may serve as an electrode, but in this study, the high-frequency signal was applied only through sample electrodes, not through the scanning tip. Thus, in all cases the electric field was approximately perpendicular to electrodes regardless of scanning direction.

Another point to note is that PFM experiments are often arranged to yield a mixed response signal of the form $A\cos\theta$, where A represents measured amplitude of sample surface vibrating in response to applied high frequency excitation signal, θ represents phase shift between driving signal and sensed mechanical response. (A calibration factor

allows conversion of photodetector output voltage to distance.) In this experiment, amplitude and phase were recorded separately. As will be discussed, brightness in plotted magnitude images corresponds to an absolute value of piezoelectric coupling coefficient ($|d_{EFF}|$). (In plotted phase images, opposite polarity would be indicated, as usual, by bright and dark plotted images, or perhaps blue to green for the interval [–180, 0) and green to red for the interval [0 , 180]. As it turned out, this was not an issue.)

Since the PZT layer in the actuator section was slightly less than 200 μm thick, we chose to acquire traces of several 40μm by 40μm areas. The initial scan started "very close to the top surface," and so was said to be 5μm away. However, in some cases, the edge of the PZT is visible at top and bottom in sets six of plotted images, taken at 5, 40, 80, 120, 160 and 190 μm from the top surface. Figure 3.5—1 depicts the orientation of the trace of PFM scans relative to the face of the cross-sectioned piece and relative to the whole actuator.

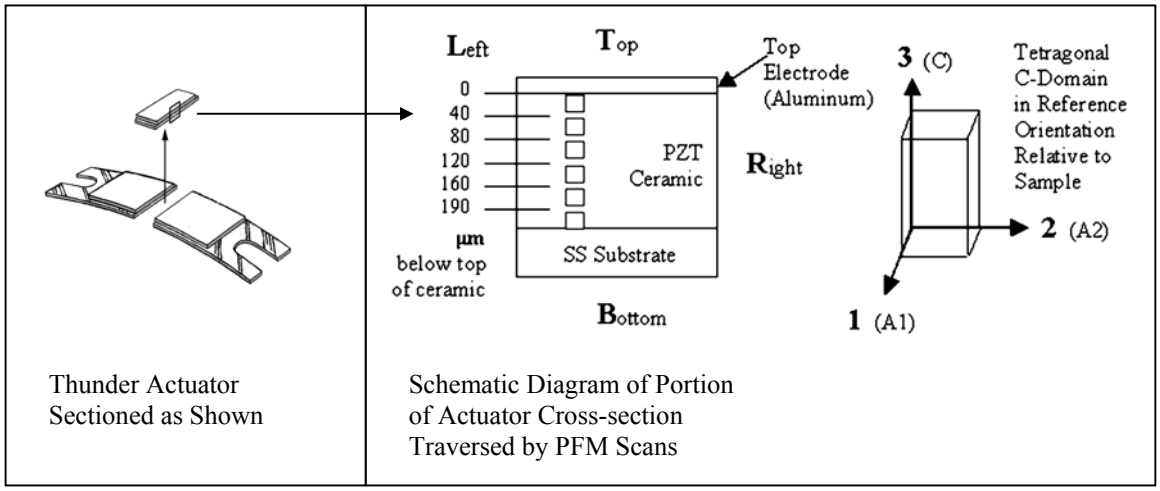

Figure 3.5—1. Conventions adopted for describing the set of PFM images and their relationship to the whole actuator. Given a poling direction perpendicular to top and bottom edges, C domains would contain unit cells oriented as shown relative to the whole actuator and to the cross-section face. A1 and A2 axes were likewise oriented as shown.

Pairs of scans were taken in lateral mode and in vertical mode. In each pair, a trace of scanned areas across the sample cross-section was conducted so that cantilever scanning direction was parallel to the electrodes in one case and perpendicular to the electrodes in the other. The actual procedure involved taking one scan in lateral mode, the next scan in vertical mode in approximately the same location on the sample surface. In VPFM mode, of course, the AFM tip scanned parallel to the sample surface, but piezoelectric response was detected in the perpendicular direction. Figures 3.5—2a through 3.5—2d clarify scanning directions relative to sample orientations and their assigned orthogonal directions.

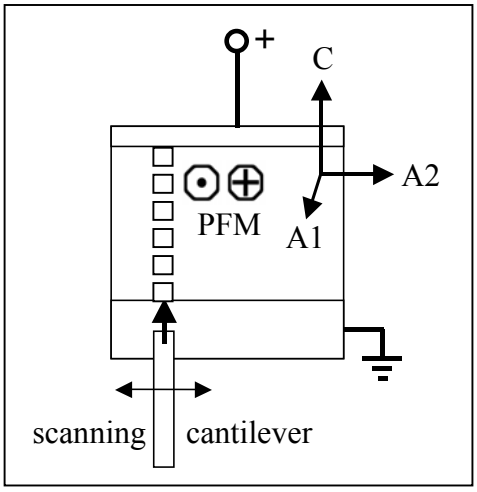

Figure 3.5—2A

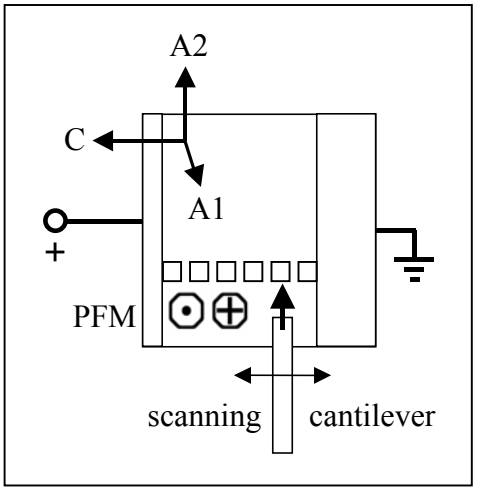

Figure 3.5—2B

Figure 3.5—2.

(A) Vertical PFM with scanning direction parallel to electrodes; out-of-plane response in A1 direction is sensed.

(B) Vertical PFM with scanning direction perpendicular to electrodes; out-of-plane response in A1 direction is sensed.

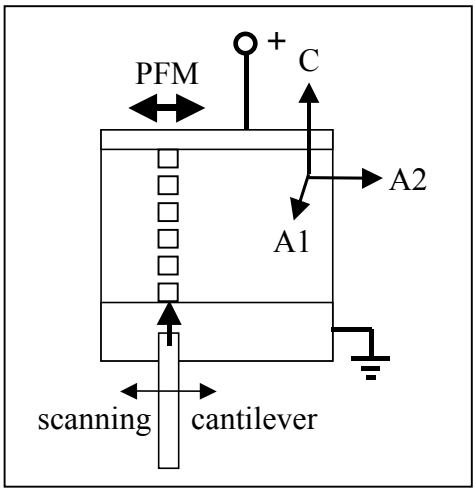

Figure 3.5—2C

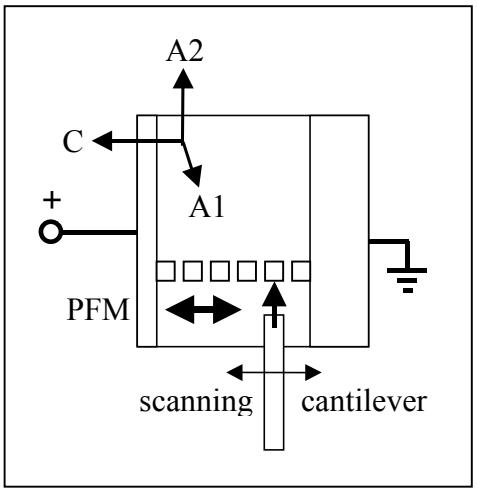

Figure 3.5—2D

Figure 3.5—2.

(C) Lateral PFM with scanning direction parallel to electrodes; in-plane response in A2 direction is sensed.

(D) Lateral PFM with scanning direction perpendicular to electrodes; in-plane response in C direction is sensed.

The AFM software saved image data as files in hdf-format. Each scan generated four files containing 256 x 256 data points. Two files related to physical topography of the sample surface; the others contained image data for magnitude ($|d_{EFF}|$) and phase (θ) of piezoelectric response. A macro-driven spreadsheet calculated $|d_{EFF}|$ and θ arrays in a point to point application of formulas (3.5—1) and (3.5—2) to the AFM voltage signal output arrays. The spreadsheet produced numeric arrays that represented a map of calculated $|d_{EFF}|$ values onto the scanned area. (This spreadsheet was devised by Brian Rodriguez, whose doctoral work contributed significantly to broadening utility and applicability of PFM. [43])

(3.5—1) $$|d_{33}| = \frac{\alpha V_{SENS}}{V_{DRIVE}}\left(\frac{Z_R}{32768} - \frac{V_{OFFSET}}{10}\right) \quad [\text{Å} / \text{V}]$$

In (3.5—1), α is a conversion constant [Å/mV] resulting from calibration, V_{SENS} is the sensitivity setting of the lock-in amplifier (typically 1-5 mV_{RMS} during PFM). Thus, αV_{SENS} [=] Å, and the pre-factor [=] Å / V. The A/D conversion between lock-in amplifier and AFM interface module introduces a small voltage offset (V_{OFFSET} = –0.084 V). In essence, Z_R represents a coded integer output from the AFM processing software, and the various elements in (3.5—1), including the integral values in the bracketed factor, simply reverse the coding and apply the distance offset calibration.

(3.5—2) $$|d_{33}^{\theta}| = Z_{\theta}\left(\frac{3600}{(7.07)(32768)}\right) - 180 \quad [\text{degrees}]$$

In (3.5—2), Z_θ is the integral pixel value in the PFM phase image file. As in (3.5—1), the values reverse the output software coding to yield phase difference between applied signal and coupled mechanical response. (The function generator in the PFM system is set to have a maximum output of 7.07 V_{RMS}, which accounts for the non-integral value in (3.5—2).)

The numeric arrays generated by the macro-driven spreadsheet developed by Rodriguez, as mentioned above, were primarily suitable for statistical analysis. An additional spreadsheet was developed by me to process the numeric arrays into images that mapped the numeric data onto an area representing the original scan.

The numeric data in an output array was classified into intervals representing sub-divisions of the total distribution of the data for a particular set of PFM scans. By assigning one of nine colors in a violet to red spectrum to each classification interval, pixels could be color-coded for mapping the calculated d-coefficient magnitudes at each position in the numeric array to a corresponding position in the image. The color of each image pixel represented the classification interval in which its associated $|d_{EFF}|$ value

belonged, relative to the overall range of $|d_{EFF}|$ values occurring in a set of scans. Black and white were included for values above or below endpoints of a chosen range. (Red and white were assigned to high magnitudes.) The overall range was chosen to include most of the values across the set of images in a cross-section trace (in which distributions were found to shift relative to one another), such that regions of similar response could be resolved into as much of the entire spectrum of colors (including black and white) as possible throughout all images in a set. In other words, low resolution images of mostly two or three colors were to be avoided, if possible.

A data treatment was applied to LPFM magnitude values because plotted images appeared "noisy" due to a speckle of tiny regions that seemed inappropriately colored relative to their surroundings. An explanation is that LPFM senses only response from the immediate sample surface, whereas VPFM is much more of a bulk response and should provide stronger trends with lower variability. Each LPFM data point was adjusted, or not, based on the average and standard deviation of differences between its value and the values of eight immediately surrounding and sixteen (next nearest) neighboring data points within the rectangular array, using essentially inverse square proximity weighting.

The idea was that points isolated in rings of differing color temperature with small standard deviations (uniform surroundings) would tend to change. Points surrounded by rings of differing color temperature with high standard deviations were probably at the border between regions and tended not to change. In other words, borders around similar regions were to remain immobile rather than shift location. Careful examination of resulting images showed that borders around regions with similar response had not shifted, while "speckle" was greatly diminished. Figures 3.5—3A and 3.5—3B provide an example. To see the difference, first look at the smallest black areas, then the smallest purple areas, and so forth. These figures also give some indication of the high resolution provided by the data images, since the entire set of images cannot be presented at the scale of Figures 3.5—3A and 3.5—3B.

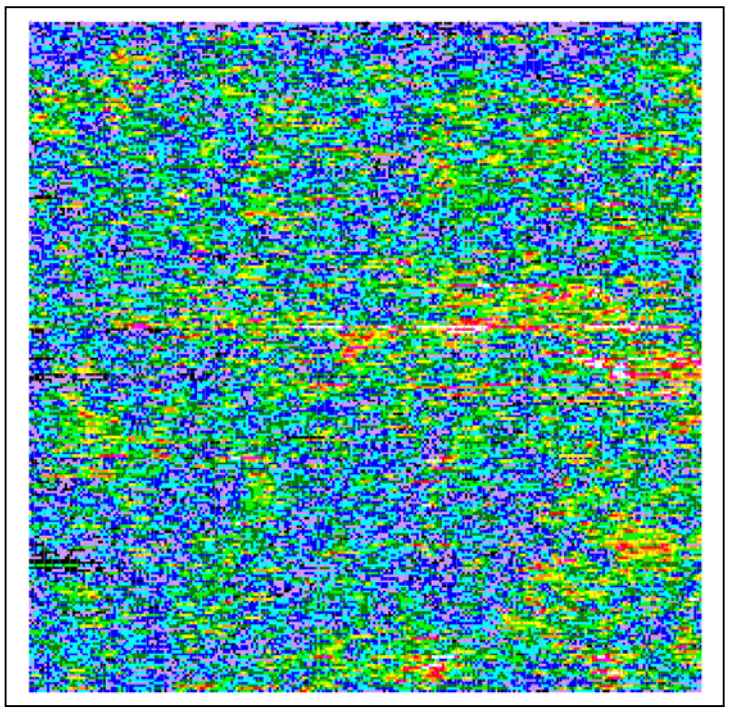

Figure 3.5—3A. (color) No contrast

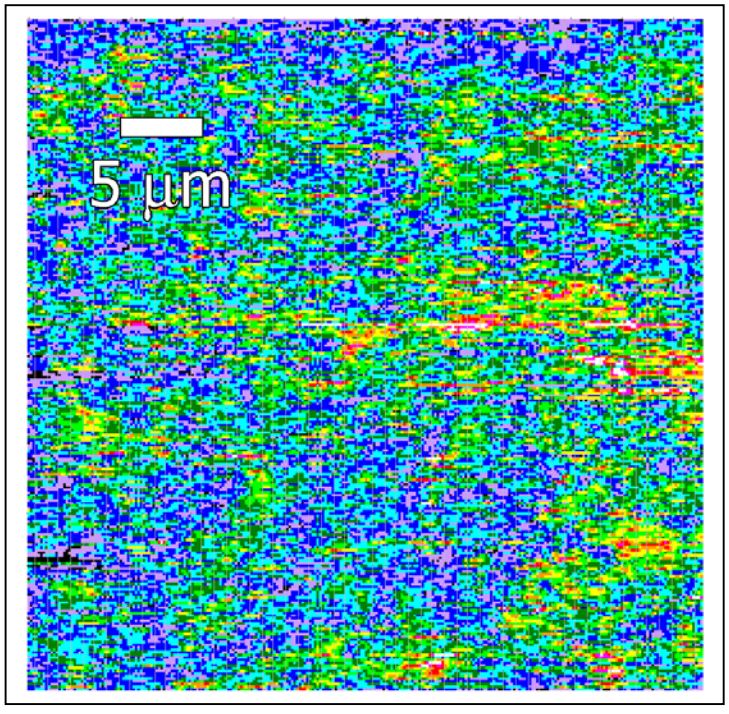

Figure 3.5—3B. (color) Contrast applied

3.6 References

[1] S. Wise. Displacement properties of Rainbow and Thunder piezoelectric actuators. Sensors and Actuators A, 69, 33-38 (1998).

[2] K. M. Mossi, G. V. Selby, R. G. Bryant. Thin-layer composite unimorph ferroelectric driver and sensor properties. Materials Letters, 35, 39-49 (1998).

[3] X. Li, W.Y. Shih, I. A. Aksay, and W.-H. Shih. Electromechanical behavior of PZT-brass unimorphs. Journal of the American Ceramic Society, 82, 1733-1740 (1999).

[4] U.S. Patent 5,741,883 to Robert G. Bryant. Tough, soluble, aromatic thermoplastic copolyimides (April 21, 1998).

[5] U.S. Patent 5,632,841 to R. F. Helbaum, R. G. Bryant, R. L. Fox. Thin layer composite unimorph ferroelectric driver and sensor (May 27, 1997).

[6] U.S. Patent 5,849,125 to Stephen E. Clark. Method of manufacturing flextensional transducer using pre-curved piezoelectric ceramic layer (December 15, 1998).

[7] K. Mossi. (1998) Thin-layer pre-stressed composite ferroelectric driver and sensor characterization with application to separation flow control, PhD dissertation, Old Dominion University, Richmond, VA.

[8] B. Jaffe, W.R. Cook, and H. Jaffe. *Piezoelectric Ceramics* (Academic Press Ltd., 1971). (See p.264.)

[9] D. Shetty and R.A. Kolk. *Mechatronic System Design* (Boston, MA: PWS Publishing Co., 1997).

[10] R.O. Cook and C.W. Hamm. Fiber optic lever displacement transducer. Applied Optics, 18, 3230-3241 (1979).

[11] U.S. Patent 3,327,584 to C.D. Kissinger. Fiber Optic Proximity Probe (27 Sept. 1967).

[12] U.S. Patent 3,273,447 to W.E. Frank. Detection and Measurement Device having a Small Flexible Fiber Transmission Line (20 Sept. 1966).

[13] Technical Manual: Ångstrom Resolver^{R} Series Dual Channel Models 201. Opto Acoustic Sensors, Inc. (Raleigh, NC).

[14] Ångstrom Resolver® Noncontacting Displacement Sensors Fact Sheet, Opto Acoustic Sensors, Inc. (Raleigh, NC), 5/91.

[15] M. Kurtz. *Handbook of Applied Mathematics for Engineers and Scientists* (McGraw-Hill, 1991).

[16] P. E. Bennet. *Advanced Circuit Analysis* (Harcourt Brace Jovanovich / Saunders College Publishing, 1992).

[17] R.O. Cook, private communication.

[18] H.V. Malmstadt, C.G. Enke, S.R. Crouch. *Electronic Measurements for Scientists* (W.A. Benjamin, Inc., 1974).

[19] S. Yakowitz and F. Szidarokvszky. *An Introduction to Numeric Computations* (Macmillan Publishing, Co., 1986).

[20] P. Stark. *Introduction to Numerical Methods* (The Macmillan Co., 1970).

[21]. A. Gruverman, O. Auciello, H. Tokumoto. Nanoscale investigation of fatigue effects in $Pb(Zr,Ti)O_3$ films. Applied Physics Letters, 69, 3191-3193 (1996).

[22] T. Idaka, T. Maruyanma, I. Sakai, M. Saitoh, L.A. Wills, R. Hiskes, S.A. Dicarolis, J. Amano, and C.M. Foster. Characteristics of PZT thin films as ultra-high density recording media. Integrated Ferroelectrics, 17, 319-327 (1997).

[23] O. Auciello, A. Gruverman, and H. Tokumoto. Scanning force microscopy study of domain structure in Pb(ZrxTi1-x)O3 thin films and Pt/PZT/Pt and RuO_2/PZT/RuO_2 capacitors. Integrated Ferroelectrics, 15, 107-114 (1997).

[24] A. Gruverman, O. Auciello, and H. Tokumoto. Imaging and control of domain structures in ferroelectric thin films via scanning force microscopy. Annual Review of Material Science, 28, 101-123 (1998).

[25] J.A. Christman, R.R. Woolcott, A.I. Kingon, R.J. Nemanich. Piezoelectric measurements with atomic force microscopy. Applied Physics Letters, 73, 3851-3853 (1998).

[26] J.A. Christman, S.-H. Kim, H. Miawa, J.-P. Maria, B.J. Rodriguez, A.I. Kingon and R.J. Nemanich. Spatial variation of ferroelectric properties in Pb(Zr0.3, Ti0.7)O3 thin films studied by atomic force microscopy. Journal of Applied Physics, 87, 8031-8034 (2000).

[27] S. V. Kalinin, and D.A. Bonnell. Imaging mechanism of piezoresponse force microscopy of ferroelectric surfaces. Physics Review B (Condensed Matter and Materials Physics), 65, 125408/1-11 (2002).

[28] A. Gruverman, B.J. Rodriguez, R.J. Nemanich, and A.I. Kingon. Nanoscale observation of photoinduced domain pinning and investigation of imprint behavior in ferroelectric thin films. Journal of Applied Physics, 92, 2734-2739 (2002).

[29] S. Hong, E.L. Colla, E. Kim, D.V. Taylor, A.K. Tangantsev, P. Muralt, K. No, and N. Setter. High resolution study of domain nucleation and growth during polarization switching in Pb(Zr,Ti)O3 ferroelectric thin film capacitors. Journal of Applied Physics, 86, 607-613 (1999).

[30] M. Alexe, A. Gruverman, C. Harnagea, N.D. Zakharov, A. Pignolet, D. Hesse and J.F. Scott. Switching properties of self-assembled ferroelectric memory cells. Applied Physics Letters, 75, 1158-1160 (1999).

[31] M. Alexe, C. Harnagea, D. Hesse, and U. Gosele. Polarization imprint and size effects in mesoscopic ferroelectric structures. Applied Physics Letters, 79, 242-244 (2001).

[32] I. Stolichnov, E. Colla, A. Tagantsev, S. Bharadwaja, S. Hong, N. Setter, J.S. Cross, and M. Tsukada. Unusual size effect on the polarization patterns in micron-size Pb(Zr,Ti)O3 film capacitors. Applied Physics Letters, 80, 4804-4806 (2002).

[33] A. Gruverman, B.J. Rodriguez, A.I. Kingon, R.J. Nemanich, J.S. Cross, and M. Tsukada. Spatial inhomogeneity of imprint and switching behavior in ferroelectric capacitors. Applied Physics Letters, 82, 3071-3073 (2003).

[34] A. Gruverman, B.J. Rodriguez, A.I. Kingon, R.J. Nemanich, J.S. Cross, and M. Tsukada. Mechanical stress effect on imprint behavior of integrated ferroelectric capacitors. Applied Physics Letters, 83, 728-730 (2003).

[35] L.M. Eng, H.-J. Guntherodt, G. Rosenman, A. Skliar, M. Oron, M. Katz, and D. Egar. Nondestructive imaging and characterization of ferroelectric domains in periodically poled crystals. Journal of Applied Physics, 83, 5973-5977 (1998).

[36] L.M. Eng, M. Abplanalp, P. Gunter. Ferroelectric domain switching in tri-glycine sulphate and barium-titanate bulk single crystals by scanning force microscopy. Applied Physics A, 66, S679-S683 (1998).

[37] M. Abplanalp, L.M. Eng, P. Gunter. Mapping the domain distribution at ferroelectric surfaces by scanning force microscopy. Applied Physics A, 66, S231-S234 (1998).

[38] L.M. Eng, H.J. Guntherodt, G.A. Schneider, U. Kopke and J. Munoz-Saldana. Nanoscale reconstruction of surface crystallography from three-dimensional polarization distribution in ferroelectric barium-titanate ceramics. Applied Physics Letters, 74, 233-235 (1999).

[39] A. Roelofs, U. Bottger, R. Waser, F. Schlahof, S. Trogisch, L.M. Eng. Differentiating 180° and 90° switching of ferroelectric domains with three-dimensional piezoresponse force microscopy. Applied Physics Letters, 77, 3444 – 3446 (2000).

[40] C.S. Ganpule, V. Nagarajan, B.K. Hill, A.L. Roytburd, E.D. Williams, S.P. Alpay, A. Roelofs, R. Waser, and L.M. Eng. Imaging three-dimensional polarization in epitaxial polydomain ferroelectric thin films. Journal of Applied Physics, 91, 1477-1481 (2002).

[41] S. Hong, J. Woo, H. Shin, J.U. Jeon, Y.E. Pak, E.L. Colla, N. Setter, E. Kim, K. No. Principle of ferroelectric domain imaging using atomic force microscope. Journal of Applied Physics, 89, 1377-1386 (2001).

[42] A.L. Kholkin, V.V Shartsman, A.Y. Emelyanov, R. Poyato, M.L. Calzada, L. Pardo. Stress-induced suppression of piezoelectric properties in PbTiO3:La thin films via scanning force microscopy. Applied Physics Letters, 82, 2127-2129 (2003).

[43] B.J. Rodriguez. 2003. Doctoral dissertation, North Carolina State University, Raleigh, NC.

[44] J. Friend and D. Stutts. Bonding suggestions for the piezoelectric motor system. http://www.umr.edu/~piezo/MotorAnalysis/BondingNote/BondingNote..html, 6/7/99.

[45] R.W. Messler, Jr. *Joining of Advanced Materials* (Butterworth-Heinemann, 1993).

Chapter 4. Effect of Structure and Boundary Conditions on Actuator Performance

Fabrication methods can be expected to affect the performance of pre-stressed unimorphs (PSUs), since the operation of solid state devices generally is dependent on processing conditions. A fundamental goal of this research was to reliably manufacture pre-stressed unimorph actuators and determine which processing conditions most favorably affect performance. Commercially-manufactured THUNDER^{TM} actuators (Face International Corporation, Norfolk, VA) provided benchmark comparison of both design and performance. Consequently, both commercial and in-house actuators were characterized and compared. The present work also sought possible refinements in how pre-stressed unimophs are made and how they are used.

The project began as a systematic investigation of the effect on performance of each input variable to the reported method of fabricating THUNDER actuators. Actuators were fabricated using different metals as substrates, and with varying relative thickness of ceramic to substrate. Although these experiments partially duplicated work reported by others, establishing reliable fabrication capability was itself a goal. Reliable fabrication would enable previously unconsidered aspects of design and function to be examined.

It was found, however, that refining the in-house process for heat and pressure bonding with LaRC-SI adhesive (discussed in Chapter 3) could have dominated this work, primarily due to variability in completed actuator performance. Performance might vary as widely within a batch (two to six specimens) processed under presumably identical conditions as between batches subjected to intentionally different conditions. Although a number of researchers have reported manufacturing pre-stressed unimorphs and presumably obtaining results to their satisfaction [1-5], the brief information provided by Face International Corporation about their facilities suggests that considerable resources were committed to achieving refined and stable commercial production. [6] A set of commercial actuators was tested to determine how much variability occurs in their performance.

As a supplemental goal, developing a quicker, simpler fabrication route to an actuator with performance as good as, or better than, commercial PSUs would be worthwhile in itself. In discussing the prior art which THUNDER actuator prototypes were intended to surpass, Hellbaum, Bryant and Fox conclude that, "it is yet another object of the present invention to accomplish the foregoing objects in a simple manner." [7] Accordingly, the polyimide-based fabrication process was supplemented with simple variants with the intent of finding a design element which stood out for its association with good performance.

The primary variable was adhesive type. As discussed in Section 2.3.1.4, any acceptable alternative to polyimide as a bonding adhesive is likely to be an epoxy (or epoxy derivative). Given that a large number of epoxy adhesive products with a range of characteristics and properties are available, this is not such a limited field as it may seem. The secondary variable involved selection of epoxy adhesives yielding both very thin and very thick bonds, with some thickness variation. The bond in THUNDER actuators, on the order of ten microns, is considered "thin," while "thick" bonds, say 40 to 100 μm, result in a composite substrate—part metal, part epoxy. A third variable was thin or thick substrate, with "thin" defined as near the optimal ratio of one-third total thickness determined by many studies, and "thick" as twice that or more. Substrates for the model 8R THUNDER actuator are closer to thick than thin by this definition, probably to enable good performance at high load in exchange for slight reduction in no-load deflection.

Fabrication at lower temperature and ambient pressure simplifies fabrication but reduces the opportunity for differential thermal contraction (DTC) to generate internal stress bias. Consequently, investigations included introduction of stress bias by means other than DTC and determining whether actuators made at lower temperature than polyimide-bonded PSUs actually had substantially lower curvature or performance. In addition, considerable work was devoted to developing a fabrication route for actuators bonded at high temperature with zinc to evaluate the effects of large DTC. It was believed that fabrication with zinc might eventually be accomplished by a relatively simple process

it spite of the higher temperature. Some interesting observations were made, but a reliable procedure was not achieved.

4.1 Background for Presentation of Results and General Observations

In keeping with the theme of maximizing both actuator force and displacement, unloaded deflection and blocking force were both used as performance metrics. Measurements were made using the load-displacement test equipment and methods described in Section 3.1.4. A brief explanation of analysis and presentation of data will be given, along with some general trends observed. The first general observation concerns patterns in plotted data and what is indicated. The second general observation concerns changing performance within a set of repeated tests and between re-tests conducted after months have elapsed.

Figure 4.1—1 shows position (relative to starting point) of the actuator center as a function of load and voltage. As discussed in Section 2.3.2, pre-stressed unimorphs are typically operated in the indirect actuation mode, in which piezoelectric strain acts in parallel with the load to create a larger deflection than is appropriate for the load acting on a comparable static beam. When electric field is turned off, elastic rebound displaces the load. In Figure 4.1—1, line (A) traces deflection due to load alone; line (B) traces the additional deflection due to applied electric field. Free (unloaded) deflection for this actuator would be the extrapolation to zero load of the difference between the two lines as marked at bottom left. Blocking force would occur where the two lines intersect, somewhere well beyond the upper right corner of the figure. The lines must be extrapolated to obtain free displacement because the mass of the shaft resting on the actuator (connected to the LVDT core) applies some force with no additional mass added. (It weighs about 100 g.) The slopes of lines (A) and (B) give the static and energized compliance of the actuator.

To isolate actuator displacement due to piezoelectric strain alone, the zero volt position line is subtracted from the position lines at non-zero electric field. Figure 4.1—2

shows the resulting displacement of the actuator center across a range of voltage and load levels. Free displacement and blocking force for this actuator are clearly the intersections of the extrapolated line of displacement at maximum voltage with the vertical axis and horizontal axis respectively. The “max” and “min” values are displacement data points at either end of the load range.

The particular actuator associated with test data plotted in Figure 4.1—1 was selected to provide a simplified example because of its unusual stability and linearity. Typically, performance plots show less idealized behavior which falls into several types. Some examples will be shown. In Figure 4.1—3 we see a type involving two or three different approximately linear displacement regimes in response to increasing load. The actuator at left is a commercial THUNDER actuator; the actuator at right is not pre-stressed (bonded with J.B. Weld epoxy setting at room temperature).

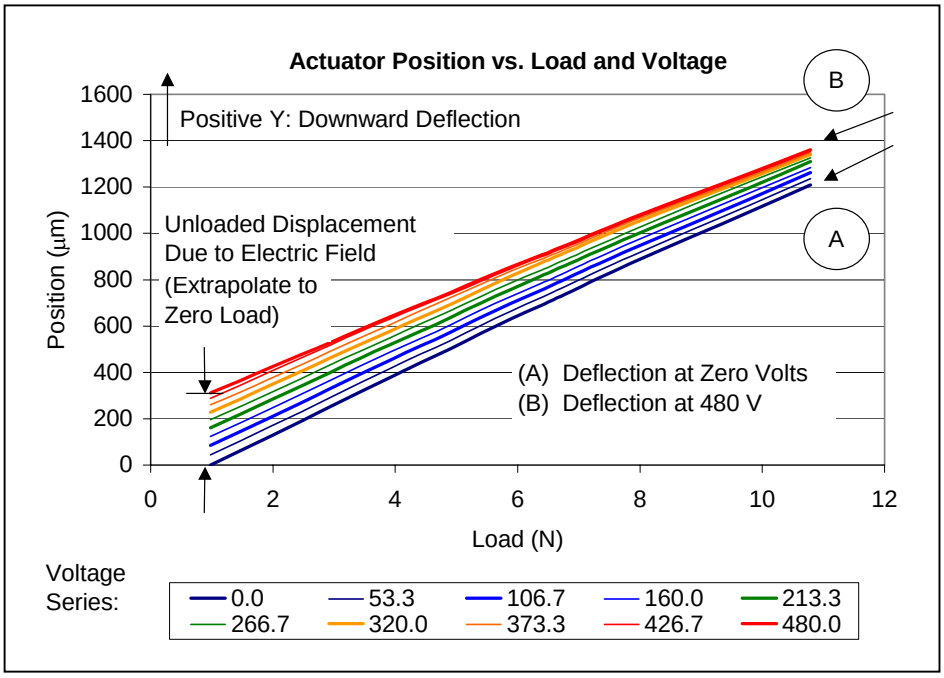

Figure 4.1—1. (color) Example of plotted actuator (center point) positions due to applied load and electric field

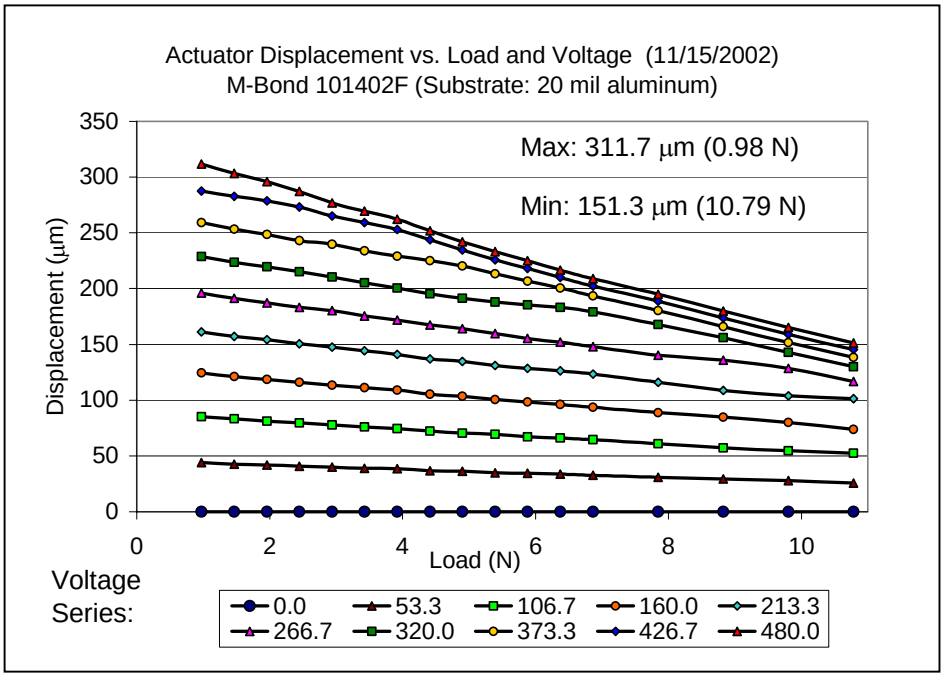

Figure 4.1—2. Example of plotted actuator (center point) displacements due to applied load and electric field

One possible explanation for upturn in the THUNDER data at low load and high voltage may come from the pre-stress enhancement of the extrinsic piezoelectric strain discussed in Section 2.3.4. Schwartz, Cross, and Wang suggest that at low electric field, a stress-biased device behaves more like a non-pre-stressed unimorph, whereas higher field activates the mechanism of reorienting stress aligned domains, resulting in non-linear plots. [8] The bend at higher load might come from some characteristic common to unimorphs whether stress-biased or not.

At high load, these thin plate beams are bent into a small radius of curvature. A central region with smaller radius of curvature may develop near the point of load application. The upper material, piezoceramic, is highly compressed—which protects it from failure—but no doubt affects its polarization state. [12-19] (The deflected shape of an

actuator made with a 4-mil substrate under 10 N load bears a remarkable resemblance to a catenary curve, as long as the test fixture allows end rotation.)

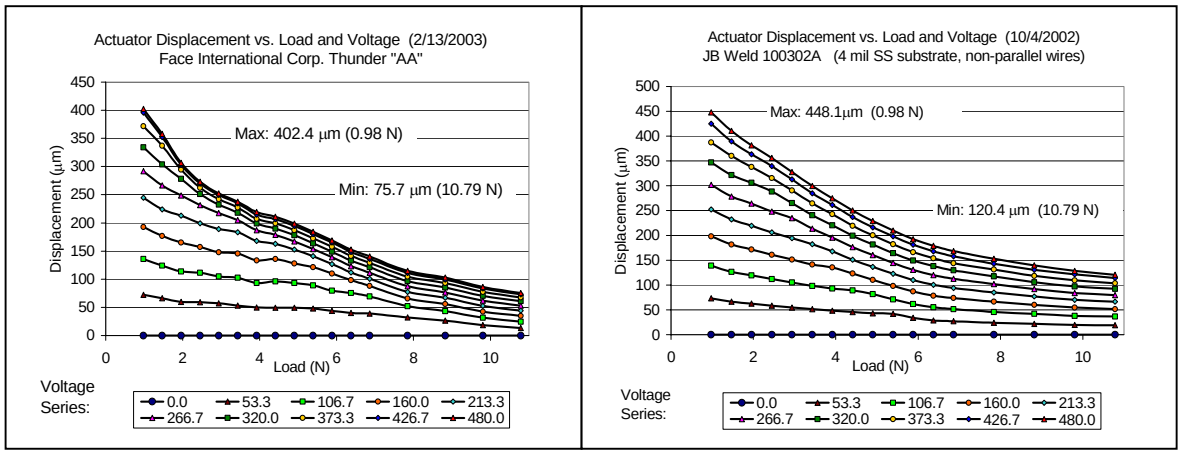

Figure 4.1—3. Examples of actuators that transition from one approximately linear load-displacement response to another

Tests on actuators bonded with M-Bond epoxy often (not always) produced load-displacement plots with a convex envelope. An interesting set is shown in Figure 4.1—4 and Figure 4.1—5. Plot A in Figure 4.1—4 shows test results for an actuator which was part of a set in which one, two, or three light coats of adhesive were sprayed during fabrication. The actuator yielding plot 4.1—4B received three coats. An average bond thickness of 35.1 μm was determined from micrographs of the cross section. The actuator yielding plot 4.1—4A received two coats, which produced an average bond thickness of 16.2 μm. (An actuator which received a single coat of adhesive, producing an average bond thickness of 5.1 μm, delaminated and cracked during fabrication.) Both actuators were made with 4-mil substrates (1 mil = 0.001 inch = 25.4 μm). Figure 4.1—5 shows test results for actuators having bond thickness between 13 and 15 μm (M-Bond adhesive). The actuator yielding plot 4.1—5A was made with an 8-mil substrate, and the actuator associated with plot 4.1—5B was made with a 12-mil substrate. (Substrate material was stainless steel in all cases.)

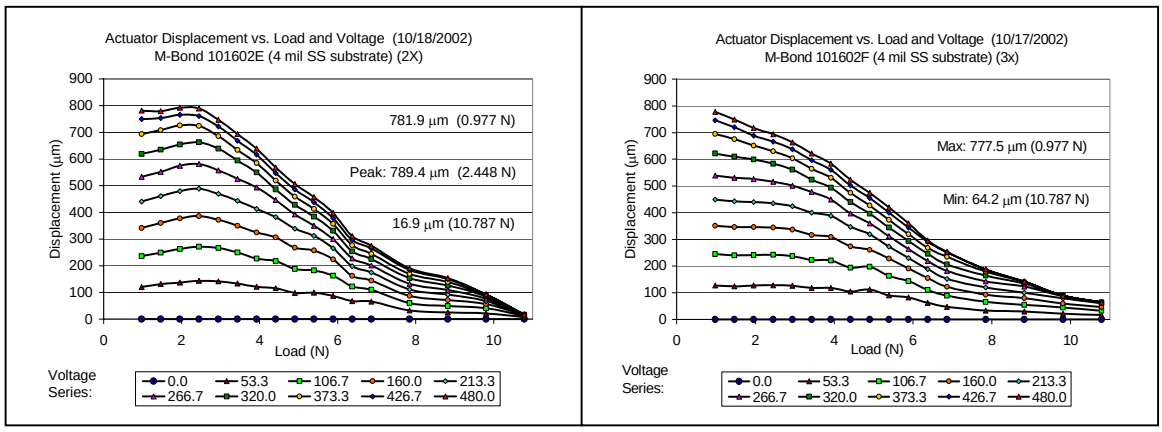

Figure 4.1—4A.
16 μm bond, 4-mil Substrate

Figure 4.1—4B.
35 μm bond, 4-mil Substrate

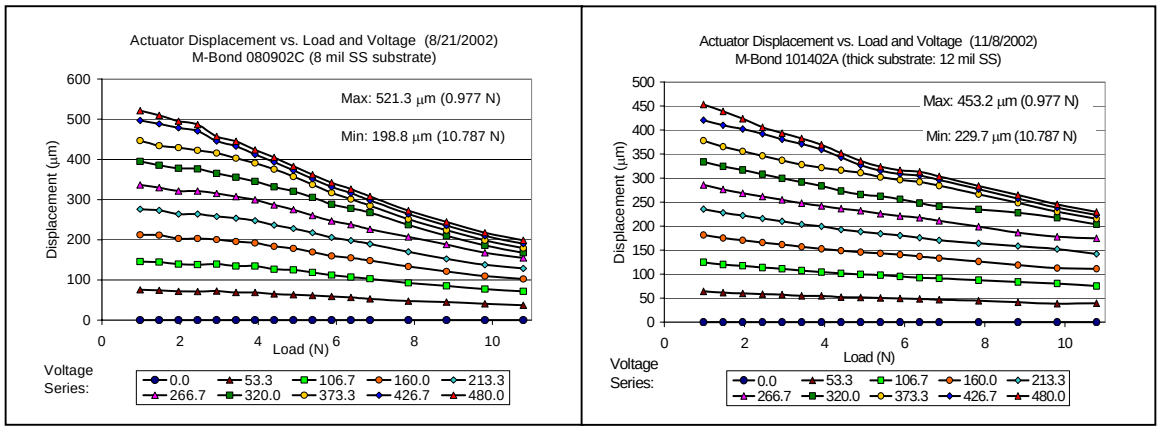

Figure 4.1—5A.
11 μm bond, 8-mil Substrate

Figure 4.1—5B.
15 μm bond, 12-mil Substrate

Figures 4.1—5 allows us to conclude that thicker substrates exchange lower free deflection for higher blocking force and tend to yield more linear load-displacement behavior. Thin bonds (less than 10 μm) appear to be associated with the phenomenon of maximum displacement developing under non-zero load. The thicker bond associated with the results plotted in Figure 4.1—4B appears to modify the effect which is slightly evident in Figure 4.1—4A, translating a small fraction of displacement capacity at small loads into improved displacement capacity at higher load. Figure 4.1—6 illustrates that performance

of actuators with thin bonds can be outstanding, or mediocre with risk of failure. An average bond thickness of 6.1 μm was determined for the actuator yielding plot 4.1—6A; an average bond thickness of 5.6μm was determined for the actuator yielding plot 4.1—6B. Both actuators were part of an experiment attempting to create very thin LaRC-SI polyimide bonds, and were both made with 4-mil substrates.

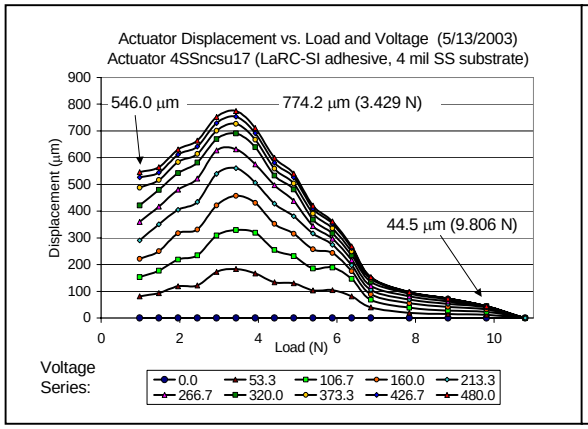

Figure 4.1—6A. Peak at non-zero load: large maximum deflection

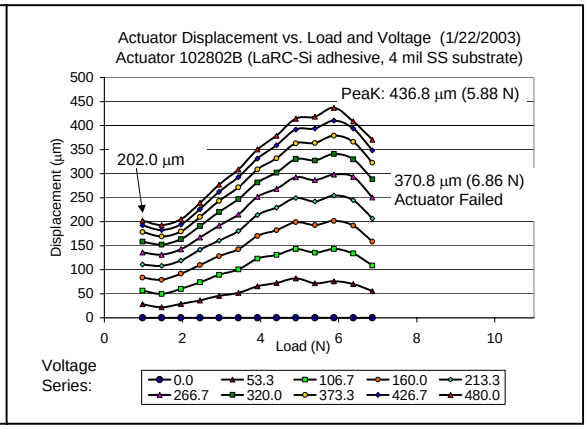

Figure 4.1—6B. Peak at non-zero load: unremarkable performance and failure

This effect is by no means without exceptions. An actuator fabricated with M-Bond adhesive with an average bond thickness of 6.9 μm yielded plotted test results which closely resemble those shown in Figure 4.1—4B (not 6B) except that the maximum data point is about 4% larger for the plot not shown. It may be true that adhesive bonds less than 10 μm thick confer some enhancement in performance but must be flawless to avoid failure.

The second general observation concerns changing performance within a set of repeated tests and between re-tests conducted after months have elapsed. Long-term change can be illustrated, as above, with load-displacement plots. Figure 4.1—7 shows results from tests on a THUNDER model 8R actuator conducted three months apart.

A decrease in deflection at low load (zero to one Newton) has been exchanged for an increase a high load (~10 N).

Figure 4.1—8 shows results from tests on an in-house actuator conducted three years apart. Actuator 19 was bonded with LaRC-SI polyimide. The "camel-shaped" plot of test results, characterized by relatively high no-load displacement followed by a drop-off and local peak at higher load, was observed in the performance of more than one actuator. For this actuator, the level of the peak at the middle of the load became lower, while displacement at both lower and higher loads improved. It is almost as though the area under the top load-displacement trace is a fixed quantity and decreased displacement in one portion of the load range will be offset by increased displacement at another portion of the load range, with the shift typically toward better performance at high loads.

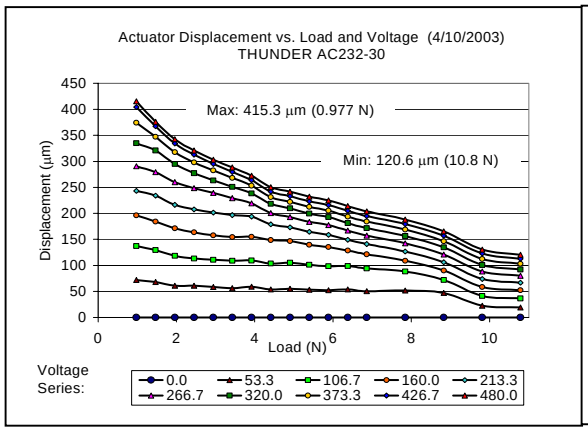

Figure 4.1—7A. Test results for THUNDER AC232-30 in April

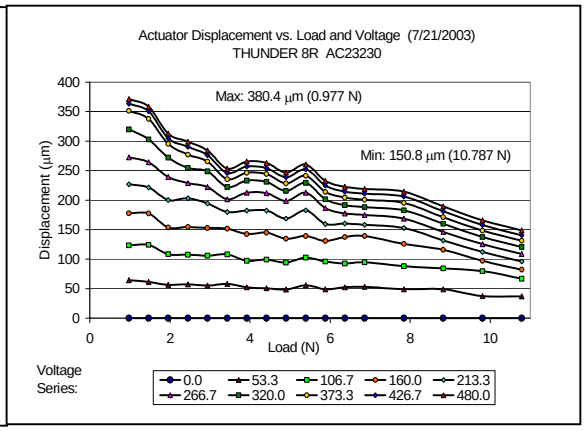

Figure 4.1—7B. Test results for THUNDER AC232-30 in July

The pattern of reduced displacement at lower loads associated with enhanced higher load displacement capacity is typical, but there are exceptions. Figure 4.1—9 shows results from tests conducted about seven months apart on an actuator fabricated with an 8-mil stainless steel substrate and bonded with M-Bond adhesive. Determination of bond

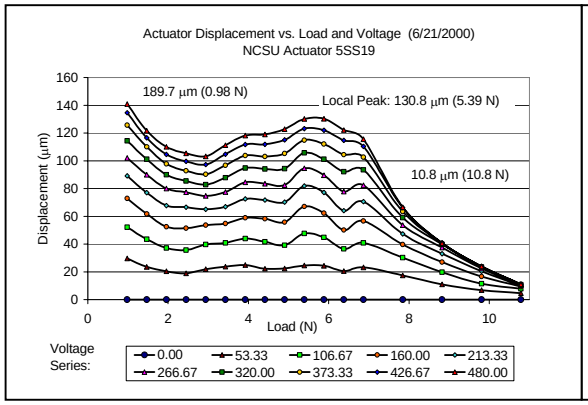

Figure 4.1—8A. Test results for NCSU actuator 19 in June 2000

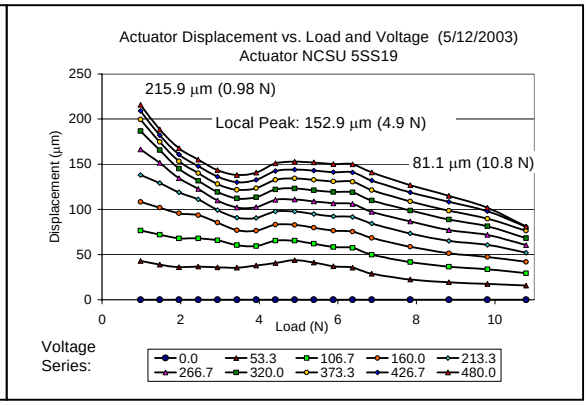

Figure 4.1—8B. Test results for NCSU actuator 19 in May 2003

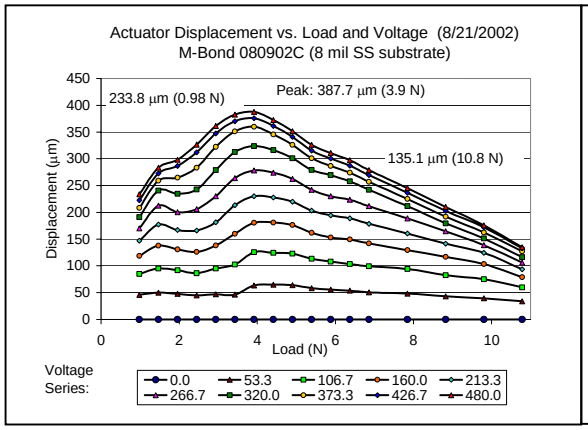

Figure 4.1—9A. Test results for MB 080902C in August 2002

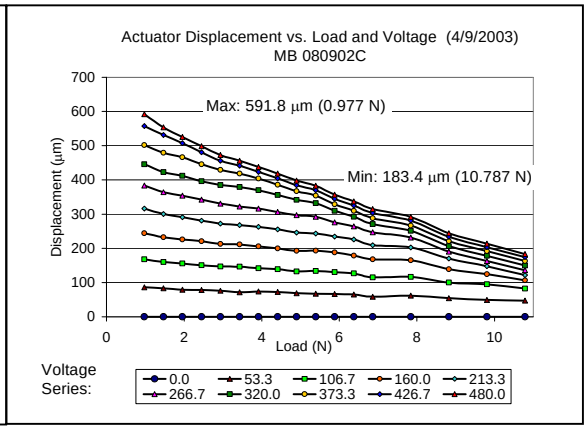

Figure 4.1—9B. Test results for MB 080902C in April 2003

thickness gave an average of 10.6 μm. The plot in Figure 4.1—9A resembles the shape associated with thinner bonds, while the shape of the plot in Figure 4.1—9B was associated with thicker substrates. Often stretching a polymer orients molecular chains and increases stiffness. (Actuators fabricated with M-Bond adhesive typically developed a permanent loss of as-fabricated curvature after an initial test.) However, the bond thickness, which is on the low side, was determined after all load-displacement tests.

An unstretched, presumably thicker bond would not seem to predict the shape seen in Figure 4.1—9A.

The standard test format for load-displacement characterization of actuators involved six repetitions of the LabView data acquisition program (TP.vi) described in Section 3.1.4. (More or fewer repetitions might have been conducted for various reasons.) Each execution of TP.vi essentially generated one of the charts depicted in previous figures, except that the particular plots shown thus far have presented a plot of averaged data for an entire set of tests. However, plots representing individual test results would have the same general appearance. Of course, load-displacement response changed from test to test within a set, but only in rare instances did the pattern of change appear random.

Most of the plots shown in previous figures indicate complex behavior, but as a gauge of changing behavior within a test set, the "max" and "min" data points indicated on each chart (and all others for which load-displacement data exists) were plotted in bar charts where bar height indicated only changes above the smallest value in a set. A selection is include in the figures below. The values indicated above each bar, however, are the full values of measured displacement, not differences from the minimum value in a set. The chart floor represents a much lower value for the set of smaller displacements at high load ("min" set) than for the larger displacements at low load ("max" set). This approach ignores any local displacement peaks that might have developed in the middle of the range of applied loads, but does capture exchanges between low-load and high-load response.

Figure 4.1—10 shows a prevalent pattern (by a small majority) developed from test results for a commercial THUNDER (at left) and an actuator fabricated in-house (at right) which was also bonded with LaRC-SI polyimide. Low-load displacement decreases in increments of decreasing size in approximately monotonic fashion toward some steady state level. Displacement at high load follows some pattern with less consistency, including small fluctuations about a constant level. Trends of increasing or decreasing displacement at high load—in the same or opposite direction as an associated trend in low load displacement—are often observed in the population of test sets but are often less persistent.

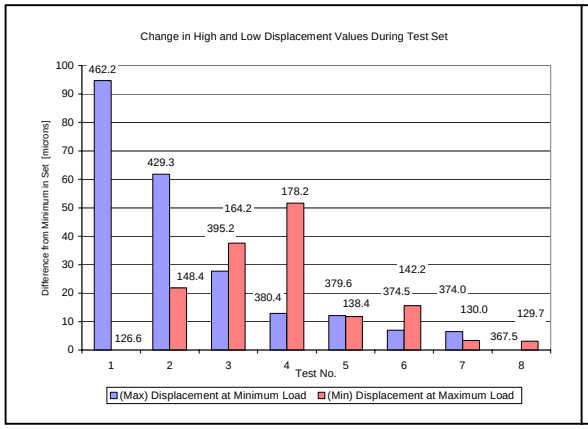

Figure 4.1—10A. (color)
Max / Min sequence:
THUNDER actuator AC229-8

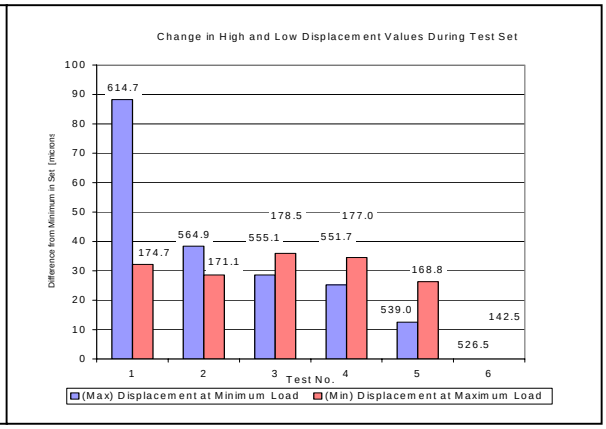

Figure 4.1—10B. (color)
Max / Min sequence:
NCSU actuator nPI060902C

Figure 4.1—11 and 4.1—12 show some variant trends in the data taken in sets of repeated tests. The plot in Figure 4.1—11A is characteristic of actuators bonded with J.B. Weld epoxy. Some type of inelastic deformation occurs during the initial test, and performance is permanently reduced although the actuator may provide a long lifetime of service at its reduced level. The bonds made with this adhesive are typically 100 to 300 μm thick. Figure 4.1—11B shows the test sequence comparison for the only J.B.Weld-bonded actuator for which displacement decreased in small increments in a series of several tests. In fabricating this actuator, the bond was made with as thin a bond as possible. An average bond thickness of 77.3 μm was determined for this “thin bond” actuator.

The examples shown in Figure 4.1—12 and in Figure 4.1—13 are test results associated with actuators bonded with M-Bond epoxy. Figure 4.1—12A shows an increasing trend of low load displacement, with high load displacement mirroring the trend in persistent fashion, although slightly out of phase at first. Figure 4.1—12B shows an unusual trend of low load performance decreasing hardly at all after rebounding from an initial test which yielded a value considerably lower than any other value in the set. A remarkable concurrent trend of substantially increasing high load displacement is also clearly evident. Figure 4.1—13 shows an equally rare instance where no clear trend is

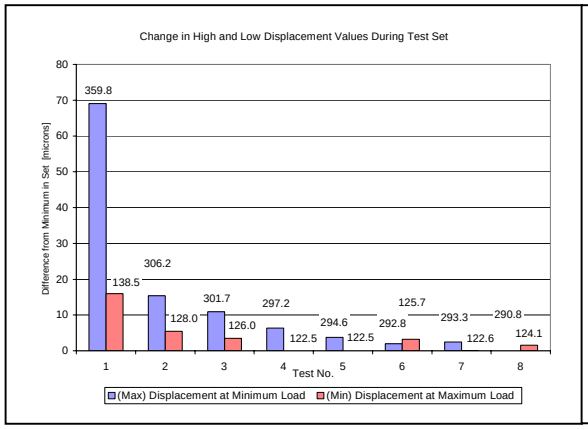

Figure 4.1—11A. (color)
Max / Min sequence:
actuator JBWthK081602C

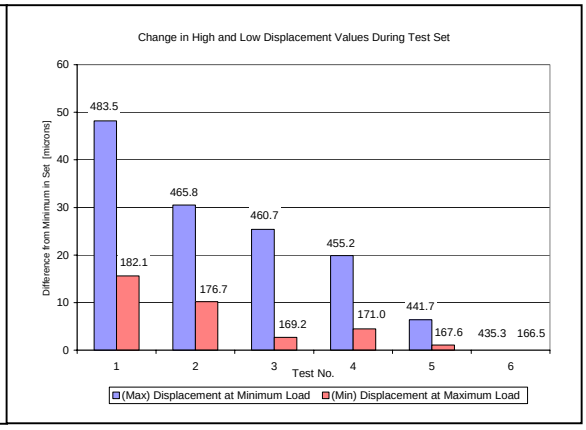

Figure 4.1—11B. (color)
Max / Min sequence:
actuator JBWthN081602A

observed even after more than the usual number of repeated tests. Measured bond thicknesses for the three actuators fabricated with M-Bond adhesive were 16.4, 12.7, and 6.9 mm, in the same order as the sequence of presentation. Although the last value is unusually thin, average load-displacement data for this actuator closely resembled that represented by Figure 4.1—4B, which shows tests results for a different actuator.

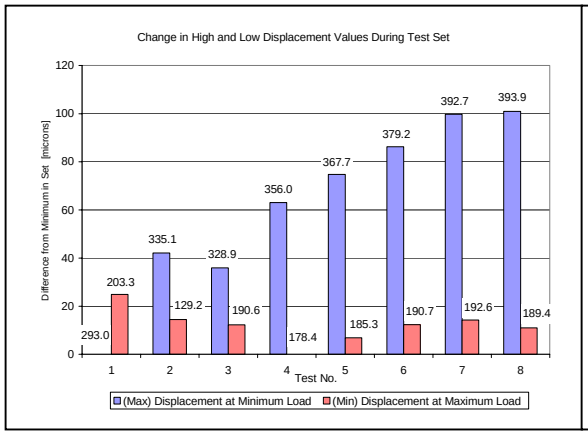

Figure 4.1—12A. (color)
Max / Min sequence:
actuator MB080902B

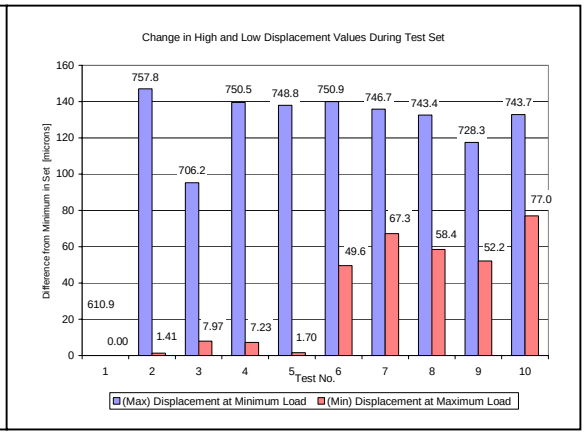

Figure 4.1—12B. (color)
Max / Min sequence:
actuator MB091102A

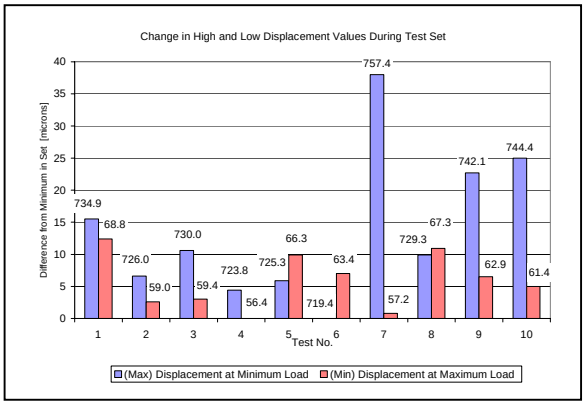

Figure 4.1—13. (color)
Max / Min sequence:
actuator MB100902E

Having made observations about patterns in plotted data and what is indicated about changing performance within a set of repeated tests and between re-tests conducted months apart, we return to analysis and presentation of data. If unloaded deflection and blocking force are to be used as performance metrics, some extrapolation of the plotted load-displacement data will be needed, both across the small gap to zero load and across the usually much larger range of increasing loads until displacement falls to zero.

It may not make sense to apply the extrapolation to plots of averaged data because the variations within test sets do not appear random. If a single uncharacteristic instance (such as the initial high value in Figure 4.1—11A or initial low value in Figure 4.1—12B) were muddled by averaging with many instances of a different sort, important implications about performance might be lost. (Each test involves considerable averaging during data acquisition, so an uncharacteristic result is unlikely to be spurious.) It was decided, then, to use the "Max / Min Sequence" plots discussed above to choose two tests which form an envelope around the entire sequence. This is slightly subjective, but the choices are usually obvious.

Earlier in this project, a single least squares line fitted to the maximum voltage displacement trace was used to determine zero load displacement and blocking force. It should be clear from the foregoing figures, however, that even in the most linear plots of

test results, projected ends of displacement traces often have different slopes. Therefore, it was decided to fit a line to the first five data points to extrapolate zero load, and a line to the last five data points to extrapolate to zero displacement. The goal was to project where the trace of displacement data was directed at either end, so fewer points were used if the direction of the data changed abruptly after its beginning or ending points. Figure 4.1—14 provides an example of the plots that result from this treatment.

In Figure 4.1—14, note that the high boundary for low-load displacement is provided by the same test data trace that provides the low boundary for high-load displacement, with the opposite case provided by the other test data trace. (In other words, the data traces cross each other in the middle.) This was often observed in addition to the situation where data from one test provides both high values with both low values provided by data from the other test. One can also see from Figure 4.1—14 that small slope differences in the lines extrapolated to zero displacement will result in considerably different values for blocking load.

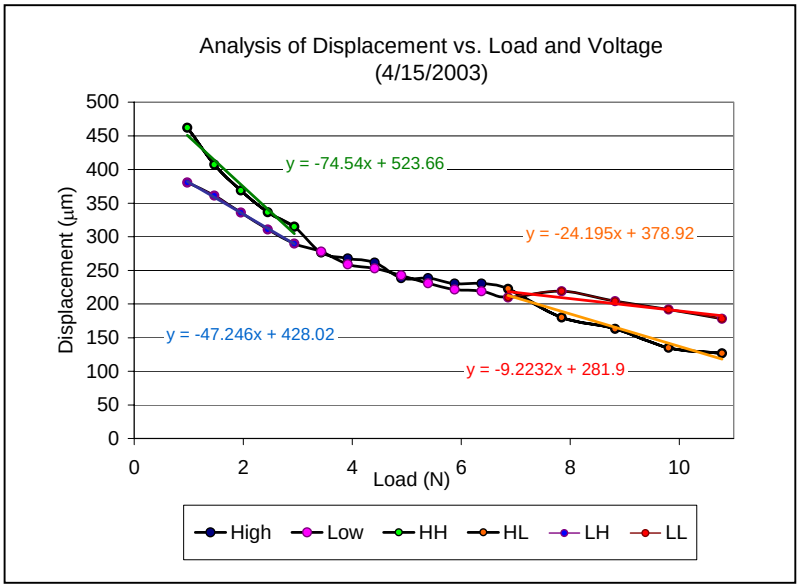

Figure 4.1—14. (color) Example of selecting test results to define high and low boundaries for extrapolated no-load displacement and blocking force

In all, it makes a lot of sense to report actuator performance and a bounded interval for both unloaded displacement and blocking force with an average value for convenience. However, since the average should indicate typical behavior, it should be based on extrapolations of the average of all test data in a set, rather than simply the average between high and low boundary values. Consequently reported averages will rarely fall at the center of the interval between high and low values.

Nonetheless, one expects it to fall somewhere within the interval, even very close to an endpoint. In several cases, the reader will notice the blocking force based on the average of all data falls a little outside the high-low interval. This results from the vagaries of selecting four or five terminal values from a fluctuating data trace to project a line for a considerable distance until it intersects the horizontal axis. An average outside the reported interval will fall close to one endpoint, and often the three values will be close together.

Having discussed data analysis involved in determining free displacement and blocking force for characterizing actuator performance, it should now be explained that adhesive bond thickness and curvature due to pre-stress were measured for a selection of actuators with the intent of correlating one or both of these attributes with performance. Bond thickness was determined by measurement of micrographs of the cross-sectioned actuators, as discussed in Section 3.1.3. The micrographs were calibrated by scale bars automatically inserted by the frame capture software in the microscope system. Curvature, which primarily means as-fabricated curvature due to pre-stress, was more difficult to measure. Both poling and testing—especially under load—change the initial curvature.

When listed in tabular form, average bond thickness values will be accompanied by number of values averaged, sample standard deviations and percentage of the average represented by the standard deviation (relative standard deviation). Each value in an average represents the average of all individual measurements made on one micrograph. Usually, five to ten micrographs were taken across the length (about 3.75 cm) of each half of a cross-sectioned actuator. However, delamination and damage to the bond layer or other issues caused some reported averages to include relatively few values. Nonetheless, a reported bond thickness is an average of averages and considerable data is represented.

In spite of careful measurements, the standard deviation typically represented at least 10 to 25% of an average, which should be considered inherent variability for the process. If the percentage of the average is higher, it is representing actual change in the bond thickness. It was discovered that all bonds, thick or thin, were thicker at the center, and thinner around the edges (or ends of the cross section). The combination of curing a bond under even modest pressure and the fact the uncured adhesive could escape near open edges, while interior adhesive was confined, caused this effect. Figure 4.1—15 shows such a trend in a thick bond made with J.B. Weld epoxy. The relative standard deviation listed is 38%, but part of this is clearly due to actual variation in bond thickness. Each of the two traces is derived from measurements made on each half of the sectioned actuator.

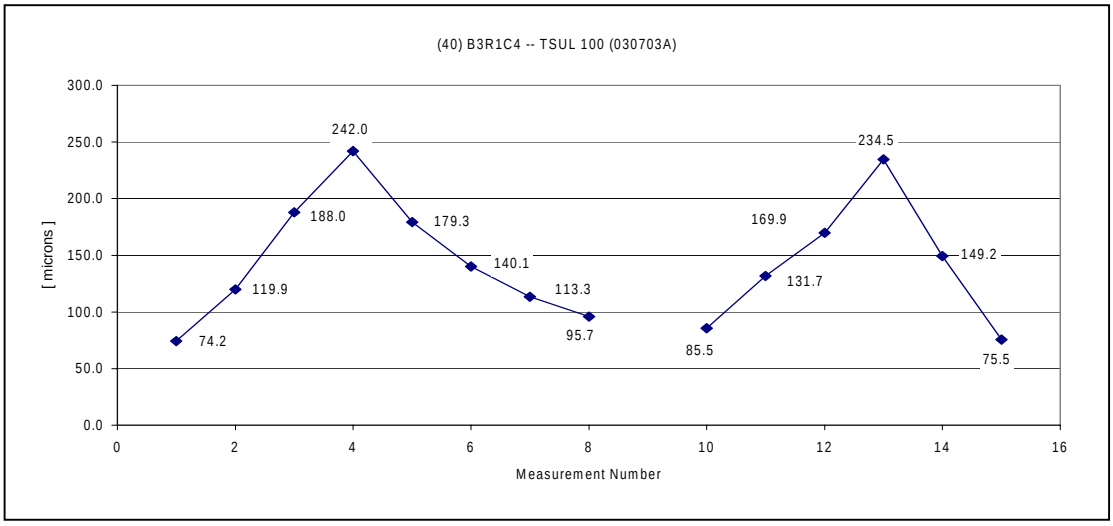

Figure 4.1—15. Illustration of actual bond thickness variation between center and ends of actuator cross section

Actuator curvature due to stress bias, on the one hand, would be the inverse of the radius of curvature, which can be determined. A more convenient indication of curvature would be flexural strain, which would be the height of the center of the simply-supported actuator relative to points of support divided by the horizontal length of actuator between supports. The vertical displacement of the actuator apex was not always measured with the

same distance between supports in some cases as in others. So, curvature due to internal stress bias will be expressed as flexural strain. On the other hand, load-displacement testing of beam actuators always involved a horizontal span (between axles in fixture) of 1.625 inches or 41.28 mm. So, displacements due to load and electric field will not be expressed as flexural strain.

Most measurements of as-fabricated curvature were made using a Mitutoyo micrometer stand while the actuator was centered on a machined block having an "H-shaped" cross section, where the tops of the "H" provided pivot points. The horizontal span between supporting edges was two inches or 50.8 mm. A light spring loading on the micrometer shaft ensured good contact with the test specimen, but introduced a small deflection of the compliant actuators. Although small (< 100 μm), the micrometer-induced deflection was never accounted for because the instrument was not always under my control, and the height of the dial and spindle were often adjusted.

At a later time, the vertical displacement of actuator centers relative to points of support were measured before load-displacement testing in the support fixture (considered part of the apparatus—see Figure 3.1.4—1). Actuators were always clamped to allow a horizontal span of 1.625 inches or 41.28 mm. First, LVDT readings were taken at each end of a clamped actuator and their average subtracted from readings taken at the center of the actuator. A technique was devised for supporting the stylus connected to the LVDT in light contact with the center of a mounted actuator, then releasing it to measure the deflection caused by the known weight of the stylus and LVDT core. This process was repeated 8–10 times before testing.

Initial flexural compliance can be obtained from the difference between flexural strain associated with stress-bias curvature when the weight of the LVDT shaft assembly is supported and is not supported by a mounted actuator. The change in height in millimeters divided by the horizontal span of 41.28 mm (1.625 inches) between clamping axles is then expressed as a percentage and divided by 0.8722 N (the weight of 89g) to give compliance based on a small applied load in the unconventional units of "percent per Newton."

The measurements made by LVDT are more reliable, but the measurements made

by micrometer are often larger. To some extent the difference is not due to measurement error. As-made actuators have the largest curvature they will ever have. Poling, mounting, and testing all reduce the curvature somewhat. It is still fair to correlate performance metrics with curvature as determined by LVDT because this curvature reflects the stress state in the actuator immediately before testing generates the measured deflection as a function of load and voltage. Nonetheless, flexural strain ("curvature") due to pre-stress must necessarily be considered approximate if for no other reason than its changeableness.

4.2 Results from Characterization of Actuators

4.2.1 Characterization of Commercial Pre-stressed Unimorphs

This section will focus on THUNDER^{TM} actuators produced by Face International Corporation (Norfolk, VA), particularly the model 8R which established the in-plane footprint for experimental actuators fabricated in this project (See Figure 3.1.1.2—1.) Another commercial actuator, manufactured by PAR Technologies LLC (Hampton VA) was also tested and was found to have generally comparable performance. The in-plane footprint for the PAR Tech specimens tested was approximately the same as that of the Face Corporation model 8R. The PAR Tech actuators appear to have been manufactured by a lower temperature process than the Face Corporation THUNDER actuators.

A micrograph of a THUNDER actuator cross-section is shown in Figure 4.2—1 with layers identified and thickness measurements shown. The microscope used did not automatically insert a scale bar, so the inset shows a micrograph of a graticule taken at the same magnification with overlaid bar created by Photoshop Image Editor. The substrate bottom edge appears to extend below the overlaid line, but this results from sample preparation. The line of darker spots indicates the actual substrate bottom edge.

The explanation is that particles of metal and embedding epoxy formed a mixture which adhered as a band of light-reflecting "smear" that was not removed in grinding. When grinding media travel from harder to softer material, there is a tendency for the level of softer material to fall below that of the adjacent harder material, facilitating such a

deposition. Note also that the bottom surface of lead zirconate titanate (PZT) ceramic has delaminated from the polyimide bond layer.

Although the ceramic grain structure does not appear to contain a significant void fraction at high magnification (Figure 4.2.1—2), there is porosity on a larger scale evident in Figure 4.2.1—1, taken at low magnification. (The polyhedral grain shapes in Figure 4.2.1—2 are associated with void exclusion, implying minimal small-scale void fraction.) It was found that the piezoceramic thin plates used for in-house fabrication (probably similar material to that used by the Face Corporation) allowed organic solvents to permeate through rapidly when placed on a perforated vacuum plate. The circles in Figure 4.2.1—2 were overlaid to determine effective ceramic grain diameter. Table 4.2.1—1 lists results based on measurements of the overlaid circles.

Results from characterization of a set of model 8R THUNDER actuators will be assembled in Table 4.2.1—2. The format of this table, which condenses experimental results from many sources, will be the same as will be used for other characterization tables presented in this chapter. The format requires explanation, which will be given now. The intent is to make the results more accessible through an organized data structure.

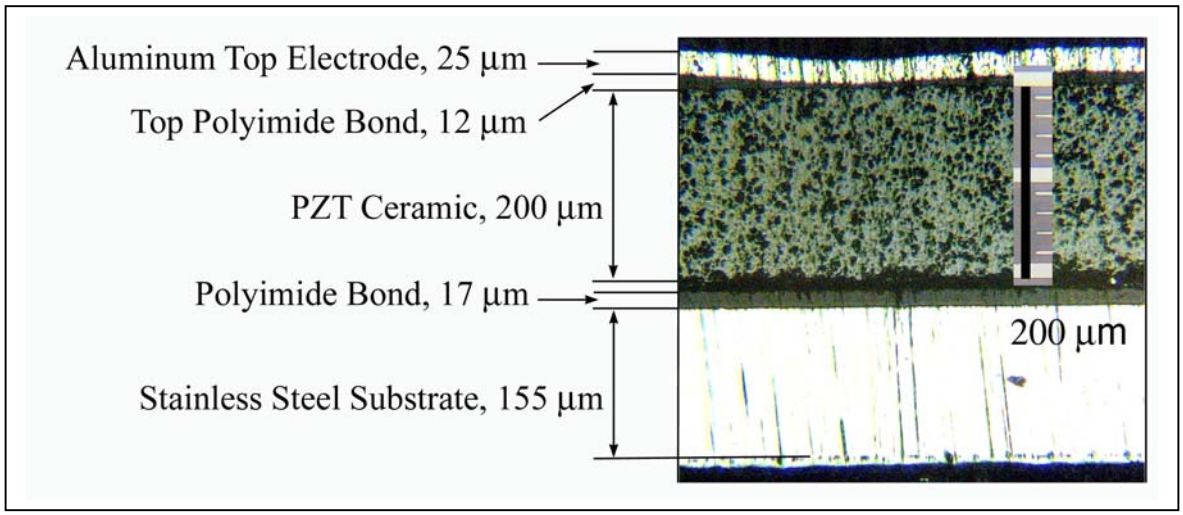

Figure 4.2.1—1. Micrograph of THUNDER actuator cross-section (Thickness values indicated are averages of five or more measurements taken across image.)

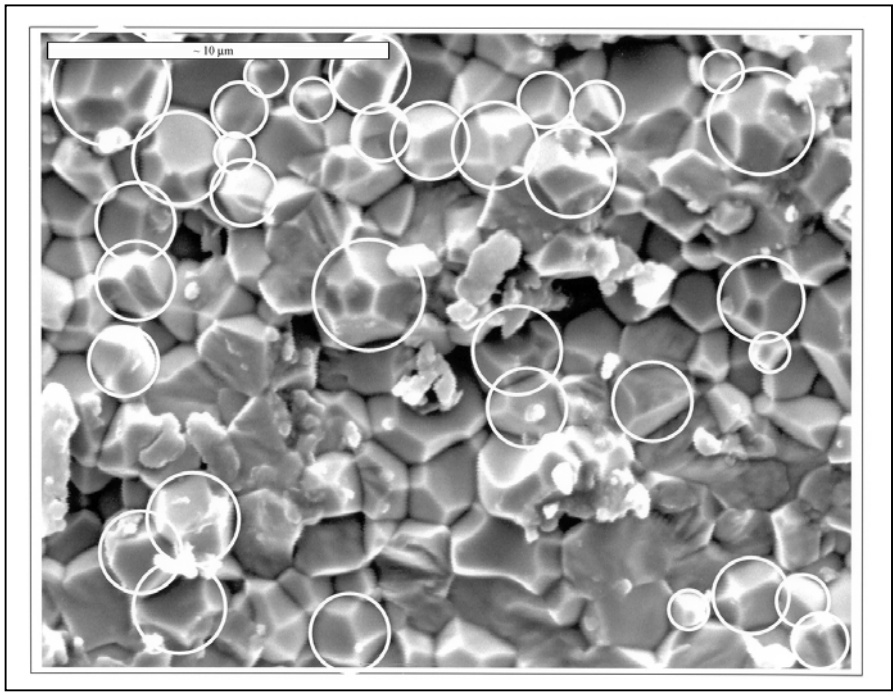

Figure 4.2.1—2. SEM Micrograph of fractured surface of the piezoceramic layer in a THUNDER actuator. (Micrograph by Chad M. Parish, Analytical Instrumentation Facility, NC State University)

Table 4.2.1—1. Approximate grain sizes in microns taken as diameters of circles over image shown in Figure 4.2.1—2.

Average (n = 33):		2.130		Maximum:		3.533	
Standard Deviation:		0.652		Minimum:		1.080	
3.53	2.73	2.54	2.37	2.29	1.97	1.58	1.25
3.32	2.73	2.49	2.37	2.27	1.70	1.54	1.24
3.12	2.60	2.44	2.35	2.27	1.64	1.50	1.21
2.74	2.58	2.41	2.34	2.08	1.58	1.26	1.16
							1.08

The tables begin, of course, with actuator identifications which are based on bond type, date of fabrication, and letter to indicate an individual specimen in a set made at the same time (two to six specimens). Earlier actuators presume bonding using LaRC-SI polyimide adhesive and focus on substrate thickness and material and are numbered in a continuing series. Subsequent columns in the tables give unloaded displacement, blocking force, bond thickness and curvature expressed as flexural strain. However, there is an internal structure within cells in each column, which is explained in Figures 4.2.1—3 and 4.2.1—4.

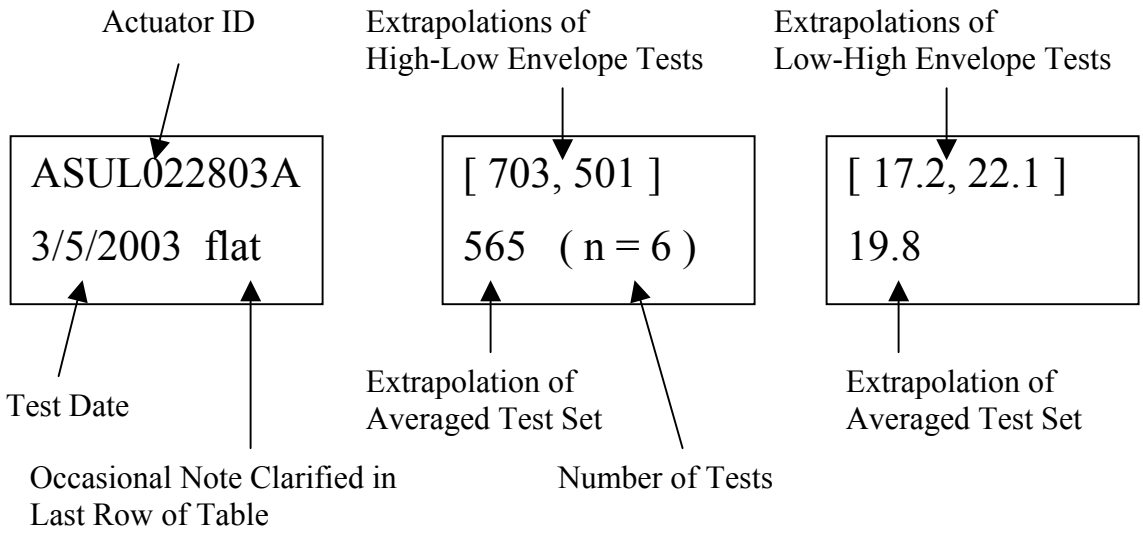

Figure 4.2.1—3. Key to organization of identification, free deflection and blocking force data (left to right) for a particular actuator

There are some additional items to mention. In some cases, the same actuator is listed two or more times with different test dates. When the same actuator was tested more than once, the separate results have been listed as though separate actuators were tested, but any bond thickness or curvature data is listed only once beside one of the multiple load-displacement listings. From the introductory examples and discussion, we know that

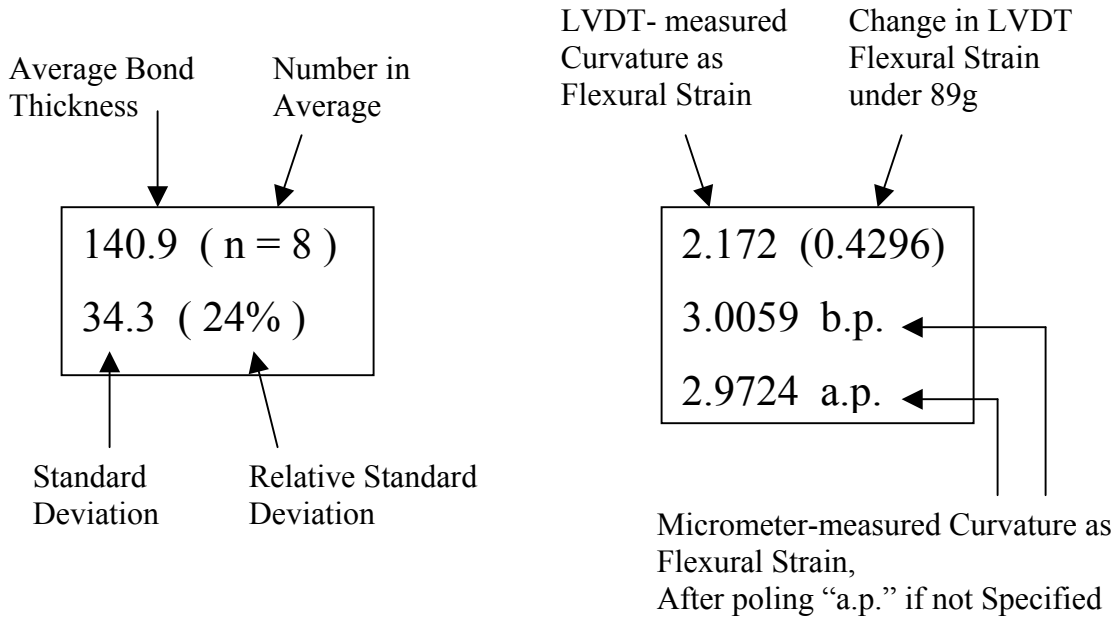

Figure 4.2.1—4. Key to organization of bond thickness and curvature data for a particular actuator

some load-displacement plots displayed a localized maximum displacement in the middle of the load range. These maxima are listed in the table with the load at which they occurred only if the values were greater than the zero load displacement. (For example, Table 4.2.2—3 lists "795.2 @ 3.43 N" beneath high / low envelope and average displacement values to indicate a maximum peak in microns at non-zero load.) The phenomenon tends to be associated with especially thin bonds. Any instance of load-displacement data based on a test set with only one test is indicated by "single test" noted where the interval for extrapolation of high-low envelope tests would normally be reported. The nearly exclusive reason for conducting only a single test was actuator failure caused by electrical short, ceramic cracking, or delamination.

Table 4.2.1—3 provides characterization results for three PAR Technologies actuators. The primary difference between these actuators and Face Corporation THUNDER actuators is that the PAR Tech actuators have thicker bonds, and the manufacturer has incorporated elements to ensure good electrical contact across the bond layer. Observations during fabrication and testing of my actuators suggest that it may not be necessary to ensure conduction across thick bonds. Either a conductive path of some kind develops during flexure, or the metal substrate and bottom and top conductive surfaces of an electroded piezoceramic plate behave as two capacitors in series. Although not captured in the data table, load-displacement plots for PAR Tech actuators tended to show a rapid drop in zero load displacement (occurring within the initial load interval of 4 – 5 N) followed by the tendency for displacement to further decrease at a very low rate as load increases.

Table 4.2.1—2. Characterization of THUNDER actuators
(Refer to text for explanation of format.)

Actuator Identification, Test Date	Unloaded Displacement [μm]	Blocking Force [N]	Bond Thickness [μm]	Curvature as Flexural Strain (percent)
AA 2/13/2003	[480, 463] 472 (n = 4)	[14.7, 18.4] 15.3		2.488 (0.4097)
AC181-15 3/4/2003	[615, 470] 543 (n = 4)	[19.5, 20.7] 20.1	12.4 (n = 10) 3.6 (29%)	3.285 (0.5404)
AC181-17 2/14/2003	[480, 372] 403 (n = 4)	[22.9, 24.0] 23.3		3.879 (0.7188)
AC229-5 5/22/2003	[Single Test] 523	[Single Test] 16.2	23.8 (n = 15) 5.7 (24%)	3.252 (0.5936)
AC229-8 4/15/2003	[524, 428] 444 (n = 8)	[15.7, 30.6] 20.3		2.918 (0.4308)

Table 4.2.1—2, Continued.

AC229-8 7/21/2003	[449, 400] 425 (n = 2)	[19.9, 30.5] 23.5		
AC232-30 4/10/2003	[562, 414] 463 (n – 6)	[15.1, 15.7] 15.6	23.6 (n = 11) 4.0 (17%)	
AC232-30 7/21/2003	[433, 404] 419 (n = 2)	[17.1, 17.5] 17.3		1.553 (0.4816)
E 4/8/2003	[457, 404] 416 (n = 5)	[15.5, 19.6] 17.4		2.798 (0.5411)

Table 4.2.1—3. Results from characterization of PAR Technologies actuators (Refer to text for explanation of format.)

Actuator Identification, Test Date	Unloaded Displacement [μm]	Blocking Force [N]	Bond Thickness [μm]	Curvature as Flexural Strain (percent)
PAR Tech A 6/21/2000	[506, 455] 460 (n = 6)	[16.3, 20.9] 18.0		
PAR Tech 3 5/20/2003	[405, 342] 368 (n = 4)	[15.1, 16.8] 16.3		
PAR Tech 6 5/20/2003	[388, 338] 369 (n = 4)	[21.7, 27.4] 24.4	68.5 (n = 13) 20.5 (30%)	

4.2.2 Characterization of NCSU-Fabricated Actuators with Polyimide Bonds

Actuators fabricated with LaRC-SI polyimide adhesive were originally fabricated using substrates five and ten mils thick (one mil = 0.001 inch = 25.4 μm). THUNDER model 8R actuators also use 5-mil substrates. The practice of also fabricating actuators on substrates twice as thick was intended to provide comparison, modeling input, and possibly improved performance at high load. Within a few months, the standard thicknesses were changed to four and eight mils. Since piezoceramic thin plates 7.5 mils thick were used throughout this project, the four mil substrates were closer to the ideal one-third fraction of total thickness reported in the literature. Tables 4.2.2—1 through 4.2.2—4 each present characterization results for actuators fabricated on substrates of the same thickness in order from thicker to thinner.

Table 4.2.2—1. Characterization of NCSU polyimide-bonded actuators fabricated on stainless steel substrates 10 mils thick (Refer to Section 4.2.1 for explanation of format.)

Actuator Identification, Test Date	Unloaded Displacement [μm]	Blocking Force [N]	Bond Thickness [μm]	Curvature as Flexural Strain (percent)
Ncsu 10SS1 6/23/2000	[172, 151] 155 (n = 6)	[20.2, 21.7] 23.0		
Ncsu 10SS1 5/5/2003	[216, 214] 215 (n = 4)	[13.4, 17.3] 13.9	6.2 (n = 3) 0.6 (10%)	2.123 (0.2030)
Ncsu 10SS21 7/12/2000	[215, 189] 207 (n = 6)	[16.2, 23.4] 18.2	14.1 (n = 10) 2.3 (17%)	

Table 4.2.2—2. Characterization of NCSU polyimide-bonded actuators fabricated on stainless steel substrates 8 mils thick (Refer to Section 4.2.1 for explanation of format.)

Actuator Identification, Test Date	Unloaded Displacement [μm]	Blocking Force [N]	Bond Thickness [μm]	Curvature as Flexural Strain (percent)
nPI060902C 1/17/2003	[691, 575] 619 (n = 6)	[16.3, 18.8] 18.3	6.9 (n = 17) 1.5 (22 %)	7.742 (1.434) 4.7815 b.p.
nPI060902C 4/7/2003	[Single Test] 693	[Single Test] 11.7		

Table 4.2.2—3. Characterization of NCSU polyimide-bonded actuators fabricated on stainless steel substrates 5 mils thick (Refer to Section 4.2.1 for explanation of format.)

Actuator Identification, Test Date	Unloaded Displacement [μm]	Blocking Force [N]	Bond Thickness [μm]	Curvature as Flexural Strain (percent)
Ncsu 5SS17 5/13/2003	[533, 487] 510 (n = 2) 795.2 @ 3.43 N	[10.8, 10.9] 10.8		
Ncsu 5SS17 5/21/2003	[Single Test] 531.1 753.1 @ 3.43 N	[Single Test] 10.1	6.1 (n = 14) 2.0 (33%)	2.662 (1.068)
Ncsu 5SS19 6/21/2000	[243, 135] 170 (n = 6)	[11.1, 11.5] 11.2	12.1 (n = 5) 0.9 (7%)	
Ncsu 5SS19 5/12/2003	[273, 242] 270 (n = 4)	[16.1, 17.2] 16.5		2.345 (0.6590)

Table 4.2.2—3, Continued.

Actuator Identification, Test Date	Unloaded Displacement [μm]	Blocking Force [N]	Bond Thickness [μm]	Curvature as Flexural Strain (percent)
Ncsu 5SS31 6/30/2000	[258, 250] 284 (n = 6)	[7.9, 7.9] 8.0	9.4 (n = 16) 4.0 (43%)	
Ncsu 5SS31 5/14/2003	[421, 386] 401 (n = 3)	[9.1, 10.8] 9.6		3.058 (1.088)

Table 4.2.2—4. Characterization of NCSU polyimide-bonded actuators fabricated on stainless steel substrates 4 mils thick (Refer to Section 4.2.1 for explanation of format.)

Actuator Identification, Test Date	Unloaded Displacement [μm]	Blocking Force [N]	Bond Thickness [μm]	Curvature as Flexural Strain (percent)
nPI062102A 1/20/2003	[Single Test] 742	[Single Test] 17.9	13.5 (n = 9) 3.3 (24%)	3.406 (1.264) 6.7282 b.p.
nPI102802B 1/22/2003	[Single Test] 220 436.8 @ 5.88 N	[Single Test] 12.4	5.6 (n = 7) 1.1 (19%)	4.034 (1.592)
nPI062102C 4/7/2003	[576, 322] 472 (n = 6) 460.2 @ 4.90 N	[10.5, 11.2] 12.0	6.5 (n = 3) 1.2 (19%)	5.692 (1.178) 6.7087 b.p.

Table 4.2.2—5 lists results for a single actuator fabricated on an aluminum substrate. Aluminum substrates might yield higher performance actuators than those made with stainless steel. [1, 3] Since the Young's modulus of aluminum is less than half that of

a typical stainless steel, actuators made with aluminum would have higher compliance and should yield greater low load displacement. Higher differential thermal contraction between aluminum and ceramic should create greater performance enhancement due to the stress-bias mechanism. In my experience, actuators made with aluminum substrates were fragile and did not perform nearly as well as actuators made with stainless steel, so few were made. The actuator represented by the data in Table 4.2.2—5 is interesting because even though its unloaded displacement is low, its high load performance and blocking force were impressive.

Table 4.2.2—5. Characterization of NCSU polyimide-bonded actuator fabricated on aluminum substrate 8 mils thick (Refer to Section 4.2.1 for explanation of format.)

Actuator Identification, Test Date	Unloaded Displacement [μm]	Blocking Force [N]	Bond Thickness [μm]	Curvature as Flexural Strain (percent)
nPI070102A 7/5/2002	[161, 138] 153 (n = 6)	[46.0, 46.7] 46.3		

4.2.3 Characterization: NCSU Actuators Fabricated with M-Bond Adhesive

In addition to effects of substrate and bond thickness and other consequences of fabricating actuators with M-Bond adhesive, the data will reflect refinements in technique. Although refinements in technique are desirable, they introduce yet another factor into the data. The 080902 set was made by brushing M-Bond with the brush installed in the cap of one of the mixing bottles supplied by the manufacturer. (In case the reader has not guessed, the numeric part of actuator identification is simply the date the particular actuator set was made.) Application of M-Bond adhesive by airbrush was first used with the 091102 set,

and an improved assembly process was combined with airbrush application for the 100902 set.

Of course, substrate thickness has a strong influence, and the 080902 set consisted entirely of actuators made with 8 mil substrates. The 091102 set consisted entirely of actuators made with 4 mil substrates, and the 100902 set used both. In general, the thinner substrates provide higher unloaded displacements, while thicker substrates provide higher blocking loads. Characterization results are given in Tables 4.2.3—1 through 4.2.3—4.

Table 4.2.3—1. Characterization of NCSU actuators bonded with M-Bond adhesive fabricated on stainless steel substrates 8 mils thick
(Refer to Section 4.2.1 for explanation of format.)

Actuator Identification, Test Date	Unloaded Displacement [μm]	Blocking Force [N]	Bond Thickness [μm]	Curvature as Flexural Strain (percent)
MB080902A 8/12/2002	[539, 491] 514 (n = 6)	[9.9, 10.0] 9.8	14.1 (n = 20) 4.9 (35%)	4.418 (0.5276) 3.4055 b.p.
MB080902A 8/22/2002	[360, 64] 278 (n = 6)	[16.6, 18.6] 18.0		
MB080902A 3/4/2003	[693, 648] 657 (n = 4)	[16.8, 18.0] 17.2		
MB080902A 4/11/2003	[652, 646] 632 (n = 3)	[15.6, 16.2] 16.3		
MB080902B 8/16/2002	[410, 107] 299 (n = 8)	[9.7, 18.3] 18.2	16.4 (n = 15) 9.0 (55%)	3.3209 b.p. 3.0217 a.p.
MB080902C 8/21/2002	[213, 168] 182 (n = 6)	[13.8, 16.0] 14.6	10.6 (n = 20) 1.9 (18 %)	2.172 (0.4296) 3.0059 b.p. 2.9724 a.p.

Table 4.2.3—1, Continued.

Actuator Identification, Test Date	Unloaded Displacement [μm]	Blocking Force [N]	Bond Thickness [μm]	Curvature as Flexural Strain (percent)
MB080902C 4/9/2003	[676, 659] 646 (n = 6)	[14.2, 18.3] 16.0		
MB080902D 8/21/2002	[587, 531] 559 (n = 3)	[14.7, 18.0] 17.7	13.4 (n = 5) 4.5 (33%)	3.2756 b.p. 2.5354 a.p.
MB100902A 4/25/2003	[542, 491] 501 (n = 10)	[18.2, 19.2] 18.9	8.0 (n = 17) 1.3 (17%)	5.842 (0.3435)
MB100902B 10/10/2002	[746, 604] 633 (n = 6)	[16.6, 17.0] 17.0	10.5 (n = 15) 2.3 (22%)	
MB100902C 4/30/2003	[509, 486] 507 (n = 6)	[17.1, 21.1] 16.2	7.8 (n = 13) 2.0 (25%)	

Table 4.2.3—2. Characterization of NCSU actuators bonded with M-Bond adhesive fabricated on stainless steel / aluminum substrates 8 mils thick (Refer to Section 4.2.1 for explanation of format.)

Actuator Identification, Test Date	Unloaded Displacement [μm]	Blocking Force [N]	Bond Thickness [μm]	Curvature as Flexural Strain (percent)
MB101602A 10/22/2002 4 SS / 4Al	[678, 593] 631 (n = 7)	[13.3, 14.6] 14.6		4.062 (0.4502) 4.6339
MB101602A 4/22/2003 4 SS / 4 Al	[593, 537] 558 (n = 6)	[13.8, 15.3] 14.2	14.9 (n = 14) 1.7 (11%)	

In spite of the influence of fabrication technique as well as the more evident effect of substrate thickness on actuator performance, variability in performance is high enough that some actuators made with earlier technique out-perform some actuators made with supposedly improved technique. Reduction in process variability would be a useful next step, which would be facilitated by the fact that actuator fabrication with M-Bond adhesive is relatively simple once good techniques have been devised. Actuators made using 4-mil substrates in the 100902 set, which incorporated both improved assembly techniques and application of adhesive by airbrush do indeed stand out for uniformly high performance.

Although M-Bond adhesive was selected based on manufacturer's claim that the product provides an exceptionally thin glue-line, the data suggest that some actuators were made with too thin a bond for optimal performance. Other actuators may have had bonds too thick for optimal performance although performance apparently degrades gradually as bond thickness increases. The bond thickness listed as 60.1 μm for the first actuator in the next table (Table 4.2.3—3) is suspect. Some samples used for bond thickness determination had delaminated and the gap had completely filled with consolidated foreign material. The high number was reported because of other relatively thick bonds in the set, but a re-measurement of the cross-section assuming presence of foreign material gave a bond thickness of 12.7 μm, which may or may not be correct.

Table 4.2.3—3. Characterization of NCSU actuators bonded with M-Bond adhesive fabricated on stainless steel substrates 4 mils thick
(Refer to Section 4.2.1 for explanation of format.)

Actuator Identification, Test Date	Unloaded Displacement [μm]	Blocking Force [N]	Bond Thickness [μm]	Curvature as Flexural Strain (percent)
MB091102A 9/16/2002	[823, 555] 771 (n = 10)	[11.4, 15.5] 11.7	60.1? (n = 9) 7.6 (13%)	5.398 (0.9973)
MB091102A 2/13/2003	[814, 784] 798 (n = 4)	[12.5, 13.0] 12.7		

Table 4.2.3—3, Continued

Actuator Identification, Test Date	Unloaded Displacement [μm]	Blocking Force [N]	Bond Thickness [μm]	Curvature as Flexural Strain (percent)
MB091102B 3/3/2003	[Single Test] 1189 (n = 10)	[Single Test] 11.0	33.0 (n = 7) 6.8 (18%)	2.745 (1.272) 3.9291
MB091102C 4/16/2003	[1061, 498] 825 (n = 7)	[11.9, 17.9] 13.3	28.4 (n = 21) 12.5 (44%)	2.803 (1.015) 3.6122
MB091102D 5/23/2003	[947, 464] 685 (n = 6)	[8.6, 9.2] 8.9	29.2 (n = 6) 11.1 (38%)	4.805 (0.7664) 3.6358
MB100902D 10/11/2002	[911, 802] 849 (n = 2)	[8.8, 9.6] 9.7		 4.2657
MB100902D 1/27/2003	[753, 692] 691 (n = 6)	[10.9, 11.5] 11.5		 2.5917
MB100902D 4/24/2003	[663, 643] 643 (n = 6)	[10.8, 10.8] 10.7	5.8 (n = 8) 5.8 (12%)	
MB100902E 4/29/2003	[789, 771] 788 (n = 10)	[10.8, 11.0] 10.8	6.9 (n = 19) 1.3 (19%)	1.226 (0.8865) 4.2382
MB100902F 4/21/2003	[827, 697] 754 (n = 6)	[11.0, 11.0] 11.0	7.1 (n = 23) 1.8 (26%)	2.475 (1.218) 4.1713
MB101602E2x 10/18/2002	[889, 634] 802 (n = 6)	[11.0, 11.1] 11.2	16.2 (n = 6) 2.3 (14%)	 4.2677
MB101602F3x 10/17/2002	[934, 788] 833 (n = 6)	[10.5, 12.3] 11.9	35.1 (n = 12) 7.5 (21%)	 4.1535

Table 4.2.3—4. Characterization of NCSU actuators bonded with M-Bond adhesive fabricated on thick substrates (Refer to Section 4.2.1 for explanation of format.)

Actuator Identification, Test Date	Unloaded Displacement [μm]	Blocking Force [N]	Bond Thickness [μm]	Curvature as Flexural Strain (percent)
MB101402A 11/8/2002 12 mil SS	[519, 470] 481 (n = 6)	[22.1, 22.7] 22.7		2.5610
MB101402B 11/8/2002 12 mil SS	[497, 422] 446 (n = 5)	[18.6, 19.5] 19.3	14.6 (n = 17) 4.8 (33%)	2.5197
MB 101402D 11/15/2002 20 mil Al	[168, 113] 142 (n = 3)	[21.3, 31.8] 20.9		3.0394
MB 101402E 11/15/2002 20 mil Al	[337, 289] 304 (n = 6)	[18.1, 18.3] 18.2	14.8 (n = 18) 3.7 (25%)	3.0787
MB 101402F 11/15/2002 20 mil Al	[358, 315] 329 (n = 6)	[20.6, 21.0] 21.0	14.5 (n = 24) 3.1 (21%)	3.0177

One final result in this sub-section should be noted. Table 4.2.3—2 lists actuator MB101602A, which was made with an upper (adjacent to ceramic) stainless steel substrate layer and lower aluminum layer, each 4 mils thick. The idea was to use the higher coefficient of thermal expansion in the aluminum layer to introduce additional curvature due to pre-stress since actuators bonded with M-Bond adhesive were cured at a lower temperature than those made with polyimide adhesive. This design resulted in curvature as high as, but no higher than other actuators using 8-mil stainless steel substrates, and performance as good as, but no better than actuators made with 8-mil stainless steel substrates.

4.2.4 Characterization: NCSU Actuators Fabricated with J.B.Weld Adhesive

Actuators made with this consumer product were unlike actuators previously discussed in that the bond was approximately the same thickness as substrate and ceramic, or at least the same order of magnitude in the case of "thin" bonds with J.B. Weld epoxy. Hence these were composite material actuators. The motivation for trying J.B. Weld epoxy was to use a truly different adhesive in case the envelope of other adhesive types was too limited and to make unimorphs at room temperature for comparison with pre-stressed unimorphs. A general description of this adhesive was given in Section 3.1.1.4.2. The first actuator made with J.B. Weld epoxy (JW 013002A) generated over one millimeter maximum displacement. Although this maximum performance was never duplicated, performance of these composite unimorphs was generally comparable to other actuator types made and tested in-house.

Two micrographs in Figure 4.2.4—1 show cross-sections of actuators bonded with J.B. Weld adhesive. The bright circle inside the bond (middle) layer is the section of an embedded wire used to create a bond of uniform, known thickness. Nomarski contrast has been used in both images. In the image at left it aids in defining the top edge of the metal substrate. Particles of polymer and metal produced by grinding tend to mix and produce light-reflecting "smear" which obscures the edges in actuator cross sections. In both

images, the existence of embedded, spherical voids scattered throughout the bond layer is revealed. The metal flecks are probably not actually present in uncut actuator bond layers, but are deposited during sawing and grinding. Since the bond material is softer than material on either side, it is probably slightly hollowed and retains the particles.

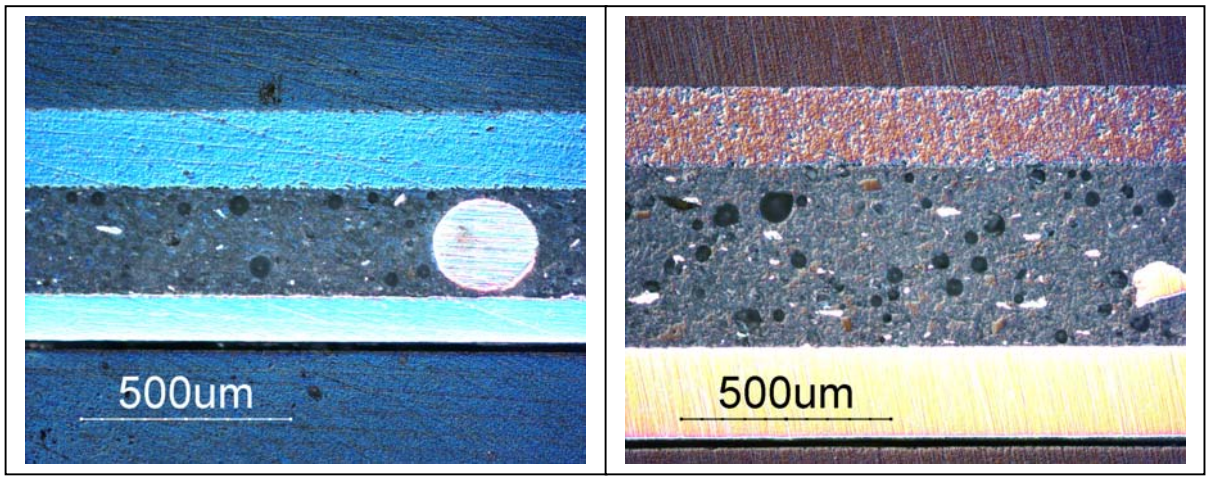

Figure 4.2.4—1. (color) Cross-sections of actuators bonded with J.B.Weld epoxy showing open voids in bond layer and embedded wire at left

Tables 4.2.4—1 and 4.2.4—2 present data resulting from characterization of actuators made with J.B. Weld epoxy. It was quickly realized that with the added rigidity of such thick bonds that it was pointless to use metal substrates thicker than 4 mils. However, one can see from the data that keeping the bond thickness well below 100 μm facilitates good performance as much or more than substrate thickness. The embedded wires noted in three entries in Table 4.2.4—2 were features in an experiment to determine the effect of preferential stiffening in the axial direction (without stiffening the transverse direction). There is a suggestion of modest performance gain, but the performance of actuators made with wires 7.5 mils in diameter is clearly hampered by the rigidity of these large wires.

Table 4.2.4—1. Characterization of NCSU actuators bonded with J.B.Weld adhesive fabricated on stainless steel substrates 8 mils thick (Refer to Section 4.2.1 for explanation of format.)

Actuator Identification, Test Date	Unloaded Displacement [μm]	Blocking Force [N]	Bond Thickness [μm]	Curvature as Flexural Strain (percent)
JW K081602C 8/19/2002	[352, 309] 319 (n = 8)	[18.5, 20.0] 19.5		
JW N081602A 8/19/2002	[486, 457] 476 (n = 6)	[18.1, 18.4] 18.5	77.3 (n = 15) 16.3 (21%)	1.5762
JW N081602B 8/19/2002	[750, 597] 622 (n = 6)	[15.2, 17.3] 16.3	59.3 (n = 11) 4.6 (8%)	

Table 4.2.4—2. Characterization of NCSU actuators bonded with J.B.Weld adhesive fabricated on stainless steel substrates 4 mils thick (Refer to Section 4.2.1 for explanation of format.)

Actuator Identification, Test Date	Unloaded Displacement [μm]	Blocking Force [N]	Bond Thickness [μm]	Curvature as Flexural Strain (percent)
JW 013002A 2/1/2002	[1057, 715] 778 (n = 6)	[12.4, 12.6] 12.4		
JW 091102G 4/18/2003	[335, 293] 314 (n = 3)	[12.5, 13.0] 21.9	271.2 (n = 6) 16.0 (6 %)	2.985 (0.465)
JW 100302A 10/4/2002 (non | | wires)	[636, 465] 503 (n = 6)	[18.1, 21.1] 20.4	261.4 (n = 10) 16.7 (6%)	

Table 4.2.4—2, Continued.

Actuator Identification, Test Date	Unloaded Displacement [μm]	Blocking Force [N]	Bond Thickness [μm]	Curvature as Flexural Strain (percent)
JW 100302B 10/4/2002 (| | wires)	[672, 473] 520 (n = 6)	[18.1, 21.0] 20.2	249.4 (n = 12) 29.9 (12%)	
JW 101402G 10/15/2002 (| | wires, 7.5)	[488, 406] 422 (n = 8)	[17.2, 18.5] 18.2	308.6 (n = 11) 63.7 (21%)	
JW K082602D 8/28/2002	[621, 589] 602 (n = 3)	[16.1, 16.3] 16.3		
JW K082602E 8/28/2002	[686, 568] 616 (n = 3)	[14.3, 16.9] 16.0	98.8 (n = 13) 17.4 (18%)	
"non | | wires" indicates embedded wires in a zig-zag line unaligned with actuator axis " | | wires" indicates embedded wire aligned parallel to actuator long axis. " | | wires, 7.5" indicates aligned, embedded wires with a diameter of 7.5 mils.				

4.3 Comparison and Evaluation of Actuator Characterization Results

Figure 4.3—1 plots free displacement values determined for all actuators tested, as reported in the twelve tables in Section 4.2. Figure 4.3—2 provides the complementary spectrum of blocking force for all actuators tested. In fact, the pair of plots reveal that high free displacements typically correspond with low blocking force and *vice versa*. (The "actuator type codes" along the bottom of Figures 4.3—1 through 4.3—3 are listed in Table 4.3—1 together with the names given in the tables in Section 4.2. as a cross reference)

If the tendency for one aspect of performance to gain in proportion to what the

other loses is based on something inherent in the mechanics of a unimorph, pre-stressed or not, then the product of blocking force and free displacement for all unimorphs should fall within a horizontal interval. It might be more appropriate to take one-half the product because this would represent area under a straight line connecting the value of free displacement with blocking force.

Figure 4.3—3 shows that the half-products (divided by 100 to cause resulting numbers to fit approximately between zero and one hundred) tend to fall within the interval between 30 and 60. (The combination of units in microns and Newtons with scaling by 100 means that a plotted value of 100 corresponds to 0.01 J, a plotted value of 50 corresponds to 0.005 J, and so forth.) Since the size of the numbers for displacement are so much larger than the numbers for blocking force, plotted values falling above or below this interval tend to indicate unusually high or low displacement with less implication regarding blocking force. Any attempt to scale either displacement or blocking force simply scales the product.

So essentially, division by 100 for convenience has either divided displacement by 100 or multiplied blocking force by 100. However, this does not address the fact that although a change from 10 to 11 N blocking force influences the product more than a change between 401 and 402 μm in displacement, the magnitude of the product is much closer to the magnitude of the displacements than to the magnitude of the blocking forces. Attempts to develop an indicator which treats each performance metric equally produced somewhat contrived comparisons which are not worth presenting here. It is interesting, however, that the scaled half-products tend to fall within an interval.

This suggests there may be a physical envelope for unimorphs which make it difficult to increase both free displacement and blocking force because increasing one property tends to decrease the other. In spite of this possible constraint, it is evident from Figure 4.3—1 that actuators bonded to 4-mil substrates with M-Bond adhesive stand out for free displacement capability among all types of actuators characterized. Modest deficiency in high-load displacement in this sub-group (that is, having relatively lower blocking force) compensates for outstanding low-load (free displacement) performance.

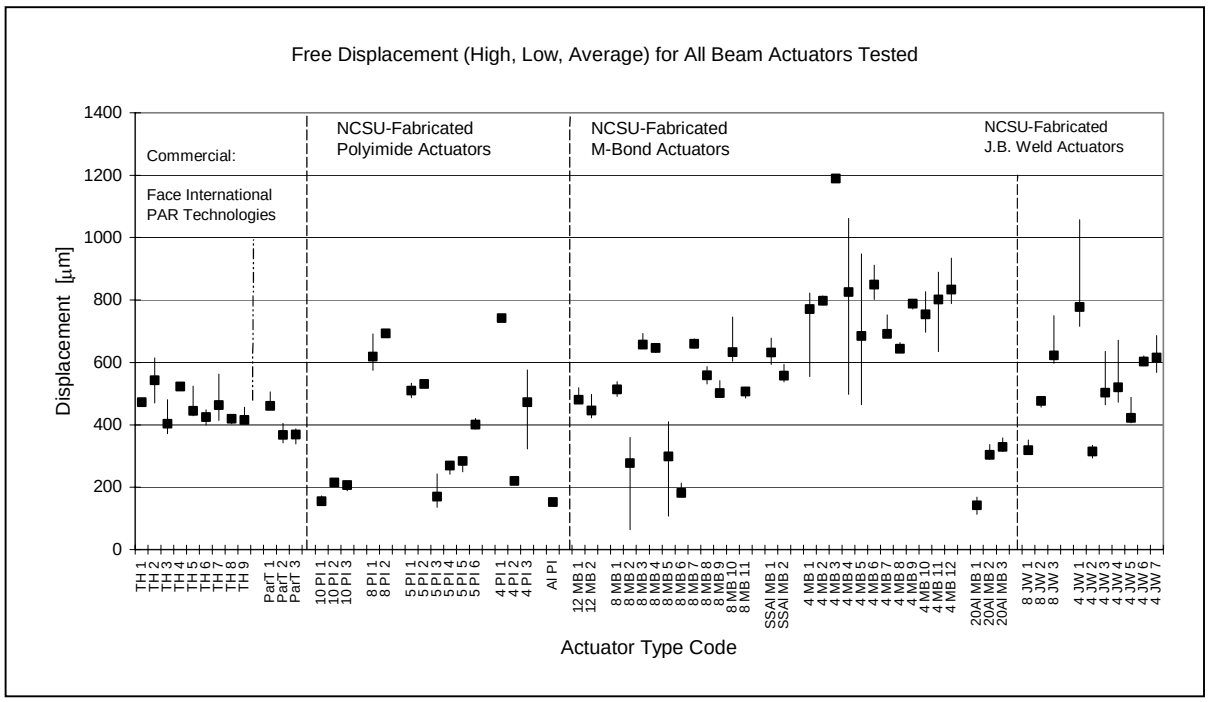

Figure 4.3—1. High, low, and average free displacement for all actuators tested

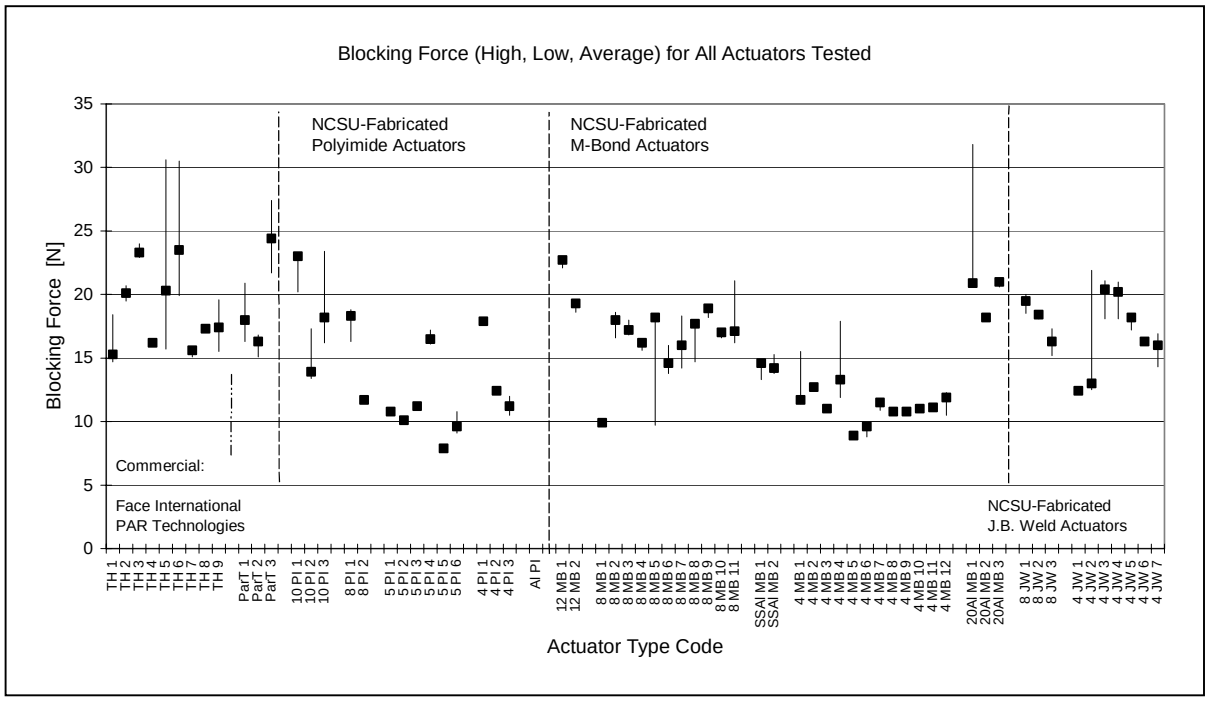

Figure 4.3—2. High. low, and average blocking force for all actuators tested

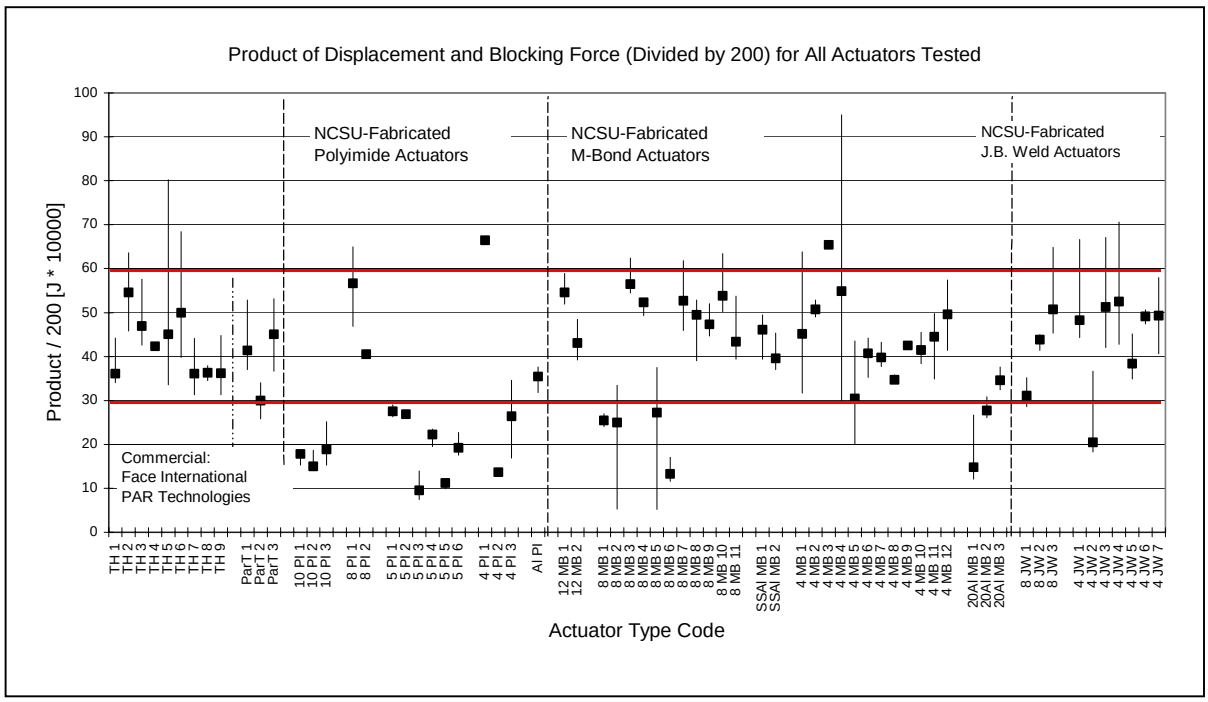

Figure 4.3—3. Approximate capacity for work output in Joules multiplied by 10^4

Table 4.3—1. "Actuator type codes" used in Figures 4.3—1 through 4.3—3 referenced to actuator identifications used in Section 4.2 (Repeated ID's refer to the same actuator tested on different dates from earliest to latest.)

Type Code	Actuator ID	Type Code	Actuator ID	Type Code	Actuator ID
THUNDER		4 PI 1	nPI062102A	4 MB 5	091102D
TH 1	AA	4 PI 2	nPI102802B	4 MB 6	100902D
TH 2	AC181-15	4 PI 3	nPI062102C	4 MB 7	100902D
TH 3	AC181-17	NCSU, M-Bond Adhesive		4 MB 8	100902D
TH 4	AC229-5	20Al MB 1	101402D	4 MB 9	100902E
TH 5	AC229-8	20Al MB 2	101402E	4 MB 10	100902F
Each Column Continued to the Same Column in "Table 4.3—1, Continued"					

Table 4.3—1, Continued.

Type Code	Actuator ID	Type Code	Actuator ID	Type Code	Actuator ID
TH 6	AC229-8	20Al MB 3	101402F	4 MB 11	101602E2x
TH 7	AC232-30	12 MB 1	101402A	4 MB 12	101602F3x
TH 8	AC232-30	12 MB 2	101402B	NCSU, J.B. Weld Adhesive	
TH 9	E	8 MB 1	080902A	8 JW 1	K081602C
PAR Technologies		8 MB 2	080902A	8 JW 2	N081602A
ParT 1	Par Tech A	8 MB 3	080902A	8 JW 3	N081602B
ParT 2	Par Tech 3	8 MB 4	080902A	4 JW 1	01302A
ParT 3	Par Tech 6	8 MB 5	080902B	4 JW 2	091102G
NCSU, Polyimide Adhesive		8 MB 6	080902C	4 JW 3	100302A
10 PI 1	10SS1	8 MB 7	080902C	4 JW 4	100302B
10 PI 2	10SS1	8 MB 8	080902D	4 JW 5	101402G
10 PI 3	10SS21	8 MB 9	100902A	4 JW 6	K082602D
8 PI 1	nPI060902C	8 MB 10	100902B	4 JW 7	K082602E
8 PI 2	nPI060902C	8 MB 11	100902C		
5 PI 1	5SS17	SSAl MB 1	101602A		
5 PI 2	5SS17	SSAl MB 2	101602A		
5 PI 3	5SS19	4 MB 1	091102A		
5 PI 4	5SS19	4 MB 2	091102A		
5 PI 5	5SS31	4 MB 3	091102B		
5 PI 6	5SS31	4 MB 4	091102C		

The group of actuators most lacking in an identifiable pattern are the NCSU actuators bonded with polyimide adhesive. Except for the fact that blocking values for actuators made with 10 and 5-mil substrates are consistent with those of commercial actuators having substrates of the same thickness, there is more scatter in this group than in any other. This was one of the reasons, as mentioned at the beginning of the chapter, that it seemed advisable to also develop fabrication techniques using other adhesives.

In an attempt to expose measurable factors contributing to performance, free displacement and blocking force can be plotted against bond thickness, curvature due to pre-stress, and initial flexural compliance. Initial flexural compliance can be obtained from the difference between flexural strain associated with stress-bias curvature when the weight of the LVDT shaft assembly is supported and is not supported by a mounted actuator. The change in height in millimeters divided by the horizontal span of 41.28 mm (1.625 inches) between clamping axles is then expressed as a percentage and divided by 0.8722 N (the weight of 89g) to give compliance based on a small applied load in the unconventional units of "percent per Newton".

Figure 4.3—4 attempts to separate effect of bond thickness from the larger effect of substrate thickness by plotting free displacement against bond thickness only for actuators bonded with either polyimide or M-Bond adhesives on substrates either 4 or 5 mils thick. However, bond thickness has also been plotted for the group of actuators bonded on 8-mil substrates with M-Bond adhesive (red circles) to show that they are clearly segregated from values for actuators bonded with M-Bond adhesive on 4 mil substrates (green circles).

There is a hint of a trend among the values plotted for M-Bond actuators on 4-mil substrates, but the most appropriate conclusion is that there is no correlation between decreasing bond thickness and increasing displacement. No trend is apparent within other plotted groups due to a combination of variability and not a wide enough range of existing bond thicknesses. Blocking force plotted against bond thickness for this reduced set of actuator shows no apparent pattern.

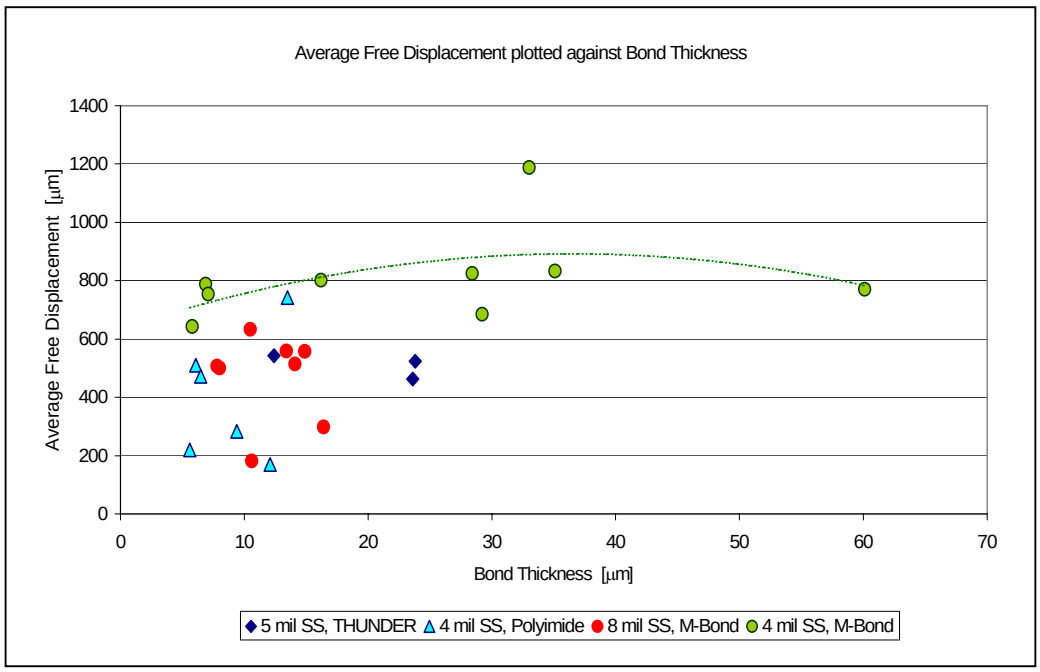

Figure 4.3—4. (color) Average free displacement plotted against bond thickness for actuators with similar substrate thickness

Plots of free displacement and blocking force against stress-bias-induced "curvature," measured as percent flexural strain, revealed no increasing or decreasing trend, except a slight, possible indication that blocking force of THUNDER actuators benefits from greater initial curvature. Such an observation would stand to reason, if more clearly indicated by the data, since a load would have to first displace the negative curvature due to pre-stress before causing an actuator to "sag".

Figures 4.3—5 and 4.3—6 test the idea that the flexural stiffness of the actuator is a strong factor in determining free displacement and blocking force. The idea is not entirely original: Li *et al* speculate that displacement in RAINBOW actuators is enhanced by poling, which reduces curvature and therefore geometrical stiffness. [20] Again, comparison of relative stiffness between actuators having nearly equivalent substrate thickness is necessary because of the internal mechanics that derive from the relative thicknesses of laminated layers in an actuator.

Data plotted in Figures 4.3—5 and 4.3—6 do indicate that for substrates of

comparable thickness, higher flexural compliance (lower stiffness) facilitates actuator free displacement accompanied to a lesser extent by smaller blocking forces. To establish the effect of adhesive type, we would like to see a difference between adhesive types indicated by segregation of the plotted points or different apparent slopes in the response trends. Again, additional data for the performance of three actuators made with M-Bond adhesive using 8-mil substrates have been plotted for comparison.

The three points are well segregated from data for M-Bond actuators made using 4-mil substrates, and indeed, appear to form a contiguous trend between both subsets. It is interesting that actuators bonded with M-Bond adhesive using 8-mil substrates exhibit free displacement and blocking force values generally comparable to those for commercial THUNDER actuators made with 5-mil substrates. Note also that blocking force performance for polyimide-bonded actuators decreases more rapidly with increasing flexural compliance than does blocking force performance for actuators bonded with M-Bond. This suggests that transition to a blocked state happens abruptly for actuators bonded with M-Bond no matter what the initial flexural stiffness.

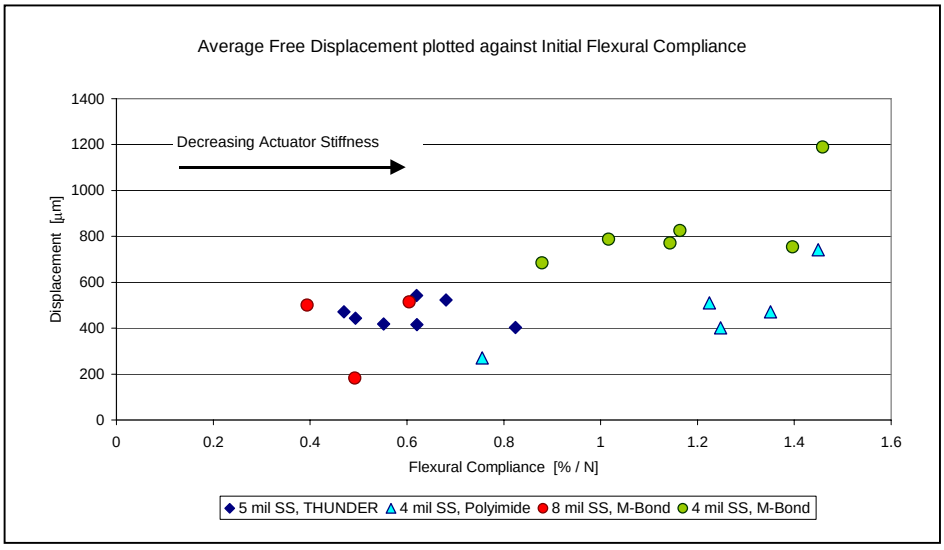

Figure 4.3—5. (color) Average free displacement plotted against initial flexural compliance for actuators with similar substrate thickness but different adhesive types

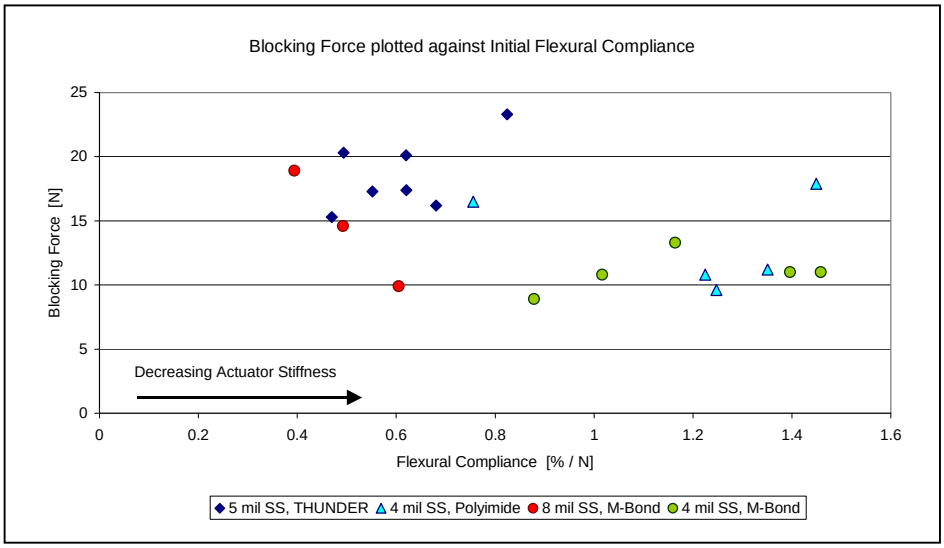

Figure 4.3—6. (color) Blocking force plotted against initial flexural compliance for actuators with similar substrate thickness but different adhesive types

The plots suggest that for actuators of comparable initial flexural stiffness, those bonded with M-Bond adhesive tend to yield higher free displacement and lower blocking force than those bonded with polyimide, and *vice versa*. Although, it has already been observed that actuators bonded with M-Bond adhesive provided higher free displacement but lower blocking force than those made with polyimide adhesive, the fact that this difference occurs when the actuators have comparable flexural compliance (and substrate thickness) reveals that the type of adhesive indeed has an effect on performance.

Examination of characterization data has thus far not generated many strong conclusions about the role of various design and fabrication parameters in actuator performance, let alone evidence for performance enhancement due to stress bias. Since this effect is of considerable interest in this project, a closing conjecture will be considered. In Section 4.1, a speculation was made that one possible explanation for the upturn in THUNDER displacement data at low load and high voltage (Figure 4.1—3) may come from the pre-stress enhancement of the extrinsic piezoelectric strain discussed in Section 2.3.4.

An otherwise very similar plot, also in Figure 4.1—3, of test data from a non-pre-stressed actuator (bonded with J.B. Weld adhesive) did not show a similar upturn. It was noted that Schwartz, Cross, and Wang have suggested that at low electric field, a stress-biased device behaves more like a non-pre-stressed unimorph, whereas higher field activates the mechanism of reorienting stress aligned domains, resulting in non-linear plots. [8]

A conjecture proposed here is that the stress-bias mechanism for enhancement of extrinsic piezoelectric strain is also activated only within regions of applied *load* which maintain the curvature necessary to maintain the stress bias. Stress-bias-induced curvature is a negative curvature (center of curvature below elastic line). The associated beam deflection is termed "hogging" in texts on beam theory, as opposed to "sagging," which is the deflection associated with load-induced positive curvature. It is further proposed that at the positive curvature which is the mirror image of the initial stress-bias-induced negative curvature, a lesser enhancement occurs within the mid-range of load.

A plot of load-displacement data for a THUNDER actuator was selected to demonstrate the proposed ideas, shown in Figure 4.3—7 . From the LVDT measurement of initial curvature, we know how much higher the center of the actuator originally was than its clamped ends. From position data acquired by load-displacement testing, we can determine how large a load was required to displace the actuator apex by a distance equal to its original curvature height. (See Figure 4.1—1 as an example of a plot of position vs. load) To isolate actuator displacement due to piezoelectric strain alone, the zero volt position line is subtracted from the position lines at non-zero electric field, but it is possible to mark the load (determined from curvature and position data) on a displacement plot where the deflection due to pre-stress is negated by applied load, that is, the load necessary to flatten the actuator. (See Figure 4.1—2 as an example of a plot of displacement vs. load) Likewise, one can mark the load needed to induce positive curvature of the same magnitude as the negative curvature due to pre- stress. These loads have been determined and are marked on the plot shown in Figure 4.3—7.

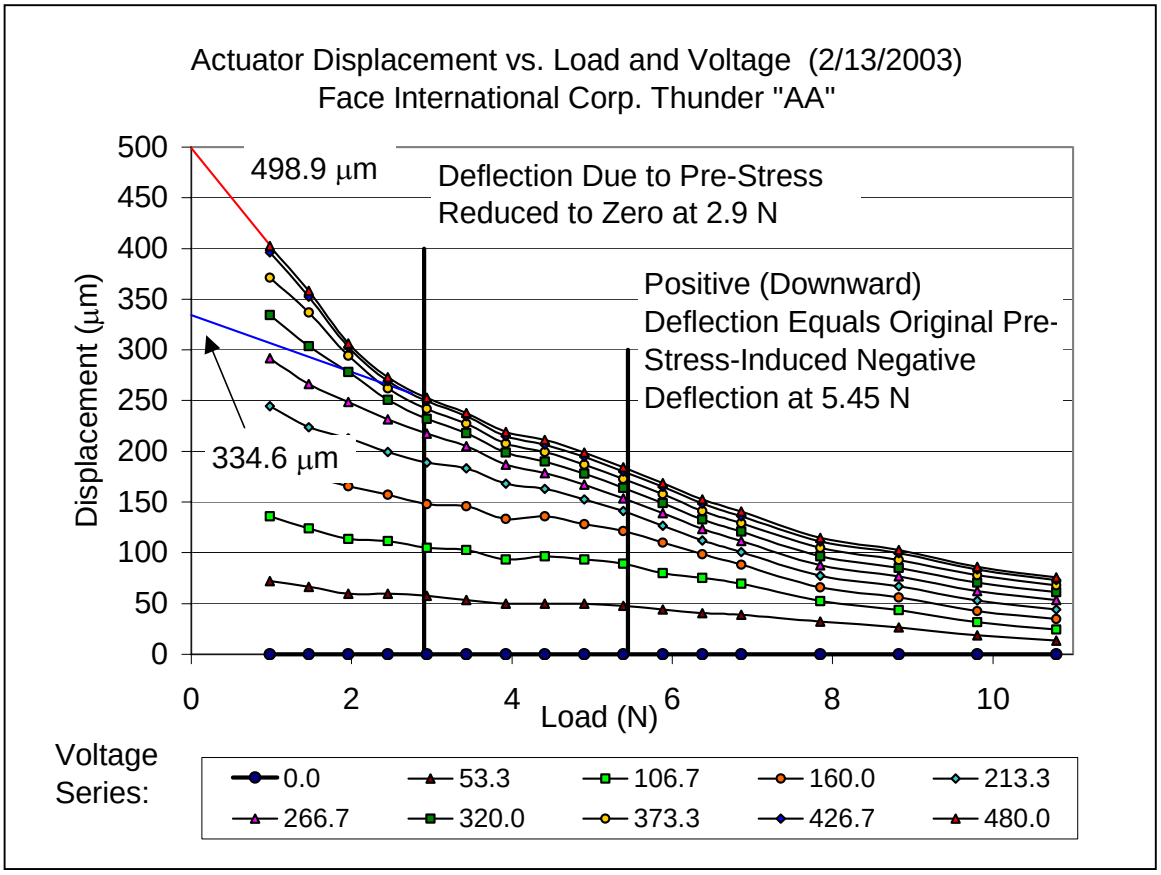

Figure 4.3—7. (color) Displacement test results for THUNDER actuator showing loads needed to flatten actuator and to induce mirror-image positive curvature

One can see that stress-bias-enhanced displacement actually falls off in approaching and crossing through the load that flattens the actuator. Displacement then recovers slightly as a load inducing mirror-image positive curvature is approached, then falls off again. The lower blue line extrapolating data in the mid-section of the data trace to zero load suggests that without stress-bias enhancement of low load displacement, the free displacement would be about 335 μm, in contrast with the 499 μm free displacement determined by extrapolating the low-load upturn in the data trace. This represents nearly

50% enhancement of free displacement, but such performance is degraded as soon as the actuator begins to flatten under load.

In actuators bonded with M-Bond adhesive the upturn in displacement is apparently a very fleeting state. Not only are they more compliant, in general, but something about the bond must change with loading. Most average test data sets for M-Bond actuators show reduced slope rather than increased slope in the data trace in the neighborhood of zero load (albeit with considerable displacement still available). A plot shown in Figure 4.3—8 reveals a significant upturn in data obtained from an actuator bonded with M-Bond upon which only one test was conducted. The load necessary to induce flatness and mirror-image positive curvature are marked on the plot shown in Figure 4.3—8.

Of course, one of the observations about pre-stressed unimorph performance which has been highlighted in this chapter is that the profile of load-displacement data changes during re-testing. The increased slope in displacement near zero load, which has just been nominated as a signature of stress-bias-enhancement of performance, is not always evident in the test data for THUNDER actuators, robust as they appear to be. Even when PSUs retain pre-stressed-induced curvature and good performance, the upturn may not be visible, although data for a new actuator often does show it. However, many actuators do repeatedly show some kind of localized drop in displacement performance under a load of 1 to 2 N, which probably flattens the actuators. One might expect the tendency of a flattened actuator to buckle with additional piezoelectric strain to compensate for loss of stress bias, but in most cases, the localized behavior in this transitional range of loading is toward reduced displacement, which typically recovers to some extent with increasing load, sometimes to a large extent.

In conclusion, this section has shown that overall patterns in load-displacement test data for pre-stressed and non-pre-stressed unimorphs typically change both within a repeated series of tests and when re-tested after some months or years have elapsed. The changes do not appear to be vary randomly, but occur in too many complicated forms to categorize easily. One unconventional form involves a peak of maximum displacement occurring at loads well above zero. It appears associated with very thin bonds, typically

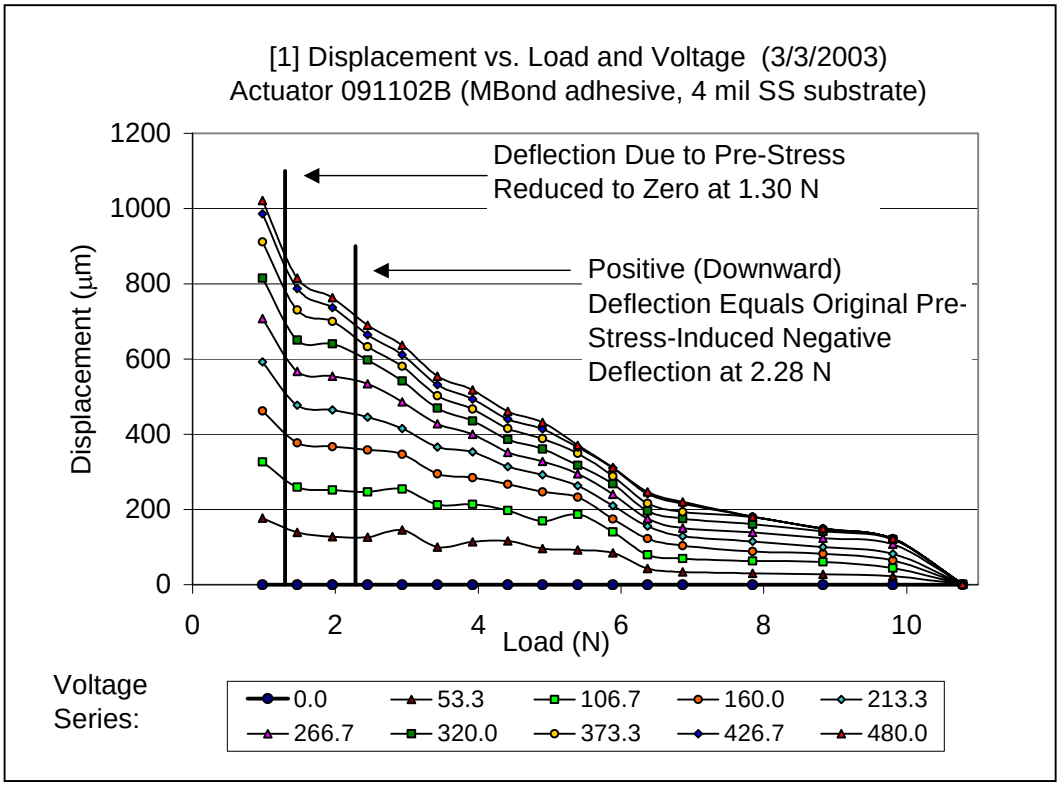

Figure 4.3—8. Displacement test results for an M-Bond for actuator showing loads needed to flatten actuator and to induce mirror-image positive curvature

less than 10 µm thick. Examination of the spectrum of performance metrics plotted for all actuators indicated that actuators achieving high free displacement typically also exhibited low blocking forces, and that the association may reflect a fundamental property of unimorphs which even clever design may have difficulty circumventing.

Plots of performance against bond thickness indicated that bond thickness corresponding to optimal performance may not be the thinnest achievable. Although performance metrics plotted against flexural strain due to pre-stress did not reveal visible trends, when plotted against initial flexural strain, actuators with different adhesives fell at slightly different locations for the same initial flexural strain. Finally, it appears that some plots of test data for pre-stressed unimorphs suggest that stress-bias-enhancement of

displacement is clearly evident at low load but diminishes as applied load flattens the actuator, only to re-appear slightly when increased load creates a mirror image of the flexural strain due to stress bias.

4.4 An Experiment on Stress Bias Induced by Bending During Fabrication

A set of actuators was fabricated at room temperature using J.B. Weld epoxy as an adhesive. Curvature was introduced by mechanical bending while the adhesive cured. The motivation was to compare load-displacement test results with a pair of flat unimorphs made with the same materials and technique to determine if the residual internal stress which developed during fabrication favorably affected performance. The fabrication process, which had two variants, is described in Section 3.1.2. The initial method used three-point bending created by a circular mass and two round supports. A subsequent method involved bending by pure moment imposed upon actuator parts sandwiched between sheets of flexible material. Actuators were fabricated at what was intended to be a series of three diminishing radii of curvature, with a pair of actuators made at each radius of curvature.

Variability in final curvature between and within sample pairs turned out rather high, although it is possible to select one sample in each pair to better represent a series of three increasing curvatures. In this analysis, the actuators have simply been arranged in order of increasing measured curvature (expressed as flexural strain) regardless of the order intended during fabrication. Table 4.4—1 summarizes characterization results using the same tabular format as previous data tables in this chapter have used, as explained in Section 4.2.1. Figure 4.4—1 shows average free displacement for the series; Figure 4.4—2 shows blocking force.

Following the pattern of previous data analysis, plots of performance metrics relative to stress-bias-induced flexural strain (curvature due to pre-stress) and initial flexural compliance were examined . (Determination of initial flexural compliance was initially explained at the end of Section 4.1.) No discernable pattern was evident, so these

plots have not been included in this report. Instead, the curvature and flexural compliance data for each actuator have been overlaid on Figures 4.4—1 and 4.4—2.

The reason for the order in which the actuators are shown is this. The flat actuators (ASUL FLAT 1 and ASUL FLAT 2) are consider controls for the effect of mechanically-induced stress bias because they were not bent. Next ASUL030703A, also known as "ASUL 100," is shown as a single representative of an ASUL made by three-point bending (induced by a mass load of 100g). The next five actuators, arranged in order of increasing curvature (or decreasing radius of curvature) were bent during fabrication by application of pure applied moment, which should give them a more uniform curvature in the form of a nearly circular arc. During fabrication of the specimen subjected to three-point bending, it was clearly evident that the arc of curvature was not circular. Instead, curvature increased toward the point of load application while the actuator remained less curved toward the ends. The alternative method for bending by applied moment was devised in an attempt to bend every part of the actuator uniformly, which mimics the uniform curvature produce by differential thermal contraction.

Table 4.4—1. Characterization of actuators bonded under load fabricated with J.B.Weld adhesive on 4 mil thick stainless steel substrates (Refer to Section 4.2.1 for Explanation of Format.)

Actuator Identification, Test Date	Unloaded Displacement [μm]	Blocking Force [N]	Bond Thickness [μm]	Curvature as Flexural Strain (percent)
ASUL022803A 3/5/2003 (Flat 1)	[703, 501] 565 (n = 6)	[17.2, 22.1] 19.8	140.9 (n = 8) 34.3 (24%)	0.5528 (0.3846)
ASUL022803B 3/20/2003 (Flat 2)	[736, 524] 609 (n = 7)	[14.0, 15.2] 14.7	128.6 (n = 13) 12.4 (10%)	0.5975 (0.3706)

Table 4.4—1, Continued.

ASUL030703A 3/10/2003 (3-pt)	[699, 436] 491 (n = 6)	[28.2, 29.6] 28.9	142.8 (n = 14) 54.5 (38%)	2.656 (0.4768)
TSUL031203A 3/27/2003 (1A)	[698, 473] 543 (n = 6)	[15.3, 15.5] 15.5	141.8 (n = 9) 13.2 (9%)	1.735 (0.4281)
ASUL031203B 3/19/2003 (1B)	[848, 451] 545 (n = 6)	[20.6, 22.3] 22.1	148.1 (n = 6) 6.7 (5%)	2.076 (0.5746)
ASUL031703A 3/17/2003 (2)	[Single Test] 732	[Single Test] 16.1		2.900 (0.4593)
ASUL032103A 3/21/2003 (3A)	[753, 529] 573 (n = 6)	[21.1, 22.3] 22.2	127.0 (n = 11) 30.5 (24%)	2.866 (0.4042)
ASUL032103B 3/25/2003 (3B)	[711, 435] 501 (n = 7)	[23.3, 27.0] 23.5	134.8 (n = 15) 19.0 (14%)	2.689 (0.3226)

Examination of data plotted Figure 4.4—1 and Figure 4.4—2 suggests that bending during fabrication accomplished no definitive enhancement of performance relative to the flat actuators, since apparent trends are nearly on the same scale as apparent variability . The fact that one of the flat actuators had one of the larger bond thicknesses listed, while the other had one of the smaller bond thickness listed in Table 4.4—1 probably explains the difference in their performance. (The actuator with the thinner bond has higher displacement, but lower blocking force than its counterpart.) Based on the single specimen produced by three-point bending, it appears that this form of curvature enhanced blocking force performance at the expense of slightly reduced displacement capability. The increasing curvature toward the center of this actuator probably does facilitate performance at high load.

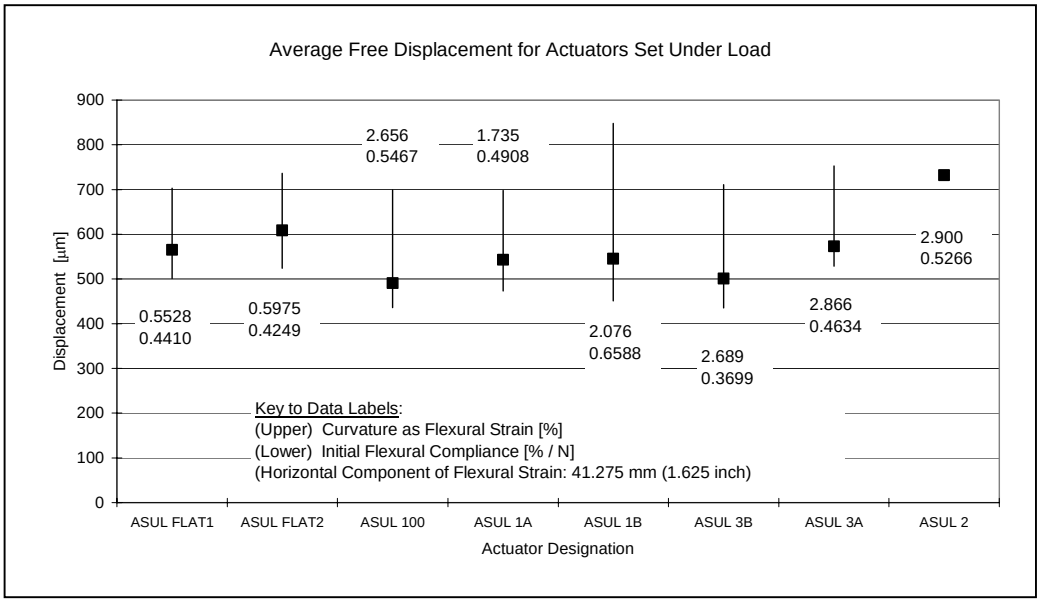

Figure 4.4—1. Average free displacement plotted against bond thickness for actuators with similar substrate thickness

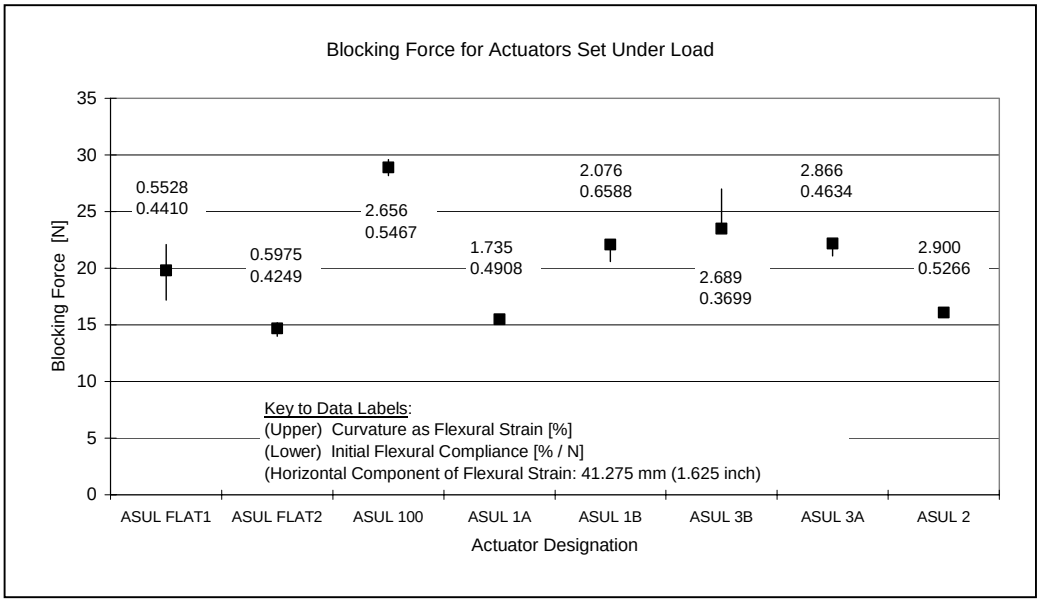

Figure 4.4—2. Average blocking force plotted against bond thickness for actuators with similar substrate thickness

Discerning a trend among the actuators produced by pure moment bending is difficult without forcing the issue. Superficially, it appears that modest bending produced little change (especially not for the better) relative to flat unimorphs. Then, perhaps blocking force capability was enhanced while displacement was slightly reduced, followed by generally better displacement performance with corresponding reduction in blocking force.

However, ASUL 2 (ASUL031703A) plays a strong role in helping this observation, and it failed after a single test and its bond thickness was not determined. As has been mentioned, actuators generally do give higher displacement performance on their initial test, so if average data for a test set had been plotted for ASUL 2 instead of single test results, one would probably have not observed any overall trend. So, except for the observation about three-point bending enhancing high load performance, one would have to stay with the conclusion that bending during fabrication accomplished no definitive enhancement of performance relative to the flat actuators. A follow-up experiment with thinner or different adhesive would be appropriate for researchers interested in this fabrication technique.

4.5 Effect of End Conditions on Compliant Actuator Performance

Mounting and end conditions for piezoelectric actuators have not been widely treated in the literature. As mentioned in Section 2.3.2, Giurgiutiu *et al* present a comprehensive analysis of stiffness issues, account not only for the intrinsic stiffness of an induced strain actuator (ISA) and that of its load, but also for the stiffness of the actuator support. [21] Nonetheless, their consideration of actuator support does not extend to the additional degrees of freedom one must consider in mounting a very compliant actuator; that is, will the means of mounting allow or block the potential for end rotation and translation during actuation.

In [22], the authors clamped the corners of THUNDER actuators with modeling clay for displacement testing. In [23], the authors note that different results will be obtained

depending on how a bimorph or THUNDER actuator is held and recommend supporting it at a particular distance from the edge of the "active" parts. Various mounting considerations are mentioned in [24], such as mounting rectangular actuators (with slotted end tabs) on pin-guided fixtures such that they are simply supported across the thin edges of wedge blocks. The authors also present a diagram of a fixture for clamping the ends of actuators in split axles to allow end rotation. A mirror mounted on a pre-stressed unimorph as part of a single axis piezoelectric gimbal was reported in [2]. The authors described how the ends of the PSU were affixed to a polypropylene mount with cuts in the polymer to create hinges. In [1], THUNDER actuators were equipped with clamps and hinges in the first phase of developing a linear motor to position satellite instrumentation. The ends of THUNDER actuators were joined together by a plastic film junction in [25] to test a system intended for underwater propulsion.

We attempted to systematically control the rotation and translation aspects of end conditions for mounted THUNDER (model 8R) actuators using the fixture depicted in schematic form in Figure 3.1.4—1, and reported our work in [26]. Load displacement tests were conducted while selectively blocking or allowing translations or rotations of one or both ends of the actuator to determine the effect on actuator stiffness and consequent implications for displacement under low and high loads.

As designed, the test fixture blocks or allows rotation in the left axle, right axle, or both axles. The means for allowing or blocking translation was available only in the right axle. In the depiction of test apparatus and fixture in Figure 3.1.4—1, it is clear that some kind of bolt blocks translation, but nothing was included in the drawing to suggest how rotation was blocked. The bolt for blocking translation has a ball bearing tip, and the axles are mounted in bearings. When machine screws that are not shown are tightened, the axle bearings lock and prevent rotation.

Of the eight possible permutations of either blocking or allowing right axle rotation or translation, or left axle rotation (only), two were omitted because blocking *rotation* of the right axle of the actuator fixture effectively blocks translation. (However, blocking *translation* of the right axle does not block its rotation. Table 4.5—1 lists the eight possible

combinations, including the two omitted conditions. Letters "A" through "F" are used to identify the six which were applied, which effectively constitutes the basis for an experimental plan. In [26], some statements unfortunately refer to the wrong end condition letter designations, although commentary is appropriate for the correct designations. The present discussion includes corrected statements. The end conditions range from complete freedom of both translation and rotation to total restriction of both translation and rotation.

Each end condition shown in Table 4.5—1 constituted a test set in which five individual tests or data sets were gathered using the LabView™ -driven data acquisition program known as "TP.vi," described in Section 3.1.4. In each test set, the five tests were gathered without changing the test arrangement in any way. In actuality, six tests were conducted and the first omitted from the average because, as has been observed elsewhere in this chapter, the first test tends to be the most different in a set of repeated tests. The apparatus applied a maximum of 480 V, then dropped the voltage in nine increments to yield a total of ten different applied voltages, including zero. Seventeen load levels were

Table 4.5—1. Experimental plan: Six sets of three end conditions, designated by letters A-F, applicable to the actuator test fixture described in text

End Condition	Rotation		Translation
	Right	Left	
A	Y	Y	Y
B	Y	N	Y
C	Y	Y	N
D	N	Y	N
E	Y	N	N
F	N	N	N
Omit	(N)	(Y)	(Y)
Omit	(N)	(N)	(Y)

applied from zero to the weight of one kilogram (plus the weight of the LVDT shaft) with LabView enlisting the human operator to change the slotted masses.

Figure 4.5—1 shows the plot resulting from the average of values (for the particular load and voltage) from the five test sets generated under end condition A, which allowed free rotation and translation of actuator ends. We see a maximum displacement somewhat above 400 μm. Since the spacing decreases between data traces for increasing voltage levels, it is evident that increasing toward the maximum operating voltage generates decreasing returns in the form of greater displacement.

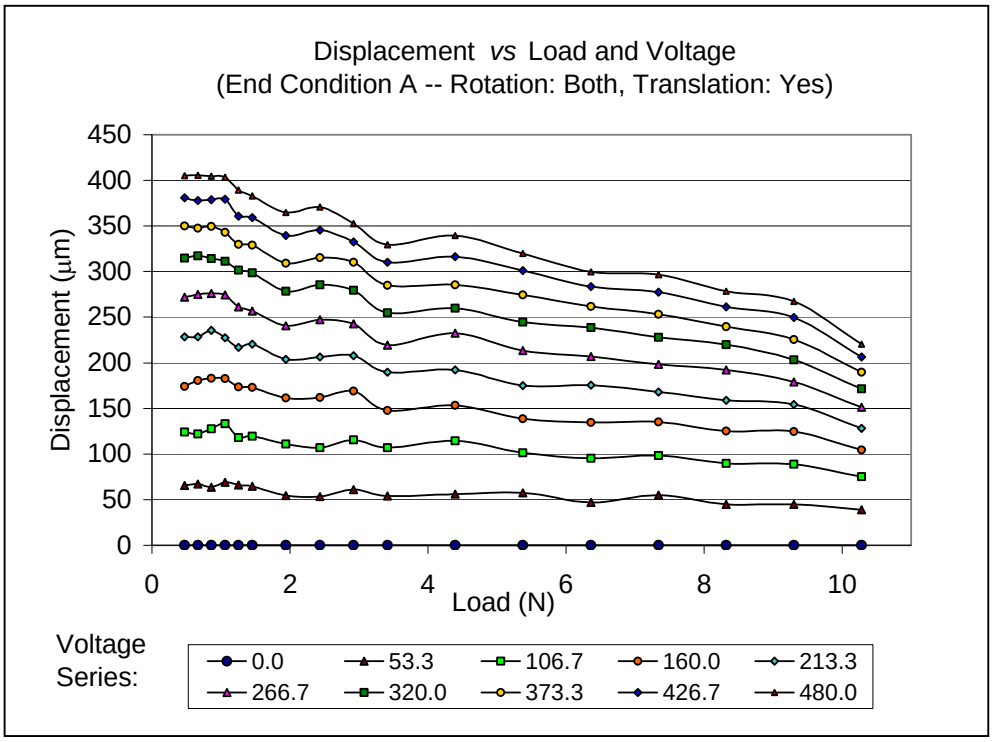

Figure 4.5—1. Average test data gathered under end condition A: Both axle rotations and translation allowed

The effect of introducing even a small end constraint is evident from data for end condition B, in which only rotation in one axle has been blocked. Data plotted in Figure

4.5—2 indicate that zero load displacement has fallen to approximately half that for the unconstrained end condition. Since the slope of displacement plotted against load represents compliance (inverse stiffness), a decreasing slope when a more restrictive end is applied represents increased structural stiffness for the actuator and mounting fixture system.

As actuator ends are further constrained, the reduction of displacement in return for increased stiffness continues, but successive further constraints have diminishing effect. Data plotted in Figure 4.5—3 indicate that zero load displacement falls to approximately 80 μm when rotation is allowed, but translation is blocked (End Condition C). Since this is less than half the effect of blocking one axle rotation, it would appear that the effect of blocking translation is greater than that of blocking rotation. (It was not possible to block

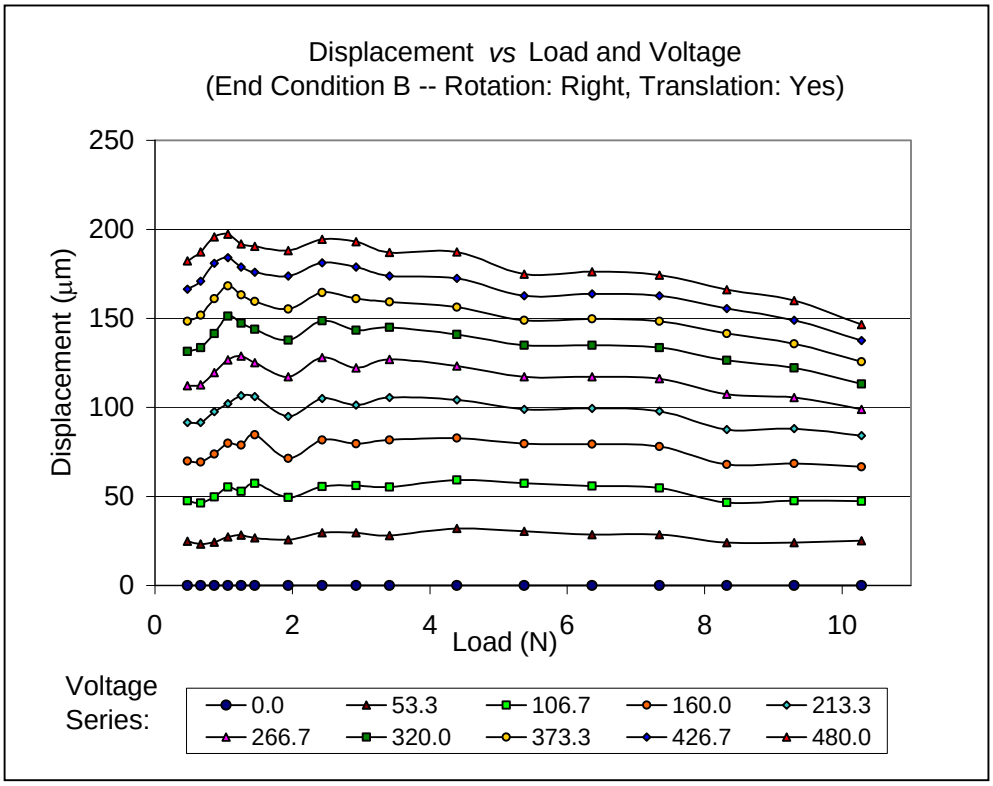

Figure 4.5—2. Average test data gathered under end condition B: Translation allowed, right rotation blocked

both rotations and allow translation.) When both rotation and translation are blocked, the minimum level of zero-load displacement was approximately 60 μm.

When translation is blocked (rotation might also be blocked), an *increase* in displacement is observed with increasing load, an effect which can be seen in Figure 4.5—3. Eventually a point of instability is reached and the actuator buckles. The buckling phenomenon is an abrupt transition or collapse from negative curvature (concave downward) to positive curvature (concave upward). While an unconstrained actuator flattens under increasing load and then sags into positive curvature, the transition is a gradual settling, not an abrupt collapse. Figure 4.5—3 has been truncated beyond an applied load of 7 N and does not show data through the buckling transition. However, non-linearity at the high ends of the data traces indicates that buckling is imminent.

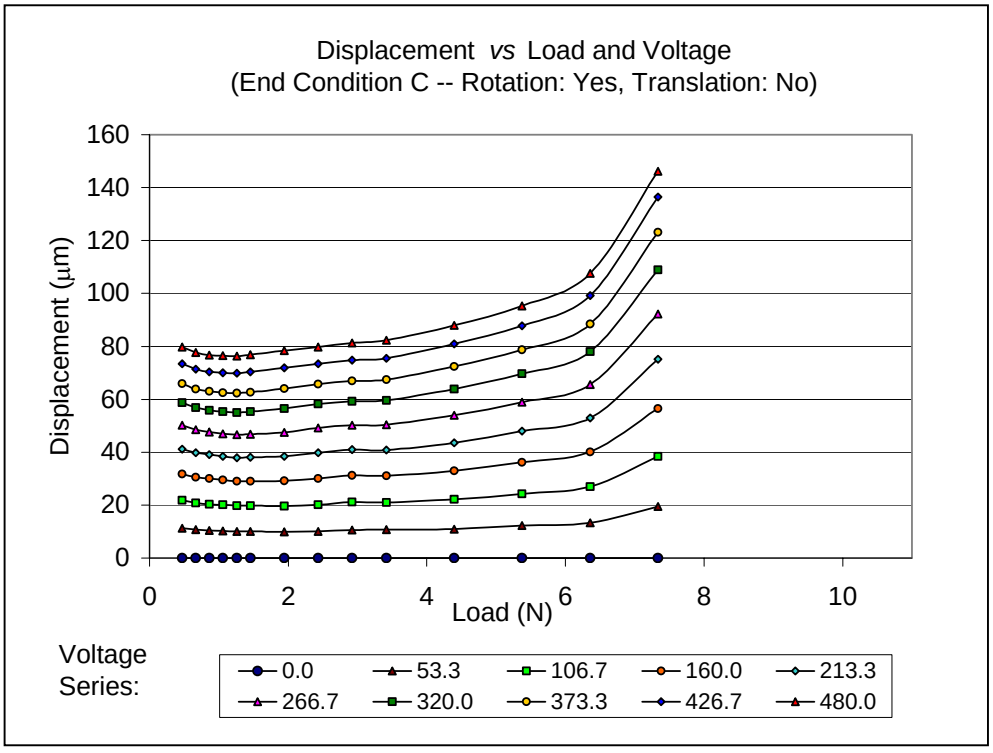

Figure 4.5—3. Average test data gathered under end condition C: Rotation allowed, translation blocked

Finally, a summary is presented in Figure 4.5—4, which maps measurements taken at each end condition on a stiffness versus displacement plane. Measurements on unconstrained actuators fall into a zone of high displacement and low stiffness. An intermediate point from end condition B, where blocked rotation of the left axle was the only constraint falls at approximately half the displacement and twice the stiffness of the

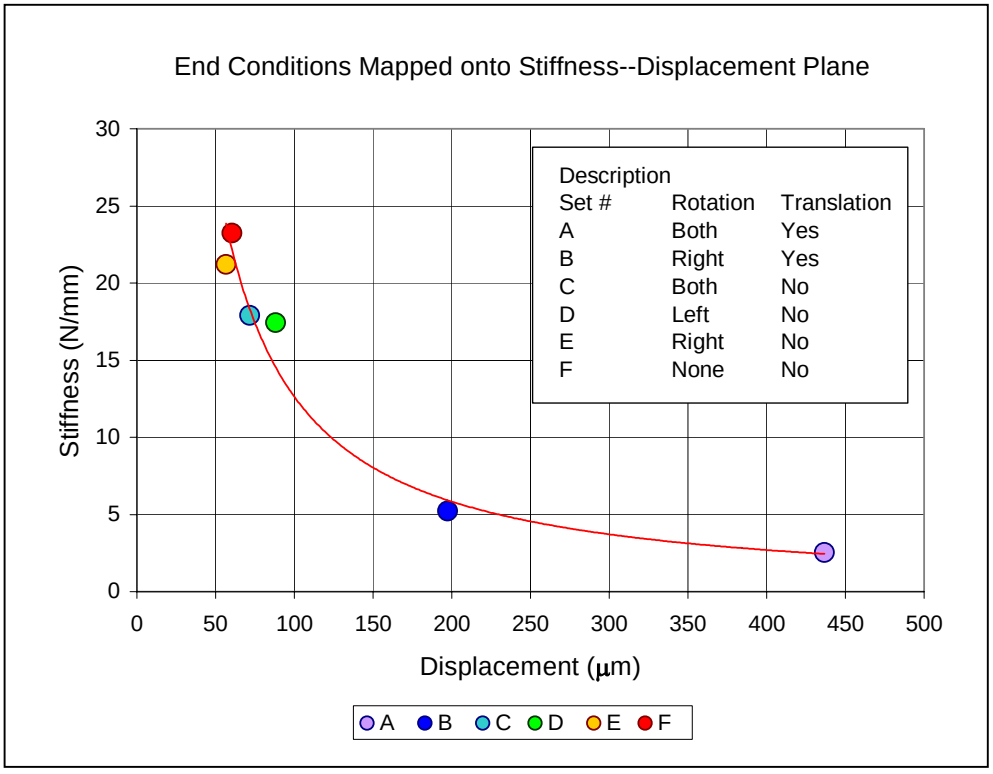

Figure 4.5—4. (color) Summary of experimental data showing the reciprocal relation between stiffness and zero load displacement

unconstrained actuator. Several points characterized by blocked translation fall into a zone of high stiffness and low displacement. These plotted points approximately follow a hyperbolic trace, that is, the product of stiffness and displacement remains approximately constant when end conditions are modified. This can be verified by multiplying the same-row values from columns in Table 4.5—2 for “no-load displacement” and “stiffness at 0

V", which correspond to Figure 4.5—4. (However, a power law trend line fit the data well in producing the chart for Figure 4.5—4: the equation of fit generated was $y = 2141.5\ x^{-1.1145}$.)

Table 4.5—2. Summary table relating end conditions with stiffness and displacement

End Condition	Displacement [μm]		Inc / Dec with Load?	Stiffness [N/mm]		% Stiffness Change
	No-Load	10 N		0 V	480 V	
A	436.63	2.54	Decreases	2.54	2.67	4.86
B	197.43	158.64	Decreases	5.22	5.32	2.04
C	71.63	116.26	Increases	17.89	16.57	–7.68
D	88.03	17.42	Decreases	17.42	19.41	–10.80
E	56.53	21.22	Increases	21.22	19.81	–6.88
F	60.51	71.41	Increases	23.23	22.66	–2.50

The data in Table 4.5—2 show correlation between percent change in actuator stiffness due to applied voltage, the trend of either increasing or decreasing displacement with increasing load, and degree of constraint from end conditions. Note that displacement increased with increasing load whenever translation was blocked, with the exception of end condition D. In this case, rotation and translation were not blocked on the same axle. It is possible that some asymmetry in the test fixture allowed this configuration to produce a slightly lower degree of constraint for end condition E, where rotation and translation have been blocked on the same axle. Otherwise, the two end conditions were symmetrical and should have given nearly the same results. Likewise, values in the column for "percent stiffness" change positively under end conditions which allow translation, and negatively when translation is blocked. Percent change was calculated by subtracting 0 V stiffness from 480 V stiffness and dividing by the average of the two. Note also that stiffness values

given in Table 4.5—2 are the inverse of the slopes of fitted lines to the data in a given set simply because the graphs are more easily interpreted by viewing displacement as response to a given load. As mentioned before, the slopes of data traces in graphs would give compliance rather than stiffness.

In summary, end conditions involving blocked translation or higher degrees of constraint tended to result in increased stiffness (reduced downward displacement) with applied voltage and with increasing displacement with increasing load. The last observation suggests that constrained actuators do more work as load increases. Calculations of load-displacement work performed support this, although other experiments have shown that the actuators must operate in a continuously loaded state, as in these tests, rather than seeing their load intermittently, as in inchworm motors, for higher work output to occur.

In the case of a loaded actuator, constraining the end conditions results in a stiffer actuator, therefore enhanced load capabilities, but at the cost of reduced low-load displacement. In particular, blocking end translation substantially reduces free displacement and increases stiffness, more so than blocking end rotation. In addition, the buckling phenomenon is more associated with blocked translation than with blocked rotation. With translation blocked, the actuator displaces less in response to low load, increases displacement under increasing load, then reaches a point of instability and collapses abruptly into the inverted curvature, which was our definition of buckling.

The effect of end conditions provides an option for increasing beam actuator stiffness. Either the actuator itself can be made stiffer, or the ends can be constrained, most effectively achieved by blocking translation. If operation were confined within a load range below the buckling transition, an actuator with the property of increasing stiffness with increasing load can be obtained by blocking translation.

4.6 Characterization of Circular THUNDER Actuators and Effect of Variable Thickness Substrate on Performance

Although not extensively studied in the project, circular THUNDER actuators offer a useful variant in actuator geometry. In particular, they are stiffer than beam actuators of comparable size because the dome shape of circular actuators is an inherently stiffer structure than an arc (which is not an arch until the ends of an arc are blocked from outward movement). Face International Corporation offers a model 5C circular actuator, but we were interested in using circular actuators for motor applications (see Figure 8.1.1—5) for which design would be facilitated by including a hole at the center of the actuator. Face Corporation was able to fill a custom order for circular actuators with holes (see Figure 8.1.1—4), which were subjected to load-displacement characterization, but not bond thickness analysis and curvature measurements. Results are listed in Table 4.6—1.

Figure 4.6—1 shows a representative load-displacement curve for a circular THUNDER actuator, 1.75 inches in diameter. Based on conclusions drawn from the finite element analysis to be presented, this particular actuator, designated as AC240-10, was modified and load-displacement testing repeated. Results are given in Figure 4.6.2—2, which will be discussed.

Note that within the load range encountered during load-displacement testing, the actuator may not have achieved maximum displacement, which appears to be increasing with load. Since this enormous load capacity is partly due to geometrical stiffening rather than material stiffening, it might be possible to produce an actuator with both improved displacement and load capability by modifying the thickness profile of the actuator substrate. The bottom rim of a dome-shaped actuator acts like a retaining ring which opposes flattening of the actuator. However, within the perimeter of the actuator, the stiffness of the laminated structure opposes deflection due to piezoelectric strain. It might be profitable to thin the substrate toward the actuator center to facilitate piezoelectric displacement, while leaving a thick perimeter to provide load-bearing capability.

Table 4.6—1. Results from characterization of circular THUNDER actuators
(Refer to Section 4.2.1 for explanation of table format.)

Actuator Identification, Test Date	Unloaded Displacement [μm]	Blocking Force [N]	Diameter [inch, mm]
AC240-10 11/19/2000	[99, 85] 97 (n = 7)	[40.4, 44.9] 40.6	1.75, 44.45
AC240-10 Modified 5/24/2003	[354, 342] 342 (n = 4)	[16.0, 18.0] 17.5	1.75, 44.45
AC249-2 10/13/2000	[47, 44] 46 (n = 6)	111 (best estimate)	0.875, 22.22
AC249-3 10/14/2000	[51, 46] 48 (n = 8)	[43.0, 54.4] 46.2	0.875, 22.22
AC253-23 10/25/2000	[38, 34] 37 (n = 6)	131 (best estimate)	0.700, 17.78
AC253-23 5/5/2003	[42, 41] 41 (n = 5)	[55.0, 71.5] 59.7	0.700, 17.78
AC253-27 10/12/2000	[37, 35] 36 (n = 6)	[60.2, 75.0] 72.2	0.700, 17.78
AC253-28 10/11/2000	[36, 35] 36 (n – 6)	[62.1, —] 85.9	0.700, 17.78
AC261 9/6/2000	[21, 20] 21 (n = 6)	[41.2, 45.0] 43.5	0.525, 13.34
AC261-5 9/11/2000	[22, 21] 22 (n = 6)	[47.7, 59.3] 53.8	0.525, 13.34

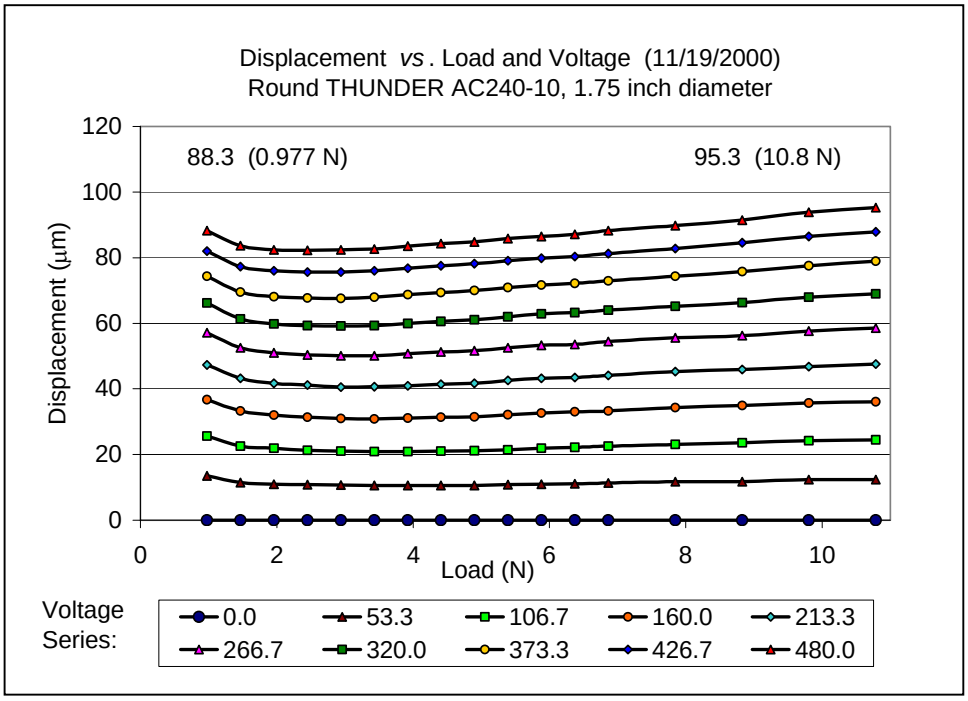

Figure 4.6—1. Representative plot of load-displacement test results for a circular THUNDER actuator with a diameter of 1.75 inches

A study was conducted using finite element analysis (FEA) to model a simplified cross-section of a circular THUNDER and to answer the following question. Is it possible to increase no-load displacement by allowing the substrate to have a variable, radially-symmetric cross-section? The metal sheet typically used in the construction of THUNDER actuators has circular symmetry and constant thickness. What if the thickness profile of the metal sheet were thinner at the edges or in the center of a circular thunder? Would displacement change as a result? It will be necessary for the model to provide for holes at the center of the circular actuator because the actuators, when used as active elements in piezoelectric motors, drive an assembly along a metal rod extending through the central hole.

4.6.1 The Model: Plan and Assumptions

The plan was to simulate the performance of a real actuator using actual test data for the real actuator, then modify the shape of the cross-section in the model to extrapolate the effects such modifications would be expected to have on real actuator performance. If the extrapolations produced consistent results, then qualitative conclusions could be drawn regarding the type of substrate cross-sectional profile most likely to provide maximum displacement in a round THUNDER actuator. As a reference, a round THUNDER custom-made by Face International Corporation, having a diameter of 0.875 inch, was used. Figure 4.6.1—2 and Table 4.6.1—1 give its dimensions, the displacement of center relative to edge due to curvature (arc height), and average no-load displacement as measured by standard load-displacement test procedure. The substrate material was stainless steel and the ceramic material was lead zirconium titanate (PZT).

This structure satisfies the conditions for an axisymmetric model in terms of both geometry and loading. That is, all dimensional aspects of the cross-section and applied loads or other effects are constant throughout 360º of rotation. Consequently, the model was defined using the axisymmetric option for the PLANE42 element type available in ANSYS 5.5 Finite Element Modeling software package. Given the nature of an axisymmetric model, only one-half the cross-section was defined (from the central axis to the right edge of the perimeter). The half cross-section resembles a 2-D object, but the software accounts for the fact that it actually represents a solid of revolution.

Table 4.6.1—1. Input data to the model
(All dimensions in inches unless otherwise indicated)

substrate thickness	0.008	substrate outer diameter	0.875
ceramic thickness	0.008	substrate inner diameter	0.125
arc height at center	0.0103	ceramic O.D.	0.750
avg. no-load displacement	0.00196	ceramic I.D.	0.188
elastic modulus of metal [psi]	30E+6	elastic modulus of ceramic [psi]	10E+6

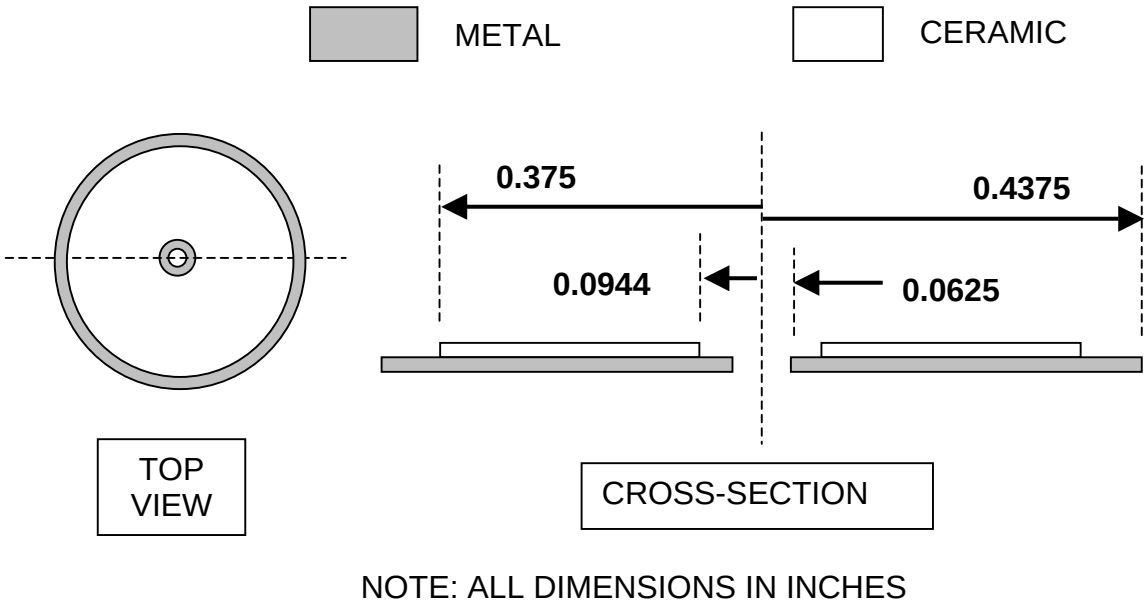

Figure 4.6.1—2. Dimensions relating to the specific actuator used as model input

Since the (half) cross-section is thin relative to the actuator radius, the actuator thickness (or height of the cross-section) dictated that a sufficient number of elements needed to be defined to maintain the aspect ratio of all elements within acceptable limits. Furthermore, complex effects occurring within the narrow dimension required partitioning increments of the thin dimension between several elements. In the final model, elements 0.002 inches in both width and height form the reference mesh. This is shown in Figure 4.6.1—3. However, nodes were defined according to variable formulas, as will be explained, which allowed the substrate profile to vary in thickness or follow polynomial curves along the bottom edge.

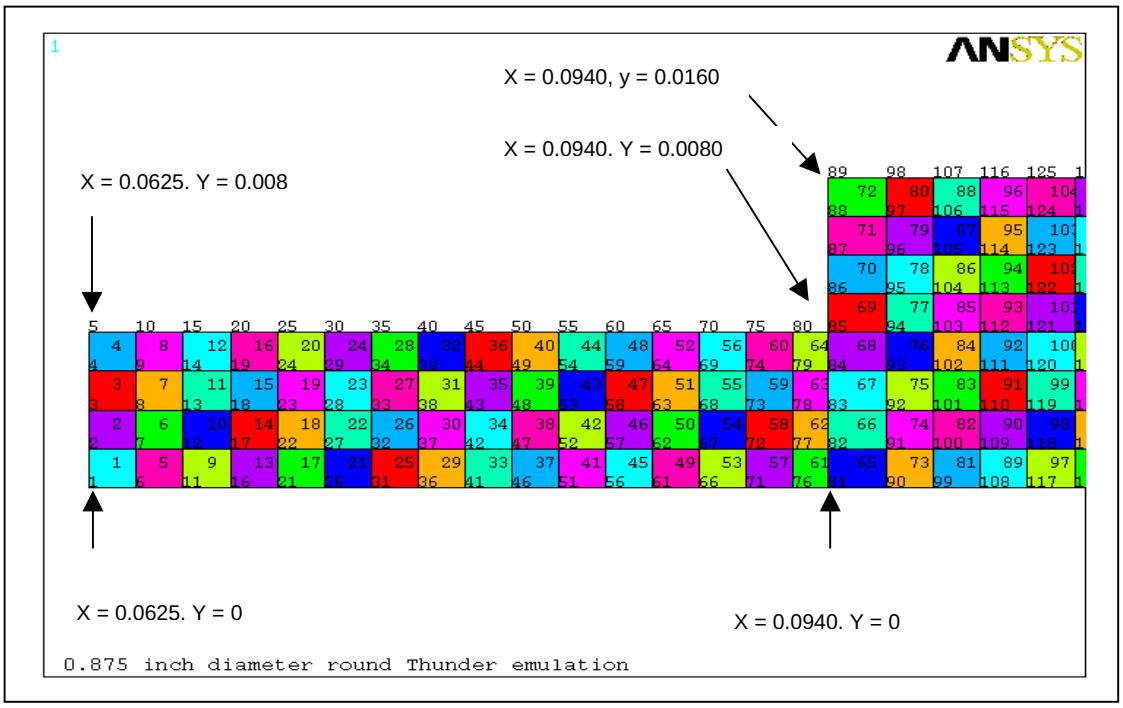

Figure 4.6.1—3. (color) Left (most central) end of element plot for ANSYS model showing transition from bare metal inner circle to start of ceramic layer inner circle

The key to the versatility of this model, which allowed a wide variety of simulations to be conducted by simply modifying a few constants in the input file, was in defining each vertical column of nodes according to variable formulas. A representative declaration of a column of nodes, is given in Figure 4.6.1—4.

```
X=.0940              !distance from central axis
    Y=(A*(X**K))+B   !curve defining bottom edge of profile
    N,81,X,Y         !location of bottom node
    N,85,X,.008      !top edge of substrate at constant height
    FILL,,,,,(.008-Y)/4  !scale three node locations in between
    N,86,X,.01       !first node above metal-ceramic interface
    N,89,X,.016      !top of ceramic at constant height
    FILL,,,,,.002    !two additional nodes in between
```

Figure 4.6.1—4. Representative declaration for a column of nodes

All bottom edge profile curves of interest had the form $\mathbf{Y = AX^N + B}$ since all curves were symmetric about the y-axis or x-axis. A positive value of y "cuts into" the bottom of the substrate by locating the bottom surface above the level, y = 0, which is the original, flat bottom surface. Figure 4.6.1—5 shows cases considered, which included even-power polynomials where N = 1, 2, 4, 6, and "reverse" (mass concentrated on inside rather than outside edge) curves where N = 1, 1/2, 1/4, and 1/6. Therefore, constants A and B were determined in each case simply by substituting two points into the desired form and solving for the constants. In cases for which mass was concentrated around the outside perimeter, the equations were fitted to $(x_1 , y_1) = (0.0625, 0.006)$ and $(x_2 , y_2) = (0.4355,$

0). Reverse cases were fitted to $(x_1 , y_1) = (0.0645, 0)$ and $(x_2 , y_2) = (0.4375, 0.006)$. The points were chosen such that the curves would not intersect flat edges of the profile at sharp points, but would leave a small flat area 0.002 inches across.

The reference shape used A = B = 0 and N = 1, which defined a zero baseline. In addition, a number of constant substrate profiles thinner or thicker than the reference shape was tested by setting A = 0, N = 1, and B = 0.004, 0.002, –0.002, and –0.004. Positive constants (offset to a level above y = 0) resulted in thinner substrates, while negative constants (offset to a level below y = 0) resulted in thicker substrates.

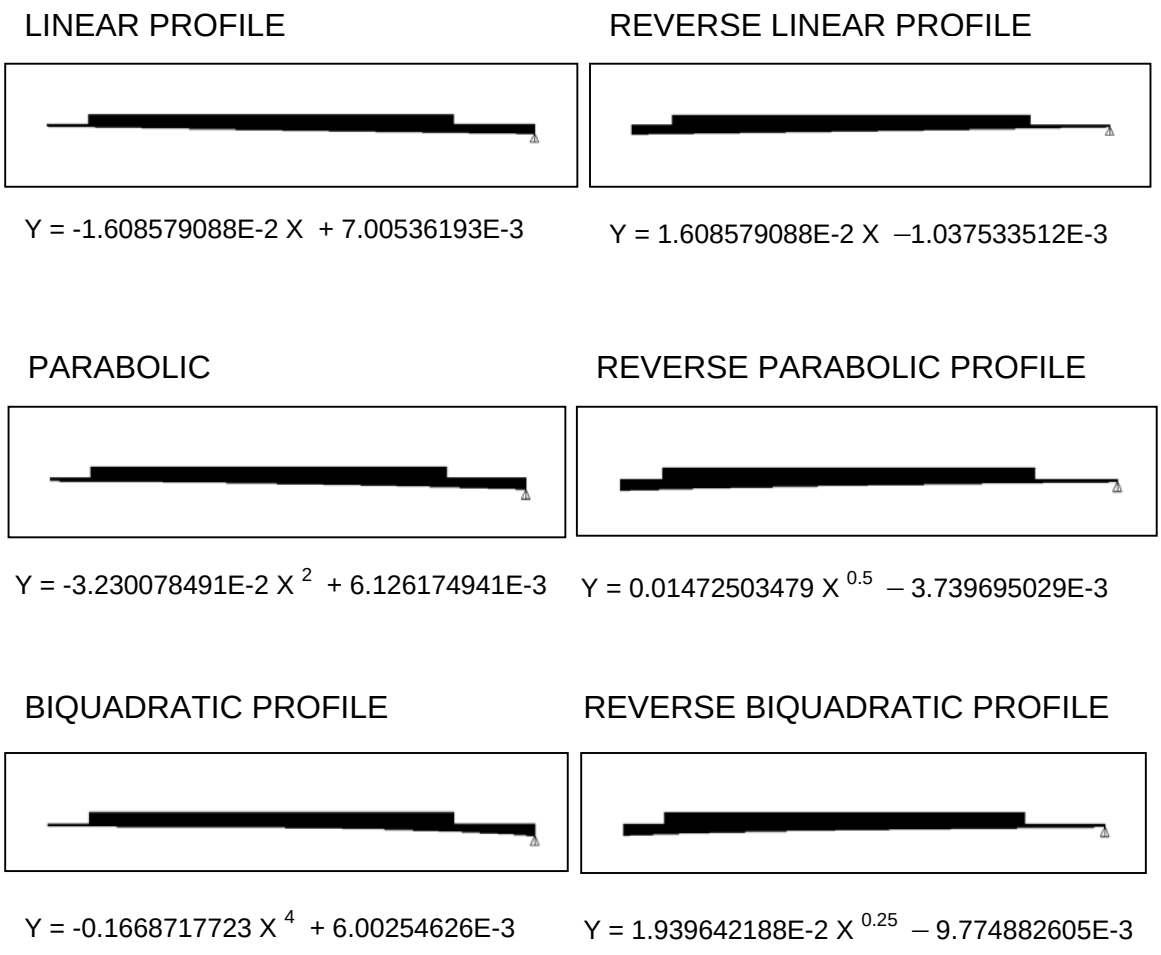

Figure 4.6.1—5. Cases evaluated by the analysis (See continuation.)

TRIQUADRATIC PROFILE

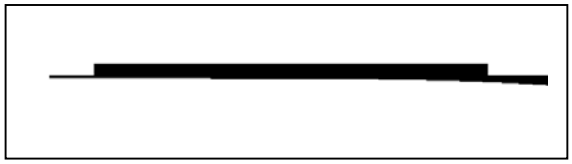

Y = -0.8794802449 X ^{6} + 6.000052421E-3

REVERSE TRIQUADRATIC PROFILE

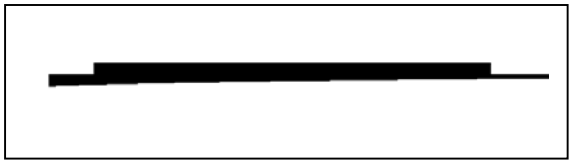

2.52085128E-2 X $^{1/6}$ – 1.596399894E-2

REFERENCE PROFILE

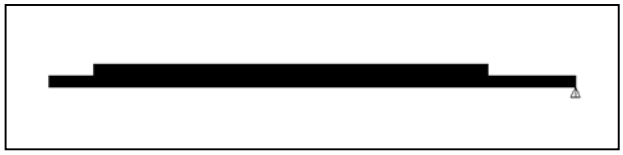

Y = 0 X ^{1} + 0

THINNED BY 0.002 INCH

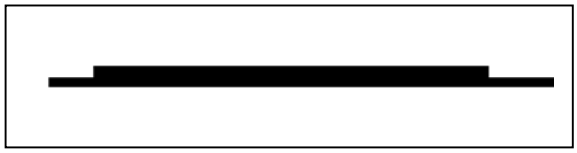

Y = 0 X ^{1} + 0.002

THICKENED BY 0.002 INCH

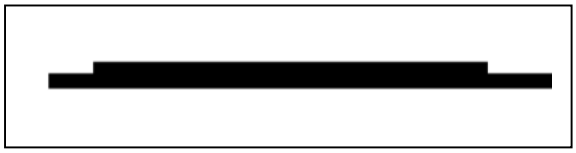

Y = 0 X ^{1} – 0.002

THINNED BY 0.004

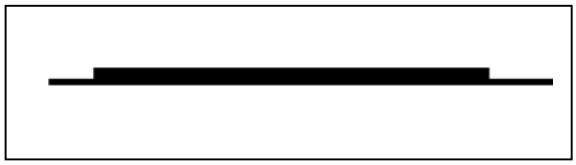

Y = 0 X ^{1} + 0.004

THICKENED BY 0.004

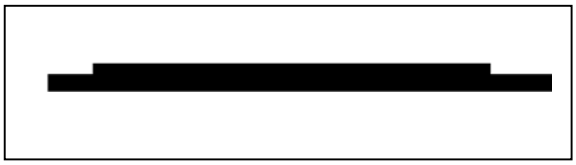

Y = 0 X ^{1} – 0.004

Figure 4.6.1—5, Continued.

Although ANSYS has the capability for coupling strain with electric field to model the inverse piezoelectric effect, a simpler model was sought for this project. Both the initial curvature developed by the fabrication process and the deflection resulting from voltage applied across the piezoceramic were modeled by assigning different expansion coefficients to elements representing substrate and those representing ceramic. A calibration of the reference shape was accomplished by setting TUNIF=0 ("uniform temperature") and varying TREF ("reference temperature") until the arc height (see Table 4.6.1—1.) of the deformed shape matched that of the real actuator. Then, TUNIF was varied until a downward deflection was produced matching the average no-load deflection of the actuator. (Recall that the domed actuator deflects downward and then springs back when voltage is removed.)

The structure was not considered to exist at any real temperature. Rather the temperature difference was merely used as a device to introduce the stress profile into the structure that would accurately simulate the deformed shape and its deflection. This was appropriate since differential contraction does indeed produce the shape assumed by real actuators, which actually do start as flat layers before high temperature bonding. If real actuators were warmed, they would indeed deflect downward, and the in-plane contraction of piezoceramic when an electric field is applied would resemble thermal contraction in every way except one. When piezoceramic contracts under applied electric field, volume is approximately conserved and an expansion occurs normal to the biaxial contraction. However, this out-of-plane expansion cannot affect the curvature of structure, or flexural displacement. As a result, the out-of-plane effect was ignored in this project.

The actual coefficients of expansion used were somewhat arbitrary. Elements representing ceramic were assigned $\alpha = 0$, and elements representing substrate were assigned $\alpha = 5E\text{-}6$, roughly equal to the expansion coefficient of stainless steel. Since the fictitious temperature could be varied and set to whatever ΔT gave correct results, it really did not matter what the actual values were as long as they were different. The search history used to find the appropriate TREF and TUNIF values is recorded in Table 4.6.2—1.

4.6.2. Results Obtained from the FEA Model

After calibration, two ANSYS solutions were obtained for each thickness profile variation. First, the model was run with TREF = 273 and TUNIF = 0 to determine the arc height that would have been obtained under identical conditions if only substrate thickness profile were varied. Then, the model was run with TREF = 273 and TUNIF = 52 to simulate flexural deflection of the structural variant under applied voltage. The difference between these two values was taken as the simulated actuator displacement.

Table 4.6.2—1. Calibration of reference profile

Seeking arc height: Target = 0.0103 inch			Seeking deflection: Target = 0.00834 inch		
TREF = 195	UX	**UY**	TUNIF = 26	UX	**UY**
MAXIMUM ABSOLUTE VALUES			MAXIMUM ABSOLUTE VALUES		
NODE	1505	1	NODE	1505	1
VALUE	-0.51653E-03	0.73604E-02	VALUE	-0.65427E-03	0.93232E-02
TREF = 225	UX	**UY**	TUNIF = 43	UX	**UY**
MAXIMUM ABSOLUTE VALUES			MAXIMUM ABSOLUTE VALUES		
NODE	1505	1	NODE	1505	1
VALUE	-0.59600E-03	0.84928E-02	VALUE	-0.60924E-03	0.786816-02
TREF = 265	UX	**UY**	TUNIF = 46	UX	**UY**
MAXIMUM ABSOLUTE VALUES			MAXIMUM ABSOLUTE VALUES		
NODE	1505	1	NODE	1505	1
VALUE	-0.70195E-03	0.10003E-01	VALUE	-0.60129E-03	0.85683E-02

Table 4.6.2—1, Continued.

Seeking arc height: Target = 0.0103 inch			Seeking deflection: Target = 0.00834 inch		
TREF = 275	UX	**UY**	TUNIF = 51	UX	**UY**
MAXIMUM ABSOLUTE VALUES			MAXIMUM ABSOLUTE VALUES		
NODE	1505	1	NODE	1505	1
VALUE	-0.72844E-03	0.10380E-01	VALUE	-0.58805E-03	0.83796E-02
TREF = 274	UX	**UY**	TUNIF = 52	UX	**UY**
MAXIMUM ABSOLUTE VALUES			MAXIMUM ABSOLUTE VALUES		
NODE	1505	1	NODE	1505	1
VALUE	-0.72579E-03	0.10342E-01	VALUE	-0.58540E-03	0.83414E-02
TREF = 273	UX	**UY**			
MAXIMUM ABSOLUTE VALUES					
NODE	1505	1			
VALUE	-0.72314E-03	0.10305E-01			

For real actuators, free boundary conditions have been found to yield the greatest displacement. Constrained boundary conditions result in a stiffer actuator at the expense of reduced displacement. For THUNDER actuators, free boundary conditions means they are simply supported from below. In other words, rotation and translation of the outside edges is accommodated by their mountings. The bottom edges of the actuator model, then, are constrained only by the condition D,1505,UY,0, where node 1505 was the bottom, outside edge node. Translation and rotation due to deformation or flexure were not constrained. Data is presented in Table 4.6.2—2. Figure 4.6.2—1 shows the deformation effect resulting from ΔT.

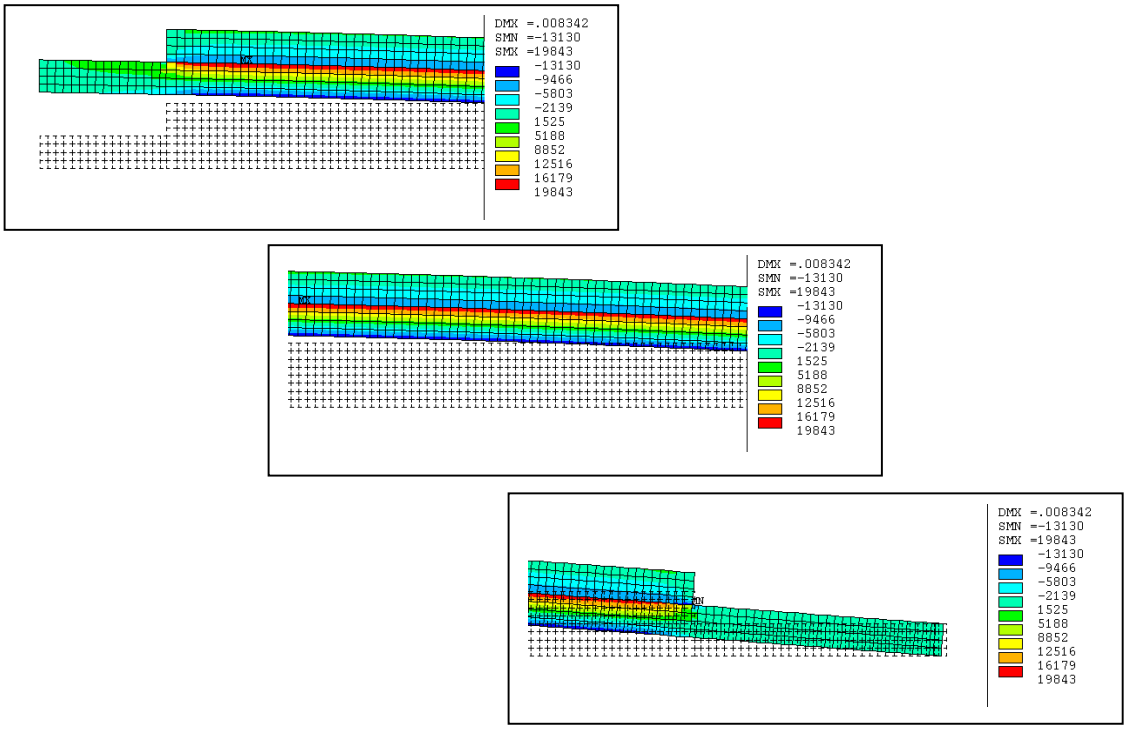

Figure 4.6.2—1. (color) Zoomed-in views of center, mid-radius, and outside edge of model (left top to bottom right) comparing deformed and undeformed shapes (Reference profile)

Table 4.6.2—2. Results of simulations

Profile	Initial UY (Inches)	Deflected UY (Inches)	Displacement (Inches)	Displacement (Microns)
Reference	0.010305	0.0083418	0.0019632	49.8
Linear	0.013187	0.01675	0.002512	63.8
Parabolic	0.013923	0.011271	0.002652	67.4

Table 4.6.2—2, Continued.

Profile	Initial UY (Inches)	Deflected UY (Inches)	Displacement (Inches)	Displacement (Microns)
Biquadratic	0.014785	0.11969	0.002816	71.5
Triquadratic	0.015244	0.01234	0.002904	73.8
Thinned 0.002 Inch	0.012829	0.010385	0.002444	62.1
Thinned 0.004 Inch	0.015499	0.012547	0.002952	75.0
Reverse Linear	0.013330	0.010791	0.002539	64.5
Reverse Parabolic	0.013929	0.011276	0.002653	67.4
Reverse Biquadratic	0.014235	0.011524	0.002711	68.9
Reverse Triquadratic	0.014336	0.011605	0.002731	69.4
Thickened 0.002 Inch	0.0082349	0.0066664	0.0015685	39.8
Thickened 0.004 Inch	0.0066274	0.0053651	0.0012623	32.1

The results are self-consistent, and the following conclusions can be drawn. Any variable thickness profile which removes material and thins the substrate results in enhanced displacement. Profiles which remove more material exhibit higher displacement. The enhancement is more effective if material is removed toward the center of the actuator than if the edges are thinned (i.e., reverse profiles). It turns out, however, that equally good or better results can be achieved simply by using a thinner constant thickness substrate, which is easily available as thinner shim stock. The model also confirms that thicker substrates result in reduced deflection. This is useful information since machining an accurate thickness profile in a real actuator at this scale would be difficult and expensive.

Round THUNDERs have the advantage that they are inherently stiffer because of their geometry (dome vs. beam). Given this, the current model suggests that selective thinning of round THUNDER substrates might be used to boost displacement up to 48% (contrast triquadratic thickness profile with reference profile). Such an actuator would probably retain most of the stiffness of an actuator with constant thickness substrate because of the stiffening effect of a thick rim. However, likelihood of failure by shell buckling might increase.

Is there experimental evidence to verify these conclusions? Circular THUNDER AC240-10, for which load-characterization results were presented in Figure 4.6.1—1, was mounted in a drill press arbor, using the center hole to fasten the actuator. It was rotated by a drill motor while using a Dremel^{TM} grinding tool to remove metal across / around the substrate, but selectively toward the center. Rotating the workpiece during grinding helped obtain radial symmetry in the grinding profile. The resulting “thinned” actuator was subjected to load-displacement testing, and the results presented in Figure 4.6.2—2.

Results plotted in Figure 4.6.2—2 clearly indicate that the circular actuator has exchanged very little high-load displacement for considerably improved low-load performance. The general appearance of the plotted test data strongly resembles that of a beam actuator.

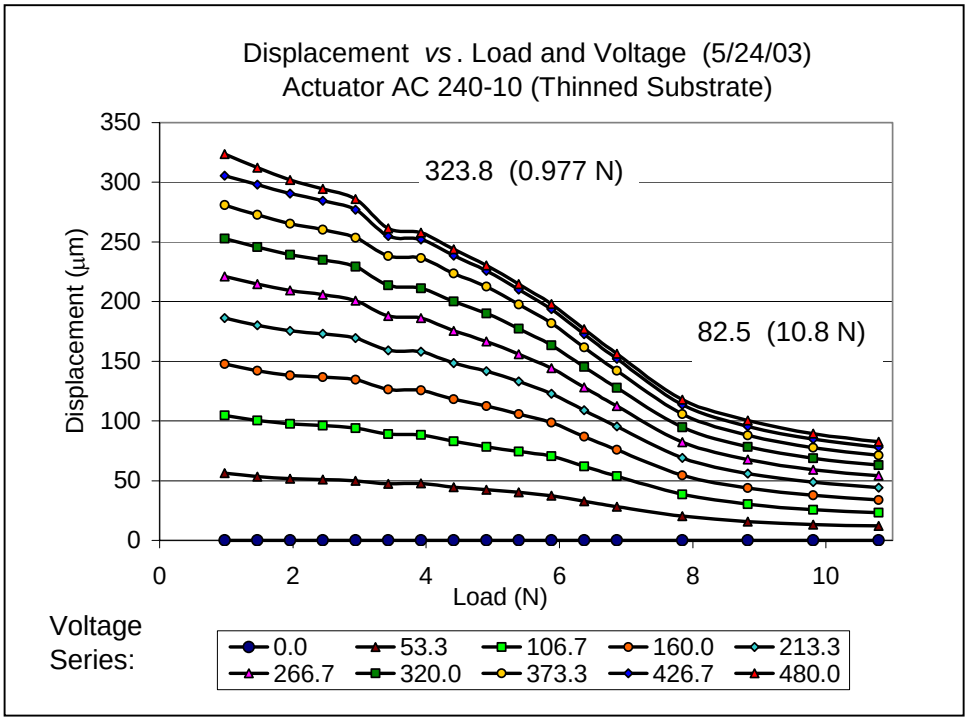

Figure 4.6.2—2. Plot of load-displacement test results for a circular THUNDER AC240-10 after thinning substrate by grinding

The change in thickness profile due to thinning was recorded and is shown by Figure 4.6.2—3. If the actuator is considered a circular area of a flat plane rather than a shallow dome, four radial lines 90º apart were marked as reference lines on the actuator from center to edge (as though the center of a circle were located at the origin of x-y coordinate axes and one measured in the z-direction at intervals along each of the four +/– axial directions). On each of the radial segments, actuator thickness was measured at the center, the edge (perimeter), and three points in between, all approximately equally-spaced on any given line and with corresponding points in the sequence at the same distance from the center on all four lines. The actual center could not be ground because it was clamped in an arbor to provide an axis of rotation.

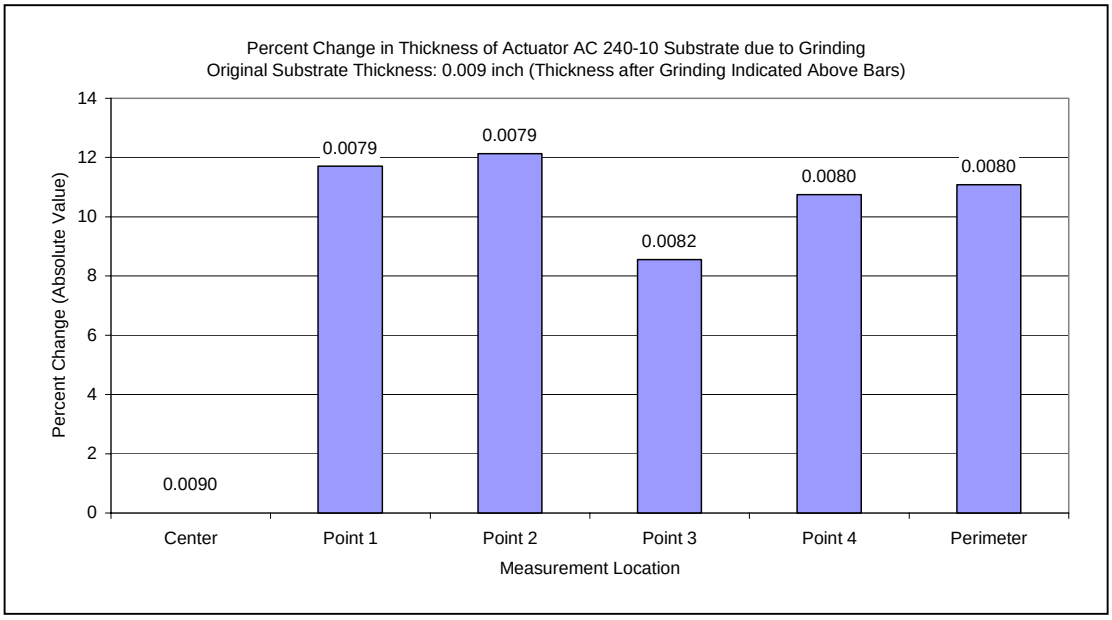

Figure 4.6.2—3. Percent **reduction** (plotted as positive values) in actuator AC240-10 substrate thickness due to grinding from center (left) to perimeter (right). Values above bars are final thickness after grinding

4.7 Summary of Chapter Conclusions

Since this chapter combined various topics related to actuator fabrication, characterization, modification, and conditions for use, here is an overall summary of what was determined from experiments and analysis of results. Shorter summaries were given at the ends of individual sections which differ slightly from this overall conclusion in that certain ideas or connections with the results might have been highlighted which have not been repeated here.

1. Performance of PSU actuators changes in a number of ways over time.

Poling and exposure to load changes curvature due to pre-stress. Repeated tests of displacement response between zero load and loads approaching blocking force generally

yield a sequence of plots indicating a non-random shift in performance between low and high load regimes.

Decline in free displacement while retesting a particular actuator is generally accompanied by improved high load displacement. Occasionally, the opposite effect also occurs.

Not only do high free displacement and high blocking force appear to interchange for certain actuators, but low variability in free-displacement performance is often accompanied by high variability in blocking loads, and vice versa.

If a particular actuator is retested after a period of months or years, the plot of load-displacement data may look very different. Generally, performance at low load has degraded while performance at high load is somewhat improved, but sometimes overall performance is degraded.

In rare instances, the overall performance of an actuator improves over time. A similar phenomenon observed more often is that "camel-shaped" traces of load-displacement data where peak displacement occurs at non-zero load can transform over time (either during short-term repeated testing or when retested after longer periods). What typically happens is that the mid-range displacement peak drops and overall performance becomes more linear, usually with gains in both free displacement and blocking force.

2. Effects of substrate / ceramic thickness ratio (and substrate material properties) are more subtle than previously shown.

As has been previously reported, thicker substrates yield smaller free displacement and larger high-load displacement than thinner substrates.

The current work has shown that thicker substrates yield more linear displacement response between zero load and loads approaching blocking force. In the context of this project, the upper limit for a "thin substrate" would be a little more than half the thickness of the ceramic element. A mid-range of thickness would extend to about the same

thickness as that of the ceramic element. Substrates thicker than the ceramic element can provide linearity in displacement response which approaches the idealized straight line.

Candidate substrate materials often come down to a choice between stainless steel and aluminum. Aluminum has been favored by some researchers [1,3] for high displacement. In this study, performance of actuators with aluminum substrates often permanently deteriorated after exposure to high load and was sometimes substandard at low loads also.

However, the conclusions just given can be combined to obtain a noteworthy result. A pair of actuators made with an aluminum substrate three times as thick as the ceramic element displayed rather good performance at low load, excellent performance at high load, and idealized linear response. Had the substrate in this actuator been stainless steel, it probably would have been too stiff to simultaneously yield all three results.

3. Bond material and thickness both affect the general character of actuator performance.

There is no strong correlation between increasing displacement and decreasing bond thickness. In other words, the apparent advantage of an integral bond of zero effective thickness in RAINBOW actuators does not carry over to bonds made with organic adhesives of finite thickness in pre-stressed unimorphs. There may be optimal thicknesses for particular adhesives, but if so, the optimal thickness is not necessarily the thinnest possible.

Thin bonds (less than 10 mm for actuators of the scale used in this project) appear to be associated with the phenomenon of maximum displacement developing under loads at some mid-level between low and high. The effect is enhanced by using a thin substrate. Thin bonds and thin substrates both appear correlated with nonlinear load-displacement plots and increased chances of electrical or mechanical failure. Peak displacement at whatever load is seldom any better, and may be considerably worse, than peak displacements for actuators with not-so-thin bonds.

Of the two adhesives used for making pre-stressed unimorphs in this project (LaRC-SI polyimide and M-Bond epoxy), actuators bonded with the epoxy were better suited to high displacements at zero and low loads, while polyimide-bonded actuators were better suited to high load performance, given comparable bond thickness and dimensions of the elements. The fact that products of free displacement and blocking force for each group of actuators were roughly equivalent suggests all well-made PSU actuators have a comparable work capacity that can be biased toward better performance at low or high loads by the adhesive type.

4. The signature of enhanced performance due to pre-stress can sometimes be seen in load-displacement data by plotting the load which flattens initial curvature.

Pre-stressed unimorphs at times display a distinct upturn in the trace of their load-displacement data approaching zero load from the high load direction followed by a dip at some fairly low level of load. By consulting the parent data of position versus load, one can mark on the displacement plot the load which produces a passive displacement equal to the initial pre-stress-induced curvature of the actuator. The load corresponding to a flattened actuator will fall near the center of the "dip" just described.

The slope of the "upturn" is steeper than the general linear trend of the plot and is ascribed to enhanced displacement according to the mechanism first described by Haertling. [20] The dip in the trace of data as load flattens the actuator is of course followed by at least a modest rebound or the dip would not be described as a dip, but rather a bend or change in slope. The rebound is indeed a modest convexity, but one can determine that its approximate center corresponds to the "mirror image" of the original curvature due to pre-stress, that is, a positive (sagging) curvature of magnitude equal to the original negative (hogging) curvature cause by internal stress bias.

The conclusion is that these features indicate localized regions in which stress-bias enhancement of displacement actually operates. At higher loads, the phenomenon is lost in the large displacements and stresses which result from applied load.

5. Attempts to mimic pre-stress-induced performance enhancement due to stress bias by mechanical bending during fabrication at room temperature gave inconclusive results.

The experiment may have shown that bending stress bias without axial tension and compression do not provide pre-stress-induced performance enhancement. Alternatively, it may have shown that a different room-temperature-setting epoxy providing a thinner glue-line should have been used.

6. End conditions strongly influence compliant actuator performance.

End conditions involving blocked translation or higher degrees of constraint tended to result in increased stiffness (reduced downward displacement) with applied voltage and with increasing displacement with increasing load. The last observation suggests that constrained actuators do more work as load increases. Calculations of load-displacement work performed support this, although other experiments have shown that the actuators must operate in a continuously loaded state, as in these tests, rather than seeing their load intermittently, as in inchworm motors, for higher work output to occur.

In the case of a loaded actuator, constraining the end conditions results in a stiffer actuator, which enhances load capabilities, but at the cost of reduced low-load displacement. In particular, blocking end translation substantially reduces free displacement and increases stiffness, more so than blocking end rotation. In addition, the buckling phenomenon is more associated with blocked translation than with blocked rotation. With translation blocked, the actuator displaces less in response to low load,

increases displacement under increasing load, then reaches a point of instability and collapses abruptly into the inverted curvature, a working definition of buckling.

7. Finite element analysis has shown that selective thinning of a circular actuator substrate can substantially enhance low load displacement while retaining most of its former high load displacement.

Any variable thickness profile which removes material and thins the substrate results in enhanced displacement. Profiles which remove more material exhibit higher displacement. The enhancement is more effective if material is removed toward the center of the actuator than if the edges are thinned (i.e., reverse profiles). It turns out, however, that equally good or better results can be achieved simply by using a thinner constant thickness substrate. The model also confirms that thicker substrates result in reduced deflection.

Round THUNDERs have the advantage that they are inherently stiffer because of their geometry (dome vs. beam). Given this, the current model suggests that selective thinning of round THUNDER substrates might be used to boost displacement up to 48%. Such an actuator would probably retain most of the stiffness of an actuator with constant thickness substrate because of the stiffening effect of a thick rim. However, likelihood of failure by shell buckling might increase.

4.8 References

[1] R.G. Bryant, S.A. Evans, E.R. Long Jr., and R.L. Fox. Thermal and Mechanical Characterization of NASA High Displacement Actuators for Satellite Instrumentation. Proceedings of the SPIE—The International Society for Optical Engineering, 3991, 195-201 (2000).

[2] G. Horner and B. Taleghani. Single axis piezoelectric gimbal. Proceedings of SPIE - The International Society for Optical Engineering, 3674, 371-378 (1999).

[3] S. Wise. Displacement properties of Rainbow and Thunder piezoelectric actuators. Sensors and Actuators A, 69, 33-38 (1998).

[4] K. M. Mossi, G. V. Selby, R. G. Bryant. Thin-layer composite unimorph ferroelectric driver and sensor properties. Materials Letters, 35, 39-49 (1998).

[5] C. Hyder, G. C. Horner, W. W. Clark. Linear traveling wave motor. Proceedings of the SPIE—The International Society for Optical Engineering, 3674, 205-211 (1999).

[6] Face International Corporation (Norfolk, VA) http://www.face-int.com/thunder/thunder.htm

[7] U.S. Patent 5,632,841 to R. F. Helbaum, R. G. Bryant, R. L. Fox. Thin layer composite unimorph ferroelectric driver and sensor (May 27, 1997).

[8] R. W. Schwartz, L. E. Cross, and Q.-M. Wang. Estimation of the effective d31 coefficients of the piezoelectric layer in Rainbow actuators. Journal of the American Ceramic Society, 84, 2563-2569 (2001).

[9] Q.M. Zhang, J. Zhao, K. Uchino, J. Zheng. Change in the weal field properties of Pb(Zr,Ti)O3 piezoceramics with compressive uniaxial stresses and its link to the effect of dopants on the stability of the polarization in materials. Journal of Materials Research, 12, 226-234 (1997).

[10] G. Yang, S.F. Liu, W. Ren, and B.K. Mukherjee. Uniaxial stress dependence of the piezoelectric properties of lead zirconate titanate ceramics. Proceedings of the SPIE—The International Society for Optical Engineering, 3992, 103-113 (2000).

[11] K. Uchino. Materials issues in design and performance of piezoelectric actuators: An overview. Acta Materialia, 46, 3745-3753 (1998).

[12] G. H. Haertling. Stress-induced effects in PLZT ceramics. IEEE International Symposium on Applications of Ferroelectrics, 1, 65-68 (1996).

[13] K. Franke, H. Huelz, and M. Weihnacht. Stress-induced depolarization in PZT thin films, measured by means of electric force microscopy. Surface Science, 416, 59-67 (1998).

[14] S.W. Meeks and R.W. Timme. Effects of one-dimensional stress on piezoelectric ceramics. Journal of Applied Physics, 46, 4334-4338 (1975).

[15] S. Stotz. Shift of the morphotropic phase boundary in the PZT system under the influence of electrical fields and uniaxial stresses. Ferroelectrics, 76, 123-132 (1987).

[16] H. Arndt, G. Schmidt, and N. Vogel. Influence of uniaxial pressure on the properties of PLZT ceramics. Ferroelectrics, 61, 9-18 (1984).

[17] V.A. Isupov. Some Aspects of the physics of ferroelectric ceramics. Ferroelectrics, 46, 217-225 (1983).

[18] H. A. Krueger. Stress sensitivity of piezoelectric ceramics: Part 1. Sensitivity to compressive stress parallel to the polar axis. Journal of the Acoustical Society of America, 42, 636-645 (1967).

[19] H. A. Krueger and D. Berlincourt. Effects of high static stress on the piezoelectric properties of transducer materials. Journal of the Acoustics Society of America, 33, 1339-1344 (1961).

[20] G. Li, E. Furman, and G. Haertling. Stress-enhanced displacements in PZLT Rainbow Actuators. Journal of the American Ceramics Society, 80, 1382-1388 (1977).

[21] V. Giurgiutiu, Z. Chaudhry, C. A. Rogers. Stiffness issues in the design of ISA displacement amplification devices: Case study of a hydraulic displacement amplifier. Proceedings of the SPIE—The International Society for Optical Engineering, 2443, 105-119 (1995).

[22] K. M. Mossi, G. V. Selby, R. G. Bryant. Thin-layer composite unimorph ferroelectric driver and sensor properties. Materials Letters, 35, 39-49 (1998).

[23] K.M. Mossi, R.P. Bishop, R.C. Smith and H.T. Banks. Evaluation criteria for Thunder actuators. Proceedings of the SPIE—The International Society for Optical Engineering, 3667, 738-743 (1999).

[24] K.M. Mossi, R.P. Bishop. Characterization of different types of high performance Thunder actuators. Proceedings of the SPIE—The International Society for Optical Engineering, 3675, 43-52 (1999).

[25] C. Niezecki and S. Balakrishnan. Power characterization of Thunder actuators as underwater propulsors. Proceedings of the SPIE—The International Society for Optical Engineering, 4327, 88-98 (2001).

[26] J. Mulling, T. Usher, B. Dessent, J. Palmer, P. Franzon, E. Grant, A. Kingon. Load characterization of high displacement piezoelectric actuators with various end conditions. Sensors and Actuators A: Physical, 94, 19-24 (2001).

5. Analysis of Butterfly Loops for a Cross-Section of Actuator Types

5.1 Experiment to Obtain Butterfly Loops for a Matrix of Conditions

5.1.1 Introduction and Presentation of Results

An experiment was conducted to characterize a sample of actuators representing the prominent design and fabrication variables for the project reported on in this thesis, using so-called butterfly loops which show strain as a function of applied electric field. Butterfly loops represent the bipolar, large-signal behavior of an actuator that originates in the piezoceramic element. In particular, they capture switching of net poling direction which occurs at the coercive field strengths for a particular piezoceramic element, given its material properties and the influence of stress from internal bias or load. They also show saturation in the alignment of polarization at high positive and negative field strengths.

Stress due to load would be modulated by such characteristics as substrate stiffness, which mostly depends on Young's modulus of substrate material and its thickness, and effect of adhesive type on load transfer through its thickness. In the case of actuators made with J.B. Weld adhesive, the especially thick bonds form part of the substrate, so that adhesive and substrate effects on piezoelectric strain are combined. One important consequence is that the butterfly loops show asymmetric response which results from internal stress bias. An unbiased unimorph, by contrast, should produce symmetric butterfly loops. By taking a series of butterfly loops under load, the combined effect of load and internal stress bias can be seen.

Experimental results will not be presented in the form of strain as a function of electric field, but rather displacement as a function of applied voltage. Applied voltage divided by the thickness (7.5 mils or 0.190 mm) of the piezoceramic element would give electric field strength [V / m], and displacement divided by the horizontal length (1.625 inch or 41.28 mm) of the actuator between support points would give flexural strain [fraction or percent]. Given that the ceramic thickness and flexural length for all actuators was constant, it was decided that comparisons based on the direct experimental quantities of voltage and displacement would seem more concrete. However, the result is that the

data are tied to the particular dimensions of these actuators and cannot be independently compared with test data for other actuators without making conversions to flexural strain and electric field strength. Nonetheless, conversion is simply a matter of linear scaling, and plotted results would have the same shape, although plotted against different scales.

The experimental plan is summarized in Table 5.1.1—1. Three adhesive types are crossed with two levels of substrate thickness, with the additional subdivision that two levels of the thick bonds provided by J.B. Weld epoxy are included. For each actuator, paired large-signal displacement-voltage tests were conducted for a series of loads from zero load the weight of 1100g, in 100g increments. After testing under the highest load, a final pair of tests was conducted with the load again at zero. Two loops were acquired in each test. The pairs of tests show the adjustment of the actuator polarization state to a new load level. (There may be charge effects, but it was verified that actuators which remain connected to the high-voltage amplifier are effectively shorted through the amplifier when it is not applying a voltage signal.)

Table 5.1.1—1. Matrix of variables represented by selected actuators

	LaRC-SI	M-Bond	JB Weld
Thick Substrate (Stainless steel, 8 mils thick)	060902B Bond Thickness = 18.8 μm	100902C Bond Thickness = 7.8 μm	K081602A (Thick Bond, 384.5 μm) N081602A (Thin Bond, 77.3 μm)
Thin Substrate (Stainless Steel, 4 mils thick)	062102A Bond Thickness = 13.5 μm	100902E Bond Thickness = 6.9 μm	K121002 (Thick Bond, 131.2 μm) N121002A (Thin Bond, 109.2 μm)

Since the sets of butterfly loops are difficult to include as figures, but are fascinating to look at and reveal many things that might not be commented on here, they have been included in their entirety as Appendix 1. The remainder of this section will present quantitative data associated with key features on a butterfly loop that were determined from the various test sets in the experiment. Figure 5.1.1—1 shows the features of interest as they appear on plots. Operating ranges are approximate intervals of applied voltage and resulting displacement for a given polarization direction without switching the poling of the actuator. The range corresponding to "downward" (see Figure 2.3.2—4A) poling has positive slope and is the top side of the lobes on the right. The range corresponding to upward poling has negative slope and is the top side of the lobes at left.

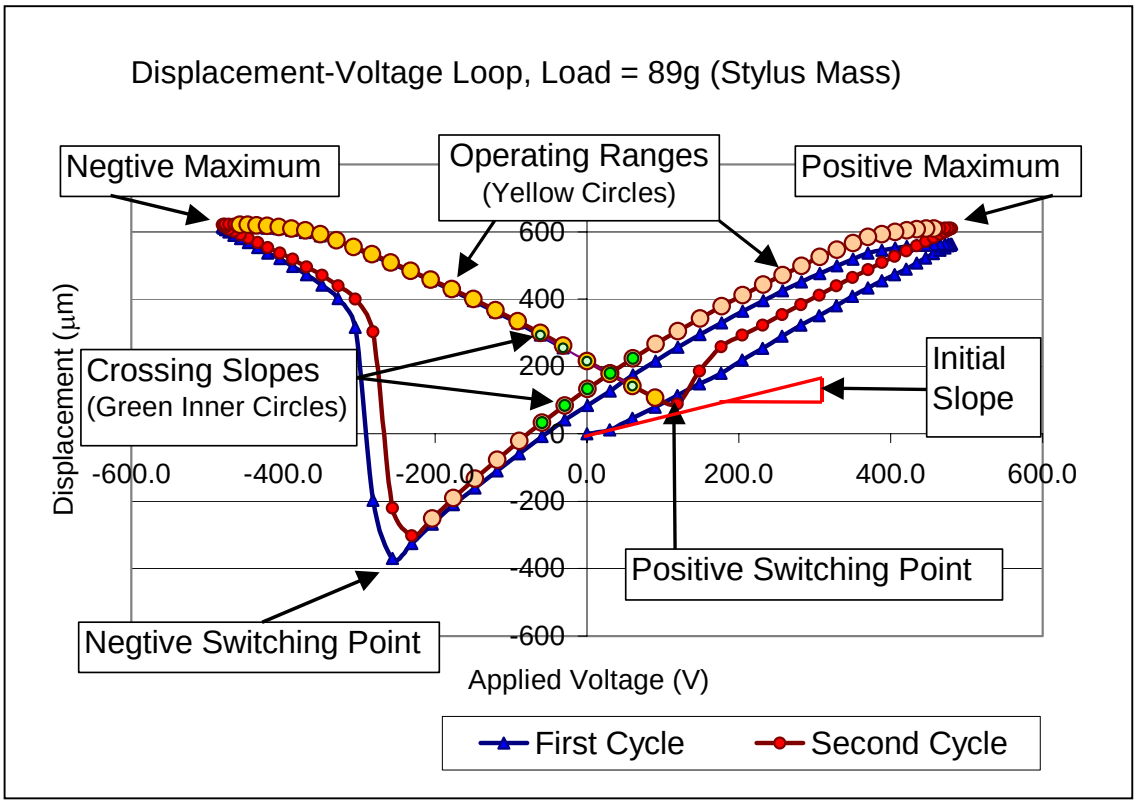

Figure 5.1.1—1. (color) Sample voltage-displacement loop pair showing landmark features to be compiled as characterization data

As in Figure 5.1.1—1, the lobes will be asymmetric when pre-stressed actuators are tested. One range will be larger and steeper from its negative-voltage end at left to its positive-voltage end at right. Thus, the pre-stress provides enhancement of performance under one poling direction which would be used to obtain enhanced performance. To obtain maximum performance, pre-stressed unimorphs should be operated within the larger range without switching the net polarization.

It can be confusing to navigate through the sequential loops and follow the complete path. Although the tests simply start at zero voltage, apply a maximum positive voltage, return to zero, apply a maximum negative voltage, then return to zero (then repeat), the crossover due to switching and the fact that the end of the first loop leads continuously into the second loop does complicate things. Figure 5.1.1—2 shows the order in which the data trace traverses through landmark features in the two loops.

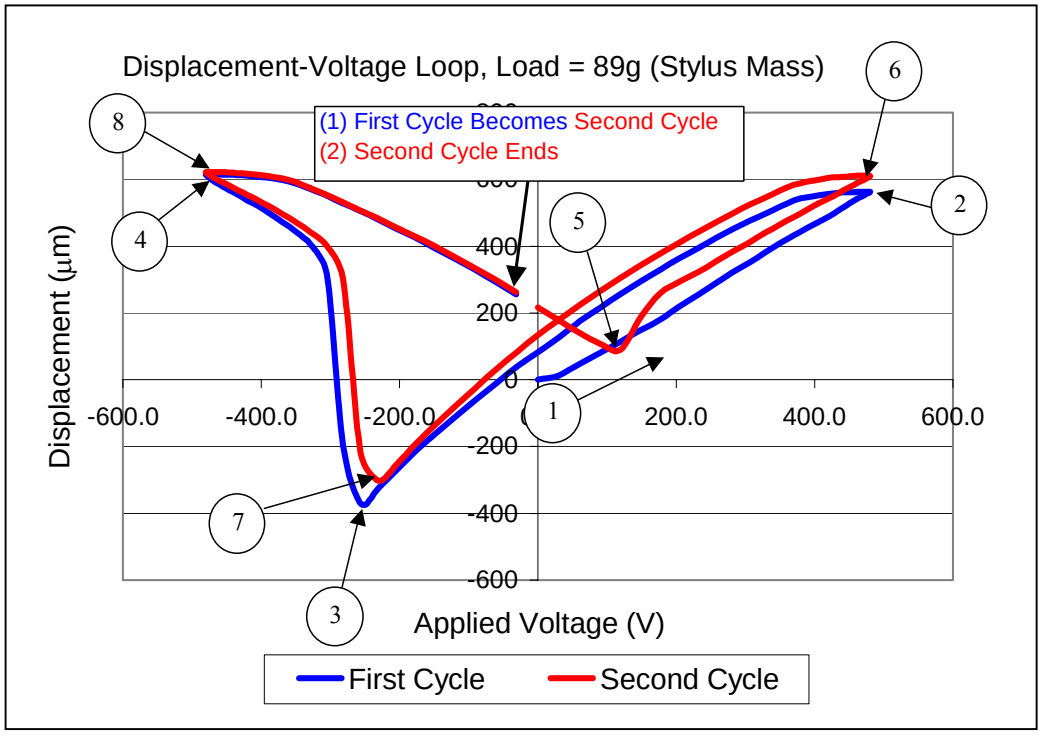

Figure 5.1.1—2. (color) Sample voltage-displacement loop pair showing continuous path through first then second loop

Table 5.1.1—2 present data for polyimide-bonded actuator (LaRC-SI adhesive) made using an 8-mil substrate. Table 5.1.1—3 presents data for the polyimide-bonded actuator made using a 4-mil substrate. The same pattern continues to the column for M-Bond actuators on thick and thin substrates, then to the column for actuators fabricated with J.B. Weld adhesive in each of the four cases. Landmark data points are given as displacement at a corresponding voltage; slopes as rise-over-run ratios, and ranges are given as maximum to minimum endpoints, followed by a displacement interval and a voltage interval.

The operating ranges for either direction of polarization have been truncated just before switching points at lower ends and before displacement response flattens on the "saturation edges" approaching maximum positive and negative voltages. The first five points as voltage recedes from the maximum (after approaching the maximum) were omitted. If a table were included for each actuator type at each load, however, the plethora of data would be unhelpful. Transition in the shape of the butterfly loops with increasing load is actually rather gradual. It will be adequate to include tables for zero, 500g, and 1000g load.

Table 5.1.1—2. Characterization of actuator 060902B: 8-mil substrate, polyimide adhesive

	Zero Load	500g Load	1000g Load
Initial Slope	0.4115 μm / V	–0.3390	–0.124
Positive Maximum	563 μm at 480 V 611 μm at 479 V	67 μm at 479 V 69 μm at 480 V	80 μm at 476 V 81 μm at 480 V
Negative Maximum	616 μm at –476 V 622 μm at –479 V	87 μm at –480 V 89 μm at –480 V	74 μm at –480 V 75 μm at –480 V
Positive Switching	90 μm at 119 V	–47 μm at 119 V	–16 μm at 90 V
Negative Switching	–370 μm at -256 V –303 μm at –230 V	–280 μm at -204 V –279 μm at –204 V	–109 μm at -176 V –109 μm at –176 V
Positive Crossing Slope	1.596 μm / V	0.843 μm / V	0.309 μm / V
Negative Crossing Slope	–1.231 μm / V	–0.439 μm / V	–0.192 μm / V
Positive Range	–252 μm at –204 V 610 μm at 457 V 861 μm, 661 V	–264 μm at –176 V 68 μm at 457 V 332 μm, 633 V	–92 μm at –148 V 79 μm at 457 V 172 μm, 605 V
Negative Range	621 μm at –457 V 108 μm at 90 V 729 μm, 547 V	88 μm at –457 V –41 μm at 90 V 129 μm, 547 V	74 μm at –457 V –16 μm at 90 V 90 μm, 547 V

Table 5.1.1—3. Characterization of actuator 062102A: 4-mil substrate, polyimide adhesive

	Zero Load	500g Load	1000g Load
Initial Slope	1.0622 μm / V	–1.3366	–0.3338
Positive Maximum	749 μm at 476 V 913 μm at 480 V	318 μm at 479 V 317 μm at 480 V	88 μm at 480 V 108 μm at 476 V
Negative Maximum	1004 μm at –476 V 1045 μm at –479 V	343 μm at –479 V 345 μm at –479 V	108 μm at –480 V 127 μm at –480 V
Positive Switching	824 μm at 231 V	-190 μm at 119 V	–20 μm at 119 V
Negative Switching	26 μm at -256 V –230 μm at –310 V	–451 μm at -204 V –450 μm at –204 V	–113 μm at -204 V –89 μm at –204 V
Positive Crossing Slope	1.641 μm / V	1.232 μm / V	0.452 μm / V
Negative Crossing Slope	–0.116 μm / V	–1.251 μm / V	–0.407 μm / V
Positive Range	372 μm at –148 V 913 μm at 457 V 1285 μm, 605 V	–365 μm at –176 V 312 μm at 457 V 677 μm, 633 V	–76 μm at –176 V 108 μm at 457 V 184 μm, 633 V
Negative Range	1045 μm at –457 V 905 μm at 60 V 1950 μm, 5517 V	341 μm at –457 V –127 μm at 90 V 467 μm, 547 V	128 μm at –457 V –15 μm at 90 V 143 μm, 547 V

Table 5.1.1—4. Characterization of actuator 100902C: 8-mil substrate, M-Bond adhesive

	Zero Load	500g Load	1000g Load
Initial Slope	1.0625 μm / V	–1.1581	–0.3591
Positive Maximum	458 μm at 479 V 459 μm at 476 V	169 μm at 476 V 172 μm at 479 V	79 μm at 480 V 81 μm at 479 V
Negative Maximum	498 μm at –479 V 499 μm at –472 V	203 μm at –479 V 203 μm at –480 V	106 μm at –480 V 107 μm at –476 V
Positive Switching	–247 μm at 148 V	–172 μm at 148 V	–57 μm at 148 V
Negative Switching	–455 μm at –204 V –447 μm at –204 V	–252 μm at –176 V –247 μm at –176 V	–78 μm at -148 V –78 μm at –148 V
Positive Crossing Slope	1.672 μm / V	1.054 μm / V	0.319 μm / V
Negative Crossing Slope	–1.619 μm / V	–1.079 μm / V	–0.316 μm / V
Positive Range	–402 μm at –176 V 456 μm at 457 V 859 μm, 633 V	–213 μm at –148 V 172 μm at 457 V 385 μm, 605 V	–66 μm at –119 V 81 μm at 457 V 147 μm, 576 V
Negative Range	496 μm at –457 V –200 μm at 119 V 696 μm, 576 V	203 μm at –457 V –139 μm at 119 V 341 μm, 576 V	106 μm at –457 V –45 μm at 119 V 151 μm, 576 V

Table 5.1.1—5. Characterization of actuator 100902E: 4-mil substrate, M-Bond adhesive

	Zero Load	500g Load	1000g Load
Initial Slope	1.2964 μm / V	–0.8829	–0.0121
Positive Maximum	599 μm at 479 V 616 μm at 479 V	177 μm at 479 V 180 μm at 479 V	7 μm at 480 V 12 μm at 480 V
Negative Maximum	668 μm at –476 V 650 μm at –476 V	205 μm at –479 V 208 μm at –479 V	22 μm at –480 V 26 μm at –476 V
Positive Switching	306 μm at 177 V	–133 μm at 148 V	5 μm at 148 V
Negative Switching	–518 μm at –204 V –501 μm at –204 V	–191 μm at -176 V –279 μm at –204 V	–5 μm at -176 V 0 μm at –204 V
Positive Crossing Slope	3.320μm / V	0.746 μm / V	0.015 μm / V
Negative Crossing Slope	–2.184 μm / V	–0.776 μm / V	–0.043 μm / V
Positive Range	–463 μm at –176 V 609 μm at 457 V 1072 μm, 683 V	–154 μm at –148 V 180 μm at 457 V 334 μm, 605 V	0 μm at –148 V 12 μm at 457 V 12 μm, 605 V
Negative Range	645 μm at –457 V –281 μm at 148 V 926 μm, 605 V	208 μm at –457 V –106 μm at 119 V 315 μm, 576 V	26 μm at –457 V 8 μm at 119 V 34 μm, 576 V

Table 5.1.1—6. Characterization of actuator K081602A: 8-mil substrate, J.B.Weld adhesive, **thick** bond

	Zero Load	500g Load	1000g Load
Initial Slope	0.4861 μm / V	–0.5836	–0.1679
Positive Maximum	303 μm at 480 V 308 μm at 479 V	147 μm at 480 V 149 μm at 480 V	64 μm at 479 V 64 μm at 480 V
Negative Maximum	264 μm at –479 V 266 μm at –479 V	140 μm at –480 V 139 μm at –480 V	64 μm at –480 V 65 μm at –479 V
Positive Switching	–265 μm at 177 V	–108 μm at 177 V	–29 μm at 177 V
Negative Switching	–286 μm at -230 V –285 μm at –230 V	–137 μm at –204 V –136 μm at –204 V	–40 μm at -176 V –38 μm at –176 V
Positive Crossing Slope	0.998 μm / V	0.562 μm / V	0.173 μm / V
Negative Crossing Slope	–1.034 μm / V	–0.539 μm / V	–0.151 μm / V
Positive Range	–268 μm at –204 V 304 μm at 457 V 572 μm, 661 V	–116 μm at –176 V 146 μm at 457 V 262 μm, 633 V	–32 μm at –148 V 63 μm at 457 V 95 μm, 605 V
Negative Range	261 μm at –457 V –265 μm at 177 V 526 μm, 634 V	136 μm at –457 V –88 μm at 148 V 224 μm, 605 V	63 μm at –457 V –25 μm at 148 V 88 μm, 605 V

Table 5.1.1—7. Characterization of actuator N081602A: 8-mil substrate, J.B.Weld adhesive, **thin** bond

	Zero Load	500g Load	1000g Load
Initial Slope	0.7150 μm / V	–0.8381	–0.4129
Positive Maximum	521 μm at 479 V 473 μm at 476 V	243 μm at 479 V 69 μm at 480 V	136 μm at 480 V 129 μm at 479 V
Negative Maximum	362 μm at –479 V 353 μm at –476 V	221 μm at –480 V 233 μm at –472 V	117 μm at –479 V 124 μm at –480 V
Positive Switching	–491 μm at 177 V	–150 μm at 177 V	–65 μm at 177 V
Negative Switching	–394 μm at -256 V –500 μm at –230 V	–152 μm at -204 V –157 μm at –204 V	–62 μm at -176 V –60 μm at –176 V
Positive Crossing Slope	1.541 μm / V	0.856 μm / V	0.329 μm / V
Negative Crossing Slope	–1.700 μm / V	–0.873 μm / V	–0.366 μm / V
Positive Range	–421 μm at –204 V 470 μm at 457 V 891 μm, 661 V	–145 μm at –176 V 242 μm at 457 V 387 μm, 633 V	–60 μm at –176 V 128 μm at 457 V 188 μm, 633 V
Negative Range	346 μm at –457 V 438 μm at 148 V 784 μm, 605 V	230 μm at –457 V –130 μm at 148 V –360 μm, 605 V	120 μm at –457 V –62 μm at 148 V 182 μm, 605 V

Table 5.1.1—8. Characterization of actuator K121002: 4-mil substrate, J.B.Weld adhesive, **thick** bond

	Zero Load	500g Load	1000g Load
Initial Slope	–2.3606 μm / V	–1.0332	–0.2949
Positive Maximum	587 μm at 480 V 589 μm at 480 V	199 μm at 480 V 210 μm at 476 V	96 μm at 480 V 109 μm at 472 V
Negative Maximum	561 μm at –479 V 559 μm at –479 V	162 μm at –479 V 208 μm at –480 V	98 μm at –461 V 112 μm at –465 V
Positive Switching	–466 μm at 204 V	–218 μm at 119 V	–36 μm at 177 V
Negative Switching	–522 μm at –204 V –517 μm at –204 V	–256 μm at -204 V –247 μm at –204 V	–46 μm at –176 V –29 μm at –176 V
Positive Crossing Slope	1.968 μm / V	0.994 μm / V	0.266 μm / V
Negative Crossing Slope	–2.044 μm / V	–0.889 μm / V	–0.275 μm / V
Positive Range	–421 μm at –176 V 586 μm at 457 V 1007 μm, 633 V	–224 μm at –176 V 209 μm at 457 V 433 μm, 633 V	–16 μm at –148 V 109 μm at 457 V 125 μm, 605 V
Negative Range	556 μm at –457 V 373 μm at 148 V 928 μm, 605 V	207 μm at –457 V –165 μm at 148 V 372 μm, 605 V	112 μm at –457 V –28 μm at 148 V 141 μm, 605 V

Table 5.1.1—9. Characterization of actuator N121002A: 4-mil substrate, J.B.Weld adhesive, **thin** bond

	Zero Load	500g Load	1000g Load
Initial Slope	1.6161 μm / V	–1.2922	–0.3197
Positive Maximum	828 μm at 479 V 936 μm at 479 V	164 μm at 496 V 168 μm at 480 V	87 μm at 476 V 94 μm at 480 V
Negative Maximum	913 μm at –476 V 931 μm at –476 V	162 μm at –479 V 166 μm at –479 V	89 μm at –479 V 96 μm at –479 V
Positive Switching	–298 μm at 177 V	–248 μm at 177 V	–43 μm at 177 V
Negative Switching	–549 μm at –230 V –364 μm at –204 V	–253 μm at –176 V –244 μm at –176 V	–51 μm at –176 V –42 μm at –176 V
Positive Crossing Slope	2.297 μm / V	0.947 μm / V	0.301 μm / V
Negative Crossing Slope	–2.493 μm / V	–0.949 μm / V	–0.302 μm / V
Positive Range	–239 μm at –176 V 932 μm at 457 V 1171 μm, 633 V	–190 μm at –148 V 168 μm at 457 V 358 μm, 633 V	–34 μm at –176 V 94 μm at 457 V 129 μm, 633 V
Negative Range	927 μm at –457 V –187 μm at 148 V 1114 μm, 605 V	166 μm at –457 V –199 μm at 148 V 365 μm, 605 V	96 μm at –457 V –40 μm at 148 V 135 μm, 605 V

5.1.2 Analysis of Butterfly Loop Characteristics

The butterfly loops in Appendix 1 show that some sets of loops are considerably more symmetric or asymmetric than others. Let us assume that actuator pre-stress is reflected in butterfly loop asymmetry, and find out if consistent observations can be made. The premier evidence for pre-stress is initial curvature upon fabrication. Perhaps a means of correlating "asymmetry" with initial actuator curvature (expressed as flexural strain) should be devised. First, a dependable numeric measure of butterfly loop asymmetry must be developed.

The presence of asymmetry in a butterfly loop indicates that some influence, such as an asymmetric stress state, is causing one polarization direction to be preferred over the other. In other words, the actuator piezoceramic will more readily switch to one polarization direction than the other. As was mentioned in Section 2.3.1.3, pre-stressed unimorphs are typically poled "down" and operated with the applied field in parallel such that actuator response typically follows the top edge of the right lobe of the butterfly loop. (See Figure 2.3.1.3—1.) The operating range can extend to negative voltages lower in magnitude than the negative switching voltage.

It would seem that this preferential polarization would be indicated by lower switching voltage, and indeed positive switching voltages are lower than the negative switching voltages for almost all the loops obtained in this experiment. However, the situation is slightly complicated by the fact that the displacement level at switching can vary dramatically depending on how symmetric or not the loops are. The combination of switching voltage and displacement at switching determines the slope of actuator response as electric field changes direction after reaching a positive or negative saturation voltage.

Data given in previous tables were analyzed by considering simplified traces around two butterfly loop cycles as follows. (Refer to Figure 5.1.1—2 as a key for numbers in parentheses.) Start at positive saturation displacement (2), go to negative switching voltage (3), then to negative saturation displacement (4), then positive switching voltage (5), then positive saturation displacement (6), then negative switching voltage (7),

then negative saturation displacement (8), then back to the positive switching voltage (5).

Upon consideration, the best indicator of asymmetry would be the (absolute) ratio of positive slope along the top of the right lobe to negative slope along the top of the left lobe. Figure 5.1.2—1 shows how this would work for what appears to be the most symmetric set of butterfly loops. Figure 5.1.2—2 shows the same method applied to one of the most asymmetric sets of butterfly loops. The temptation is to consider only the ratio

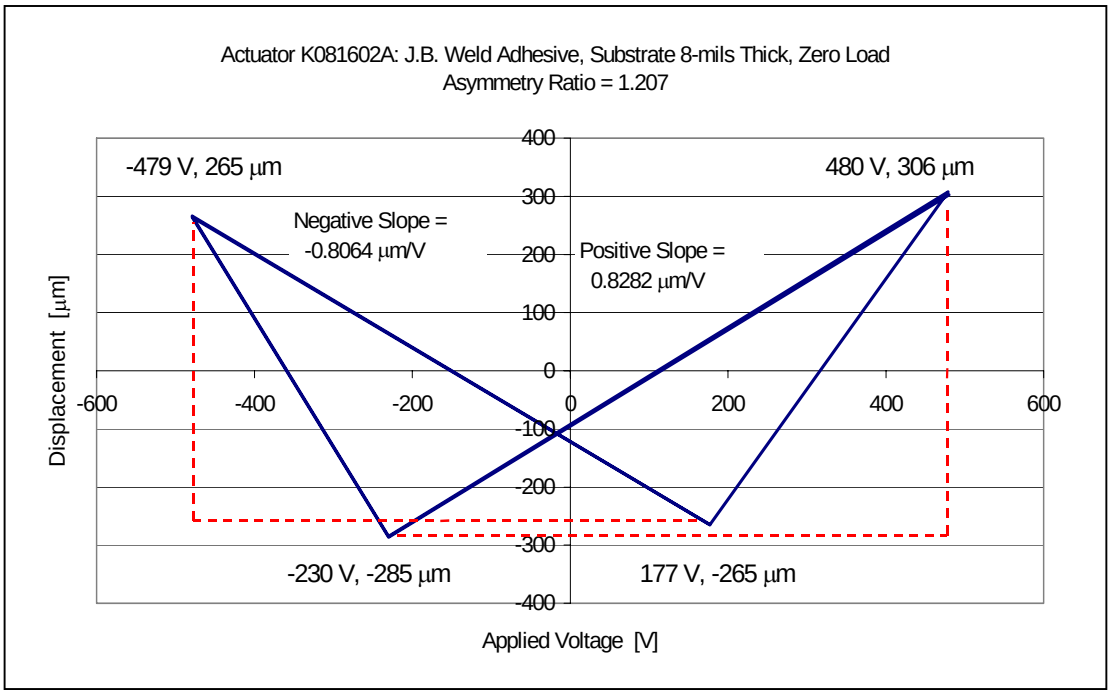

Figure 5.1.2—1. (color) Example of how absolute (asymmetry) ratio of positive and negative slopes would be calculated for an unusually symmetric case

of *displacements* along each slope. However, it was found that the ratio of slopes resulted in better differentiation between the various actuators. Hence, this was chosen as the better metric. In other words, we are seeking a measure that better separates the actuators according to differences between left and right sides of the butterfly loop (which represent response to polarization in opposite directions).

Stated more precisely, the asymmetry ratio would be the absolute ratio of positive slope between positive saturation displacement and negative switching point to the negative slope between negative saturation displacement and positive switching point. Its calculated values correlate well with visual evaluation and have the useful property of indicating that a voltage step causing one micron of displacement on the negative slope will give, say, 1.38 or 1.21 microns of displacement on the positive slope.

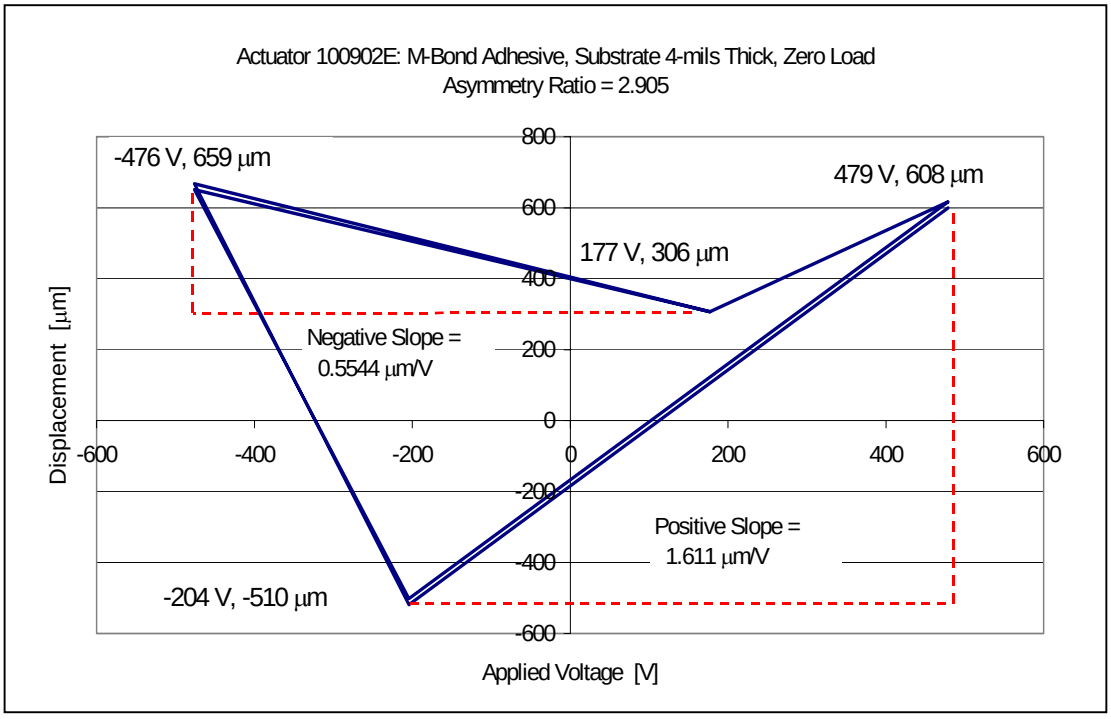

Figure 5.1.2—2. (color) Example of how absolute (asymmetry) ratio of positive and negative slopes would be calculated for an unusually **a**symmetric case

In general, by considering only butterfly loops produced at zero load, good correlation can be demonstrated between initial curvature of the actuators (as flexural strain) and the asymmetry metric just described. A secondary metric would be the absolute ratio of negative switching voltage to positive switching voltage. Previously this type of

measure was rejected as a primary indicator of butterfly loop asymmetry, but as a supplementary measure, the ratio of switching voltages is useful. Figure 5.1.2—3 presents the comparison. Observations based on the comparison are discussed in Section 5.1.3.

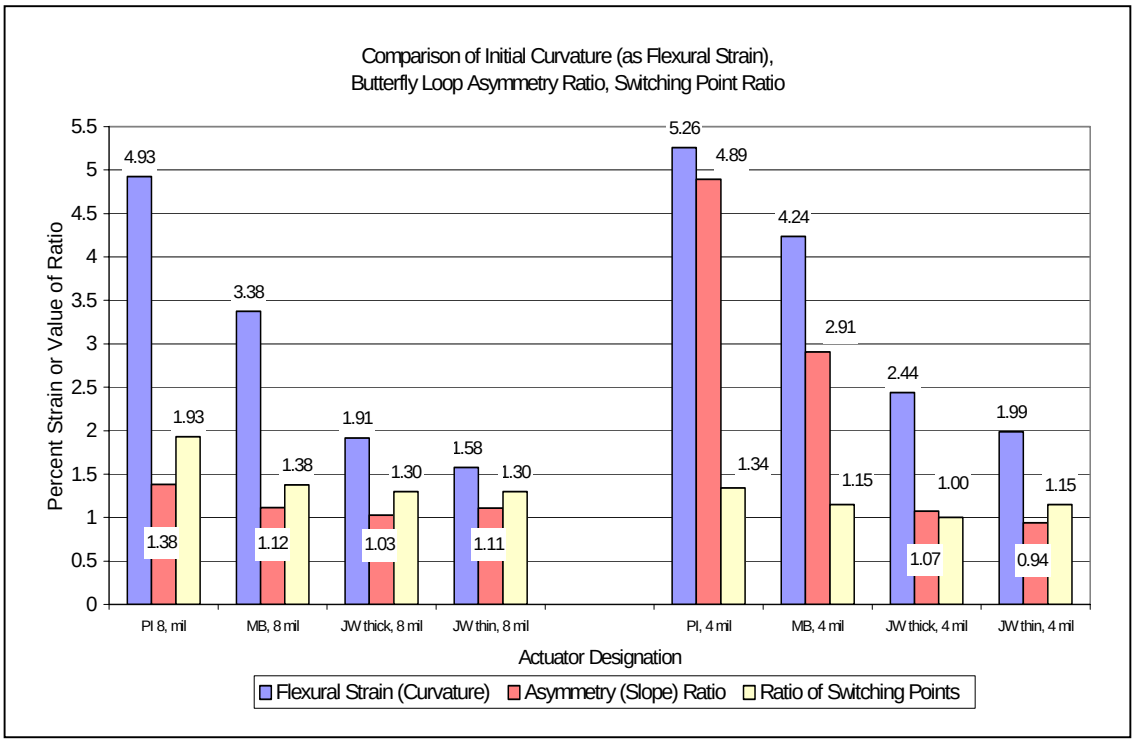

Figure 5.1.2—3. (color) Comparison of initial curvature, asymmetry ratio and switching voltage ratio for the selection of actuators tested in this experiment.

The correspondence of asymmetry ratio with load is less clear. Figure 5.1.2—4 shows the spectrum of asymmetry ratios for each actuator at zero load, weight of 500g, and of 1000g. Aside from observing that highly asymmetric butterfly loops belonging to actuators made with 4-mil substrates become more symmetric under the influence of load, no clear patterns are apparent.

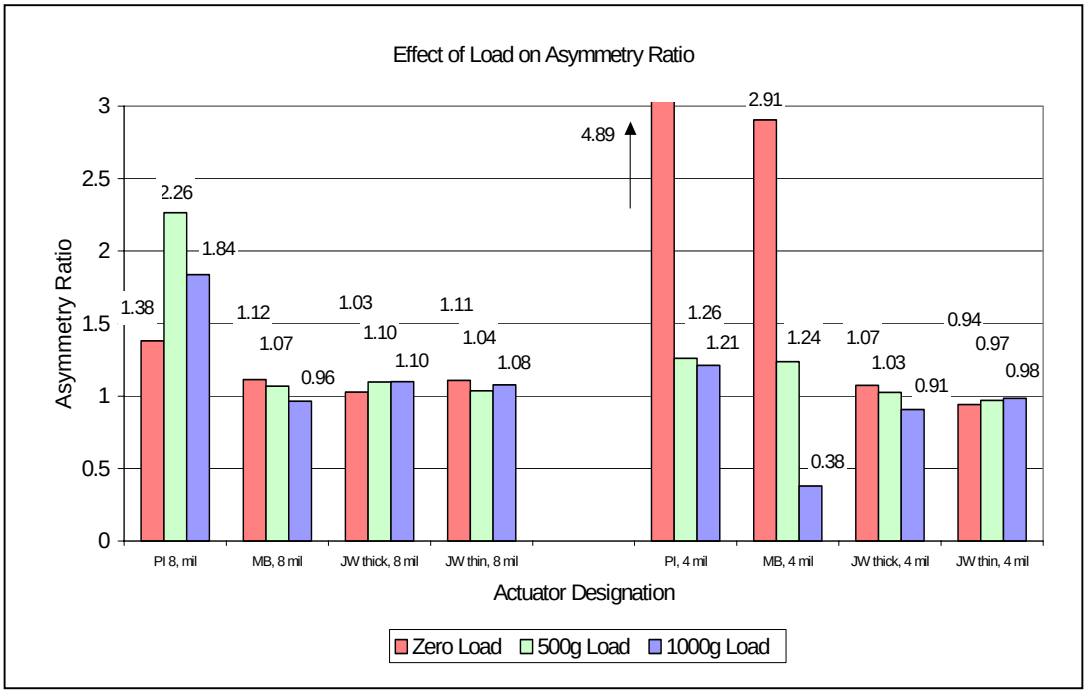

Figure 5.1.2—4. (color) Effect of load on butterfly loop asymmetry ratios obtained from the selection of actuators tested in this experiment

5.1.3. Conclusions Regarding the Butterfly Loop Experiment

Calculated asymmetry (slope) ratios and switching voltage ratios correlate well with each other and with the initial curvature measured after fabrication. Of course, this applies to butterfly loops obtained under zero load. For pre-stressed actuators made with 4-mil substrates, large asymmetry ratios match large initial curvature. Switching voltage ratios provided a more subdued correlation in general, but are more strongly differentiated for actuators made with 8-mil substrates than for actuators made with 4-mil substrates. Note that even actuators made at room temperature (J.B. Weld adhesive) developed some initial curvature because the relatively thick bonds shrank during curing.

General conclusions, which can be seen more quickly by examining the sets of images in Appendix 1, are as follows. Actuators made with LaRC-SI polyimide and with

M-Bond epoxy both display asymmetric butterfly loops, with polyimide-bonded loops having stronger asymmetry. The polyimide-bonded actuator made with an 8-mil substrate occupies a smaller area on the displacement-voltage plane, but is not unduly distorted by high load. However, as load increases, saturation edges close into nearly non-hysteretic traces. By contrast, results generated in testing the polyimide-bonded actuator made with a 4-mil substrate displays bizarre distortion at *zero load and low loads*. As load increases, the butterfly loops actually become less distorted, showing about the same asymmetric shape under the weight of 1000g as the previous actuator did at zero load. The final retest at zero load again displays the extremely distorted shape.

Both actuators bonded with M-Bond adhesive are only somewhat asymmetric and have a characteristic, well-formed shape. The actuator made with an 8-mil substrate did not change shape substantially under increasing load, although the right saturation edge thinned to a mostly non-hysteretic segment. They simply occupied less area on the displacement-voltage plane. The actuator made with a 4-mil substrate followed the same general pattern except that at 800g load and higher, the butterfly loops became severely distorted. Clearly, the weight of 1100g was effectively a blocking force for this actuator.

Actuators made with J.B.Weld epoxy adhesive using 8-mil substrates are generally not asymmetric. That is, they are symmetric.The actuator having the thicker bond is well-balanced, and shows the closing of the top ends of both lobes into mostly non-hysteretic segments at high load. The actuator with the thinner bond was a bit unstable, which is why it was only tested to a maximum load of 500g. Some pairs of butterfly loops show a slight asymmetry which is reversed from the asymmetry typical of a pre-stressed unimorph (reversed in that the right lobe is larger than the left).

Actuators made with J.B.Weld epoxy adhesive using 4-mil substrates display well-balanced butterfly loops. Table 5.1.1—1 reveals that the thinner bond in the second actuator is actually not much thinner than the thicker bond in the other actuator (109 μm versus 131 μm), which puts the bond in the thin-bond actuator at about the same thickness as the substrate. Both actuators made with 4-mil substrates continue to generate almost undistorted butterfly loops at high loads, which occupy a smaller area on the displacement-

voltage plane as usual. The actuator with the thicker bond began to show slight distortion in its loops at 1000g load and higher.

5.2 A Transform to Convert Actuator Loops to Piezoelectric Strain Loops

One would like to know how the stress conditions under which piezoelectric elements in pre-stressed unimorphs are operating modify their strain characteristics. Given that the unimorph structure acts as an integral amplifier for piezoelectric strain, the displacements given in the previous section (even if expressed as strain) do not quantitatively represent the actual transverse strain within the piezoelectric element. Instead, the piezoelectric strain is transformed by the mechanics of the unimorph, considered here as a thin beam although plate mechanics are also applicable. In addition, differential thermal contraction (DTC) occurring in actuators fabricated at high temperature also induces an amplified displacement (initial curvature) which is an indirect measure of the level of resulting internal pre-stress.

This section explores how a transform, or rather an inverse transform, might be created to convert the displacement-voltage behavior of a pre-stressed unimorph to in-plane strain response of the piezoelectric element. The idea is to apply the transform to a butterfly loop or the type obtained in the experiment previously discussed. Such transformed loops would provide an indication of the magnitude of the effective in-plane piezoelectric coupling coefficient, or d-coefficient (as a variable quantity) during the large-signal actuation because the slope of the plotted curve is the value of the coupling coefficient for a particular load and voltage. If the behavior of a stress-biased actuator is associated with unusually high values of the coupling coefficient, then evidence is provided for the effect of stress bias and its magnitude.

The transform is derived from [1], Timoshenko's analysis of bimetal thermostats. Recognizing that the bending moment generated by the difference between piezoelectric strain in the ceramic layer and no induced strain in the electrically-inactive layer is equivalent to the effects of differential thermal contraction between two layers with

different coefficients of expansion, the bimetallic strip model was adapted to include terms of both kinds. This modification was used by Wang and Cross in [2].

The reason why pains were taken to examine the opening stages of their model development in Section 2.3.3 in this thesis and highlight what appeared to be an inconsistency was that by developing their model from the same starting point as bimetallic strip analysis in 1925, an endorsement from recent times was obtained. If the inconsistency is amended, then the model to be developed here is in general agreement with theirs. Consequently, the older model has not been entirely superceded by newer approaches and may be regarded as having enduring utility as an approach for modeling pre-stressed unimorph actuators.

In the development of the model to be outlined here, a further modification was introduced to help account for the effect of the bond layer in an adhesive-bonded actuator. By contrast, Wang and Cross were modeling a RAINBOW cantilever which has an integral bond of effectively zero thickness. Accounting for the effects of a bond layer is not entirely new [3-6], but it was accomplished rather simply in the model to be given here by inserting a term allowing the bond layer to become a shear spring and "lose" some of the strain difference between layers. On the other hand, the particular application may be new: that is, using a unimorph model to transform butterfly loops so that the actual strain in the piezoelectric layer of pre-stressed actuators can be estimated.

Following Timoshenko's article was useful in creating a spreadsheet to apply the model because it was clear how to separate axial stress from stress due to bending moment. To calculate a stress profile across the cross section of the actuator, the axial component (considered constant but opposite in sign in each layer), is superimposed on bending stress (a function of location within the cross section). First, a brief review of the mechanics of mutually-interfering layers bonded together will be given.

An unconstrained material experiences a change in length equal to $\alpha L \Delta T$ when subjected to a change in temperature equal to ΔT, where α is the coefficient of linear expansion and L is the original length of the bar or strip of material. Except in the unlikely situation where two materials have exactly the same rate of expansion across ΔT,

a bilayer strip of different materials rigidly joined together arrives at a compromise in which the following descriptions apply. [7]

(a) Extension of one material + Compression of other material = Difference in "free" lengths, where a free length is the length either material would attain if it could expand or contract freely without restraint by the other material.

(b) Tensile force in one material = compressive force in other material, to satisfy the requirements of static equilibrium.

The difference in free lengths is given by $\alpha_1 L \Delta T - \alpha_2 L \Delta T = (\alpha_1 - \alpha_2) L \Delta T$, and the change in length, δ , is given by $\delta = \frac{\sigma L}{E}$, from the definition of Young's modulus. Statement (a), above, can then be expressed as follows (5.2—1).

(5.2—1) $$\frac{\sigma_1 L}{E_1} + \frac{\sigma_2 L}{E_2} = (\alpha_2 - \alpha_1) L \, \Delta T \quad \rightarrow \quad \frac{\sigma_1}{E_1} + \frac{\sigma_2}{E_2} = (\alpha_2 - \alpha_1) \Delta T$$

Since average stress equals force acting normal to a cross-sectional area divided by the area, the forces, P_1 and P_2 , which develop in the constrained layers as a result of the temperature change are given by $\sigma_1 = P_1 / A_1$, and $\sigma_2 = P_2 / A_2$. Statement (b), above, also allows us to say the $P_1 = P_2 = P$. We can also make the assumption that the bilayer strip has unit width. Then, $A_1 = (1) h_1$ and $A_2 = (1) h_2$, where h_1 and h_2 are the thicknesses of layer one and layer two, respectively. Incorporating these additional features into (5.2—1) yields the following.

(5.2—2) $$P \left[\frac{1}{E_1 h_1} + \frac{1}{E_2 h_2} \right] = (\alpha_2 - \alpha_1) \Delta T$$

The right side of (5.2—2) could be replaced by other sources of strain imposed on a rigidly-joined two-material structure such as the axial movement of a nut on a threaded rod

(where the rod extends as it compresses a concentric sleeve), or piezoelectric strain in a bilayer unimorph (where a non-piezoelectric layer has a strain coefficient equal to zero).

The presence of axial force modifies the transverse stiffness of a beam. From the instant a long, shallow beam—typically the shape used for a bimetallic strip or piezoelectric unimorph—becomes displaced from a straight position, axial force produces a bending moment in addition to axial compression or tension. If a compressive axial force is applied, the bending produced by the moment facilitates further bending, a key principle of buckling theory. A combined stress state develops as follows (5.2—3).

(5.2—3) $\sigma = \frac{P}{A} \quad \rightarrow \quad \sigma = \frac{P}{A} + \frac{M\ y}{I}$, where the first term is the axial component, the second is the bending component of the combined stress state. [8]

5.2.1 The Bimetal Thermostat Model

The following analysis is adapted from Timoshenko's 1925 article [1]. The resulting simple model has been helpful to a number of researchers. Riethmuller and Benecke [9] used the so-called bimetal effect developed in [1] to predict the thermal deflection of a bimaterial transducer element micromachined from silicon substrate. In [10], the authors adapted the expression given in [9] to estimate the transverse piezoelectric coefficient, d_{31} , in a PZT thin film deposited on a silicon cantilever the size of an AFM probe. In [13], the authors note that the ratio of layer thicknesses which give maximum predicted deflection in RAINBOW actuators is in qualitative agreement with Timoshenko's model of a bimetal thermostat.

Consider an extracted element of a bilayer structure with a central bond, shown as a free body diagram in Figure 5.2.1—1.

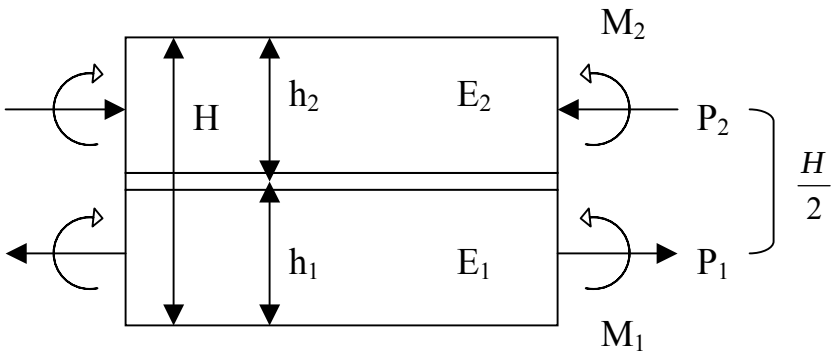

Figure 5.2.1—1. Extracted element of bilayer structure with central bond

Although a central layer has been depicted in Figure 5.2.1—1, let us assume initially that it has no thickness and is perfectly rigid. Since no external forces act on the bilayer strip, all forces and moments acting on the cross-section must be in equilibrium.

(5.2.1—1) $P_1 = P_2 = P$ (5.2.1—2) $\frac{P\,H}{2} = M_1 + M_2$

The relationship between moments M_1 and M_2 and radius of curvature, r, induced by the couple, ½ PH, is given by (5.2.1—3) and (5.2.1—4).

(5.2.1—3) $M_1 = \frac{E_1\,I_1}{\rho}$ (5.2.1—4) $M_2 = \frac{E_2\,I_2}{\rho}$

Substitute (5.2.1—3) and (5.2.1—4) into (5.2.1—2) to give (5.2.1—5).

(5.2.1—5) $\frac{P\,H}{2} = M_1 + M_2 = \frac{E_1\,I_1 + E_2\,I_2}{\rho}$

Once again, assume the width of the bilayer strip equals unity. Consequently the area of either layer is numerically equal to its thickness, h_1 or h_2. On the bearing surface between layers (direct bond), unit elongation from (5.2.1—1) and (5.2.1—2) must be equal. Thus, the sum of thermal, axial and bending strain on one side equals the sum of the counterparts on the other.

(5.2.1—6) $$\alpha_1 \, \Delta T + \frac{P_1}{E_1 \, h_1} + \frac{h_1}{2\rho} = \alpha_2 \, \Delta T + \frac{P_2}{E_2 \, h_2} + \frac{h_2}{2\rho}$$

Recall that $P_1 = P_2 = P$, and that $H = h_1 + h_2$, and rearrange (5.2.1—6) to give (5.2.1—7).

(5.2.1—7) $$P\left[\frac{1}{E_1 \, h_1} + \frac{1}{E_2 \, h_2}\right] + \frac{H}{2\rho} = \left(\alpha_2 - \alpha_1\right)\Delta T$$

Combine this with (5.2.1—5) to obtain (5.2.1—8).

(5.2.1—8) $$\frac{H}{2\rho} + \frac{2\left(E_1 \, I_1 + E_2 \, I_2\right)}{H \, \rho}\left[\frac{1}{E_1 \, h_1} + \frac{1}{E_2 \, h_2}\right] = \left(\alpha_2 - \alpha_1\right)\Delta T$$

This yields (5.2.1—9).

(5.2.1—9) $$\frac{1}{\rho} = \frac{\left(\alpha_2 - \alpha_1\right)\Delta T}{\frac{H}{2} + \frac{2\left(E_1 \, I_1 + E_2 \, I_2\right)}{H}\left[\frac{1}{E_1 \, h_1} + \frac{1}{E_2 \, h_2}\right]}$$

5.2.2 Shear Deformation in Central Layer

Now suppose that the central layer (layer 3) depicted in Figure 5.2.1—1 has finite thickness and is non-rigid. However, its thickness, t, is much less than h_1 or h_2 (one or two orders of magnitude). In addition, its stiffness, as indicated by Young's modulus, is considerably less (several orders of magnitude) than that of material 1 (in layer 1) or material 2 (in layer 2). That is, $E_3 << E_1$ or E_2 .

Since the central layer is much less stiff than the much thicker layers above and below it, let us assume that in response to the differential contraction of adjacent layers, it deforms only in shear. Furthermore, we assume that its own thermal contraction has little effect on the final stress profile of the composite structure. Figure 5.2.2—1 depicts a simplified model of the shear deformation of the central layer.

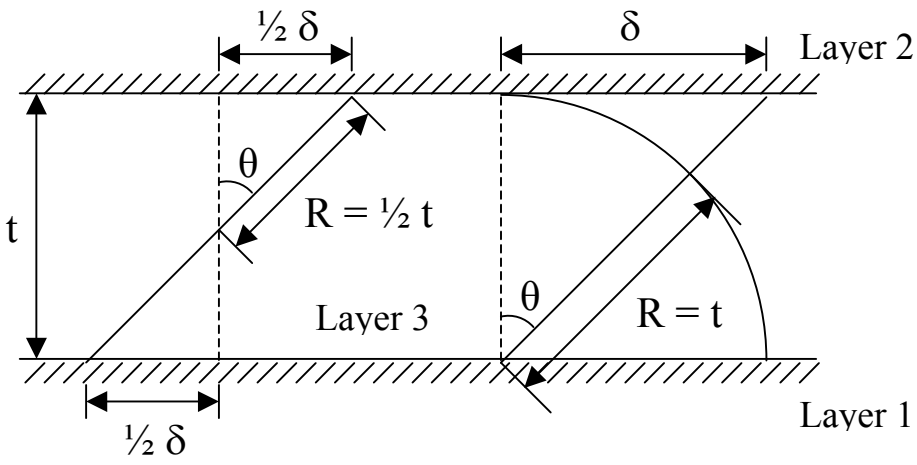

Figure 5.2.2—1. Simple model of shear deformation in central layer

The left part of figure 5.2.2—1 is more intuitively satisfying since it suggests a balanced shear resulting from the "leftward" sliding of Layer 1 and "rightward" sliding of Layer 2, but the right part of the figure allows the easier calculation given in (5.2.2—1) and gives the same result as can be determined from the left diagram.

(5.2.2—1) $\delta = t \tan\theta = t\,\gamma$, where δ is shear deflection, t is thickness (equals the radius, R) of Layer 3, and γ is shear strain.

Using the left part of Figure 5.2.2—1, the calculation is as follows.

(5.2.2—2) $$R = \frac{\frac{1}{2}t}{\cos\theta}, \quad \tfrac{1}{2}\delta = R\sin\theta = \frac{\frac{1}{2}t\,\sin\theta}{\cos\theta} = \tfrac{1}{2}\,t\,\tan\theta, \quad etc.$$

On either side of the plane of symmetry, as depicted in Figure 5.2.2—2, the following statements hold.

(5.2.2—3) $$\gamma = \frac{\delta}{t} = \frac{\tau}{G} \quad \rightarrow \quad \delta = \frac{t\,\tau}{G} = \frac{t\,\frac{P}{(1)\frac{L}{2}}}{G} = \frac{2\;t\;P}{G\;L}$$

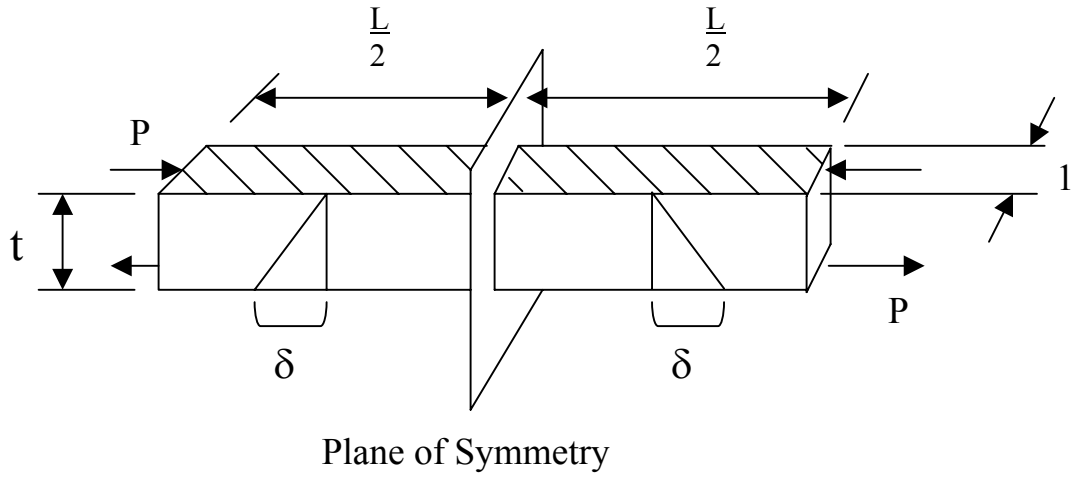

Figure 5.2.2—2. Shear forces and deformations in central layer

Thus, according to this model, total shear displacement (sum of left and right halves) is given by the following (5.2.2—4).

(5.2.2—4) $$\delta_{TOTAL} = \frac{4\ t\ P}{G\ L}$$

Return to equation (5.2.1—7) to proceed with incorporating this slippage element into the larger bilayer model. If all terms in (5.2.1—7) were moved to the left side, the resulting statement would indicate that the sum of net thermal strain and resulting tension, compression, and bending in the two bonded layers equals zero. However, given a central layer of non-zero thickness, t , yet another mechanical deformation occurs in distributing the effects of thermal strain—the slippage due to shear—as shown in (5.2.2—5).

(5.2.2—5) $$P\left[\frac{1}{E_1\ h_1} + \frac{1}{E_2\ h_2}\right] + \frac{H}{2\rho} - (\alpha_2 - \alpha_1)\Delta T \neq 0$$ However,

$$P\left[\frac{1}{E_1\ h_1} + \frac{1}{E_2\ h_2}\right] + \frac{4\ t\ P}{G\ L} + \frac{H}{2\rho} - (\alpha_2 - \alpha_1)\Delta T = 0$$

Combining as before with equation (5.2.1—5) and rearranging yields (5.2.2—6):

(5.2.2—6) $$\frac{1}{\rho} = \frac{(\alpha_2 - \alpha_1)\Delta T}{\frac{H}{2} + \frac{2(E_1\ I_1 + E_2\ I_2)}{H}\left[\frac{1}{E_1\ h_1} + \frac{1}{E_2\ h_2} + \frac{4\ t}{G\ L}\right]}$$

An argument must be included to justify adding a displacement, δ , to quantities which were associated with strains. To make (5.2.2—4) a statement about shear strain requires dividing through by the thickness, t. But t is perpendicular to the direction of axial stress and doesn't interact with it. The change in shear displacement with t, however, does have an impact on the axial direction. In other words, the loss to the axial-force couple

changes with shear displacement (and thus depends on t), not shear strain. Note also, that equation (5.2.2—6) becomes equation (5.2.1—9) if t = 0.

The radius of curvature changes in direct proportion with the denominator on the right side of (5.2.2—6). As t increases, both terms in the denominator becomes larger, and hence, the radius becomes larger. In other words the actuator flattens. When values are actually calculated for a series of thicknesses, however, one discovers that the first term, half of the total thickness of all layers (H / 2) contributes a much larger share to increasing the radius than does the second term. Even though increasing H also acts to decrease the first factor in the second term in the denominator, the effect is lessened by algebraic combination with all the other quantities in that term. The expression devised for loss of curvature due to shear displacement actually has only a small effect on the final calculated value.

5.2.3 Maximum Deflection Resulting from Differential Thermal Strain

Maximum deflection is calculated as follows. Assume that a bilayer strip is simply supported and bent due to heating or cooling. Since the arc depicted at the base of Figure 5.2.3—1 is a circular arc having radius ρ , it follows that (5.2.3—1):

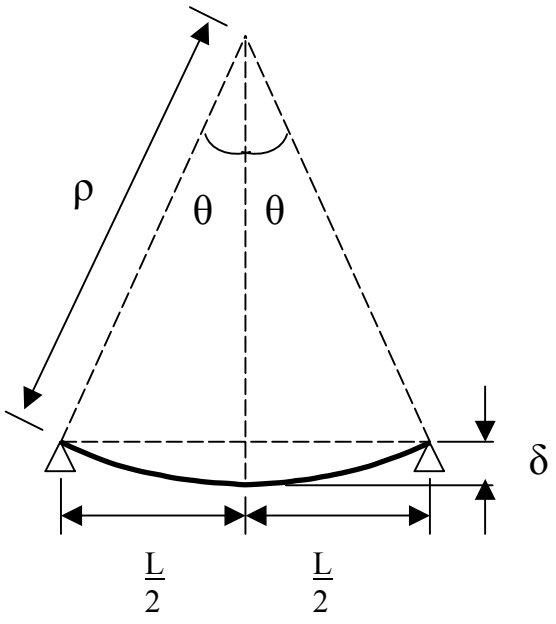

Figure 5.2.3—1. First arc diagram

(5.2.3—1) $$\delta\,(2\rho - \delta) = \left(\frac{L}{2}\right)^2$$

If $\delta << \rho$, the square of d can be omitted and (5.2.3—1) can be simplified as follows from (5.2.3—2).

(5.2.3—2)

$$2\,\rho\,\delta - \delta^2 = \frac{L^2}{4} \quad \rightarrow \quad 2\,\rho\,\delta \approx \frac{L^2}{4} \quad \rightarrow$$

$$\delta_{MAX} \approx \frac{L^2}{8\,\rho}$$

The derivation of (5.2.3—1) is as follows—from (5.2.3—3).

(5.2.3—3) $\rho\cos\theta = \rho - \delta\,, \quad \rho\sin\theta = \left(\frac{L}{2}\right)^2 \;\rightarrow\; \left(\frac{L}{2}\right)^2 + (\rho - \delta)^2 = \rho^2 \;\rightarrow$

$$\left(\frac{L}{2}\right)^2 = \rho^2 - \left(\rho^2 - 2\,\rho\,\delta + \delta^2\right) \;\rightarrow\; 2\,\rho\,\delta - \delta^2 = \left(\frac{L}{2}\right)^2 \;\rightarrow\; \delta(2\rho - \delta) = \left(\frac{L}{2}\right)^2$$

The exact solution of (5.2.3—1), however, is as follows (5.2.3—4).

(5.2.3—4) $$-\delta^2 + 2\,\rho\,\delta - \left(\frac{L}{2}\right)^2 = 0 \;\rightarrow\; \delta^2 - 2\,\rho\,\delta + \frac{L^2}{4} = 0$$

Apply the quadratic formula, where a = 1, b = -2 ρ, $c = \frac{L^2}{4}$, and

$b^2 - 4\,ac = 4\,\rho^2 - 4(1)\left(\frac{L^2}{4}\right) = 4\,\rho^2 - L^2$, to get (5.2.3—5).

(5.2.3—5) $\delta_{MAX} = \frac{2\,\rho \pm \sqrt{4\,\rho^2 - L^2}}{2} = \rho \pm \sqrt{\rho^2 - \frac{L^2}{4}}$ *iff* $4\rho^2 > L^2$, which is nearly

always true, that is, L is less than twice the radius of curvature. Figure 5.2.3—2 shows the significance of the positive and negative roots of the quadratic solution.

From the foregoing, it is evident that (5.2.3—1) allows one to determine ρ without knowing θ, provided one knows the half-horizontal displacement, L/2 , the counterpart of δ , rather than half-arc length, s/2. For small deflections, the two quantities are nearly equivalent, and the difference is difficult to measure. The vertical deflection, ρ(1- cosθ), changes as sinθ, whereas the horizontal deflection, ρsinθ, changes as cosθ. Between zero

and one degree, sinθ changes 115 times as much as cosθ, 38 times as much between one degree and two, 23 times as much between two and three degrees, and so forth.

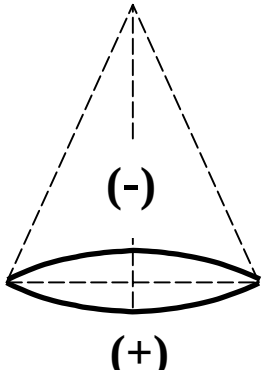

Figure 5.2.3—2. Curvatures signified by signed solutions of (5.2.3—5)

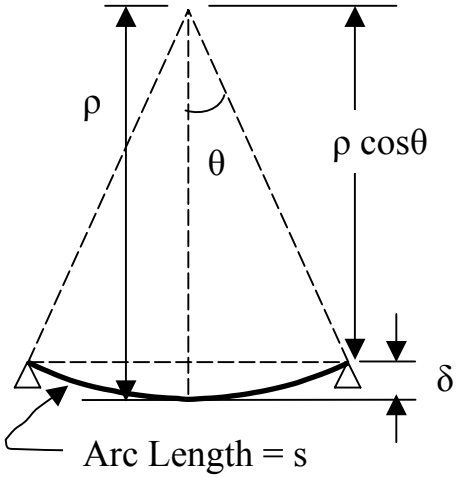

Figure 5.2.3—3. Second arc diagram

If the half-horizontal displacement, L/2 , is not known, the following approach can be used to calculate δ_{MAX} using the half-arc length s/2, which is almost always known from fabrication design.

Since $\frac{s}{2} = \rho\,\theta \quad \rightarrow \quad \theta = \frac{s}{2\,\rho}$, then (5.2.3—6).

(5.2.3—6) $$\delta_{MAX} = \rho\left(1 - \cos\theta\right) = \rho\left(1 - \cos\left(\frac{s}{2\,\rho}\right)\right)$$

While (5.2.3—6) might be simpler to use than (5.2.3—1), the latter allows one to develop an expression for thermal (or piezoelectric) strain in terms of deflection because it is purely an algebraic expression with no transcendental function included. This has an

especially useful application in the present work. Various experiments were conducted to measure large signal strain-displacement or butterfly loops using PSU actuators. However, the displacement correlated with applied voltage in the experimental data is the transverse displacement of the actuator, not the voltage-induced strain of the piezoelectric layer. Conversion of actuator displacement to piezoceramic displacement allows one to estimate its actual d_{31} values, which would be the slope of the butterfly loop as a function of voltage. A formula of this sort is derived as follows (5.2.3—7).

From (5.2.3—1) $$\delta\left(2\,\rho-\delta\right)=\frac{L^2}{4}\quad\rightarrow\quad 2\,\rho\,\delta=\frac{L^2}{4}+\delta^2\quad\rightarrow\quad\rho=\frac{\frac{L^2}{4}+\delta^2}{2\,\delta}\ ,$$

which gives (5.2.3—7).

(5.2.3—7) $$\rho=\frac{1}{2\,\delta}\left(\frac{L^2}{4}+\delta^2\right)=\frac{L^2}{8\,\delta}+\frac{\delta^2}{2\,\delta}=\frac{L^2}{8\,\delta}+\frac{\delta}{2}\quad\rightarrow\quad\frac{1}{\rho}=\frac{1}{\frac{L^2}{8\,\delta}+\frac{\delta}{2}}$$

Equate (5.2.3—7) to (5.2.**2**—6) and re-arrange to get (5.2.3—8).

(5.2.3—8) $$\left(\alpha_2-\alpha_1\right)\Delta T=\frac{\frac{H}{2}+\frac{2\left(E_1\,I_1+E_2\,I_2\right)}{H}\left[\frac{1}{E_1\,h_1}+\frac{1}{E_2\,h_2}+\frac{4\,t}{G\,L}\right]}{\frac{L^2}{8\,\delta}+\frac{\delta}{2}}$$

The thermal strain could of course be replaced by piezoelectric strain. If this were done, however, the resulting expression would apply to an unstressed unimorph actuator. In a pre-stressed unimorph, stress from thermal strain is superimposed on stress from piezoelectric strain. To reflect this, equation (5.2.3—8) should be changed to the expression given in (5.2.3—9). The electric field, E = V / t is determined by the ceramic thickness, while the strain depends upon the change in length of the in-plane dimension, L.

Multiplying (5.2.3—9) through by L would give in-plane displacement associated with the piezoelectric material strain.

(5.2.3—9)

$$\frac{\Delta L}{L} = \frac{d_{31} V}{t} = \frac{\frac{H}{2} + \frac{2\left(E_1 I_1 + E_2 I_2\right)}{H}\left[\frac{1}{E_1 h_1} + \frac{1}{E_2 h_2} + \frac{4t}{G L}\right]}{\frac{L^2}{8\delta} + \frac{\delta}{2}} - \left(\alpha_2 - \alpha_1\right)\Delta T$$

5.2.4 Internal Stress Resulting from Differential Thermal Strain

Maximum stress resulting from differential thermal strain will occur on the bearing surface between layers. A central sheared layer acts to dissipate some of it. In either layer of the bilayer strip, stress has an axial component and a bending component. Bending stress is at a maximum at the layer surface, as (5.2.4—1).

(5.2.4—1) $$\sigma = \frac{-E\, y}{\rho}, \quad y = \frac{h}{2} \quad \rightarrow \quad \sigma_{MAX} = \frac{E\, h}{2\, \rho}$$

For layer 1, maximum stress is given by (5.2.4—2).

(5.2.4—2) $$\sigma_{MAX} = \frac{P}{h_1} + \frac{E_1\, h_1}{2\, \rho}$$

From (5.2.1—5), the following expression can be substituted for the force, P , in (5.2.4—2) to get (5.2.4—3), which leads to (5.2.4—4).

(5.2.4—3) $$\frac{P\, H}{2} = \frac{E_1\, I_1 + E_2\, I_2}{\rho} \quad \rightarrow \quad P = \frac{2}{H}\left[\frac{E_1\, I_1 + E_2\, I_2}{\rho}\right]$$

(5.2.4—4) $$\sigma_{MAX} = \frac{2}{H\ h_1}\left[\frac{E_1\ I_1 + E_2\ I_2}{\rho}\right] + \frac{E_1\ h_1}{2\ \rho} = \frac{1}{\rho}\left[\frac{2}{H\ h_1}\left(E_1\ I_1 + E_2\ I_2\right) + \frac{E_1\ h_1}{2}\right]$$

Since the formula provides a result in proportion to whatever value is substituted for curvature, 1/r , it would provide a good estimate of how much a sheared central layer reduces maximum stress. Stress across a layer could be calculated by leaving the variable y in place in (5.2.4—1) rather than substituting the half-layer thickness. Taking positive y as upward in either layer, the resulting expression is as follows.

(5.2.4—5) $$\sigma = \frac{1}{\rho}\left[\frac{2}{H\ h_1}\left(E_1\ I_1 + E_2\ I_2\right) + E_1\ y\right]$$, for which these cases hold (5.2.4—6):

(5.2.4—6)

$$\begin{cases} \text{If} \quad y = +\dfrac{h_1}{2}, \quad \sigma = \dfrac{1}{\rho}\left[\dfrac{2}{H\ h_1}\left(E_1\ I_1 + E_2\ I_2\right) + \dfrac{E_1\ h_1}{2}\right] \\ \text{If} \quad y = -\dfrac{h_1}{2}, \quad \sigma = \dfrac{1}{\rho}\left[\dfrac{2}{H\ h_1}\left(E_1\ I_1 + E_2\ I_2\right) - \dfrac{E_1\ h_1}{2}\right] \end{cases}$$

5.2.5 Centroid of Non-Homogenous Cross-Section

Consider the more typical two-layer case. Let material 1, which would be the most rigid material (metal substrate) in the present situation, be the reference material. In Figure 5.2.5—1, the centroids of each layer are marked with crosses; the centroid of the bilayer composite, placed at an assumed location, is marked with a circled cross. The displacement of the composite centroid from the top surface of the structure is denoted as C.

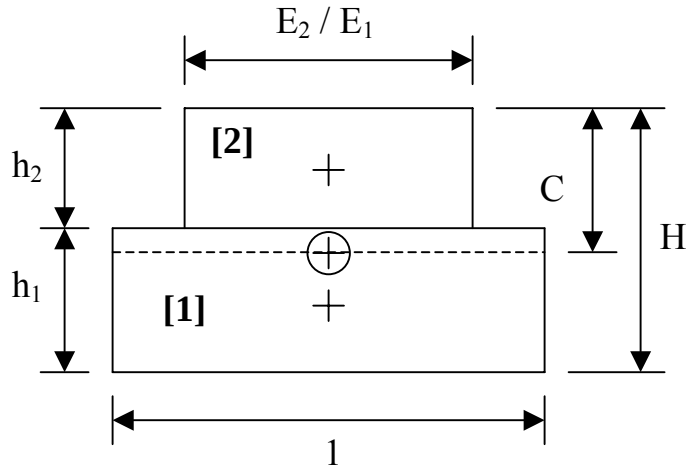

Figure 5.2.5—1. Diagram for finding centroid in two-layer case

In many textbook examples, more rigid materials are transformed to have a greater width than the least rigid material. In this derivation the most rigid material keeps the given width of one unit, while less rigid materials are contracted to proportionally smaller widths. Following the style of Timoshenko's analysis, let $n = E_1 / E_2$. After transformation, section 1 has an area of h_1 , section 2 an area of $(1 / n)\, h_2$. Taking displacements as originating at the top of the structure as drawn, an expression for the location of C is found as follows.

(5.2.5—1)
$$\left(\frac{1}{n} h_2\right)\left(C - \frac{h_2}{2}\right) + (h_1)\left(C - \left(h_2 + \frac{h_1}{2}\right)\right) = 0$$

$$\frac{1}{n} h_2\, C - \frac{1}{n}\frac{h_2^{\,2}}{2} + h_1\, C - h_1\, h_2 - \frac{h_1^{\,2}}{2} = 0$$

$$\frac{1}{n} h_2\, C + h_1\, C - \left[\frac{1}{n}\frac{h_2^{\,2}}{2} + h_1\, h_2 + \frac{h_1^{\,2}}{2}\right] = 0$$

$$C\left(h_1 + \frac{h_2}{2}\right) = \left(\frac{h_1^{\,2}}{2} + h_1\, h_2 + \frac{h_2^{\,2}}{2}\right) - \frac{h_2^{\,2}}{2} + \frac{1}{n}\frac{h_2^{\,2}}{2}$$ (Continued …)

(5.2.5—1) Series , Continued

$$C\left(h_1+\frac{h_2}{n}\right)=\frac{(h_1+h_2)^2}{2}+\left(\frac{1}{n}-1\right)\frac{h_2{}^2}{2}$$

$$C=\frac{\dfrac{(h_1+h_2)^2}{2}-\left(1-\dfrac{1}{n}\right)\dfrac{h_2{}^2}{2}}{h_1+\dfrac{h_2}{n}}$$

In [1], the expression derived is slightly different because material 1 is above material 2 in that article. If Figure 5.2.5—1 were inverted bottom to top and displacements taken from what is the bottom surface in the uninverted orientation, the expression derived here would agree with the Timoshenko article. However, the expression given in [1] contains a misprint. The denominator of the first term in the numerator of the complex fraction should be 2n in the Timoshenko article, as can be verified by using the corrected expression to get the result given in the example which follows the general expression containing the misprint.

Suppose the structure shown in Figure 5.2.5—1 had the following dimensions and properties, typical of a unimorph actuator. The layers have thicknesses $h_1 = h_2 = 200$ μm. Layer 1 is stainless steel with a modulus of $E_1 = 200$ GPa; layer 2 is PZT ceramic with a modulus of $E_2 = 66$ GPa. Therefore, $1 / n = 0.33$. Using (5.2.4—5), the centroid of the composite section is located at a distance $C = 250.4$ μm from the top surface, that is, about one-quarter of a layer thickness below the junction between layers.

Now consider a three-layer case, which differs from the two layer case in that a central layer of thickness h_3 is sandwiched between the layers in the previous case. It has a Young's modulus, E_3, which is less than that of material 1. (Figure 5.2.5—2 also implies that $E_3 < E_2$, which is expected but does not have to be true.)

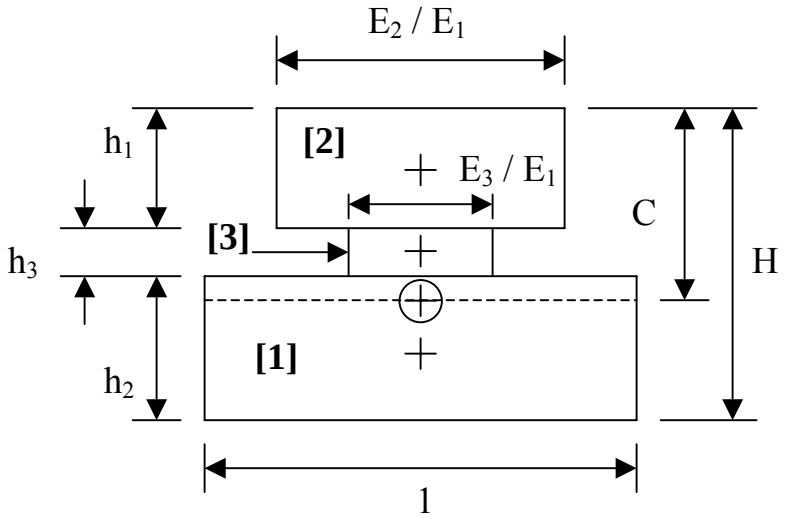

Figure 5.2.5—2. Diagram for finding centroid in three-layer case

In addition to the ratio $n = E_1 / E_2$, let $m = E_1 / E_3$. After transformation, the area of section 1 is h_1 ; the area of section 2 is $(1 / n)\, h_2$; the area of section 3 is $(1 / m)\, h_3$. Again taking displacements as originating at the top of the structure as drawn, an expression for the location of C is found as follows (5.2.5—2).

(5.2.5—2)

$$\left(\frac{1}{n} h_2\right)\left(C - \frac{h_2}{2}\right) + h_1\left(C - \left(h_2 + h_3 + \frac{h_1}{2}\right)\right) + \left(\frac{1}{m} h_3\right)\left(C - \left(h_2 + \frac{h_3}{2}\right)\right) = 0$$

$$\frac{1}{n} h_2 C - \frac{1}{n}\frac{h_2^{\,2}}{2} + h_1 C - h_1 h_2 + h_1 h_3 \frac{h_1^{\,2}}{2} + \frac{1}{m} h_3 C - \frac{1}{m} h_2 h_3 - \frac{1}{m}\frac{h_3^{\,2}}{2} = 0$$

$$h_1 C + \frac{1}{n} h_2 C + \frac{1}{m} h_3 C = \frac{1}{n}\frac{h_2^{\,2}}{2} + h_1 h_2 + \frac{h_1^{\,2}}{2} + h_1 h_3 + \frac{1}{m} h_2 h_3 + \frac{1}{m}\frac{h_3^{\,2}}{2}$$

(Continued …)

(5.2.5—2) Series, Continued

$$\ldots \qquad = \left(\frac{h_1^{\,2}}{2} + h_1 h_2 + \frac{h_2^{\,2}}{2} \right) - \frac{h_2^{\,2}}{2} + \frac{1}{n}\frac{h_2^{\,2}}{2} + h_1 h_3 + \frac{1}{m} h_2 h_3 + \frac{1}{m}\frac{h_3^{\,2}}{2}$$

$$C = \frac{\dfrac{(h_1 + h_2)^2}{2} - \left(1 - \dfrac{1}{n}\right)\dfrac{h_2^{\,2}}{2} + h_1 h_3 + \dfrac{1}{m} h_2 h_3 + \dfrac{1}{m}\dfrac{h_3^{\,2}}{2}}{h_1 + \dfrac{1}{n} h_2 + \dfrac{1}{m} h_3}$$

One can see that the final result in (5.2.5—2) is similar to (5.2.5—1), but contains additional terms related to the middle layer. Suppose the structure in Figure 5.2.5—2 has the same dimensions and properties previously given for layers 1 and 2, but the middle layer has a thickness of 5 μm, and a Young's modulus of 4 GPa. The centroid of the composite is now 254.1 μm below the top surface using the final result from (5.2.5—2), rather than 250.4 μm, as calculated with the final result from (5.2.5—1) for two layers only.

5.2.6 Implementation in Spreadsheet Format

To make the model represented by these various expressions more interactive, a spreadsheet program can be developed. As input cells, one needs to have layer thicknesses, elastic moduli, coefficients of expansion, and length of the composite structure. One can then calculate $1 / n$ and $1 / m$ and the location, C, of the centroid below the top surface using (5.2.5—2), $1 / \rho$ using (5.2.2—6), and maximum deflection using (5.2.3—2) which readily gives an exact value.

In calculating the inverse radius of curvature, one must use moments of inertia about the centroid of the composite, which involves knowing the distances between layer centroids and the centroid of the composite and use of the parallel axis theorem. Table

5.2.6—1 provides the various formulas that would be needed. Assume h_1 , h_2 , and all variable names used thus far retain the same definitions.

To plot an interactive stress profile, it is helpful to separate axial stress and bending stress because bending stress will depend on vertical location within cross-section, whereas axial stress is taken as constant within each layer—compressive in Layer 2 and tensile in

Table 5.2.6—1. Formulas needed for spreadsheet implementation

Distance between layer centroids and centroid of composite structure	
Layer 1	$\overline{y_1} = C - \left(h_2 + h_3 + \frac{h_1}{2} \right)$
Layer 2	$\overline{y_2} = C - \frac{h_2}{2}$
Layer 3	$\overline{y_3} = C - \left(h_2 + \frac{h_3}{2} \right)$
Moments of inertia of the sections	
Layer 1	$I_1 = \frac{1}{12}(h_1)^3 + h_1\left(\overline{y_1}\right)^2$
Layer 2	$I_2 = \frac{1}{n}\left[\frac{1}{12}(h_2)^3 + h_2\left(\overline{y_2}\right)^2 \right]$
Layer 3	$I_3 = \frac{1}{m}\left[\frac{1}{12}(h_3)^3 + h_3\left(\overline{y_3}\right)^2 \right]$
Boundaries in terms of distance from the centroid of the composite structure (These formulas give correct values even when h_3 is set to zero.)	
Top Surface	C
Surface Between Layer 3 and Layer 2	C – h_2
Surface Between Layer 3 and Layer 1	C – (h_2 + h_3)
Bottom Surface	C – (h_1 + h_2 + h_3)

Layer 1, since differential contraction rather than expansion is envisioned. Plotted stress vs. y-coordinate is the sum of both parts. Table 5.2.6—2, based on (5.2.4—5), summarizes the details of this partitioned calculation.

Table 5.2.6—2. Partitioning the calculations into cases, depending on distance from top of upper layer

If Within Layer 2 ($y > C - h_2$), then	
Axial Stress	$P_{AXIAL} = -\frac{1}{\rho}\left(\frac{2}{H\ h_2}\right)\left(E_1 I_1 + E_2 I_2\right)$
Bending Stress	$P_{BEND} = \frac{1}{\rho}\left(\frac{1}{n}\right)\left(E_2\right) y$
If Within Layer 1 ($y < C - (h_2 + h_3)$), then	
Axial Stress	$P_{AXIAL} = +\frac{1}{\rho}\left(\frac{2}{H\ h_1}\right)\left(E_1 I_1 + E_2 I_2\right)$
Bending Stress	$P_{BEND} = \frac{1}{\rho}\left(E_1\right) y$
Else, Within Layer 3 (which includes "y =" as opposed to ">" or "<" cases)	
Axial Stress	Neglect: thin, compliant layer located toward center—shear stress only
Bending Stress	$P_{BEND} = \frac{1}{\rho}\left(\frac{1}{m}\right)\left(E_3\right) y$

One implementation of these guidelines is shown in Figure 5.2.6—1, which is a "test pattern" of sorts because a number of sources which discuss the bimetal thermostat model simplify the general case by assuming that the rigid layers have the same Young's modulus and same thickness, differing only in coefficient of thermal expansion.

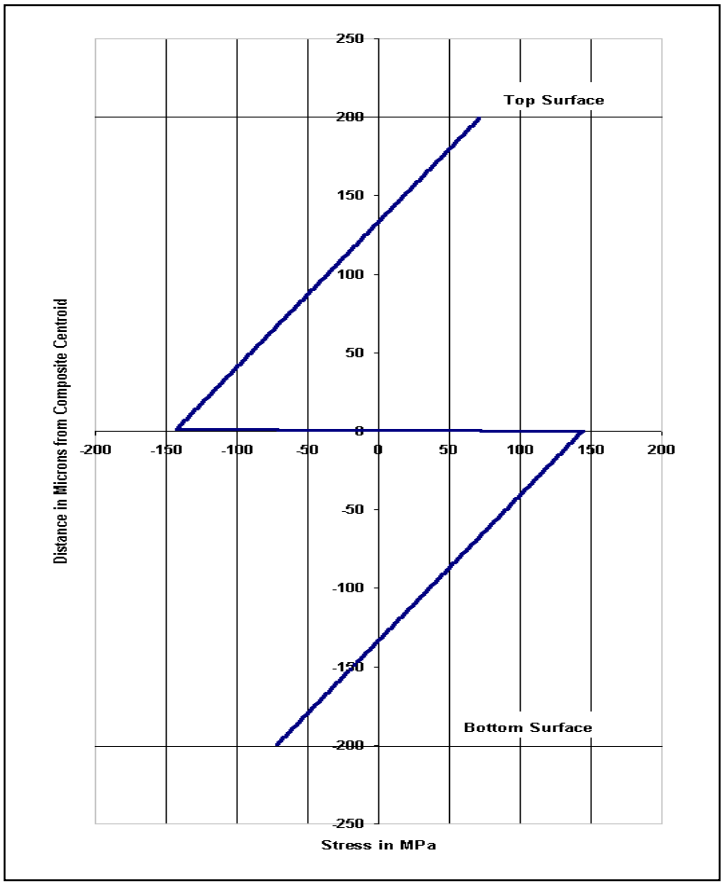

Figure 5.2.6—1. Stress profile assuming equal elastic moduli and equal thicknesses

The calculations for Figure 5.2.6—2 assume that the thicknesses of Layer 1 and Layer 2 are each 200 μm, the elastic modulus of each layer equals 200 GPa, the approximate modulus of stainless steel. The thickness of Layer 3 is zero. The expansion coefficient of Layer 1 (bottom) is 16.6 μm / m ºC, comparable to that of Type 302 stainless steel; the expansion coefficient of Layer 2 is 4.0 μm / m ºC, comparable to that of PZT ceramic. They have experienced differential thermal contraction through 200ºC. The key observation, as noted in [8], is that the transition from compressive to tensile stress or vice versa occurs at one-third the layer thickness below the top or bottom surface. Given equal elastic moduli and thickness, the centroid of the composite structure is at its center.

However, rarely would two materials with different expansion coefficients have the same elastic modulus. Figures 5.2.6—2 and 5.2.6—3 show the effect of reducing the modulus of the upper layer below that of stainless steel. (The modulus of PZT-5A thin plates used in actuators fabricated for this project was given as 66 GPa by the supplier.) In Figure 5.2.6—2, upper layer modulus has been reduced to 150 GPa; in Figure 5.2.6—3, it has been reduced to 100 GPa.

The effect is that the upper area in tension in Layer 2 is reduced until the entire upper layer is in compression. In addition, the centroid of the composite section moves closer to the centroid of the lower layer. The range of maximum to minimum stress is reduced in the upper layer but becomes more extreme in the substrate, but this occurs asymmetrically in that stress on the bottom surface of the upper layer is lessened while stress on the bottom surface on the lower layer increases. (Stress on the top surfaces of each layer change also, but by not as much.

Now suppose that each layer again has the same elastic modulus (200 GPa) and initial thickness (200 μm). Figure 5.2.6—4 shows the effect of reducing the thickness of the lower layer to 150 μm, Figure 5.2.6—5 the effect of reducing the thickness to 100 μm. Although the maximum tensile and compressive stress values at the bearing surface become slightly more extreme as the thickness of the lower layer is reduced, the primary effect is that more of each layer, particularly the lower layer, is in tension.

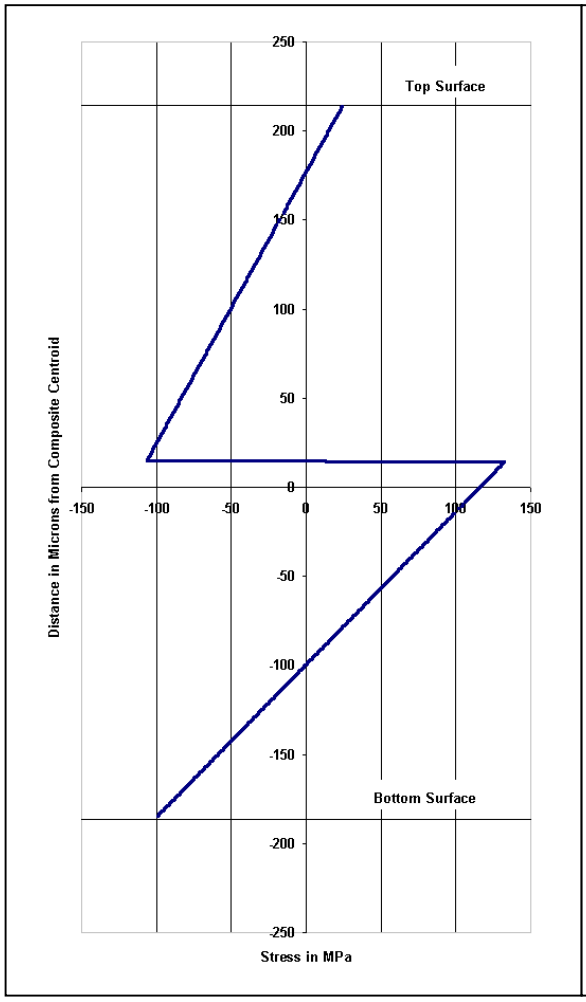

Figure 5.2.6—2.
Left: Top layer modulus = 150 GPa

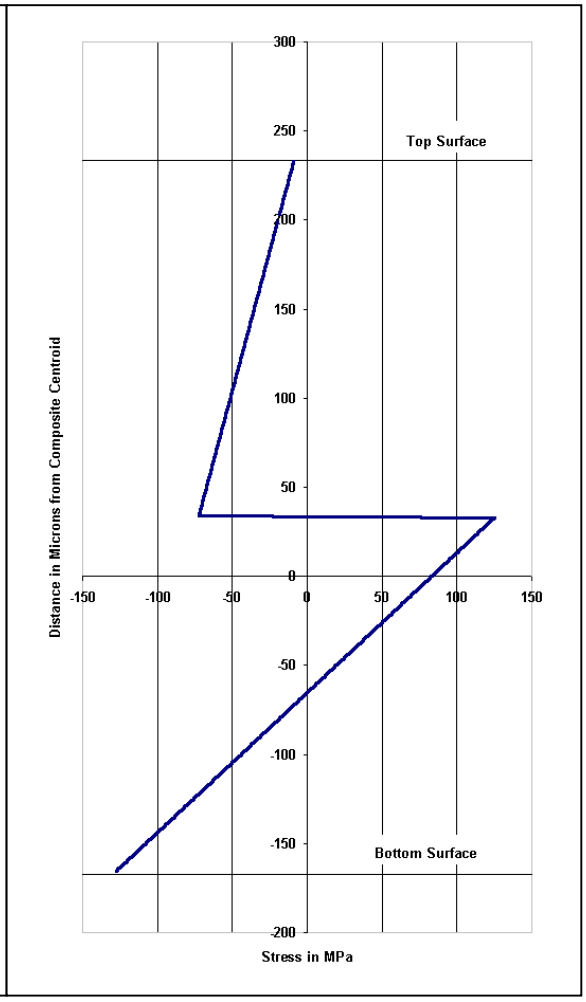

Figure 5.2.6—3.
Right: Top layer modulus = 100 GPa

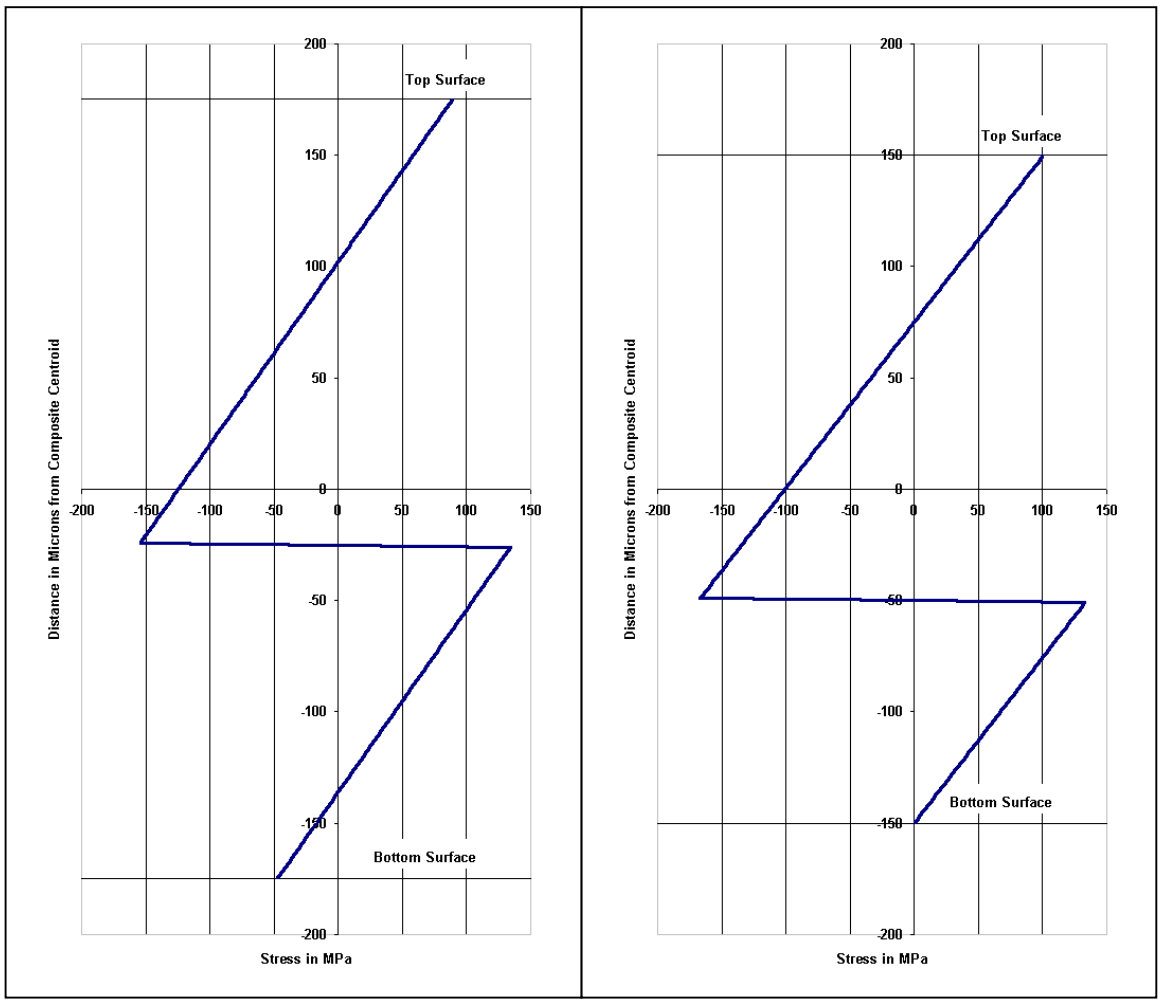

Figure 5.2.6—4.
Left: Lower layer thickness = 150 μm

Figure 5.2.6—5.
Right: Lower layer thickness = 100 μm

Now consider the calculated stress profile of a structure with elastic moduli and layer thicknesses typical of a commercial Face THUNDER 8R actuator. The upper layer has a Young's modulus of 66 GPa, a thickness of 196 μm. The lower layer has a Young's modulus of 200 GPa, a thickness of 165 μm. The result is shown in Figure 5.2.6—6. In Figure 5.2.6—7, a central layer has been added, which, like LaRC-SI polyimide adhesive, has a modulus of 3.8 GPa and a thickness of 16 μm. The central layer allows a slight reduction in maximum tensile and compressive stresses at the surfaces on either side of the

adhesive, but also transfers some of the compressive stress at the bottom surface of the lower layer to the top surface of the upper layer.

Figure 5.2.6—8 shows the effect of decreasing lower layer thickness to 100 μm. In Figure 5.2.6—9, the lower layer thickness has been further reduced to 50 μm. Although the top surface of the upper layer develops slightly lower compressive stress, the lower layer cannot generate tension in the upper layer. In Figure 5.2.6—9, the lower layer has become thin enough that the upper layer is determining its stress state. Likewise, the lower is less able to affect the stress state of the thicker upper layer.

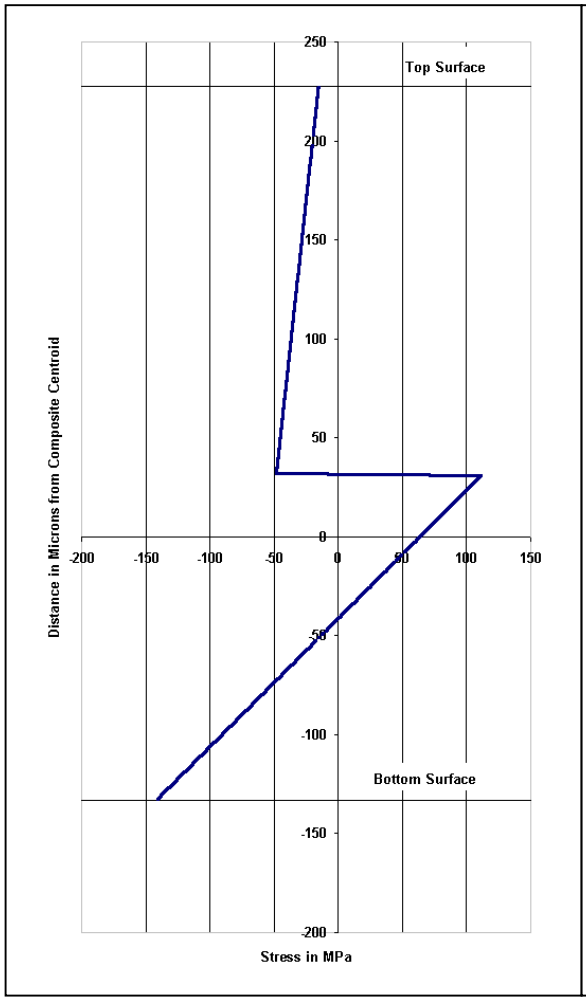

Figure 5.2.6—6. THUNDER actuator properties

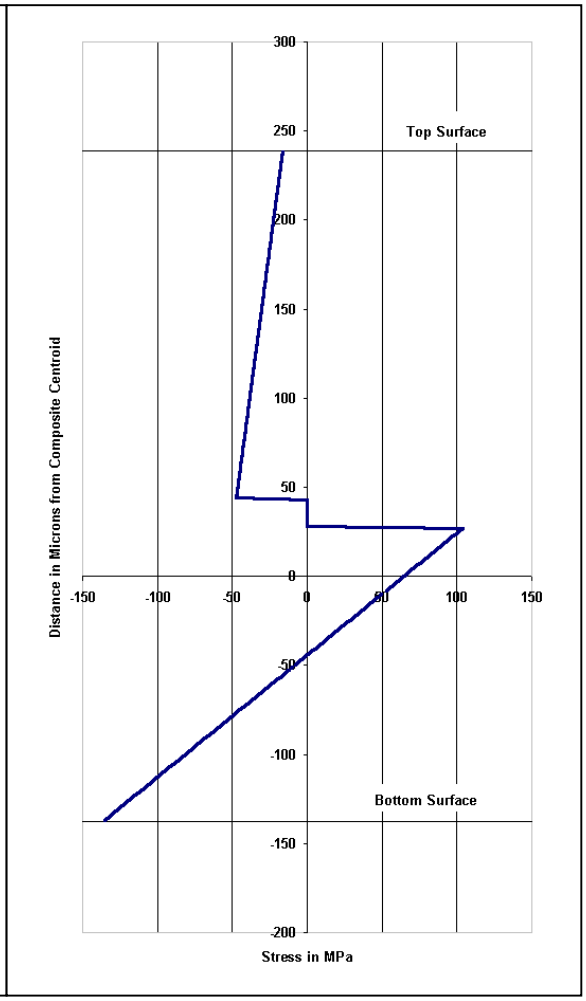

Figure 5.2.6—7. Add central bond layer

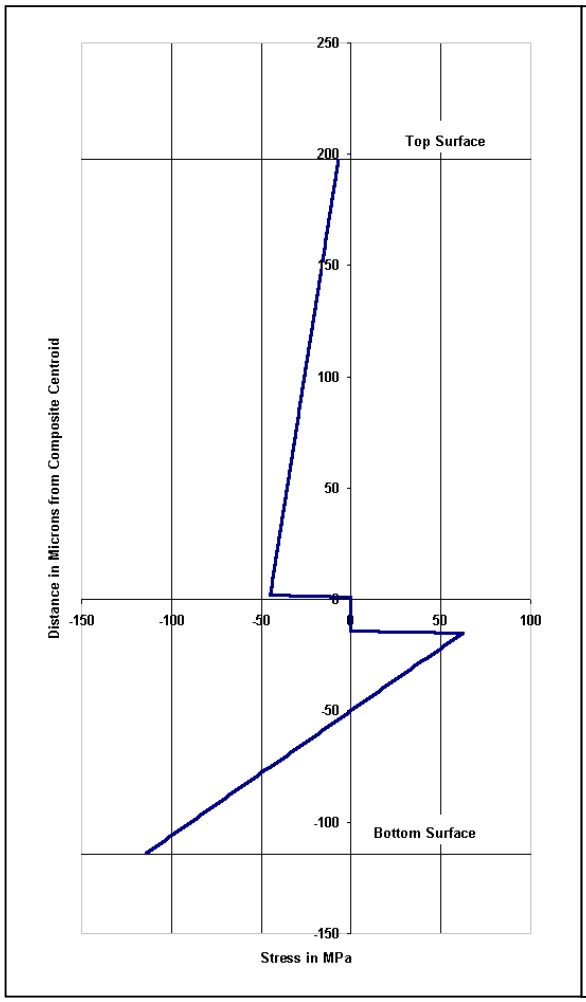

Figure 5.2.6—8.
Substrate thinned to 100 μm

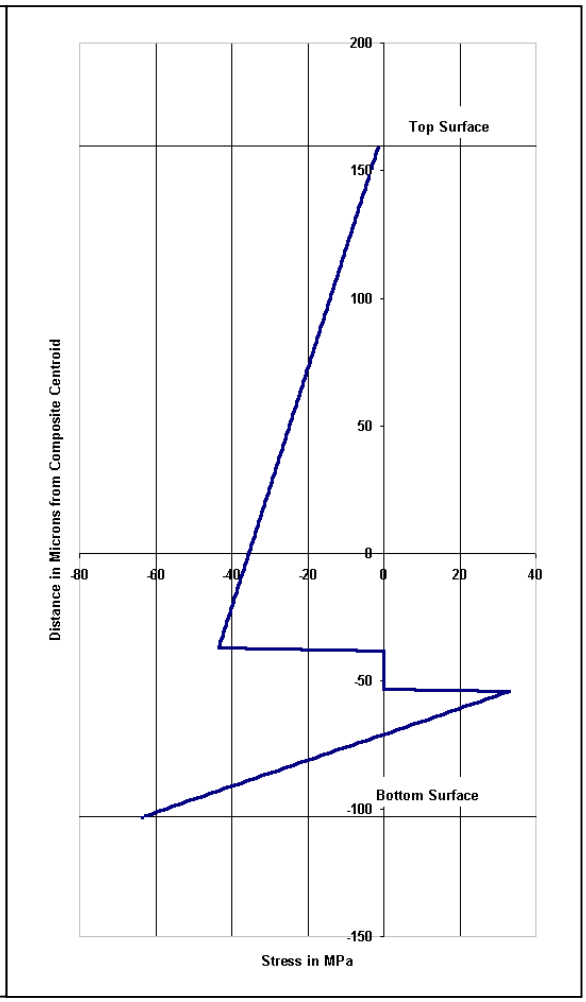

Figure 5.2.6—9.
Substrate thinned to 50 μm

5.2.7 Using Equation 5.2.7—1 as a Transform to Determine d_{31}

A number of displacement-voltage loops, also known as butterfly loops because of their shape, were measured for a selection of pre-stressed unimorph actuators. In a pre-stressed unimorph, stress from piezoelectric strain is superimposed on stress from thermal strain, a constant value determined upon fabrication. The butterfly loops directly measure actuator displacement as a function of applied voltage. In the small-signal case (that is, applied voltage much less than coercive voltage), the relationship is approximately linear; in the large-signal case, the piezoelectric coupling coefficient is a non-linear function of applied voltage.

As defined, the coupling coefficient, or d-coefficient, relates not displacement and voltage, but elastic strain and electric field. Suppose the relationship is linear. If mechanical response occurs in the same direction as electrical input, the slope of displacement-voltage loops and the slope of strain-field loops will be numerically equivalent because one divides through a linear equation by the thickness of the material. However, in the case of electric field applied in the 3-direction and mechanical response determined in the 1-direction, the tensorial relationship requires that a length to thickness ratio be applied, as will be demonstrated.

Figure 5.2.7—1 plots displacement vs. applied voltage for a particular actuator. Initial displacement was normalized to zero. The transform which is then applied to each data point plotted in Figure 5.2.7—1 is given by (5.2.7—1), a close relative of (5.2.3—9). The input quantity is of course δ , actuator deflection normalized to start at zero, whereas the output quantity is average in-plane deflection of the piezoceramic layer, ΔL. The transformed butterfly loop is plotted in Figure 5.2.7—2.

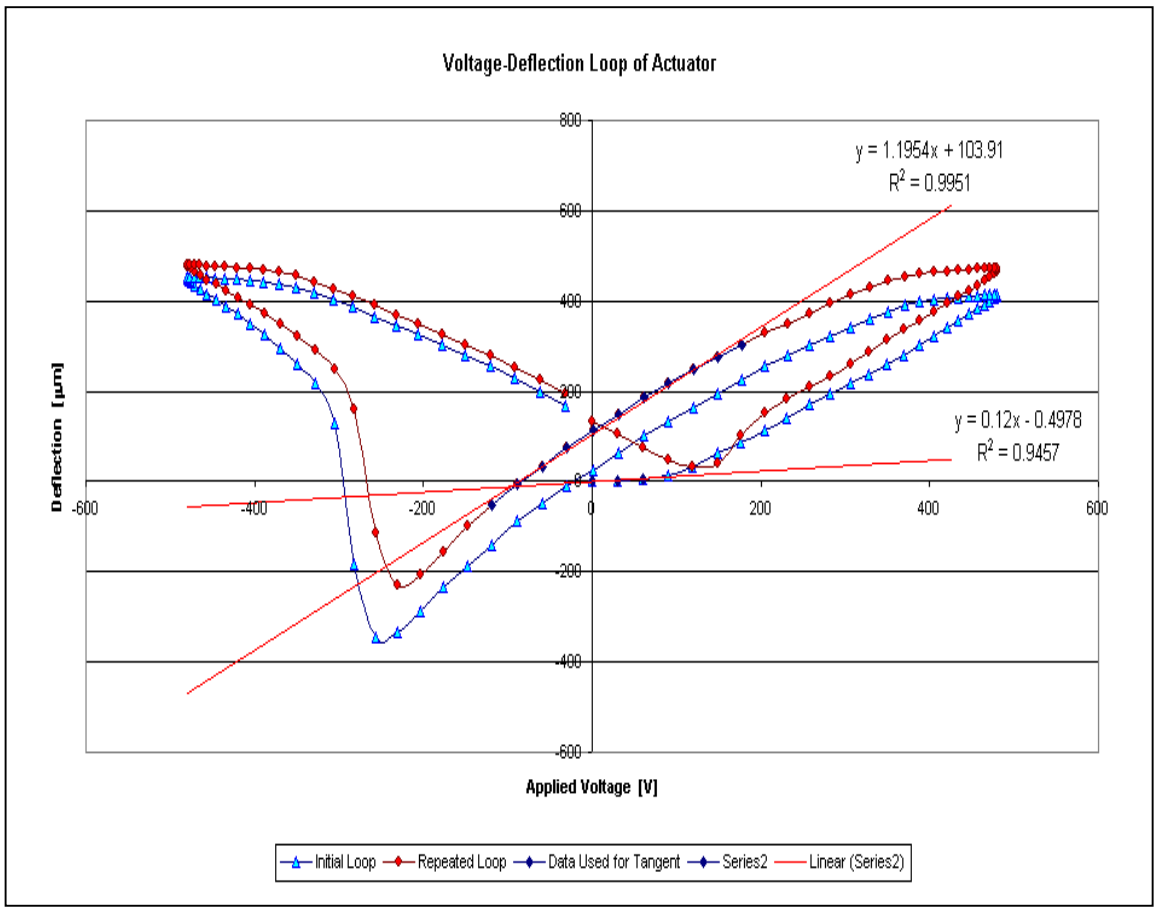

Figure 5.2.7—1. (color) Example of butterfly loop derived from actuator characterization

(5.2.7—1)

$$\Delta L = \frac{d_{31}\, V\, L}{t} = \left[\frac{\frac{H}{2} + \frac{2\left(E_1\, I_1 + E_2\, I_2\right)}{H}\left[\frac{1}{E_1\, h_1} + \frac{1}{E_2\, h_2} + \frac{4\, t}{G\, L}\right]}{\frac{L^2}{8\,\delta} + \frac{\delta}{2}} - \left(\alpha_2 - \alpha_1\right)\Delta T \right] L$$

Keeping in mind that the theoretical relationship between d_{33} loops and d_{31} loops is – ½ , the resulting plot should be upside down relative to the actuator loops and half as

large in extreme values relative to a d_{33} loop (not determined here). For comparison with published d_{31} values, the initial slope of the butterfly curve can be determined using a tangent line, as has been plotted against the first loop. The tangent shown at the crossing point of the second loop follows an example given in [11], which reports an experimental characterization of PLZT subjected to stress and electric field above the coercive field. However, the slope of a tangent line to the loop at some appropriate point is not a direct measure of the d_{31} coupling coefficient. If ΔL is plotted against applied voltage, the slope of a linear segment would be $(L / t)/ d_{31}$, as can be seen from (5.2.7—2). (Note that $d_{31} = d_{13}$.) Hence the slope values determined by linear fit must be multiplied by (t / L), the thickness-to-length ratio of the ceramic layer, to recover the coupling coefficient.

(5.2.7—2) $$\varepsilon_1 = d_{13}\, E_3 \quad \rightarrow \quad \frac{\Delta L}{L} = d_{31}\, \frac{V}{t} \quad \rightarrow \quad \Delta L = \left(\frac{L}{t}\, d_{31} \right) V$$

Note that the plots in Figures 5.2.7—1 and 5.2.7—2 show deflections in microns rather than meters, which must be accounted for in calculations.

The calculations are overlaid on Figure 5.2.7—2, giving –66 pm/V based on initial slope and –440 pm/V based on the tangent at the crossing point. Considering that reported d_{31} values for PZT would typically fall in a range between –100 pm/V to –350 pm/V, the first value is low while the second is a bit high. However, the calculated values have the correct order of magnitude and might serve as approximate values for relative comparisons between actuators.

However, other researchers have reported large d_{31} values. In [11], a d_{31} value of –590 pm/V, based on a tangent at the crossing point, was determined from experimental measurements on a PLZT relaxor ferroelectric. In [12], Schwartz *et al* report d_{31} coefficients ranging from –300 pm/V to –600 pm/V based on a model of the piezoelectric layer in RAINBOW actuators.

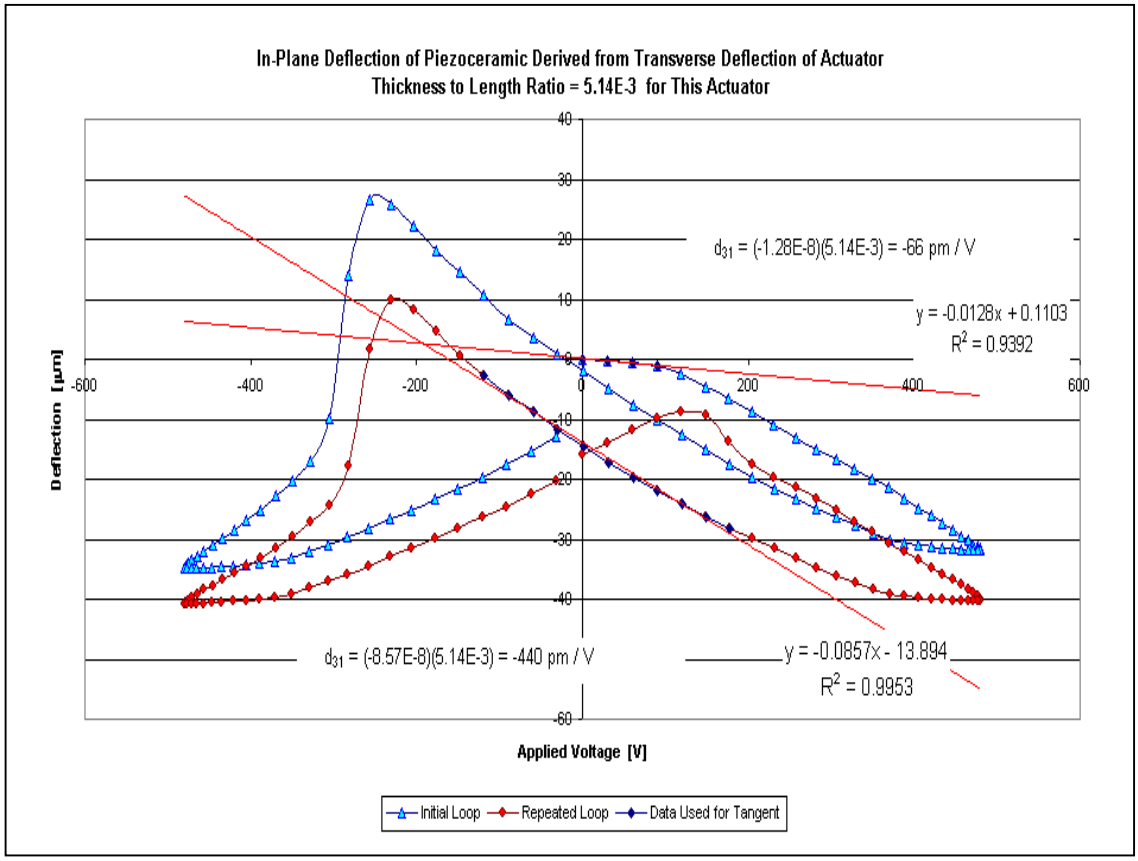

Figure 5.2.7—2. (color) Example of transformed butterfly loop

5.3 References

[1] S. Timoshenko. Analysis of Bi-metal Thermostats. Journal of the Optical Society of America and Review of Scientific Instruments, 11, 233-255 (1925).

[2] Q.M. Wang and L.E. Cross. Tip deflection and blocking force of soft PZT-based cantilever Rainbow actuators. Journal of the American Ceramic Society, 82, 103-110 (1999).

[3] E. F. Crawley and J. de Luis. Use of piezoelectric actuators as elements of intelligent structures. AIAA (American Institute of Aeronautics and Astronautics) Journal, 25, 1373-1384 (1987).

[4] E.F. Crawley and E.H. Anderson. Detailed models of piezoelectric actuation in beams. Journal of Intelligent Materials and Structures, 1, 4-25 (1990).

[5] D.H. Robbins and J.N. Reddy. Analysis of piezoelectrically actuated beams. Computers and Structures, 41, 265-279 (1991).

[6] B. N. Agrawal and K. E. Treanor. Shape control of a beam using piezoelectric actuators. Smart Materials and Structures, 8, 729-740 (1999).

[7] E.J. Hearn. *Mechanics of Materials* (2^{nd} ed.; Pergammon, 1985).

[8] D. Rosenthal. *Resistance and Deformation of Solid Media* (Pergamon, 1974).

[9] W. Riethmuler and W. Benecke. Thermally exited silicon microactuators. IEEE Transactions on Electron Devices, 35, 758-763 (1988).

[10] S. Watanabe, T. Fujiu, and T. Fujiu. Effect of poling on piezoelectric properties of lead zirconate titanate thin films by sputtering. Applied Physics Letters, 66, 1481-1483 (1995).

[11] C. S. Lynch. Electro-mechanical coupling in 8/65/35 PLZT. IEEE International Symposium on Applications of Ferroelectrics, 357-360 (1994).

[12]. R. W. Schwartz, L. E. Cross, and Q.-M. Wang. Estimation of the effective d_{31} coefficients of the piezoelectric layer in Rainbow actuators. Journal of the American Ceramic Society, 84, 2563-2569 (2001).

[13] E. Furman, G. Li, and G.H. Haertling. Electromechanical properties of Rainbow devices. Ninth IEEE International Symposium on Applications of Ferroelectrics, 146-149 (1995).

Chapter 6. Polarization Orientation Across Planar Section as Determined by PFM

6.1. Context for the Experiment

This experiment explored how a variant of atomic force microscopy (AFM) known as piezoresponse force microscopy (PFM) can be used to elucidate the effect of internal stress field on polarization state in a THUNDER™ actuator. Internal stress bias, or pre-stress, appears to enhance actuator performance relative to non-stress-biased unimorphs [1-4]. Determining polarization state corresponding to the internal stress function should indicate a materials explanation for the enhanced performance. As discussed in Chapter 2, both THUNDER and RAINBOW™ actuators achieve internal stress bias through differential contraction of component materials during fabrication at high temperature, acquiring a curved equilibrium shape at room temperature due to internal stress.

As has been occasionally noted, a stress biased actuator develops an internal stress profile resembling that of a bimetallic thermostat strip. [9,10, 56] The internal stress of differential expansion in a bimetallic strip generates an internal moment which causes deflection as though it were experiencing an external load. Thus, regions of material will be in compression, other regions in tension, and transitions will be marked by stress-free surfaces.

Figure 6.1—1 shows the idealized stress profile of a bimetallic strip experiencing differential contraction, where the lower layer has the larger coefficient of expansion with the layers unstressed at an initially higher temperature. The same stress profile would result during differential expansion if the upper layer had the larger coefficient of expansion with the layers unstressed at an initially lower temperature.

However, the symmetric stress profile in Figure 6.1—1 is a “test pattern” of sorts in keeping with presentations typically given in textbooks which simplify the general case of the thermostat model by assuming that the layers have the same Young’s modulus and same thickness, differing only in coefficient of thermal expansion. In the simplified case, the transition from compressive to tensile stress or vice versa occurs at one-third the layer

thickness below the top or bottom surface. [58] Given equal elastic moduli and thickness, the centroid of the composite structure is at its center. For comparison with Figure 6.1—1, refer to Figure 2.3.4—1 in Chapter 2 which shows the stress profile for a RAINBOW actuator determined from a finite element model.

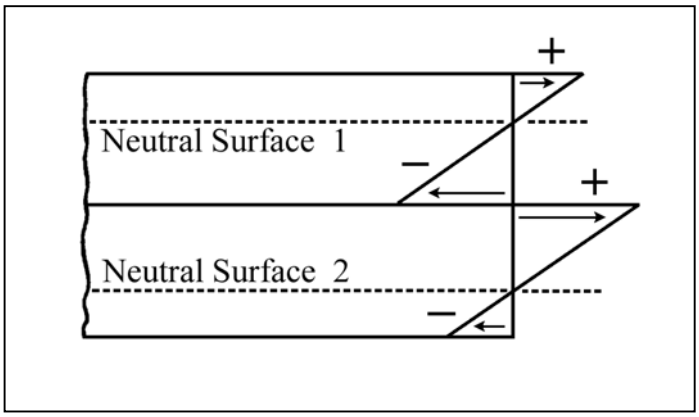

Figure 6.1—1. Schematic stress profile of a two-layer bimetallic strip after differential contraction. Tensile stress is considered positive (+); compressive stress negative (–). Given equal thickness layers, the neutral planes are displaced somewhat toward outside surfaces.

In 1997, Li *et al* found that RAINBOWs exhibited 30%—40% higher displacement than flat, adhesive-bonded unimorphs of the same dimensions [11]. The internal stress distribution was investigated by x-ray diffraction (XRD). Their proposed mechanism for stress-enhanced displacement contends that in-plane stress causes domain alignment, which allows augmented extrinsic contribution to electric field-induced strain. Specifically, surface tensile stress causes the elongated direction in the tetragonal order of PZT and PLZT domains to preferentially align parallel to the ceramic upper surface. The stress-enhanced population of a-domains, as was discussed in Chapter 2, can undergo 90˚ reorientation to align with an electric field applied perpendicular to the ceramic surface.

The same XRD analysis, apparently has not been performed on THUNDER actuators, but the general observations and conclusions should be transferable. Despite differences in fabrication, the principle of introducing internal stress bias through differential contraction is the same. Given equivalent curvature and location relative to a neutral surface, an equivalent stress field must exert an equivalent effect on preferential domain orientation. Any localized enhancement of electric field-induced strain should occur in both cases, even if its effect on relative performance of the two actuator types differs for structural reasons. That is, equivalent stress-modified piezoelectric strain can produce different deflections in actuators with compositional and structural differences.

One can expect XRD analysis at the tension side of an actuator to probe to a depth of a few microns when a reflection technique is used. Even a transmission technique yields data strongly weighted in terms of material just below the surface, an effect which strong absorption by high atomic number ions in PZT reinforces. [12] Investigating preferential domain orientation as a function of depth through the entire 200 μm thickness of the actuator ceramic requires cutting a cross-section. It would also be possible to conduct XRD on such a cross-section, but it would not be possible to observe variation in results at the micron level.

Although it would be preferable to conduct investigation on an uncut actuator, sectioning may not have introduced undue difficulties. Cumulative deflection of a cross-sectioned THUNDER actuator is clearly smaller than for an entire actuator. However, the radius of curvature is not greatly altered, since fabrication introduces a constant, distributed internal moment. Also, the sectioned sample still had crosswise dimensions much larger than the actuator thickness, which limits the effect of introducing a new edge. In addition, the actuator was embedded in rigid epoxy before cutting, helping to preserve its uncut shape. Even so, out-of-plane stress must fall to zero at the cut surface, and there will be some edge effect. A feature of vertical PFM which is advantageous in this circumstance is that measuring piezoelectric response normal to the surface integrates bulk material response below the surface.

Domain structures in polarized materials have been imaged using scanning electron microscopy, polarized light optical microscopy, and surface etching or decoration techniques.[13] Net polarization can be obtained by electronic measurement of bulk surface charge [14] and d-coefficient values can be obtained by interferometry. [15-18] Although the vertical resolution of interferometry can exceed that of scanning probe methods, the lateral resolution is essentially macroscopic. AFM imaging techniques have the advantages of exceptionally high spatial resolution and relatively uncomplicated sample preparation.[19] STM (scanning tunneling microscopy) has also been used for domain imaging, but has the disadvantage of requiring a conductive surface. Spatial resolution has been compromised by preparing conductive samples.[20, 21]

The present study determined trends in distribution of effective d-coefficient values by vertical PFM (VPFM) [22-35] and lateral PFM (LPFM) imaging [36-43], which have been described elsewhere as useful tools for detecting out-of-plane and in-plane polarization components. One would like to reconstruct the three-dimensional polarization gradient at the sub-grain level as a function of position between top and bottom edges of the ceramic plate cross-section. Given the approximately linear relationship between the coupling coefficient and polarization vector, we can see the proportional change in polarization vector orientation from the trends in distribution of effective d-coefficient values.

Various researchers have utilized the idea that information from one vertical PFM scan and two lateral PFM scans, taken before and after sample rotation through 90º, provide orthogonal components P_X, P_Y, and P_Z of the polarization vector **P**. [39-41, 48, 55] Values of P_X, P_Y, and P_Z obtained by scanning across a planar surface can be mapped onto the area to see the relative change in polarization components from place to place, allowing reconstruction of **P** by the collective evaluation of all the components.

The current experiment involves a somewhat unusual arrangement in that electric field was applied in one direction and mechanical response sensed in a perpendicular direction in every case except one. Typically, researchers using the term VPFM, for example, are measuring piezoelectric response perpendicular to the surface of something

like a thin-film capacitor, in which case surface displacement is sensed in parallel with applied field. (The AFM tip often serves as a contact electrode.) In our experiment, (see Section 3.5) VPFM measurements were indeed taken for surface displacement perpendicular to the sample surface, but the electric field was applied in a different orthogonal direction. Likewise, LPFM measurements also sensed shear displacement perpendicular to applied field direction in one case, and parallel to the field direction in the other. Trends in three-dimensional polarization have been deduced by considering the entire set of results.

As was discussed in Section 3.5, each AFM scan acquired in this experiment generated four files containing 256 x 256 data points. One file in each set of four represented the mechanical response of the piezoelectric sample surface to a high frequency excitation signal. A macro-driven spreadsheet calculated effective piezoelectric coupling coefficient, $|d_{EFF}|$, and phase shift arrays in a point to point application of formulas (3.5—1) and (3.5—2) to the AFM voltage signal output arrays. The spreadsheet produced numeric arrays that represented a mapping of calculated $|d_{EFF}|$ values onto the scanned areas. Further processing by another spreadsheet assigned color values to each number in the $|d_{EFF}|$ arrays to yield a color-coded pixel representing the classification interval in which each number belonged, relative to the overall range of $|d_{EFF}|$ values occurring in a set of scans. The numeric arrays could then be displayed as color images showing variation in $|d_{EFF}|$ across scanned areas.

A gallery of images resulting from plotted d-coefficient magnitude data ($|d_{EFF}|$) is presented at reduced scale in Figure 6.2—1 . At the expense of diminishing available resolution, the entire set can be viewed together to better detect trends. All plotted images represent a square area, 40 μm by 40 μm. The ceramic grain size in this actuator was found to vary between 1.5 and 2.75 μm (± one standard deviation around average, n = 33) based on analysis of SEM images of a fractured surface.

An important initial observation is that the images map intervals of the range of calculated $|d_{EFF}|$ values onto surface area, showing both the topographic patterns formed by regions of similar response as well as the fraction of total area covered by various levels of

response. To better summarize the relative fractions of total image area experiencing various levels of response, the image data are plotted as sets of histograms in Figure 6.2—2. Since each image plots 256 x 256, or 65536 data points acquired by scanning an area $(40\ \mu m)^2$, each image pixel represents an area about 156 nm across. The area fraction occupied by regions of similar mechanical response is given by the fraction of total pixels falling within an interval.

Note that overall trends in image coloration and histogram modal values for the two VPFM image sets should closely resemble each other, since both represent vibrations sensed perpendicular to the sample surface (A1 direction) although the AFM cantilever scanning direction (parallel to the surface) differed by 90º. So the four experimental conditions represent only three orthogonal directions. It appears that the two VPFM sets are indeed quite similar. The fact that they are not identical arises because slightly different paths were traced across the cross-section as a result of turning the sample by 90º.

The range of values derived from all five scans in a set (e.g., LPFM parallel to electrodes) has been divided into the same bin intervals with the same color coding for all images and histograms within a given set. Different intervals and color coding, however, apply to each different test condition set. Therefore, in Figure 6.2—1, trends formed by the sequence of images in a column are meaningful, whereas images in a row do not form a trend. However, the conclusions drawn from each columnar trend are related in that they must be consistent. Given a change in the net orientation of the polarization vector, results from sensing PFM response in three orthogonal directions must provide a consistent view of the change resolved into orthogonal components.

6.2 Presentation of Experimental Results

Results are largely summarized in the next two figures. The caption for Figure 6.2—1 is on page 324, following. Figure 6.2—1 is on page 325.

Figure 6.2—1. (color) Gallery of plotted | d_{EFF} | images. (Refer to Figure 6.2—3 for color codes.)

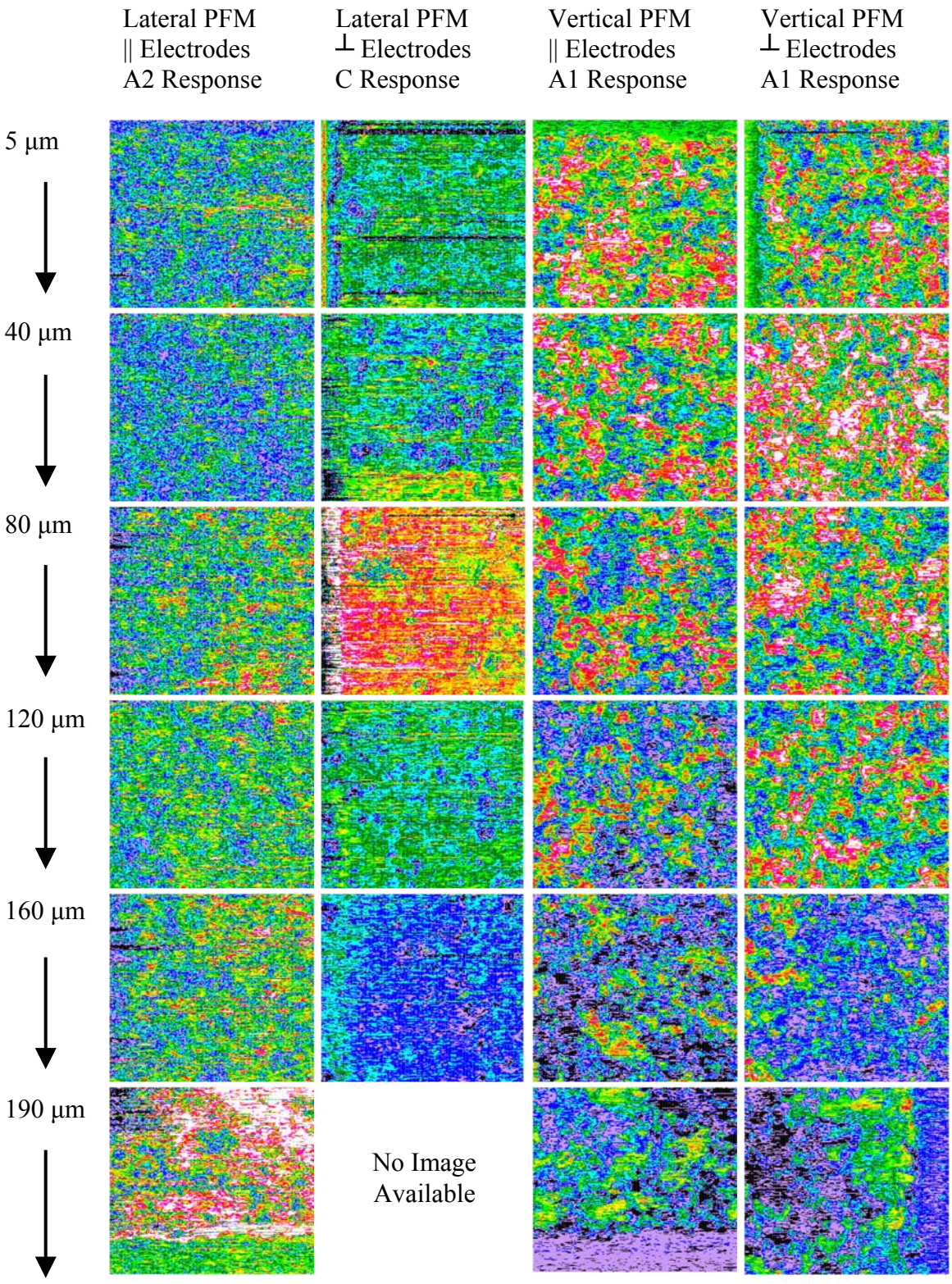
Lateral PFM
|| Electrodes
A2 Response
Lateral PFM
⊥ Electrodes
C Response
Vertical PFM
|| Electrodes
A1 Response
Vertical PFM
⊥ Electrodes
A1 Response
5 µm
40 µm
80 µm
120 µm
160 µm
190 µm
No Image
Available
Distance from Top Electrode Toward Bottom Electrode

Lateral PFM

Parallel to Electrodes
(Response in A2 Direction)

Perpendicular to Electrodes
(Response in C Direction)

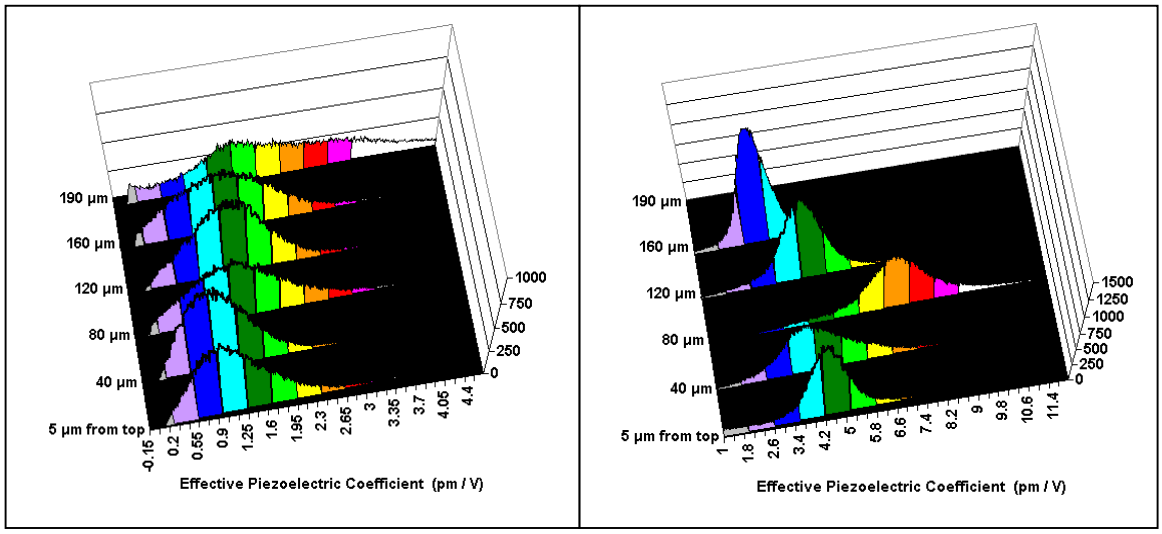

Vertical PFM

Parallel to Electrodes.
(Response in A1 Direction)

Perpendicular to Electrodes
(Response in A1 Direction)

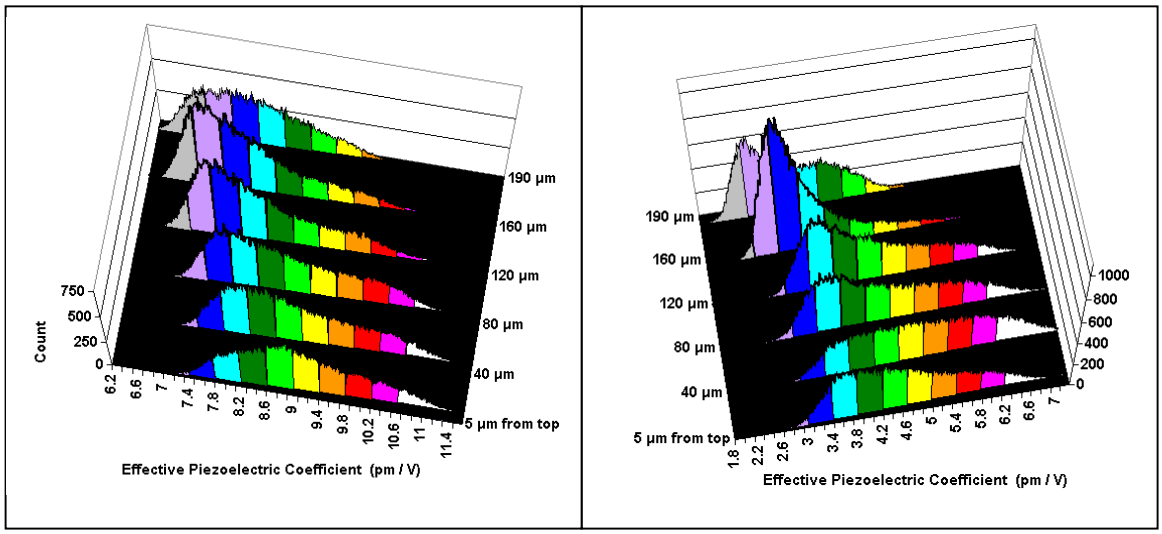

Figure 6.2—2. (color) Histogram sets compiled from $|d_{EFF}|$ data. (Refer to Figure 6.2—3 for color codes.)

Lateral PFM || Electrodes A2 Response		Lateral PFM ⊥ Electrodes C Response		Vertical PFM || Electrodes A1 Response		Vertical PFM ⊥ Electrodes A1 Response	
	< 0.2		< 1.8		< 7.0		< 2.6
	> 0.2—0.55		> 1.8—2.6		> 7.0—7.4		> 2.6—3.0
	> 0.55—0.9		> 2.6—3.4		> 7.4—7.8		> 3.0—3.4
	> 0.9—1.25		> 3.4—4.2		> 7.8—8.2		> 3.4—3.8
	> 1.25—1.6		> 4.2—5.0		> 8.2—8.6		> 3.8—4.2
	> 1.6—1.95		> 5.0—5.8		> 8.6—9.0		> 4.2—4.6
	> 1.95—2.3		> 5.8—6.6		> 9.0—9.4		> 4.6—5.0
	> 2.3—2.65		> 6.6—7.4		> 9.4—9.8		> 5.0—5.4
	> 2.65—3.0		> 7.4—8.2		> 9.8—10.2		> 5.4—5.8
	> 3.0—3.35		> 8.2—9.0		> 10.2—10.6		> 5.8—6.2
	>3.35		>9.0		>10.6		>6.2

Relative size and position of classification ranges plotted on a comprehensive scale

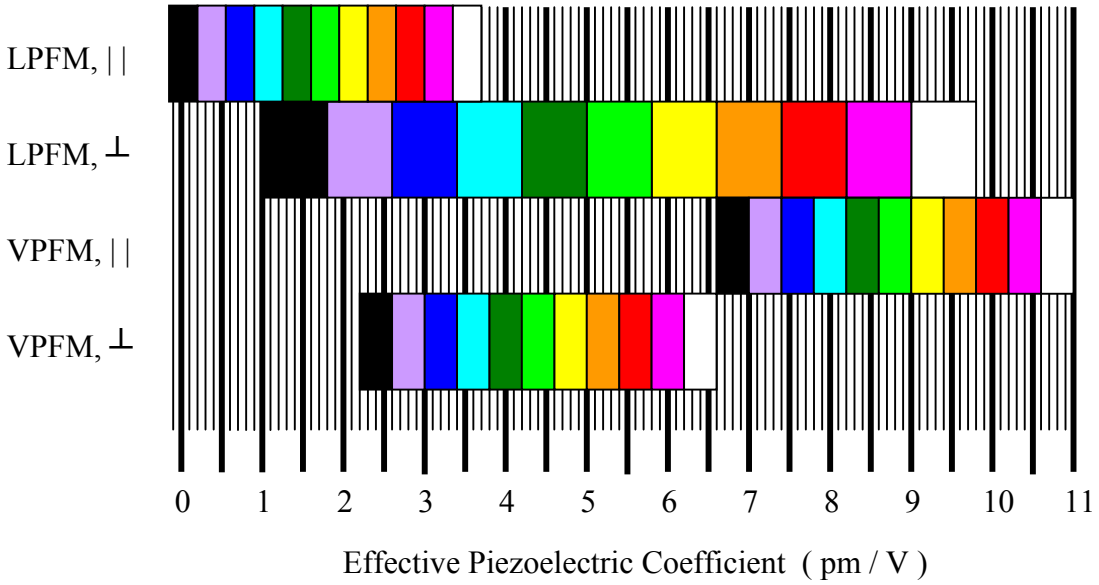

Figure 6.2—3. (color) Key to the color-coded scales used in each scanning set (All Values: effective piezoelectric coefficient [pm / V])

6.3. Discussion

As was discussed by Rodriguez *et al* [55], even slightly off-axis domain crystallographic orientations (relative to bulk sample, in this case) result in "effective" coupling coefficient measurements which incorporate a number of single crystal dij values. Vertical PFM signals will be proportional to the d_{33} coefficient if the polarization vector happens to be normal to the cross-section surface which is imaged. However, if there is an angle between the normal to the thin plate surfaces and the polarization vector, the measured piezoelectric coefficient d_{ZZ} (i.e., measured response in the direction normal to the surfaces) is not equal to d_{33} and not proportional to spontaneous polarization.[44-48]

For sample composition resulting in tetragonal order, the measured piezoelectric factor d_{ZZ} is given by (6.3—1).

$$d_{ZZ}(\theta) = (d_{31} + d_{15}) \sin^2 \theta \cos \theta + d_{33} \cos^3 \theta, \quad (6.3—1)$$

where θ is the angle between measurement direction and the [001] crystallographic axis.

Effective d-coefficient magnitudes resulting from in-plane sample response are also related to the polarization vector by functions which may incorporate a number of single crystal dij values. Modulation voltage is still applied parallel to the sample's z direction, though mechanical response is measured along the x or y directions. (In this discussion, x, y, and z directions are synonyms for 1, 2, and 3 directions.) For sample composition with tetragonal order, the measured values of d_{ZX} and d_{ZY} are given by (6.3—2) and (6.3—3).

$$d_{ZX}(\theta) = d_{31} \cos \theta \quad (6.3—2)$$

$$d_{ZY}(\theta) = (d_{33} - d_{15}) \sin^2 \theta \cos \theta + d_{31} \cos^3 \theta, \quad (6.3—3)$$

where θ is the angle between measurement direction and the [001] crystallographic axis. The essential point is that measured piezoresponse will depend on d_{33}, d_{31} and d_{15} piezoelectric coefficients, as described elsewhere.[48]

In fact, we do not know the individual grain's crystallographic orientation at any specific region in the bulk sample. Therefore, we have to rely on three-dimensional analysis of VPFM and LPFM signals. This approach takes into account the values of d_{33}, d_{31}, and d_{15} and their signs, and provides approximate average orientation of the material at a given place. [55] By repeating the process, we can get an idea how the average orientation changes with distance from the sample surfaces.

We know, based on supplier information, that the piezoceramic elements in the THUNDER actuators are poled downward. That is, when voltage is applied in the polarity shown, resulting in the electric field direction shown, the polarization vector has been defined such that the d_{33} coefficient will be positive, indicating that the ceramic will expand in the 3-direction (perpendicular to electrodes). However, when domains have off-axis orientations, as discussed above, we obtain not d_{33} and d_{31}, but d_{ZZ}, d_{ZX}, and d_{ZY} responses.

Initially, researchers used PFM primarily to acquire information about the phase difference between modulation signal and sample mechanical response. [49-53] Suppose that the block of electroded piezoceramic depicted in Figure 6.3—1 is a portion of a thin film capacitor and mechanical response is measured in the direction perpendicular to the top electrode by PFM. Then, downward poling (+Pzz) would result in mechanical vibrations occurring in-phase with the modulation voltage, and would conventionally be represented in phase images by white regions. Conversely, upward poling (–Pzz) would result in mechanical vibration out-of-phase with applied modulation voltage and would be represented as black in a phase image. Gray might represent a non-coupled region.[29]

However, phase images should be interpreted with caution. Phase contrast can arise from different levels of signal-to-noise ratio in regions of low $|d_{EFF}|$ and regions of high $|d_{EFF}|$, and non-piezoelectric regions in contact with material responding to PFM modulation voltage will be visible in phase images. [26] Also, phase difference can be altered by parasitic capacitance of the tip-sample structure. [54]

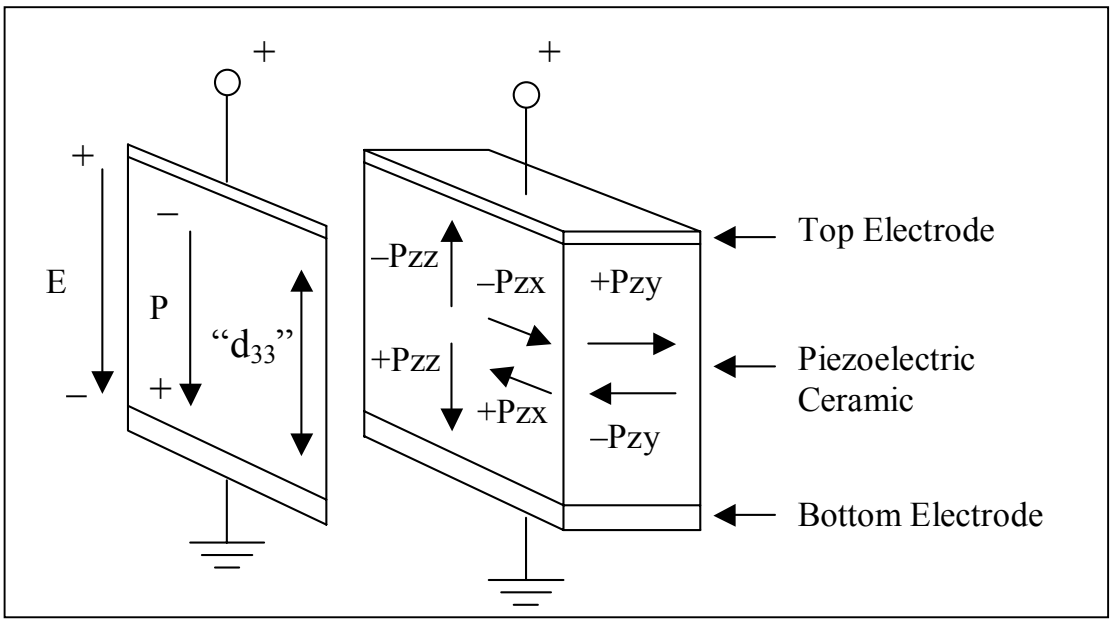

Figure 6.3—1. Orientation of effective polarization components relative to schematic depiction of sample

The significance of phase images resulting from this study is difficult to determine. Although not presented here, plotted images show topographic variation as do the d-coefficient magnitude images. Phase images from VPFM data scanned parallel to sample electrodes show little spatial resolution unless plotted against a narrow interval because the distributions have very narrow ranges. All phase distributions fall within the interval between –180º and 0º, implying that both in-plane and out-of-plane mechanical responses were out-of-phase with the PFM modulation signal by a certain amount, but displacements were all either positive or negative at the same time.

This may not be physically possible. Intrinsic d-coefficients are cross-coupled in a way resembling the Poisson effect in solid mechanics: a PZT ceramic plate with net poling parallel (not anti-parallel) to applied electric field expands in the field direction and contracts in the lateral direction (i.e., $d_{33} > 0$, $d_{31} < 0$).

Our interpretation draws on two related facts. Since the PFM modulation signal was applied to the sample electrodes rather than between sample surface and tip, the measured phase values result from a capacitive structure formed by the sample and AFM. This may have introduced a self-consistent phase response of constant sign that did not reflect the phase of the mechanical response in different directions across the sample surface. As was noted in Chapter 3.4 , PFM experiments are often arranged to yield a mixed response signal of the form $A\cos\theta$, where A represents measured amplitude of sample surface vibrating in response to applied high frequency excitation signal, θ represents phase shift between driving signal and sensed mechanical response. In this experiment, amplitude and phase were recorded separately, which is why brightness in plotted magnitude images corresponds to an absolute value of piezoelectric coupling coefficient. The independent phase response data probably also represents unsigned magnitude. While absolute value of effective piezoelectric coefficient is still useful, undirected phase response is less useful since the phase data is primarily expected to provide directionality to $|d_{EEF}|$. Nonetheless, a summary of phase results is included for the sake of completeness.

Figures 6.3—2A through 6.3—2D present phase results as sets of histograms. The observation can be made that phase difference is not strongly correlated with location relative to top and bottom surfaces of the ceramic cross-section. The apparent central tendencies within sets of histograms indicates that phase offset is about 20º smaller for LPFM results than for VPFM results, and VPFM distributions are showing a tendency toward bimodality. Note also that LPFM histograms appear to have higher variability associated with scanning parallel to sample electrodes, while VPFM histograms associated with scanning perpendicular to electrodes have the higher variability. This trend is likewise seen in the d-coefficient magnitude histograms presented in Figure 6.2—2, in that the corresponding cases are marked by more irregular histograms and more irregular progressions of histograms.

Despite some uncertainty about the meaning of the phase measurements, consistent trends in $| d_{EEF} |$, as indicated by the images in Figure 6.2—1, nonetheless provide a strong

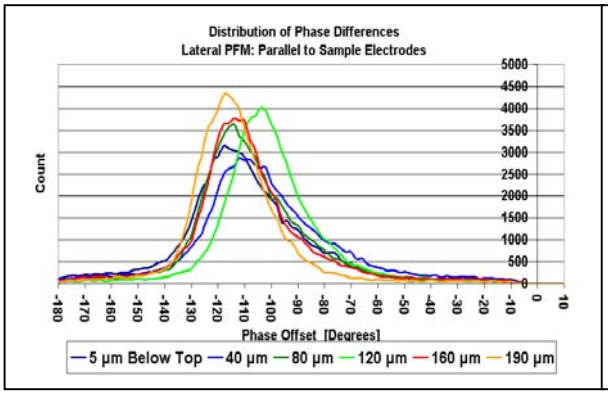

Figure 6.3—2A. (color) LPFM phase offset histograms as a function of position on cross-section surface (Scanning direction parallel to sample electrodes—lateral response sensed)

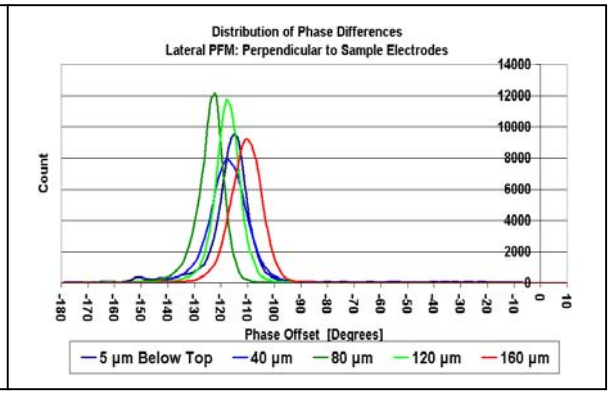

Figure 6.3—2B. (color) LPFM phase offset histograms as a function of location on cross-section surface (Scanning direction perpendicular to sample electrodes—lateral response sensed)

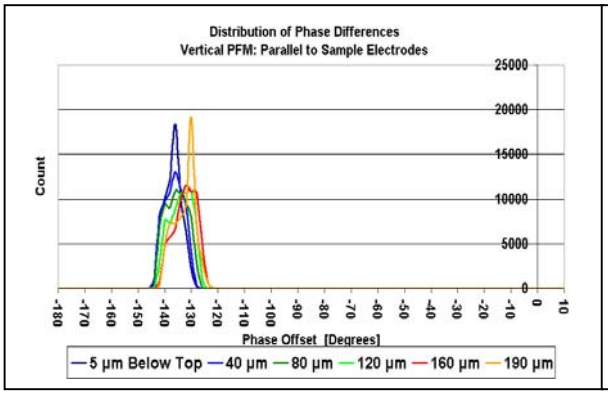

Figure 6.3—2C. (color) VPFM phase offset histograms as a function of position on cross-section surface (Scanning direction parallel to sample electrodes—vertical response sensed)

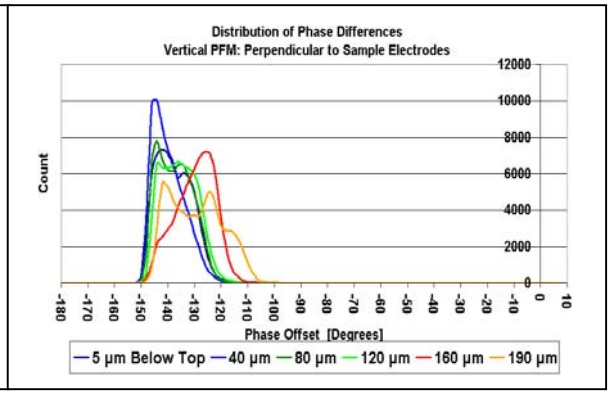

Figure 6.3—2D. (color) VPFM phase offset histograms as a function of location on cross-section surface (Scanning direction perpendicular to sample electrodes—vertical response sensed)

basis for useful conclusions. On one hand, higher color temperature (toward red end of spectrum) in plotted results indicates polarization strongly oriented in the direction electric field is applied and large mechanical response, but not direction. Since the data were not obtained using a mixed signal, effects of polarization orientated –180º to zero (relative to sensing direction) are indistinguishable from those resulting from zero to +180º orientations. On the other hand, while measuring (effective d-coefficient) magnitudes, we are getting information about orientation by acquiring three orthogonal responses at several areas across the sectioned face of the actuator ceramic. Four scans (with two VPFM scans giving the same information) indicate something conclusive between them.

Although the values of $|d_{EFF}|$ calculated from AFM data using equations (3.5—1) and (3.5—2) and plotted in Figure 6.2—1 have stronger foundations in physical theory than, say, image analysis of AFM-generated pictures, the experiment has not managed to produced strictly quantitative results. While VPFM measurement of out-of-plane displacement has been calibrated by measuring AFM cantilever tip deflection during a calibrated shift in the vertical position of the AFM scanning system, calibration of LPFM measurements is necessarily more indirect. Since LPFM is measuring torsional response of the cantilever to lateral motion of the sample surface, one would need to find the torsional stiffness of the cantilever and determine a coefficient of friction between a specific tip and the sample surface. Then LPFM measurements could be connected to VPFM calibration.

Other factors decrease the quantitative value of these results. When rotating the sample to obtain LPFM scans in orthogonal directions, ideally the same 40 μm square areas of sample surface would be scanned in both cases, but in fact the location of the second scan was only approximately the same as that of the first. The two sets of VPFM results should fall within the same order of magnitude. With the lower and upper limits of the composite range extending from 2 to 11.2 pm/V, and individual ranges occupying intervals 5.2 and 5.0 pm/V wide, they are close to the same order of magnitude. An important point is that unlike AFM studies of thin film electrical domain structure, which typically involve “through domains”, the integrated response of bulk samples can arise

from a diversity of physical and electrical microstructures beneath a scanning tip. In a way, it was surprising to get the level of detail we see in the plotted images.

Although both sets of LPFM results are consistent with the magnitude of VPFM results, the range of LPFM results sensed in the A2 direction occupies a range one-third to one-half as large as other ranges. Aside from the point about scanning slightly different places before and after rotating the sample, surface effects can play a role in the discrepancy since LPFM measurements are much more sensitive to surface contact than VPFM measurements. Surface roughness might have varied slightly or there may have been something on the surface such as charge or an adsorbed film of water.

Finally, we must consider why the measured d-coefficient magnitudes are so much smaller than the reported values for bulk ceramics. Reported values for d_{33} coefficients (referred to poling direction rather than crystallographic axis) typically fall between 200 and 700 pm/V; d_{31} values are typically about half the corresponding d_{33} value. Typical values obtained in this experiment range from 0.2 to 11 pm/V.

When PFM experiments are conducted using the AFM tip as an electrode, small values of $|d_{EFF}|$ have been obtained and the explanation is that material surrounding the excited region acts to constrain its movement. In our experiment the modulation signal was applied through top and bottom electrodes. However, if the embedding epoxy was able to constrain the actuator sections well enough to preserve the stress state of the entire actuator, then perhaps the external constraint created a clamping effect. In addition, out-of-plane response might have been reduced by introducing the cut surface, which requires that out-of-plane stress components must fall to zero at the surface. And last, when connecting wires under magnification, examination of the embedded actuator section did reveal occasional evidence of cracking and delamination at a few places on the surface. This minor damage was incurred during cutting, grinding and polishing and is difficult to avoid entirely.

6.4 Additional Discussion and Conclusions

Two essential conclusions can be drawn from the images in Figure 6.2—1. Strong response in the A1 direction (perpendicular to cut surface) transitions to strong response in the A2 direction (in plane with left-right orientation), implying that a large A1 polarization component rotates toward the A2 direction in traversing from top to bottom of the ceramic. We cannot say whether rotation occurred in a clockwise or counterclockwise fashion (about some appropriately defined axis), but given the symmetry of the actuator the direction is mostly immaterial.

In addition, an initially weak response at the top surface in the C direction (in plane with top-bottom orientation) develops into a strong response toward the center, then diminishes again toward the bottom surface. This implies one of two possible transitions for the polarization vector C component: either it rotates into alignment and reverses the rotational direction to return (approximately) to its original direction, or it rotates into alignment and out of alignment without reversing direction of rotation so that its final direction is opposite its initial direction. Combining observations, the possible reorientations of net polarization are shown in Figure 6.4—1 in schematic form (excluding cases resulting from permutations of alternate directions for A1 and A2).

One promising interpretation of the overall pattern includes the issue of poling direction. We know that the actuator has been poled downward and would expect an overall alignment to be evident in the case of a non-stress-biased unimorph. But a stress gradient is also present. Which effect dominates? In general, the $|d_{EFF}|$ images suggest that internal stress bias dominates and that we do not even see the initial poling.

However, this may not be strictly true. One place we might see strong indication of initial poling is near a neutral plane in the stress gradient of the actuator. If the stress profile of the pre-stressed actuator actually did resemble the upper layer profile shown in Figure 6.1—1, the location labeled “Neutral Surface 1” would correspond approximately to the location where the LPFM image taken while scanning perpendicular to sample electrodes (C direction) becomes remarkably bright. Is there evidence that a typical

THUNDER actuator piezoceramic actually does have a neutral surface at approximately one-third to one-half its total thickness relative to the top surface?

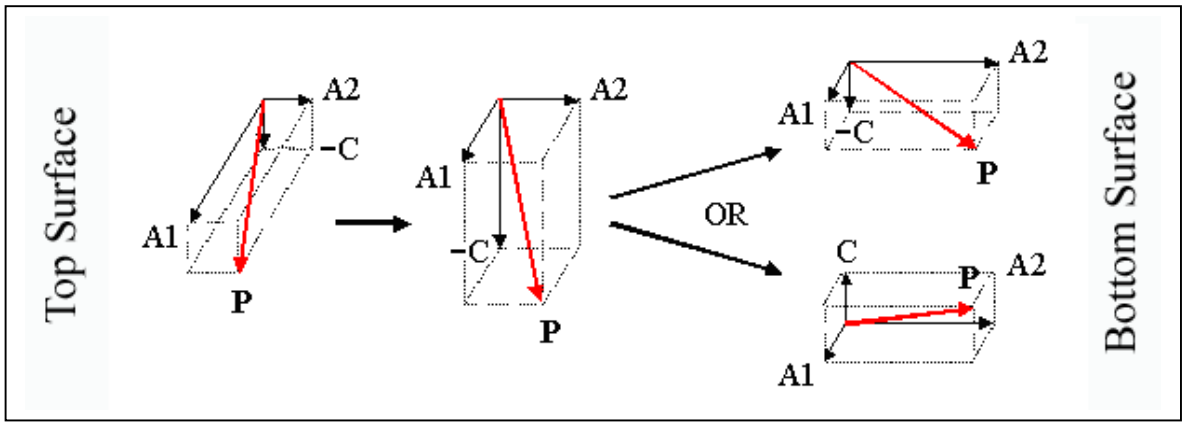

Figure 6.4—1. (color) Schematic depiction of two possible reorientations of the polarization vector **P** occurring upon crossing from top to bottom electrodes (Permutations resulting from alternate directions for A1 and A2 have been omitted.)

On the one hand the model developed in Section 5.2, after Timoshenko's analysis of a bimetal thermostat, predicts that when the Young's moduli of ceramic and metal layers are as different as in commercial PZT and stainless steel, the top of the ceramic layer approaches zero stress from the direction of compression, but never actually goes into tension. Since aluminum has less than half the Young's modulus of stainless steel (76 GPa for a general purpose aluminum alloy, 210 GPa for austenitic stainless steel [59]), the analytical model would probably show the occurrence of tension in the top ceramic material of actuators made with aluminum substrates.

On the other hand, the finite element model in Sections 4.6.1 and 4.6.2 indicates tensile stress of low magnitude in the top surface material of its ceramic element. Although the circular geometry has a significant influence on the actuator characteristics, the model

assumes both substrate and ceramic layers 8 mils thick (see Table 4.6.1—1) , which is about the same as a beam actuator fabricated in-house using a substrate 8 mils thick.

Figure 6.4—2 reproduces the first section of Figure 4.6.2—1 at larger scale to show where in the piezoceramic element the transition from compressive to tensile stress occurs. Although top regions of some finite element model cells have gone into tension, the overall picture is much like that given by the analytical model in Section 5.2. That is, not much of the actuator ceramic actually experiences tensile stress.

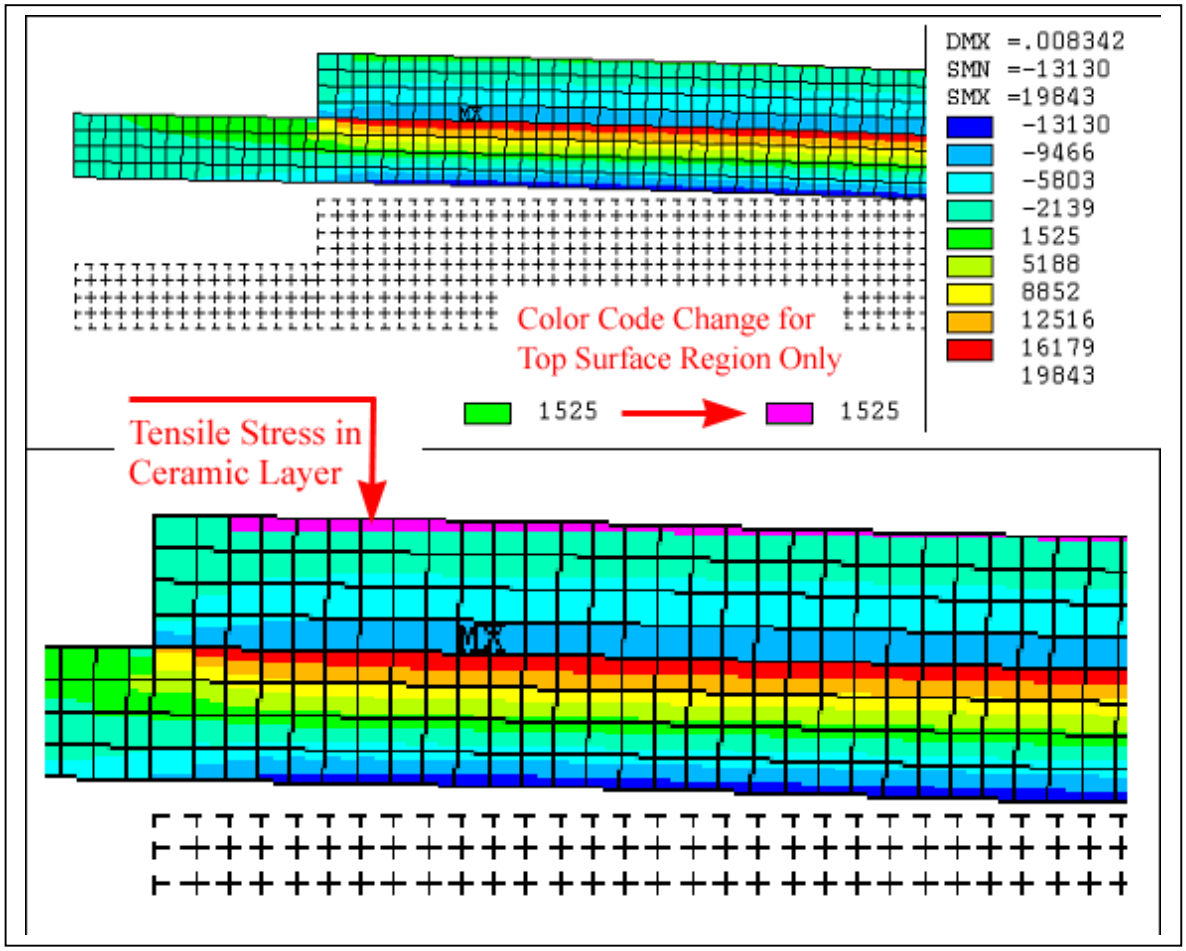

Figure 6.4—2. (color) Reproduction of first section of Figure 4.6.2—1 at larger scale to show where transition from compressive to tensile stress occurs—with change to complementary color in lower enlargement to improve clarity (Stress in units of psi)

While it would be nice to explain why the LPFM image taken while scanning perpendicular to sample electrodes shows unusually strong response where it does, still a strong case already exists for why actuators with internal polarization changing direction as shown in Figure 6.4—1 would show enhanced piezoelectric strain. The role of tensile stress in the operation of pre-stressed unimorphs was to cause some portion of preferential domain alignment to shift to a direction *not* parallel to the poling direction. Thus, when electric field was applied parallel to the poling direction, the possibility of reorienting mechanical-stress-induced a-domains by electrical stress arises, thereby regenerating c-domains and providing the basis for an enhanced extrinsic component of piezoelectric strain. The foremost implication of Figure 6.2—1 and its analysis in Figure 6.4—1 is that throughout most of the piezoceramic cross section, the polarization vector is pointing *anywhere but* in the c-direction (poling direction). Clearly, the polarization state of this actuator is well-arranged for enhanced extrinsic contribution to piezoelectric strain to occur.

Supposing, regardless of the implications of available models, that there is indeed some material in tension in upper regions of the actuator ceramic, we can also suggest why the rotation of A1 polarization component to an A2 component occurs from top to bottom electrodes across the cross-section. In general, the tetragonal order of polarization domains in the PZT element is influenced by tensile directions in the three-dimensional stress field. Tensile stress in the A1 direction near the top actuator surface creates preferential out-of-plane alignment (i.e., plane of cross section), as was detected by VPFM. Near the bottom electrode, compression in the A1 direction suppresses this alignment. However, the Poisson effect of compression in the A1 direction is a tensile stress component in A2 and C directions which is superimposed on other contributions to stress in those directions.

Orientation in either the A2 or C direction is not equally likely because of the bicurvature of the actuator lamina and the fact that the ceramic element is about three times longer (A1 direction) than wide (A2 direction). Differential contraction during fabrication induces transverse as well as axial curvature. Poisson counter-stress from compression in the A1 direction is superimposed on the primary stress in the A2 direction and vice versa.

One might think that the combined Poisson counter-stress in the C direction resulting from both A1 and A2 primary stresses would facilitate C-domain alignment in the compressive region of ceramic near the bottom electrode, but evidently this is not the case. The relative dimensions of the ceramic thin plate probably determine which primary stress directions have dominant effects, and evidently longer dimensions win. (Approximate relative dimensions of the actuator ceramic involved in this study are 3 : 1 : 0.008, length to width to thickness—defined as A1, A2, C directions—where width is 0.5 inch or 12.7 mm.)

This study has shown that analysis of the piezoresponse of a cross-sectioned THUNDER actuator surface can provide useful insight into the relationship between internal stress bias and orientation of the net polarization as a function of distance through the thickness of the ceramic element. The approach can offer evidence for verifying or elaborating upon current models regarding effect of stress-bias on actuator shape and deflection. Our results give indications that a section of an embedded actuator maintains approximately the same stress profile as the entire actuator.

Although definite quantitative measurements of effective piezoelectric coupling coefficients in all three orthogonal scans would require refinements of the procedure used in this experiment, sufficiently consistent results were obtained to allow useful conclusions. The technique of plotting color images from calculated values of $|d_{EEF}|$ was useful in making trends evident within a trace of scans and in revealing the complex topographic variation in piezoresponse across areas on the micron scale.

Although it would be helpful to resolve the difficulty we encountered interpreting phase measurements, the information about orientation obtained by taking three sets of scans in orthogonal directions confirms the value of this method in reconstructing three-dimensional orientations of net polarization.

Our analysis indicates that both tensile stresses in the ceramic near the actuator top electrode and compressive stresses near the bottom electrode of the ceramic element in a THUNDER actuator tend to suppress domain alignment in the C direction. However, near the neutral surface of the internal stress profile, overall C-direction poling strongly favors a

preponderance of C domains. In-plane polarization components (A1 and A2) contribute to a rotation of the polarization vector between top and bottom surfaces of the cross section. In regions of the ceramic under compression, it appears that the tensile Poisson counter-stress associated with the long dimension of the ceramic plate selects the preferential orientation of domain structure.

The final word is that the polarization state of the actuator probed by PFM in this experiment is ideally set for enhanced extrinsic contribution to piezoelectric strain. Since the polarization vector points in any direction but the c-direction throughout most of the actuator cross-section, a substantial opportunity exists for domain reorientation by an electric field applied in the c-direction.

6.5 References

[1] C.D. Near. Piezoelectric actuator technology. Proceedings of the SPIE—The International Society for Optical Engineering, 2717, 246-258 (1996).

[2] G.H. Heartling. Rainbow ceramic—a new type of ultra-high displacement actuator. Bulletin of the American Ceramics Society, 73, 93-96 (1994).

[3] C. Shakeri, C.M. Bordonaro, M.N. Noori, R. Champagne. Experimental study of Thunder: A new generation of piezoelectric actuators. Proceedings of the SPIE—The International Society for Optical Engineering, 3675, 63-71 (1999).

[4] R. W. Schwartz, M. Narayanan. Development of high performance stress-biased actuators through the incorporation of mechanical pre-loads. Sensors and Actuators A, 101, 322-333 (2002).

[5] U.S. Patent no. 5,471,721 to G.H. Haertling. Method for making monolithic prestressed ceramic devices (1995).

[6] U.S. patent no. 5,632,841 to R.F. Hellbaum, R.G. Bryant, R.L. Fox. Thin layer composite unimorph driver and sensor (1997).

[7] K.M. Mossi, G.V. Selby, R.G. Bryant. Thin-layer composite unimorph ferroelectric driver and sensor properties. Materials Letters, 35, 39-49 (1998).

[8] S.A. Wise. Displacement properties of Rainbow and Thunder piezoelectric actuators. Sensors and Actuators A, 69, 33-38 (1998).

[9] E. Furman, G. Li, G.H. Haertling. Electromechanical properties of Rainbow devices. Ninth IEEE International Symposium on Applications of Ferroelectrics, 146-149 (1995).

[10] D.H. Robbins, J.N. Reddy. Analysis of piezoelectrically actuated beams. Computers and Structures, 41, 265-279 (1991).

[11] G. Li, E. Furman, G.H. Haertling. Stress-enhanced displacements in PZLT Rainbow Actuators. Journal of the American Ceramic Society, 80, 1382-1388 (1997).

[12] B.D. Cullity. *Elements of x-ray diffraction* (2nd ed.; Addison-Wesley, 1978).

[13] M.E. Lines and A.M. Glass. *Principles and applications of ferroelectrics and related materials* (Clarendon, Oxford, 1977).

[14] C.Z. Rosen, B.V. Hiremath, and R. Newnham. *Piezoelectricity (*American Institute of Physics, 1992).

[15] A.L. Kholkin, C. Wuetchrich, D.V. Taylor, and N. Setter. Interferometric measurements of electric field-induced displacements in piezoelectric thin films. Review of Scientific Instruments, 67, 1935-1941 (1996).

[16] J.-F. Li, P. Mosesm and D. Viehland. Simple, high-resolution interferometer for the measurement of frequency-dependent complex piezoelectric responses in ferroelectric ceramics. Review of Scientific Instruments, 66, 215-221 (1995).

[17] Q. Zhang, W. Pan, and L.E. Cross. Laser interferometer for the study of piezoelectric and electrostrictive strains. Journal of Applied Physics, 63, 2492-2496 (1988).

[18] Q. Zhang, S. Jang, and L.E. Cross. High-frequency strain response in ferroelectrics and its measurement using a modified Mach-Zehnder interferometer. Journal of Applied Physics, 65, 2807-2813 (1989).

[19] G. Binnig, C.F. Quate, and C.H. Gerber. Atomic Force Microscope. Physics Review Letters, 56, 930-933 (1986).

[20] H. Birk, J. Glatz-Reichenbach, L. Jie, E. Schreck, and K. Dransfield. The local piezoelectric activity of thin polymer films observed by scanning tunneling microscopy. Journal of Vacuum Science and Technology B, 9, 1162-1165 (1991).

[21] L. Jie, C. Baur, B. Koslowski, and K. Dransfield. Study of the microscopic ferroelectric properties of copolymer P(VDF-TrFE) films. Physica B: Condensed Matter, 204, 318-324 (1995).

[22] A.Gruverman, O.Auciello, H.Tokumoto. Nanoscale investigation of fatigue effects in Pb(Zr,Ti)O3 films. Applied Physics Letters, 69, 3191-3193 (1996).

[23] T. Hidaka, T. Maruyanma, I. Saitoh, L.A. Wills, R. Hiskes, S.A. Dicarolis and J. Amano. Characteristics of PZT thin films as ultra-high density recording media. Integrated Ferroelectrics, 17, 319-327 (1997).

[24] O. Auciello, A. Gruverman, and H. Tokumoto. Scanning force microscopy study of domain structure in Pb(ZrxTi1-x)O3 thin films and Pt/PZT/Pt and RuO2/PZT/RuO2 capacitors. Integrated Ferroelectrics, 15, 107-114 (1997).

[25] A. Gruverman, O. Auciello, and H. Tokumoto. Imaging and control of domain structures in ferroelectric thin films via scanning force microscopy. Annual Review of Material Science, 28, 101-123 (1998).

[26] J.A. Christman, R.R. Woolcott, A.I. Kingon, R.J. Nemanich. Piezoelectric measurements with atomic force microscopy. Applied Physics Letters, 73, 3851-3853 (1998).

[27] J.A. Christman, S.-H. Kim, H. Miawa, J.-P. Maria, B.J. Rodriguez, A.I. Kingon and R.J. Nemanich. Spatial variation of ferroelectric properties in Pb(Zr0.3, Ti0.7)O3 thin films studied by atomic force microscopy. Journal of Applied Physics, 87, 8031-8034 (2000).

[28] S. V. Kalinin, and D.A. Bonnell. Imaging mechanism of piezoresponse force microscopy of ferroelectric surfaces. Physics Review B (Condensed Matter and Materials Physics), 65, 125408/1-11 (2002).

[29] A. Gruverman, B.J. Rodriguez, R.J. Nemanich, and A.I. Kingon. Nanoscale observation of photoinduced domain pinning and investigation of imprint behavior in ferroelectric thin films. Journal of Applied Physics, 92, 2734-2739 (2002).

[30] S. Hong, E.L. Colla, E. Kim, D.V. Taylor, A.K. Tangantsev, P. Muralt, K. No, and N. Setter. High resolution study of domain nucleation and growth during polarization switching in Pb(Zr,Ti)O3 ferroelectric thin film capacitors. Journal of Applied Physics, 86, 607-613 (1999).

[31] M. Alexe, A. Gruverman, C. Harnagea, N.D. Zakharov, A. Pignolet, D. Hesse and J.F. Scott. Switching properties of self-assembled ferroelectric memory cells. Applied Physics Letters, 75, 1158-1160 (1999).

[32] M. Alexe, C. Harnagea, D. Hesse, and U. Gosele. Polarization imprint and size effects in mesoscopic ferroelectric structures. Applied Physics Letters, 79, 242-244 (2001).

[33] I. Stolichnov, E. Colla, A. Tagantsev, S. Bharadwaja, S. Hong, N. Setter, J.S. Cross, and M. Tsukada. Unusual size effect on the polarization patterns in micron-size Pb(Zr,Ti)O3 film capacitors. Applied Physics Letters, 80, 4804-4806 (2002).

[34] A. Gruverman, B.J. Rodriguez, A.I. Kingon, R.J. Nemanich, J.S. Cross, and M. Tsukada. Spatial inhomogeneity of imprint and switching behavior in ferroelectric capacitors. Applied Physics Letters, 82, 3071-3073 (2003).

[35] A. Gruverman, B.J. Rodriguez, A.I. Kingon, R.J. Nemanich, J.S. Cross, and M. Tsukada. Mechanical stress effect on imprint behavior of integrated ferroelectric capacitors. Applied Physics Letters, 83, 728-730 (2003).

[36] L.M. Eng, H.-J. Guntherodt, G. Rosenman, A. Skliar, M. Oron, M. Katz, and D. Egar. Nondestructive imaging and characterization of ferroelectric domains in periodically poled crystals. Journal of Applied Physics, 83, 5973 (1998).

[37] L.M. Eng, M. Abplanalp, P. Gunter. Ferroelectric domain switching in tri-glycine sulphate and barium-titanate bulk single crystals by scanning force microscopy. Applied Physics A, 66, S679-S683 (1998).

[38] M. Abplanalp, L.M. Eng, P. Gunter. Mapping the domain distribution at ferroelectric surfaces by scanning force microscopy. Applied Physics A, 66, S231-S234 (1998).

[39] L.M. Eng, H.J. Guntherodt, G.A. Schneider, U. Kopke and J. M. Saldana. Nanoscale reconstruction of surface crystallography from three-dimensional polarization distribution in ferroelectric barium-titanate ceramics. Applied Physics Letters, 74, 233-235 (1999).

[40] A. Roelofs, U. Bottger, R. Waser, F. Schlahof, S. Trogisch, L.M. Eng. Differentiating 180 ° and 90 ° switching of ferroelectric domains with three-dimensional piezoresponse force microscopy. Applied Physics Letters, 77, 3444-3446 (2000).

[41] C.S. Ganpule, V. Nagarajan, B.K. Hill, A.L. Roytburd, E.D. Williams, S.P. Alpay, A. Roelofs, R. Waser, and L.M. Eng. Imaging three-dimensional polarization in epitaxial polydomain ferroelectric thin films. Journal of Applied Physics, 91, 1477-1481 (2002).

[42] S. Hong, J. Woo, H. Shin, J.U. Jeon, Y.E. Pak, E.L. Colla, N. Setter, E. Kim, K. No. Principle of ferroelectric domain imaging using atomic force microscope. Journal of Applied Physics, 89, 1377-1386 (2001).

[43] A.L. Kholkin, V.V Shartsman, A.Y. Emelyanov, R. Poyato, M.L. Calzada, L. Pardo. Stress-induced suppression of piezoelectric properties in PbTiO3:La thin films via scanning force microscopy. Applied Physics Letters, 82, 2127-2129 (2003).

[44] X. Du, U. Belegundu, K. Uchino. Crystal orientation dependence of piezoelectric properties in lead zirconate titanate: Theoretical expectation for thin films. Japanese Journal of Applied Physics, Part 1: Regular Papers & Short Notes & Review Papers, 36, 5580-5587 (1997).

[45] X. Du, J. Zheng, U. Belegundu, K. Uchino. Crystal orientation dependence of piezoelectric properties of lead zirconate titanate near the morphotropic phase boundary. Applied Physics Letters, 72, 2421-2423 (1998).

[46] X. Du, Q.-M. Wang, U. Belegundu, A. Bhalla, K.Uchino. Crystal orientation dependence of piezoelectric properties of single crystal barium titanate. Materials Letters, 40, 109-113 (1999).

[47] S. Kalpat, X. Du, I.R. Abothu, A. Akiba, H. Goto, and K. Uchino. Effect of crystal orientation on dielectric properties of lead zirconium titanate thin films prepared by reactive RF-sputtering. Japanese Journal of Applied Physics, 40, 713-717 (2001).

[48] C. Harnagea, A. Pignolet, M. Alexe, and D. Hesse. Piezoresponse scanning force microscopy: What quantitative information can we really get out of piezoresponse measurements on ferroelectric thin films. Integrated Ferroelectrics, 38, 23-29 (2001).

[49] K. Franke, J. Besold, W. Haessler, C. Seegebarth. Modification and detection of domains on ferroelectric PZT films by scanning force microscopy. Surface Science Letters, 302, L283-L288 (1994).

[50] P. Guthner and K. Dransfeld. Local poling of ferroelectric polymers by scanning force microscopy. Applied Physics Letters, 61, 1137-1139 (1992).

[51] T. Hidaka, T. Maruyama, M. Saitoh, N. Mikoshiba, M. Shimizu, T. Shiosaki, L.A.Wills, R. Hiskes, S.A. Dicarolis, and J. Amano. Formation and observation of 50 nm polarized domains in PbZr1-xTixO3 thin film using scanning probe microscope. Applied Physics Letters, 68, 2358-2359 (1996).

[52] A. Gruverman, O. Auciello, H. Tokumoto. Scanning force microscopy for the study of domain structure in ferroelectric thin films. Journal of Vacuum Science and Technology B, 14, 602-605 (1996).

[53] E.L. Colla, S. Hong, D.V. Taylor, A.K. Tagantsev, and N. Setter. Direct observation of region by region suppression of the switchable polarization (fatigue) in Pb(Zr,Ti)O3 thin film capacitors with Pt electrodes. Applied Physics Letters, 72, 2763-2765 (1998).

[54] B.J. Rodriguez, A. Gruverman, A.I. Kingon, R.J. Nemanich, and O. Ambacher. Piezoresponse force microscopy for polarity imaging of GaN. Applied Physics Letters, 80, 4166-4168 (2002).

[55] B.J. Rodriguez, A. Gruverman, A.I. Kingon, R.J. Nemanich and J.S. Cross. Three-dimensional high-resolution reconstruction of polarization in ferroelectric capacitors by piezoresponse force microscopy. Journal of Applied Physics, 95, 1958-1962 (2004).

[56] S. Timoshenko. Journal of the Optical Society of America and Review of Scientific Instruments, 11, 233-255 (1925).

[57] B.J. Rodriguez. 2003. Doctoral dissertation, North Carolina State University, Raleigh, NC.

[58] Daniel Rosenthal. *Resistance and Deformation of Solid Media* (Pergamon, 1974).

[59] D. Roylance. *Mechanics of Materials* (John Wiley and Sons, 1996).

7. Motors Driven by THUNDER Actuators: Design and Performance

7.1. The Thunder-worm Linear Motor: Directly Coupled Motors

Several prototype motors were designed and built in an ongoing attempt to transform the compliance of THUNDER actuators from limitation to strength. Motors to be discussed in Section 7.1 were directly coupled to loading force, which was generated by movement along a metal rod encircled by a compression spring constrained lengthwise between the body of the motor and an end block.

The metal rod extended through an open bore along the central axis of each linear motor, allowing the motor to react against the rod and follow it as a guiding rail. The project goal was to store as much elastic energy as possible in the spring to be available for sudden release. As a traveling motor compressed the spring, the actuators in the motor experienced load-induced deflection from the force of the spring pushing back.

During indirect actuation, piezoelectric strain causes additional deflection, storing a larger strain energy in the actuator structure than appropriate for the loading force. With electric field off, elastic rebound introduces additional compression into the external spring load. Unfortunately, the external load thereby generates additional passive deflection in the actuator, which limits additional electrical field-induced deflection.

The purpose of the motor as a device is to allow the actuators to perform work on an external load in multiple steps. This involves clamping mechanisms to hold the position of the motor and block load resistance during the parts of the deflection cycle when the actuator recovers to a starting point. Clamping is seldom perfect, and clamp losses can limit the performance of a stepwise displacement motor.

In a piezoelectric motor of the this type, supporting the load across multiple actuators configured in parallel produces an additive increase in their collective stiffness. We would like to obtain the strain-amplified displacement of a unimorph while compensating for the stiffness and force capability surrendered in exchange for this amplification. The flexural actuator already incorporates intrinsic strain amplification due

to the mechanics of beams (or domes). Hence, as shown by Giurgiutiu [1], the load has a mechanical (force) advantage relative to active elements in the actuator.

Using a parallel actuator arrangement, the motor blocking force is increased, but if the goal is to store energy in a spring load, then the stiffness of the load must be matched to the stiffened actuator arrangement in the motor. As discussed in Chapter 2, energy transfer is maximized when load and actuator have equal stiffness. (Substantial displacement of a load which cannot apply comparable resisting force for lack of stiffness accomplishes little work.) If the structures supporting actuators introduce additional compliance, then actuator work output is also reduced.

7.1.1 Linear Motor Design and Principles of Operation

A linear motor was designed and built with two features in mind. First, 20 model 8R rectangular THUNDER actuators from Face International Corporation acted in parallel against the load, with the intent of assembling compliant actuators into a relatively stiff collective actuator. Second, passive clamps were used, simplifying the displacement cycle considerably. (The name, "Thunder-worm," is a contraction of THUNDER actuator and inchworm cycle motor.)

Passive clamps dispense with the need for timed pulses sent to powered clamps (actuated by solenoids, for example) in coordination with driving pulses sent to extensional actuators (the THUNDERs). An ideal passive latch would consist of a mechanism that simply did not allow movement in the blocked direction no matter how large the force behind the blocked movement or how high the frequency of back and forth movement. Conversely, movement in the allowed direction would encounter minimal resistance without force or time constraints.

The clamp design that was used is not new, although using it for an inchworm cycle piezoelectric motor may be a new application. [2] Essentially, a pivoting plate attached to a motor clamp assembly has a hole slightly larger than the diameter of the axial rod which threads through the plate and through the entire motor. The plate is slightly

angled so that the rod passing through in one direction tends to rotate the plate toward perpendicularity with the rod axis, allowing unblocked passage through the enlarged hole. Motion in the other direction immediately draws the plate further from perpendicularity, binding the rod as the projected diameter of the angled hole presents insufficient clearance along the axial direction. A weak pre-load spring ensures that the plate remains in a position where the difference between allowing and blocking movement of the rod involves a tiny angular shift. The schematic operation of this mechanism is shown in Figure 7.1.1—1. A detailed analysis of its operation as piezoelectric motor clamp was given in [3] and summarized in [14], which examines various features of the Thunder-worm linear motor operation. As with all inchworm cycle stepwise displacement motors, our motors have a front clamp and a rear clamp.

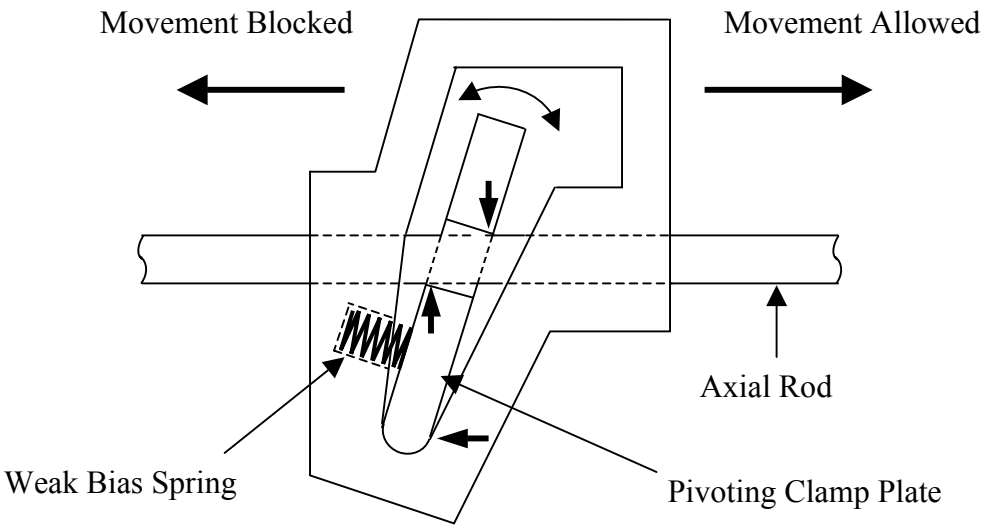

Figure 7.1.1—1. Schematic passive clamp permitting travel in one direction only. Binding points indicated by three short arrows. (Assume rod is stationary.)

The design of two versions of the Thunder-worm motor will be evident from photographs presented in Figures 7.1.1—2 through 7.1.1—5. Figure 7.1.1—2 shows the Thunder-worm previously described, driven by 20 model 8R rectangular THUNDER actuators. An important point is that the front and back sections are not connected except through the stacked actuators. The rear section consists of both the rear clamp and the shells of the actuator boxes. A gap between the inner pair of actuator boxes allows the metal rod to thread through the device. Figure 7.1.1—3 shows a close view of actuator boxes, where the parallel stack of THUNDER actuators are separated by a line of brass rod segments that have small, parallel holes drilled through their cross-sectional diameters on each side, with clearance for the actuators. Two 0-80 machine screws thread through each

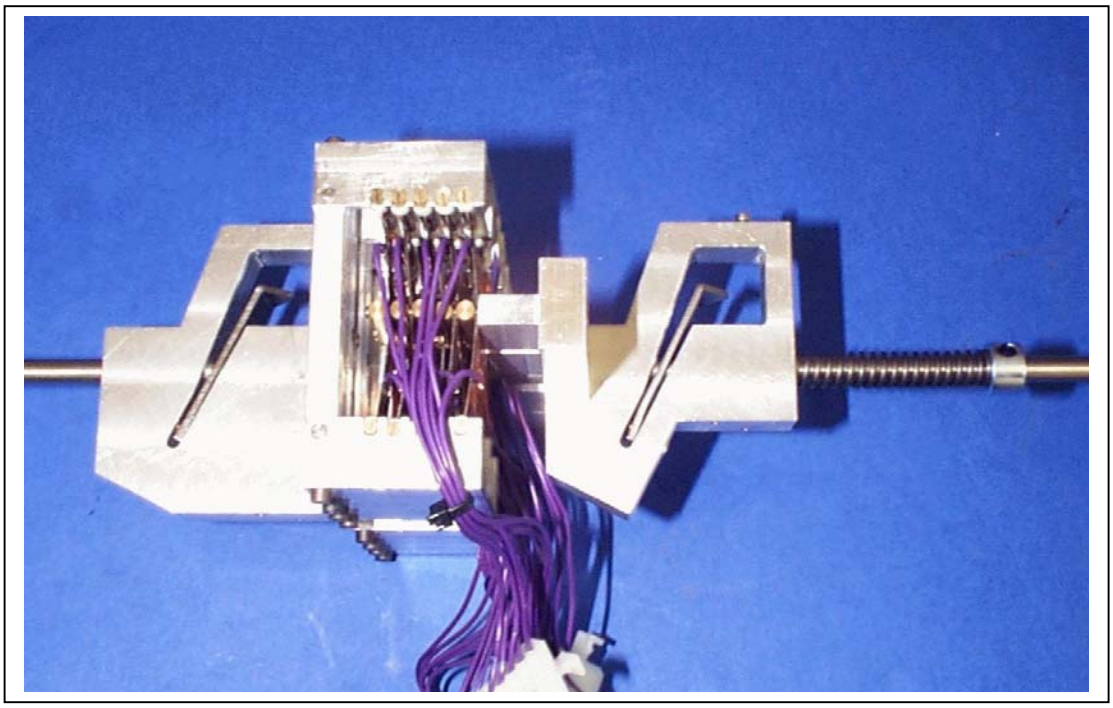

Figure 7.1.1—2. (color) Linear Thunder-worm using 20 rectangular beam actuators (Photograph by graduate student, N.C. State University Center for Robotics and Intelligent Machines)

set of brass rod segments and fasten all five actuators in a set to the front bar. The orange strips are Kapton polyimide film used for electrical insulation. Figure 7.1.1—4 shows a group of circular actuators custom manufactured by Face International Corporation to our requirement for a central hole. A stacked set of circular THUNDER actuators formed the basis for a Round Thunder-worm linear motor shown in Figure 7.1.1—5.

Figure 7.1.1—3. (color) Close-up of parallel arrangement in each actuator box, showing end axles and center pivots (Photograph by graduate student, N.C. State University Center for Robotics and Intelligent Machines)

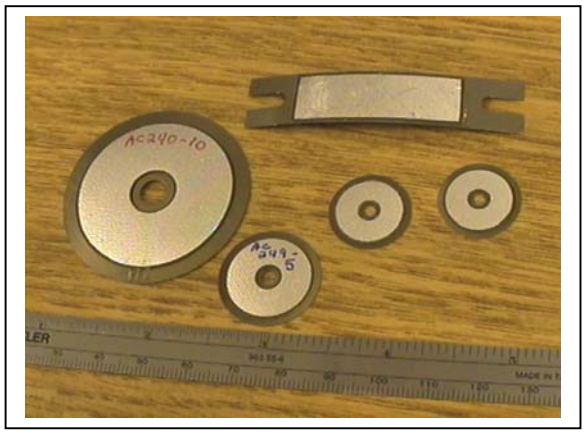

Figure 7.1.1—4. (color) Circular THUNDER actuators custom–made with central hole, shown alongside model 8R THUNDER

As with the motor built using rectangular actuators, the front and back sections of the Round Thunder-worm are not connected except through the set of stacked circular actuators. A threaded sleeve, visible in Figure 7.1.1—5, fastens the center of each actuator to the body of the front clamp. The cylindrical actuator shell is fastened to the rear clamp.

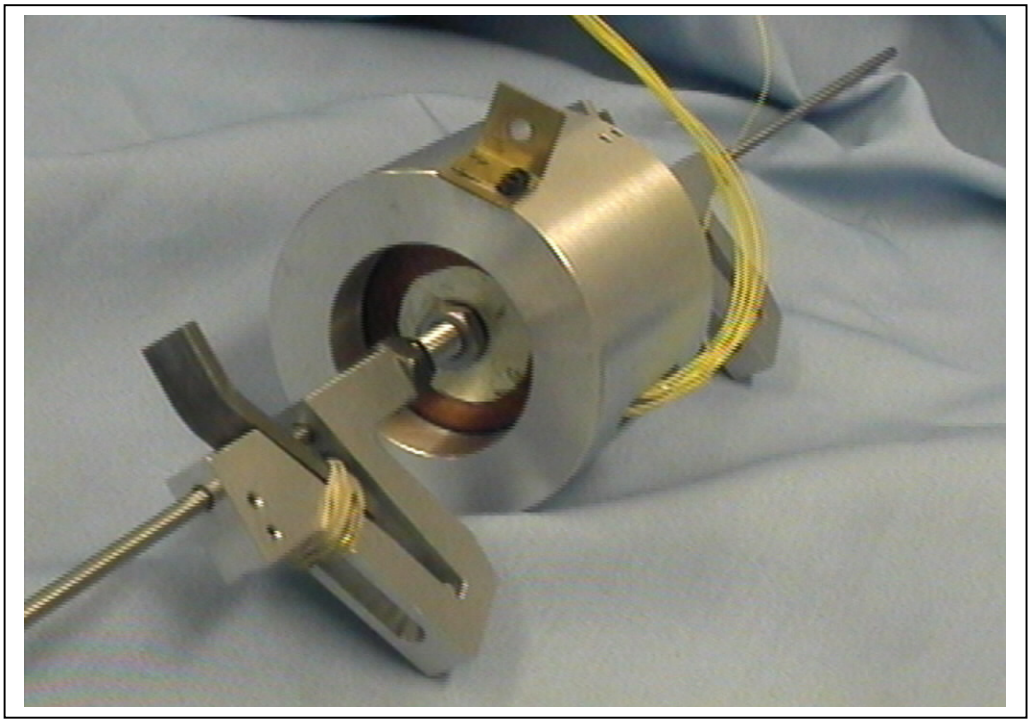

Figure 7.1.1—5. (color) Linear Thunder-worm using nine circular THUNDER actuators stacked in parallel, threaded by axial rod (Photograph by graduate student, N.C. State University Center for Robotics and Intelligent Machines)

The metal rod threads through each clamp and through the sleeve. The Round Thunder-worm also has its own version of the brass rod segments serving as end axles and center pivots. On either side, both the center and perimeter actuator surfaces are supported by closely fitting brass rings of circular cross-section. This is effectively the same as a simply supported beam actuator on knife-edge supports for any arc-shaped cross-section of the circular actuators. Of course, any misalignment, gaps, or play in the supports causes appreciable loss in the output of the collective actuators. Attempting to circumvent this problem by too-tight clearances or undue compression of actuator stacks also causes appreciable loss in the output of the collective actuators.

Circular THUNDER actuators are geometrically stiffer than beam THUNDER actuators of comparable size because a dome is an inherently stiffer structure than an arc. Essentially, every cross-section of a dome about its axis is an arc, and they are mutually self-reinforcing against axial loads. The trade-off is that a stiffer pre-stressed unimorph generally provides lower displacement for the same piezoelectric strain. Based on actuator stiffness alone, the Round Thunder-worm linear motor should exhibit superior performance in comparison with the Thunder-worm motor driven by rectangular THUNDER actuators. The displacement step size of the former would be less than that of the latter, but blocking force against a spring resistance of comparable stiffness should be greater.

7.1.2 Summary of Characterization Results

From among many experiments conducted on the round and rectangular linear motors by me and by other researchers in our group, the following results will illustrate which factor was found to control the performance of a piezoelectric motor of the design given here. However, some background information should be provided. First, note that an inchworm cycle based on indirect actuation is slightly different than the usual cycle based on a direct extensional actuation such as is provided by a piezoelectric stack.

In the latter case, forward movement occurs when the electric field is on and the actuator expands, performing work against any load present. When the electric field is off, actuator contraction pulls the back end of the device forward as well. The indirect actuation cycle differs in that when the electric field is on, the actuators flatten (relatively speaking) and pull the back end of the device forward. When the electric field is off, elastic rebound pushes against the load and achieves forward movement. As the actuators flatten and pull the back end of the device forward in the first half of the cycle, the job of the rear clamp is to hold the back end at however far a forward position it has attained while the front end rebounds forward from this newly advanced position.

Figure 7.1.2—1 illustrates the explanation just given. The front and rear clamps are indicated by electronic diode symbols, with the idea that only forward motion (to the right) is allowed. Neither clamp can move leftward regardless of the distance between them. The metal rod along which the Thunder-worms travel has not been portrayed in the figure, but it would thread through both clamps without interfering with actuator movement. The lightning bolt symbol indicates that the electric field is on during step B, which causes the actuator to flatten. During this step, the back part of the motor advances, then remains at its maximum forward position. When the electric field is off in step C, the elastic rebound of the actuator moves the front part of the motor forward, accomplishing work against any load present. Net forward displacement for one cycle is indicated by the dotted lines.

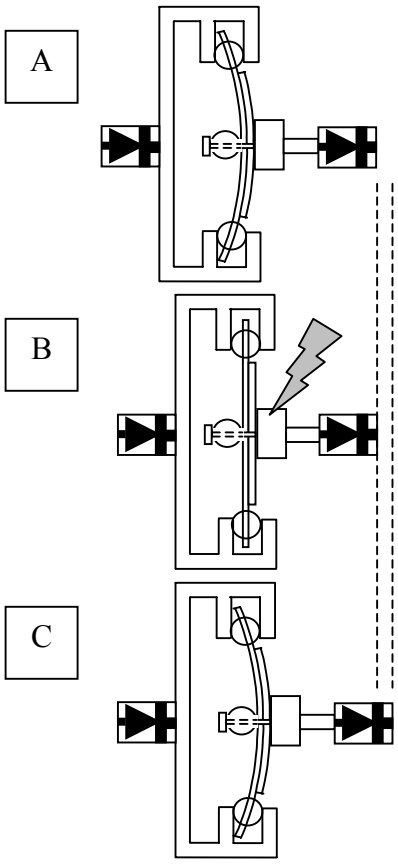

Figure 7.1.2—1. Illustration of the inchworm cycle based on indirect actuation (Steps explained in text)

This careful explanation of the inchworm cycle based on indirect actuation will aid in interpreting Figure 7.1.2—2. The performance of the linear motors was measured by mounting the metal rod previously mentioned in ringstands clamped to the lab bench. A spring of known stiffness (music wire compression springs, MSC Industrial Supply Co.) was sandwiched between the front of the Thunder-worm motor and a split collar ("end block") with slight initial compression to ensure lack of play. The gap between motor and end block was measured as needed with digital calipers. A pair of LVDT displacement gauges was attached to the front half and to the rear half of the Thunder-worm motor, with the idea of independently

tracking the displacement of each part. A LabView Program provided a train of square wave pulses as an input to the high-voltage amplifier, as discussed in Chapter 3, which drove the linear motor for a specific number of cycles, such as fifty. The drive signal had a frequency of 2 Hz. Results were captured on the oscilloscope by pressing the "hold" button.

In Figure 7.1.2—2, the blue trace indicates movement of the back section of the motor; red indicates movement of the front section. The green trace follows applied electric field (as voltage difference): top horizontal segments indicate field on, bottom horizontal segments indicate field off. The magenta (violet-purple) trace is actuator

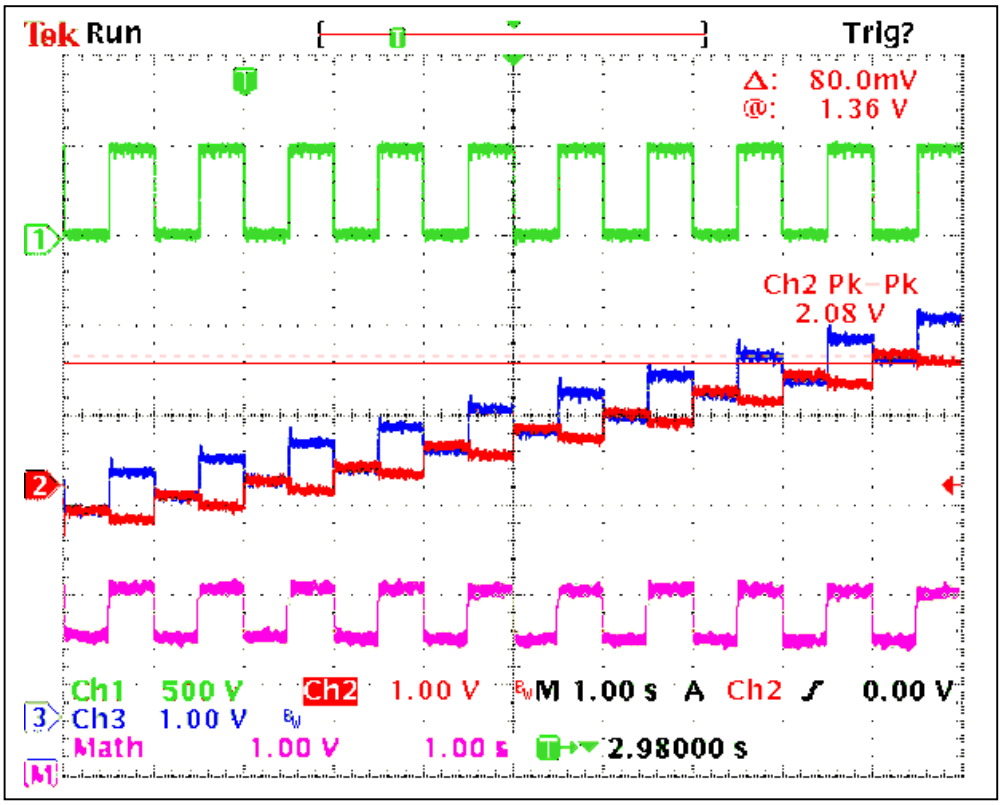

Figure 7.1.2—2. (color) An oscilloscope screen shot showing (red and blue) a portion of the displacement trace of front and back sections of a Thunder-worm linear motor producing compression of a spring load during forward movement

displacement, the difference between blue and red traces, which is provided by the math function in the oscilloscope. There are more subtle definitions of actuator displacement based on separating the differences during actuation and rebound, but careful analysis has shown that the alternatives produce more confusion, less insight, and approximately the same quantitative results.

Conditions were arranged so that any movement "upward" (screen orientation) is forward motion by the front or back parts of the Thunder-worm motor (red and blue traces). Any downward movement of the red or blue traces indicates backslip. In the magenta trace indicating actuator displacement, "upward" movement corresponds to actuator flattening as electric field is applied. While this is leftward displacement relative to the motor sign conventions as diagrammed, it is consistent with definitions elsewhere that "downward" actuator displacement occurs in the "+ y" direction.

Figure 7.1.2—3 shows a schematic breakdown of how various intervals on the oscilloscope trace correspond to relative displacements of front and back sections of the motor during two actuation cycles. The lines have been staggered for clarity. Note that the vertical distance between front and back traces, whether in the figure or on the oscilloscope screen shot, do not indicate distance between points of measurement on the front and back sections. The vertical separation only indicates relative displacements of each section from where it was when the motor was started. The various relative displacement intervals were measured on the oscilloscope using "h-bars," and the image was later measured using Photoshop graphic editing software. (The screen grid serves as a scale reference.) The resulting data forms the basis for analyzing motor performance.

During tests, the motors were subjected to several runs at increasing load. Consequently, forward movement diminished as spring resistance approached the motor blocking force. Before each run, the length of the space confining the spring was measured with digital calipers to provide an external frame of reference since LVDT gauges were reset to the beginning of their range. Given the initial spring length before testing, the benchmark intermediate lengths at the start of each run, and the net forward motion in each displacement cycle, displacements of the front and back sections of the motors could be

associated with incrementally increasing spring loads. By mapping actuator displacement, net forward movement, and backslip in each clamp against resistance force, the interaction of factors contributing to motor performance can be evaluated.

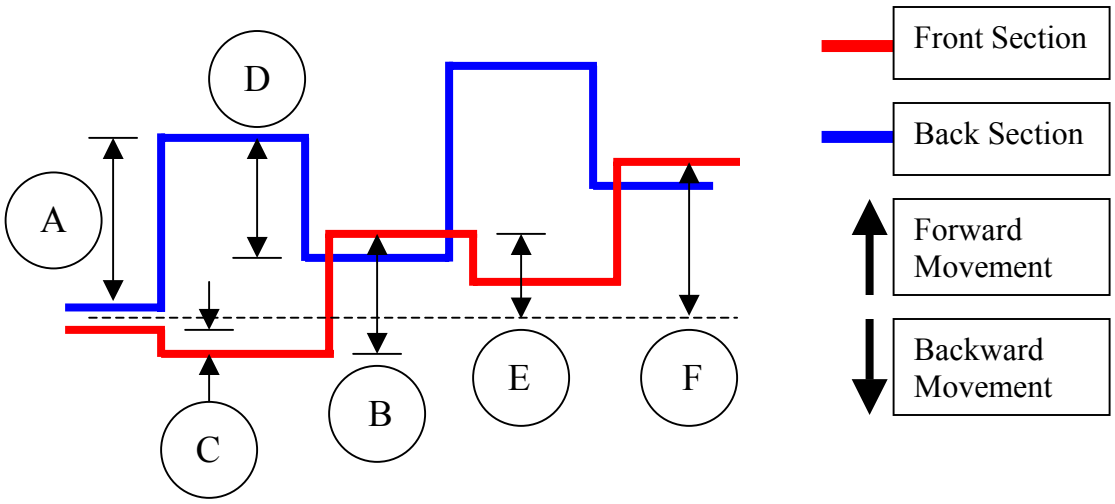

Figure 7.1.2—3. (color) Features of linear motor displacement cycle determined from oscilloscope traces

(A) Back section forward shift when electric field is on
(B) Forward movement of front section from elastic rebound when field is off
(C) Backslip of front section when back section shifts forward
(D) Backslip of back section when actuators rebound and push forward
(E) and (F) Net forward movement determined at front of motor

Two examples will illustrate what the various experiments have shown. In each case, key results are shown in two plots for clarity, but relate to the same data set, as will be explained. Figure 7.1.2—4 shows the results of an experiment on a Round Thunder-worm linear motor in which were installed four circular actuators made by Edward O'Malley of Clemson University. [4] The upper plot shows measured backslip of front

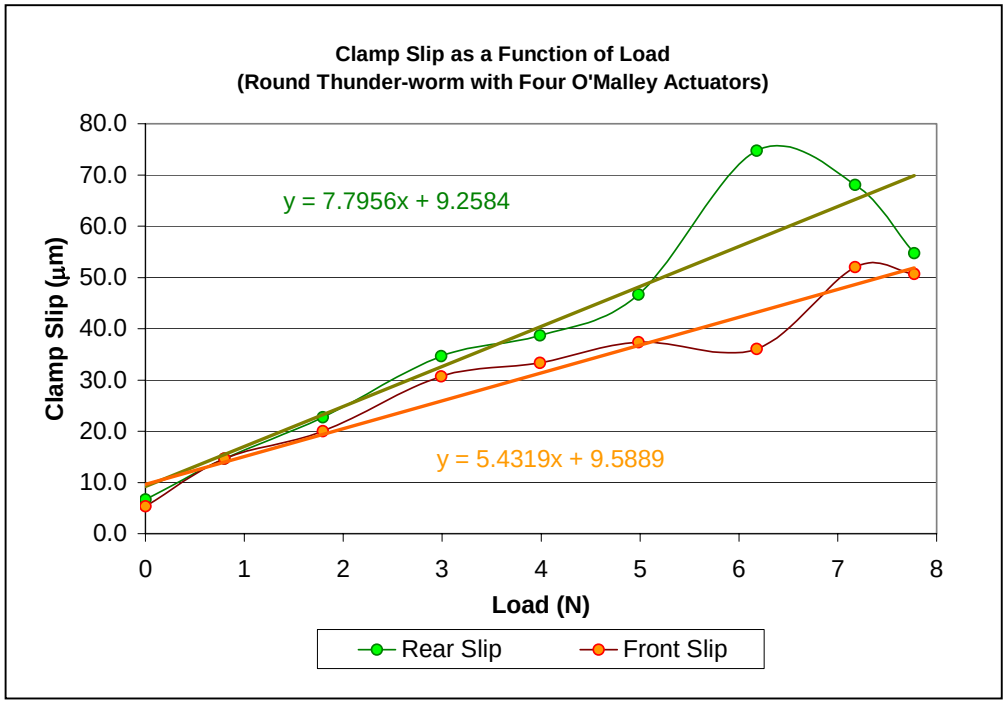

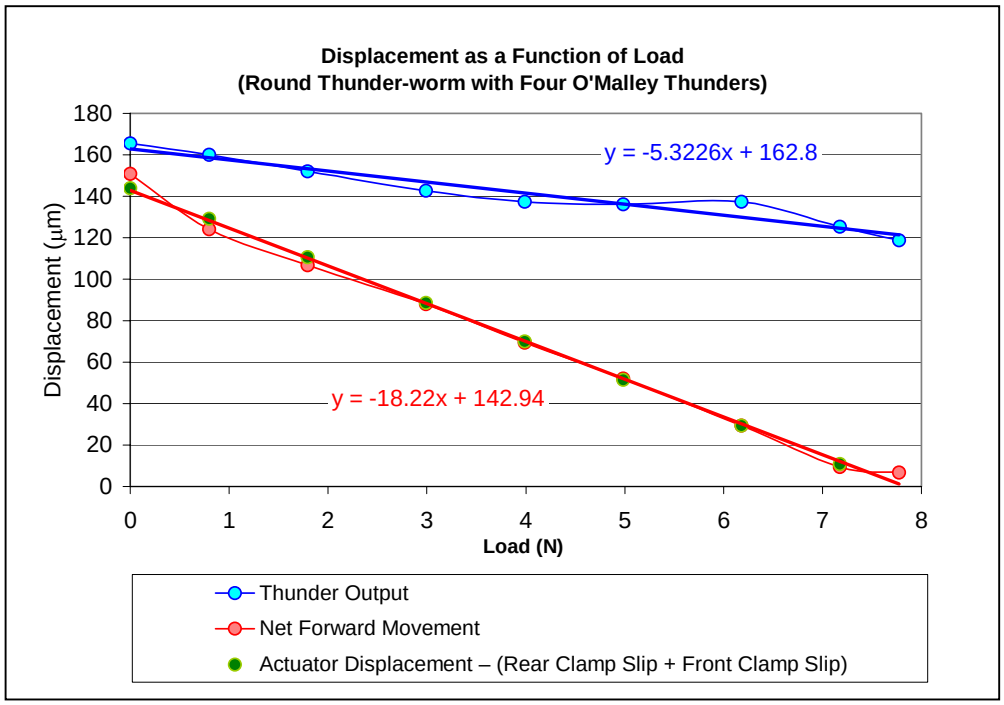

Figure 7.1.2—4. (color) Example of round Thunder-worm performance (Both plots relate to the same data set, as explained in text.)

and back clamps. Lines have been fitted to the data using the least squares method, and equations of the fitted lines are shown on the plot. The lower plot shows actuator displacement, "Thunder Output," and resulting motor displacement, "Net Forward Movement," with lines fitted to the data and equations of the fitted lines as shown in the other plot. The x-intercept (displacement goes to zero) of the lines is blocked force for the actuators and for the motor. Clearly, the motor blocked force is much smaller than the actuator blocked force (7.8 N as opposed to 30.6 N). Therefore, a portion of the displacement capacity of the actuators under load is unavailable to the motor. The logical suspect, of course, is the combination of clamp losses.

To test this hypothesis, the value of the actuator displacement trend line equation less the sum of the front and rear backslip equations (i.e, $y = (-5.3226 x + 162.8) - ((5.4319 x + 9.5889) + (7.7956 x + 9.2584))$) was calculated and plotted at each force value for which any displacement value was measured. The plotted values appear on the bottom plot as the green circles which fall precisely on the trend line for net forward movement. It appears that these are the data points to which the trend line for net forward movement has been fitted, but in fact they just fall on the line. Excluding variability, the difference in the trend of actuator displacement and motor movement is entirely accounted for by the combined trends in front and rear clamp slip. Of the two, backslip in the rear clamp causes greater loss.

This is reasonable because it occurs when actuators are rebounding and working against the load. During this short time, the front clamp probably cannot both allow forward movement and block the force of the load—so the rear clamp is supporting both the force of the load and providing a reaction to the rebound. It happens quickly: acceleration and vibration are probably both involved.

Figure 7.1.2—5 shows the results of an experiment on the Thunder-worm linear motor photographed in Figure 7.1.1—2. This motor uses 20 rectangular THUNDER actuators. Data for the experiment was taken in six runs, which have been kept separate in these plots. Also, total displacement of the motor, amounting to about 12 mm, has been plotted for reference. In this trace, one can see the data points getting closer together as

incremental forward movement of the motor diminishes under increasing load. Again, lines have been fitted to the data using the least squares method, and equations of the fitted lines are shown on the plot. Again, the upper plot shows measured backslip of front and back clamps, the lower plot shows actuator displacement, "Thunder Output," and resulting motor displacement, "Net Forward Movement."

The motor blocked force is not quite as much smaller than the actuator blocked force (12.8 N as opposed to 26.7 N) as was the case with the Round Thunder-worm. (We have to keep in mind that actuator blocked force refers to the collective structure of many individual actuators although an individual circular THUNDER actuator is considerably stiffer than an individual rectangular THUNDER actuator.) Once again, the value of the actuator displacement trend line equation less the sum of the front and rear backslip equations (i.e, $y = (-16.989\ x + 453.06) - ((-4.2163\ x + 171.58) + (12.693\ x - 40.017))$) was calculated and plotted at each force value for which any displacement value was measured.

The plotted values appear on the bottom plot as the bright green circles which fall precisely on the trend line for net forward movement. The correspondence is nearly exact at the scale of the plotted data, despite the considerable variability of the individual data points to which the lines were originally fitted. The variability of the data is interesting, but no attempt will be made to explain it. At loads less than about 5 N, there appear to be starting effects, possibly from acceleration, possibly from parts of the motor finding dynamic configurations which were not present when the motor was started. Again, the difference in the trend of actuator displacement and motor movement is entirely accounted for by the combined trends in front and rear clamp slip.

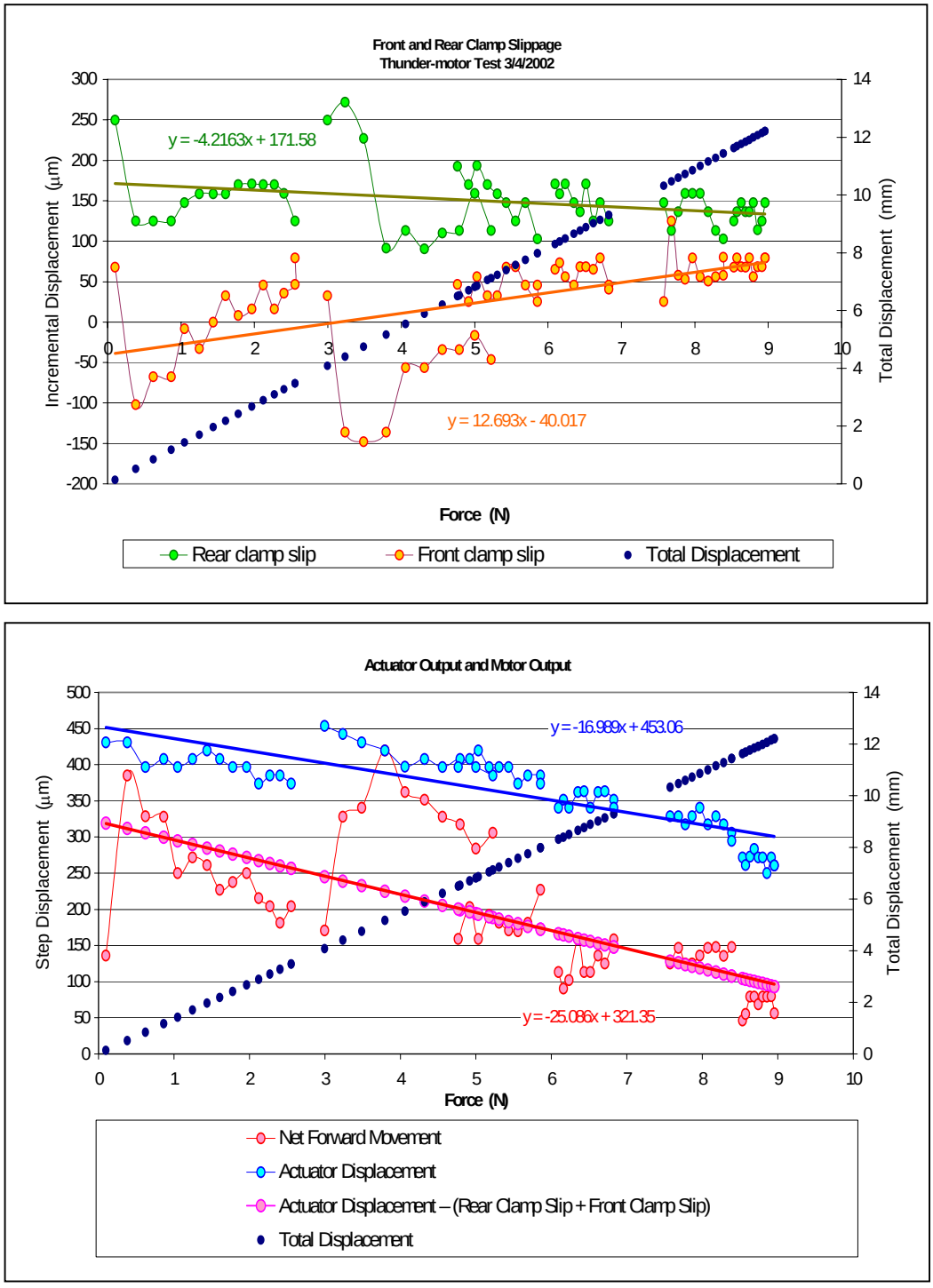

Figure 7.1.2—5. (color) First example of Thunder-worm performance (Both plots relate to the same data set, as explained in text.)

Figure 7.1.2—6 presents results of an earlier test of the Thunder-worm linear motor built with rectangular THUNDER actuators. The same experimental apparatus and load spring was used, but the test was conducted by another member of our group (Brian Dessent, 2000). It is not clear why the plots shown in Figure 7.1.2—5 appear to contain higher variability than Dessent's results shown in Figure 7.1.2—6. Motor performance is comparable, however. Results shown in Figure 7.1.2—5 correspond to an actuator blocking force of 26.8 N and a motor blocking force of 12.8 N. The results shown in Figure 7.1.2—6 correspond to an actuator blocking force of 22.6 N and a motor blocking force of 12.6 N.

The same procedure was followed in accounting for the difference between motor and actuator blocking force values. However, there is the difference that a linear fit was not adequate for representing the front clamp slip data; instead a cubic fit was needed. Consequently, the data for motor displacement (Net Forward Movement) was also fitted with a cubic equation, although a quadratic or even a linear fit would have been adequate. Again, the value of the actuator displacement trend line equation less the sum of the front and rear backslip equations (i.e, $y = (-19.436 x + 439.88) - ((4.0703 x + 44.699) + (0.2169 x^3 - 6.8335 x^2 + 66.574 x - 110.83))$) was calculated and plotted at each force value for which any displacement value was measured.

Calculated results were plotted as circles in the lower plot. While the calculated values do not appear to fall on top of the green fitted curve as in the two previous cases, the coincidence is quite good. In determining trend lines for clamp slip data and net forward movement for the plots shown in Figure 7.1.2—6, the first data point was omitted in each case since it clearly did not belong with the other data. (Whatever caused the unusually large, negative clamp slip, it created a net forward movement larger than the actuator output in this instance. Finally, "displacement efficiency" or "step efficiency" is simply the ratio of actuator output to net forward movement. It dramatizes how much of the actuator output is becoming lost to clamp slip.

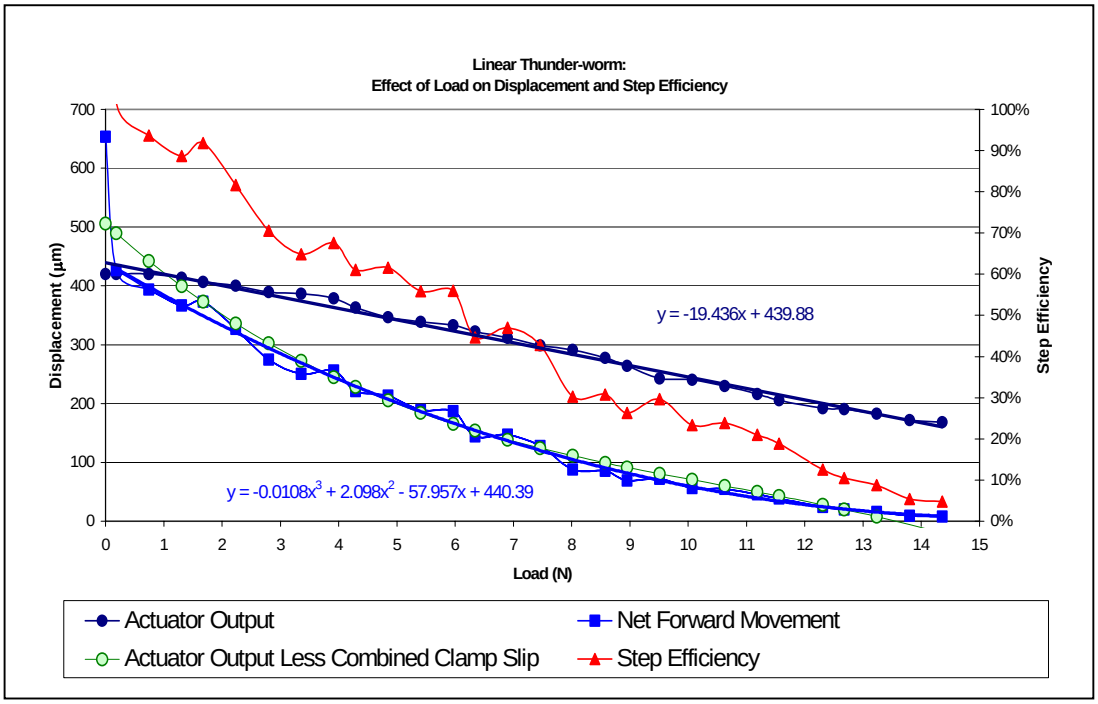

Figure 7.1.2—6. (color) Second example of Thunder-worm performance (Both plots relate to the same data set, as explained in text.)

Two additional plots are presented for general information. Figure 7.1.2—7 is important because no data for motor speed has been given as of yet. Unloaded motor speed peaks at a respectable 1.6 cm / s at what is clearly a resonant frequency—almost exactly 100 Hz. Since step size at low frequencies (e.g., 12 Hz) is relatively large, while motor speed is relatively low (but increases even as step size temporarily drops off), it is likely that energy storage effects due to frequency are enhancing motor performance, particularly since step sizes from 8-16 mm would be two to three times larger than dynamic displacement for an isolated THUNDER actuator.

Figure 7.1.2—8 simply shows that blocking force is not stable as frequency is increased. In fact, the plot may provide an indication of anti-resonant / resonant behavior at 80 Hz and 90 Hz, respectively. Above 90 Hz, blocking force may simply become a more variable quantity, given that higher frequency vibrations probably make it more difficult for passive clamps to hold their position.

At higher frequencies, mechanical vibration creates higher energy density within an object, facilitating loss of contact between surfaces held in place by static friction. This is an unstable equilibrium because dynamic friction is lower than static friction. If the static frictional contact is resisting a force (such as the motor spring load) that will shift the clamp position if not opposed, then higher frequency vibration can trigger loss of contact, followed by an immediate drop to the lower dynamic friction force, then slip to a position where the opposed force is reduced.

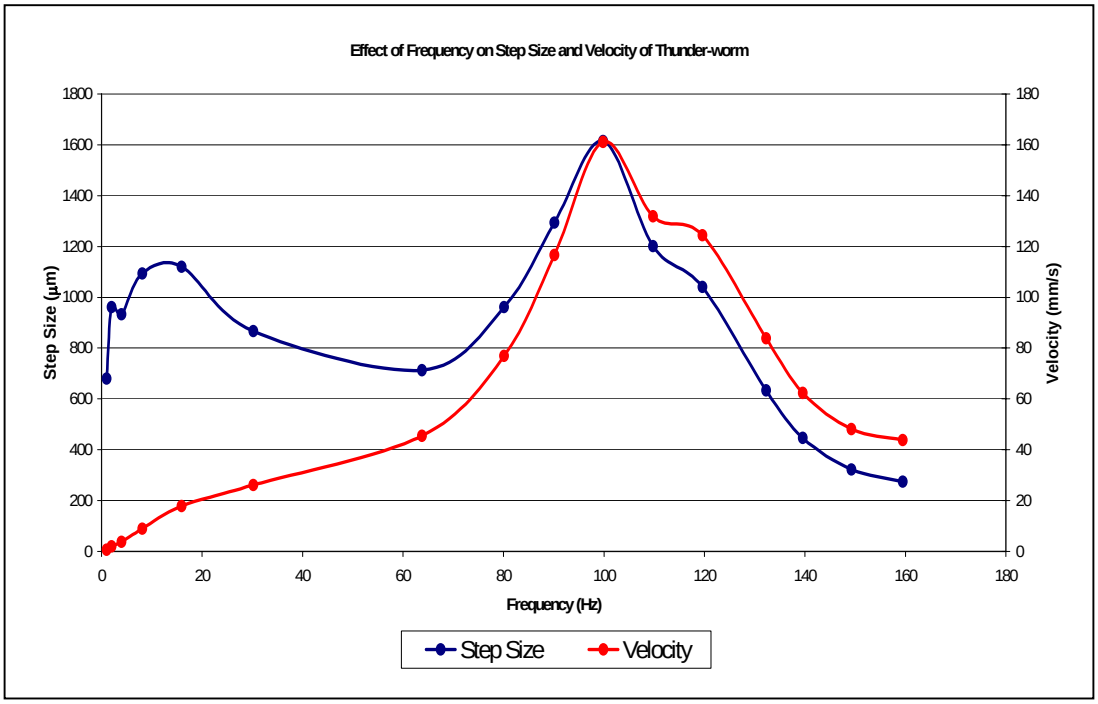

Figure 7.1.2—7. (color) Effect of frequency on motor speed and step size

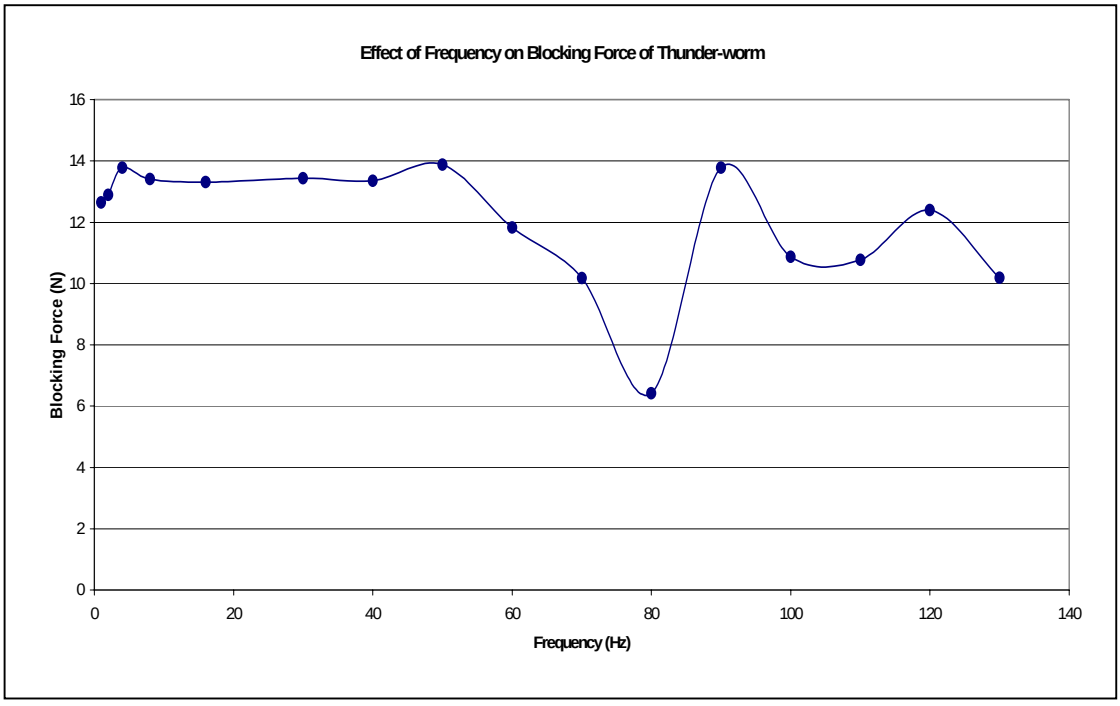

Figure 7.1.2—8. Effect of frequency on motor blocking force

7.1.3 Conclusions Regarding Linear Motor Results

Primary conclusions, then, are that clamp slip limits achievable blocking force, and accounts for the entire difference between actuator output and motor output. In addition, back clamp loss is larger than front clamp loss. Higher frequency operation probably degrades clamp performance. Nonetheless, it is difficult to make a conclusive statement about how clamp slip varies with increasing load.

The clamp design was the same for both the round actuator motor and rectangular actuator motor. In our experience, however, it was found that small factors, such as exact pivot point, specific pre-load spring placement and force, and wear of the edges of the clamp plate hole, can all affect how well the clamps operate.

For whatever reason, clamp losses in the Round Thunder-worm motor experiment started quite small (10 μm) and increased to between 40-60 μm at 8 N resistance force. At that point, the combined clamp losses (about 100 μm) were nearly as high as actuator displacement (about 120 μm). Initially, the losses were consuming only about one-eighth of the actuator output.

In the other Thunder-worm motor experiment, rear clamp losses started at about 170 μm and fell slightly to about 140 μm (disregarding initial excursions in the first two runs). At 8 N resistance force, it appears that both front and rear clamp losses were converging to about 100 μm. At the calculated motor blocking force of 12.8 N, actuator output would be 235 μm (using the trend line equation), so that again the combined clamp losses (about 200 μm) would be nearly as high as actuator displacement. However, initially the losses were consuming as much as one-third of the actuator output, a larger fraction than for the Round Thunder-worm motor.

Then, there is also the matter of negative front clamp loss in the first two runs of the motor with rectangular actuators, which partially offsets the higher losses in the rear clamp. Positive values of "slip" mean the clamp moved backward when it should have stayed still; negative "slip" values mean the clamp moved forward when it should have stayed still. Based on observations of the motor in operation, negative slip in the front

clamp happens when the forward movement of the back section of the motor under applied electric field occurs with such acceleration applied through a sufficiently long stroke that instead of only pulling the front clamp backward in reaction, it drives it forward due to impact. (In other words, instead of only providing a reaction to the actuators pulling the back section forward, the front section has to stop the motion of the back section after it has acquired substantial kinetic energy.) At higher resistance loads, this effect attenuates.

Based on these observations, the conjecture could be advanced that clamp losses do not necessarily always increase or decrease with load, but that higher actuator displacements are associated with higher losses. It could be that in the absence of kinetic effects (energy of internal motions), clamp losses do tend to start small and increase with increasing load, while presence of kinetic effects introduces initially divergent loss behavior that converges to a steady state at higher loads.

Finally, the experiments showed that the linear motor with stiffer actuators and higher actuator blocking force does not necessarily have the higher motor blocking force. The fact that the actuator output and net forward movement lines are much less divergent under increasing load for the rectangular actuator motor in spite of its large clamp losses suggests that high displacement is always helpful. In addition, kinetic effects probably introduce no overall advantage or disadvantage in terms of ultimate blocking force. The final conclusion (Figure 7.1.2—7) is that motor speed peaks at a resonant frequency.

7.2 The Rotary Thunder-motor: An Indirectly Coupled Motor

This section will describe how a rotary motor design originated. The working device achieved its best performance with actuators vibrating in resonance, as was the case with linear motors described above. An important observation which must not be lost in the following discussion , however, is that the resonant behavior of the rotary motor is not dependent on load, and in fact is little affected by load. This is why the section is subtitled, “an indirectly-coupled motor”.

The linear motors were directly-coupled because load force was directly applied through the front end of the motor to the center of the actuators, while reactions were applied through the back half of the motor to the mounted ends of the actuators. The actuators experienced increasing passive deflection under increasing load, which diminished their capability for additional deflection under applied electric field. Although not explicitly demonstrated by the data given, the resonant behavior of the actuators was strongly influenced by force and stiffness of the load. Clearly, the motor and load together formed a single elastic system. A sufficiently large load could completely suppress actuator deflection.

As will be seen, actuators in the rotary motor transfer deflection only through end rotation accompanying flexure. In the design soon adopted for the re-configurable prototype, actuators were mounted as vibrating cantilevers, that is, as though one end were embedded in a wall. A blocking torque would correspond to an unyielding wall, while a wall unable to constrain actuator end rotation would allow some transmission of rotation to an unseen external load. Actuator deflection is probably maximized, not suppressed, by an unyielding rather than "lossy" end mount (where loss occurs as rotation transferred out). The stiffness of the end condition can affect resonant behavior, but only weakly.

7.2.1 Conceptual Basis and Key Components

Some time after characterization of the linear motors had been completed, a new design for a rotary motor was developed and a prototype built. The original concept came from watching THUNDER actuators mounted in the test fixture (Figure 3.1.3—1) during operation. The angular displacement of the axles clamped to the ends of an actuator was clearly visible and noteworthy. By coupling the oscillatory movement of the THUNDER actuator to the axle through a "mechanical diode" that transfers torque in one direction but not in the other, continuous axle rotation would result. The one-way mechanism would lock actuator and axle together in the transfer direction but rotate freely around the axle in the other.

It happened that my advisor had once before directed the attention of our group to the work of Frank *et al* [5] in our previous attempts to develop piezoelectric stack- based motors. They reported a number of passive clamp designs based on wedges and rollers, and we had on hand a number of commercially available devices known as roller clutches or clutch bearings which they had found useful in their work. By adding clutch bearings to a mounting fixture for THUNDER actuators, a design emerged for a rotary Thunder-motor. Since the original design resembled the two-axle fixture shown in Figure 3.1.3—1, two axles are shown in Figure 7.2.1—1, which accompanies an explanation of how the motor works.

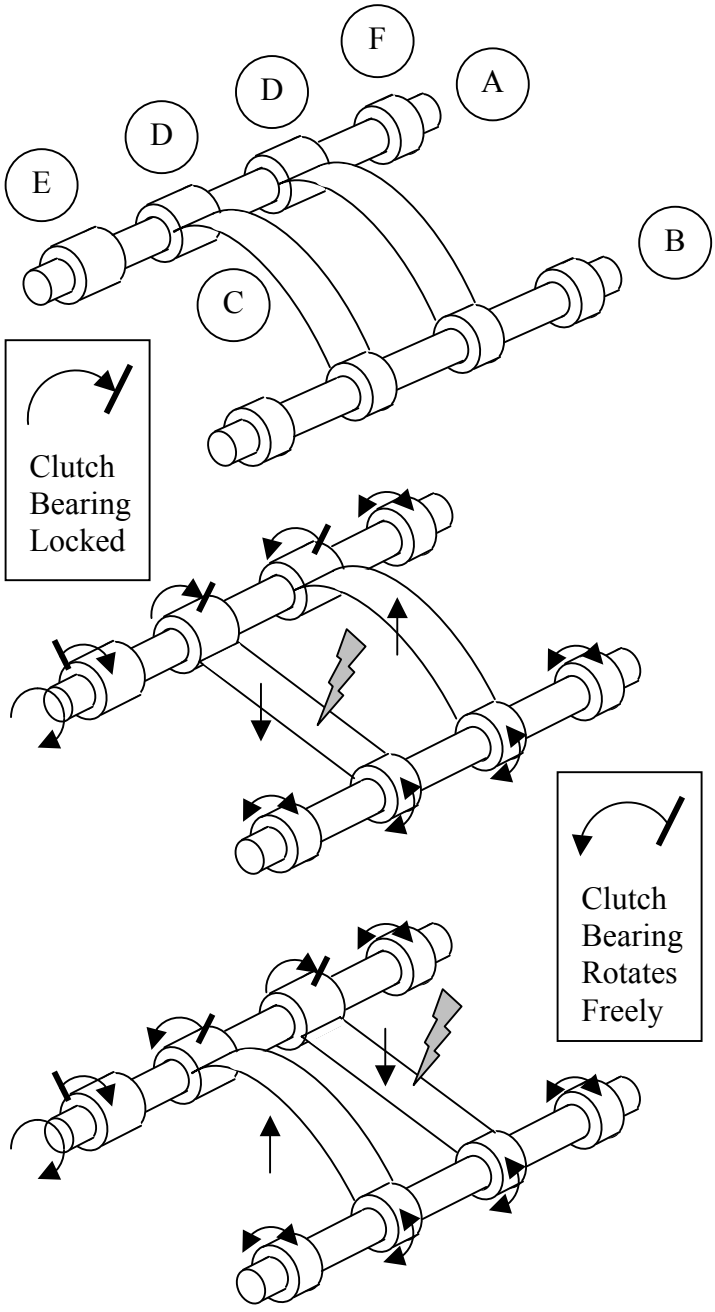

Figure 7.2.1—1.
Conceptual operation of rotary motor: components and actuation cycle (Steps explained in text)

The top drawing in Figure 7.2.1—1 shows the various components depicted in schematic form. Parts (A) and (B) are axles (e.g., hardened, polished steel rods).

The short, concentric, cylindrical segments around the axles at intervals are needle bearings. Although not explicitly indicated, it is assumed that the four bearings at the ends of the axles are clamped into support blocks that do not allow the bearings themselves to rotate.

Front (at left) and back (right) THUNDER actuators (C), shown with exaggerated curvature, are attached to roller clutch bearings (D) at one end in such a way that no hinge point results. In other words, a rotational moment at the end of the actuator is transferred to the bearing, in the same way that a loaded cantilever beam creates a resisting moment in the supporting structure in which its fixed end is embedded. The attachment is aligned so that the axial line of the axle is the center of transferred moments. Torque is applied to axle (A) when either actuator deflects in a direction that locks the clutch bearings.

Needle bearing (E) is also a roller clutch, but has been mounted on axle (A) so that its blocking direction (clockwise or counter-clockwise) is opposite that of the clutch bearings (D). Its job is to block back-rotation from a counter-torque-producing load. The bearings that are drawn as having shorter lengths, that is, bearing (F) and all four bearings on axle (B), are non-clutch needle bearings. They allow free rotation in both directions. This is symbolized by the double-ended arrows next to them in the middle and lower drawings. The free-rotation bearings at the ends of axle (B) are mechanically redundant.

The three-quarter round arrow shown at the front (left) of axle (A) indicates continuous output rotation. Axle (A) is considered the driven axle; axle (B) a passive hinge. However, by inserting appropriate additional clutch bearings, both axles could be driven in counter-rotation. Since clutch bearing (E) blocks back-rotation, the motor would operate if the actuators shown were driven in phase or if there were only one actuator. However, except for a possible flywheel effect, that would mean that torque would be applied to the output axle only half the time. Two actuators driven out of phase, as shown in the middle and lower drawings, means that one actuator always applies torque while the other rebounds. In the middle drawing, the front actuator flattens during applied electric field, indicated by the lightning bolt symbol, while the back actuator rebounds. The reverse situation is shown by the lower drawing. If all the clutch bearings were turned over, end-

over-end, and remounted on the axles, their blocked directions would all be reversed, and the actuators would apply torque to the driven axle during rebound. Alternatively, both actuators could be turned over, top to bottom, and achieve the same result.

The prototype motor design used roller clutch needle bearings (0.375-in. shaft diameter) from the Torrington Division of Ingersoll-Rand Corporation. Bearings to fit shaft diameter as small as 0.125 inch are also available. Needle bearing designs (clutch or not) are designed to add only a thin sectional increase to the cross-section of a shaft. In industry terminology, clutch bearings transition between lockup (blocked rotation) and overrunning (free rotation). The principle of operation is shown in Figure 7.2.1—2.

Essentially, a shell housing ball bearings or cylinder bearings has a cross-section that causes them to become wedged between inclined surfaces and the shaft surface if turned in the locking direction. Rotation in the opposite direction causes the bearings to move slightly toward the direction of greater clearance between shaft and inclined surfaces, allowing them to turn or slip freely. A simple way to accomplish this within a circular boundary is to use a regular polygonal cross-section for the inner surface because the apothem (distance from center of polygon to center of an edge) is always less than the radius (distance from center of polygon to a vertex). However, as the number of sides increases, the difference between the two rapidly becomes very small, and a toothed inner cross-section (with wedge-shaped teeth) could be used. A square section has been shown in Figure 7.2.1—2 to illustrate the polygonal approach because difference between radius and apothem is clearly evident for polygons with a small number of sides. Clutch bearings use light springs to maintain the bearings in positions where they are poised to lock up with a small angular shift toward the blocked direction.

Backlash (lost motion between engagement and disengagement of locking mechanism upon reversal of direction) of the clutch bearings is important. Indeed, analysis of linear motors in the previous sections exposed clamp losses as the limiting factor in their performance. In [5], measurements on an un-named commercial roller clutch found typical angular backlash of 0.3 degrees. While developing piezoelectric stack-based motors, our group determined angular slippage as a function of load for a 0.25-inch Torrington roller

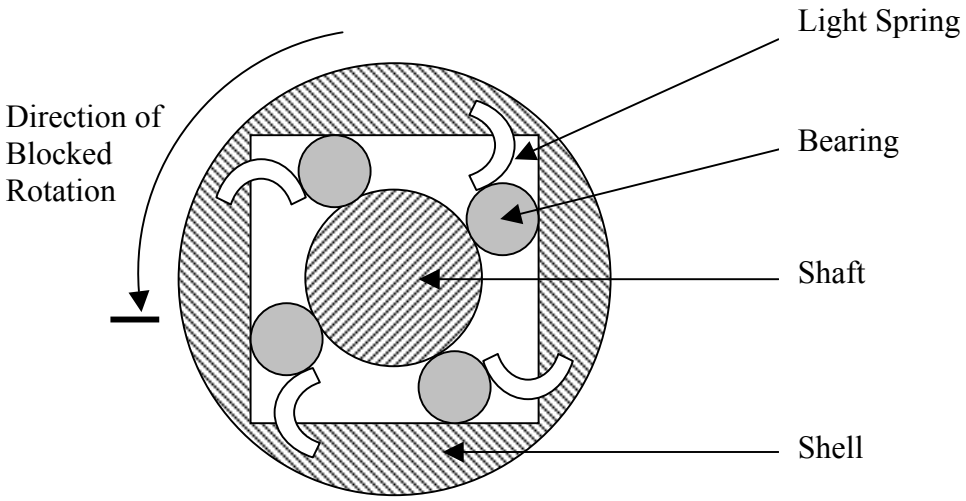

Figure 7.2.1—2. Schematic cross-section of clutch bearing with sectional taper based on radius and apothem of a square

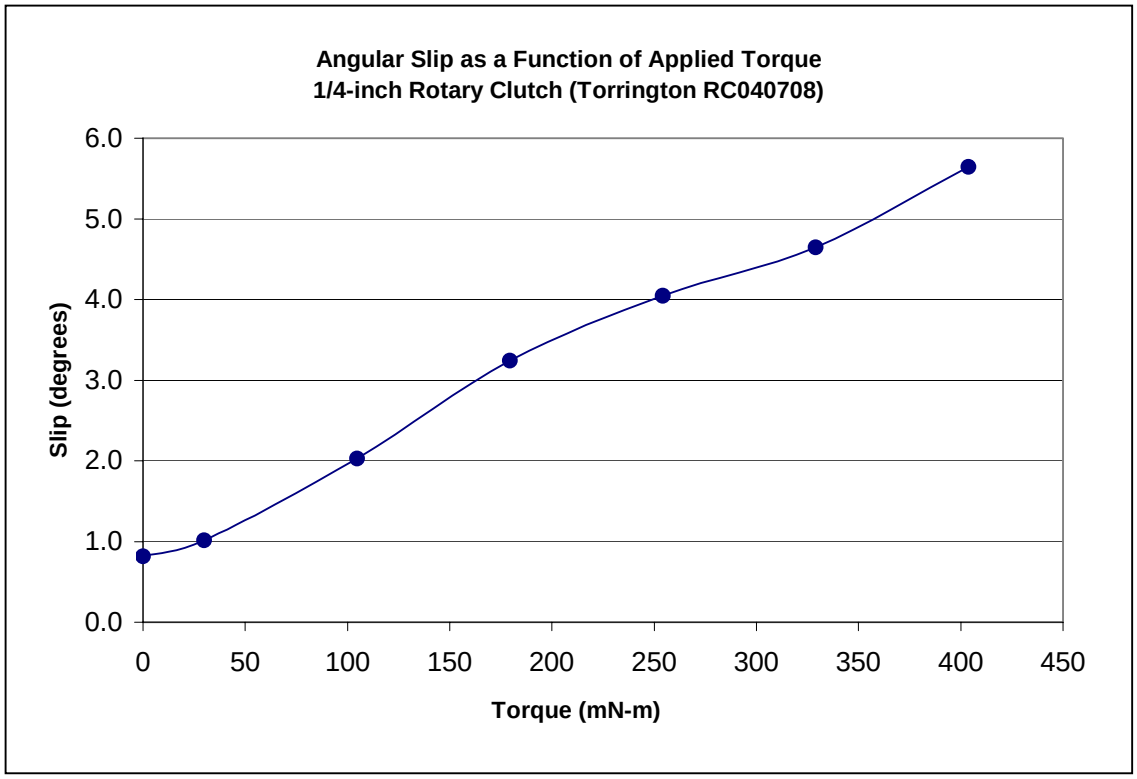

Figure 7.2.1—3. Plot of angular slip as a function of torque for 1/4-inch clutch bearing measured under static conditions

clutch bearing. The clutch bearing served as the mid-point pivot in a metal bar (about 8 inches across) on which was attached a laser pointer at one end and masses suspended at the other. The weight of the suspended mass attempted to rotate the bar in the direction blocked by the bearing. Figure 7.2.1—3 shows the results. [Brian Dessent, 2000]

It should be noted that results taken under static conditions may not correspond exactly to dynamic backlash occurring under similar loads when frequency is introduced as a new variable. Literature by the Torrington Company regarding drawn cup roller clutches places maximum engagement rates at 7000 per minute (117 Hz) for the higher-duty product line incorporating a fiberglass-reinforced nylon bearing cage with stainless steel leaf springs. [30] Rotary Thunder-motors in the current project were tested well above 117 Hz with no discontinuity in performance, and with maximum performance typically occurring above that frequency. While the clutch bearings may have introduced some losses, it must have been that the difference between rotation allowed and rotation blocked remained large enough for them to adequately serve as mechanical diodes.

After initial tests of the prototype rotary Thunder-motor, built with two axles as designed, it became apparent that the non-driven axle hampered motor performance considerably. It became apparent that the vibration spectrum of the actuator and mounts was energetic and complex. Instead of allowing simple free rotation and translation of the actuator end, the non-driven axle and collars caused small-scale warpage and binding which led to periodic stick-slip transitions, erratic changes in output speed, noise and mechanical wear. Motor performance was improved dramatically by removing the non-driven axle and collars, allowing the actuator to vibrate as a cantilever.

Small masses attached to the actuator in the cantilever configuration created a spring-mass system, also improving performance considerably. Given the initial curvature of a THUNDER actuator and consequent flexure about its centerline, the primary (usually only) attached mass was located at the center of the actuator, not the end. This implies a contribution from the second mode of flexural vibration for a cantilever in which the tips remain nearly stationary while maximum displacement occurs at mid-length.

The Rotary Thunder-motor design had evolved to resemble a rotary actuator

described by Mockensturm, Frank, Koopman, and Lesieutre in [7], providing examples of convergent design in my work and theirs. They had abandoned attempts to drive with piezoelectric stacks and had attached two, then twelve, bimorphs directly to a rotary clutch as cantilevers with large end-masses. They found, however, that their motor performed better when the bimorphs were excited into the second mode of vibration for cantilevers, in which end masses were nearly stationary and maximum flexure occurred at cantilever centers. However, when they replaced the end-masses with a slotted ring that clamped the bimorphs at their outer ends, motion was over-constrained and the motor failed to operate.

The prototype Rotary Thunder-motor was not one motor, but several different motors, depending on number and type of Thunders, whether directly or rebound driven, with drive signal in-phase or out-of-phase, or whether a smaller end-mass was attached in addition to the center-mass. All these cases were investigated, and a summary will be presented. However, it seems appropriate to introduce a motor variant assembled later in the motor development phase of this project as a design and performance benchmark because it was simpler, performed well, and was characterized using experience gained in previous testing.

After characterizing the motor performance using one or two model 8R THUNDER actuators, the predominant rectangular actuator used in my work, the Rotary Thunder-motor was re-configured by mounting a single model 6R THUNDER actuator in both rotary clutch collars. The model 6R actuator has a piezoceramic patch two inches square, centered on a stainless steel substrate three inches long. It has two cutouts in each end tab which conveniently bolted into the two rotary clutch end collars. The motivation for switching to a single actuator was that evidence had accumulated suggesting that two model 8R actuators did not necessarily provide twice the performance, may have interacted unfavorably due to coupled vibrations, and were not always equivalent at the start due to manufacturing variability and changes over time.

The Rotary Thunder-motor, assembled with a single model 6R actuator, is depicted in Figure 7.2.1—4. Figure 7.2.1—5 shows the clutch bearing collar design in detail since it is considered a key part. This and other parts, machined from polycarbonate plate, 0.5 inch

thick, were designed as components of a test bed allowing assembly of the original two-axle design and any necessary re-configuration. The concept worked in that it allowed easy transition to a single axle, cantilever-mounted actuator.

It should be mentioned that the thin plate mounted on top of the vertical support blocks (about 0.25 inch wide as seen from top) is a reaction stop. As shown, the motor in Figure 7.2.1—4 would have clutch bearings oriented for direct drive—that is, when the actuator flattens under applied electric field, the clutch bearings lock and transfer clockwise torque (as seen from end at right) to the axle, causing rotation. In response, the actuator and collar assembly would tend to rotate counter-clockwise toward the reaction stop, which would block continued rotation. Some key parts not shown are small bits of foam rubber wedged in between the neck of the bearing collar and the reaction stop. They not only make the motor much quieter, but prevent loss of vibration which actually diminishes performance.

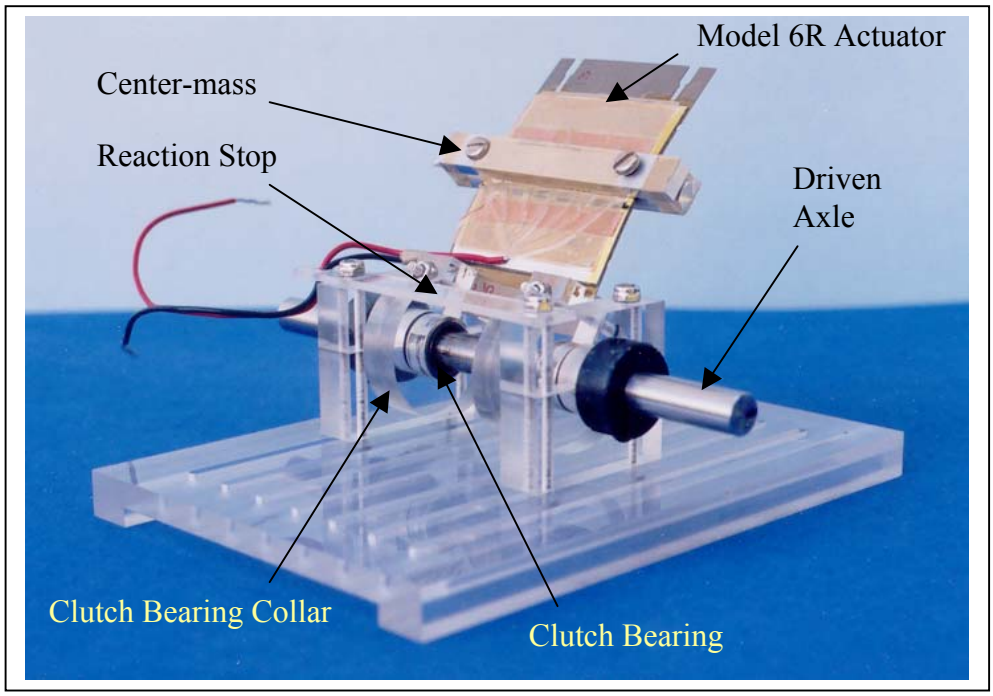

Figure 7.2.1—4. (color) Rotary Thunder-motor assembled with a single model 6R THUNDER actuator (Photograph by Kay S. Davis)

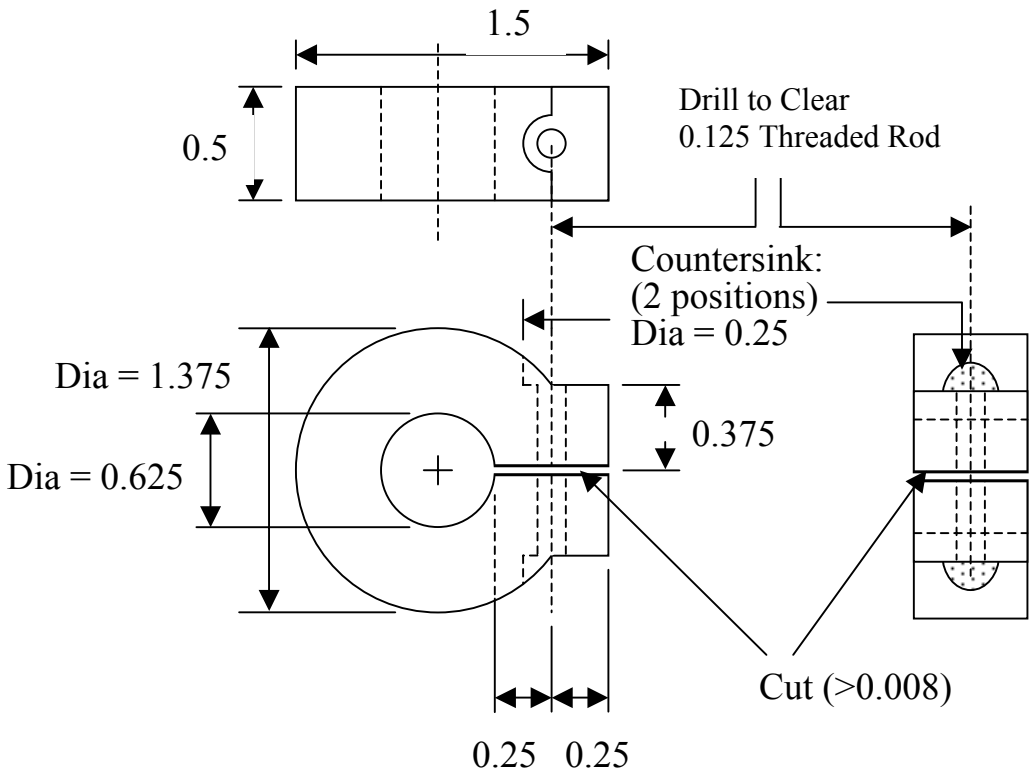

Figure 7.2.1—5. Detail of clutch bearing collar
(Material: polycarbonate, All dimensions in inches)

Two views of the Rotary Thunder-motor configured with two model 8R actuators are shown in Figures 7.2.1—6A and 7.2.1—6B. The striped wheel seen in both photographs is the tachometer wheel described in Section 3.2.3. The three bearings visible in between the two clutch bearing collar and actuator assemblies in the top photo are free rotation needle bearings used as spacers. Note center-masses attached to each actuator.

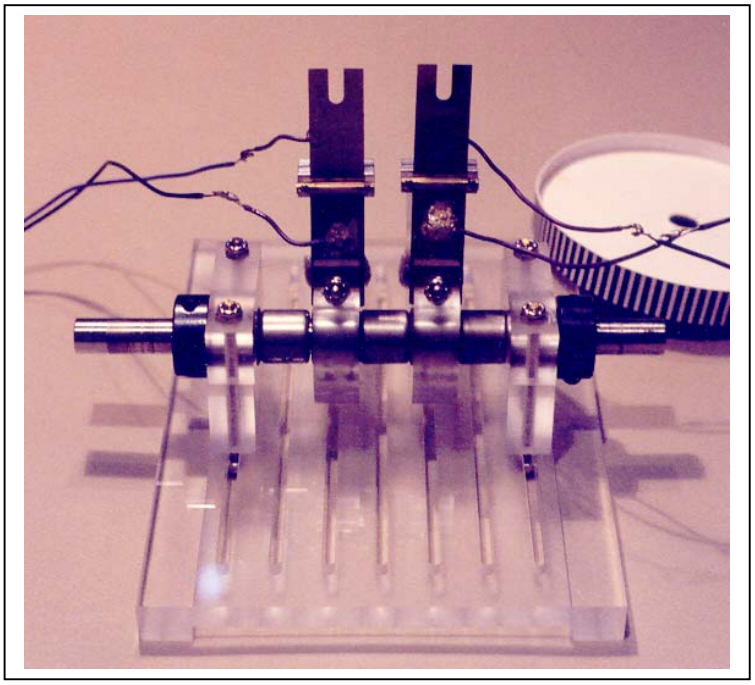

Figure 7.2.1—6A. (color)
(Photograph by Kay S. Davis)

View from side of Rotary Thunder-motor assembled with two model 8R actuators
(Shown with tachometer wheel at corner of base)

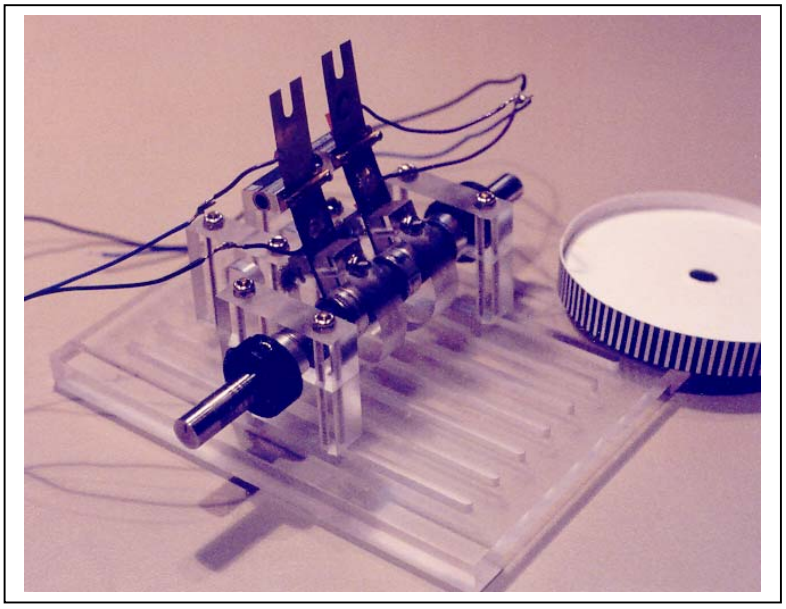

Figure 7.2.1—6B. (color)
(Photograph by Kay S. Davis)

Three-quarter view of Rotary Thunder-motor assembled with two model 8R actuators
(Shown with tachometer wheel at corner of base)

7.2.2 Analysis of Rotary Motor Configured with Single 6R THUNDER

The experimental results analyzed in this section were obtained by using an oscilloscope to capture initial accelerations of the motor-driven tachometer wheel as voltage was first applied. The objective was to determine motor torque by a means other than measuring the effect of braking force on motor speed (to estimate blocking torque).

From the fundamental physics of rotation, we have, $\Sigma\tau = I\alpha$, that is, net torque equals rotational moment of inertia multiplied by angular acceleration. Furthermore, an estimate of motor efficiency was sought. Electrical power is given by $P = V\,I$ (product of voltage and current). Both voltage and current of the applied drive signal were measured (discussed in greater depth in Section 7.2.3, following this section). Mechanical power output can be calculated from $P = \tau\omega$ (mechanical power of rotation equals torque multiplied by angular speed). Mechanical power-out as a fraction of electrical power-in provides a measure of efficiency.

Rotational moment of inertia had been determined with utmost care by repeatedly measuring dimensions of the tachometer wheel and all rotating parts (shaft, split collars) with digital calipers. The tachometer wheel was disassembled and all components weighed on an analytical balance along with other rotating parts. Even flecks of glue breaking loose from the bond between wheel disk and patterned flange during disassembly were collected and weighed. Since rotational inertia of an assembled object equals the sum of the rotational inertia of its parts—all referred to the same axis of rotation (with the parallel axis theorem applied as necessary)—standard formulas for disks, open cylinders, thin plates (for strips of tape, open spaces in split collar) could be used to determine a very accurate value for the composite rotational inertia, I_{TOTAL}.

In addition, the motor must contain internal resistance because it runs at constant speed under any specific operating conditions, which implies that angular acceleration is zero (otherwise motor speed would increase), and consequently that net torque is zero. Clearly, active elements in the motor are generating torque or the motor would not rotate,

especially if loaded. Therefore, at constant motor speed, generated torque exactly balances internal and external resistance (an effective torque of opposite sign).

Thus, net torque can be expanded into actuator-generated torque, τ_{GEN}, and opposing torque of internal resistance, τ_{RES}, as indicated by (7.2.2—1).

(7.2.2—1) $\Sigma\tau = \tau_{GEN} + \tau_{RES} = I\alpha \rightarrow \tau_{GEN} = I\alpha - \tau_{RES}$ (At $\alpha = 0$, $\tau_{GEN} = \tau_{RES}$.)

Resistance torque can be further subdivided into external motor load (e.g., a brake stand) and internal resistance, $\tau_{RES} = \tau_{LOAD} + \tau_{INT}$. However, we are not really interested in generated torque, that is, the maximum values supplied by actuators to their clutch bearings from which bearing loss is deducted before reaching the motor load. Generated torque never reaches the axle and cannot be used. Therefore, let output torque (τ_{OUT}), be defined as generated torque less internal resistance.

(7.2.2—2) $\tau_{OUT} = (\tau_{GEN} + \tau_{INT}) = I\alpha - \tau_{LOAD}$

Internal resistance was measured in a separate experiment, described in Appendix 2, in which falling masses attached to cords wrapped around the motor axle provided torque. Most of the components were removed except for the specific bearings to be tested for internal resistance. The effect of vibration was also measured by conducting falling weight tests while THUNDER actuators, clamped in the support blocks serving as bearing mounts, were operated at various frequencies at amplitudes typical of normal motor operation. The tachometer wheel and fiber-optic displacement gauge were used to measure accelerations resulting from the applied torque of the falling masses (with the rotational inertia of all rotating parts accounted for). In these experiments, as in the present experiment, an oscilloscope was used to capture the transient response of the motor or its parts under applied conditions.

In the present experiment, which sought to measure the transient acceleration before steady state rotation was established, the oscilloscope was set to acquire about one

second of data in a stopped frame to enable manual control of data acquisition. Switching to faster scales on the stopped frame enabled zooming-in on the initial region of the signal, where oscilloscope v-bars were used to measure time intervals. Movement of a black stripe and white stripe on the tachometer wheel resulted in one period in the waveform, corresponding to about 4º of angular displacement of the wheel. Dividing angular displacement by the period width in seconds gave average angular velocity during the time interval of the pulse.

It was found that the motor attains nearly full speed in a few milliseconds. Since motor response to the drive signal was indicated only by the movement of the tachometer wheel, let time zero be the instant when the tachometer trace first indicated displacement. There are two reasons for supposing that angular acceleration began a brief moment before (at a negative time, as it were). First, the ramping of the drive signal was also captured, as shown in Figure 7.2.2—1, and it typically attains most of its steady-state amplitude before tachometer trace responds. Many screen shots from other motor experiments indicate that response of unimorph actuators to drive signals is orders of magnitude faster than the millisecond scale. Although mechanical transients often occur from the sudden movement, superimposed on the transient (if one occurs) are displacement pulses with proportional amplitudes in one-to-one correspondence with voltage pulses. The second reason for postulating an actual start before time zero is that the first period of the tachometer trace indicates that considerable velocity is already present (much more than the differences in velocity indicated by the first, second, and successive periods). In other words, substantial acceleration was necessary to attain such a large first value if the start of acceleration corresponded to zero velocity (i.e., no initial velocity).

In calculated results based on the measured time intervals, average speeds were assigned to mid-points of their time increments relative to the cumulative time elapsed. (This discussion will use the terms speed and velocity interchangeably, since sign and orientation of the torque and rotation vectors are not needed except to note which torques are opposing.) To better characterize brief moments between zero velocity and full speed, oscilloscope screen-shots were re-analyzed using Photoshop graphic editing software to

measure the time between drive voltage rise and first detected movement of tachometer wheel. The change from zero velocity to first increment of measured average velocity across time elapsed gave angular acceleration. Although there is some degree of variation, Figure 7.2.2—1 shows a representative screen shot from which a series of time intervals after time zero and an interval corresponding to the rise time of driving signal would all be measured.

The top, blue trace is the fiber-optic gauge response to the tachometer wheel; the bottom, green trace is the drive voltage from the amplifier. The third display line in the upper right corner of the screen shot indicates that the first angular displacement period (the interval isolated by v-bars) required 10.4 ms to move beneath the laser gauge probe. Since the 4º angular displacement corresponds to 0.0698 radians, the average angular velocity for this time increment is 6.71 radians per second. (The angular increment is actually 0.06966 radians according to my best measurements, yielding 6.70 radians per second.)

However, 6.70 radians per second is already an appreciable velocity (equivalent to 128 rpm). The point marked “A” is where I would select a point of zero velocity. Although amplifier voltage output is starting to build, the amplitude is not significant below this point. In later experiments where actuator displacement signals were recorded, this appears to be true. There is a short delay of about 1 ½ drive signal periods, then actuator displacement also ramps up to maximum amplitude in something like 10-20 ms. The interval of 10.94 ms (as measured by Photoshop) marked “B” in Figure 1, is the time during which the motor accelerates from zero velocity to however fast it is turning at the left endpoint of the first tachometer period, which has a speed of 6.70 radians per second at its midpoint.

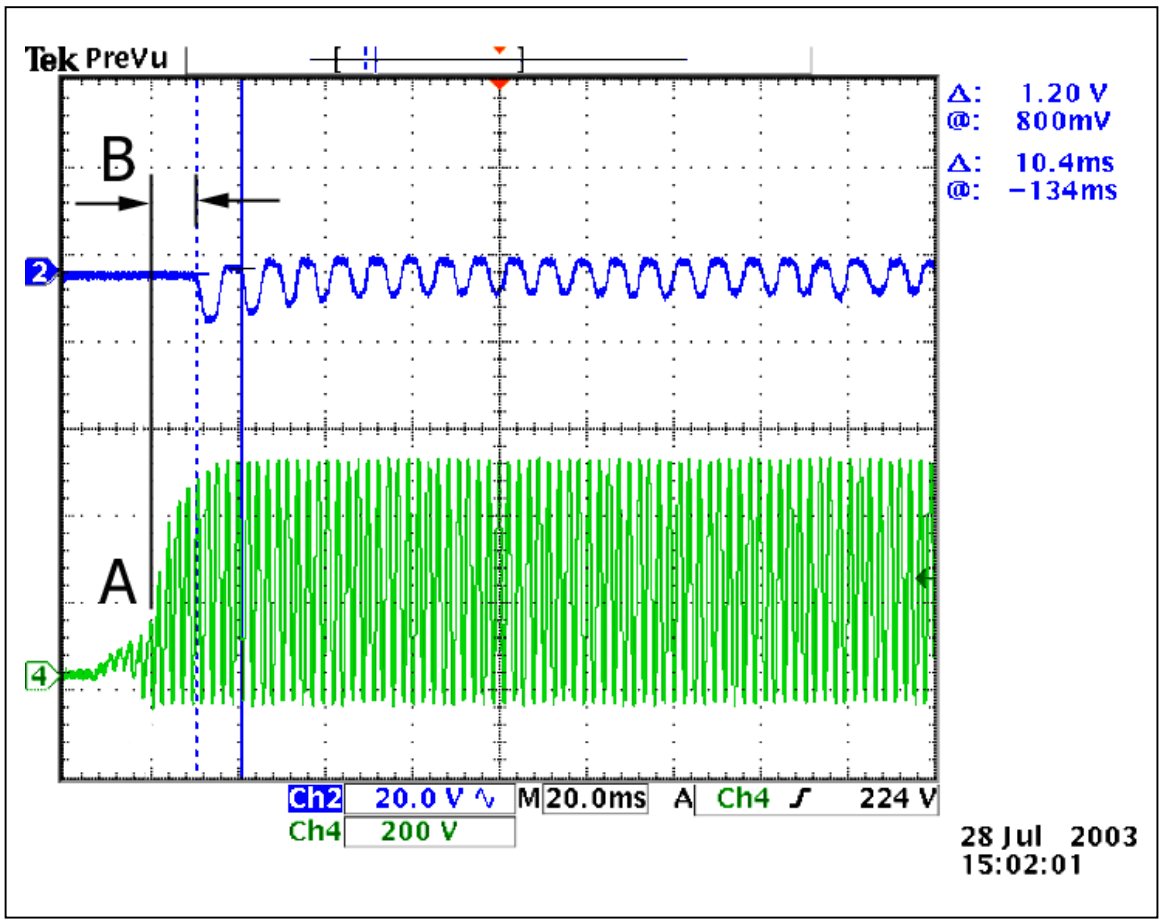

Figure 7.2.2—1. (color) Typical oscilloscope screen shot showing the ramping of drive signal by the high voltage amplifier and initial response of tachometer trace

When plotted, the first known average speed will not fall at zero time, but at the midpoint of the first interval, which is 10.4 / 2 = 5.2 ms. Therefore, it is assumed that we know the speed at the center of every tachometer interval, including the first, but that we do not know the speed at the endpoints between them (although we know where the endpoints fall on the scale of elapsed time, which is how the average speeds were determined). In the interval before time zero, we do not know the average velocity at the midpoint (since we do not know the angular increment the tachometer wheel would have turned if it had started at point A in Figure 7.2.2—1), but we do know that velocity at the

left endpoint (point A) is zero. The best we can do is to draw a line between zero velocity and the first average velocity associated with the first tachometer interval. The instantaneous velocities associated with the data taken from Figure 7.2.2—1 are plotted in Figure 7.2.2—2 in addition to the point of zero velocity. The slope of the fitted line gives an estimate of the acceleration, which in this instance, is 420.6 rad s^{-2}.

As discussed, time zero is the left endpoint of the first measured speed interval (i.e., no point plotted there). A hypothetical midpoint has been assigned to the midpoint of the interval during which most acceleration occurred. The left endpoint of this interval before time zero is the time of zero velocity. In general, it was found that assigning the square root of the first measured speed to the hypothetical midpoint gave the best fit between the first three points: zero velocity, the hypothetical midpoint, and the first measured speed.

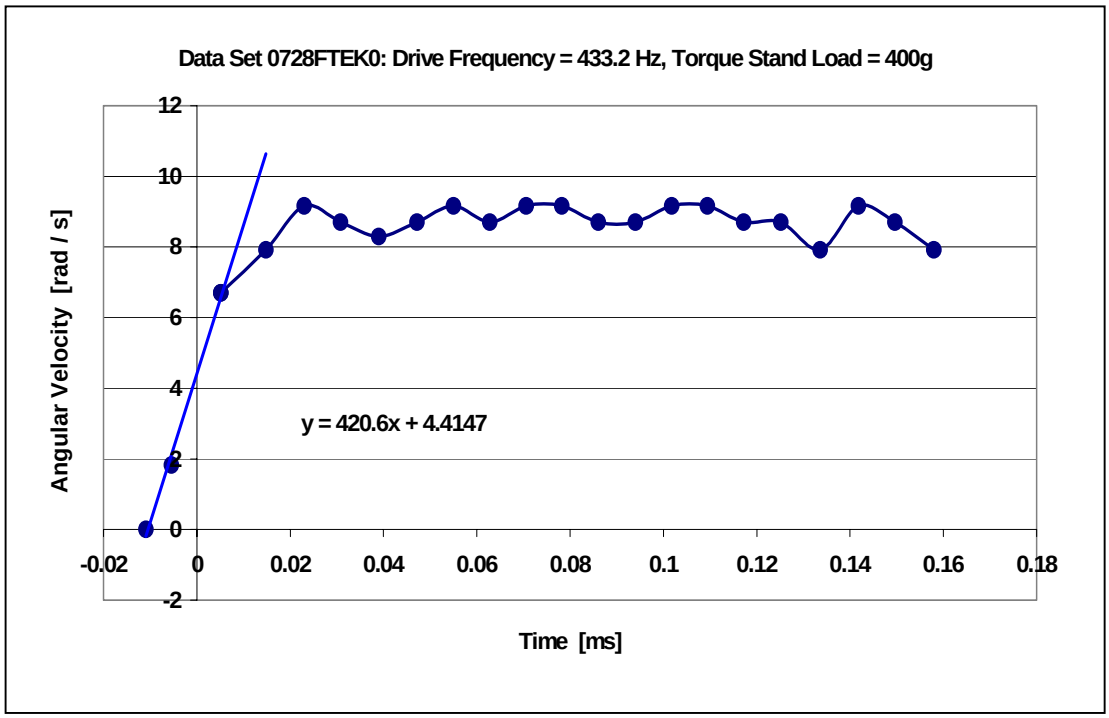

Figure 7.2.2—2. Estimated point of zero velocity (and a hypothetical midpoint explained in text) plotted with average velocities determined from data taken from an oscilloscope screen shot

There is no theoretical justification for this, only the circumstantial justification that excellent fit happened to occur in association with nearly all data sets.

As drive signal frequency was increased, it is particularly evident that the actuator must slap against its stop block, and the system "rings" in velocity space (i.e., oscillatory increasing and decreasing speed). In other words, the motor speed overshoots its average value, then damps to the average. Even so, plotted velocity values well away from the start also exhibit noisy fluctuations. The impact vibration damps and is lost in general noise fluctuations. (Other experiments indicate that in displacement space, the actuator experiences a secondary vibration from the impact which acts as a carrier wave for the driven vibration.)

Data was taken for seven frequencies spaced across the range of drive signal frequencies across for which this motor configuration operated. This was compounded by repeating at four braking loads on the torque test stand where the motor was installed—0g, 400g, 800g, and 1200g. Angular accelerations thus determined were analyzed as a group to reveal trends and estimate acceleration as a function of frequency and load. After analyzing 56 such plots (a pair of tests at each condition, four load levels including no load, at seven frequencies), the plot shown in Figure 7.2.2—3 was generated, which shows the scatter of determined acceleration values.

The figure relies heavily on color to make sense of the effect of load. "Cooler" colors represent light loading; "warmer" colors represent heavy loading. Symbol shape distinguishes the two tests in a pair. (There is a single third test represented by a triangle. It is omitted in subsequent plots since this figure shows it has no particular distinction relative to the other two.) More variation among values is observed as frequency increases. Although not readily visible at the lowest frequency, analysis has shown that an unambiguous reversal of the order of correlation occurred across the frequency range. At the lowest frequency, acceleration values increased directly with increasing load. At the highest frequency, acceleration values increased indirectly with increasing load. A fairly systematic exchange occurred at intermediate frequencies.

In attempting to reduce scatter and resolve trends more clearly, it was observed that

accelerations determined for each data set correlated strongly with the first measured speed values, which might be close to the average speed of the data set or might not. To some extent this is inherent in the fact that the first speed value controls one end of the fitted acceleration line. However, in almost every case the negative time of zero velocity, which was independently determined, fell in line with the first measured speed and the hypothetical midpoint which itself was calculated from the first measured speed. This was mostly true even before it was discovered that the square root of first measured speed yielded a better fit. Typically, the first measured speeds were about 0.8 of the average, but ranged from 0.2 to 1.4, with the sub-range between 0.6 and 1.0 representing about ± 1 standard deviation.

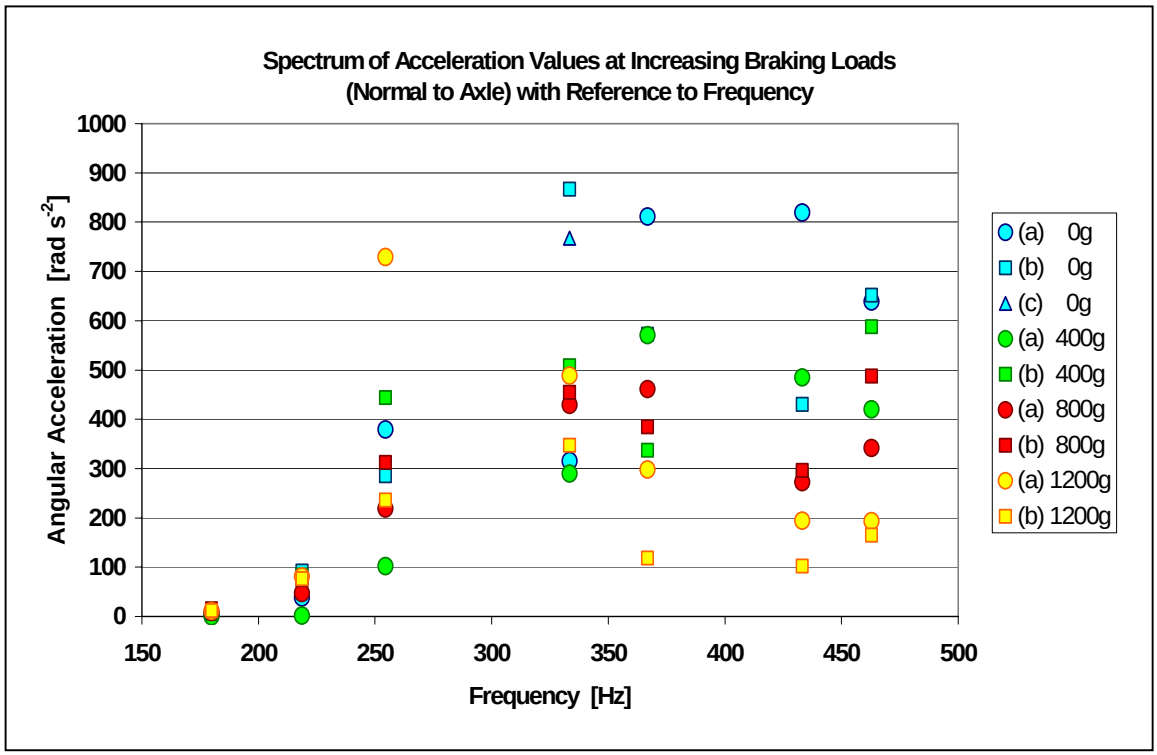

Figure 7.2.2—3. (color) Angular accelerations determined for the matrix of seven frequencies and four braking load levels, repeated twice

To reduce the collective variation in the set of first measured speeds and determined acceleration values, the acceleration values were normalized by the first measured speeds (reducing short-term variability), then multiplied by average speed (reflecting central tendency of entire data set) for the particular data set. In other words, the accelerations were multiplied by the ratio of average speed to first measured speed. In reality, the average speeds are also partially dependent on the first initial speed, but less so, or they would not be average (more data behind them).

As one might imagine, many arbitrary, hard-to-predict things probably occur during the initial acceleration, including exactly when oscilloscope data acquisition is started and stopped. One way of explaining the strategy is that dividing higher than average accelerations by higher than average first measured speeds and lower than average accelerations by lower than average first measured speeds yields a reduced range with necessarily reduced variability. A set of adjusted accelerations with reduced variability [rad s^{-2}] was then generated by multiplying the reduced range [s^{-1}] by the more stable average speed values [rad s^{-1}]. We are more interested in average behavior of the motor than arbitrary, transient behavior even though initial acceleration is an important transient phase. Figure 7.2.2—4 shows the result of this treatment.

Since we observe that a degree of variability exists among the pair values, we next average the pair values. At this point, least squares trend lines are calculated. Figure 7.2.2—5 shows the results of this operation. A consistent trend is observed between the zero load, 400g, and 1200g load lines. If minimal, partially-subjective tweaking can resolve this, it would be beneficial in creating an acceleration model for characterizing motor torque. The high-value outlier in the unloaded set was adjusted by calculating the standard value of each data point (that is, individual datum minus the average of the frequency subset; the quantity divided by standard deviation). It was only one of three data points with a standard score greater than one. Adjustments were made, but only the minimum changes needed to reduce the standard scores below a value of one.

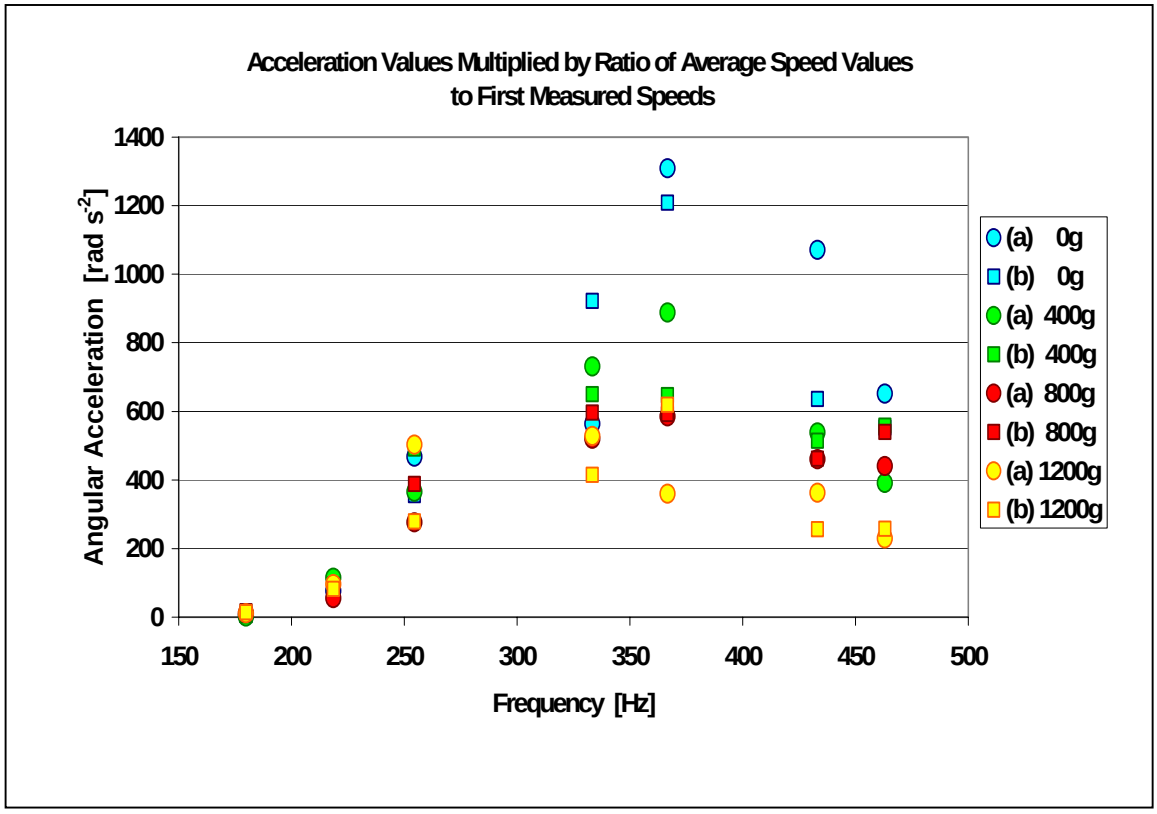

Figure 7.2.2—4. (color) The spectrum of angular accelerations as a function of frequency and load after treatment discussed in text to reduce variability and expose trends

The 800g load line was recalcitrant toward adjustment. It would seem that a trend line in keeping with the group would closely follow the data points at 333, 367, and 433 Hz. A strategy was investigated involving least squares fit of the spacing of the 800g points between the 400g and 1200g points. Results did not justify the intervention. Finally, the point at 463 Hz was adjusted by trial and error. Results are shown in Figure 7.2.2—6. The filled circles represent actual data, while the open circles represent values to which the two points were adjusted.

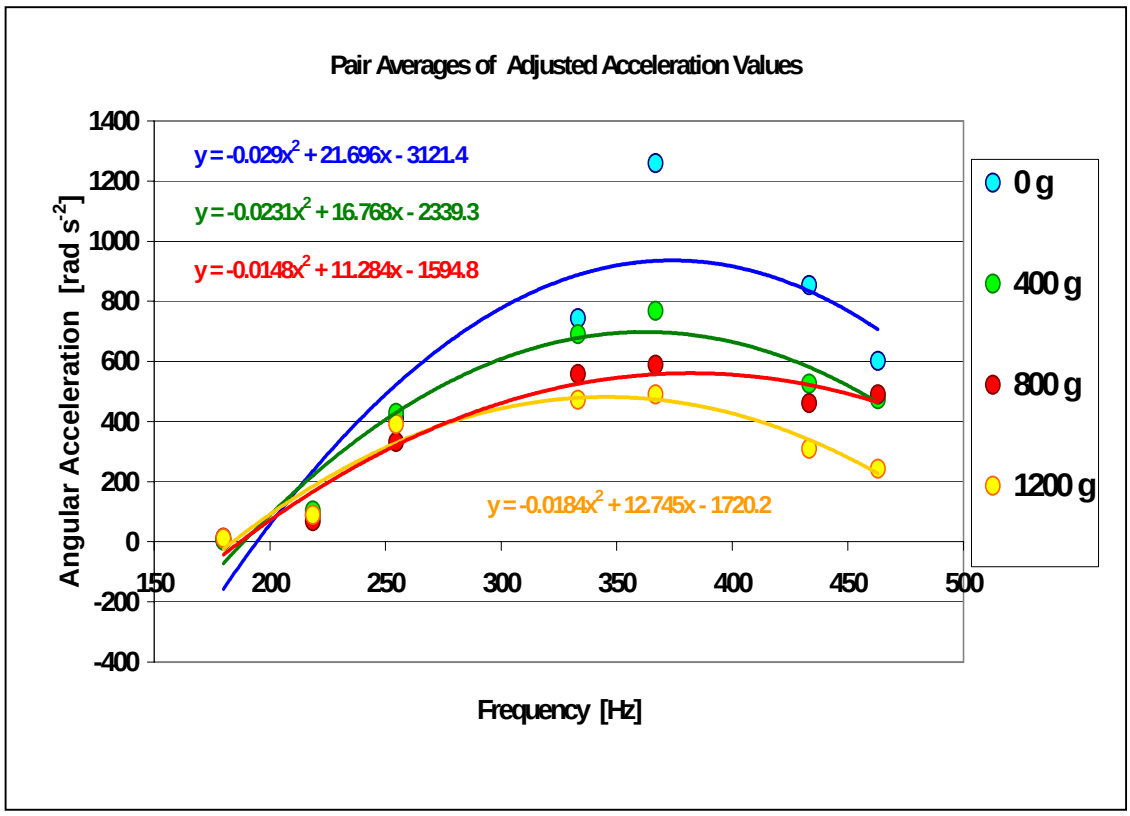

Figure 7.2.2—5. (color) The spectrum of angular accelerations as a function of frequency and load after pairwise averaging to further reduce variability

It would seem the resulting trend lines provide the basis for a reasonable evaluation of angular acceleration as a function of frequency and load. We can see that the function allows for the switching of order between direct and indirect correlation of acceleration magnitude with load.

The experiment providing acceleration data for this analysis was conducted on a motor with only one pair of clutch bearings in actuator collars. Secondary clutch bearings in axle mounts (intended to block back-rotation) had been replaced with minimal-resistance, non-clutch, needle bearings. The resisting torque of this configuration was

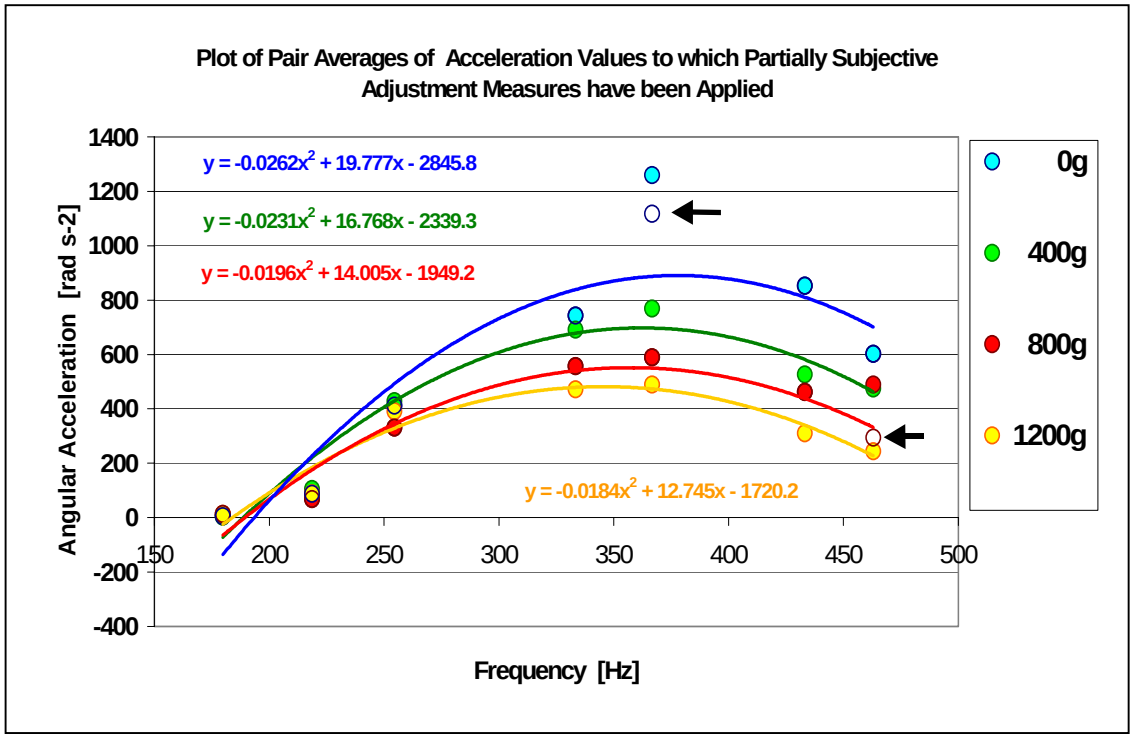

Figure 7.2.2—6. (color) The spectrum of angular accelerations as a function of frequency and load after attempts to resolve lack of fit of two points to otherwise consistent pattern

found to be –0.0199 N. For comparison, the resisting torque provided by both pairs of clutch bearings in place (actuator collars and axle mounts) was found to be –0.0226 N, and resisting torque on an axle assembly in only one pair of minimal-resistance, non-clutch bearings found to be –0.00104 N.

The cumulative resistance is not a linear combination, according to these experimental measurements. Furthermore, the values seem high, given that bearings in general (and clutch bearings in allowed direction) are not supposed to provide resistance to rotation. However, in testing the resistance of the un-powered motor with both pairs of clutch bearings in place, over 1600g attached to a thin wire wrapped around the axle was

required to turn it. A load of 1000g was not able to turn the axle at all. It would seem that the relatively high resistance is a correct observation.

The experiment to determine internal resistances also showed that vibration can reduce the internal friction of clutch bearings. Figure 7.2.2—7 shows results of an experiment in which a vibrating 6R THUNDER actuator was inserted into the mounting blocks which supported two clutch bearings. Analysis of resulting angular acceleration data suggests that internal resistance decreases with increasing frequency.

The experiment which yielded this data also provided resistances of various bearings and coefficient of friction between motor axle and brake shoe. Four sets of data were excluded from a total of 18 sets because data workup revealed they were flawed. (See Appendix 2.) One of these is the "low-confidence data point" plotted in Figure 7.2.2—7. It was plotted nonetheless because there is not much data available to make the general trend evident. On the one hand, this point suggests that bearing resistance does not continue to diminish with increasing frequency, which is probably true. On the other hand, the "low-confidence" value is exceedingly approximate. Thus, a possible general trend was devised by averaging the least squares line between the three accepted values with the second order least squares curve between all four points and weighting the linear part three to one relative to the parabolic part.

Figure 7.2.2—8 shows values determined for coefficient of friction between motor axle and test stand brake shoe at various test stand loads (acting normal to the axle). The fact that the values decrease with load is probably a true observation. Ideally, the torque test stand would have had rollers to support the motor axle as the brake shoe pressed on it. Since it did not, the contact between the surfaces probably changed as load increased. The end of the axle where the test load pressed was about 4 cm from the axle support block, creating a large moment that could tilt the motor slightly. The motor was taped into place with metal tape but not clamped. Clamping appeared to distort the plastic motor base and diminish performance. The reason the fitted curve equation displayed on Figure 7.2.2—8

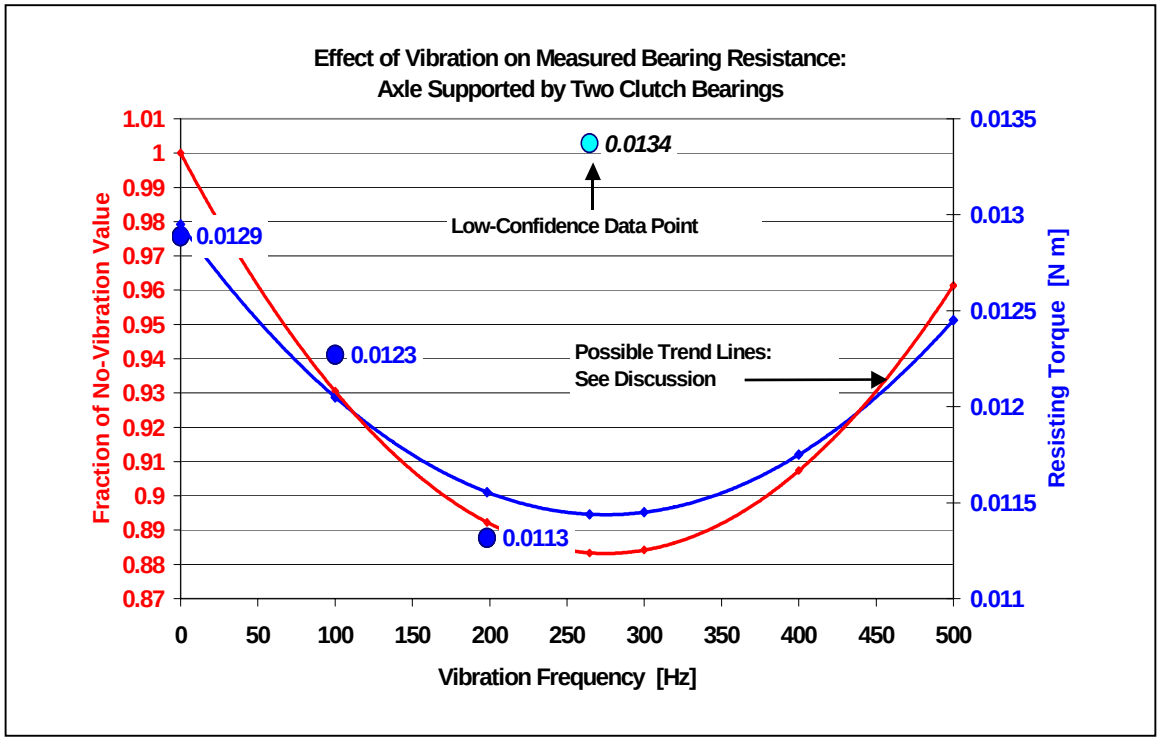

Figure 7.2.2—7. (Color) Reduction in clutch bearing internal resistance due to vibration with probable minimum inferred by including outlier in analysis and assigning low weighting

uses (0.001 x) instead of (x) as an independent variable is that the least squares algorithm results in excessively ill-conditioned matrices when the relative size of independent and dependent values differs by four orders of magnitude as in this data. (In other words, the equation of fit returned by the spreadsheet used to create the graph did not match the data when plotted.)

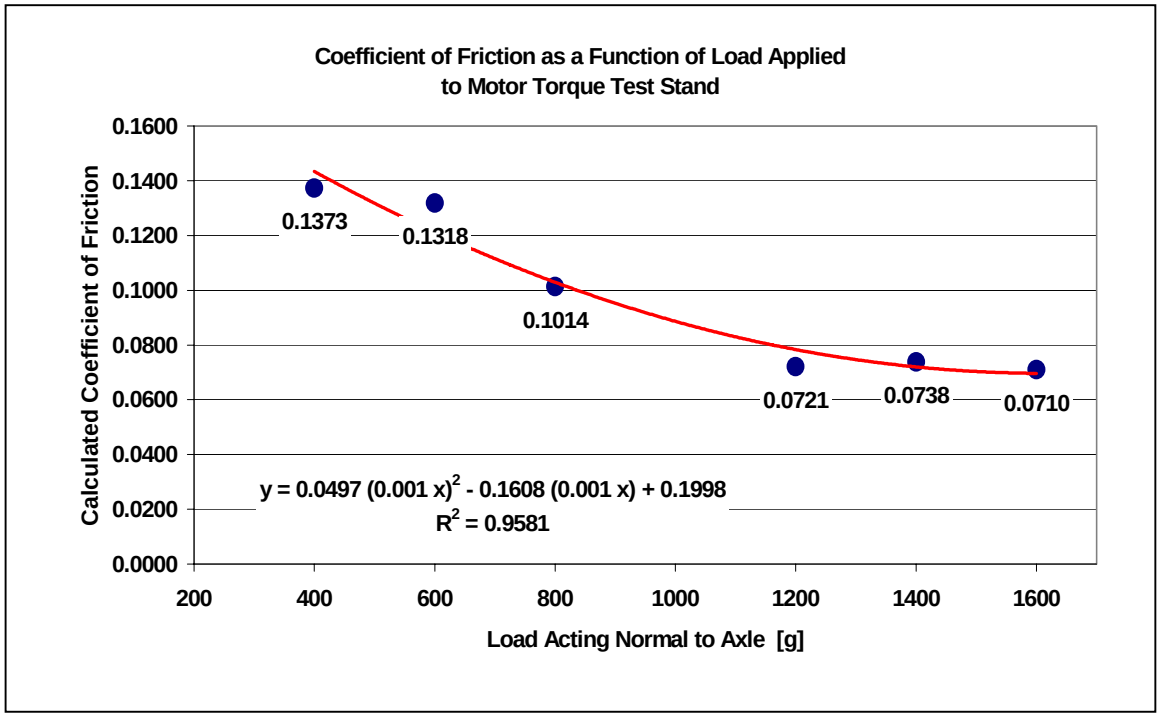

Figure 7.2.2—8. (color) Change in coefficient of friction between test stand brake shoe and motor axle with increasing load normal to axle

In the opening to this section, output torque (τ_{OUT}) was defined as generated torque less internal resistance.

(7.2.2—2: repeated) $\tau_{OUT} = (\tau_{GEN} + \tau_{INT}) = I\alpha - \tau_{LOAD}$

Although it was not necessary to define vector quantities relative to a coordinate system, torques acting in opposite directions must have opposite signs. Therefore, consider torques acting in the direction of axle rotation as positive. All resistance torques which act in the opposite direction are negative. Thus, τ_{INT}, a negative torque, will decrease τ_{GEN}, making τ_{OUT} a smaller quantity. On the other hand, τ_{LOAD}, also a negative torque, will increase τ_{OUT}

because it is subtracted from the right side of the equation. (In other words, to accelerate, the motor must generate more torque than the load, and internal resistance, consumes.)

Since angular acceleration has been determined as a function of frequency, torque can likewise be expressed as a function of frequency ($\tau(\upsilon) = I\,\alpha(\upsilon)$, where υ is frequency). Figure 7.2.2—9 shows the result of incorporating known quantities into equation (7.2.2—2). It is really not necessary to introduce τ_{INT} into calculations. The right side of (7.2.2—2) is simply equivalent to output torque.

Output torque as a function of frequency is plotted in Figure 7.2.2—9. The principal observation to be made is that Figure 7.2.2—9 shows the exchange of increasing torque with increasing load at lower frequencies with decreasing torque with increasing load at higher frequencies. Increasing torque with increasing load may not seem a real possibility, but notice that the spacing of the data points at 179.9 Hz. They become closer together, and presumably at some higher load would again fall to lower torque values. What we really want to see is output torque as a function of load. This is plotted in Figure 7.2.2—10.

The phenomenon of torque increasing directly or indirectly with increasing load is highlighted by Figure 7.2.2—10. The switchover occurs between 333.3 Hz and 366.7 Hz. How fast the motor turns when delivering a particular torque is also important because the combination defines both the work output and usefulness of the motor. The overlaid average speeds in rpm indicate that the switchover from increasing to decreasing torque with increasing load occurs at maximum speed. (Note that these are not data point labels, but external information.)

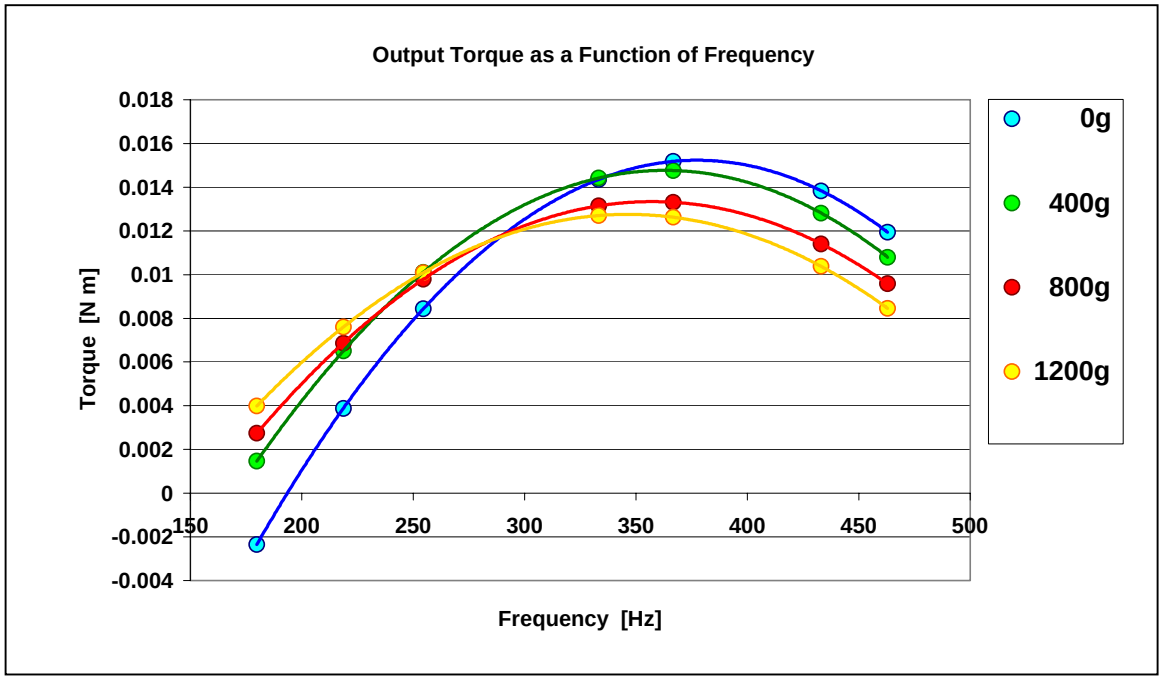

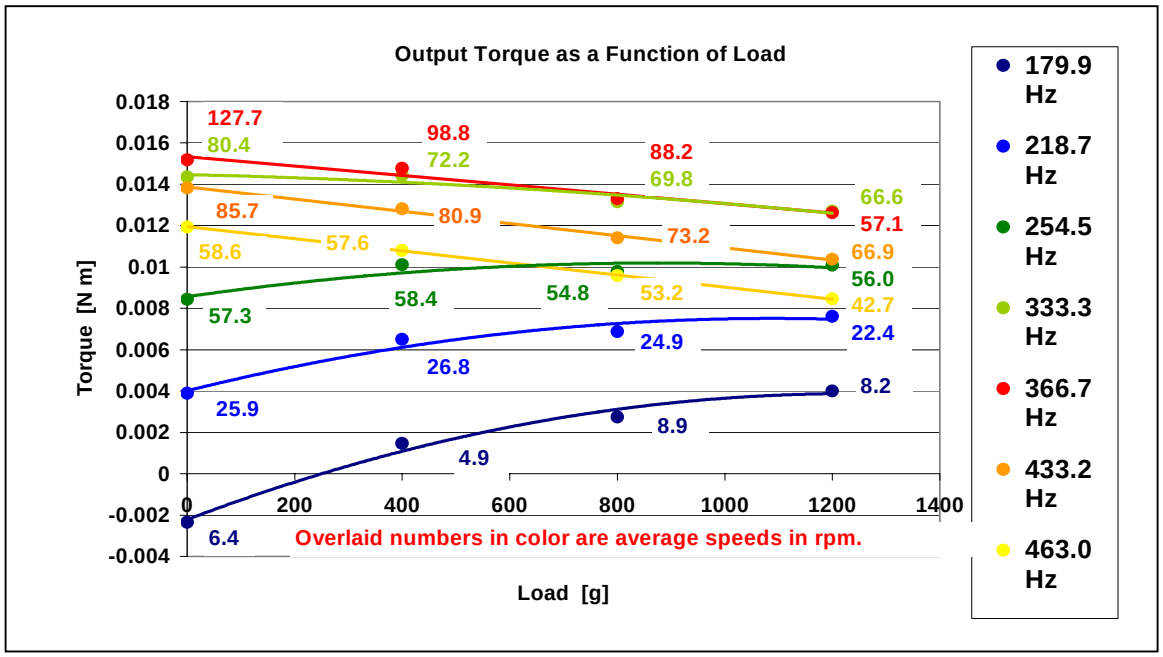

Figure 7.2.2—9. (above—color) and Figure 7.2.2—10. (below—color).

Rotary Thunder-motor output torque as a function of frequency and load showing the relationship to frequency (above) and load (below)

Since power of rotational motion is given by $P = \tau\omega$ (torque multiplied by angular speed), Figure 7.2.2—10 could be re-plotted as a graph of mechanical power as a function of load. This is shown in Figure 7.2.2—11.

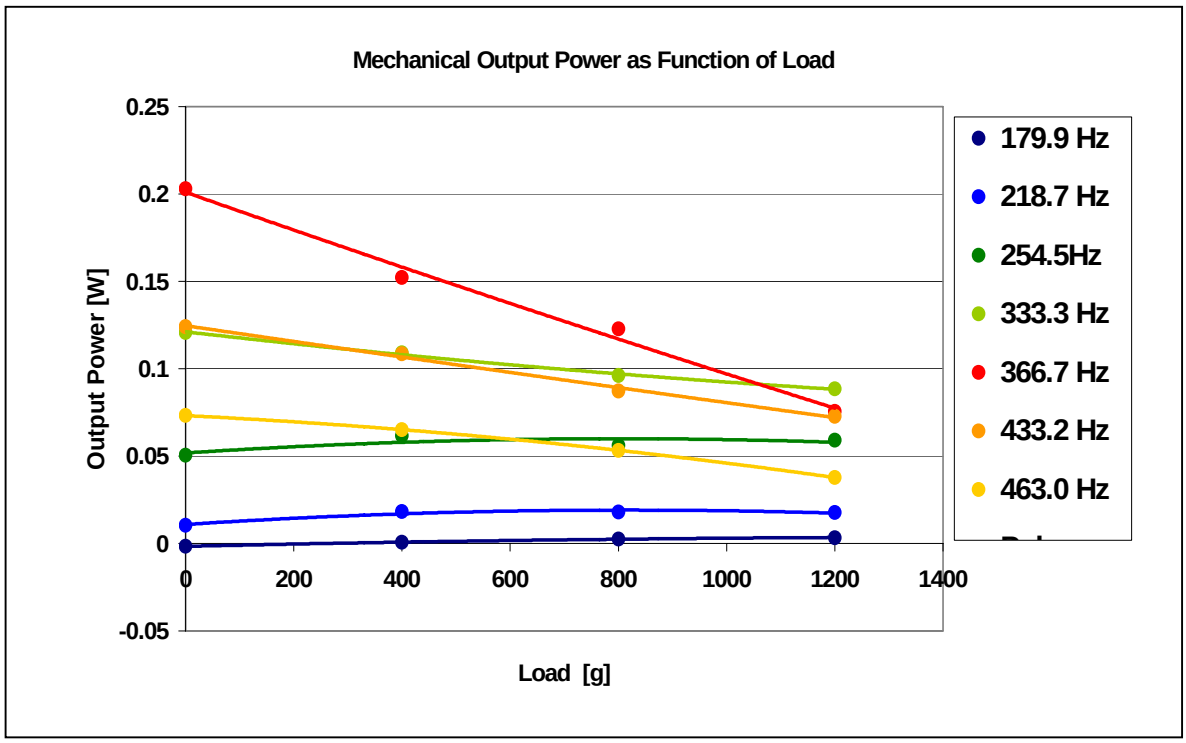

Figure 7.2.2—11. (color) Mechanical output power determined as the product of output torque and rotational speed

To calculate the efficiency of energy conversion by the motor, electrical power input as a function of load will be needed. First, consider electrical power input as a function of frequency. Experimental results for electrical power as a function of frequency are plotted in Figure 7.2.2—12. Input power as a function of frequency was measured in greater detail because load tests were typically conducted near resonant frequency of the actuator. Consequently, all the information about effect of load on power drawn by the actuator is mostly concentrated in the narrow transition band between the resonant and

anti-resonant peaks evident in Figure 7.2.2—12. The information which is available regarding power as a function of load is shown in Figure 7.2.2—13. The following data treatment attempts to extend the range over which electrical power as a function of load is known.

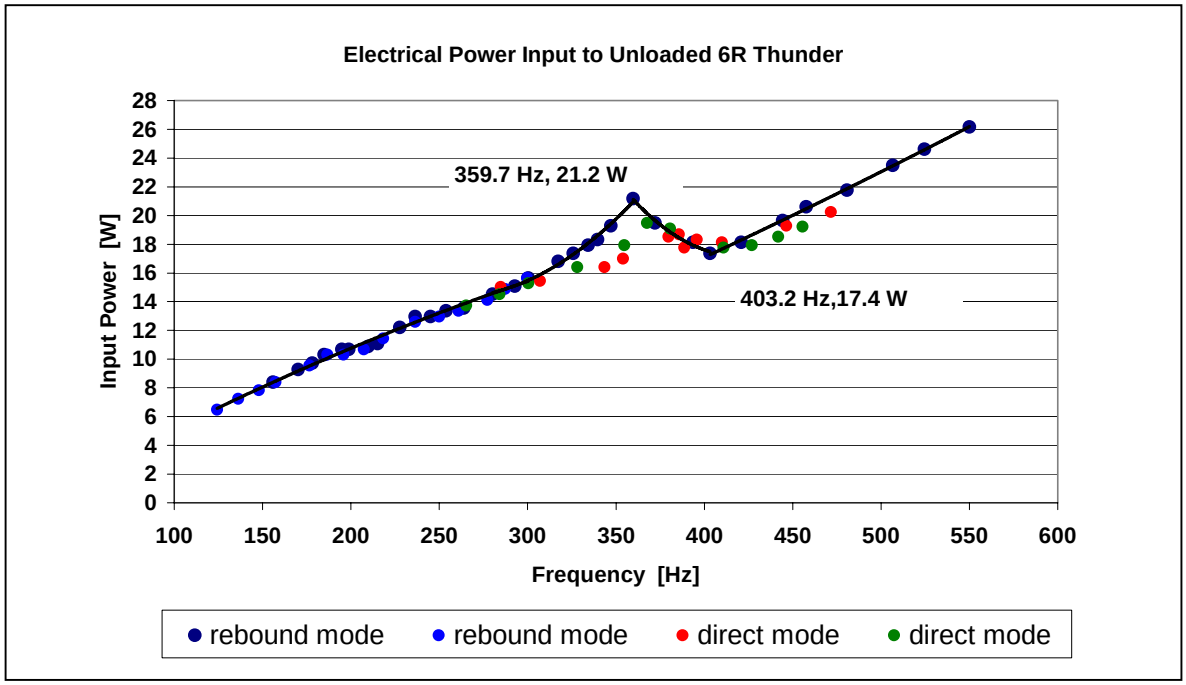

Figure 7.2.2—12. (color) Electrical input power from various tests on the rotary motor configured with model 6R actuator as determined by current drawn at constant voltage

In Figure 7.2.2—13, only the lowest data series (291.4 Hz) is actually below resonance, and we see that it is nearly linear with slight positive slope. The highest frequency data series still falls in the transition region before the anti-resonance peak. However, its behavior resembles the lowest frequency series in that it shows a slight positive slope and reduced curvature. The mechanical output power, as shown in Figure 7.2.2—11, is drawn from a wider range of frequencies. Only the red line (366.7 Hz) falls in the region of resonant transition.

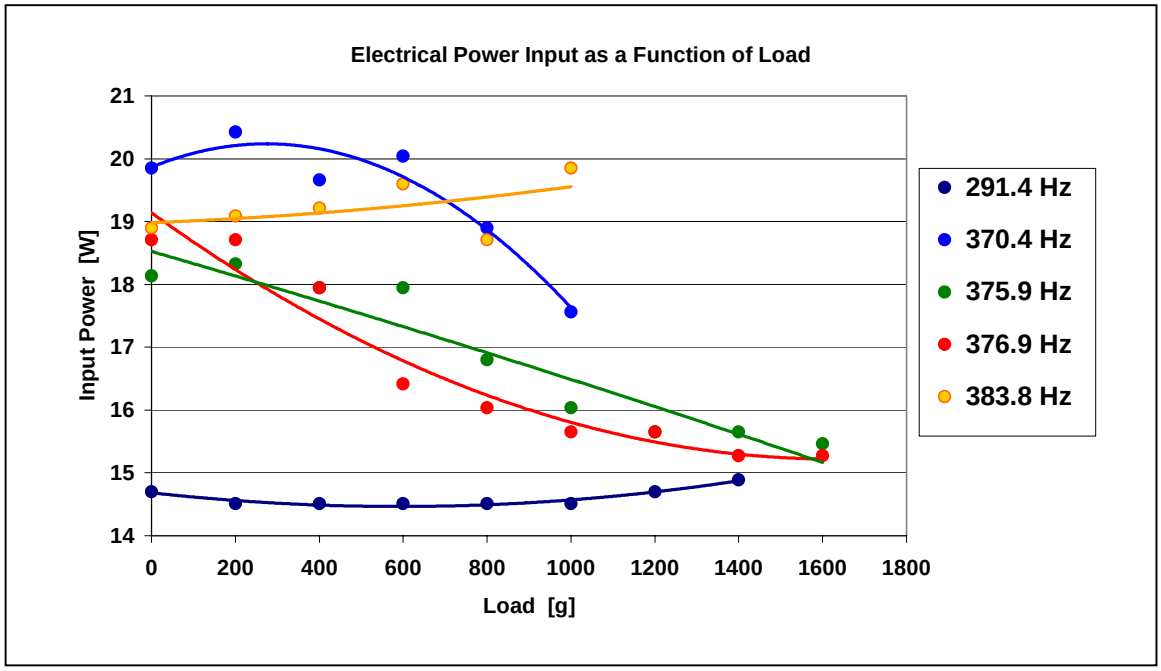

Figure 7.2.2—13. (color) Available data regarding electrical power input as a function of braking load within a range of frequencies near resonance

To determine whether there is a global behavior for change in power as a function of load, either electrical or mechanical, the fractional change ((final – initial) / initial) in power between two points (0g and 1200g) was calculated for all available load series, whether for electrical power input or mechanical power output. This approach accommodates the fact that electrical power values are on the order of one hundred times larger than mechanical power values. (This unfortunate fact suggests that conversion efficiency will be about one percent.) The proportional change is thereby separated from initial magnitude. Results are given in Figure 7.2.2—14. From the plot, it appears that all points fall on the same curve, which resembles the curve in Figure 7.2.2—12, except that signs of slopes are interchanged.

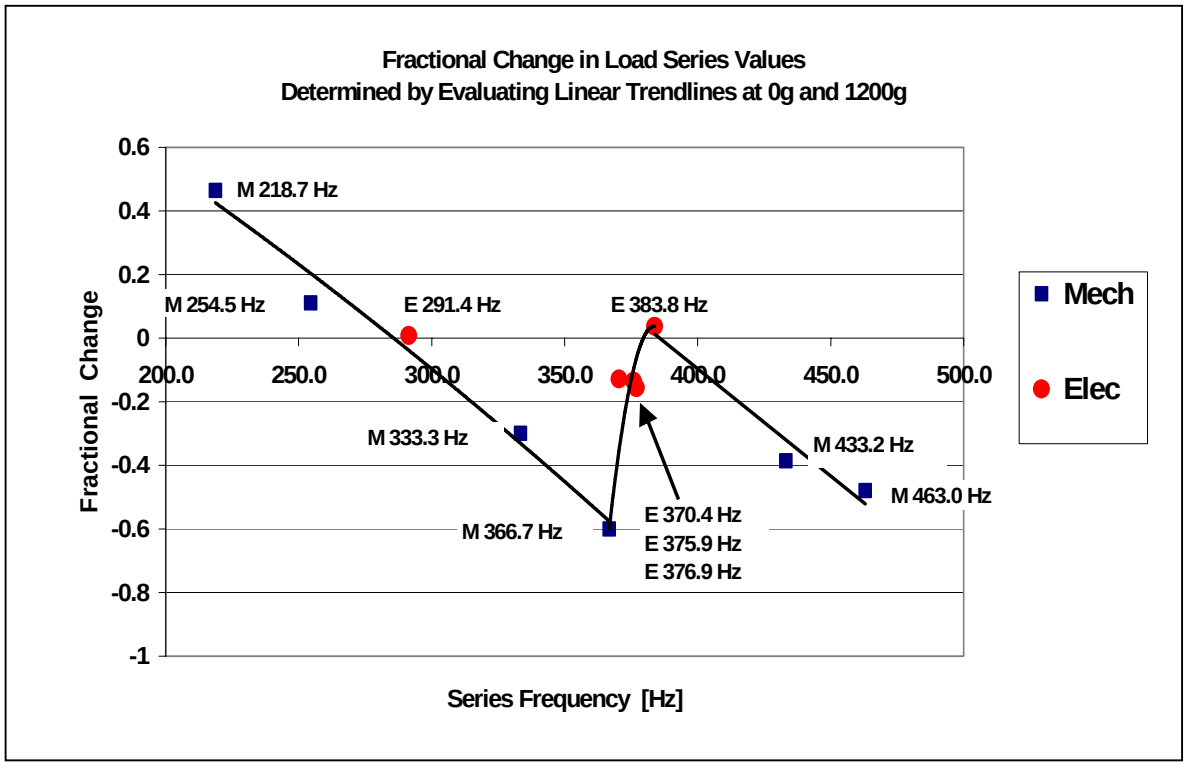

Figure 7.2.2—14. (color) Attempt to establish whether electrical power input as a function of load changes in proportion with mechanical output power as a function of load when plotted against frequency

Using equations of the fitted curve in Figure 7.2.2—12, electrical input power to the unloaded 6R THUNDER was determined for each of the same frequencies for which there are plots of mechanical output power as a function of load. The fractional changes for power input between no load and 1200g load were applied to each of the zero load electrical power inputs. Results are shown in Figure 7.2.2—15. By following the color scheme and comparing Figure 7.2.2—15 with Figures 7.2.2—12 and 7.2.2—14, one can see that it does make sense.

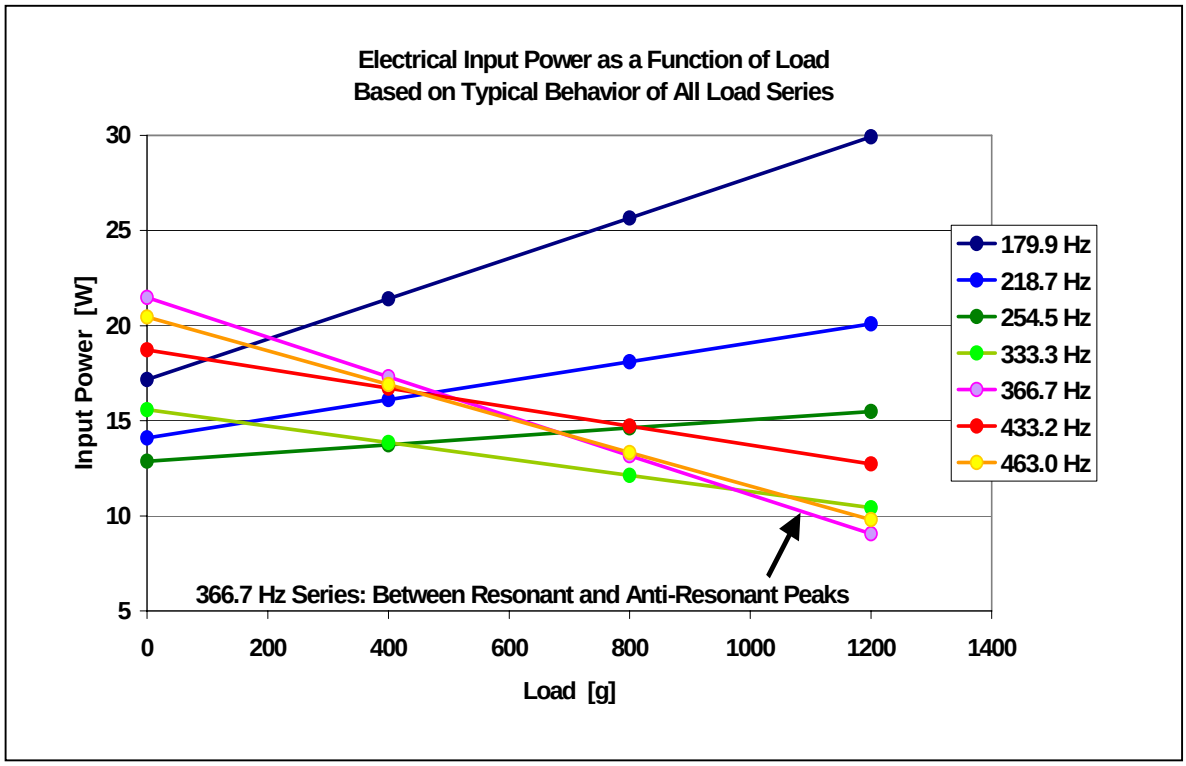

Figure 7.2.2—15. (color) Electrical input power as a function of load determined by scaling electrical input power as a function of frequency by the consistent relationship between electrical power input and mechanical power output when load is changed by a fixed amount

Note that actual data consisted of current drawn. This was measured by passing input signals through a "true RMS" Fluke multimeter. In all Rotary Thunder-motor experiments, voltage was applied in a sinusoidal waveform from –60 to 480V, that is, a peak-to-peak voltage of 540V. Since RMS power is typically reported, the RMS voltage used in calculations would be 381.8 V. Peak-to-peak power could be obtained from RMS power by multiplying by 1.4142 (square root of 2).

It is a small step, then, to determine what percentage of electrical power is converted to mechanical power. Results are presented in Figure 7.2.2—16. The unfortunate

fact is that efficiency approaching 1% is the maximum performance. (However, see the closing comment in Section 7.2.4.) Maximum efficiency occurs in association with the frequency of 366.7 Hz, which is the only resonant frequency in the set of plotted curves.

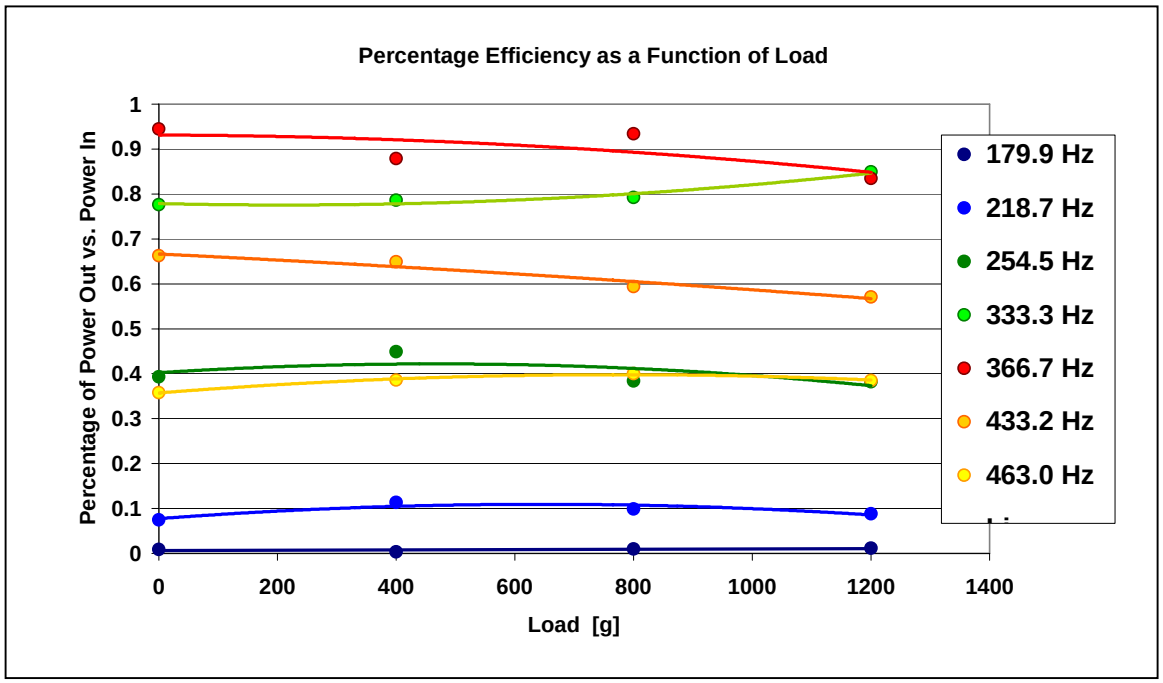

Figure 7.2.2—16. (color) Percentage efficiency as a function of load across a range of frequencies:
(Mechanical Power Out / Electrical Power In)*100

7.2.3 Summary of Experimental Results for Earlier Motor Configurations

There were a number of other motor configurations assembled before the single model 6R THUNDER actuator design which has been the focus of discussion thus far. This section presents an overview of results from earlier work for comparison. The Rotary Thunder-motor test-bed, designed to accommodate variations in assembly, facilitated evolution of the prototype. Even though a number of initial tests were conducted on a motor assembled from a single model 8R THUNDER actuator, the presumed advantage of

mounting two actuators on the driven shaft was an enduring feature of intermediate assemblies, although it was never found to be all that beneficial. This observation is what lead to the motor design using a single model 6R actuator.

The basis for using two actuators was the idea that output rotation would be discernably discontinuous without two actuators alternately applying torque in response to an out-of-phase drive signal. In reality, the performance of a motor built with a single actuator or with two actuators operating in phase never showed any deficiency.

The essential combination of clutch bearing, collar, and actuator was even quite forgiving in response to whether reactions to the generated torque were supplied by a supporting structure. In an *ad hoc* demonstration, a bearing-collar-actuator assembly held only by a long metal shaft threading through it was driven while the shaft was held in the hands. (The clutch collar must be made from electrically insulating material to protect the experimenter from ***lethal voltage***.) The vibrating structure had no difficulty turning the shaft while suspended in this fashion, with only minimal tendency to counter-rotate.

A series of tests was conducted on the motor assembled in various ways using the dual-channel Angstrom Resolver fiber optic gauge, as described in Section 3.2.3, to measure rotational speed with one probe, actuator displacement with the other probe, with the actuator mounted as a cantilever embedded in the clutch bearing collar (Figure 7.2.1—5). (In a few initial experiments, one actuator was mounted at both ends in two collars, in the manner of the conceptual illustration of Figure 7.2.1—1.)

After a few initial experiments, a multimeter was inserted into the drive signal input line to measure electrical current drawn by the motor under various operating conditions. Since the motor was invariably operated by a DC-biased sinusoidal signal from –60 to +480 V (540 V peak-to-peak), current drawn provided a measure of electrical input power.

Unfortunately, calculations have mixed peak-to-peak voltage and RMS current. True RMS input power would be about 71% of the mixed value, which would improve stated efficiency values slightly. However, since all efficiency calculations have indicated less than one percent conversion to mechanical energy, the fact that efficiency is less than

one percent was considered a sufficient result in itself. Precisely how much less than one percent was not considered important enough to justify re-calculating all the numbers. Comparison between motor configurations will be valid because the effect of using nearly constant peak-to-peak voltage will be uniform in all data.

Fiber-optic gauge output signals (tachometer wheel trace and actuator amplitude) were displayed on a four-channel oscilloscope along with the high-voltage drive signal from the amplifier. (A 100X, voltage-dividing oscilloscope probe was used to measure the drive signal magnitude, since the oscilloscope had a ± 20 V range.) Numeric data was acquired by measuring (with oscilloscope vertical-bars or horizontal-bars) a sample of tachometer signal time periods (typically about 20), amplitude of the vibration response signal (ΔV), and offset times between vibration response and drive signals to note phase shift. Data sets also included a current reading taken from the multimeter and a voltage reading from the front panel display of the fiber optic gauge—to record the DC operating point on the calibration curve around which the vibration response signal was occurring (explained in Section 3.2.1). Representative oscilloscope screen displays are shown in Figure 7.2.3—1A and Figure 7.2.3—1A B. The example shown in Figure 7.2.3—1B was partly chosen to show the superimposed complex waveforms often seen during motor testing, especially at resonant frequencies. The green and violet out-of-phase drive signals seen in Figure 7.2.3—1B are the output of the circuit described in Section 3.3.

As explained in Section 3.2.1, measured amplitudes of the vibration response signal were converted to mechanical displacement of the actuator. The tachometer response signal was converted to rotational speed in rpm, as explained in Section 3.2.3. Data was assembled and plotted in a spreadsheet (a large part of which was devoted to expediently determining physical displacement from ΔV and the non-linear calibration curve both obtained from the fiber optic displacement gauge—explained in Section 3.2.2).

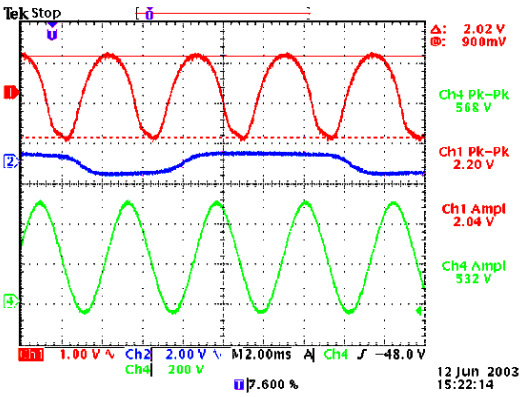

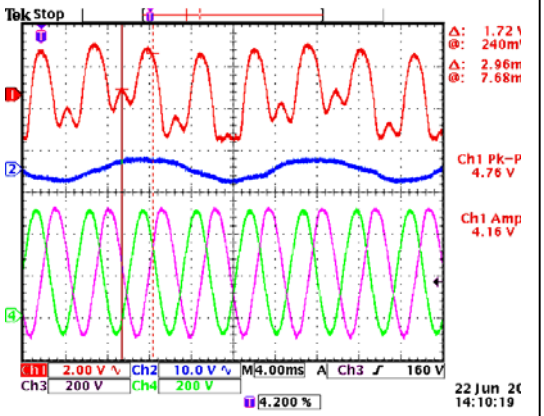

Figure 7.2.3—1A. (color)

Figure 7.2.3—1B. (color)

Representative screen shots of motor test signals showing vibration response signals in red (top), tachometer signals in blue (middle), and high-voltage drive signals in green (bottom).
In Figure 7.2.3—1B, the violet trace is a second high-voltage drive signal for driving two actuators out-of-phase.

A representative frequency sweep (vibrational amplitude, rotational speed, and input current as a function of frequency) is shown in Figure 7.2.3—2. It shows three resonant peaks, a phenomenon that was only observed so clearly when the rotary motor was configured with a pair of THUNDER model 8R actuators driven in phase. Such well-defined peaks were either not as evident or not all present when the motor was configured with a single THUNDER model 6R actuator (below 600 Hz), with in a single THUNDER model 8R actuator, or when double THUNDER model 8R motor assemblies were operated out-of-phase.

Note that high displacement at low frequency does not yield rotation, although the resonant peak has a much higher amplitude than the other two. Resonant / anti-resonant inflections are also observed in the current plot, although an inflection in current associated with the low frequency resonance is not visible at the scale of the plot. Collective evidence

suggests that motors built using double actuators driven in phase experience considerable interaction between the actuators.

To create a comparative performance summary of various motor configurations, however, results from load tests will be more useful than frequency sweeps. A motor mounted in the torque test stand described in Section 3.4 was operated at a resonant frequency where rotational speed was at a maximum. The initial data point of the load test was unloaded speed. (Data for actuator amplitude, current drawn and phase offsets were also recorded as previously described.) Weights were stacked one at a time on the test stand, while decreasing speed (and other variables) were measured. An example of load test results is provide by Figure 7.2.3—3.

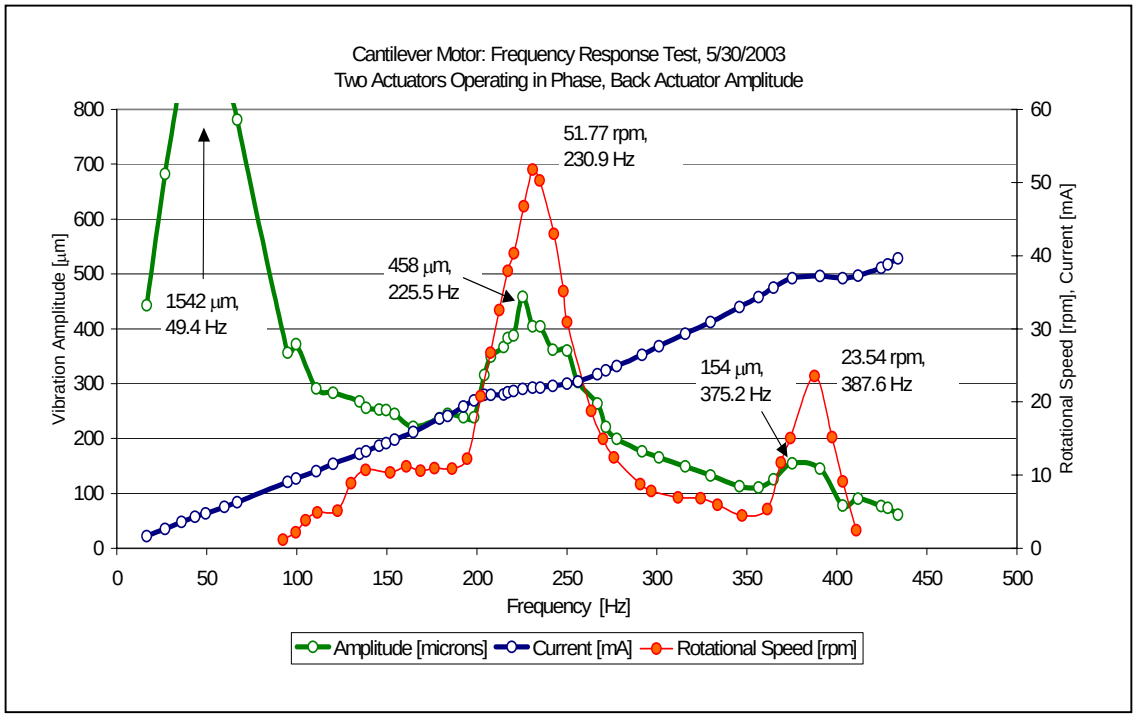

Figure 7.2.3—2. (color) Representative frequency sweep for double actuator motor driven in phase.

The equivalent of the blocking force of an actuator or linear motor is the blocking torque of a rotary motor. The data in Figure 7.2.3—3 have been plotted against amount of mass stacked on the test stand brake shaft during a load test. The weight acting through the brake shaft in a direction normal to the horizontal axis of the motor axle results in a proportional force of friction acting tangentially to the moving surface of the axle (in a direction opposing motor rotation). The proportionality is the coefficient of friction, which was found (for this particular apparatus) to be a decreasing function of load tending toward a constant value, as discussed in Section 3.4.

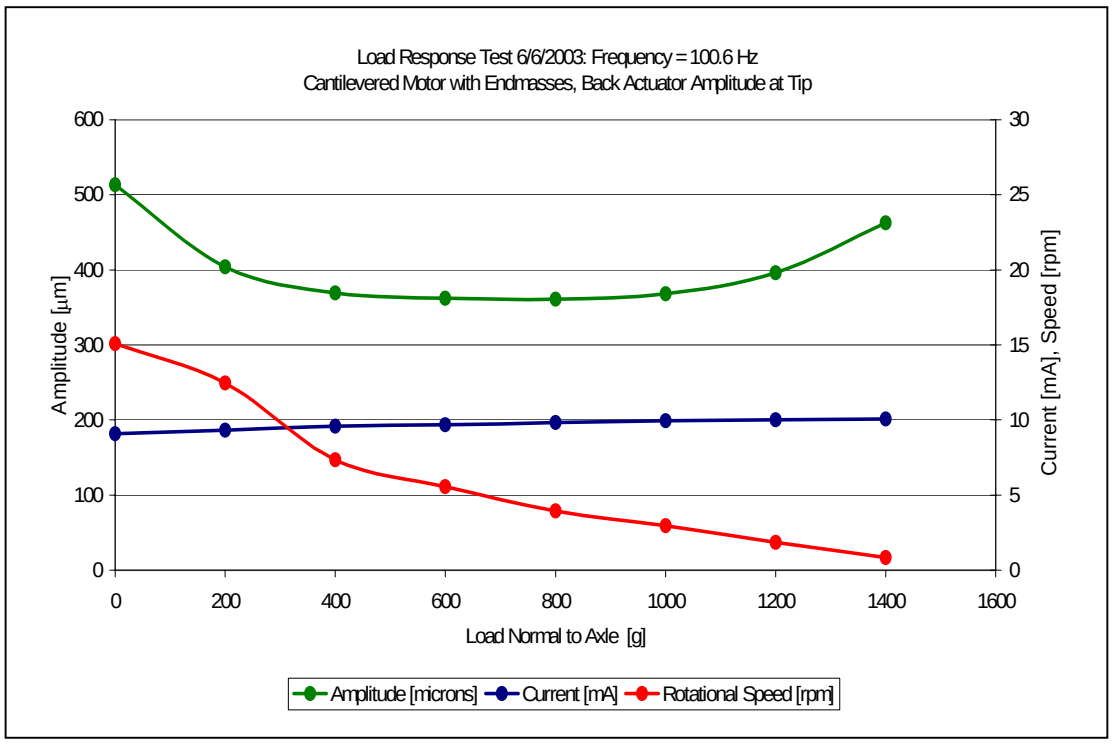

Figure 7.2.3—3. (color) Example of rotary motor load test results plotted against mass load on brake shaft of test stand

To find blocking torque, however, motor speeds must be re-plotted against resistance torque caused by brake shaft friction, not the amount of mass stacked on the test

stand. If the coefficient of friction were constant, as it typically is, the shape of the plotted curves would remain unchanged when plotted against resisting torque supplied by friction. However, since C.O.F for this apparatus is a non-linear function, the conversion alters the shape of the plotted data, as shown in Figure 7.2.3—4.

Frictional torque is developed by tangential frictional force applied to the motor axle at a distance from the axis of rotation equal to the radius of the axle, which is 0.1875 inch or $4.7625(10)^{-3}$ m. The conversion from mass, x (in grams), loaded on the brake shaft of the test stand to resistance torque (due to friction) was given by equation 3.4—2 in Section 3.4, which is repeated here. The function, F(x), where x is the mass load on the test stand brake shaft, gives the variable coefficient of friction, according to the piecewise function in equation 3.4—1, given in Section 3.4.

(3.4—2), repeated.

$$\text{Counter-Torque [Nm]} = (4.7625(10)^{-3}\ [\text{m}]) \left(9.8 \left[\frac{m}{s^2} \right] \right) \left(x\,[g] \frac{0.001\,[kg]}{[g]} \right) F(x) \left[\frac{g}{g} \right]$$

Notice that the initial downturn in motor speed between zero mass load and 400g evident in Figure 7.2.3—3 has been straightened by the re-plotting. This suggests that the changing coefficient of friction might have an observable effect on the shape of plotted data *before* re-plotting. One simply would not know what cause to attribute to the downturn. A line, fitted by the least squares method, provides an estimation of blocking torque, the zero speed which the plotted data were approaching.

Although the torque values were determined from resistance due to friction, they are equivalent to the motor-generated torque because at constant motor speed, net torque is zero, indicating that generated and opposing torques of opposite sign are canceling. Non-zero torque causes acceleration (changing speed). Every additional mass added to the brake stand increased frictional counter-torque, causing negative acceleration (slowing) while motor torque increased, restoring balance between opposing torques and constant speed

operation. Thus, the motor provides higher torque at lower speed in response to increased load.

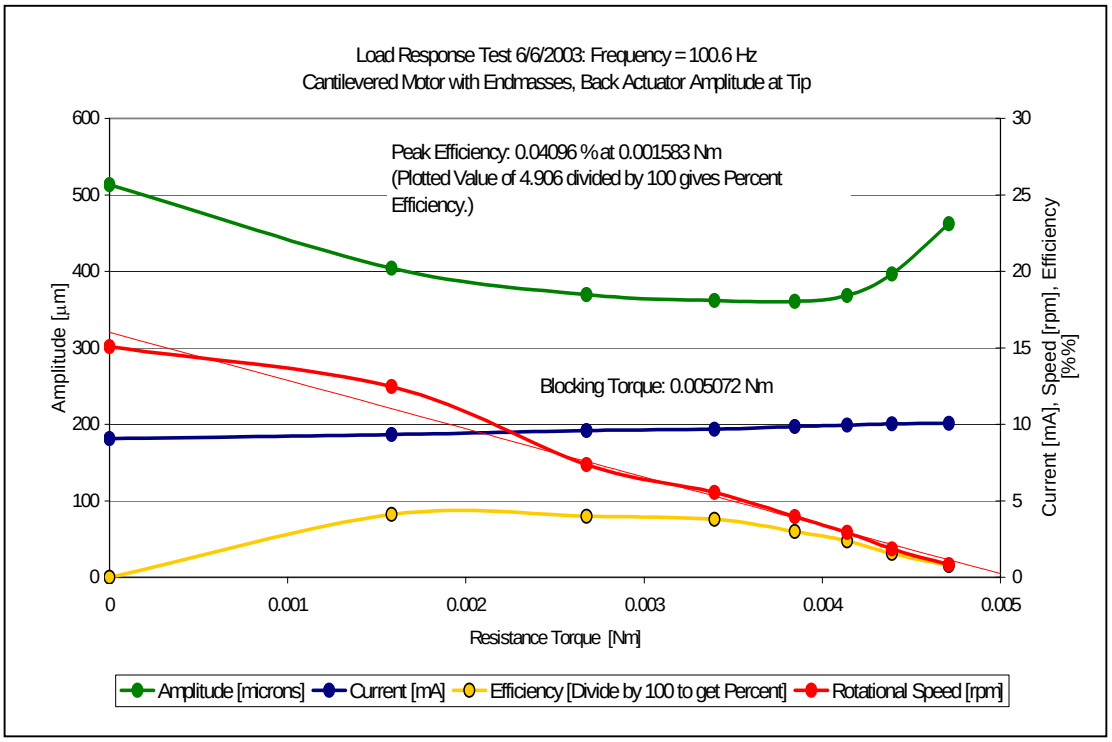

Figure 7.2.3—4. (color) Example of load test data in Figure 7.2.3—3 re-plotted against resistance torque due to friction from brake. Fitted line estimates blocking torque.

Since the rate at which mechanical work is being done by the motor and at which electrical energy is being supplied can both be determined from the given data (and known, constant operating voltage), efficiency of conversion can be determined. Mechanical output power is given by the product of torque and angular speed, electrical input power by the product of voltage and current. Speed in rpm would be multiplied by $2\pi / 60$ to convert to radians per second, and current in mA would be divided by 1000 to convert to current in Amperes.

Calculated efficiency is also plotted in Figure 7.2.3—4, which indicates not only that conversion efficiency is low, but remarkably low. (However, see closing comment in Section 7.2.4.) The plotted numbers are 100 times the percentage efficiency or 10,000 times the fractional efficiency (symbolized in some of my plots by " %% "). (As discussed previously, the calculated values should be about 40% higher since a peak-to-peak voltage was used instead of RMS voltage.) Note that maximum efficiency occurs approximately midway between zero external torque and blocking torque. This is analogous to the principle, discussed in Section 2.3.2, that maximum work is transferred from an actuator to load when deflection is constrained to one-half the free deflection, allowing one-half the blocked force to develop.

The examples chosen for Figures 7.2.3—3 and 7.2.3—4 were of course selected as the best illustrations of the points made in the preceding discussion. Although other test results do not contradict what these figures show, there is considerable variation among them. Sometimes actuator amplitude was relatively constant with increasing load; sometimes it increased or decreased. Often, it oscillated between high and low values during some portion of the test results. The initial downturn in motor speed, which was removed by re-plotting in the example provided, was sometimes evident, sometimes not.

More important, however, was the observation that the overall linear trend in decreasing speed with increasing load tended to fall into a separate regime after the first two to four measured speed values. This is slightly evident in Figure 7.2.3—4, but was more evident in almost every other plot of test data. The phenomenon could have resulted from the shift between surface and edge contact between brake shaft and motor axle. Consequently, in most cases, the first two to four data points were excluded from the data used to determine fitted lines to estimate blocking torque. As evidence for the appropriateness of this treatment, an example of fitting a trend line to a reduced data set is shown in Figure 7.2.3—5.

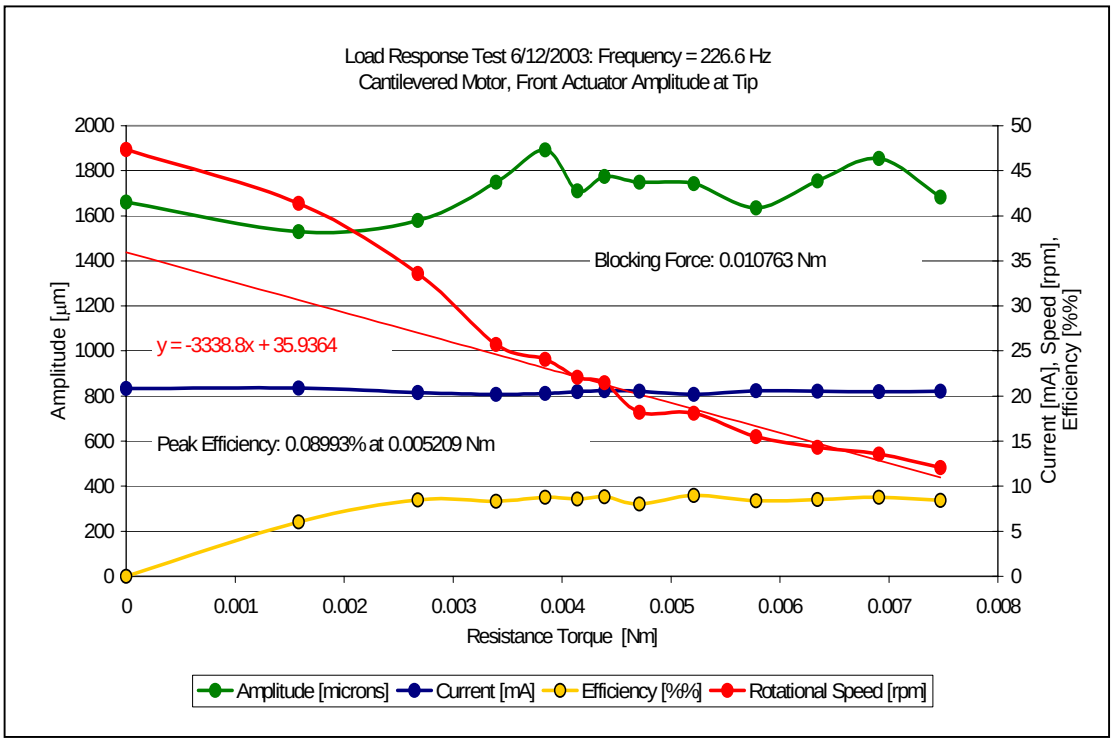

Figure 7.2.3—5. (color) An example of load test data re-plotted against resistance torque which illustrates the omission of three initial speed values from least squares approximation

Table 7.2.3—1 summarizes test results obtained during initial reconfigurations before using two actuators mounted as cantilevers. Table 7.2.3—2 summarizes characterization of a double actuator motor having small (3.4 g) end-masses attached to tips of actuators in addition to center-masses (7.8 g). Table 7.2.3—3 and Table 7.2.3—4 summarize results from characterization of a double actuator motor driven in phase, with Table 7.2.3—5 providing additional results from four additional load tests on the same motor operated at the higher-frequency operating point. In Table 7.2.3—6 double actuators are driven out of phase. Table 7.2.3—7 covers characterization of the motor driven by actuators in rebound orientation (clutch bearing locks and transmits torque not when actuators are energized but when they rebound with electric field off). Table 7.2.3—

8 provides a summary of results for the motor driven by a single 6R actuator. Finally, Table 7.2.3—9 presents a collection of parts data, such as mass, cost. To gain a sense of the relative merit of the various motor configurations tested, a visual comparison of blocking force and speed data is shown in Figure 7.2.3—10.

Note that frequency tests were conducted at constant (zero) load across a range of frequencies, while load tests were conducted at constant frequency across a range of increasing loads. Therefore, in tables listing frequency sweep results, the parenthetical values give the frequency at which the reported value (e.g., motor speed) was measured. In tables listing load test results, the parenthetical values give the load level or resistance torque at which the reported value was measured—with the exception of the value given in parentheses next to blocking torque. This parenthetical value is the (non-zero) frequency at which the motor was driven during the entire load test. This frequency was chosen simply by searching for the frequency corresponding to highest speed at the time of a test.

Table 7.2.3—1 Characterization of initial motor configurations

Blocking Torque, (Test Frequency) [Nm], [Hz]	Maximum Speed, (Frequency) [rpm], [Hz]	Max Amplitude, (Frequency) [μm], [Hz]	Operating Range [Hz]
Original Two-Axle Motor, Center-mass Not Yet Attached (aad_021903)			
0.0006156, (129)	2.57, (128.9)	332, (128.9)	110 to 147
Original Two-Axle Motor, Center-mass Attached (aae_022003)			
0.0006019, (224)	6.77, (220.9)	399, (229.5)	180 to 278
Center-mass Attached, Non-driven Axle Removed (aaf_022503)			
0.01172, (218.7)	16.19, (221.6)	2618, (227.6)	140 to 330

Table 7.2.3—2 Characterization of double-actuator motor with end-masses

Frequency Sweeps	Maximum Speed, (Frequency) [rpm], [Hz]	Max Amplitude, (Frequency) [μm], [Hz]	Operating Range [Hz]
Front Actuator, Broad Peak, 12.51 to 14.25 rpm, (98.7 to 134.6 Hz) (abc_060403)			
	14.25, (105.0)	613, (117.3)	53 to 210
Back Actuator, Broad Peak, 12.81 to 14.48 rpm, (100 to 140 Hz) (abc_060303)			
	14.48, (106.6)	529, (106.6)	53 to 210
Blocking Torque, (Test Frequency) [Nm], [Hz]	Maximum Speed, (Torque) [rpm], [Nm]	Max Amplitude, (Torque) [μm], [Nm]	Efficiency, (Torque) [%], [Nm]
Load Test, Front Actuator at Center (abe_060603)			
0.005142, (100.6)	15.05, (0)	1172, (0.004711)	0.04992, (0.003394)
Load Test, Front Actuator at Tip (abd_060603)			
0.005096, (100.5)	14.75, (0)	584, (0.004391)	0.0518, (0.00268)
Load Test, Back Actuator at Center (abf_060603)			
0.005430, (100.6)	15.09, (0)	921, (0.004711)	0.04564, (0.002678)
Load Test, Back Actuator at Tip (abf_060603)			
0.005072, (100.6)	15.09, (0)	513, (0)	0.04096, (0.001583)

Table 7.2.3—3. Characterization of double-actuator motor driven in phase

Secondary Speed, (High-Frequency) [rpm], [Hz]	Maximum Speed, (Frequency) [rpm], [Hz]	Max Amplitude, (Frequency) [μm], [Hz]	Operating Range [Hz]
Frequency Sweep, Front Actuator (abb_060103)			
21.37, (388.9)	49.54, (230.9)	434, (203.4)	50-400
Frequency Sweep, Back Actuator (abb_053003)			
22.00, (384.6)	48.65, (234.6)	458, (225.5)	80-415
Frequency Sweep, Front Actuator at Center (abh_061103)			
18.04, (372.2)	52.41, (227.3)	509, (206.6)	<40 to 400
Frequency Sweep, Back Actuator at Center (abh061003)			
17.39, (363.2)	49.27, (218.8)	591, (218.8)	<40 to 395
Frequency Sweep, Front Actuator at Tip (abf_060903)			
16.49, (378.8)	50.39, (230.9)	1677, (206.9)	30 to 400
Frequency Sweep, Back Actuator at Tip (abg_061003)			
18.52, (376.9)	50.45, (223.2)	(Inverse Peak)	70 to >450

Table 7.2.3—4. Additional characterization of double-actuator motor driven in phase.

Blocking Torque, (Test Frequency) [Nm], [Hz]	Maximum Speed, (Torque) [rpm], [Nm]	Max Amplitude, (Torque) [μm], [Nm]	Efficiency, (Torque) [%], [Nm]
Load Test, Back Actuator at Center (abba_060203)			
0.01439, (235.85)	49.29, (0)	564, (0.001583)	0.1055, (0.009207)
Load Test, Front Actuator at Center (abh_061203)			
0.010725, (228.3)	50.89, (0)	753, (0.003845)	0.0835, (0.005781)
Load Test, Front Actuator at Tip (abh_061203)			
0.010763, (226.6)	47.35, (0)	1893, (0.003845)	0.08993, (0.005209)
Load Test, Back Actuator at Center (abj_061303)			
0.008982, (226.9)	47.67, (0)	881, (0.001583)	0.08645, (0.004140)
Load Test, Back Actuator at Tip (abi_061303)			
0.0102, (226.9)	44.95, (0)	1524, (0.001583)	0.0815, (0.004140)

Table 7.2.3—5. Characterization of double-actuator motor driven in phase at high-frequency operating point

Blocking Torque, (Test Frequency) [Nm], [Hz]	Maximum Speed, (Torque) [rpm], [Nm]	Max Amplitude, (Torque) [μm], [Nm]	Efficiency, (Torque) [%], [Nm]
Load Test, Front Actuator at Center (abj_061603)			
0.004446, (373.7)	10.71, (0)	186.4, (0.004140)	0.006860, (0.002876)
Load Test, Front Actuator at Tip (abj_061603)			
0.004394, (373.1)	10.70, (0)	2329, (0.004140)	0.006597, (0.001583)
Load Test, Back Actuator at Center (abj_061503)			
0.004489, (373.1)	21.42, (0)	305, (0)	0.01173, (0.001583)
Load Test, Back Actuator at Tip (abj_061503)			
0.004562, (373.1)	12.01, (0)	2510, (0.003394)	0.007877, (0.001583)

Table 7.2.3—6. Characterization of double-actuator motor driven out of phase

Frequency Sweeps	Maximum Speed, (Frequency) [rpm], [Hz]	Max Amplitude, (Frequency) [μm], [Hz]	Operating Range [Hz]
Front, Center, Broad Peak, 39.47 to 34.94 rpm, (197.2 to 224.2 Hz) (abk_061803)			
	39.47, (197.2)	638, (197.2)	130 to 310
Front, Tip, Broad Peak, 39.47 to 34.94 rpm, (98.7 to 134.6 Hz (abk_061803)			
	38.33, (194.1)	4409, (194.1)	135 to 300
Back, Center, Broad Peak, 39.02 to 30.77 rpm, (193.5 to 225.7 Hz (abl_061903)			
	39.02, (193.5)	1353, (212.4)	125 to 290
Back, Tip, Broad Peak, 37.88 to 33.41 rpm, (195.7to 222.6 Hz (abl_061903)			
	37.88, (195.7)	2923, (187.5)	130 to 300
Blocking Torque, (Test Frequency) [Nm], [Hz]	Maximum Speed, (Torque) [rpm], [Nm]	Max Amplitude, (Torque) [μm], [Nm]	Efficiency, (Torque) [%], [Nm]
Load Test, Front Actuator at Center (abn_062403)			
0.009213, (195.7)	34.34, (0)	520, (0.005781)	0.1461, (0.003394)
Load Test, Front Actuator at Tip (abm_062403)			
0.009179, (195.7)	35.40, (0)	1348, (0.007474)	0.1338, (0.002678)
Load Test, Back Actuator at Center (abm_062303)			
0.009943, (196.3)	31.67, (0)	1279, (0.005209)	0.1365, (0.005209)
Load Test, Back Actuator at Tip (abl_062003)			
0.011107, (195.7)	35.79, (0)	5786, (0.007474)	0.2275, (0.005781)
Load Test, Back Actuator at Tip (abm_062303) (Intended to Check Test, Above)			
0.009530, (195.7)	32.75, (0)	3373, (0.004140)	0.1561, (0.003394)

Table 7.2.3—7. Characterization of motor with actuator in rebound orientation

Frequency Sweeps	Maximum Speed, (Frequency) [rpm], [Hz]	Max Amplitude, (Frequency) [μm], [Hz]	Operating Range [Hz]
Back Actuator, Center, Out of Phase, Rebound Configuration (abt_070203)			
	35.92, (227.9)	448.1, (218.2)	120 to 310
Back Actuator, Tip, Out of Phase, Rebound Configuration (abt_070303)			
	49.02, (217.7)	2224, (241.5)	120 to 300
Front Actuator, Center, In Phase, Rebound Configuration (abw_070603)			
	50.43, (223.8)	800.1, (190.8)	100 to 300
Front Actuator, Tip, In Phase, Rebound Configuration (abv_070603)			
	44.21, (225.2)	1924, (193.3)	<100 to >300
Blocking Torque, (Test Frequency) [Nm], [Hz]	Maximum Speed, (Torque) [rpm], [Nm]	Max Amplitude, (Torque) [μm], [Nm]	Efficiency, (Torque) [%], [Nm]
Load Test, Front Actuator at Center, In Phase, Rebound Configuration (abu_070603)			
0.009352, (215.5)	53.13, (0)	585, (0.001534)	0.08902, (0.005209)
Load Test, Front Actuator at Tip, In Phase, Rebound Configuration (abu_070603)			
0.007563, (215.5)	53.57, (0)	1894, (0.002678)	0.07747, (0.003845)
Load Test, Back Actuator at Center, In Phase, Rebound Orientation (abu_070403)			
0.008538, (215.5)	33.99, (0)	520, (0.005496)	0.1461, (0.003394)
Load Test, Back Actuator at Tip, In Phase, Rebound Orientation (abt_070403)			
0.010114, (215.5)	51.66, (0)	3086, (0.004391)	0.1075, (0.005209)

Table 7.2.3—8. Characterization of motor driven by a single model 6R actuator

Frequency Sweeps	Maximum Speed, (Frequency) [rpm], [Hz]	Max Amplitude, (Frequency) [μm], [Hz]	Operating Range [Hz]
Frequency Sweep, Center, (abz_071003)			
	175.91, (359.7)	334, (372.0)	<140 to 580
Frequency Sweep, Back, Center, (aca_071303R)			
	103.50, (385.6)	1822, (387.5)	<280 to >480
Frequency Sweep, Tip, (acb_071303R)			
	103.50, (385.6)	4121, (378.8)	<280 to >480
Frequency Sweep, Center, (acb_071303R)			
	132.77, (380.7)	422, (380.7)	<280 to >480
Blocking Torque, (Test Frequency) [Nm], [Hz]	Maximum Speed, (Torque) [rpm], [Nm]	Max Amplitude, (Torque) [μm], [Nm]	Efficiency, (Torque) [%], [Nm]
Load Test, Center (acb_071303)			
0.01156, (291.4)	69.45, (0)	334, (0.004140)	0.1316, (0.004711)
Load Test, Tip (abz_071203)			
0.008074, (383.8)	186.6, (0.001583)	1333.50, (0)	0.2077, (0.003394)
Load Test, Center (acc_071503)			
0.005432, (291.4)	168.88, (0)	334, (0.004140)	0.1150, (0.003394)
Load Test, Tip (acb_071403)			
0.005443, (376.9)	164.77, (0)	2687, (0)	0.1129, (0.003845)

Table 7.2.3—9. Inventory of motor parts with measured mass and approximate cost

Part	Quantity	Mass [g] (Each)	Cost , $ (Each)
Stainless Steel Axle, 0.375" Dia., 6" Long (Type 303 SS, Precision-Ground)	1	85.8213	19 (6 ft.)
Plastic Actuator Collar and Bolt	2	12.8	
Clutch Bearings, 3/8" Shaft Dia	2 or 4	7.3	14
Non-Clutch Bearings (If two Clutch Bearings)	2 or 0	5.6	4
Steel Split-Collar (A third collar for testing)	2 + 1	19.6	3
Face International. Co. Model 6R THUNDER	1	18.7	105
Wires and Tape attached to THUNDER 6R	1	0.3	
Center-mass attached to THUNDER 6R	1	16.5	
Face International. Co. Model 8R THUNDER	2	1.8	102
Center-mass attached to THUNDER 8R	2	7.8	
End-mass attached to THUNDER 8R	2	3.45	
Plastic Base	1	140.6	
Axle Bearing Blocks and Bolts	2	18.2	
Stop Blocks, Bolts and Pads (Not Used with Model 6R Configuration)	lot	16.3	

Note: Prices have generally changed over time. Listed prices have been rounded to nearest dollar since valuation is intended to be approximate. THUNDER actuator prices revised to April 2004 listing by manufacturer [8], but the prices shown (for 1—10 actuators) are discounted when actuators are purchased in larger quantities.
Parts with no cost listed were custom fabricated (or trivial, such as wire or bolts).

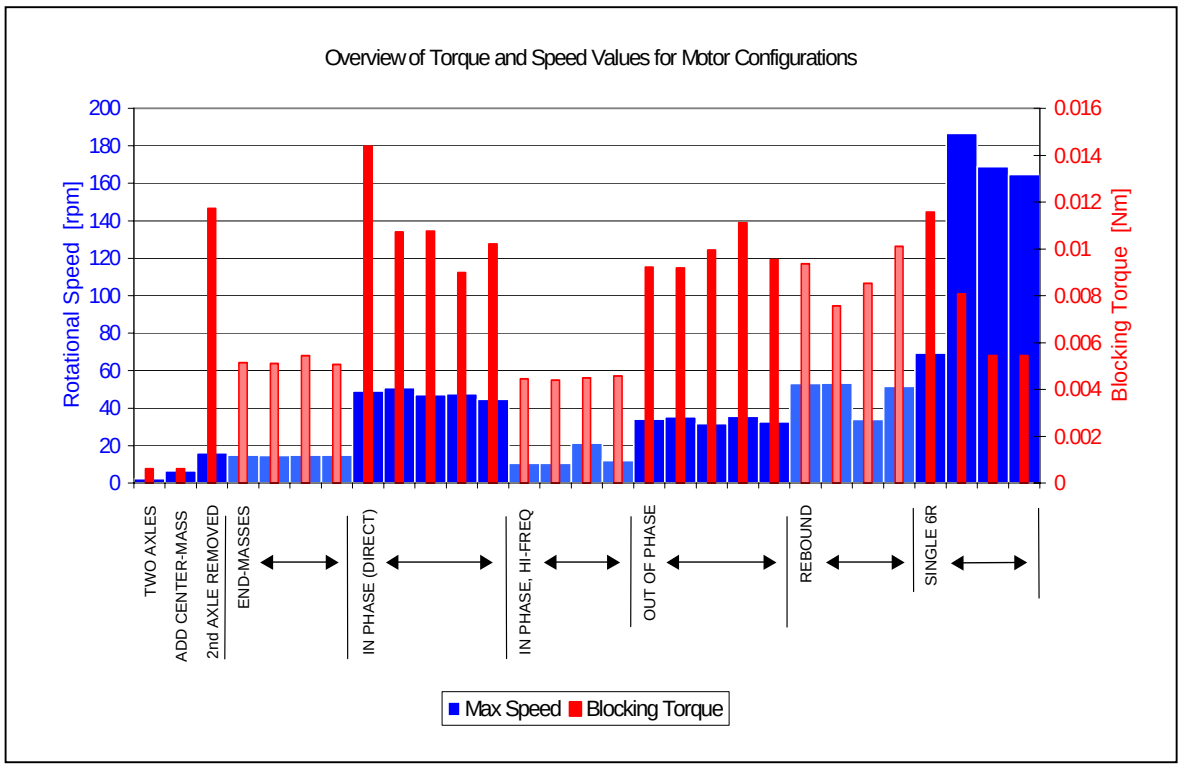

Figure 7.2.3—10. (color) Comparison of blocking force and speed results from tests for various motor configurations (Lighter vs. darker colors are intended only to distinguish data sets corresponding to each design modification.)

To add context for how large or small the torque values are, some comparisons will be given. We observe that test results for the various motor configurations tend to fall around a blocking torque of 0.010 Nm, with the range from (approximately) 0.005 to 0.015 Nm. The rotary motor by Mockensturm, Frank, Koopman, and Lesieutre, to be discussed further in the last section, attained a stall torque of 0.47 Nm using 12 bimorphs driven at maximum voltage (maximum speed on the order of 500 rpm). [7] A traveling wave ultrasonic motor, sold by Piezo Systems, Inc. (Cambridge, MA, www.piezo.com) attains a continuous torque of 0.05 Nm, and a short duration torque of 0.10 Nm or more (100-300 rpm). The smallest commercial electromagnetic motors are the Smoovy motors made by RMB Miniature Bearings Inc., a U.S. subsidiary of a Swiss Company

(www.smoovy.com). They sell a motor with a diameter of 3 mm (which has a speed on the order of 100,000 rpm), but their 8-mm-diameter motor has a continuous rated torque of 0.00066 Nm, with the capability of providing 0.00081 Nm for periods of three minutes or less (17,000 to 13,500 rpm). A survey of small DC electromagnetic motors by Glenn and Hagood [9] included a range of stall torque values from 0.0033 to 0.08 Nm (speeds from 13,500 to 5,000 rpm).

7.2.4 Summary Discussion and Conclusions Regarding Rotary Motor Results

A number of conclusions are suggested by the overview of results plotted in Figure 7.2.3—10 and by the analysis in Section 7.2.2, but first, a cautionary note. Observed trends may be stronger or not as strong as this sample of data suggests—given that this motor is an inherently "noisy" system. The Rotary Thunder-motor subjects itself and its surroundings to energetic vibration to produce rotation and work. It generates loud acoustic noise during operation. Internal parts might loosen or shift, and its position in the test apparatus or relative to fiber-optic probes might change slightly during testing. (It is necessary to use lock-nuts having Nylon inserts on all threaded rods or the motor does not remain assembled.) Two THUNDER actuators failed after periods of operation and had to be replaced with different actuators of the same model. (Results elsewhere in this thesis indicate definite variation between individual actuators of the same model, especially with time and use.)

On the other hand, care was taken to determine stability, cross-check or re-check measurements, and rebuild as necessary with well-matched parts and identical methods. All reported results are averages of at least several individual measurements. Rotational speed results have the greatest number of individual data points behind them—as many as 20-30 measurements.

That said, we note that the most definite conclusion to be drawn from the leftmost solid-color section in Figure 7.2.3—10, is that constraining the non-driving end of actuators in the rotary motor substantially diminishes output torque and speed. Blocking

torque showed a gain of almost two orders of magnitude, while speed increased six-fold greater than the speed of the two-axle motor with no center-mass and more than double the speed of the two-axle motor with center-mass. It would have been instructive to have also measured the change upon first removing the second axle, then adding the center-mass.

Larger center-masses were tried before adopting the mass given in Table 7.2.3—8. The largest was a mass of about 20g. Perhaps the larger masses caused some unmeasured amplification of torque, but speed determinations and subjective evaluations of "robust operation" indicated that the larger center-masses were not advantageous. It was further noted during many experiments that even slightly touching the free end of the vibrating cantilever caused the motor to slow. Also, clamping the base too firmly, even if structural distortion seemed unlikely, likewise caused the motor to slow (e.g., only one corner clamped).

The next most apparent conclusion is that it was difficult to improve upon motor performance with two actuators driven in phase, coupled during energized deflections (direct mode) rather than during elastic rebound (rebound mode). This configuration achieved high blocking torque at useful speeds around 50 rpm. The much-anticipated advantage of driving actuators out-of phase resulted in comparable blocking torque at perhaps slightly reduced speed. Likewise, rebound-coupled operation might have exchanged slightly-enhanced speed for slightly-reduced blocking torque, but the observation is tentative given variability, and of no great consequence.

There was a sense that the motor performance deteriorated slightly during the course of repeated testing for unidentified reasons, but no data are available to support this perception. However if this perception were valid, then testing earlier in the schedule (such as operation with two actuators directly driven in phase) would have been slightly favored.

Adding end-masses to the tips of the actuators (in addition to center-masses always used after they were first installed) resulted in reduction of both blocking torque and rotational speed. An interesting observation is that adding end-masses to the tips of the actuators reduced blocking torque and rotational speed to the general levels occurring when operating at the high-frequency resonance without attached end-masses. However,

adding them lowered the resonant frequency of operation well below the high frequency peak that occurs without the end-masses. (See Figure 7.2.3—2 for an indication of a high-frequency peak in actuator amplitude and motor speed.) Motor operation with end masses was also much quieter.

The last conclusion available from Figure 7.2.3—10 is that a motor built with a single model 6R THUNDER actuator rather than a pair of model 8R THUNDER actuators achieves mixed indications of motor performance. The model 6R actuator is larger than the model 8R (about three times greater area covered by a piezoceramic layer almost twice as thick) and draws more current. There may be subtle effects from mounting a single actuator onto both clutch bearing collars rather than one of a pair in each of them. For example, the model 6R actuator can be expected to generate transverse deflection about as large as longitudinal deflection, since the piezoceramic plate is square. The motor is not designed to use this deflection component, which may interfere somewhat with the operation of the clutch bearings.

However, the bottom line is that a single model 6R THUNDER actuator dramatically increases motor speed in exchange for either comparable or somewhat reduced blocking torque, compared with the motor driven by two model 8R THUNDER actuators vibrating in phase. Ideally, both torque and speed would have been augmented by the much larger actuator. The first blocking torque (0.012 Nm, reading from left) plotted with the data subset for characterization of the motor built with a model 6R actuator is indeed the third highest blocking torque shown in Figure 7.2.3—10. However, it appears that the high torque was achieved in exchange for reduced speed (about 70 rpm rather than, say, 170 rpm, associated with lower blocking torque).

The analysis of the motor built with a model 6R actuator based on acceleration, which was discussed in Section 7.2.2, produced slightly higher maximum values of blocking torque—in a range between 0.012 and 0.016 Nm—corresponding to resonant frequencies between approximately 350 and 400 Hz. The agreement is quite good, considering that these results were obtained by an entirely different experimental process and the analysis included many steps and inputs and data treatments. The efficiency

calculations suggest that the motor built with a model 6R actuator may achieve conversion "as high as" one percent, while friction load tests yield 0.21% as a highest calculated value. Rather than concluding that the two methods are in disagreement, it may well be that the motor is more efficient in the brief time before achieving steady state operation.

During that period, the clutch bearings would be switching between lockup and free rotation at an increasing but temporarily slower rate. Recall that the manufacturer placed a limit on the rate of transition at 117 Hz. Also, the experiment which attempted to determine effect of vibration on clutch-bearing internal resistance in the free rotation direction found the resistance reduced by about 10% in association with vibration at about 250 Hz. (See discussion regarding Figure 7.2.2—7.) This frequency is close enough to the resonant frequency of the assembled motor to suggest that the clutch bearings may play a role in determining the resonant range of motor operation. Although the effect of clamp loss was not quantified in characterizing the Rotary Thunder-motor as it was in the analysis of linear motor performance, there can be little doubt that clamp loss is one factor in limiting the rotary motor performance.

In Section 7.2.1, the similarity of the rotary motor studied in this project to the rotary actuator described by Mockensturm, Frank, Koopman, and Lesieutre in [7] was discussed. The paper reported on a mathematical model developed to better understand and refine a motor designed by engineering intuition which had performed beyond expectations. It used the resonant vibration of 12 bimorphs with large end-masses radially distributed around a central hub mounted to a commercial roller clutch, resulting in measured stall torque (blocking torque) of 0.47 Nm at 266 V_{PP} . An unloaded speed of 9 rps or 540 rpm was mentioned. The frequency corresponding to these values was not specified, but subsequent discussion suggests it was on the order of 1000 Hz. Assuming test methods were equivalent, their device outperformed the Rotary Thunder-motor by several times even if the higher number of actuators is accounted for.

They also reported experimental results from the study of clutch bearing performance. Their model incorporated a constant drag torque (internal resistance) of 0.002 Nm whenever the motor shaft was moving relative to the clutch. My study discussed

in Section 7.2.2 found an internal resistance of 0.02 Nm for a pair of clutch bearings turning in the free rotation direction. Adding a second pair to block back rotation increased the value to 0.023 Nm, which is clearly a very non-linear change. Aside from likelihood of experimental error, this may indicate a large increase in resistance torque upon simply adding a *second* clutch bearing to a single clutch.

As also noted in the article, when a vibrating actuator switches from backstroke while the clutch overruns to the torque transmission half-cycle, a perfect clutch would lock as soon as the velocity of the hub reached the velocity of the shaft. The over rotation before a *non*-perfect clutch engages is backlash. A plot of "transmitted torque versus clutch over-rotation" is referred to a number times in their discussion. In my Figure 7.2.1—3, a loading torque of 400 mN-m (0.4 N-m) yielded an approximate backlash of 5.5º, while in their figure, 0.4 N-m corresponds to a backlash of approximately 1.2º.

A useful aspect of their plot of "transmitted torque versus clutch over-rotation" is that data are shown for both static and dynamic torque transmitted through the rotary clutch, which differ significantly. Static measurements tend to characterize the compliance of the loaded structure in a locked state, while dynamic measurements tend to characterize the kinetic stick-and-slip process of needle bearings engaging and disengaging at high frequency. At a typical operating frequency of 1 kHz, their clutches were cycled about five times faster than the clutches used in the Rotary Thunder-motor.

In general, the plot in [7] indicates that higher torque transmission by the rotary clutch corresponds to lower dynamic backlash than static backlash up to a cross-over point above which dynamic backlash exceeds determined static backlash. This is not quite the same interpretation as given in the article, which says that the clutch can transmit more torque at low angular displacements ("hub rotation angles"), and *vice versa*, under dynamic as opposed to static conditions. The undisclosed link between higher angular displacements and higher backlash prompted the rephrasing.

If there is indeed a correlation, this information may offer some explanation why the Rotary Thunder-motor configured with a single 6R actuator had impressive speed but unexpectedly less-than-impressive blocking torque. (Note that motors using either model

6R or model 8R actuators were tested at comparable frequencies.) The general performance data listed with the product model price list by Face International Corporation [8] indicates that the model 6R THUNDER actuator provides about 150% the typical maximum displacement of the model 8R actuator. At no load, there would be minimal backlash, so virtually all displacement would be converted to rotation. As load was introduced, dynamic conditions would initially favor a suppression of increasing backlash, but would transition to distinctly high losses at some crossover load. If backlash were actually proportional to angular displacement, the higher displacement of the model 6R actuator would contribute to accelerated losses at high loads.

Further work is needed to explain the discrepancies between these observations, and in general, to determine if a Rotary Thunder-motor could be modified to perform as well or better than the device studied by the Mockensturm, Frank, Koopman, and Lesieutre group. Given comparable characterization, it is safe to say that their rotary clutches exhibited better performance, among other things.

In closing, consider both the foremost strength and foremost weakness of the rotary motor prototype. The design advantage is that a vibrating cantilever has a large moment arm to transmit a large moment to its embedded end. Anything mechanically linked to the embedded end of the actuator must serve as a rotational constraint. During torque transmission half-cycles, internal resistance and load on the motor must fulfill this duty. However, the vibrating actuator has a significant mechanical advantage—proportional to the effective length of the moment arm—over rotational end constraints. Consequently, the motor shaft tends to rotate in spite of internal and external resistance. This situation creates the basis for high torque, which is highly desirable in a small motor.

The most conspicuous drawback is the low efficiency of electrical to mechanical energy conversion calculated in Section 7.2.2 for the rotary motor configured with a single model 6R THUNDER actuator. The low ratio of output to input energy determined may not actually reflect the inherent efficiency of this motor. During vibration, a piezoelectric actuator stores part of electrical input energy in the electric field between electrodes, since it is a capacitor. The other part is stored in the actuator structure as mechanical energy

(strain or kinetic energy). The square of the electromechanical coupling factor, k, of a material or actuator is defined as the ratio of stored mechanical energy to input electrical energy (or the inverse if the device is a generator). However, stored electrical or mechanical energy is not all available for energy conversion in piezoelectric devices, regardless of design. Wang *et al* considered at length the derivation of coupling factors for bimorphs. [10] The authors also derived expressions for the so-called energy transmission coefficient, λ , defined as the ratio of output mechanical energy to input electrical energy, which according to Uchino [11], is a more practical metric for actual work done by piezoelectric devices.

For a commercial soft PZT ceramic having $k_{31} = 0.44$, Wang *et al* apply their derived expressions to determine that the electromechanical coupling factor for a bimorph actuator made from this ceramic would equal 0.34. However, they further determine that under optimal loading conditions, the maximum value of the energy transmission coefficient, λ , equals 0.06075. That is, "a maximum of 6.1% of input electrical energy can be transferred into mechanical output energy." Clearly, energy conversion in piezoelectric devices is subject to more fundamental limitations than device design considerations.

Giurgiutiu *et al* determine expressions to calculate the electro-mechanical coupling coefficient, k, and peak reactive power for bias-voltage operation of "induced strain actuators" (ISAs) using commercial data available from manufacturers. [12] Most ISAs are driven with a DC-biased signal to accommodate their preferred polarity. The authors show that bias voltage significantly increases the reactive power component of applied voltage. Reactive power dominates dynamic operation of piezoelectric devices, which differs significantly from the energy analysis typically applied to electromagnetic devices.

Niezrecki and Balakrishnan investigated the use of two THUNDER actuators in clamshell configuration to displace water, ultimately to propel deep sea remotely operated vehicles, which would ideally have a long range of travel by using very little power. [13] They note that very little real power is consumed during operation because the electrical load is primarily reactive, so that potential for high efficiency operation exists. A resonant

LC drive circuit would pair the capacitive actuator with an inductor, allowing fundamental principles of electronic oscillators to provide oscillatory current with minimal losses.

A large portion of the current requirements of piezoelectric devices derives from the simple, but not so simple, oscillatory transport of opposite polarity charge onto and off of the capacitive actuator structure. The oscillatory current increases with frequency because the same amount of charge must be shuffled back and forth faster. This current is otherwise (mostly) not used or consumed, and could be delivered much more efficiently by a resonant circuit matched to the resonant frequency of the actuator. In the case of the rotary motor presented in this chapter, the design of such an LC or tank circuit would be greatly simplified by being able to operate a device with a stable resonant frequency—that is, one not greatly influenced by load or other operating conditions. Thus, by suitable drive circuit design, a motor system could be developed which produces the mechanical output of the motor as characterized in this study, but consumes substantially less electrical power in the process.

7.3 References

[1] V. Giurgiutiu, Z. Chaudhry, C. A. Rogers. Stiffness issues in the design of ISA displacement amplification devices: Case study of a hydraulic displacement amplifier. Proceedings of the SPIE—The International Society for Optical Engineering, 2443, 105-119 (1995).

[2] U. S. Patent Number 4,874,155 to A.S. Goul. Fast Clamp (1989).

[3] J. A. Palmer. 2002. Development of millimeter scale motors for miniature direct drive robots. PhD dissertation, N.C. State University, Raleigh, NC.

[4] E. J. O'Malley. 1999. Boundary condition impact on performance of circular piezoelectric induced strain actuators. Master's thesis, Vanderbilt University. Nashville, TN.

[5] J. Frank, E. M. Mockensturm, W. Chen, G. H. Koopman, G. A. Lesieutre. Design and performance of a resonant roller wedge actuator. Proceedings of SPIE - The International Society for Optical Engineering, 3985, 198-206 (2000).

[6] Fact Sheet: Drawn Cup Roller Clutches. The Torrington Company, Division of Ingersoll-Rand (Torrington, CT), 1996.

[7] E. M. Mockensturm, J. Frank, G. H. Koopmann, G. A, Kesieutre. Modeling and simulation of a resonant bimorph actuator drive. Smart Structures and Materials 2001: Smart Structures and Integrated Systems. Proceedings of the SPIE—The International Society for Optical Engineering, 4327, 472-480 (2001).

[8] Face Electronics, LC (Norfolk VA) http://www.face-int.com/thunder/thunder.htm

[9] T.S. Glenn and N.W. Hagood. Development of a two-sided piezoelectric rotary ultrasonic motor for high torque. Proceedings of the SPIE—The International Society for Optical Engineering, 3041, 326-338 (1997).

[10] Q.-M. Wang, X.-H. Du, B. Xu, and L. E. Cross. Electromechanical coupling and output efficiency of piezoelectric bending actuators. IEEE Transactions on Ultrasonics, Ferroelectrics and Frequency Control, 46, 638-646 (1999).

[11] K. Uchino. *Piezoelectric Actuators and Ultrasonic Motors* (Boston, MA: Kluwer Academic Publishers, 1996).

[12] V. Giurgiutiu and C. A. Rogers. Comparison of solid-state actuators based on power and energy criteria. Proceedings of the SPIE—The International Society for Optical Engineering, 2717, 287-300 (1996).

[13] C. Niezecki and S. Balakrishnan . Power characterization of Thunder actuators as underwater propulsors. Proceedings of the SPIE—The International Society for Optical Engineering, 4327, 88-98 (2001).

[14] J.A. Palmer, B. Dessent, J.F. Mulling, T. Usher, E. Grant, J.W. Eischen, A.I. Kingon, and P.D. Franzon. The design and characterization of a novel piezoelectric transducer-based linear motor. IEEE / ASME Transactions on Mechatronics, 9, 392-398 (2004).

APPENDICES

Appendix 1. Complete Collection of Butterfly Loops

This is the collection of images associated with an experiment conducted to characterize a sample of actuators representing the prominent design and fabrication variables for the project reported on in this thesis, using so-called butterfly loops which show strain as a function of applied electric field. Discussion and referral to Appendix 1 is given in Chapter 5.

The experimental plan is summarized in Table A.1—1. Three adhesive types are crossed with two levels of substrate thickness, with the additional subdivision that two levels of the thick bonds provided by J.B. Weld epoxy are included. For each actuator, a pair of large-signal displacement-voltage tests were conducted for a series of loads from zero load to the weight of 1100g, in 100g increments. After testing under the highest load, a final pair of tests was conducted with the load again at zero. Two loops were acquired in each test. The pairs of tests show the adjustment of the actuator polarization state to a new load level. Other experimental details are included between the image sets.

Table A.1—1. Matrix of variables represented by selected actuators

	LaRC-SI	M-Bond	JB Weld
Thick Substrate (Stainless steel, 8 mils thick)	060902B Bond Thickness = 18.8 μm	100902C Bond Thickness = 7.8 μm	K081602A (Thick Bond, 384.5 μm) N081602A (Thin Bond, 77.3 μm)
Thin Substrate (Stainless Steel, 4 mils thick)	062102A Bond Thickness = 13.5 μm	100902E Bond Thickness = 6.9 μm	K121002 (Thick Bond , 131.2 μm) N121002A (Thin Bond, 109.2 μm)

1. Gallery of strain-displacement loops for actuator 060902B (LaRC-SI adhesive, 8 mil stainless steel substrate) follows.

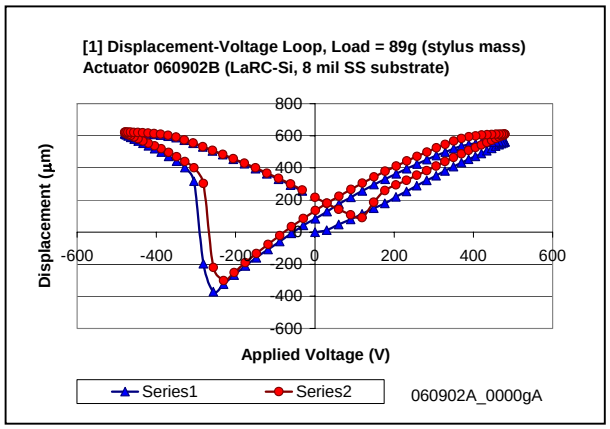

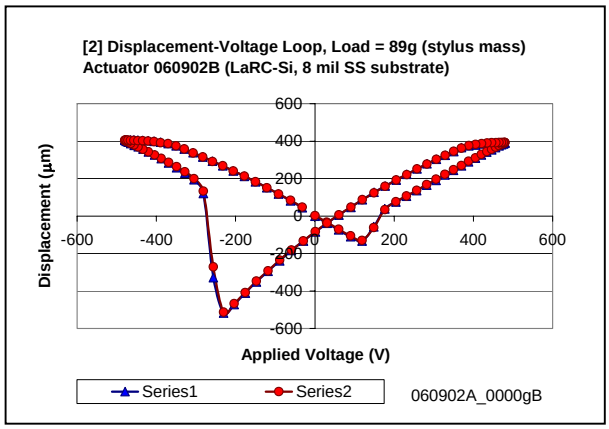

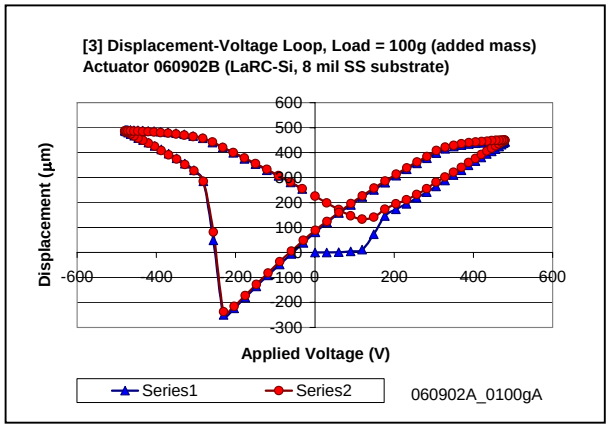

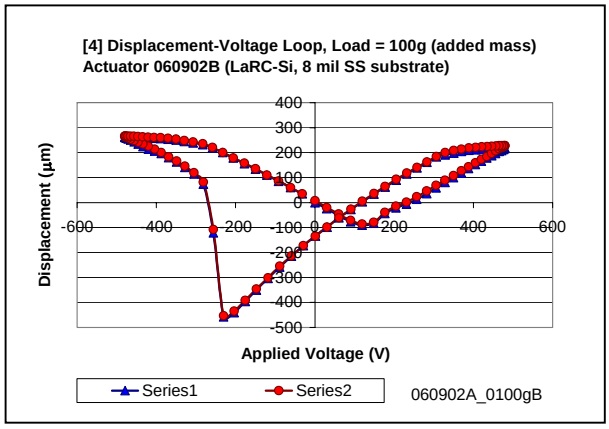

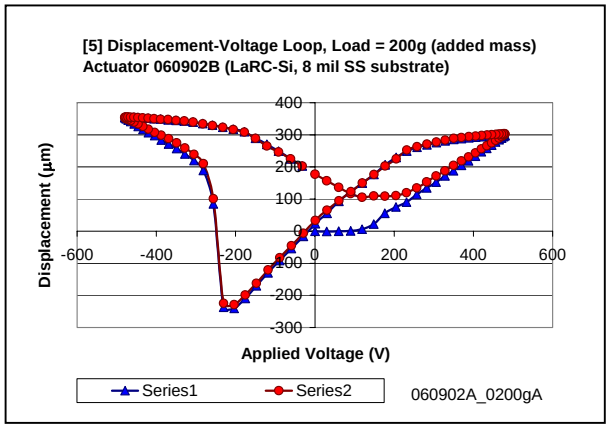

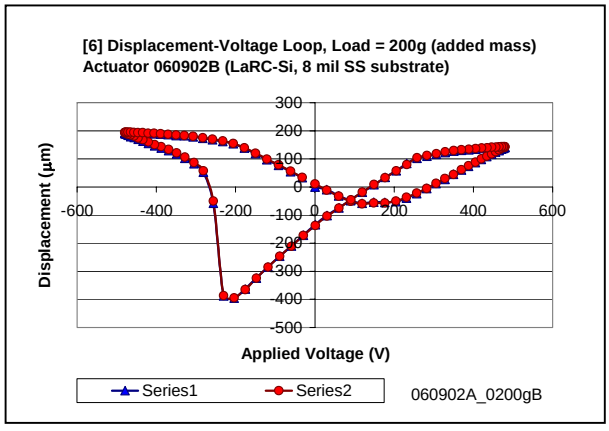

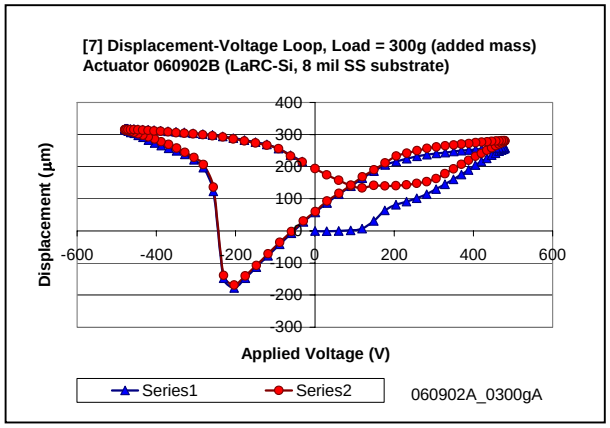
[7] Displacement-Voltage Loop, Load = 300g (added mass)
Actuator 060902B (LaRC-Si, 8 mil SS substrate)
Displacement (µm)
Applied Voltage (V)
Series1
Series2
060902A_0300gA

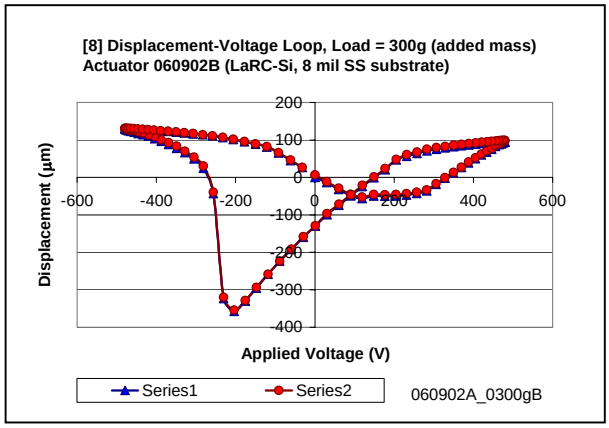
[8] Displacement-Voltage Loop, Load = 300g (added mass)
Actuator 060902B (LaRC-Si, 8 mil SS substrate)
Displacement (µm)
Applied Voltage (V)
Series1
Series2
060902A_0300gB

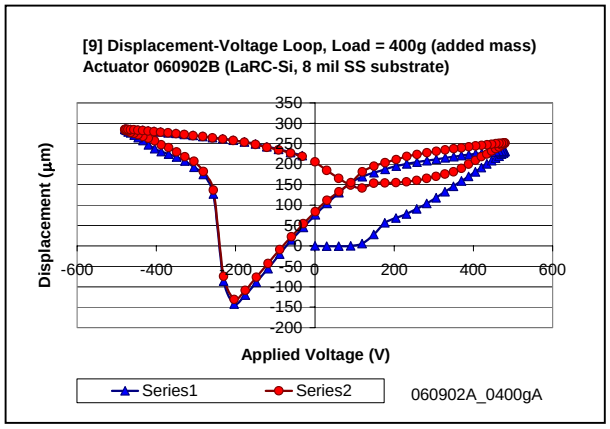
[9] Displacement-Voltage Loop, Load = 400g (added mass)
Actuator 060902B (LaRC-Si, 8 mil SS substrate)
Displacement (µm)
Applied Voltage (V)
Series1
Series2
060902A_0400gA

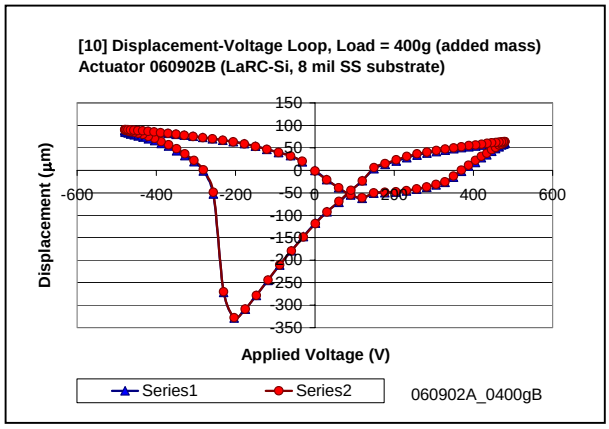
[10] Displacement-Voltage Loop, Load = 400g (added mass)
Actuator 060902B (LaRC-Si, 8 mil SS substrate)
Displacement (µm)
Applied Voltage (V)
Series1
Series2
060902A_0400gB

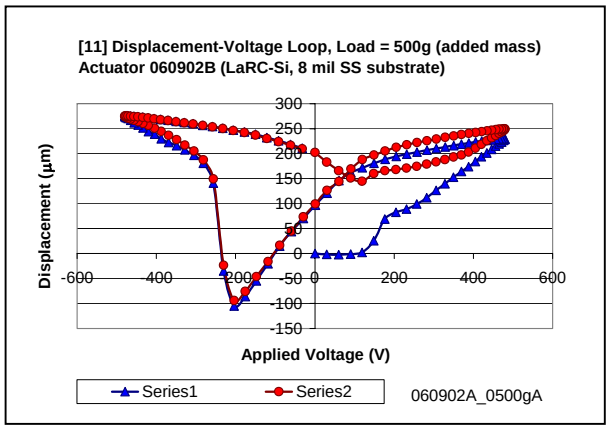
[11] Displacement-Voltage Loop, Load = 500g (added mass)
Actuator 060902B (LaRC-Si, 8 mil SS substrate)
Displacement (µm)
Applied Voltage (V)
Series1
Series2
060902A_0500gA

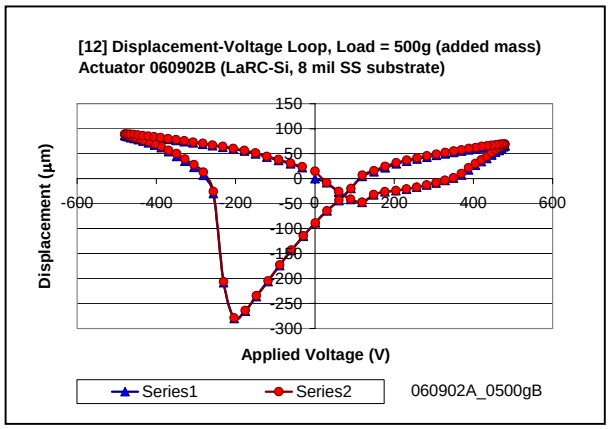
[12] Displacement-Voltage Loop, Load = 500g (added mass)
Actuator 060902B (LaRC-Si, 8 mil SS substrate)
Displacement (µm)
Applied Voltage (V)
Series1
Series2
060902A_0500gB

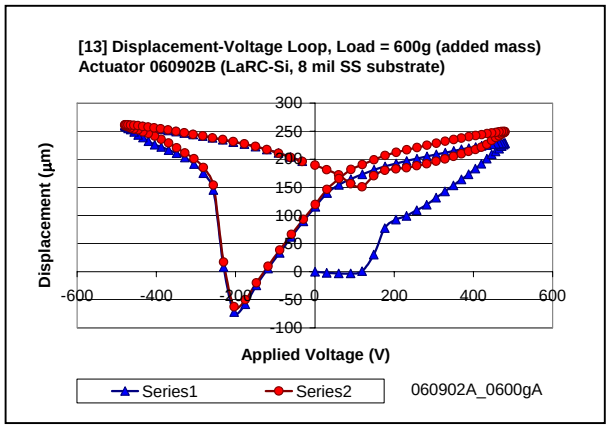
[13] Displacement-Voltage Loop, Load = 600g (added mass)
Actuator 060902B (LaRC-Si, 8 mil SS substrate)
Displacement (µm)
Applied Voltage (V)
Series1
Series2
060902A_0600gA

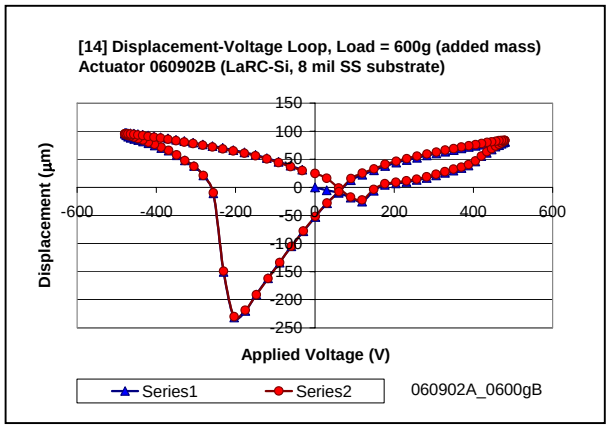
[14] Displacement-Voltage Loop, Load = 600g (added mass)
Actuator 060902B (LaRC-Si, 8 mil SS substrate)
Displacement (µm)
Applied Voltage (V)
Series1
Series2
060902A_0600gB

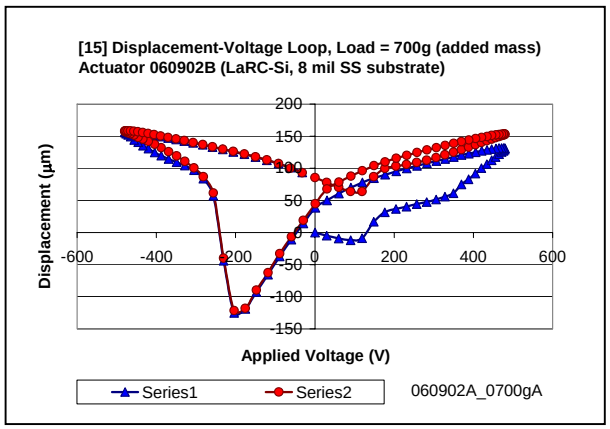
[15] Displacement-Voltage Loop, Load = 700g (added mass)
Actuator 060902B (LaRC-Si, 8 mil SS substrate)
Displacement (µm)
Applied Voltage (V)
Series1
Series2
060902A_0700gA

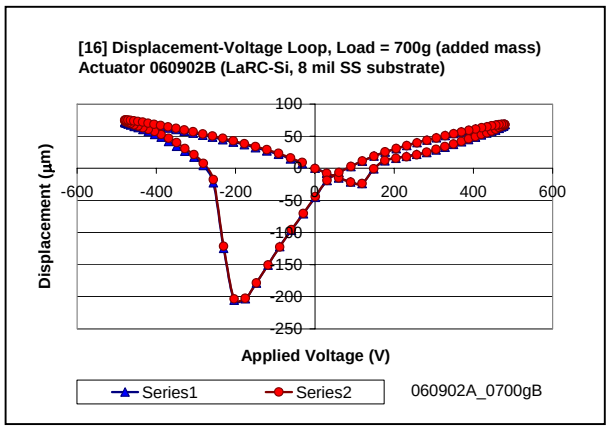
[16] Displacement-Voltage Loop, Load = 700g (added mass)
Actuator 060902B (LaRC-Si, 8 mil SS substrate)
Displacement (µm)
Applied Voltage (V)
Series1
Series2
060902A_0700gB

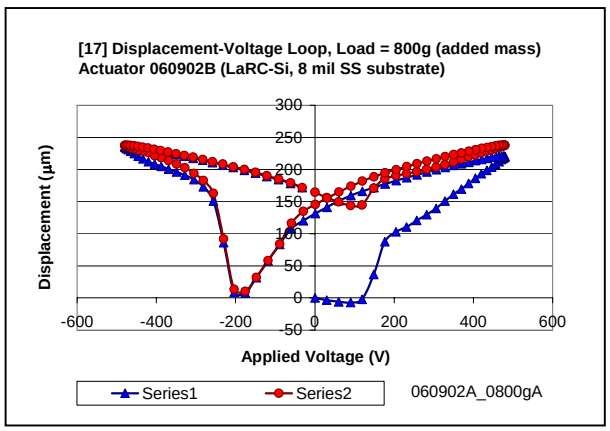
[17] Displacement-Voltage Loop, Load = 800g (added mass)
Actuator 060902B (LaRC-Si, 8 mil SS substrate)
Displacement (µm)
Applied Voltage (V)
Series1
Series2
060902A_0800gA

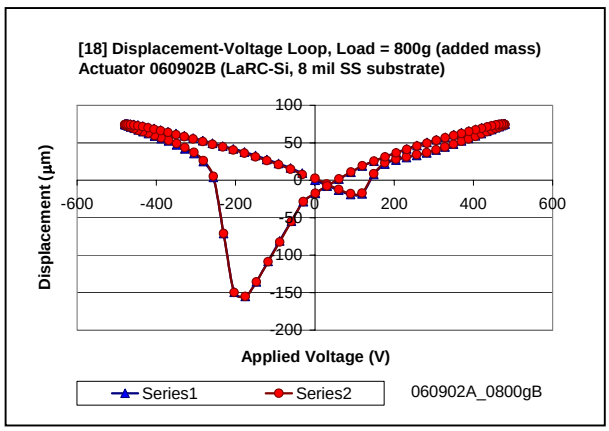
[18] Displacement-Voltage Loop, Load = 800g (added mass)
Actuator 060902B (LaRC-Si, 8 mil SS substrate)
Displacement (µm)
Applied Voltage (V)
Series1
Series2
060902A_0800gB

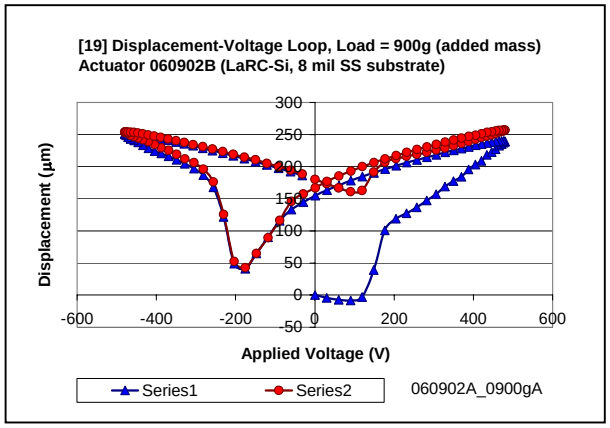
[19] Displacement-Voltage Loop, Load = 900g (added mass)
Actuator 060902B (LaRC-Si, 8 mil SS substrate)
Displacement (µm)
Applied Voltage (V)
Series1
Series2
060902A_0900gA

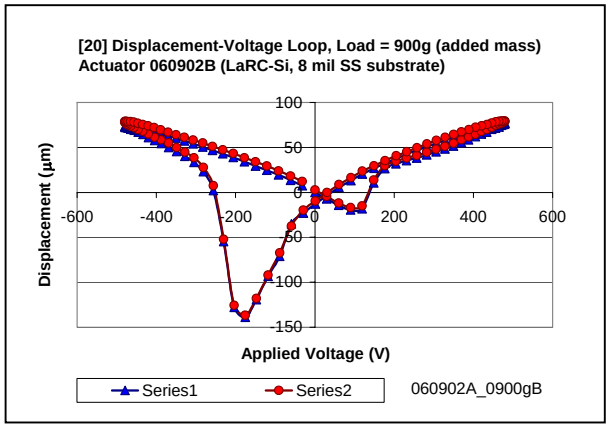
[20] Displacement-Voltage Loop, Load = 900g (added mass)
Actuator 060902B (LaRC-Si, 8 mil SS substrate)
Displacement (µm)
Applied Voltage (V)
Series1
Series2
060902A_0900gB

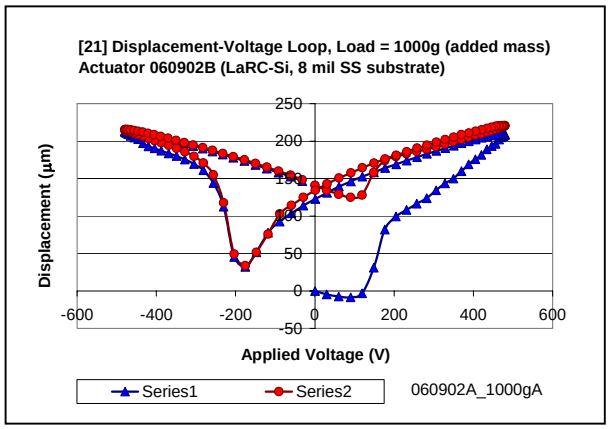
[21] Displacement-Voltage Loop, Load = 1000g (added mass)
Actuator 060902B (LaRC-Si, 8 mil SS substrate)
Displacement (µm)
Applied Voltage (V)
Series1
Series2
060902A_1000gA

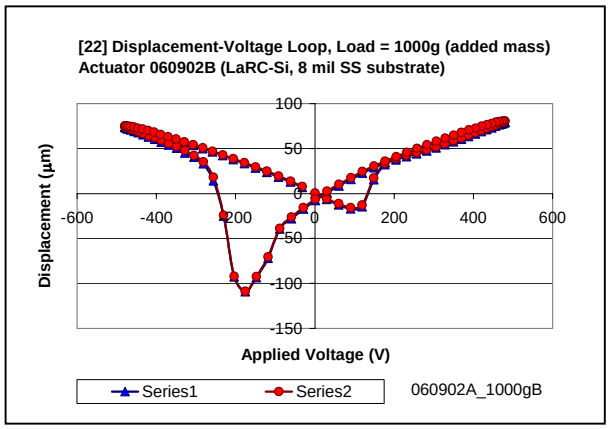
[22] Displacement-Voltage Loop, Load = 1000g (added mass)
Actuator 060902B (LaRC-Si, 8 mil SS substrate)
Displacement (µm)
Applied Voltage (V)
Series1
Series2
060902A_1000gB

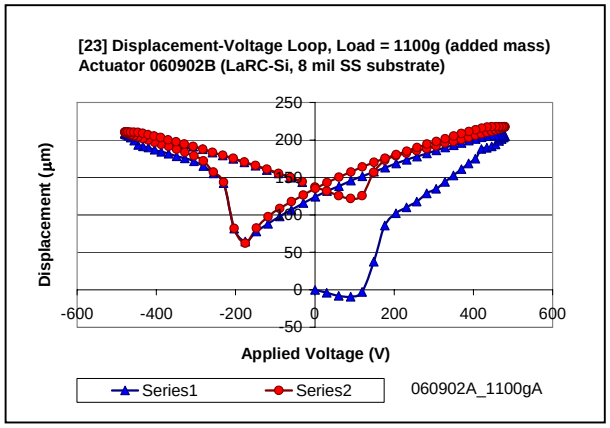
[23] Displacement-Voltage Loop, Load = 1100g (added mass)
Actuator 060902B (LaRC-Si, 8 mil SS substrate)
Displacement (µm)
Applied Voltage (V)
Series1
Series2
060902A_1100gA

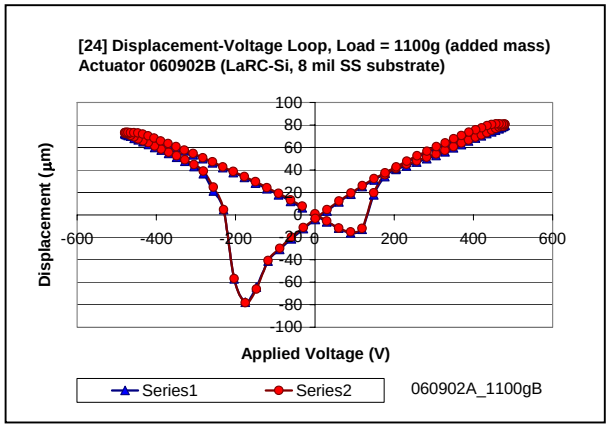
[24] Displacement-Voltage Loop, Load = 1100g (added mass)
Actuator 060902B (LaRC-Si, 8 mil SS substrate)
Displacement (µm)
Applied Voltage (V)
Series1
Series2
060902A_1100gB

Here are addendum files, that is, repeats of displacement-voltage loops at 1000 and 1100g loads, followed by a final set at zero load.

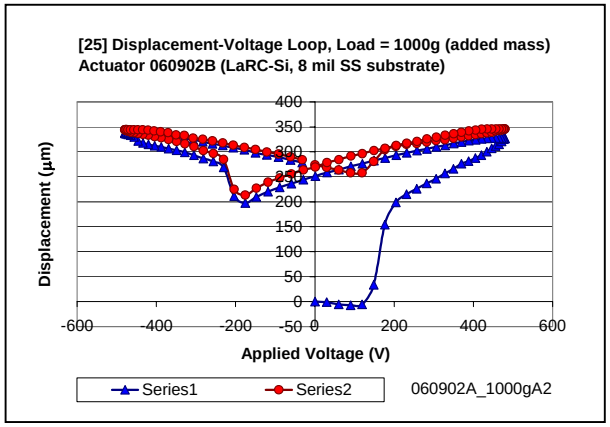

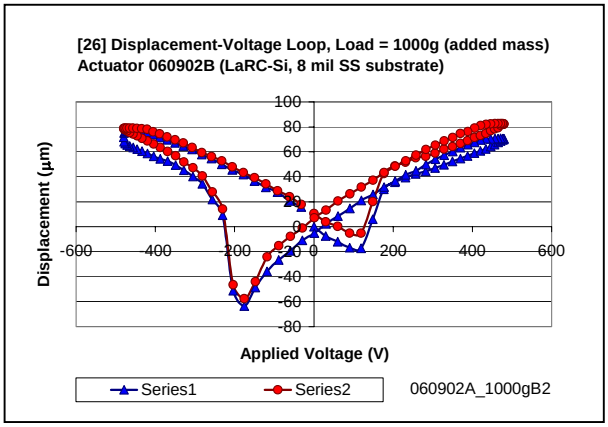

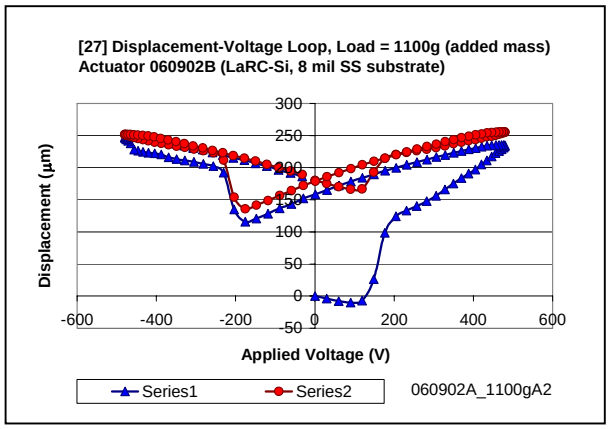

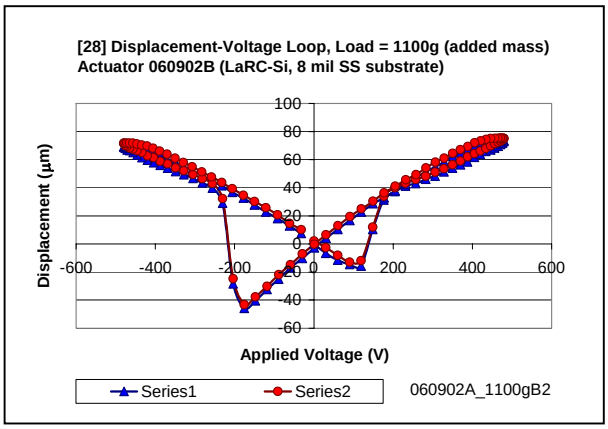

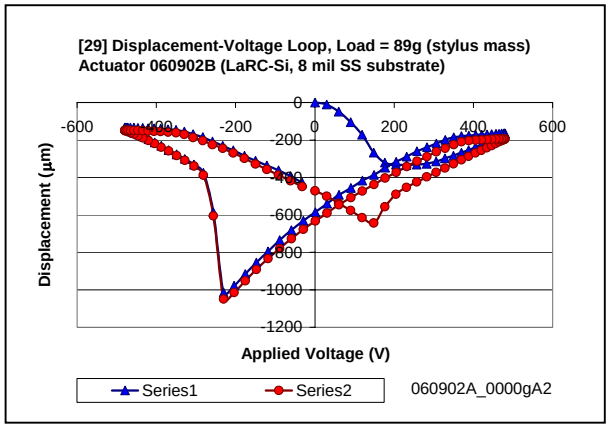

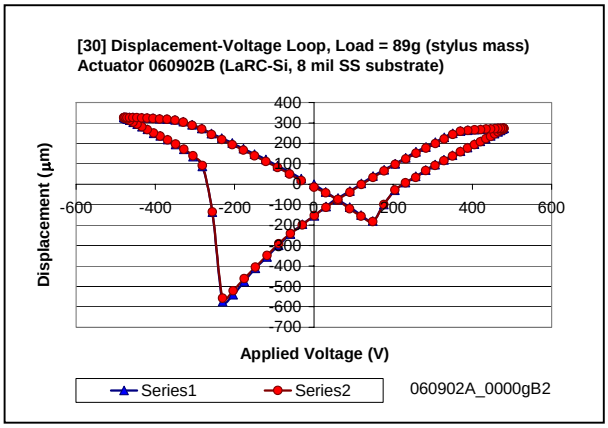

Before running sets of displacement-voltage loops (after obtaining butterfly loops, which cause switching of net poling), actuators were re-poled by stepping applied voltage to a maximum of 500 V. The resulting single-polarity loops are shown below.

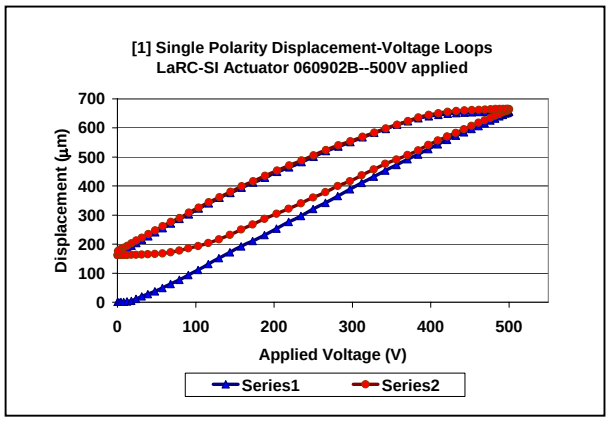

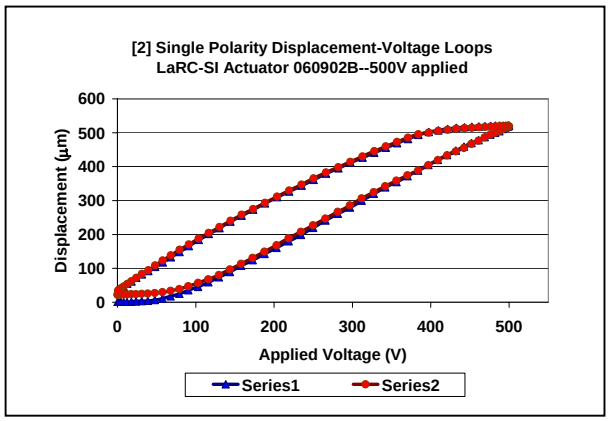

2. Gallery of strain-displacement loops for actuator 062102A (LaRC-SI adhesive, 4 mil stainless steel substrate) follows.

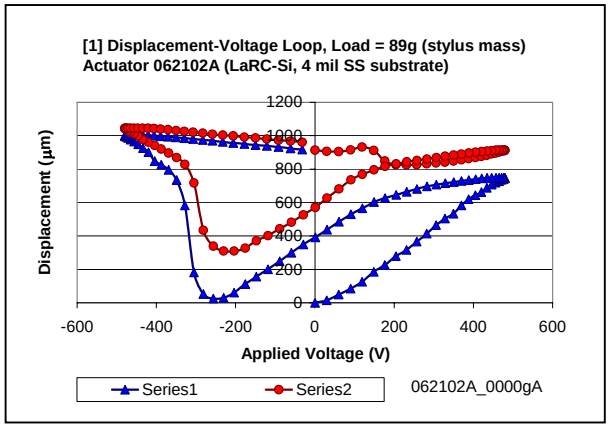

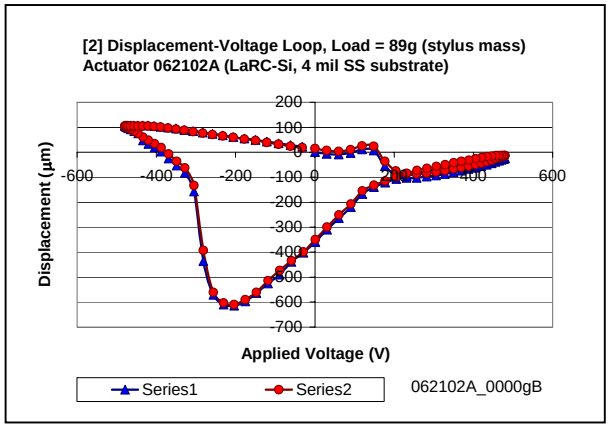

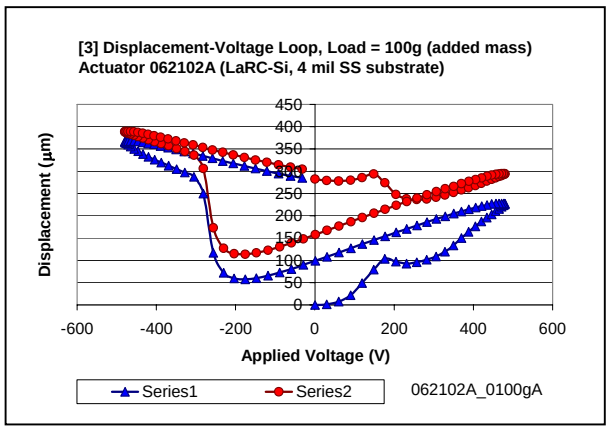
[3] Displacement-Voltage Loop, Load = 100g (added mass)
Actuator 062102A (LaRC-Si, 4 mil SS substrate)
Displacement (µm)
Applied Voltage (V)
Series1
Series2
062102A_0100gA

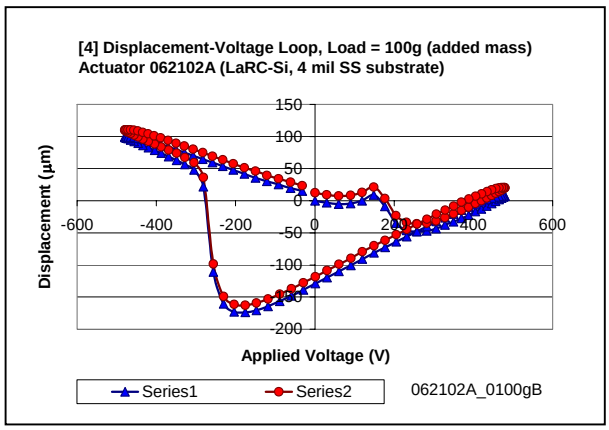
[4] Displacement-Voltage Loop, Load = 100g (added mass)
Actuator 062102A (LaRC-Si, 4 mil SS substrate)
Displacement (µm)
Applied Voltage (V)
Series1
Series2
062102A_0100gB

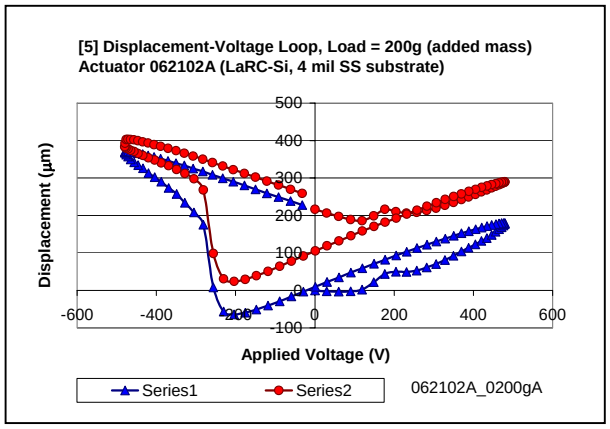
[5] Displacement-Voltage Loop, Load = 200g (added mass)
Actuator 062102A (LaRC-Si, 4 mil SS substrate)
Displacement (µm)
Applied Voltage (V)
Series1
Series2
062102A_0200gA

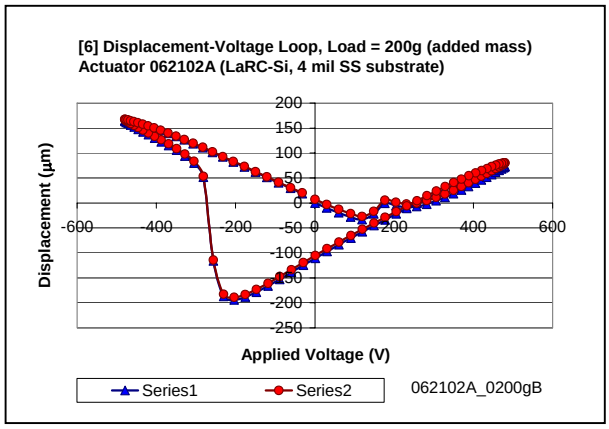
[6] Displacement-Voltage Loop, Load = 200g (added mass)
Actuator 062102A (LaRC-Si, 4 mil SS substrate)
Displacement (µm)
Applied Voltage (V)
Series1
Series2
062102A_0200gB

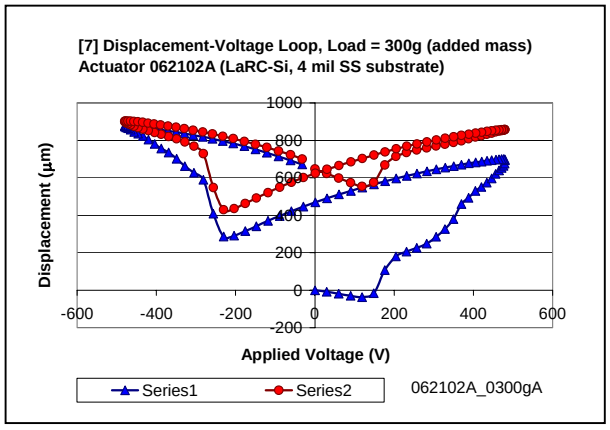
[7] Displacement-Voltage Loop, Load = 300g (added mass)
Actuator 062102A (LaRC-Si, 4 mil SS substrate)
Displacement (µm)
Applied Voltage (V)
Series1
Series2
062102A_0300gA

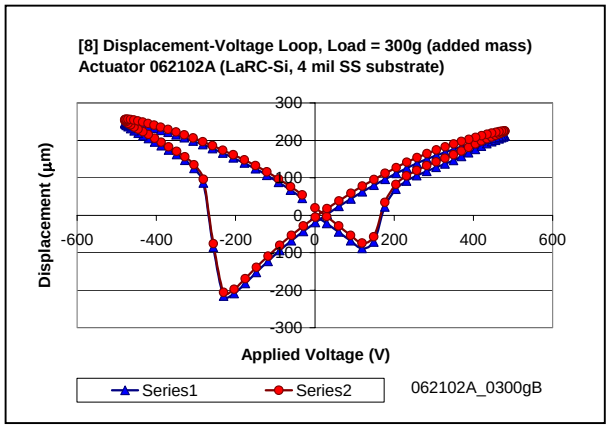
[8] Displacement-Voltage Loop, Load = 300g (added mass)
Actuator 062102A (LaRC-Si, 4 mil SS substrate)
Displacement (µm)
Applied Voltage (V)
Series1
Series2
062102A_0300gB

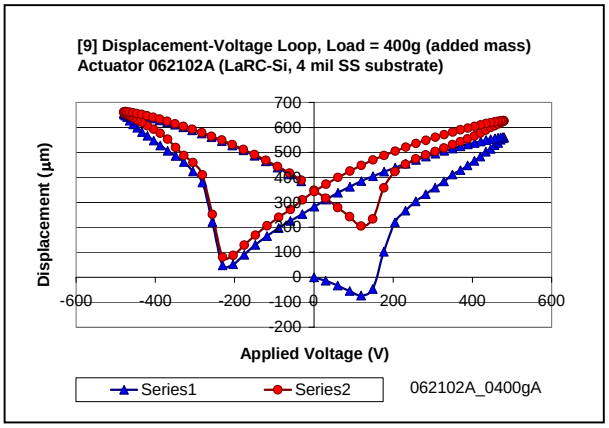
[9] Displacement-Voltage Loop, Load = 400g (added mass)
Actuator 062102A (LaRC-Si, 4 mil SS substrate)
Displacement (µm)
Applied Voltage (V)
Series1
Series2
062102A_0400gA

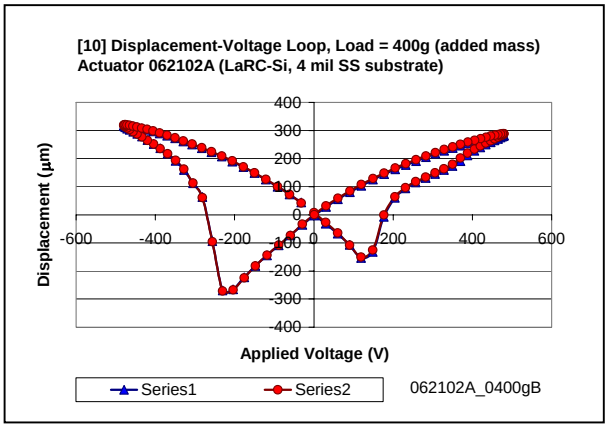
[10] Displacement-Voltage Loop, Load = 400g (added mass)
Actuator 062102A (LaRC-Si, 4 mil SS substrate)
Displacement (µm)
Applied Voltage (V)
Series1
Series2
062102A_0400gB

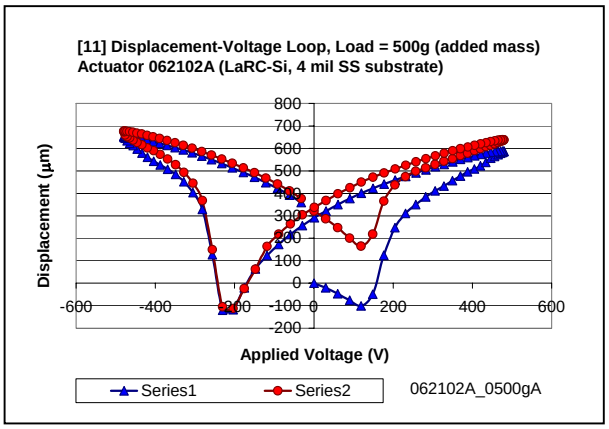
[11] Displacement-Voltage Loop, Load = 500g (added mass)
Actuator 062102A (LaRC-Si, 4 mil SS substrate)
Displacement (µm)
Applied Voltage (V)
Series1
Series2
062102A_0500gA

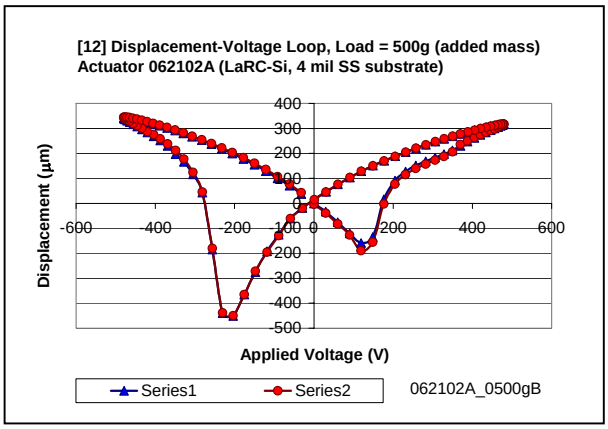
[12] Displacement-Voltage Loop, Load = 500g (added mass)
Actuator 062102A (LaRC-Si, 4 mil SS substrate)
Displacement (µm)
Applied Voltage (V)
Series1
Series2
062102A_0500gB

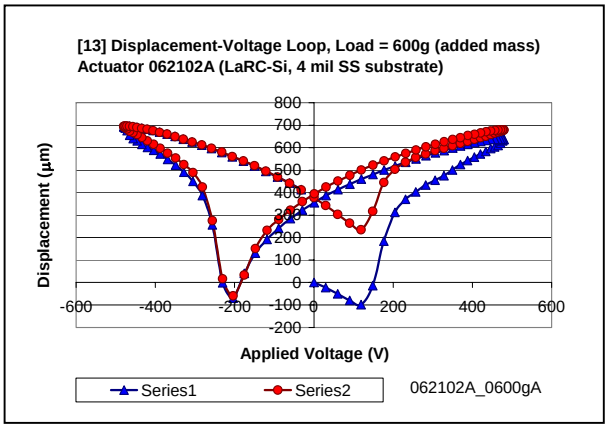
[13] Displacement-Voltage Loop, Load = 600g (added mass)
Actuator 062102A (LaRC-Si, 4 mil SS substrate)
Displacement (µm)
Applied Voltage (V)
Series1
Series2
062102A_0600gA

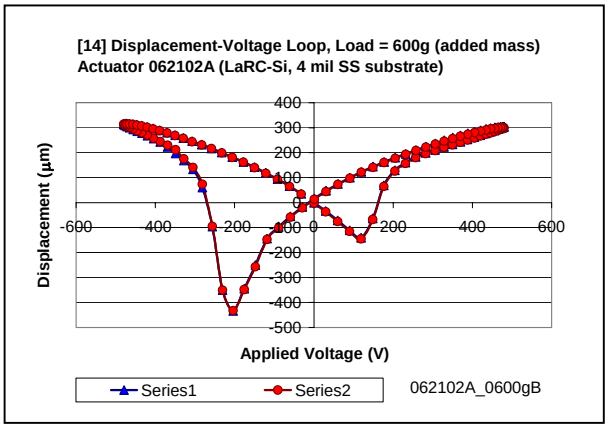
[14] Displacement-Voltage Loop, Load = 600g (added mass)
Actuator 062102A (LaRC-Si, 4 mil SS substrate)
Displacement (µm)
Applied Voltage (V)
Series1
Series2
062102A_0600gB

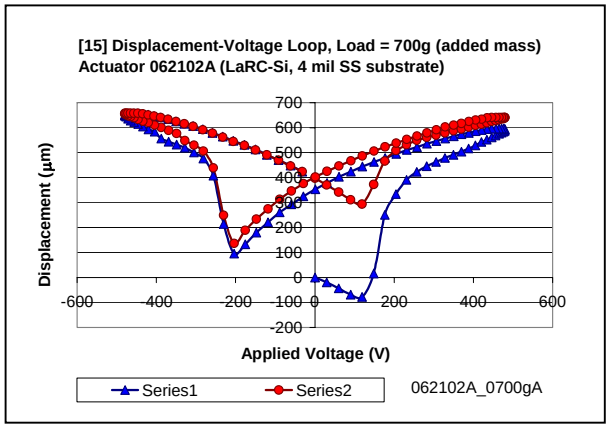
[15] Displacement-Voltage Loop, Load = 700g (added mass)
Actuator 062102A (LaRC-Si, 4 mil SS substrate)
Displacement (µm)
Applied Voltage (V)
Series1
Series2
062102A_0700gA

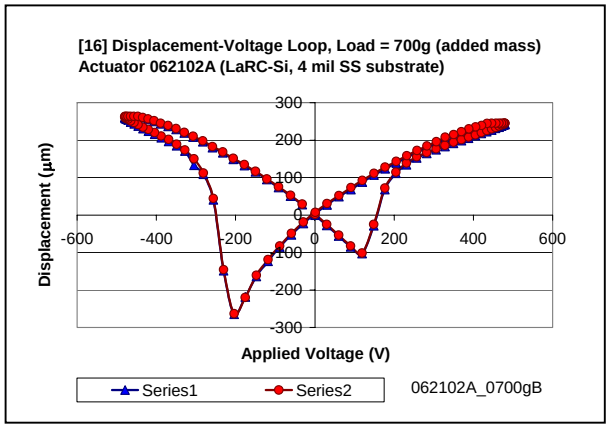
[16] Displacement-Voltage Loop, Load = 700g (added mass)
Actuator 062102A (LaRC-Si, 4 mil SS substrate)
Displacement (µm)
Applied Voltage (V)
Series1
Series2
062102A_0700gB

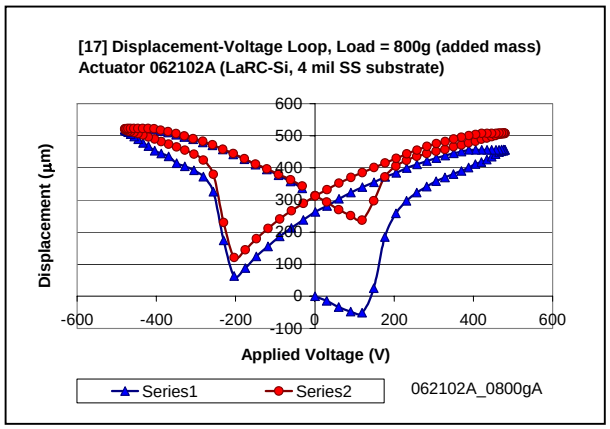
[17] Displacement-Voltage Loop, Load = 800g (added mass)
Actuator 062102A (LaRC-Si, 4 mil SS substrate)
Displacement (µm)
Applied Voltage (V)
Series1
Series2
062102A_0800gA

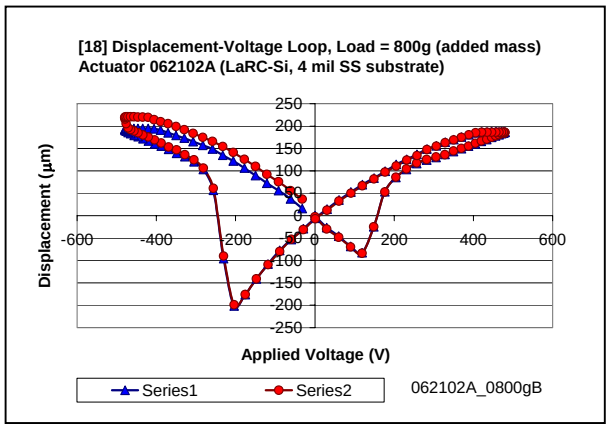
[18] Displacement-Voltage Loop, Load = 800g (added mass)
Actuator 062102A (LaRC-Si, 4 mil SS substrate)
Displacement (µm)
Applied Voltage (V)
Series1
Series2
062102A_0800gB

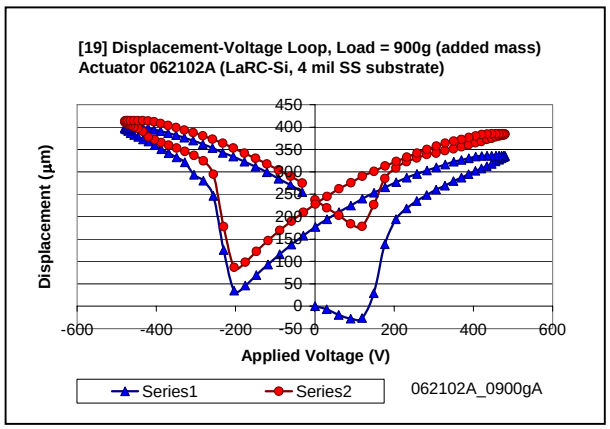
[19] Displacement-Voltage Loop, Load = 900g (added mass)
Actuator 062102A (LaRC-Si, 4 mil SS substrate)
Displacement (µm)
Applied Voltage (V)
Series1
Series2
062102A_0900gA

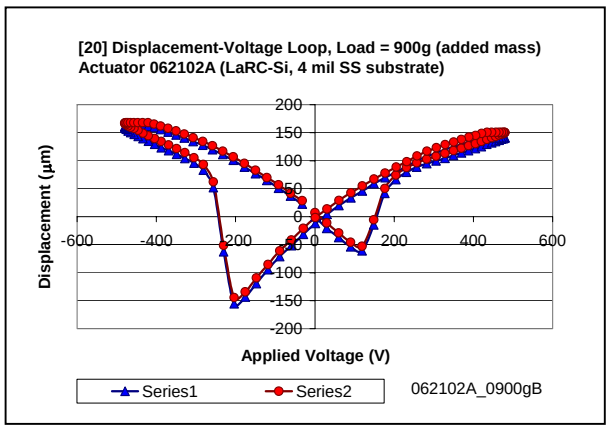
[20] Displacement-Voltage Loop, Load = 900g (added mass)
Actuator 062102A (LaRC-Si, 4 mil SS substrate)
Displacement (µm)
Applied Voltage (V)
Series1
Series2
062102A_0900gB

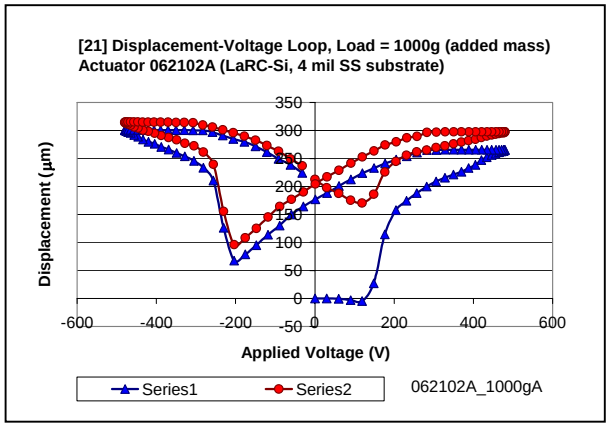

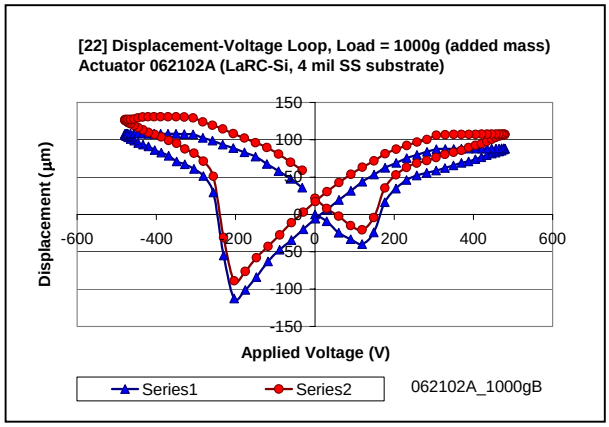

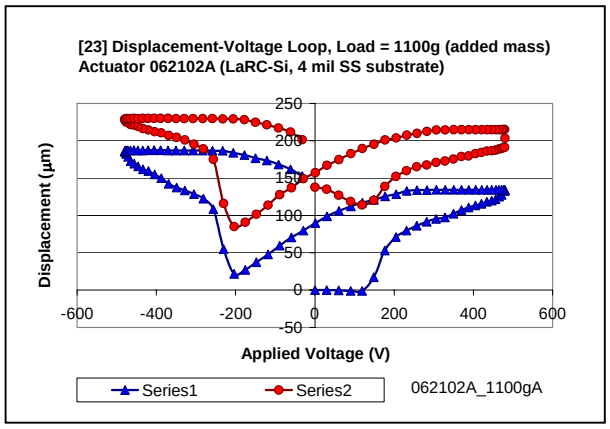

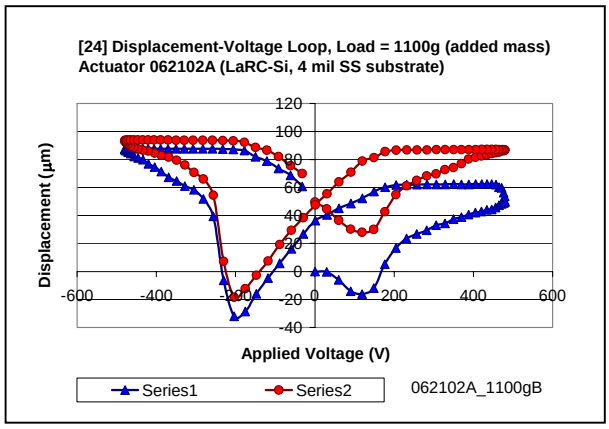

The final set at zero load was taken after the preceding loops without interruption.

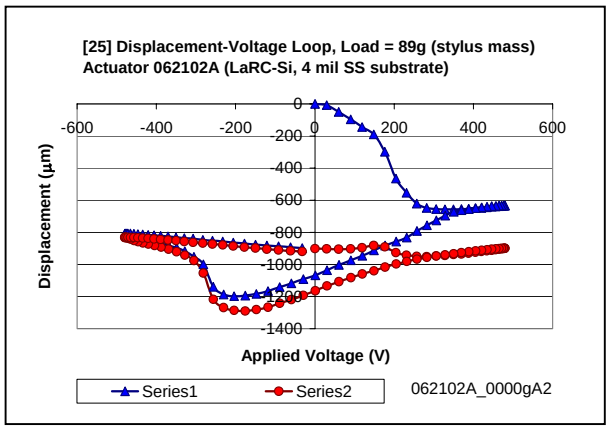

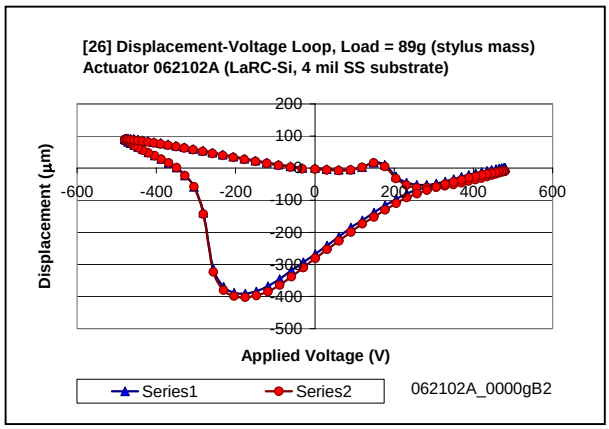

3. Gallery of strain-displacement loops for actuator 100902C (M-Bond adhesive, 8 mil stainless steel substrate) follows.

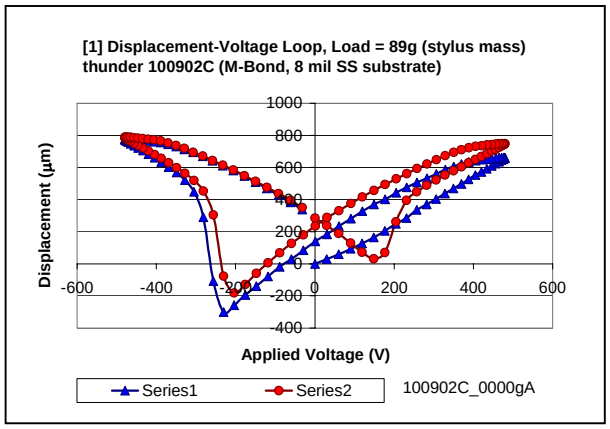

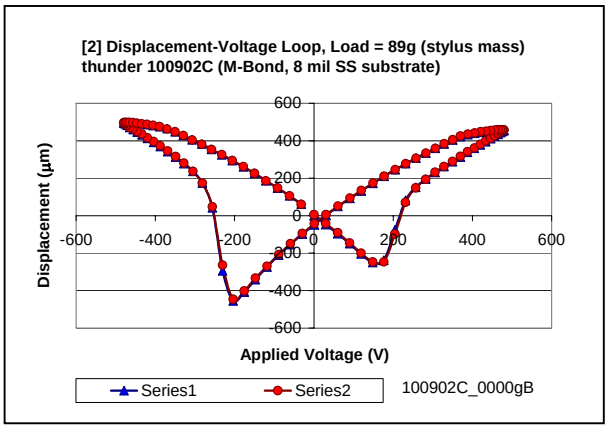

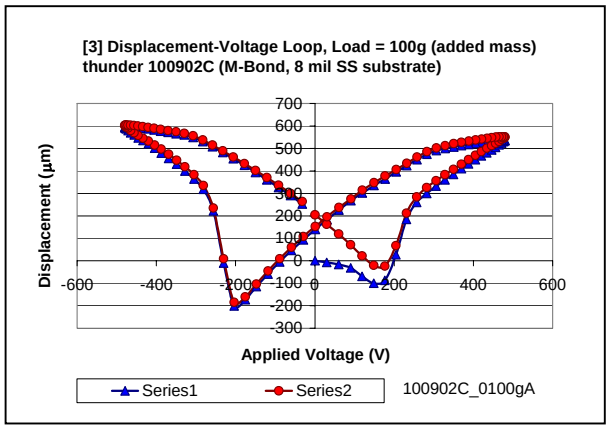

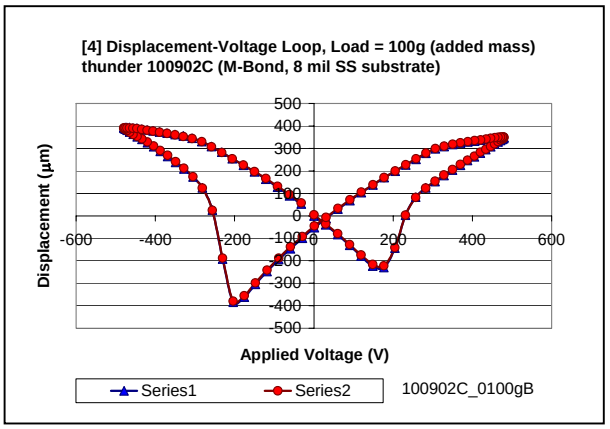

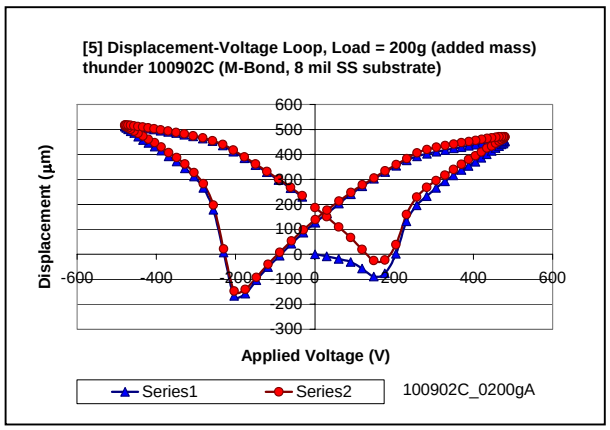

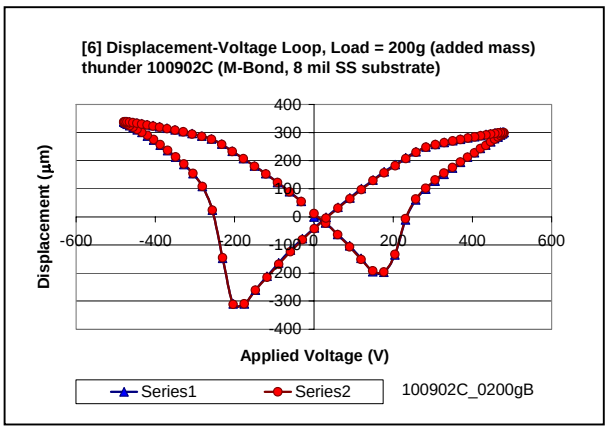

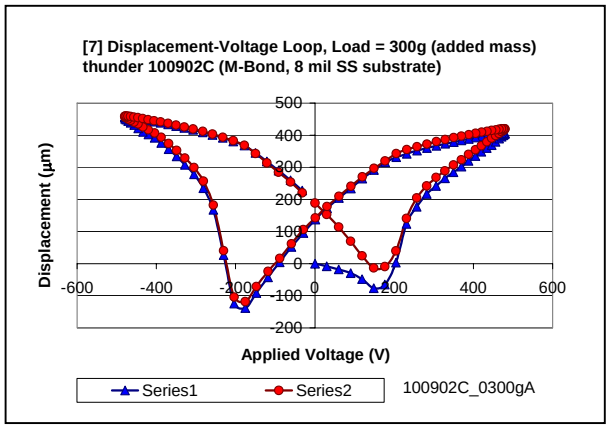
[7] Displacement-Voltage Loop, Load = 300g (added mass)
thunder 100902C (M-Bond, 8 mil SS substrate)
Displacement (µm)
Applied Voltage (V)
Series1
Series2
100902C_0300gA

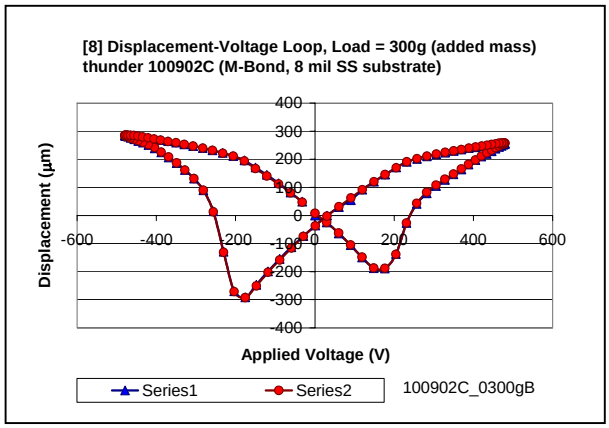
[8] Displacement-Voltage Loop, Load = 300g (added mass)
thunder 100902C (M-Bond, 8 mil SS substrate)
Displacement (µm)
Applied Voltage (V)
Series1
Series2
100902C_0300gB

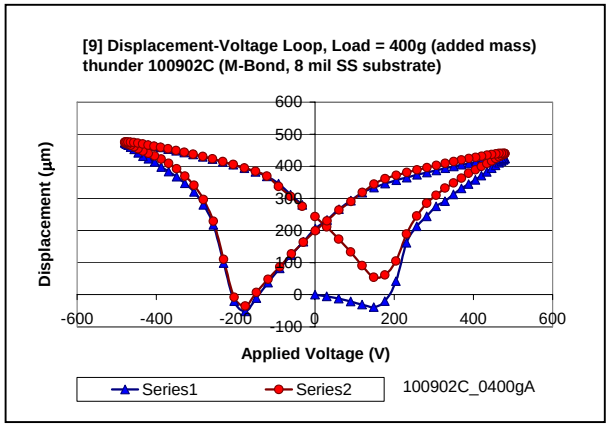
[9] Displacement-Voltage Loop, Load = 400g (added mass)
thunder 100902C (M-Bond, 8 mil SS substrate)
Displacement (µm)
Applied Voltage (V)
Series1
Series2
100902C_0400gA

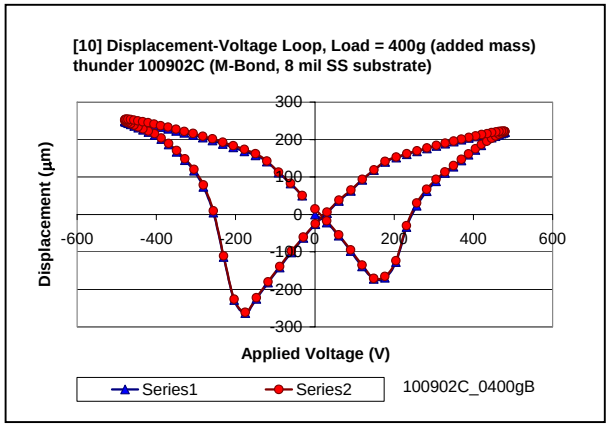
[10] Displacement-Voltage Loop, Load = 400g (added mass)
thunder 100902C (M-Bond, 8 mil SS substrate)
Displacement (µm)
Applied Voltage (V)
Series1
Series2
100902C_0400gB

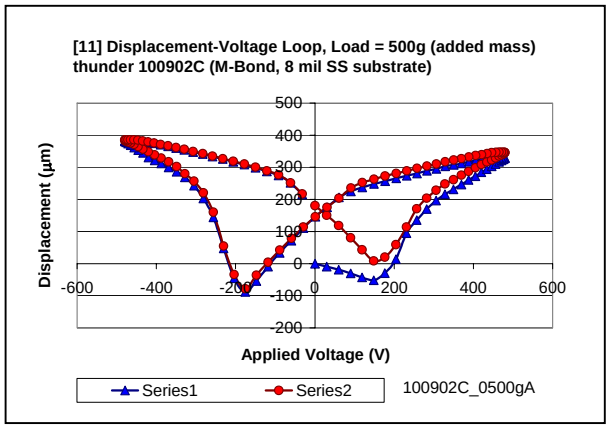
[11] Displacement-Voltage Loop, Load = 500g (added mass)
thunder 100902C (M-Bond, 8 mil SS substrate)
Displacement (µm)
Applied Voltage (V)
Series1
Series2
100902C_0500gA

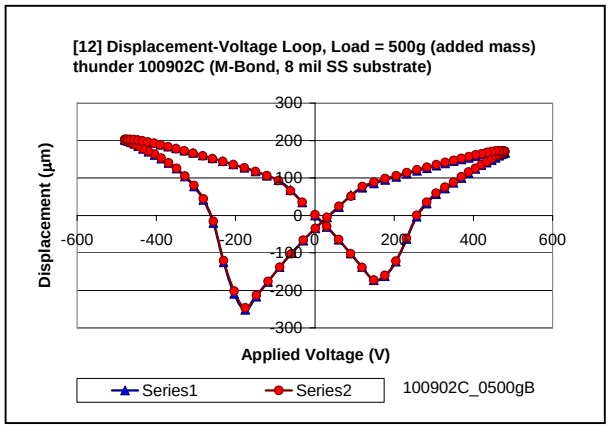
[12] Displacement-Voltage Loop, Load = 500g (added mass)
thunder 100902C (M-Bond, 8 mil SS substrate)
Displacement (µm)
Applied Voltage (V)
Series1
Series2
100902C_0500gB

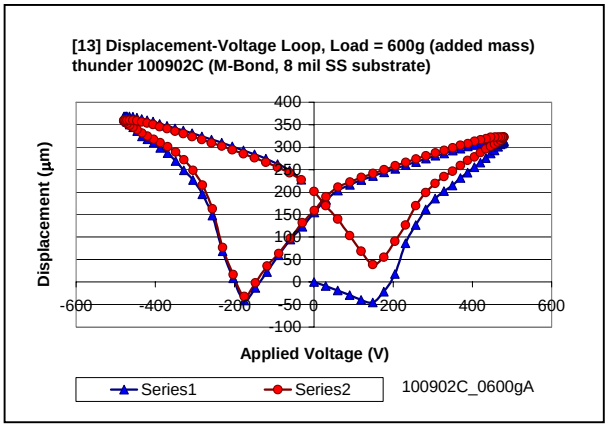
[13] Displacement-Voltage Loop, Load = 600g (added mass)
thunder 100902C (M-Bond, 8 mil SS substrate)
Displacement (µm)
Applied Voltage (V)
Series1
Series2
100902C_0600gA

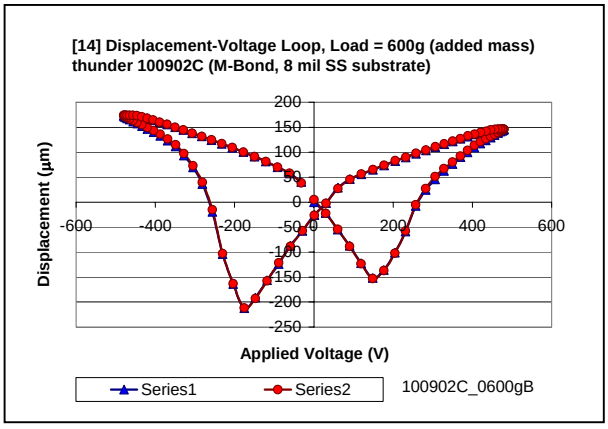
[14] Displacement-Voltage Loop, Load = 600g (added mass)
thunder 100902C (M-Bond, 8 mil SS substrate)
Displacement (µm)
Applied Voltage (V)
Series1
Series2
100902C_0600gB

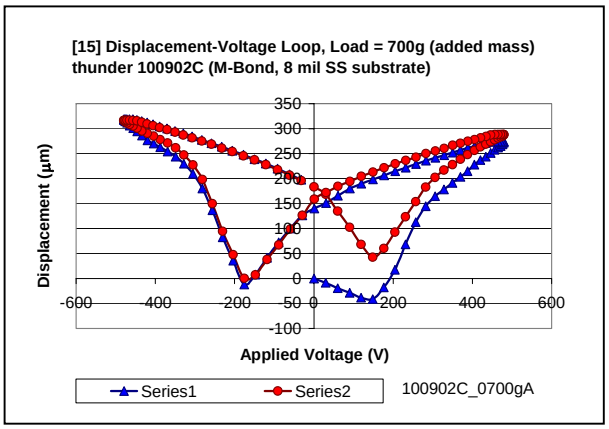
[15] Displacement-Voltage Loop, Load = 700g (added mass)
thunder 100902C (M-Bond, 8 mil SS substrate)
Displacement (µm)
Applied Voltage (V)
Series1
Series2
100902C_0700gA

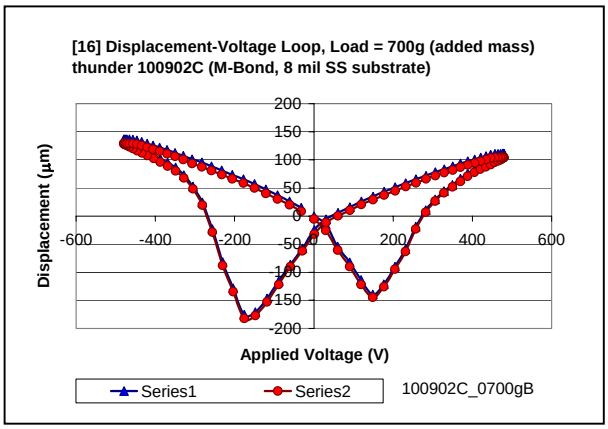
[16] Displacement-Voltage Loop, Load = 700g (added mass)
thunder 100902C (M-Bond, 8 mil SS substrate)
Displacement (µm)
Applied Voltage (V)
Series1
Series2
100902C_0700gB

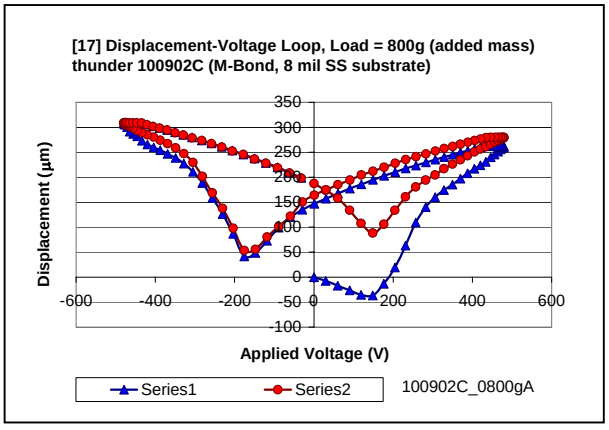
[17] Displacement-Voltage Loop, Load = 800g (added mass)
thunder 100902C (M-Bond, 8 mil SS substrate)
Displacement (µm)
Applied Voltage (V)
Series1
Series2
100902C_0800gA

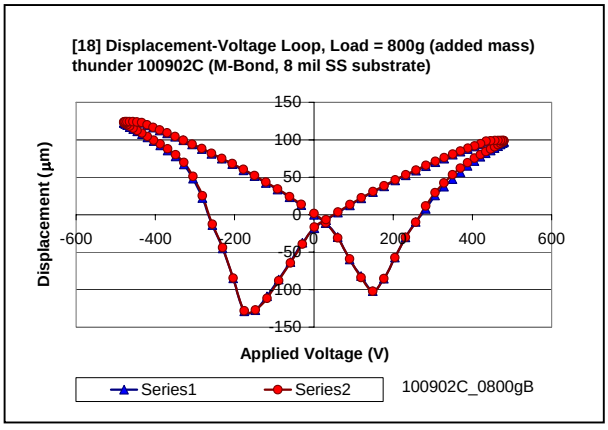
[18] Displacement-Voltage Loop, Load = 800g (added mass)
thunder 100902C (M-Bond, 8 mil SS substrate)
Displacement (µm)
Applied Voltage (V)
Series1
Series2
100902C_0800gB

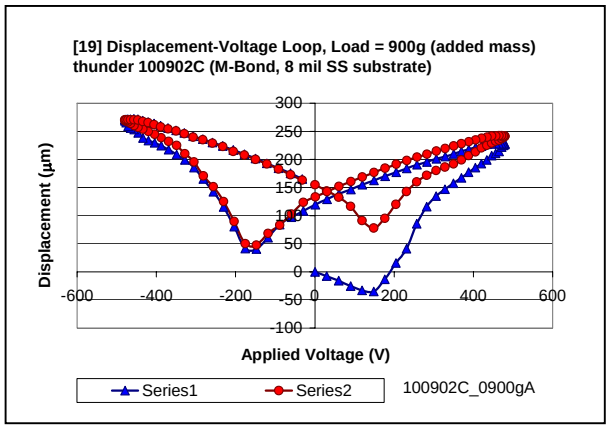
[19] Displacement-Voltage Loop, Load = 900g (added mass)
thunder 100902C (M-Bond, 8 mil SS substrate)
Displacement (µm)
Applied Voltage (V)
Series1
Series2
100902C_0900gA

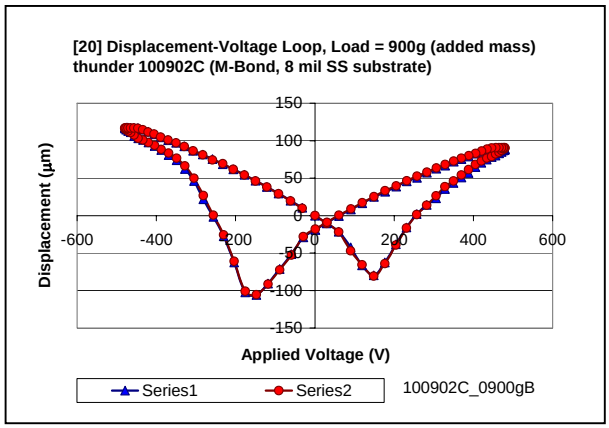
[20] Displacement-Voltage Loop, Load = 900g (added mass)
thunder 100902C (M-Bond, 8 mil SS substrate)
Displacement (µm)
Applied Voltage (V)
Series1
Series2
100902C_0900gB

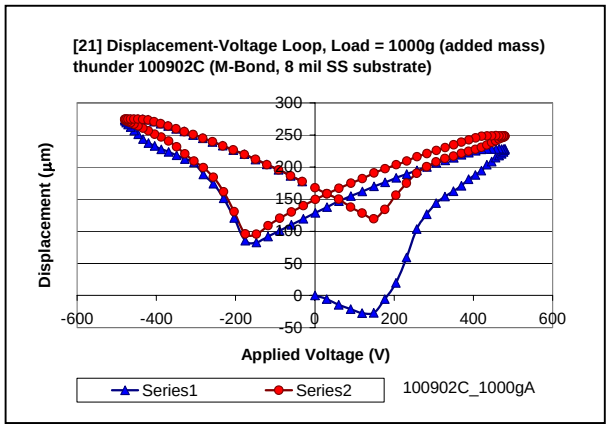
[21] Displacement-Voltage Loop, Load = 1000g (added mass)
thunder 100902C (M-Bond, 8 mil SS substrate)
Displacement (µm)
Applied Voltage (V)
Series1
Series2
100902C_1000gA

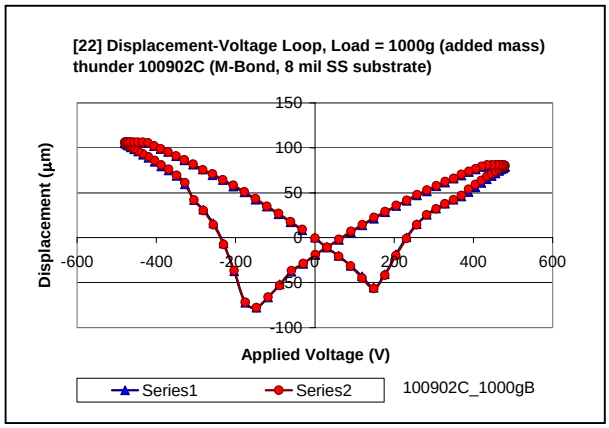
[22] Displacement-Voltage Loop, Load = 1000g (added mass)
thunder 100902C (M-Bond, 8 mil SS substrate)
Displacement (µm)
Applied Voltage (V)
Series1
Series2
100902C_1000gB

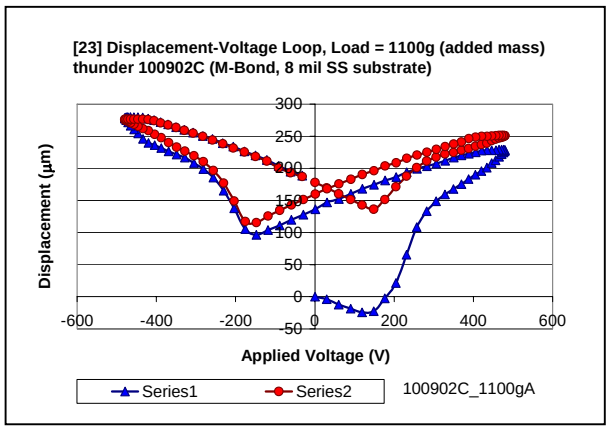
[23] Displacement-Voltage Loop, Load = 1100g (added mass)
thunder 100902C (M-Bond, 8 mil SS substrate)
Displacement (µm)
Applied Voltage (V)
Series1
Series2
100902C_1100gA

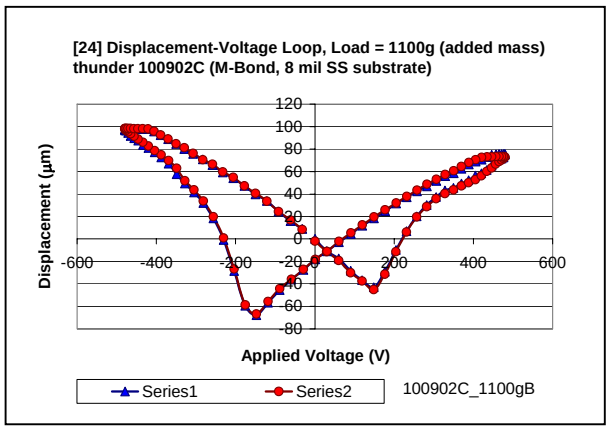
[24] Displacement-Voltage Loop, Load = 1100g (added mass)
thunder 100902C (M-Bond, 8 mil SS substrate)
Displacement (µm)
Applied Voltage (V)
Series1
Series2
100902C_1100gB

Here are addendum files, that is, repeats of displacement-voltage loops at 1000 and 1100g loads, followed by a final set at zero load.

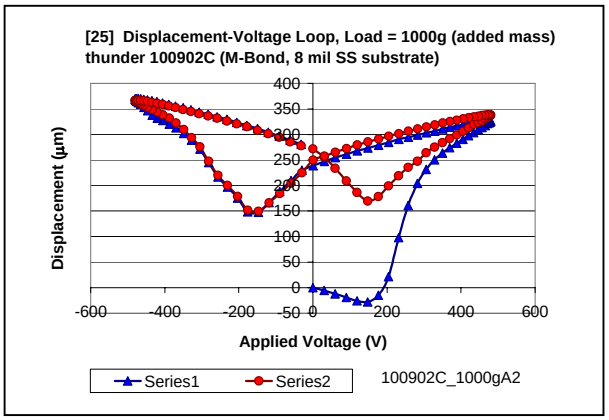

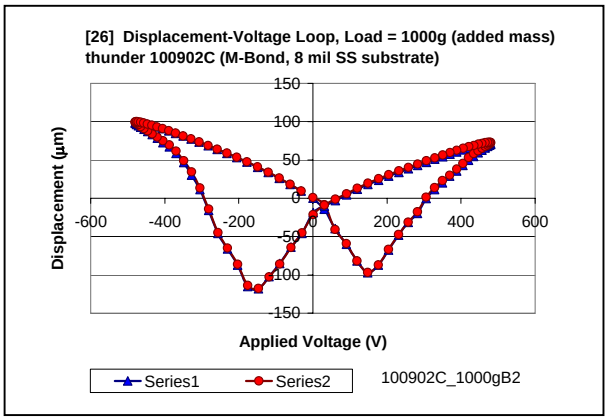

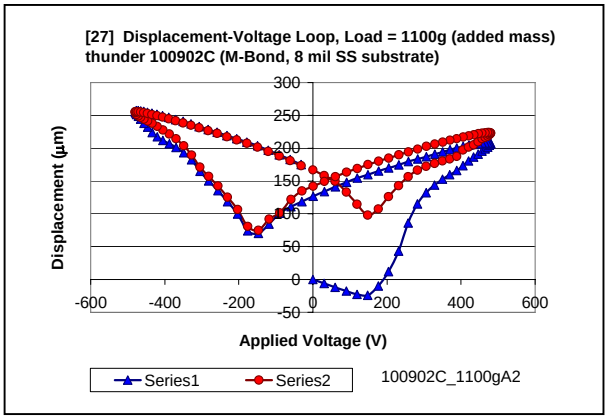

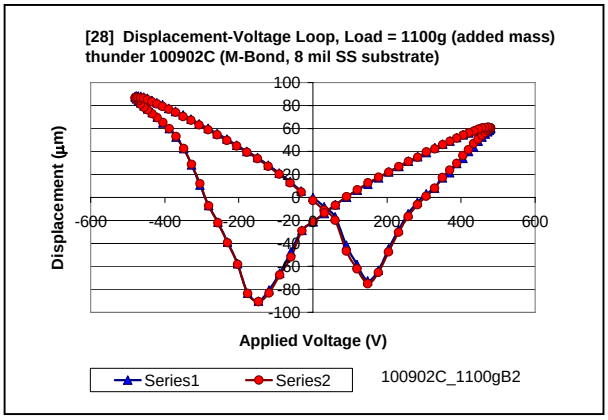

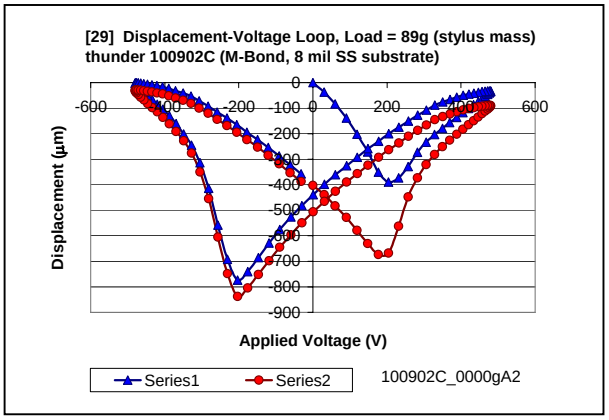

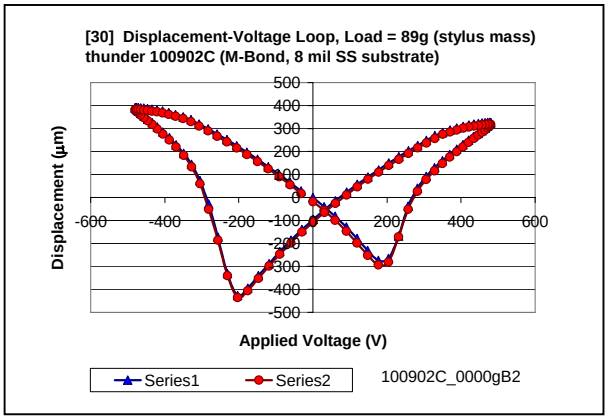

4. Gallery of strain-displacement loops for actuator 100902E (M-Bond adhesive, 4 mil stainless steel substrate) follows.

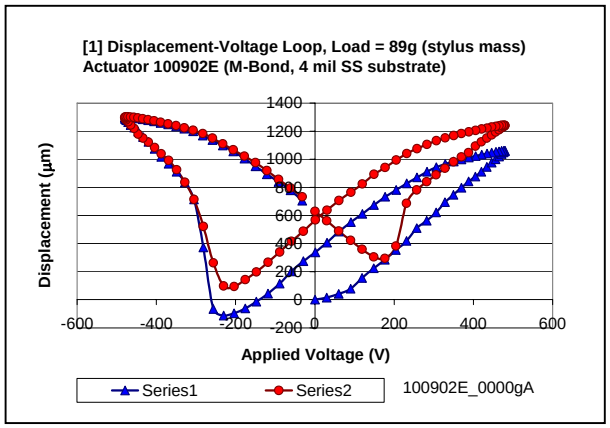

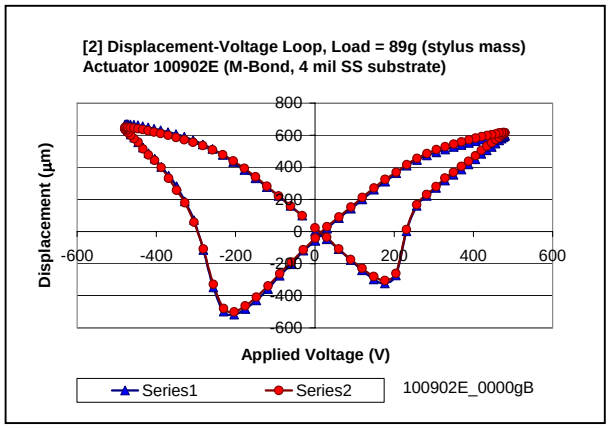

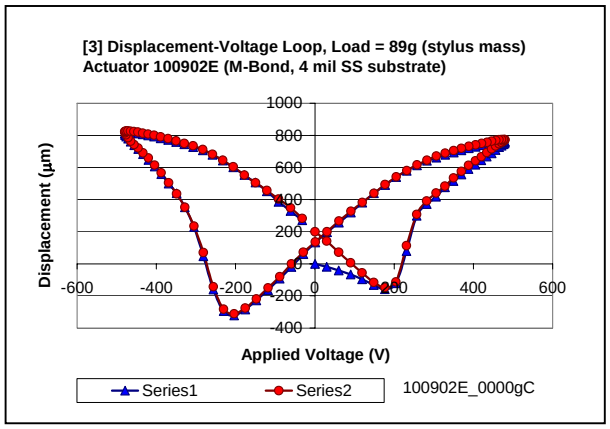

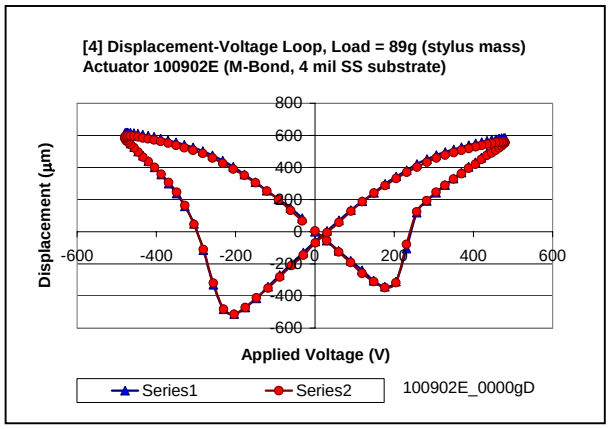

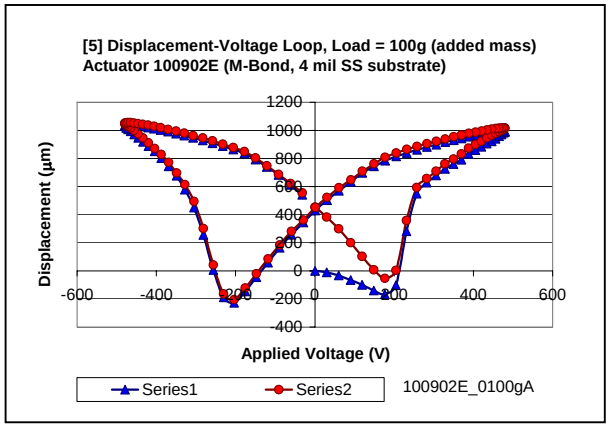

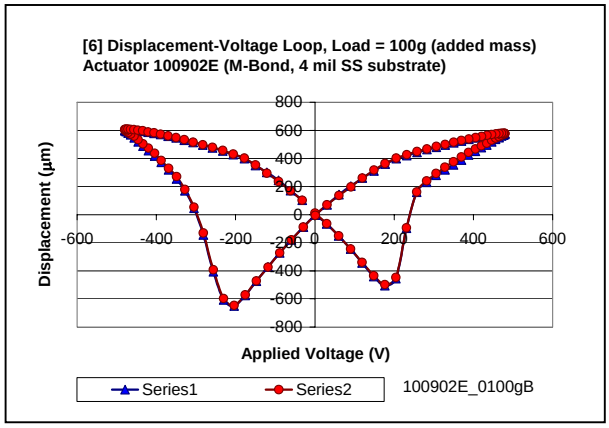

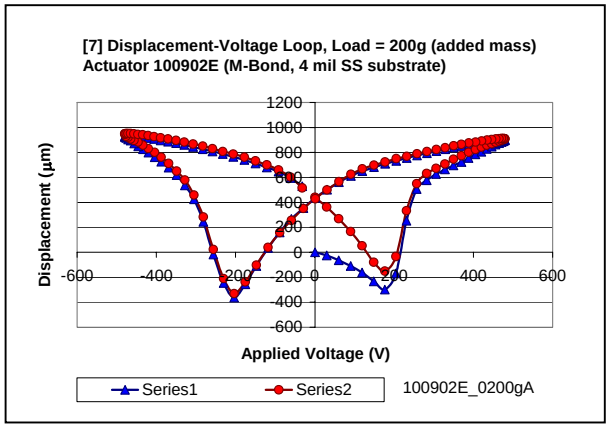
[7] Displacement-Voltage Loop, Load = 200g (added mass)
Actuator 100902E (M-Bond, 4 mil SS substrate)
Displacement (µm)
Applied Voltage (V)
Series1
Series2
100902E_0200gA

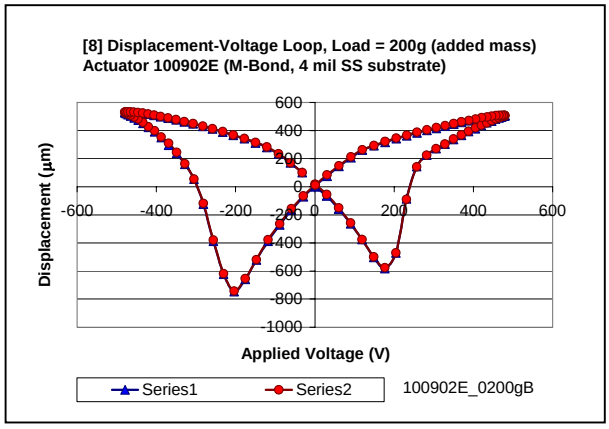
[8] Displacement-Voltage Loop, Load = 200g (added mass)
Actuator 100902E (M-Bond, 4 mil SS substrate)
Displacement (µm)
Applied Voltage (V)
Series1
Series2
100902E_0200gB

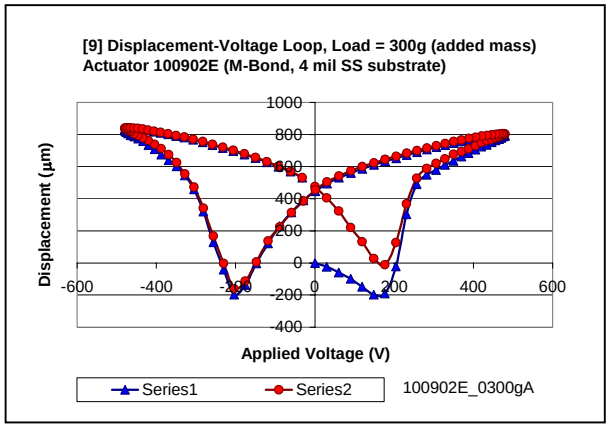
[9] Displacement-Voltage Loop, Load = 300g (added mass)
Actuator 100902E (M-Bond, 4 mil SS substrate)
Displacement (µm)
Applied Voltage (V)
Series1
Series2
100902E_0300gA

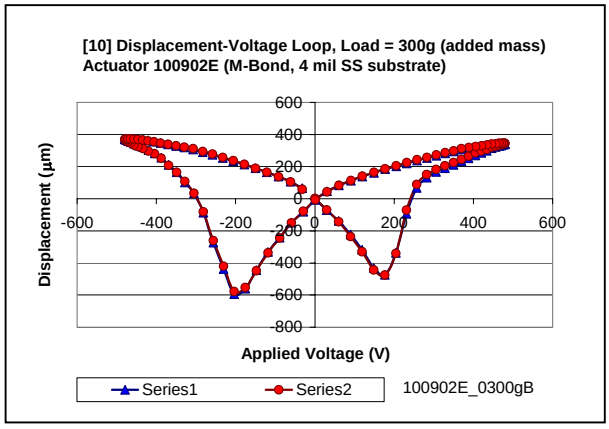
[10] Displacement-Voltage Loop, Load = 300g (added mass)
Actuator 100902E (M-Bond, 4 mil SS substrate)
Displacement (µm)
Applied Voltage (V)
Series1
Series2
100902E_0300gB

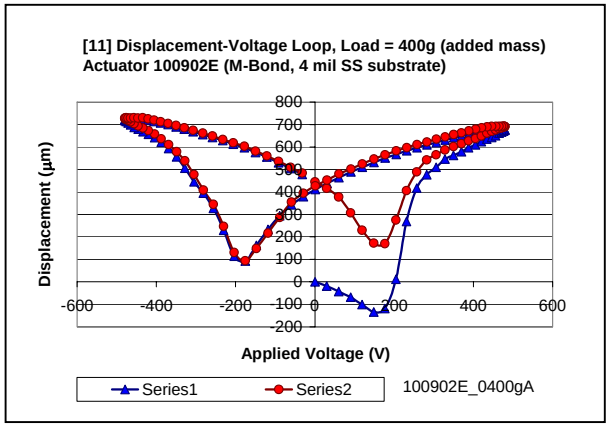
[11] Displacement-Voltage Loop, Load = 400g (added mass)
Actuator 100902E (M-Bond, 4 mil SS substrate)
Displacement (µm)
Applied Voltage (V)
Series1
Series2
100902E_0400gA

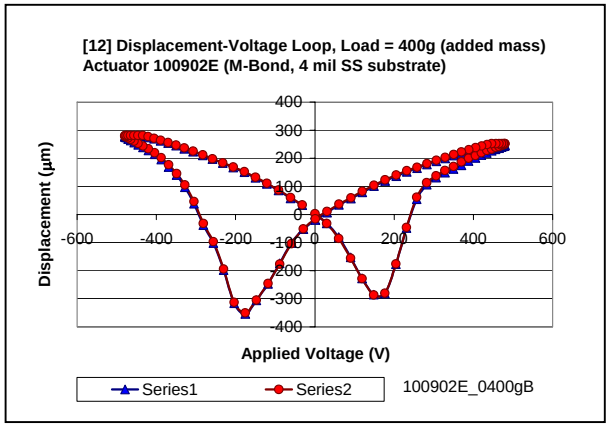
[12] Displacement-Voltage Loop, Load = 400g (added mass)
Actuator 100902E (M-Bond, 4 mil SS substrate)
Displacement (µm)
Applied Voltage (V)
Series1
Series2
100902E_0400gB

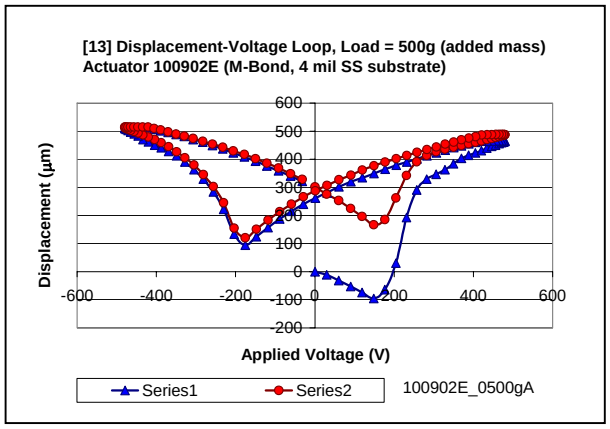
[13] Displacement-Voltage Loop, Load = 500g (added mass)
Actuator 100902E (M-Bond, 4 mil SS substrate)
Displacement (µm)
Applied Voltage (V)
Series1
Series2
100902E_0500gA

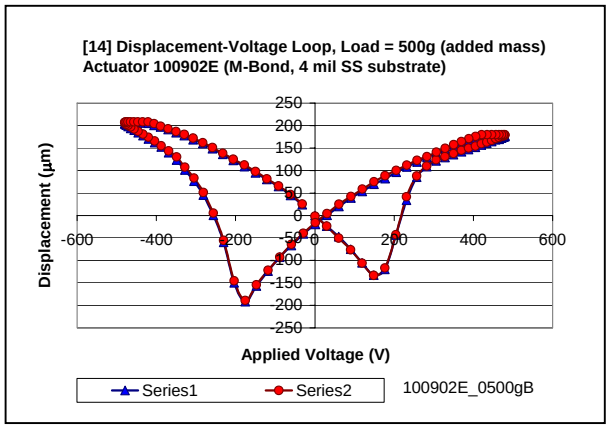
[14] Displacement-Voltage Loop, Load = 500g (added mass)
Actuator 100902E (M-Bond, 4 mil SS substrate)
Displacement (µm)
Applied Voltage (V)
Series1
Series2
100902E_0500gB

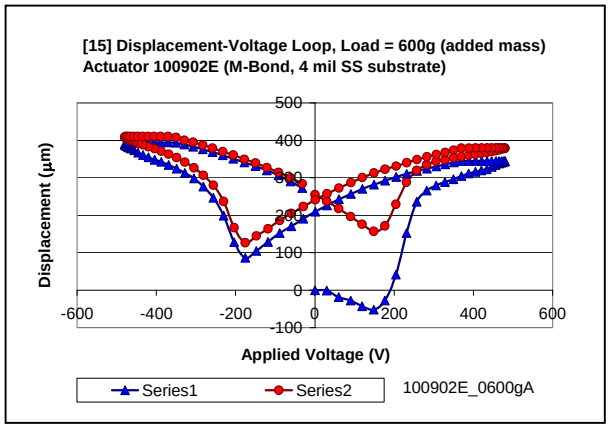
[15] Displacement-Voltage Loop, Load = 600g (added mass)
Actuator 100902E (M-Bond, 4 mil SS substrate)
Displacement (µm)
Applied Voltage (V)
Series1
Series2
100902E_0600gA

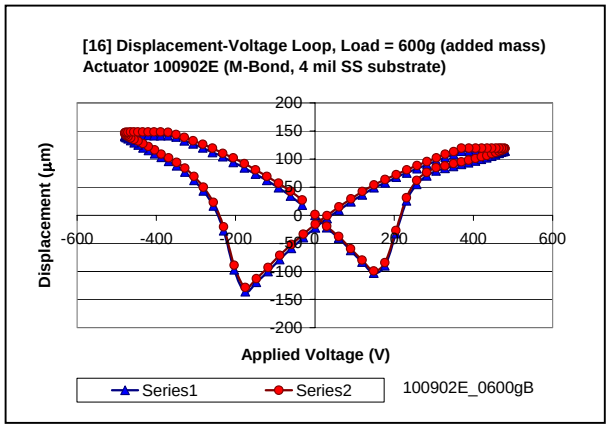
[16] Displacement-Voltage Loop, Load = 600g (added mass)
Actuator 100902E (M-Bond, 4 mil SS substrate)
Displacement (µm)
Applied Voltage (V)
Series1
Series2
100902E_0600gB

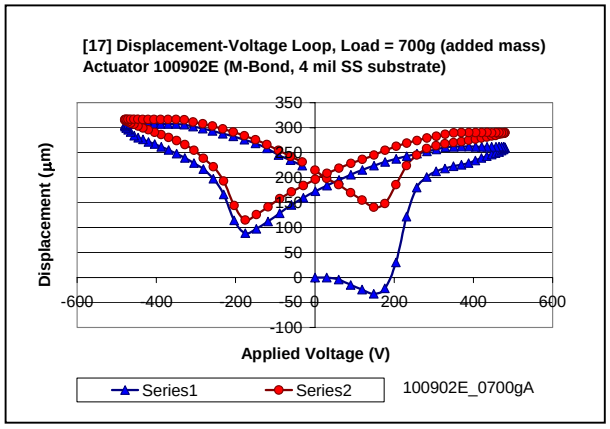
[17] Displacement-Voltage Loop, Load = 700g (added mass)
Actuator 100902E (M-Bond, 4 mil SS substrate)
Displacement (µm)
Applied Voltage (V)
Series1
Series2
100902E_0700gA

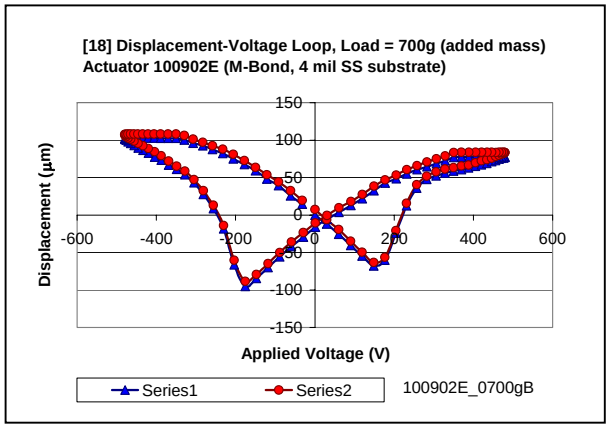
[18] Displacement-Voltage Loop, Load = 700g (added mass)
Actuator 100902E (M-Bond, 4 mil SS substrate)
Displacement (µm)
Applied Voltage (V)
Series1
Series2
100902E_0700gB

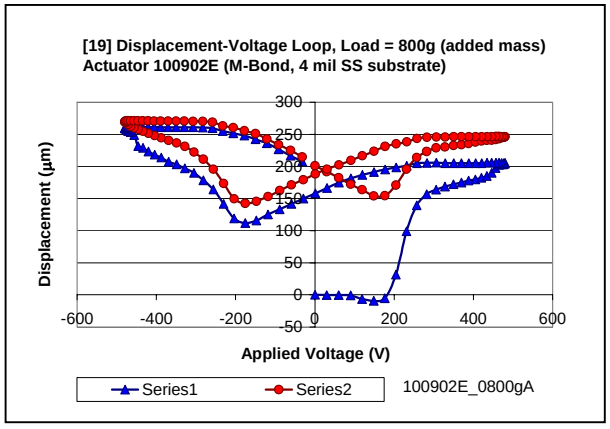
[19] Displacement-Voltage Loop, Load = 800g (added mass)
Actuator 100902E (M-Bond, 4 mil SS substrate)
Displacement (µm)
Applied Voltage (V)
Series1
Series2
100902E_0800gA

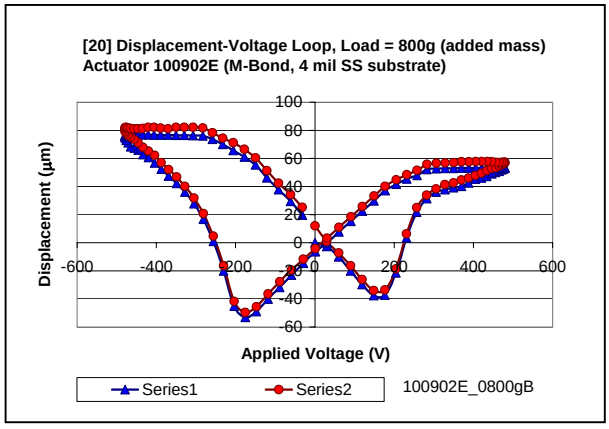
[20] Displacement-Voltage Loop, Load = 800g (added mass)
Actuator 100902E (M-Bond, 4 mil SS substrate)
Displacement (µm)
Applied Voltage (V)
Series1
Series2
100902E_0800gB

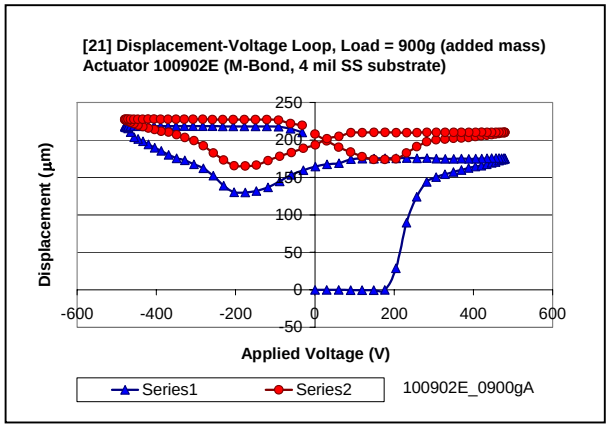
[21] Displacement-Voltage Loop, Load = 900g (added mass)
Actuator 100902E (M-Bond, 4 mil SS substrate)
Displacement (µm)
Applied Voltage (V)
Series1
Series2
100902E_0900gA

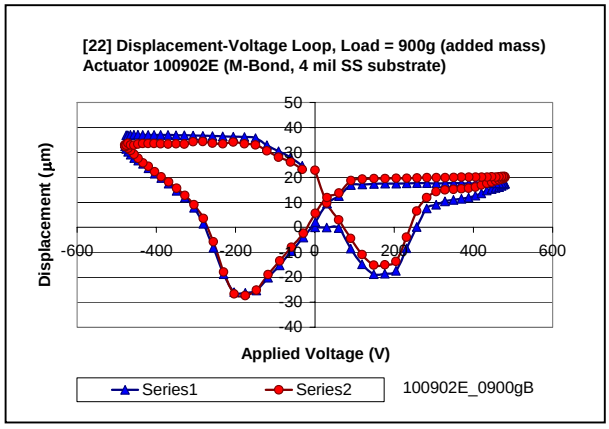
[22] Displacement-Voltage Loop, Load = 900g (added mass)
Actuator 100902E (M-Bond, 4 mil SS substrate)
Displacement (µm)
Applied Voltage (V)
Series1
Series2
100902E_0900gB

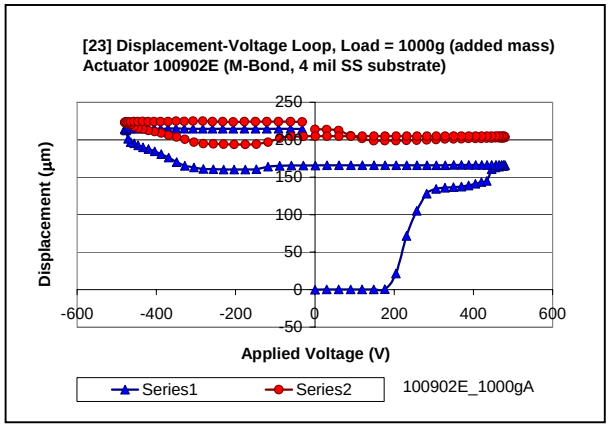
[23] Displacement-Voltage Loop, Load = 1000g (added mass)
Actuator 100902E (M-Bond, 4 mil SS substrate)
Displacement (µm)
Applied Voltage (V)
Series1
Series2
100902E_1000gA

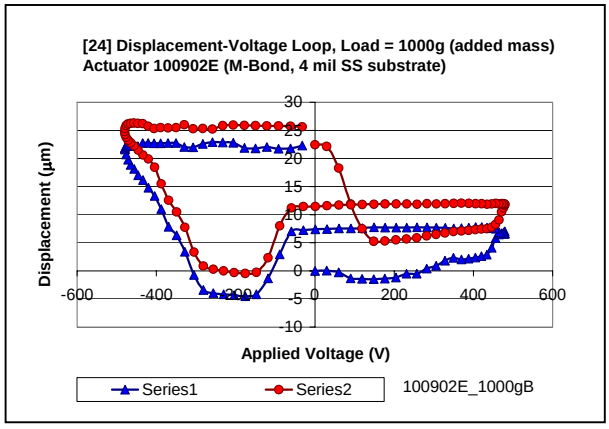
[24] Displacement-Voltage Loop, Load = 1000g (added mass)
Actuator 100902E (M-Bond, 4 mil SS substrate)
Displacement (µm)
Applied Voltage (V)
Series1
Series2
100902E_1000gB

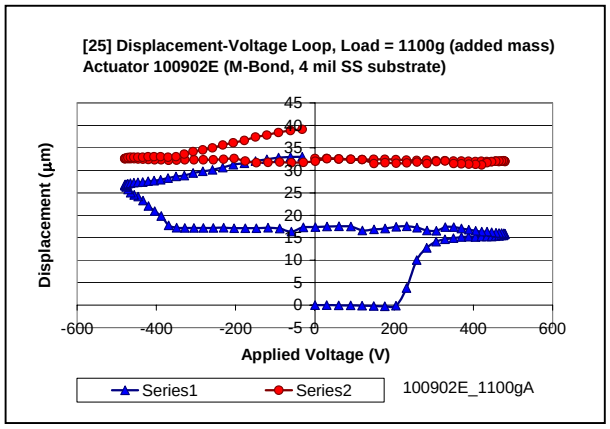

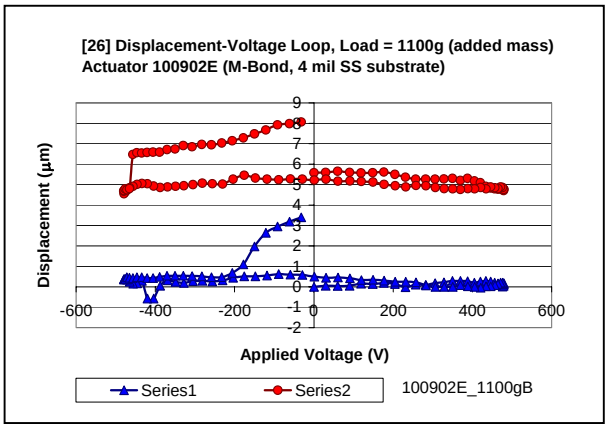

Here are addendum files, that is, repeats of displacement-voltage loops at 1000 and 1100g loads, followed by a final set at zero load.

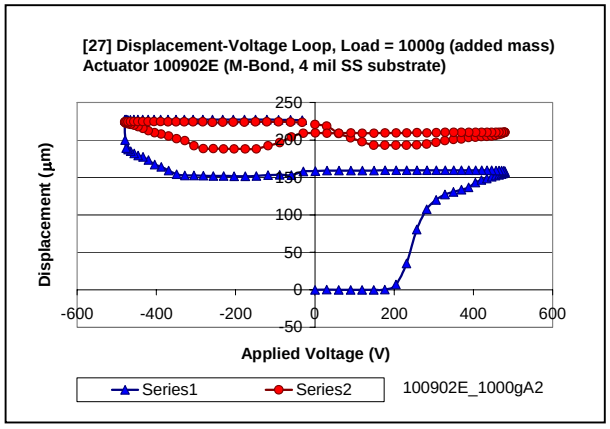

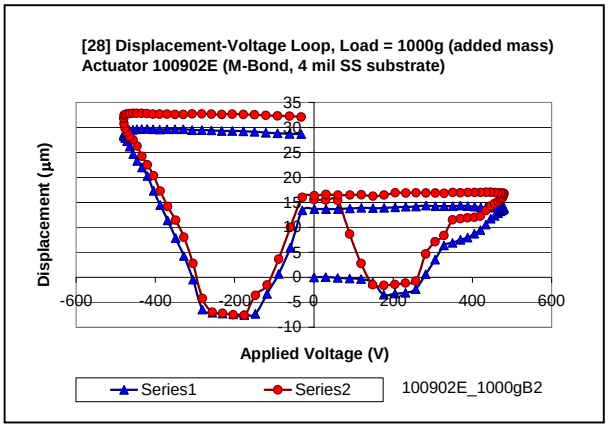

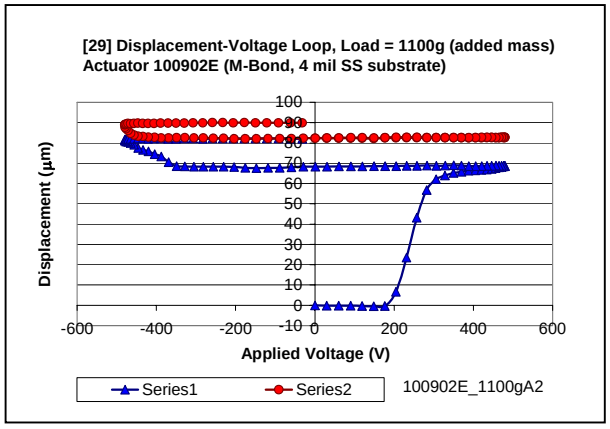

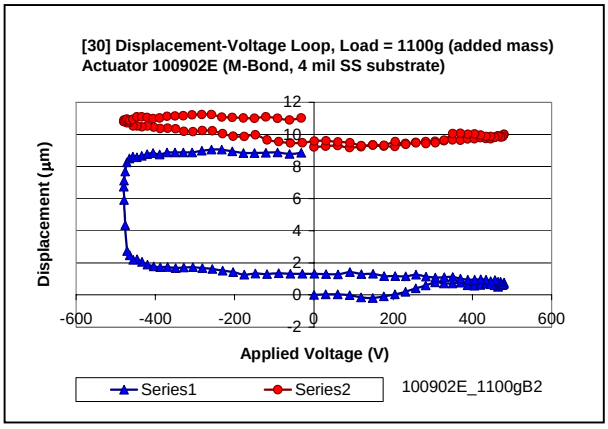

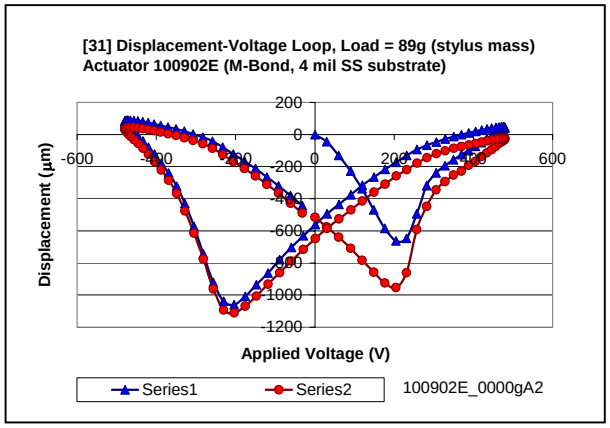

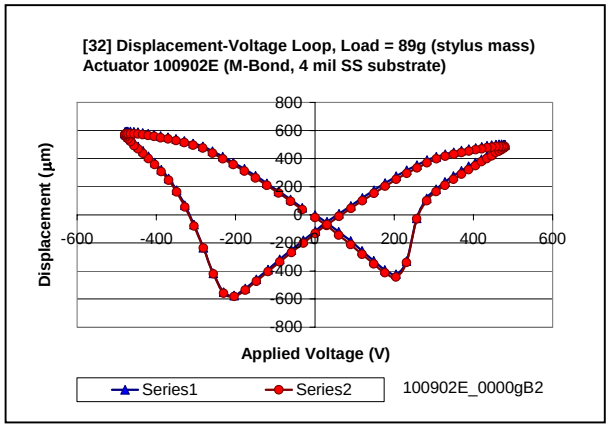

5. Gallery of strain-displacement loops for actuator K081602A (JB Weld adhesive, “thick”, 8 mil stainless steel substrate) follows.

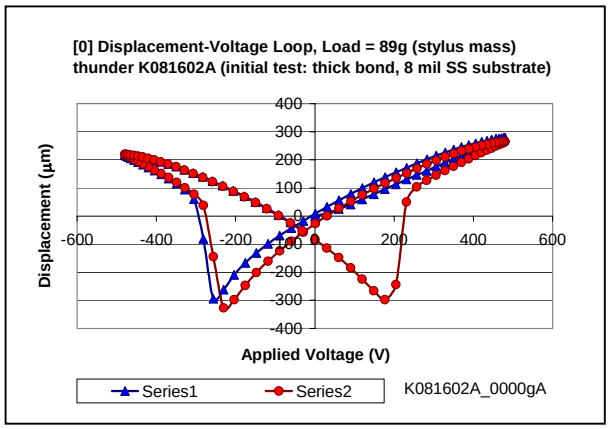

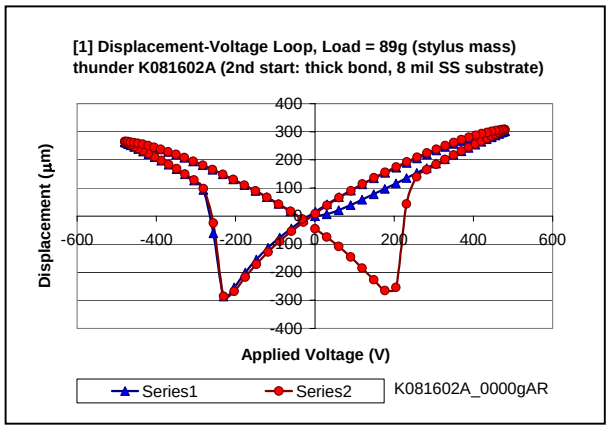

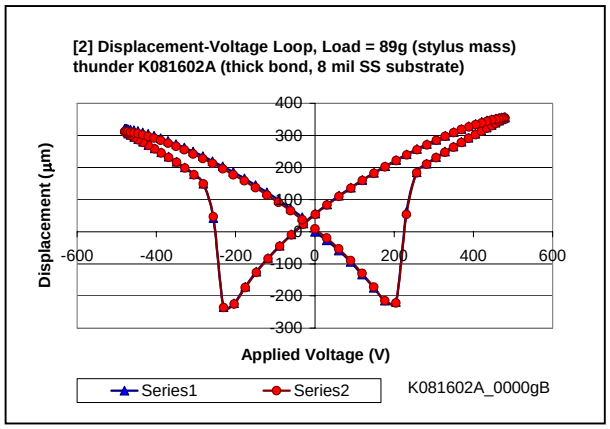

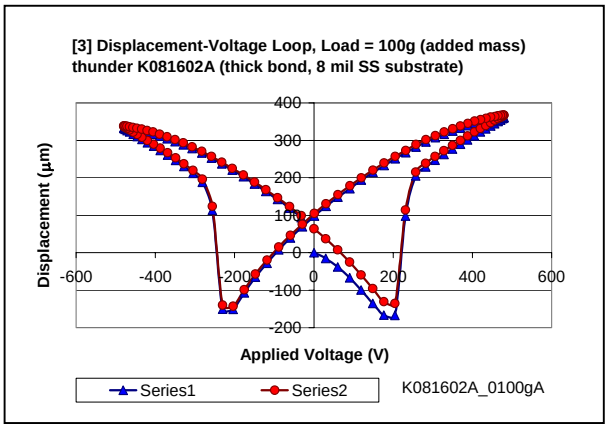
[3] Displacement-Voltage Loop, Load = 100g (added mass)
thunder K081602A (thick bond, 8 mil SS substrate)
Displacement (µm)
Applied Voltage (V)
Series1
Series2
K081602A_0100gA

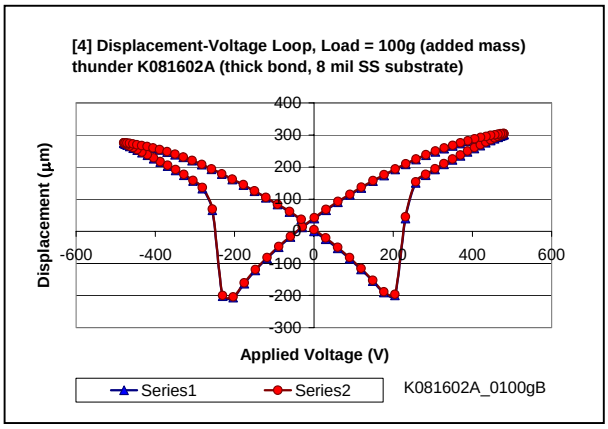
[4] Displacement-Voltage Loop, Load = 100g (added mass)
thunder K081602A (thick bond, 8 mil SS substrate)
Displacement (µm)
Applied Voltage (V)
Series1
Series2
K081602A_0100gB

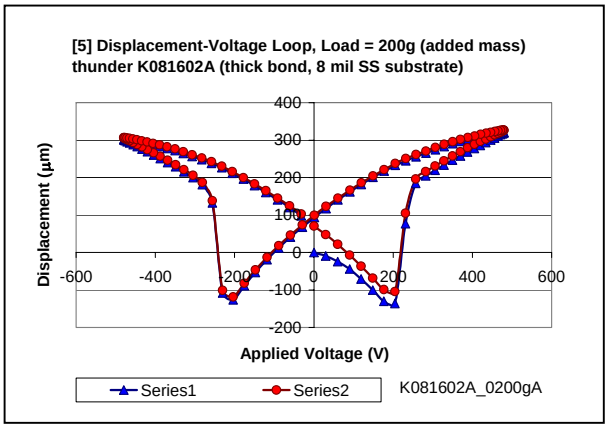
[5] Displacement-Voltage Loop, Load = 200g (added mass)
thunder K081602A (thick bond, 8 mil SS substrate)
Displacement (µm)
Applied Voltage (V)
Series1
Series2
K081602A_0200gA

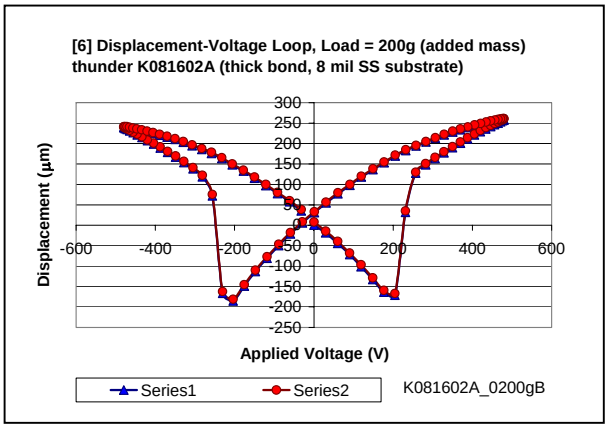
[6] Displacement-Voltage Loop, Load = 200g (added mass)
thunder K081602A (thick bond, 8 mil SS substrate)
Displacement (µm)
Applied Voltage (V)
Series1
Series2
K081602A_0200gB

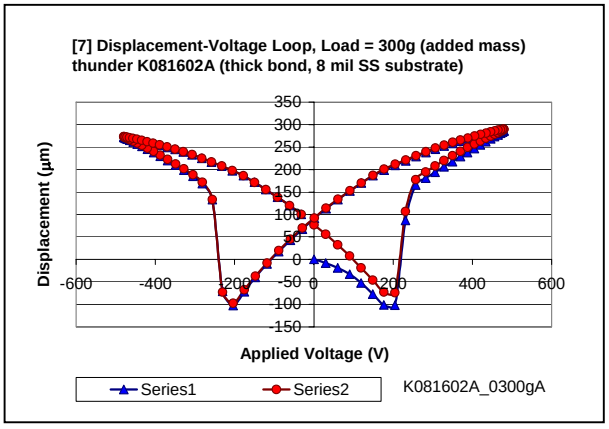
[7] Displacement-Voltage Loop, Load = 300g (added mass)
thunder K081602A (thick bond, 8 mil SS substrate)
Displacement (µm)
Applied Voltage (V)
Series1
Series2
K081602A_0300gA

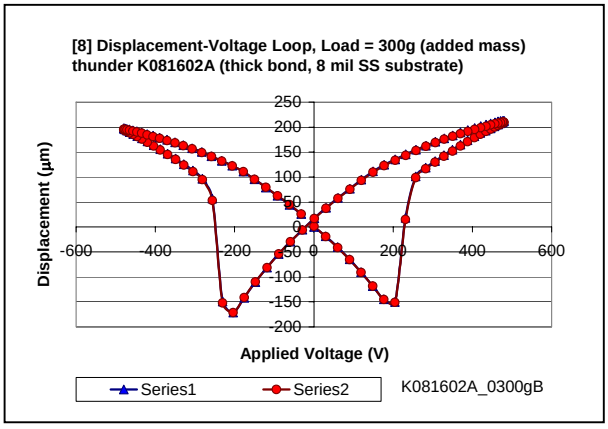
[8] Displacement-Voltage Loop, Load = 300g (added mass)
thunder K081602A (thick bond, 8 mil SS substrate)
Displacement (µm)
Applied Voltage (V)
Series1
Series2
K081602A_0300gB

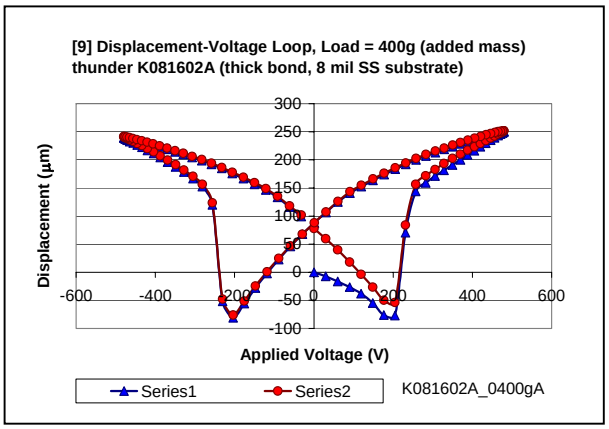
[9] Displacement-Voltage Loop, Load = 400g (added mass)
thunder K081602A (thick bond, 8 mil SS substrate)
Displacement (µm)
Applied Voltage (V)
Series1
Series2
K081602A_0400gA

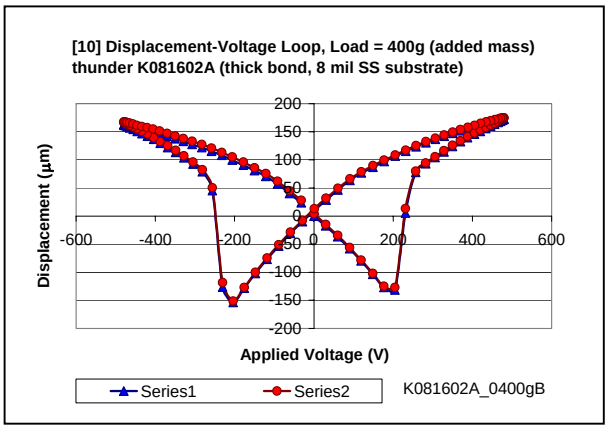
[10] Displacement-Voltage Loop, Load = 400g (added mass)
thunder K081602A (thick bond, 8 mil SS substrate)
Displacement (µm)
Applied Voltage (V)
Series1
Series2
K081602A_0400gB

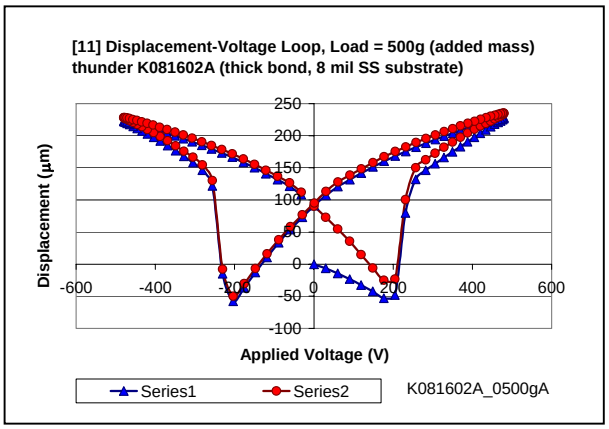
[11] Displacement-Voltage Loop, Load = 500g (added mass)
thunder K081602A (thick bond, 8 mil SS substrate)
Displacement (µm)
Applied Voltage (V)
Series1
Series2
K081602A_0500gA

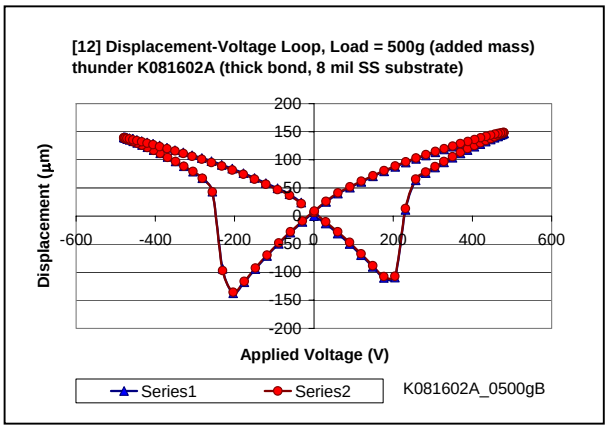
[12] Displacement-Voltage Loop, Load = 500g (added mass)
thunder K081602A (thick bond, 8 mil SS substrate)
Displacement (µm)
Applied Voltage (V)
Series1
Series2
K081602A_0500gB

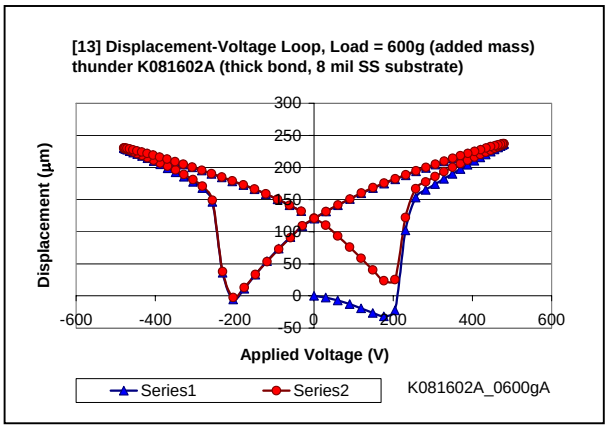
[13] Displacement-Voltage Loop, Load = 600g (added mass)
thunder K081602A (thick bond, 8 mil SS substrate)
Displacement (µm)
Applied Voltage (V)
Series1
Series2
K081602A_0600gA

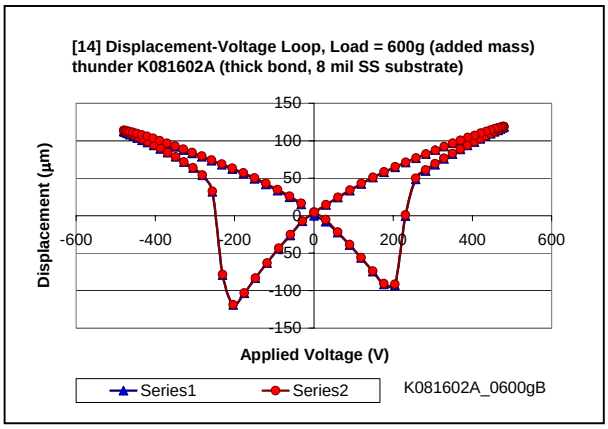
[14] Displacement-Voltage Loop, Load = 600g (added mass)
thunder K081602A (thick bond, 8 mil SS substrate)
Displacement (µm)
Applied Voltage (V)
Series1
Series2
K081602A_0600gB

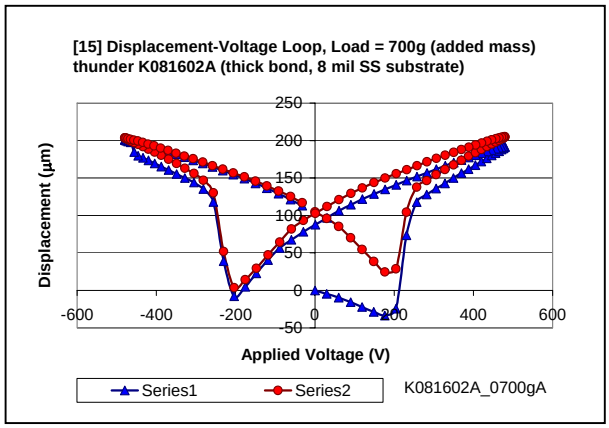
[15] Displacement-Voltage Loop, Load = 700g (added mass)
thunder K081602A (thick bond, 8 mil SS substrate)
Displacement (µm)
Applied Voltage (V)
Series1
Series2
K081602A_0700gA

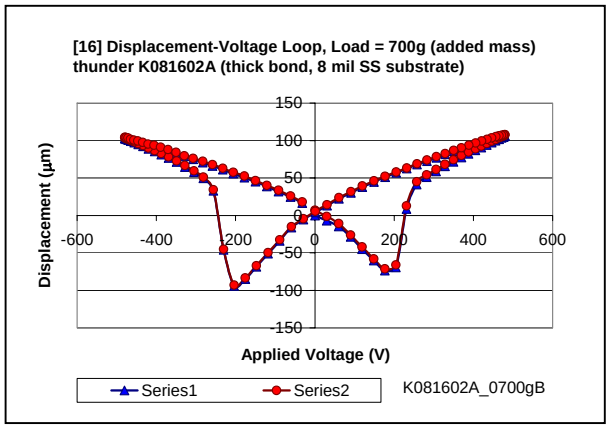
[16] Displacement-Voltage Loop, Load = 700g (added mass)
thunder K081602A (thick bond, 8 mil SS substrate)
Displacement (µm)
Applied Voltage (V)
Series1
Series2
K081602A_0700gB

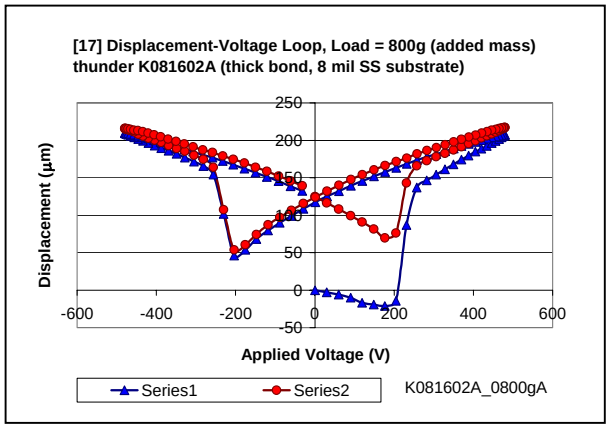
[17] Displacement-Voltage Loop, Load = 800g (added mass)
thunder K081602A (thick bond, 8 mil SS substrate)
Displacement (µm)
Applied Voltage (V)
Series1
Series2
K081602A_0800gA

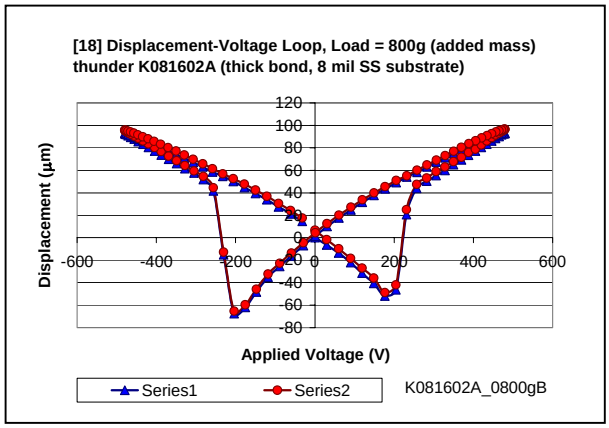
[18] Displacement-Voltage Loop, Load = 800g (added mass)
thunder K081602A (thick bond, 8 mil SS substrate)
Displacement (µm)
Applied Voltage (V)
Series1
Series2
K081602A_0800gB

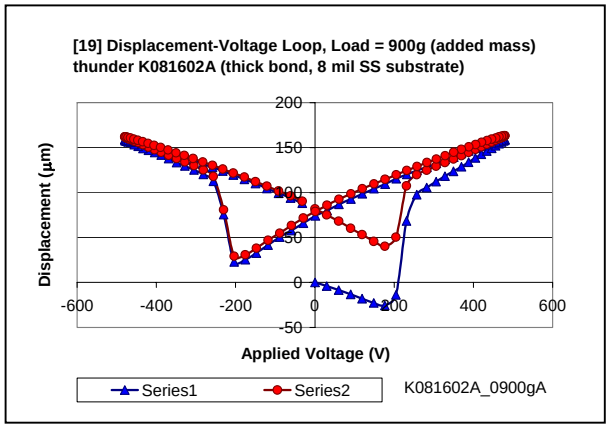
[19] Displacement-Voltage Loop, Load = 900g (added mass)
thunder K081602A (thick bond, 8 mil SS substrate)
Displacement (µm)
Applied Voltage (V)
Series1
Series2
K081602A_0900gA

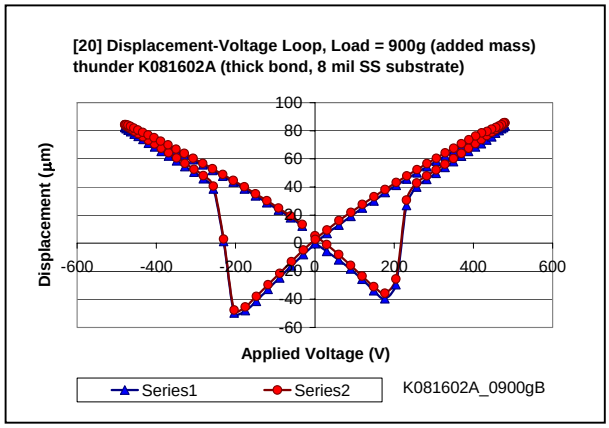
[20] Displacement-Voltage Loop, Load = 900g (added mass)
thunder K081602A (thick bond, 8 mil SS substrate)
Displacement (µm)
Applied Voltage (V)
Series1
Series2
K081602A_0900gB

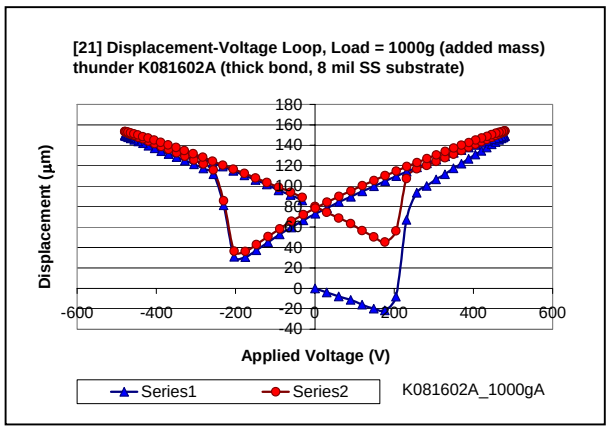

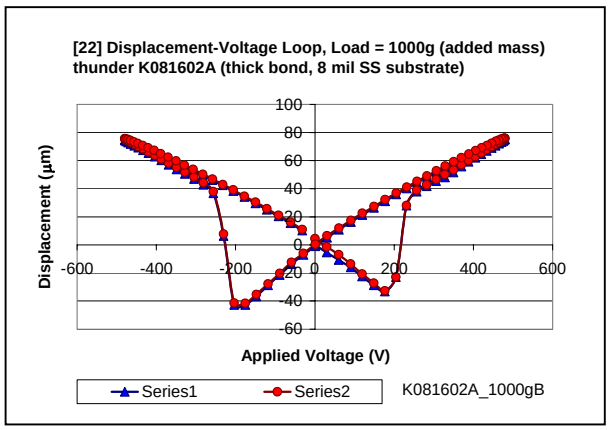

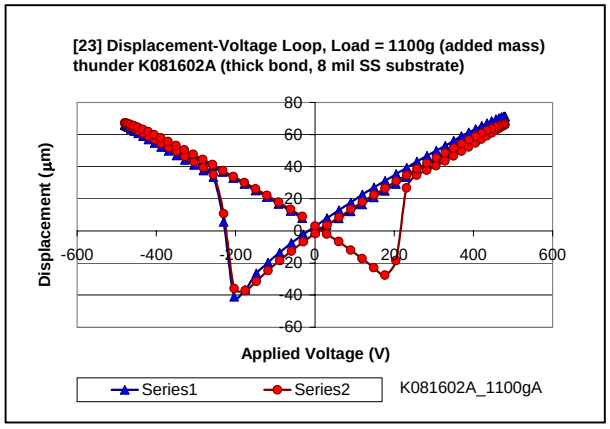

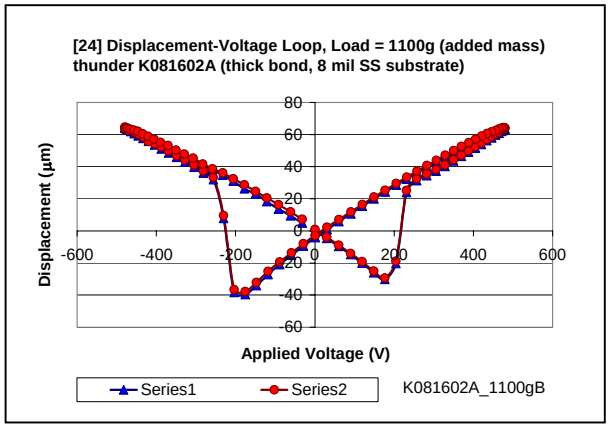

Here are addendum files, that is, repeats of displacement-voltage loops at 1000 and 1100g loads, followed by a final set at zero load.

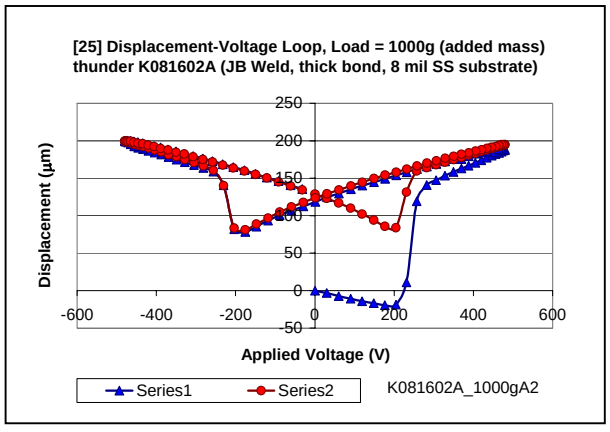

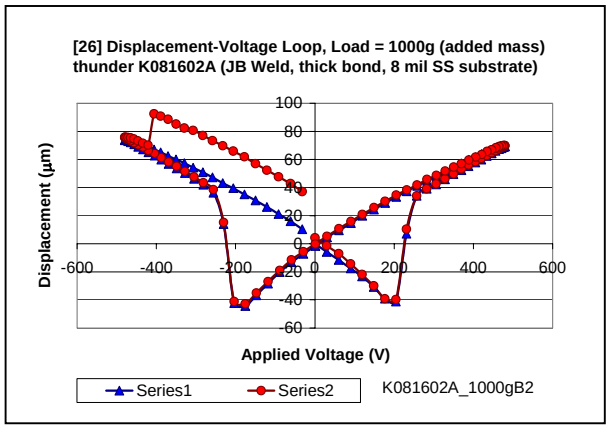

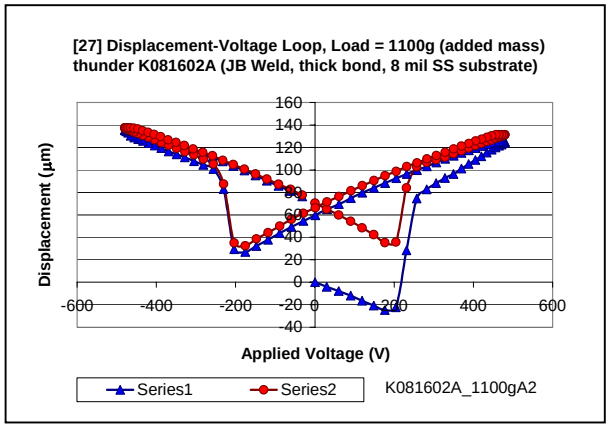

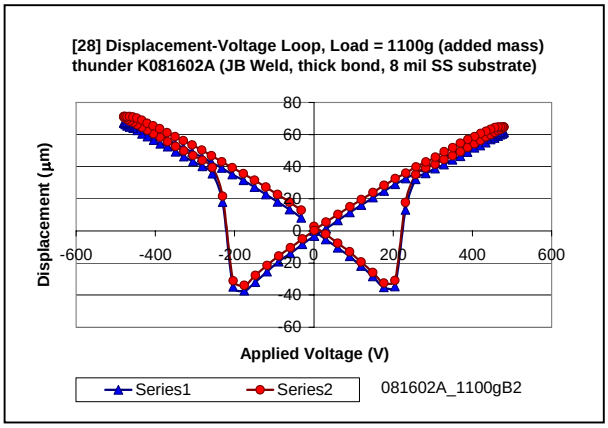

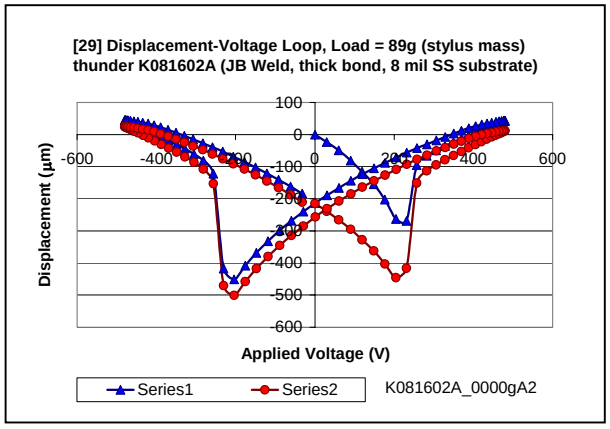

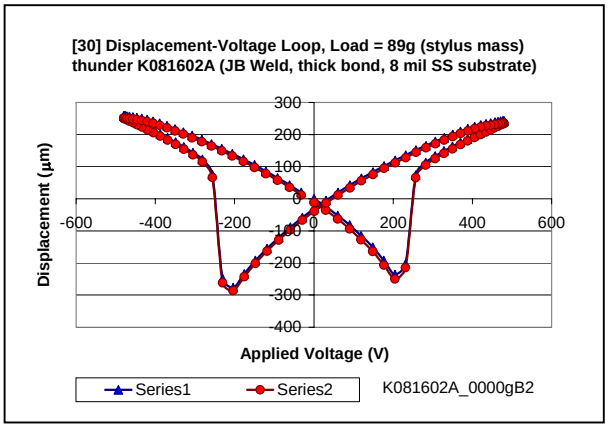

6. Gallery of strain-displacement loops for actuator N081602A (JB Weld adhesive, “thin”, 8 mil stainless steel substrate) follows.

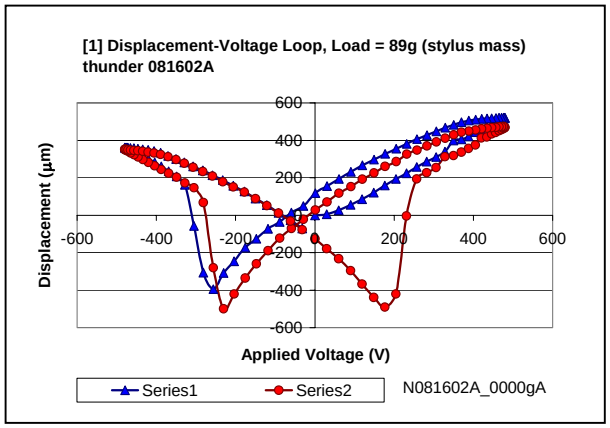

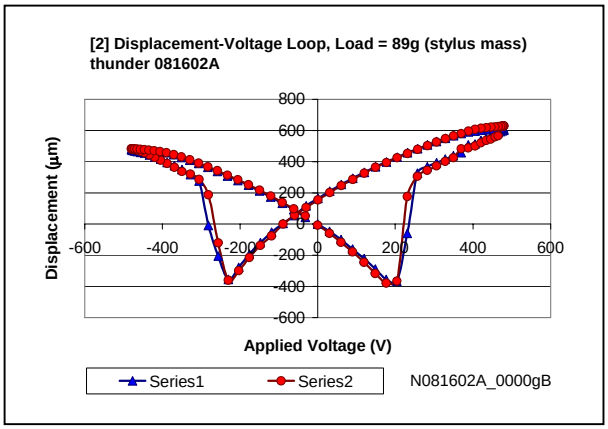

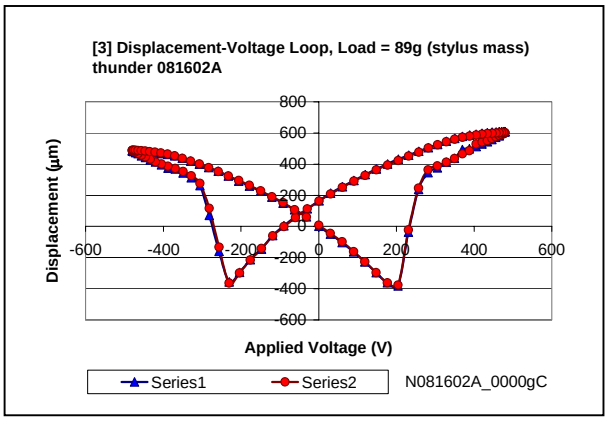
[3] Displacement-Voltage Loop, Load = 89g (stylus mass)
thunder 081602A
Displacement (µm)
800
600
400
200
0
-200
-400
-600
-600
-400
-200
0
200
400
600
Applied Voltage (V)
Series1
Series2
N081602A_0000gC

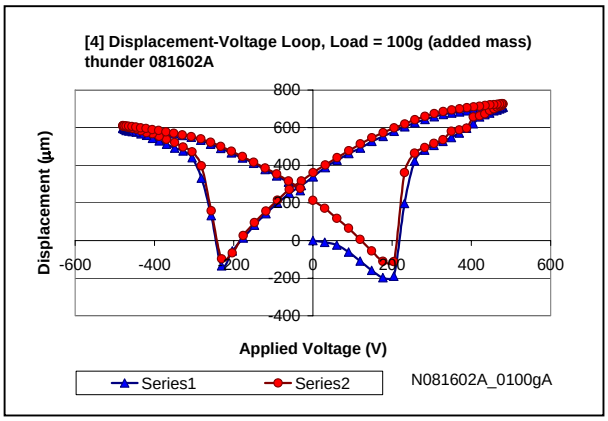
[4] Displacement-Voltage Loop, Load = 100g (added mass)
thunder 081602A
Displacement (µm)
800
600
400
200
0
-200
-400
-600
-400
-200
0
200
400
600
Applied Voltage (V)
Series1
Series2
N081602A_0100gA

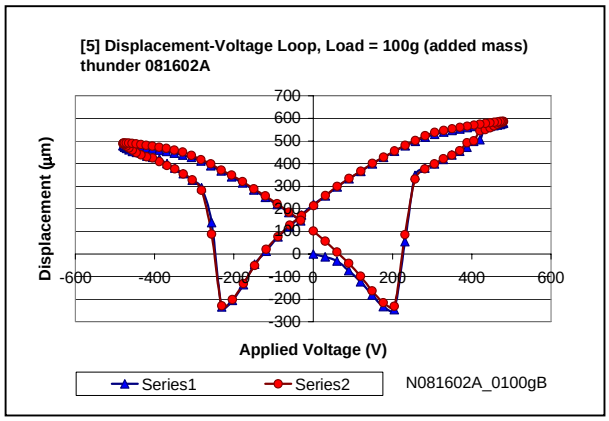
[5] Displacement-Voltage Loop, Load = 100g (added mass)
thunder 081602A
Displacement (µm)
700
600
500
400
300
200
100
0
-200
-300
-600
-400
-200
-100
0
200
400
600
Applied Voltage (V)
Series1
Series2
N081602A_0100gB

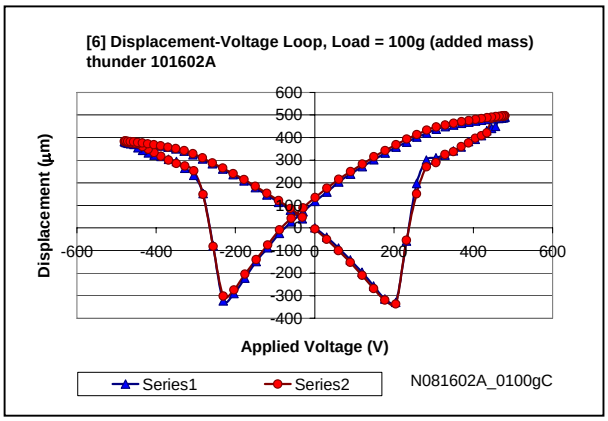
[6] Displacement-Voltage Loop, Load = 100g (added mass)
thunder 101602A
Displacement (µm)
600
500
400
300
200
100
0
-200
-300
-400
-600
-400
-200
-100
0
200
400
600
Applied Voltage (V)
Series1
Series2
N081602A_0100gC

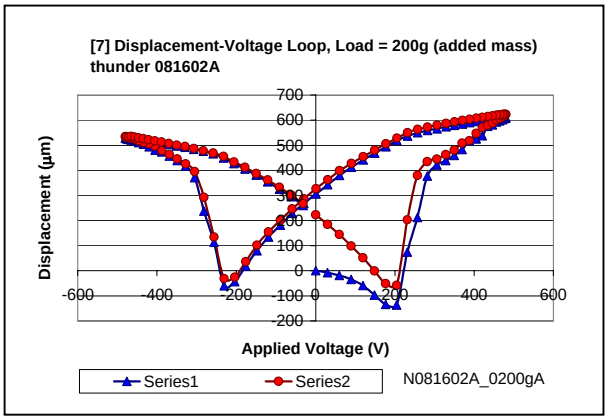
[7] Displacement-Voltage Loop, Load = 200g (added mass) thunder 081602A
Displacement (µm)
Applied Voltage (V)
Series1
Series2
N081602A_0200gA

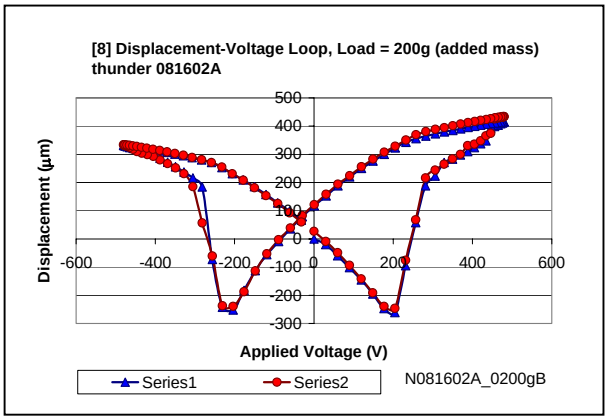
[8] Displacement-Voltage Loop, Load = 200g (added mass) thunder 081602A
Displacement (µm)
Applied Voltage (V)
Series1
Series2
N081602A_0200gB

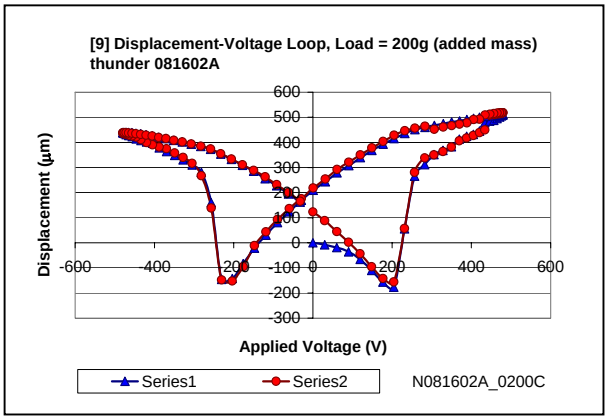
[9] Displacement-Voltage Loop, Load = 200g (added mass) thunder 081602A
Displacement (µm)
Applied Voltage (V)
Series1
Series2
N081602A_0200C

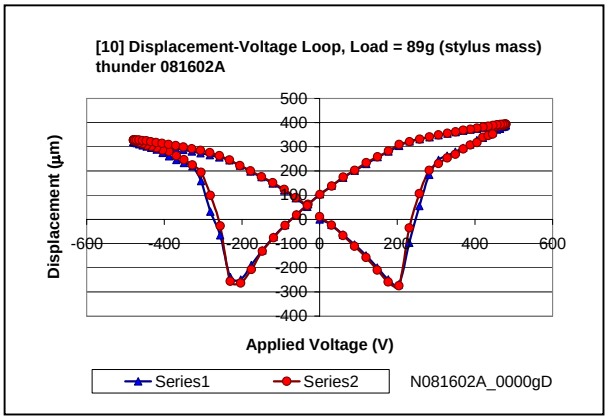
[10] Displacement-Voltage Loop, Load = 89g (stylus mass) thunder 081602A
Displacement (µm)
Applied Voltage (V)
Series1
Series2
N081602A_0000gD

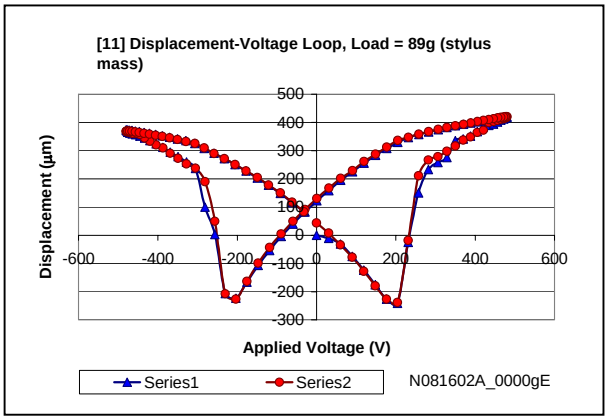
[11] Displacement-Voltage Loop, Load = 89g (stylus mass)
Displacement (µm)
Applied Voltage (V)
Series1
Series2
N081602A_0000gE

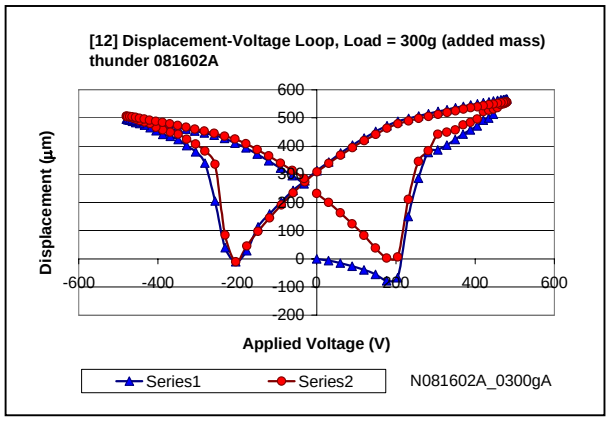
[12] Displacement-Voltage Loop, Load = 300g (added mass)
thunder 081602A
Displacement (µm)
Applied Voltage (V)
Series1
Series2
N081602A_0300gA

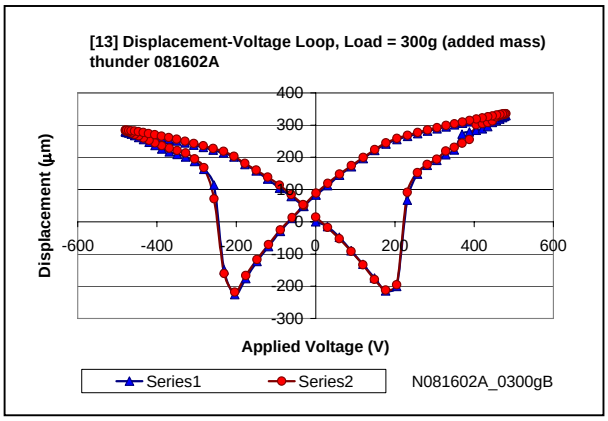
[13] Displacement-Voltage Loop, Load = 300g (added mass)
thunder 081602A
Displacement (µm)
Applied Voltage (V)
Series1
Series2
N081602A_0300gB

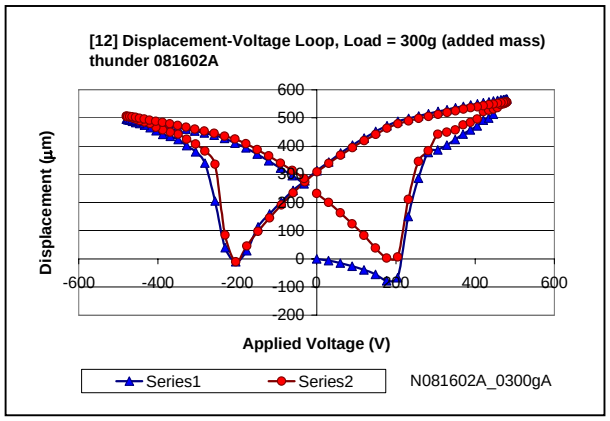
[12] Displacement-Voltage Loop, Load = 300g (added mass)
thunder 081602A
Displacement (µm)
Applied Voltage (V)
Series1
Series2
N081602A_0300gA

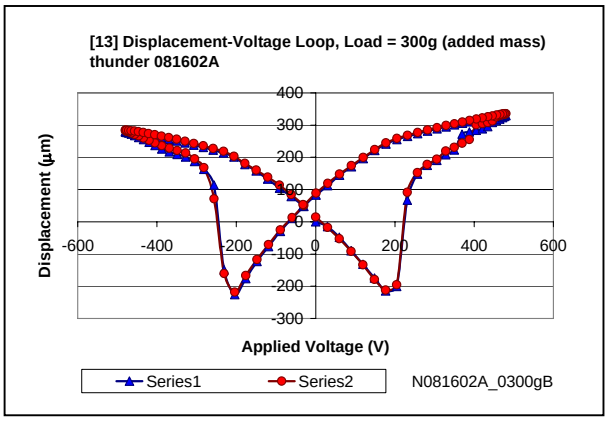
[13] Displacement-Voltage Loop, Load = 300g (added mass)
thunder 081602A
Displacement (µm)
Applied Voltage (V)
Series1
Series2
N081602A_0300gB

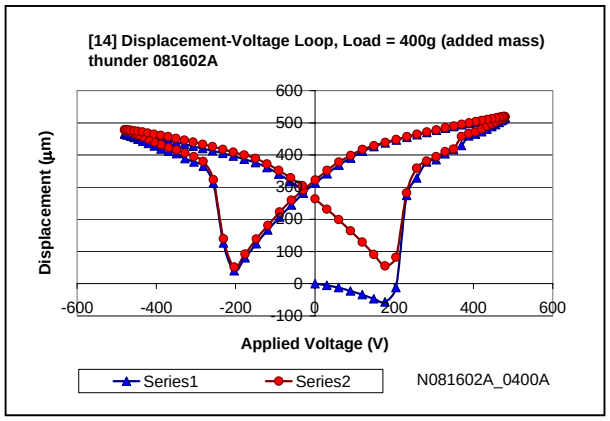
[14] Displacement-Voltage Loop, Load = 400g (added mass)
thunder 081602A
Displacement (µm)
Applied Voltage (V)
Series1
Series2
N081602A_0400A

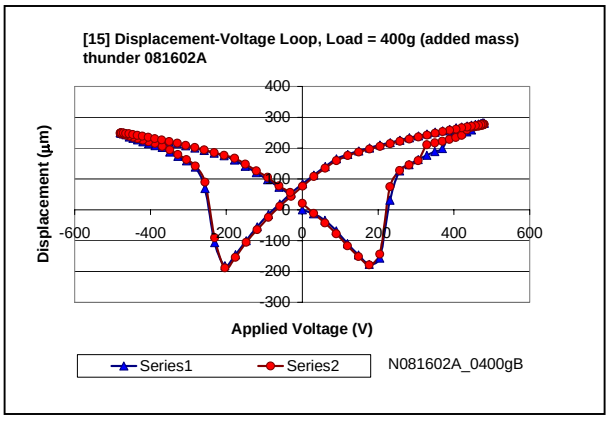
[15] Displacement-Voltage Loop, Load = 400g (added mass)
thunder 081602A
Displacement (µm)
Applied Voltage (V)
Series1
Series2
N081602A_0400gB

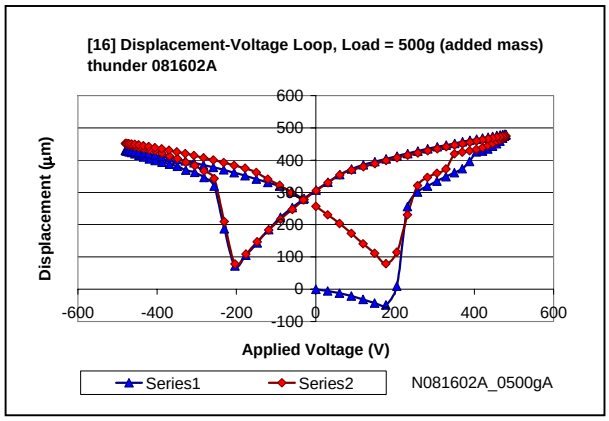

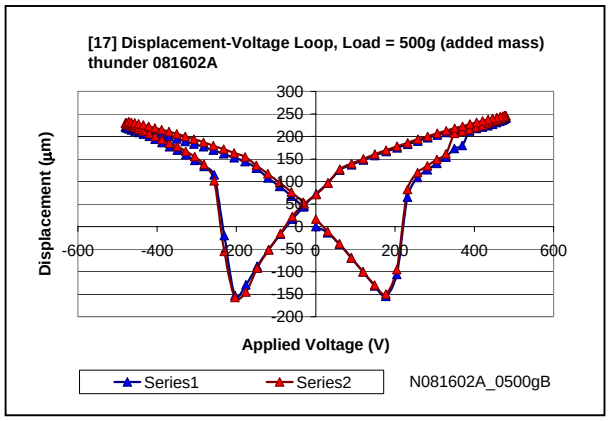

7. Gallery of strain-displacement loops for actuator K121002 (JB Weld adhesive, “thick”, 4 mil stainless steel substrate) follows.

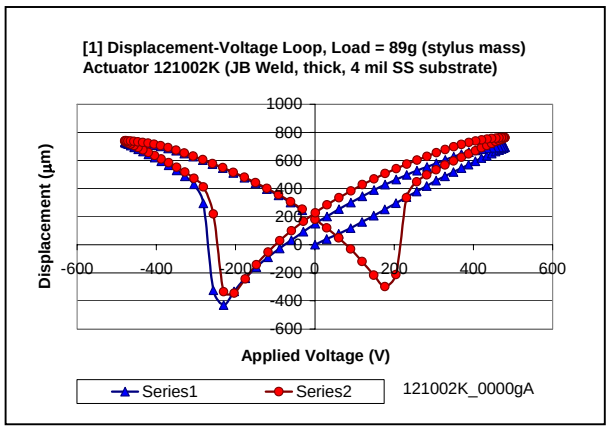

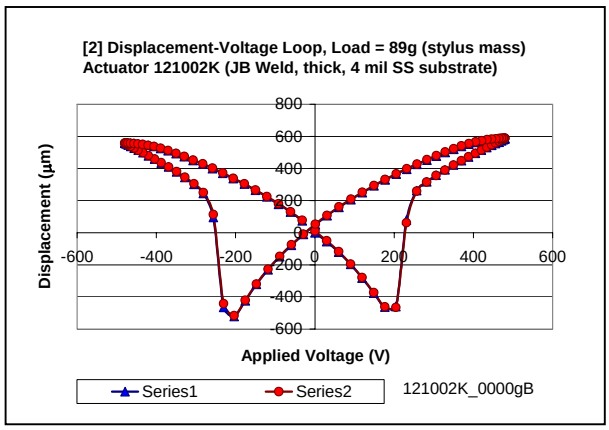

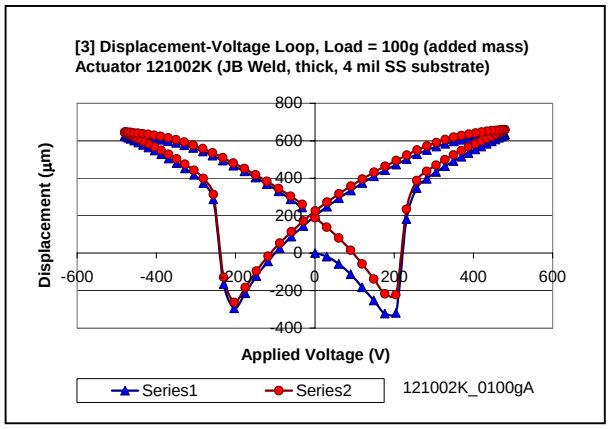

The second pair of displacement-voltage loop for 100g load was omitted accidentally. This was discovered after completing the set for 200g load. The remedy was to repeat another set for 100g load (including the omitted pair) and for 200g load.

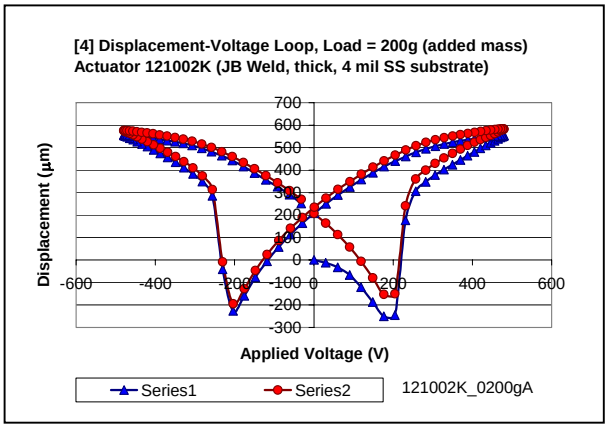

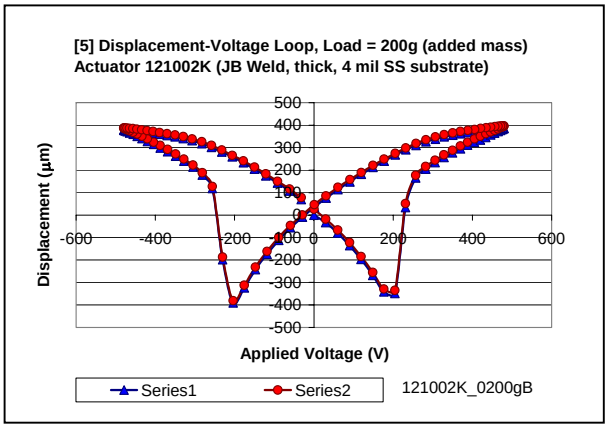

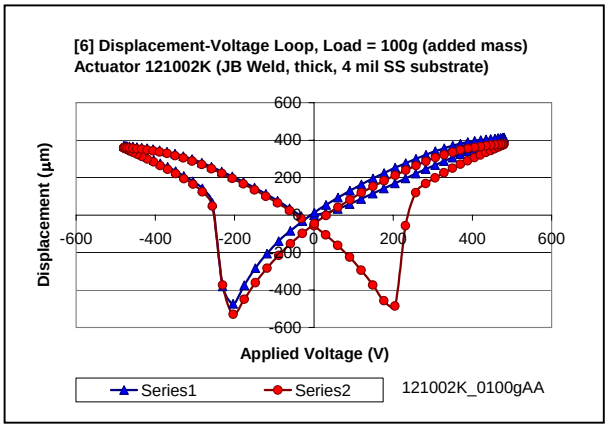

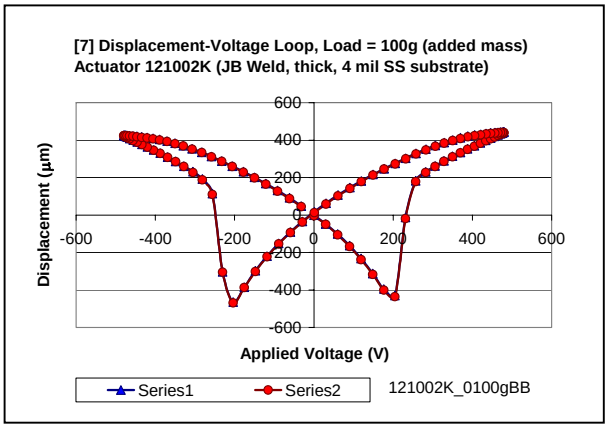

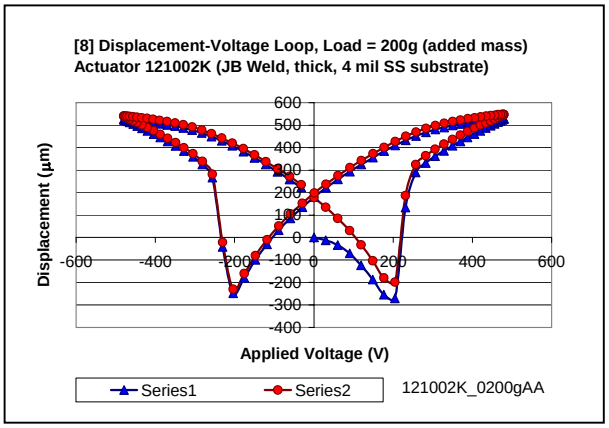

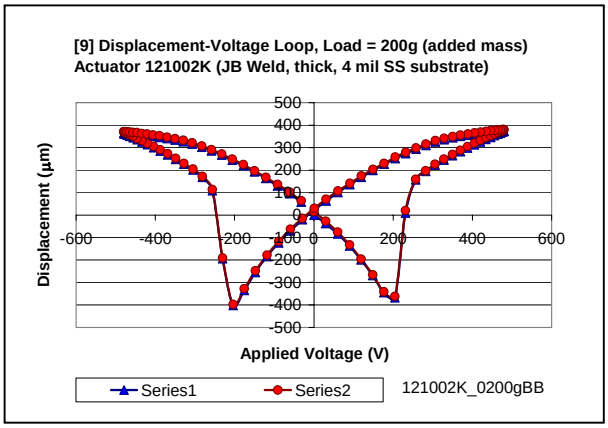

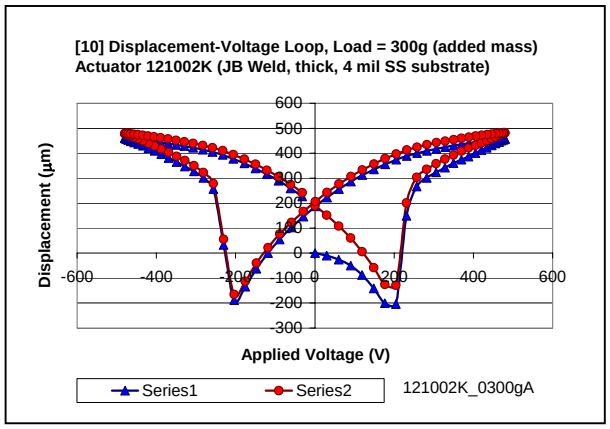
[10] Displacement-Voltage Loop, Load = 300g (added mass)
Actuator 121002K (JB Weld, thick, 4 mil SS substrate)
Displacement (µm)
Applied Voltage (V)
Series1
Series2
121002K_0300gA

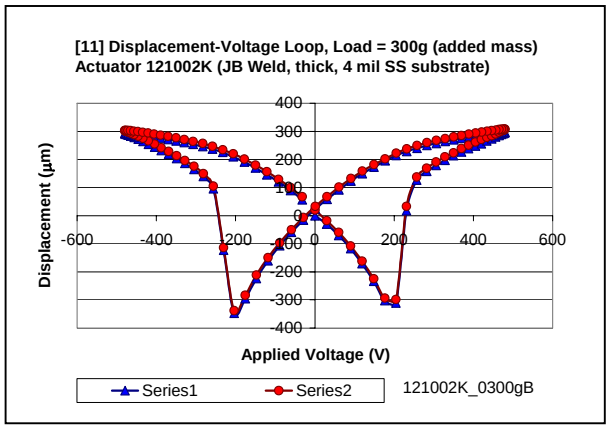
[11] Displacement-Voltage Loop, Load = 300g (added mass)
Actuator 121002K (JB Weld, thick, 4 mil SS substrate)
Displacement (µm)
Applied Voltage (V)
Series1
Series2
121002K_0300gB

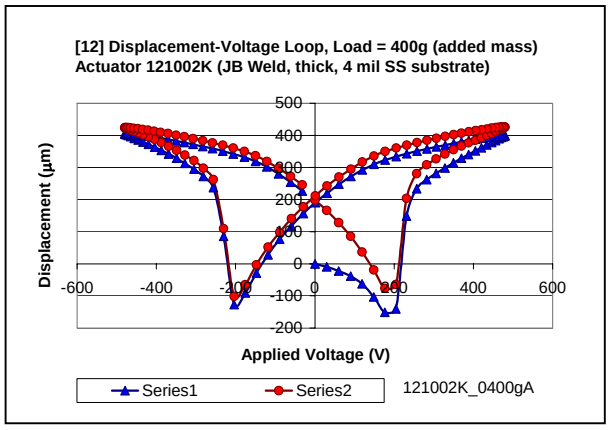
[12] Displacement-Voltage Loop, Load = 400g (added mass)
Actuator 121002K (JB Weld, thick, 4 mil SS substrate)
Displacement (µm)
Applied Voltage (V)
Series1
Series2
121002K_0400gA

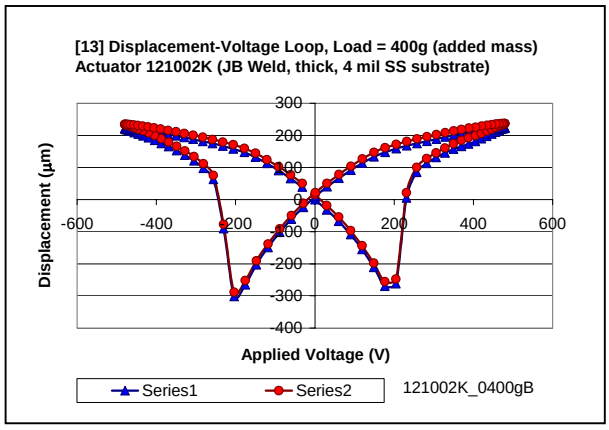
[13] Displacement-Voltage Loop, Load = 400g (added mass)
Actuator 121002K (JB Weld, thick, 4 mil SS substrate)
Displacement (µm)
Applied Voltage (V)
Series1
Series2
121002K_0400gB

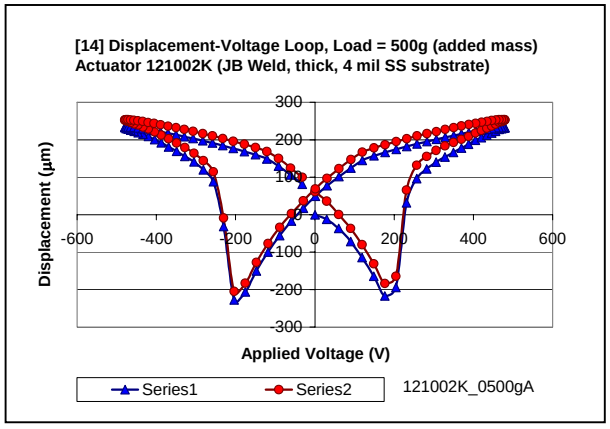
[14] Displacement-Voltage Loop, Load = 500g (added mass)
Actuator 121002K (JB Weld, thick, 4 mil SS substrate)
Displacement (µm)
Applied Voltage (V)
Series1
Series2
121002K_0500gA

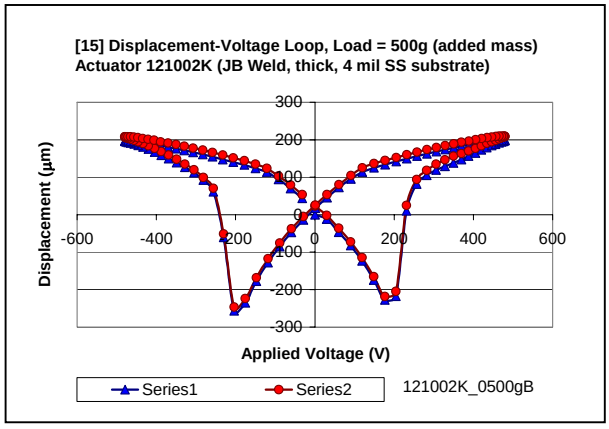
[15] Displacement-Voltage Loop, Load = 500g (added mass)
Actuator 121002K (JB Weld, thick, 4 mil SS substrate)
Displacement (µm)
Applied Voltage (V)
Series1
Series2
121002K_0500gB

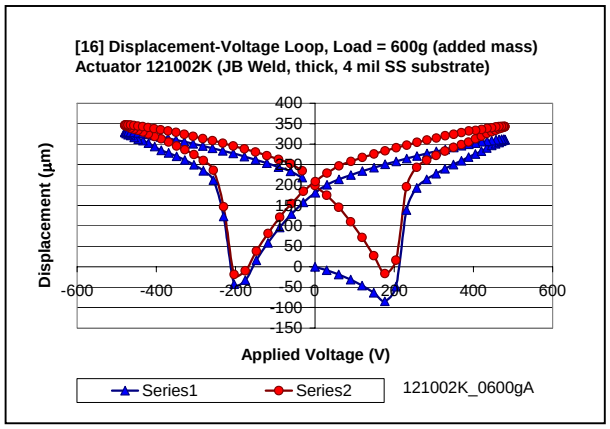
[16] Displacement-Voltage Loop, Load = 600g (added mass)
Actuator 121002K (JB Weld, thick, 4 mil SS substrate)
Displacement (µm)
Applied Voltage (V)
Series1
Series2
121002K_0600gA

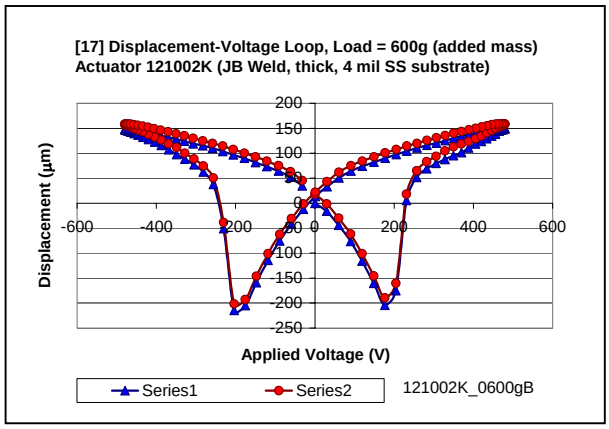
[17] Displacement-Voltage Loop, Load = 600g (added mass)
Actuator 121002K (JB Weld, thick, 4 mil SS substrate)
Displacement (µm)
Applied Voltage (V)
Series1
Series2
121002K_0600gB

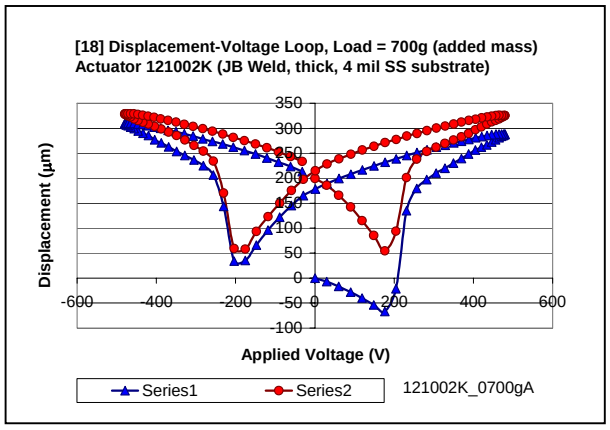
[18] Displacement-Voltage Loop, Load = 700g (added mass)
Actuator 121002K (JB Weld, thick, 4 mil SS substrate)
Displacement (µm)
Applied Voltage (V)
Series1
Series2
121002K_0700gA

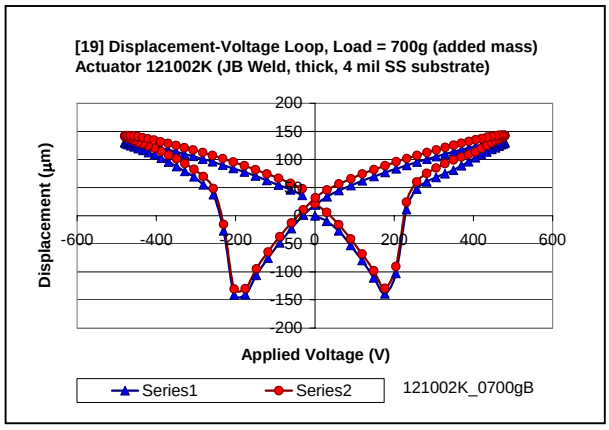
[19] Displacement-Voltage Loop, Load = 700g (added mass)
Actuator 121002K (JB Weld, thick, 4 mil SS substrate)
Displacement (µm)
Applied Voltage (V)
Series1
Series2
121002K_0700gB

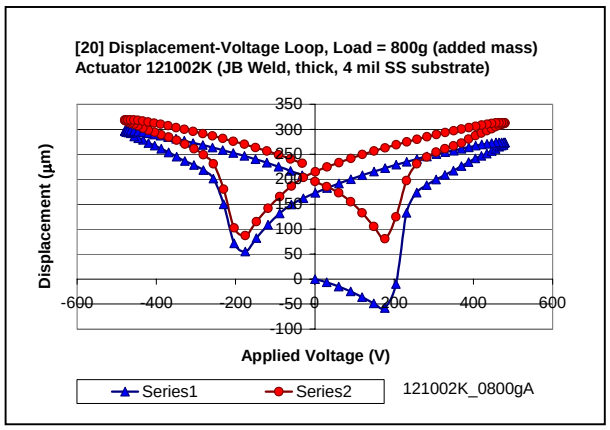
[20] Displacement-Voltage Loop, Load = 800g (added mass)
Actuator 121002K (JB Weld, thick, 4 mil SS substrate)
Displacement (µm)
Applied Voltage (V)
Series1
Series2
121002K_0800gA

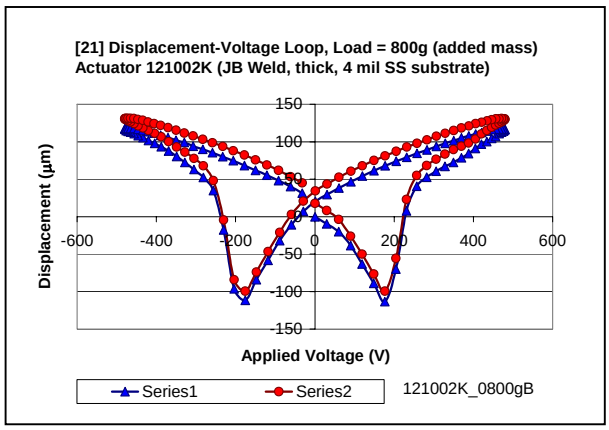
[21] Displacement-Voltage Loop, Load = 800g (added mass)
Actuator 121002K (JB Weld, thick, 4 mil SS substrate)
Displacement (µm)
Applied Voltage (V)
Series1
Series2
121002K_0800gB

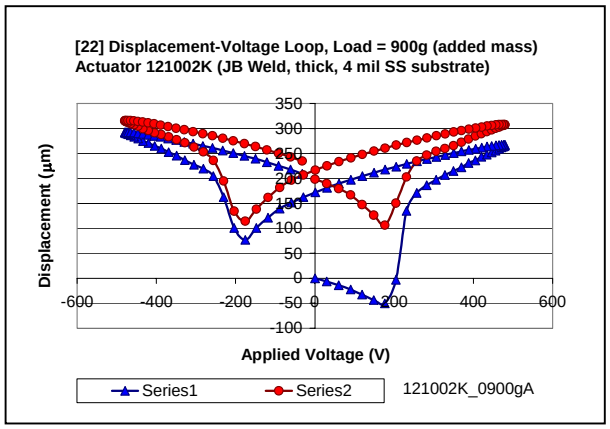

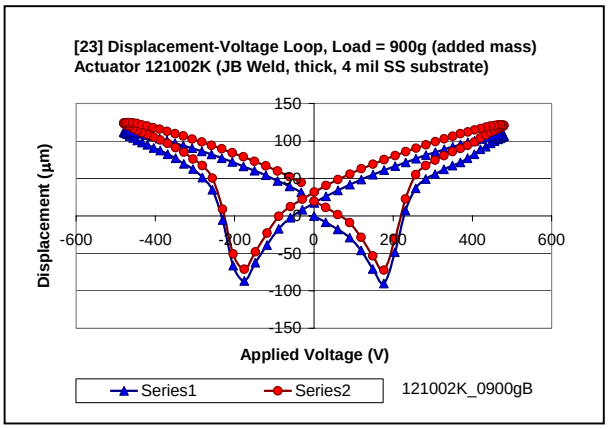

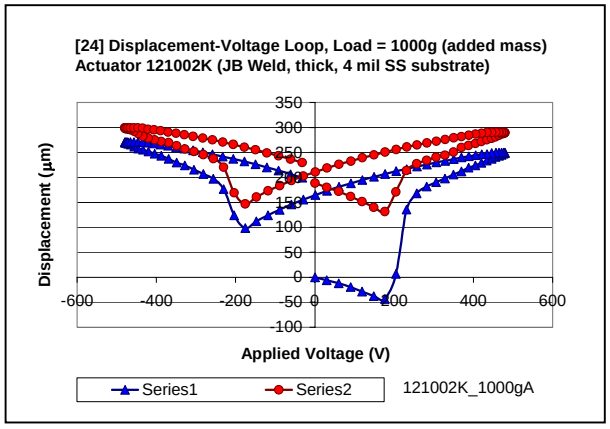

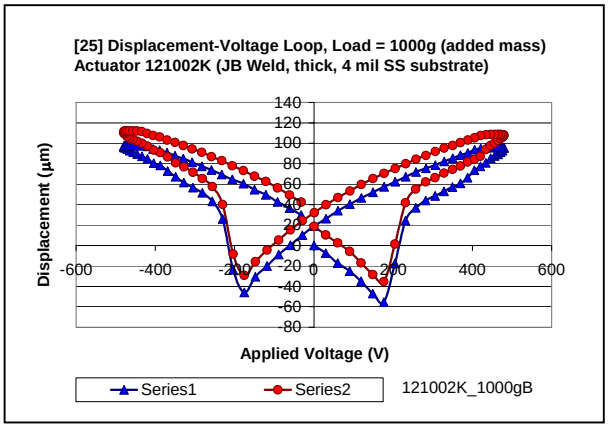

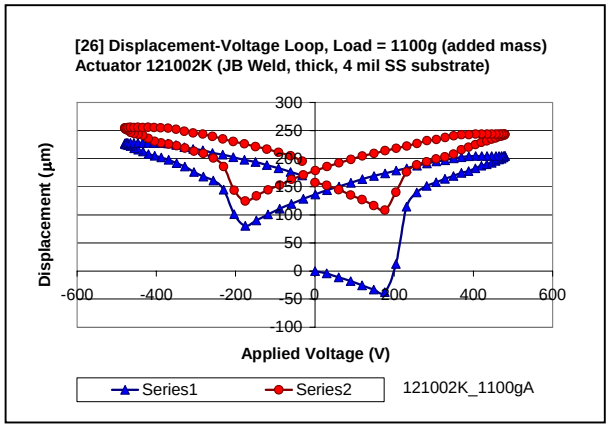

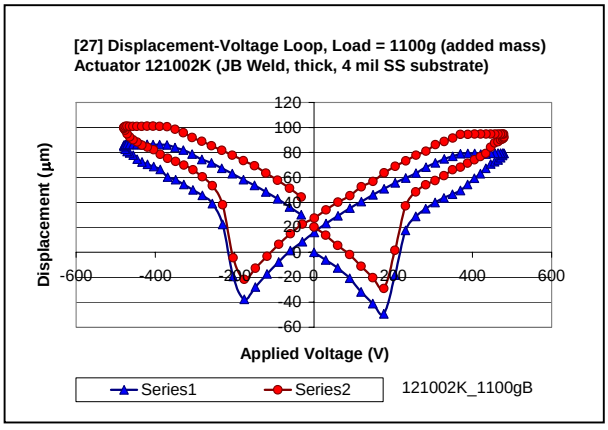

The final set at zero load was taken after the preceding loops without interruption.

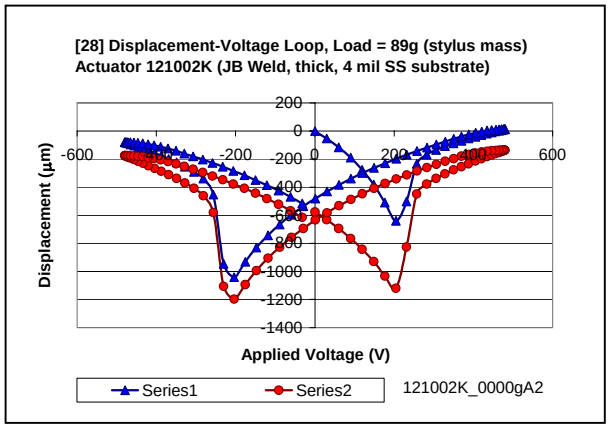

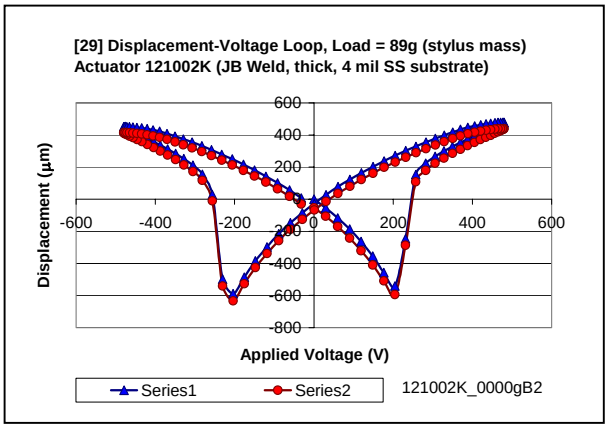

8. Gallery of strain-displacement loops for actuator N121002A (JB Weld adhesive, “thin”, 4 mil stainless steel substrate) follows.

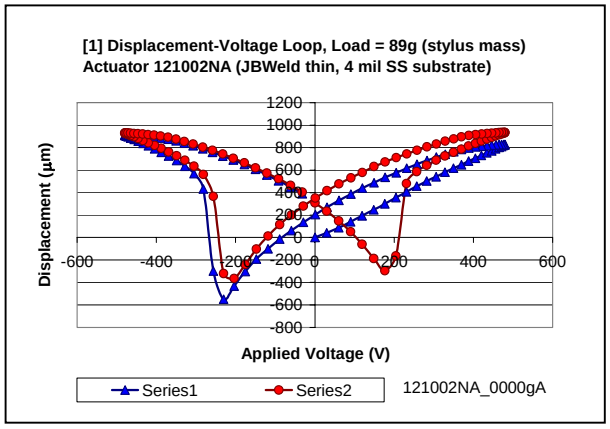

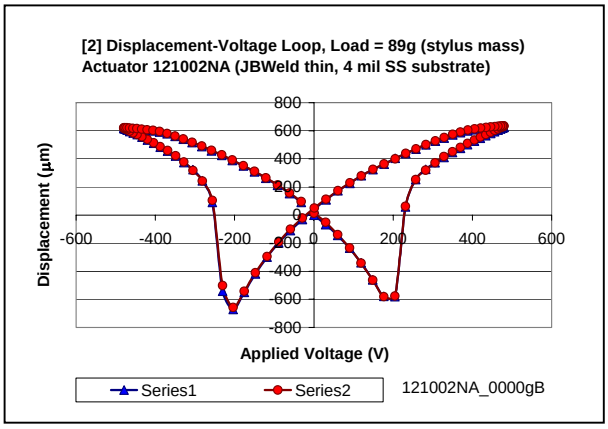

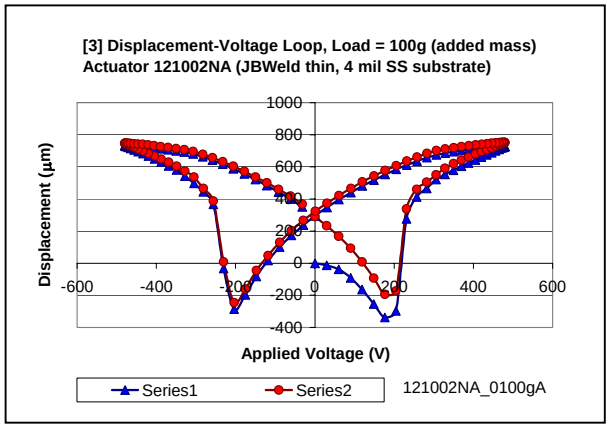

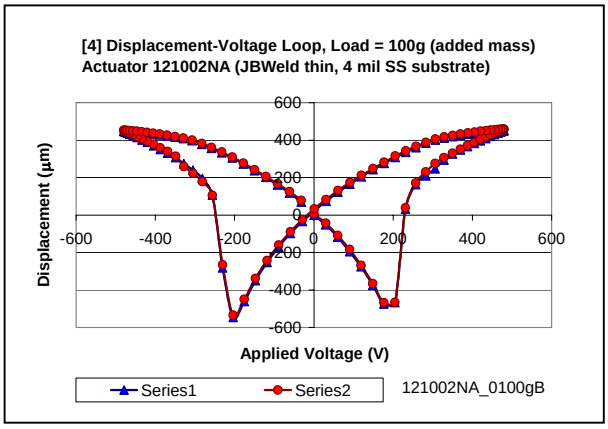

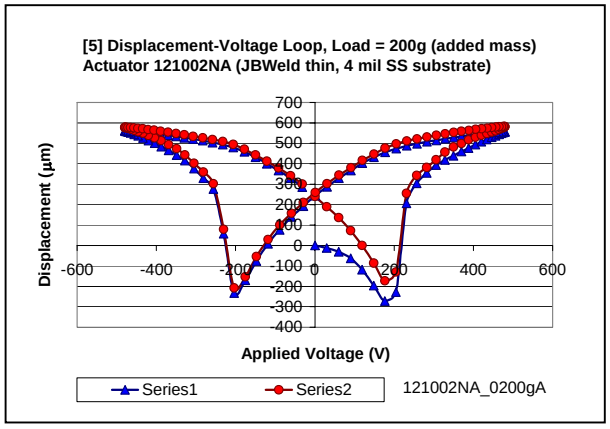
[5] Displacement-Voltage Loop, Load = 200g (added mass)
Actuator 121002NA (JBWeld thin, 4 mil SS substrate)
Displacement (µm)
Applied Voltage (V)
Series1
Series2
121002NA_0200gA

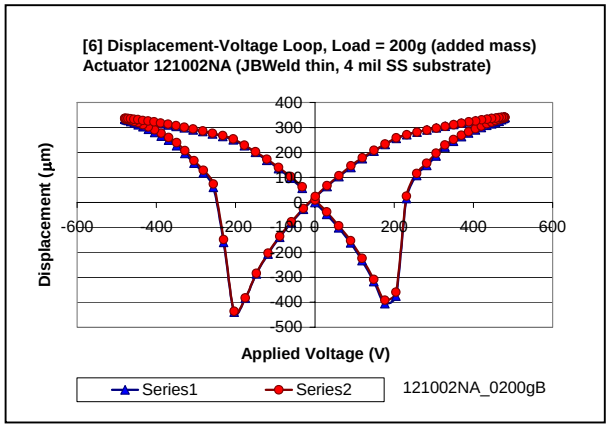
[6] Displacement-Voltage Loop, Load = 200g (added mass)
Actuator 121002NA (JBWeld thin, 4 mil SS substrate)
Displacement (µm)
Applied Voltage (V)
Series1
Series2
121002NA_0200gB

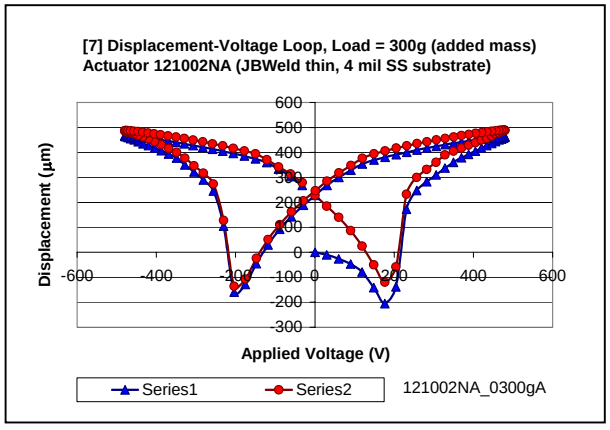
[7] Displacement-Voltage Loop, Load = 300g (added mass)
Actuator 121002NA (JBWeld thin, 4 mil SS substrate)
Displacement (µm)
Applied Voltage (V)
Series1
Series2
121002NA_0300gA

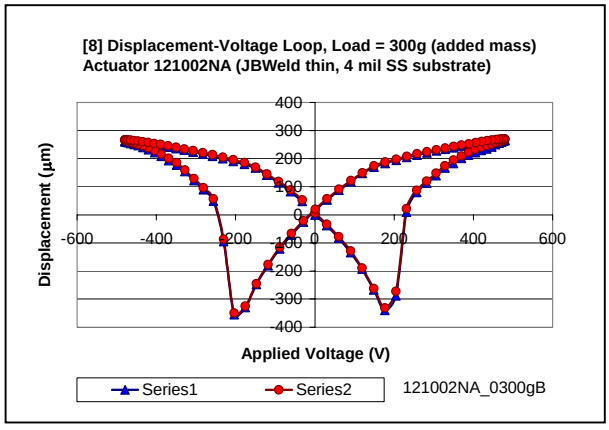
[8] Displacement-Voltage Loop, Load = 300g (added mass)
Actuator 121002NA (JBWeld thin, 4 mil SS substrate)
Displacement (µm)
Applied Voltage (V)
Series1
Series2
121002NA_0300gB

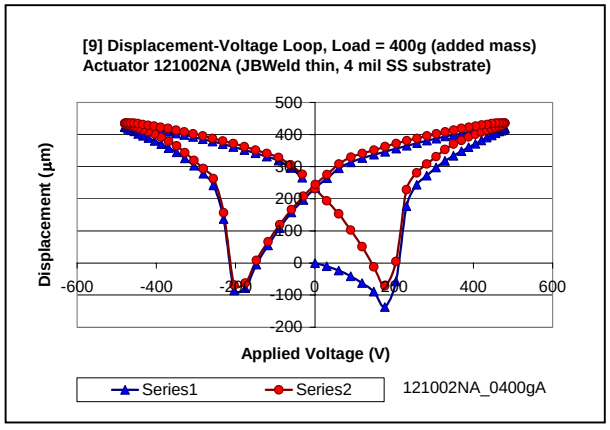
[9] Displacement-Voltage Loop, Load = 400g (added mass)
Actuator 121002NA (JBWeld thin, 4 mil SS substrate)
Displacement (µm)
Applied Voltage (V)
Series1
Series2
121002NA_0400gA

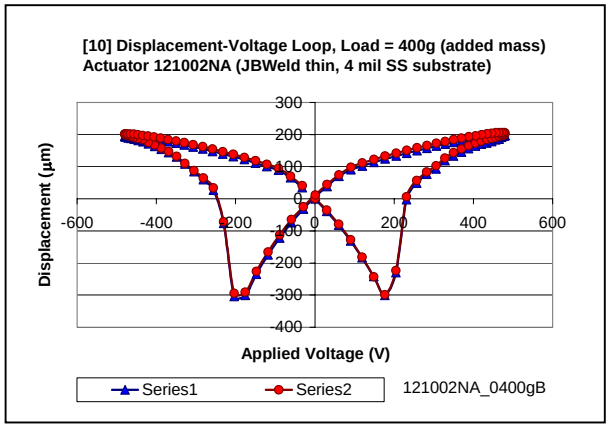
[10] Displacement-Voltage Loop, Load = 400g (added mass)
Actuator 121002NA (JBWeld thin, 4 mil SS substrate)
Displacement (µm)
Applied Voltage (V)
Series1
Series2
121002NA_0400gB

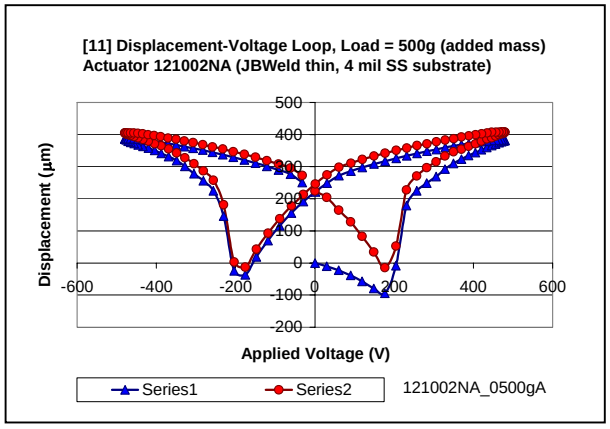
[11] Displacement-Voltage Loop, Load = 500g (added mass)
Actuator 121002NA (JBWeld thin, 4 mil SS substrate)
Displacement (µm)
Applied Voltage (V)
Series1
Series2
121002NA_0500gA

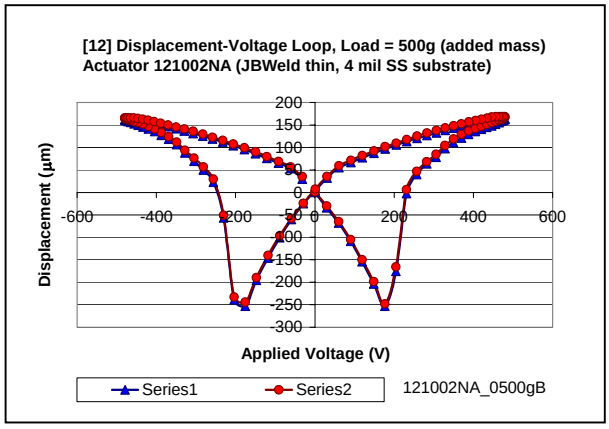
[12] Displacement-Voltage Loop, Load = 500g (added mass)
Actuator 121002NA (JBWeld thin, 4 mil SS substrate)
Displacement (µm)
Applied Voltage (V)
Series1
Series2
121002NA_0500gB

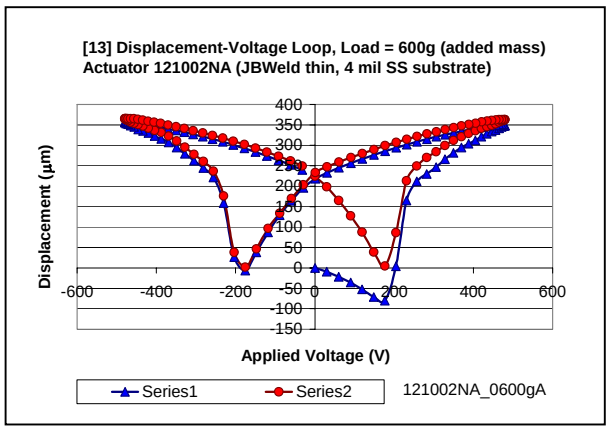
[13] Displacement-Voltage Loop, Load = 600g (added mass)
Actuator 121002NA (JBWeld thin, 4 mil SS substrate)
Displacement (µm)
Applied Voltage (V)
Series1
Series2
121002NA_0600gA

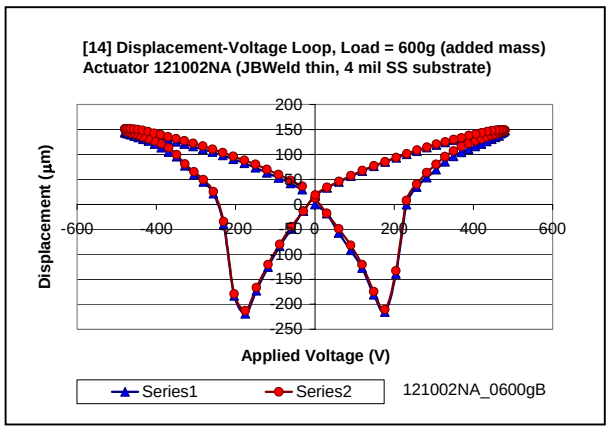
[14] Displacement-Voltage Loop, Load = 600g (added mass)
Actuator 121002NA (JBWeld thin, 4 mil SS substrate)
Displacement (µm)
Applied Voltage (V)
Series1
Series2
121002NA_0600gB

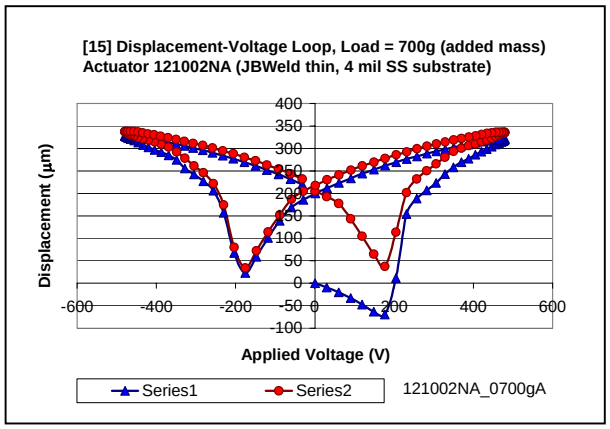
[15] Displacement-Voltage Loop, Load = 700g (added mass)
Actuator 121002NA (JBWeld thin, 4 mil SS substrate)
Displacement (µm)
Applied Voltage (V)
Series1
Series2
121002NA_0700gA

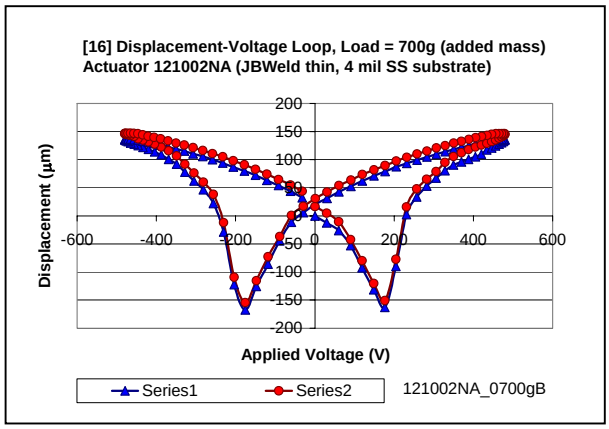
[16] Displacement-Voltage Loop, Load = 700g (added mass)
Actuator 121002NA (JBWeld thin, 4 mil SS substrate)
Displacement (µm)
Applied Voltage (V)
Series1
Series2
121002NA_0700gB

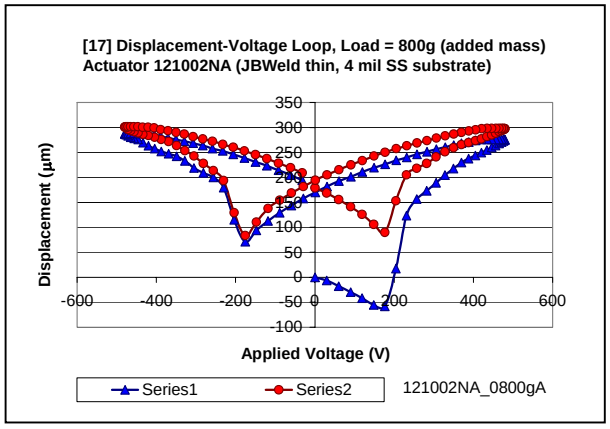
[17] Displacement-Voltage Loop, Load = 800g (added mass)
Actuator 121002NA (JBWeld thin, 4 mil SS substrate)
Displacement (µm)
Applied Voltage (V)
Series1
Series2
121002NA_0800gA

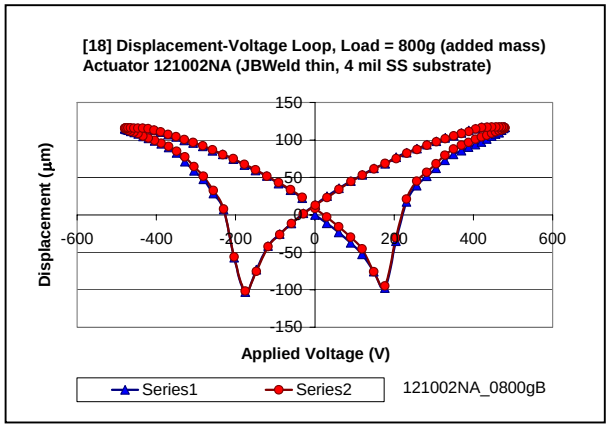
[18] Displacement-Voltage Loop, Load = 800g (added mass)
Actuator 121002NA (JBWeld thin, 4 mil SS substrate)
Displacement (µm)
Applied Voltage (V)
Series1
Series2
121002NA_0800gB

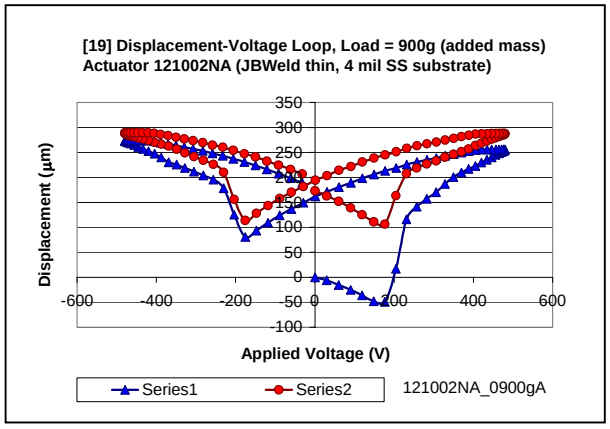
[19] Displacement-Voltage Loop, Load = 900g (added mass)
Actuator 121002NA (JBWeld thin, 4 mil SS substrate)
Displacement (µm)
Applied Voltage (V)
Series1
Series2
121002NA_0900gA

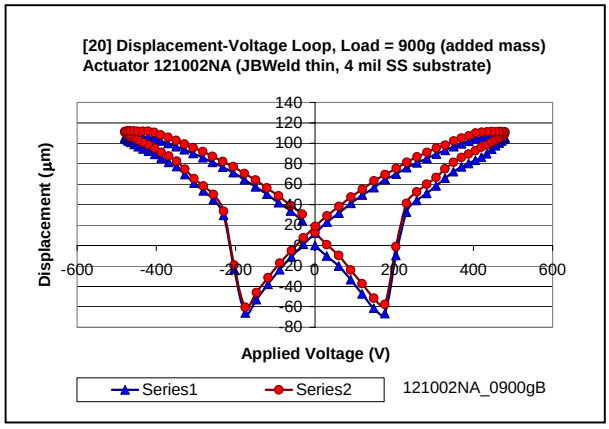
[20] Displacement-Voltage Loop, Load = 900g (added mass)
Actuator 121002NA (JBWeld thin, 4 mil SS substrate)
Displacement (µm)
Applied Voltage (V)
Series1
Series2
121002NA_0900gB

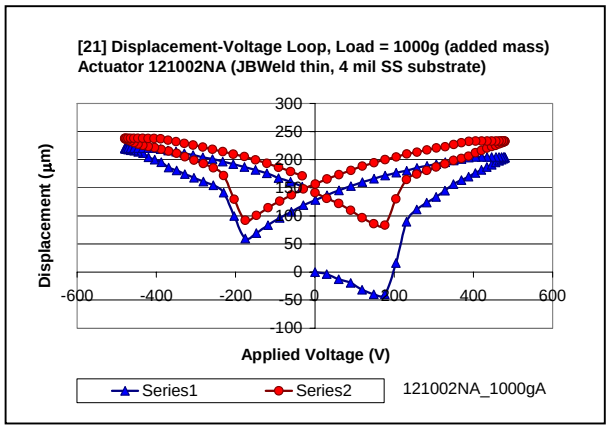
[21] Displacement-Voltage Loop, Load = 1000g (added mass)
Actuator 121002NA (JBWeld thin, 4 mil SS substrate)
Displacement (µm)
Applied Voltage (V)
Series1
Series2
121002NA_1000gA

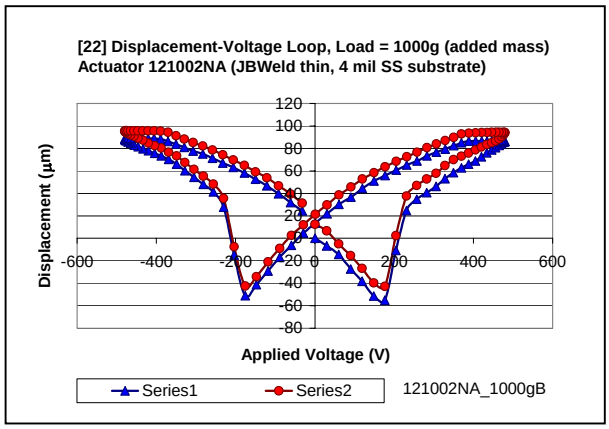
[22] Displacement-Voltage Loop, Load = 1000g (added mass)
Actuator 121002NA (JBWeld thin, 4 mil SS substrate)
Displacement (µm)
Applied Voltage (V)
Series1
Series2
121002NA_1000gB

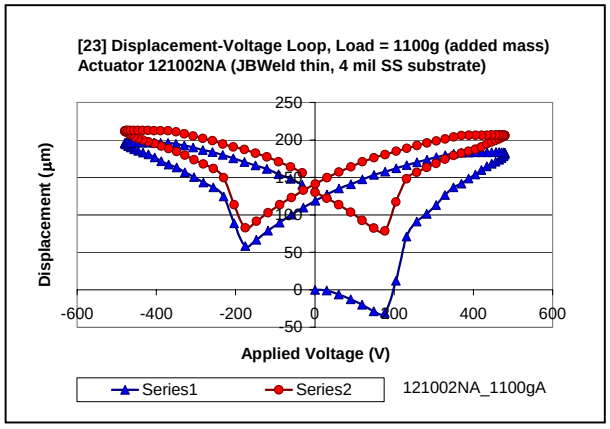

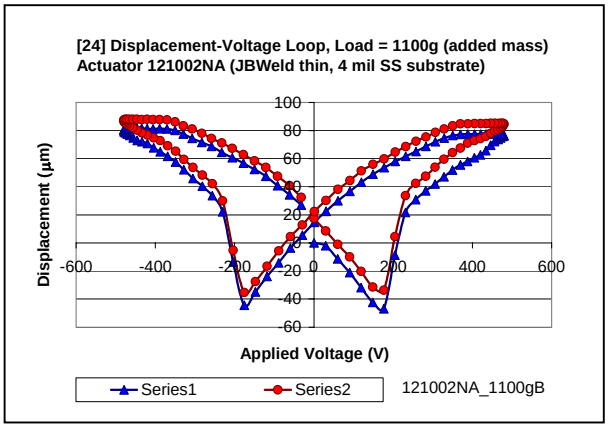

The final set at zero load was taken after the preceding loops without interruption.

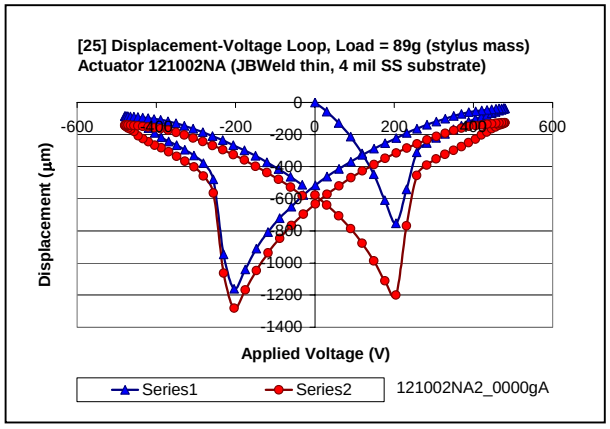

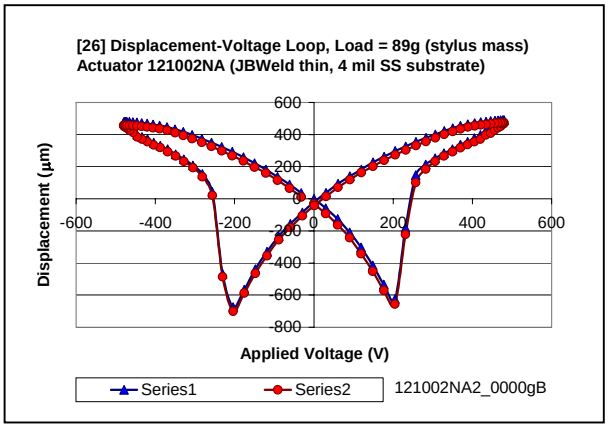

A calibration was performed with the LVDT used in this experiment. The purpose was to verify the scaling factor (μm/V) used to convert the LVDT signal (in sampled, digitized form) to displacement in microns, and to ascertain that the LVDT was linear (or not) across a substantial portion of its range. A number of tests in this experiment required as much as ± 6 V from a total range of ± 10 V.

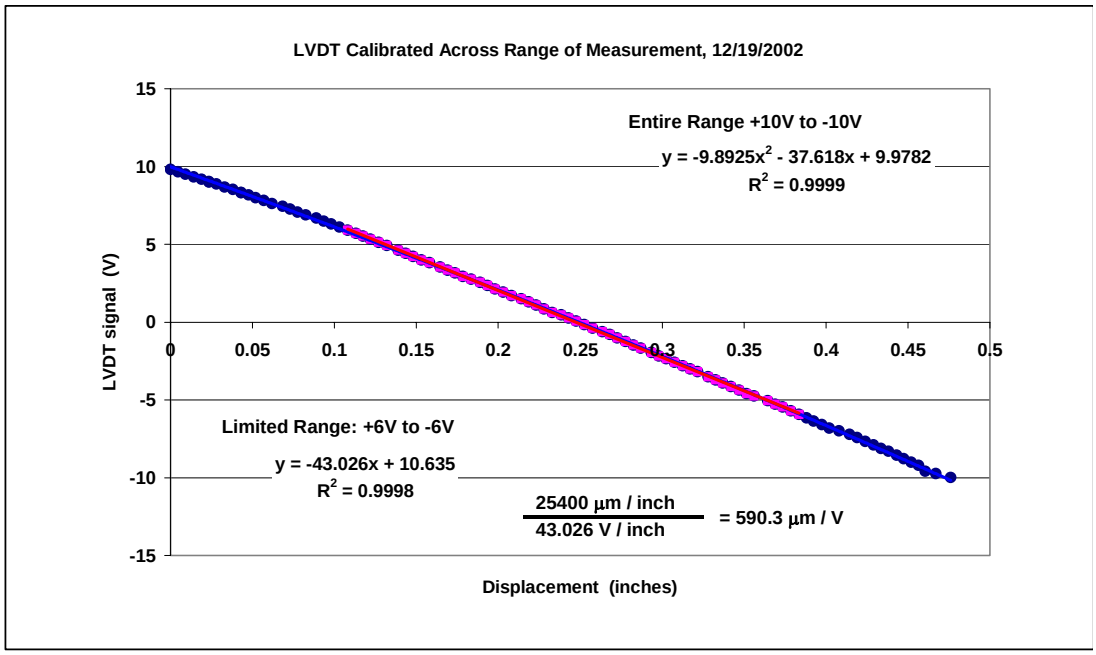

The LVDT response across the limited range from ± 6 V is sufficiently linear to use a single constant scaling factor. The full range is approximately linear, but slight non-linearities at the limits of the response range are best fitted by a quadratic curve.

Appendix 2: Supporting Theory, Data Workup, and Calculations for Rotary Motor Analysis Conducted in Section 7.2.3

A2.1 Determination of Internal Resistance in Motor Parts based on Acceleration by Falling Masses

An experiment measured resistance to axle rotation provided by bearings, especially resistance of the clutch bearings which enable the motor to function. In addition, the experiment measured coefficient of friction of the brake stand used to determine blocking force throughout this project. The approach was to measure acceleration of the shaft resulting from torque of falling masses attached to wire wound around the motor axle. The analysis produced 18 pairs of charts.

Data consists of increments in milliseconds measured on oscilloscope screen shots. The captured signal showed Angstrom Resolver non-contact laser gauge response to accelerating tachometer wheel. Oscilloscope V-bars were used to measure time intervals between peaks. The first part of such a sequence is shown in Figure A2—1, assembled from three overlapping (zoomed-in) parts of the screen shot.

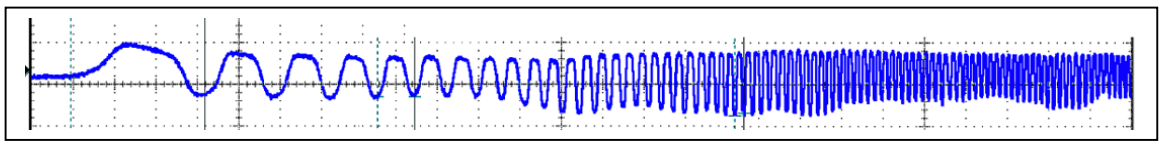

Figure A2—1. (color) Beginning of oscilloscope trace resulting from laser gauge response to tachometer wheel acceleration.

As the peaks become closer, time intervals between them become more difficult to measure. The oscilloscope zoom capability helps to expand the range of resolvable Intervals, but is limited by the fact that the oscilloscope screen capture has sampled a finite number of data points appropriate to the initial scale of the trace. After one or two zoom

levels, one sees only a tenuous trace of widely space dots. This ultimately occurs because the initial sweep rate had to be slow enough to capture the trace by hand.

Each set of data was plotted in two ways. The graphs show either calculated displacements (A-type) or speeds (B-type) plotted against the raw data (in milliseconds) converted to seconds. However, in B-type charts, calculated speeds are plotted against the mid-points of the various intervals, based on the idea that average speed across an interval most likely happens at the midpoint. An explanation of Chart A2—1A and A2—1B will illustrate how all A-type and B-type charts operate. Table A2—1 shows a portion of the data structure associated with A-type charts. Table A2—2 shows a portion of the data structure associated with B-type charts.

The chart range represented by Table A2—1A plots data in column C for its y-range (first series) against data in column B for its x-range. The calculations in column C refer both to raw data in column E and a sequence of counting numbers (0, 1, 2, 3, …) starting with zero in A10. Every other A-type chart also refers to column A instead of repeating a column of counting numbers. Column D repeats however many of the first y-values in column C that are considered reliable. Equations of fit are then based on the values in the selected subset. (In Chart A2—1A, the first 60 values were chosen.)

The chart range represented by Table A2—1B is based on a similar data structure, using column G for the x-range and column H for the y-range (first series). The selected subset of values from column H is contained in column I (first 53 values), and raw data is contained in column J. B-type charts do not refer to the counting numbers in column A.

In the chart range represented by Table A2—1A, after an initial value of zero in cell B10, the next increment is given by "=B10+(0.001*E11)," where data starts in E11, so that a cumulative elapsed time is generated. (The factor "0.001" converts milliseconds to seconds.) The next formulas are "=B11+(0.001*E12)," "=B12+(0.001*E13)," and so on. As seen in Figure 1, the intervals of time become progressively smaller as axle and tachometer wheel accelerates.

The chart range represented by Table A2—1B is a little different. Starting with a value of zero in cell G11, the next x-range value in Chart B is given by

"=G10+(0.001*J11/2)," where data starts in J11. So this produces the time of the first half interval. In this instance, half way between zero and 22.4 ms is 0.0112 s. All subsequent x-range formulas must also add the second half of the previous interval to the previous midpoint value in addition to the current half interval based on the current time increment. Thus, the next formulas are "=G11+(0.001*J11/2)+(0.001*J12/2)," "=G12+(0.001*J12/2)+(0.001*J13/2)," and so on.

Table A2.1—1. Data structure associated with A-type charts

Angular Increment (Radians) = 0.069658374 (cell $E$1)				
chart 1A	angular displacement vs. time			
	No Added Load, Outside Clutch Bearings In Place			
	Actuator Collars Also In Place			
	p.63, Supplemental Notebook 2			
	1632.8 g pulling load			
Column A	Column B	Column C	Column D	Column E
	=B10+(0.001*E11)	=$A11*$E$1	=C11	
0 (Row 10)	0			Data
1 (Row 11)	0.0224	0.069658374	0.069658374	22.4
2	0.0394	0.139316747	0.139316747	17
3	0.0536	0.208975121	0.208975121	14.2
4	0.0656	0.278633495	0.278633495	12
5	0.077	0.348291868	0.348291868	11.4
6	0.0866	0.417950242	0.417950242	9.6
7	0.0958	0.487608616	0.487608616	9.2
8	0.104	0.55726699	0.55726699	8.2
9	0.1114	0.626925363	0.626925363	7.4
10	0.1184	0.696583737	0.696583737	7

Table A2.1—2. Data structure associated with B-type charts

Angular Increment (Radians) = 0.069658374 (cell $E$1)				
chart 1B angular speed vs. time				
No Added Load, Outside Clutch Bearings In Place				
Actuator Collars Also In Place				
p.63, Supplemental Notebook 2				
1632.8 g pulling load				
Column A	Column G	Column H	Column I	Column J
	=G10+(0.001*J11/2)	=$E$1/(0.001*J11)	=H11	
0 (Row 10)	0			Data
1 (Row 11)	0.0112	3.109748826	3.109748826	22.4
2	0.0309	4.097551394	4.097551394	17
3	0.0465	4.905519274	4.905519274	14.2
4	0.0596	5.804864474	5.804864474	12
5	0.0713	6.110383657	6.110383657	11.4
6	0.0818	7.256080593	7.256080593	9.6
7	0.0912	7.571562358	7.571562358	9.2
8	0.0999	8.494923621	8.494923621	8.2
9	0.1077	9.413293742	9.413293742	7.4
10	0.1149	9.951196242	9.951196242	7

Charts plotting speed increments were actually developed first because they give the rate of change of acceleration and plots require only a linear fit. However, since average speed over each interval was plotted against elapsed time as an approximation of instantaneous speed, increasing scatter resulted as differences between peaks became too small to distinguish on the oscilloscope. The scatter is so pronounced because error in time measurements becomes incorporated in both x-range and y-range values.

The key idea is that the angular increment (about 4º of the timing wheel circumference) is traversed in shorter and shorter intervals of time. So, with G11 containing the midpoint of the interval extending between zero time and 22.4 ms, the average rotational speed at that midpoint would be given by "=$E$1/(0.001*J11)." The next y-range value is given by "=$E$1/(0.001*J12)," which is larger because J12 contains a smaller interval of time (17 ms) than J11 (22.4 ms). Cell E1 contains the angular increment of one white and black stripe pair on the tachometer wheel (0.069658 radians).

In A-type charts, cumulative (angular) displacements were plotted against elapsed time. The y-range calculation simply multiplies a count of the number of intervals between the first one measured and the current one by the same angular increment which is displaced in smaller and smaller times. Thus, the y-range formulas are "=$A11*$E$1," "=$A12*$E$1," where A11 = 1, A12 = 2, and A13 = 3, and so on. Cell E1 contains the angular increment of one white and black stripe pair on the tachometer wheel (0.069658 radians). Scatter is greatly reduced by this approach because each additional increment of cumulative displacement represents a smaller and smaller fraction of the total value. All error is contained in the x-range.

Spreadsheet data block for associating angular displacement and time

Angular increment (radians) = 0.069658374 ("=(E2/E3)*2*PI()")
Black + white pair width = 0.125 inch (E2)
Circumference = 11.275 inches (E3)
Arc length fraction of circumference = 0.011086475
(Increment in degrees = 3.99113082)

All eighteen pairs of charts are reproduced in the following pages. Discussion about how they were used resumes afterwards.

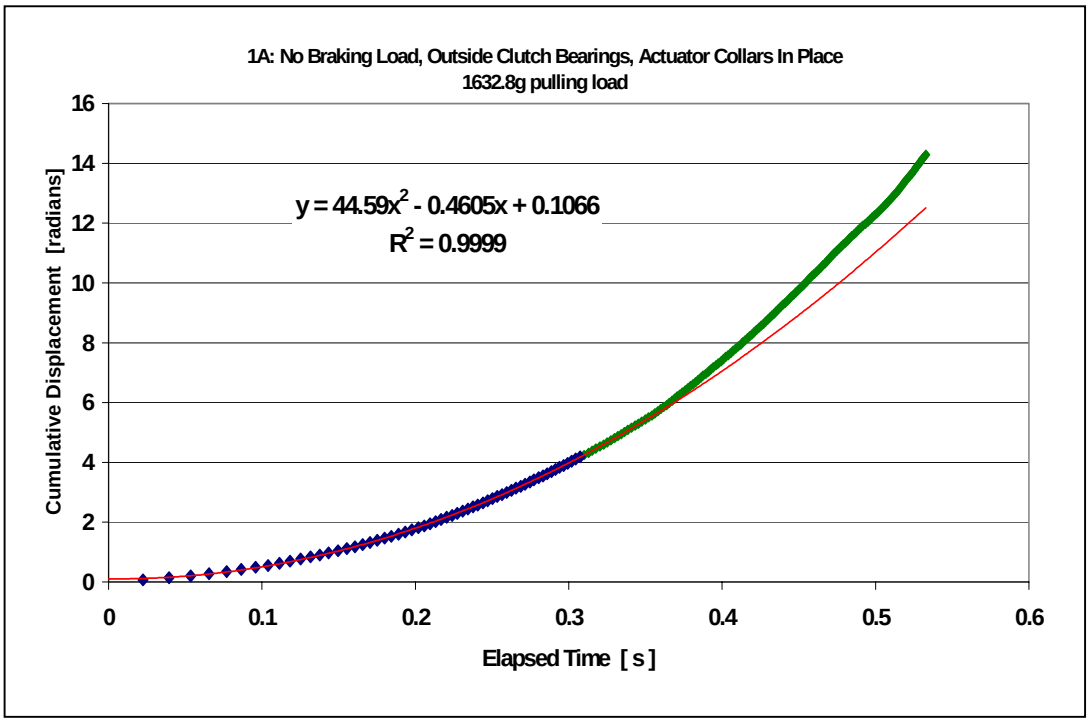

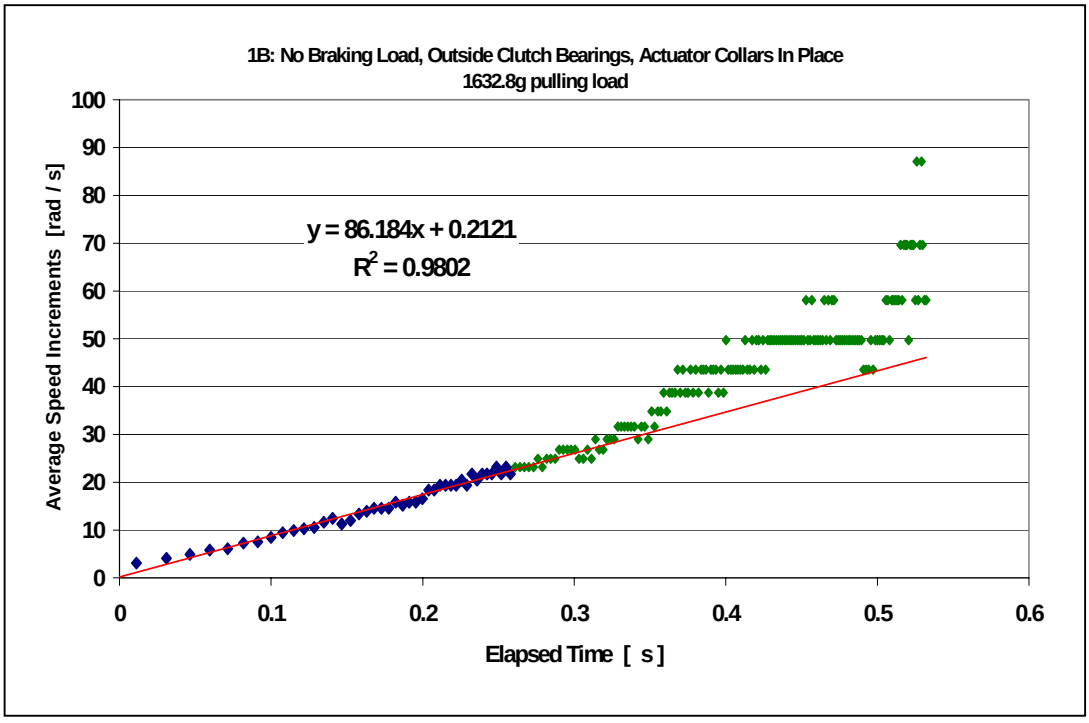

Charts A2.1—1A, 1B. (color) No added load, outside clutch bearings in place, actuator collars also in place, 1632.8 g pulling load

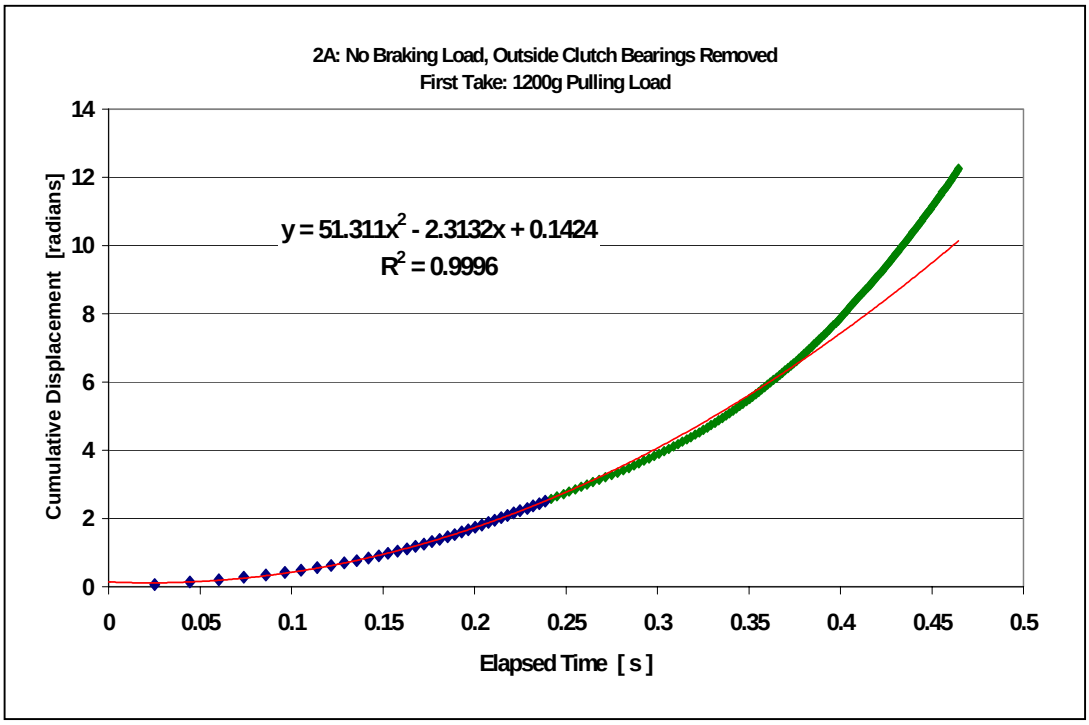

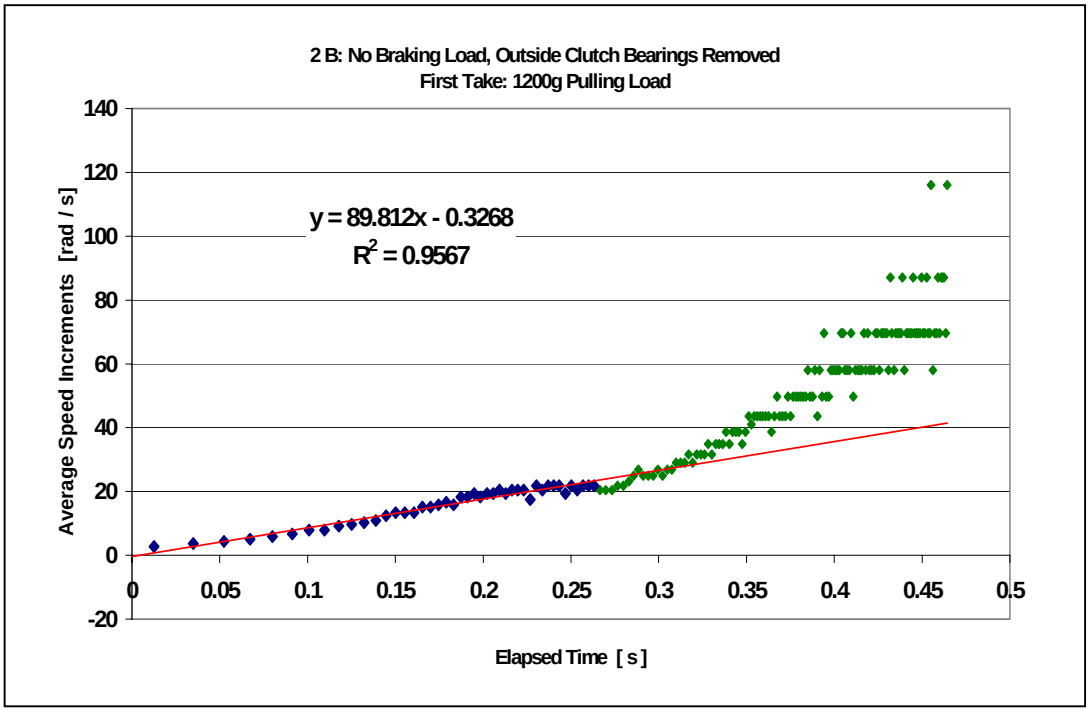

Charts A2.1—2A, 2B. (color) No added load, outside clutch bearings removed, 1200 g pulling load (First take)

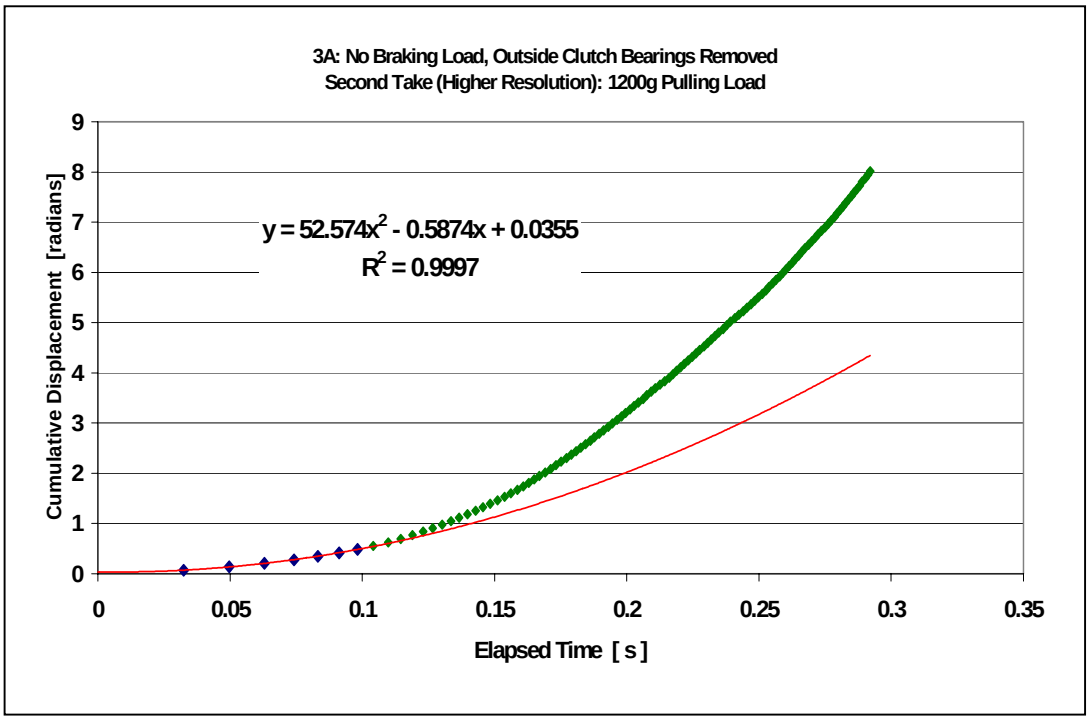

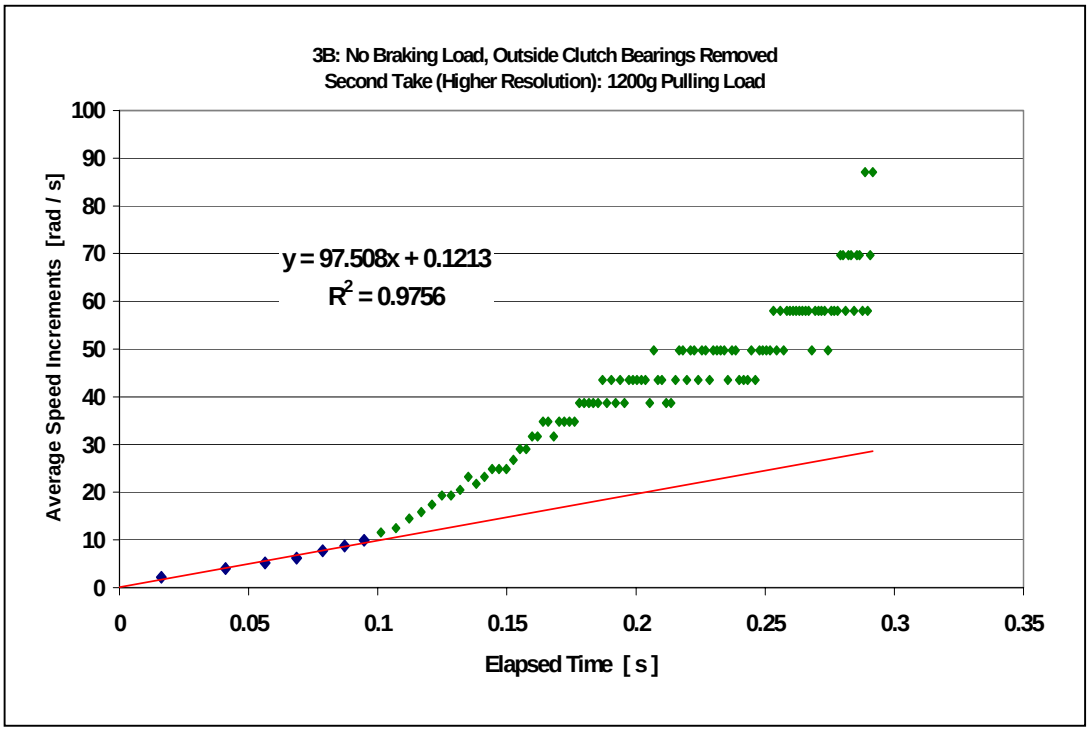

Charts A2.1—3A, 3B. (color) No added load, outside clutch bearings removed, 1200 g pulling load (Second take)

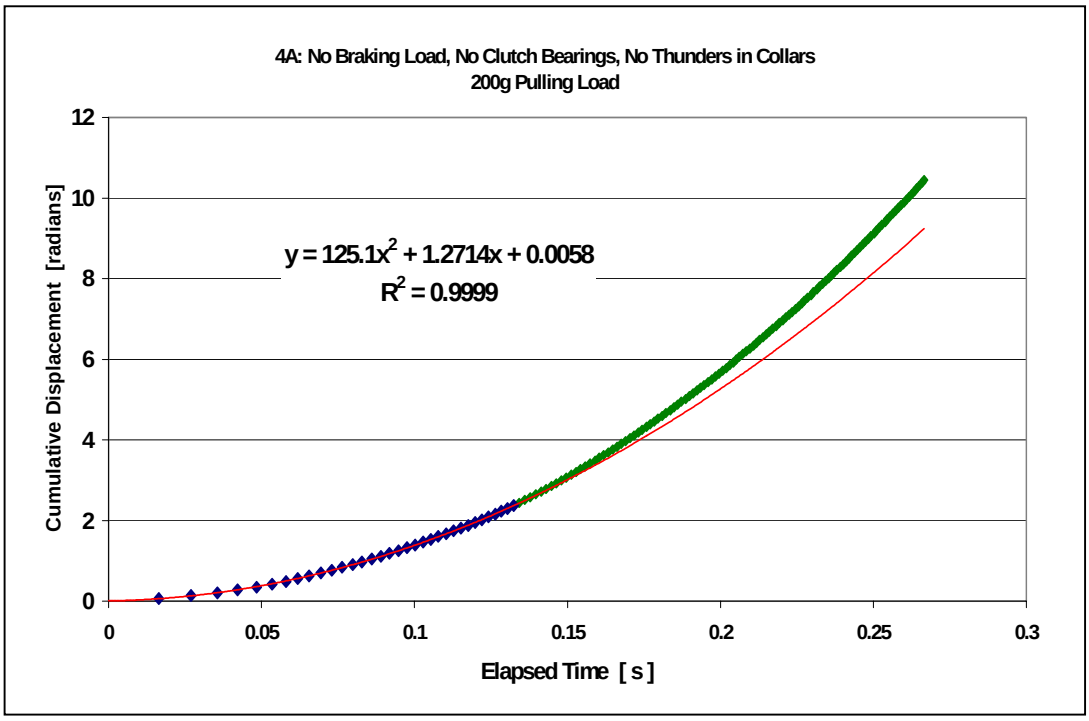

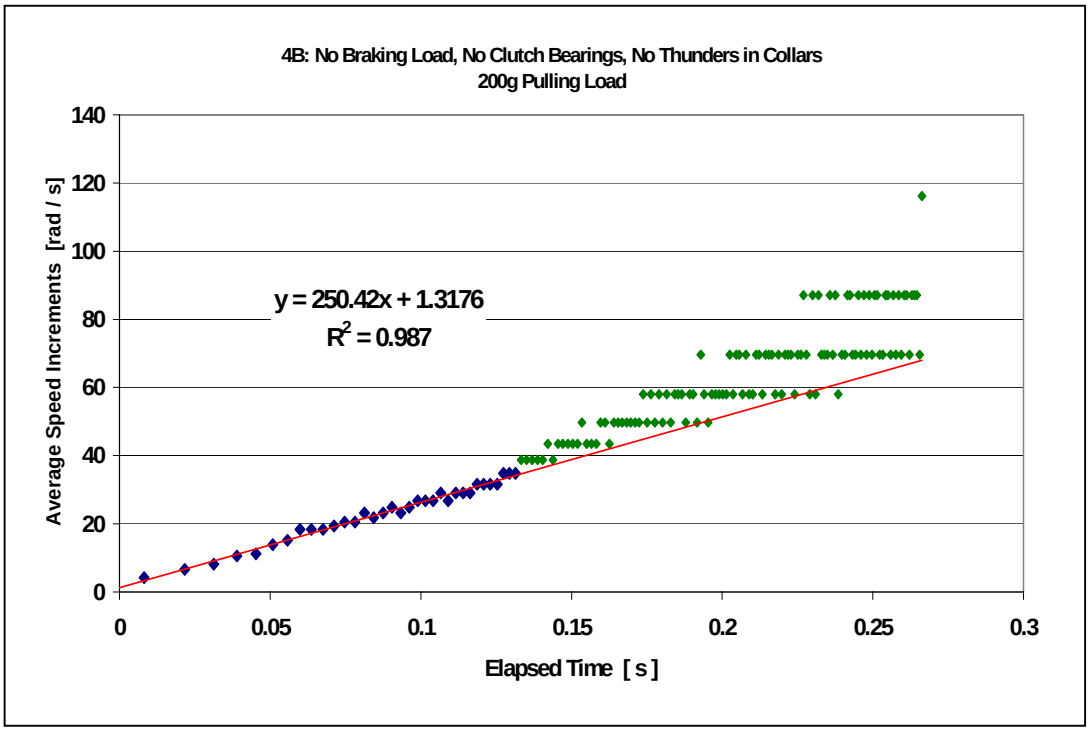

Charts A2.1—4A, 4B. (color) No braking load, no clutch bearings, no Thunders in collars, 1200 g pulling load

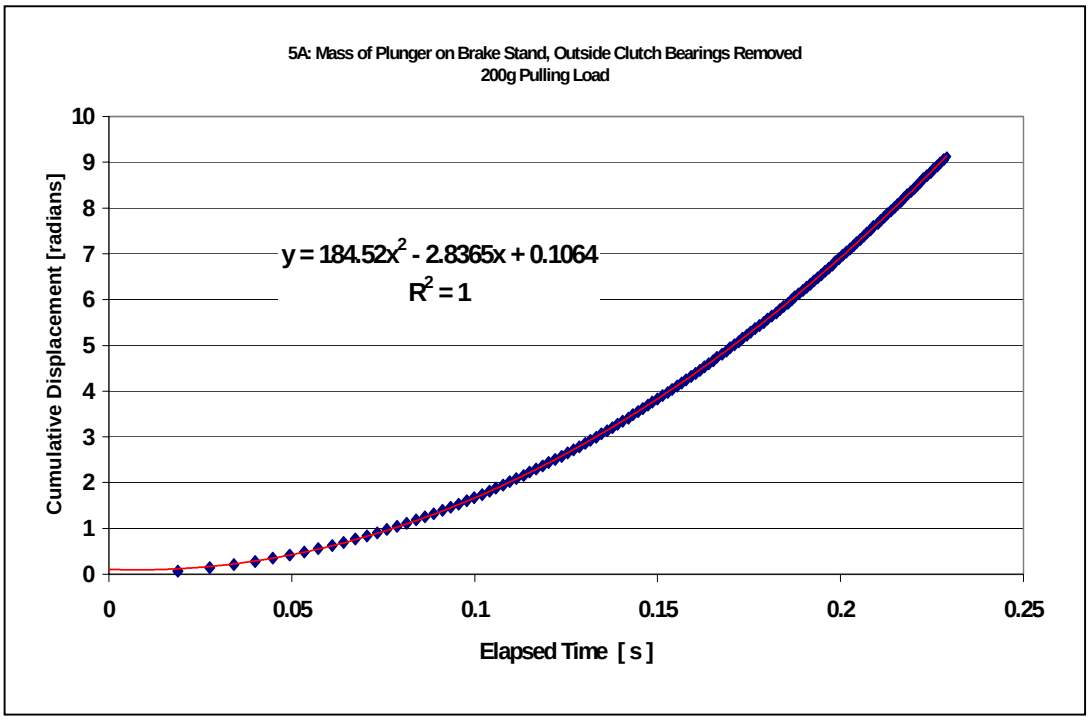

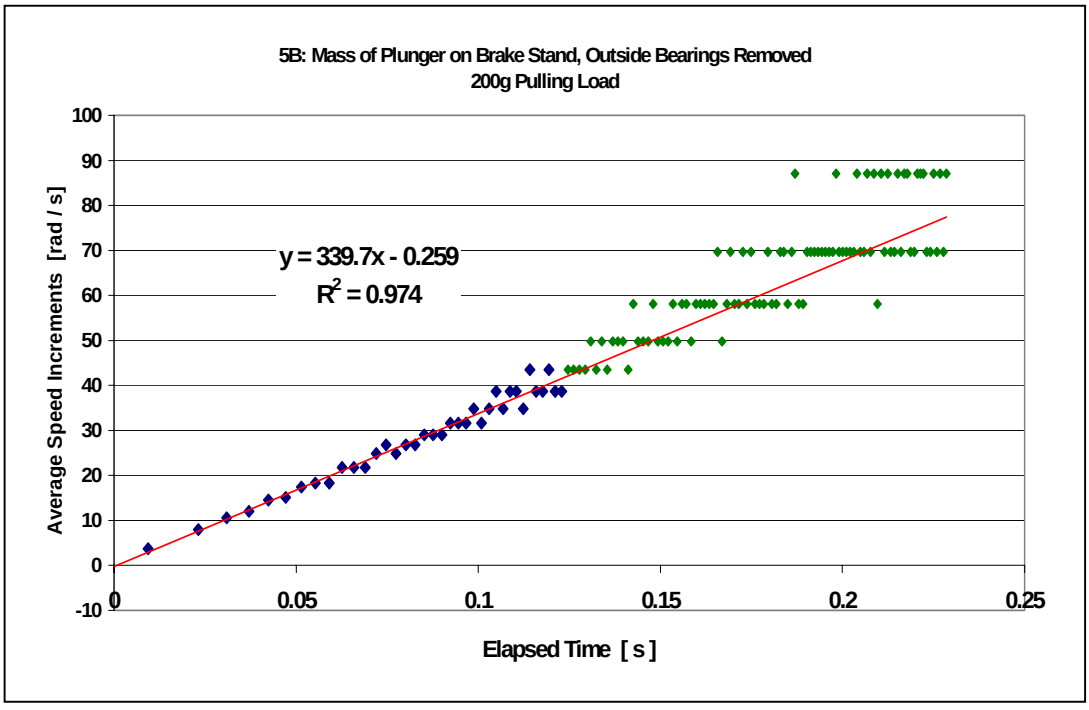

Charts A2.1—5A, 5B. (color) Mass of plunger on brake stand, outside clutch bearings removed, 200g pulling load

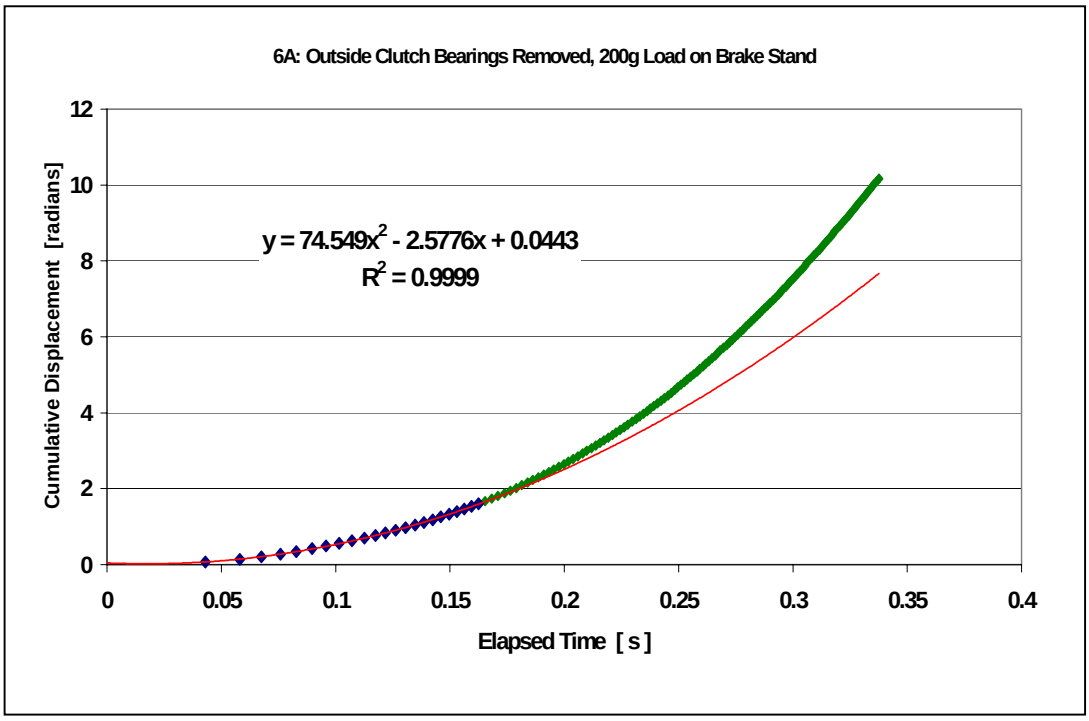

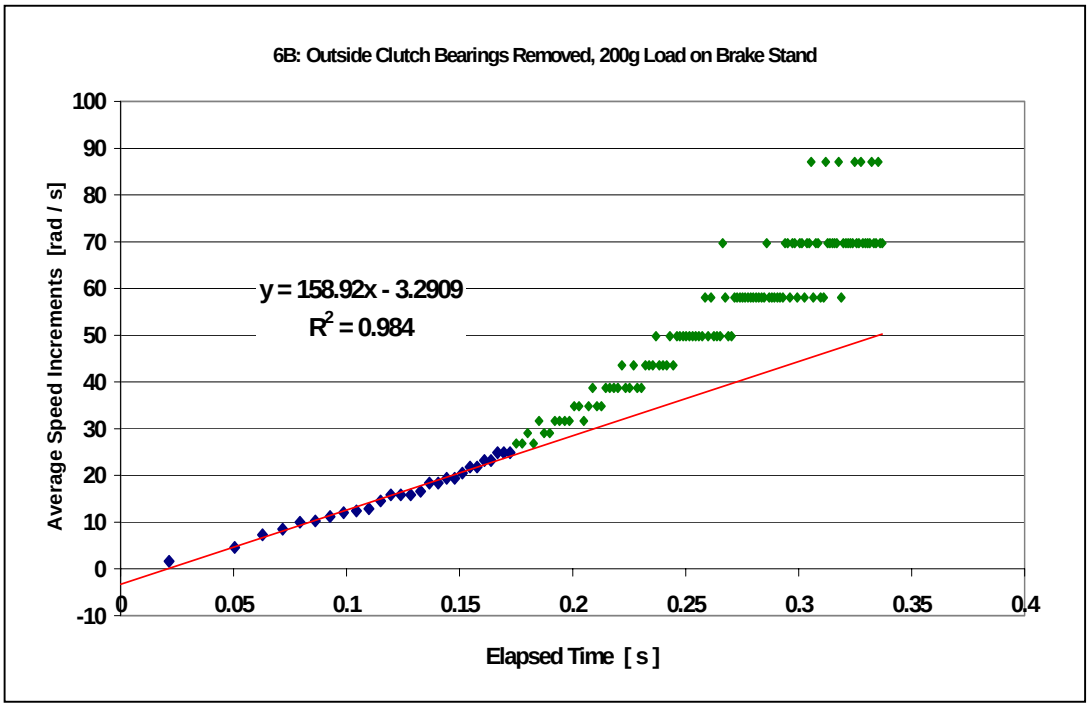

Charts A2.1—6A, 6B. (color) 200g load on brake stand, outside clutch bearings removed, 200g pulling load

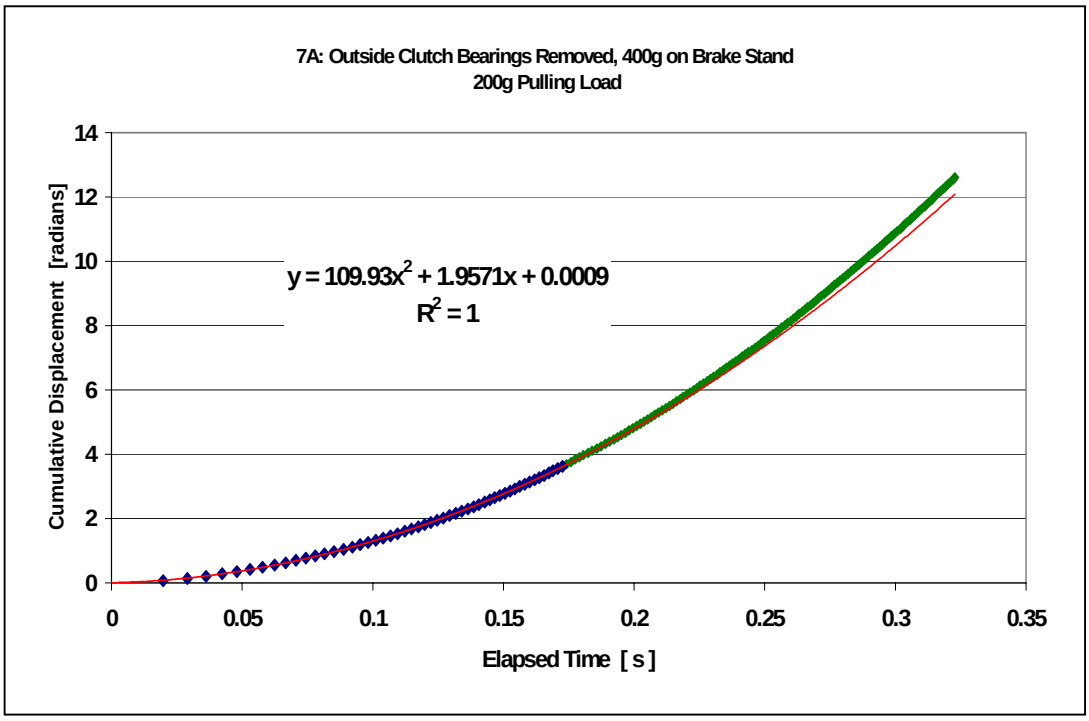

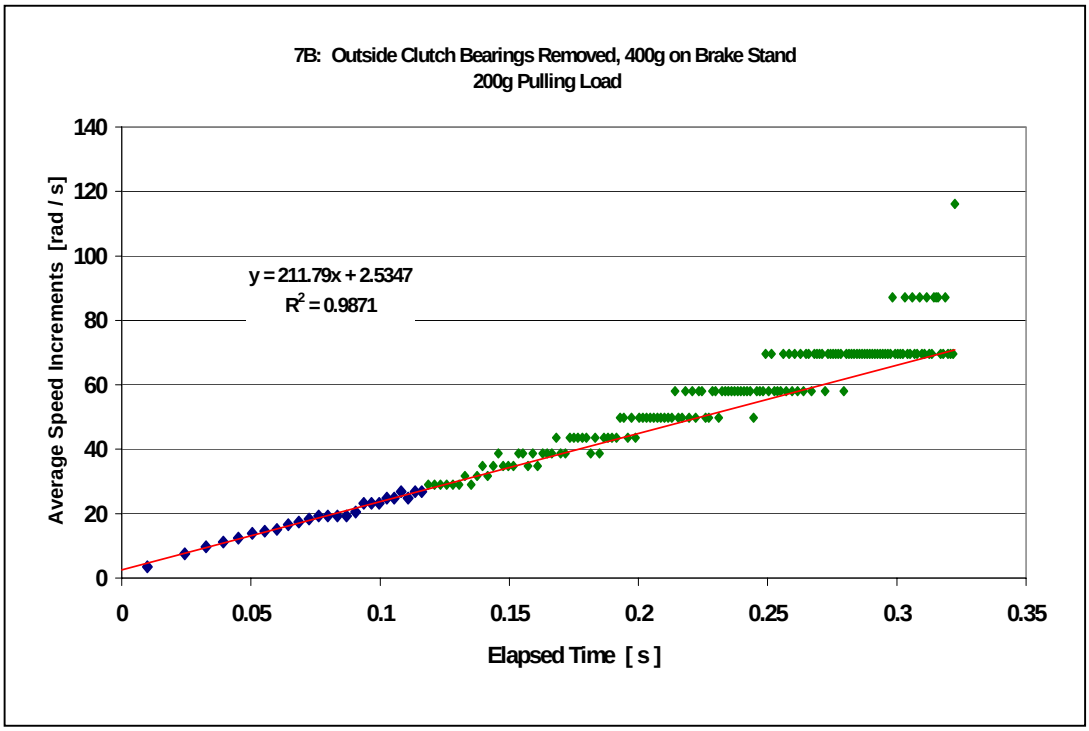

Charts A2.1—7A, 7B. (color) 400g load on brake stand, outside clutch bearings removed, 200g pulling load

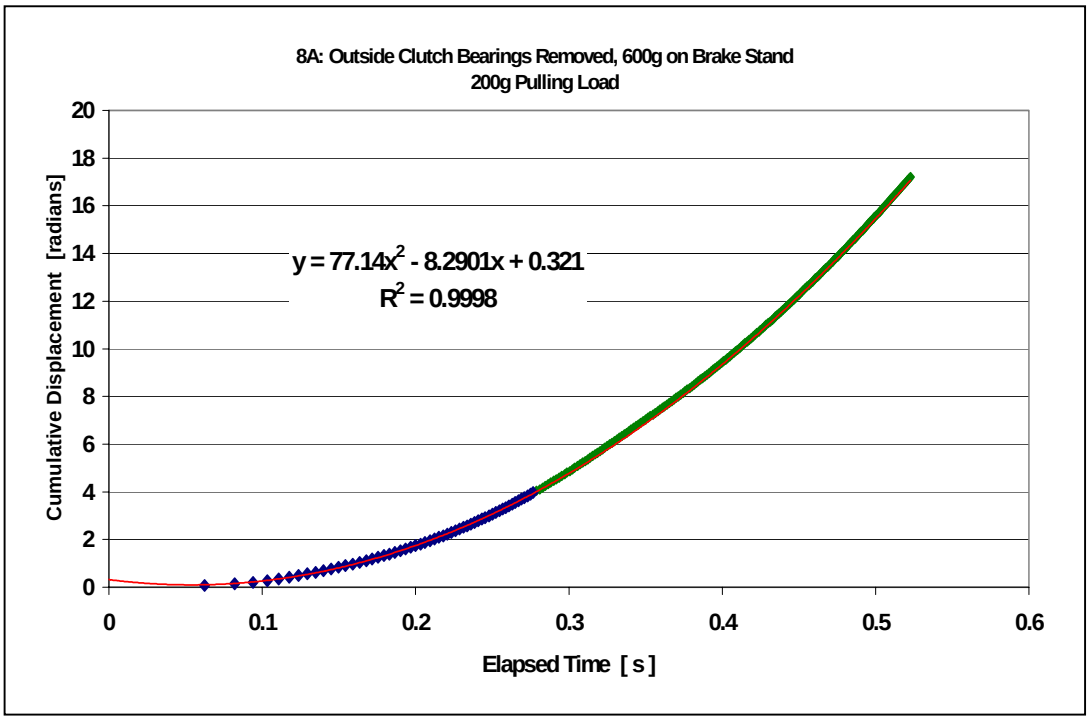

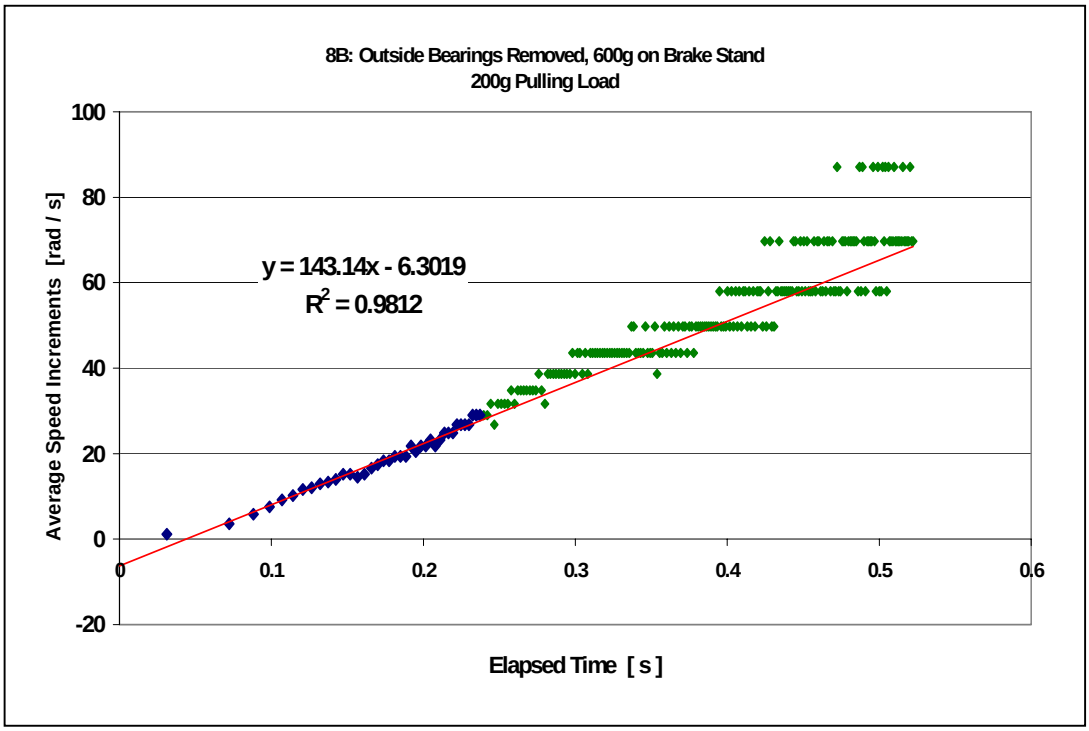

Charts A2.1—8A, 8B. (color) 600g load on brake stand, outside clutch bearings removed, 200g pulling load

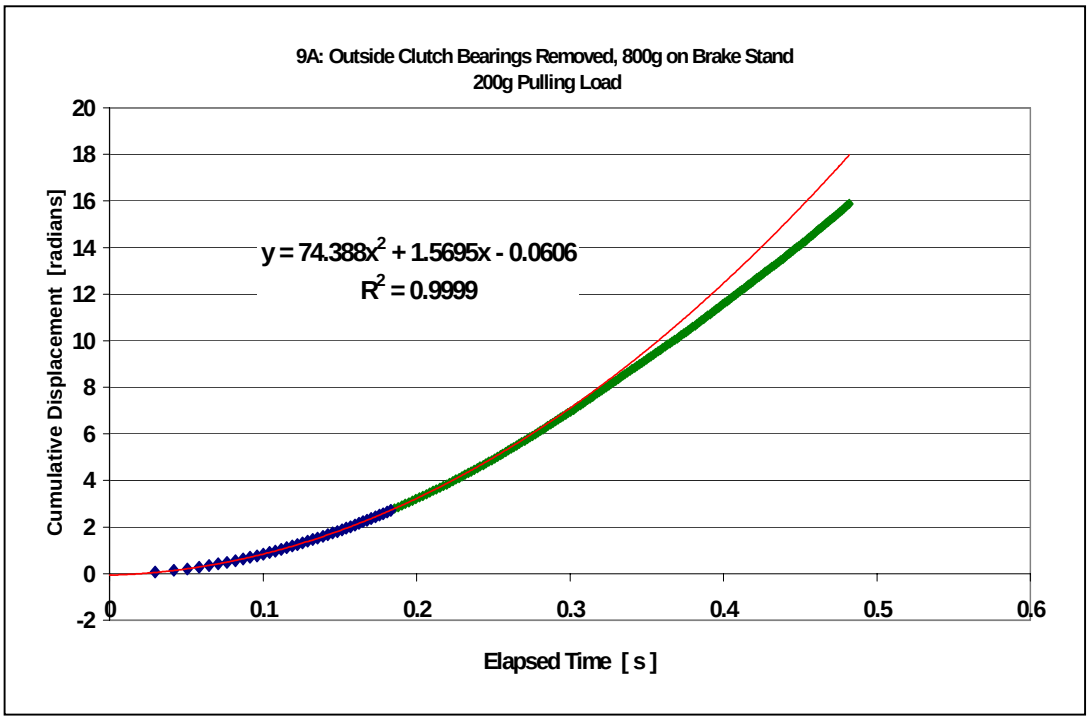

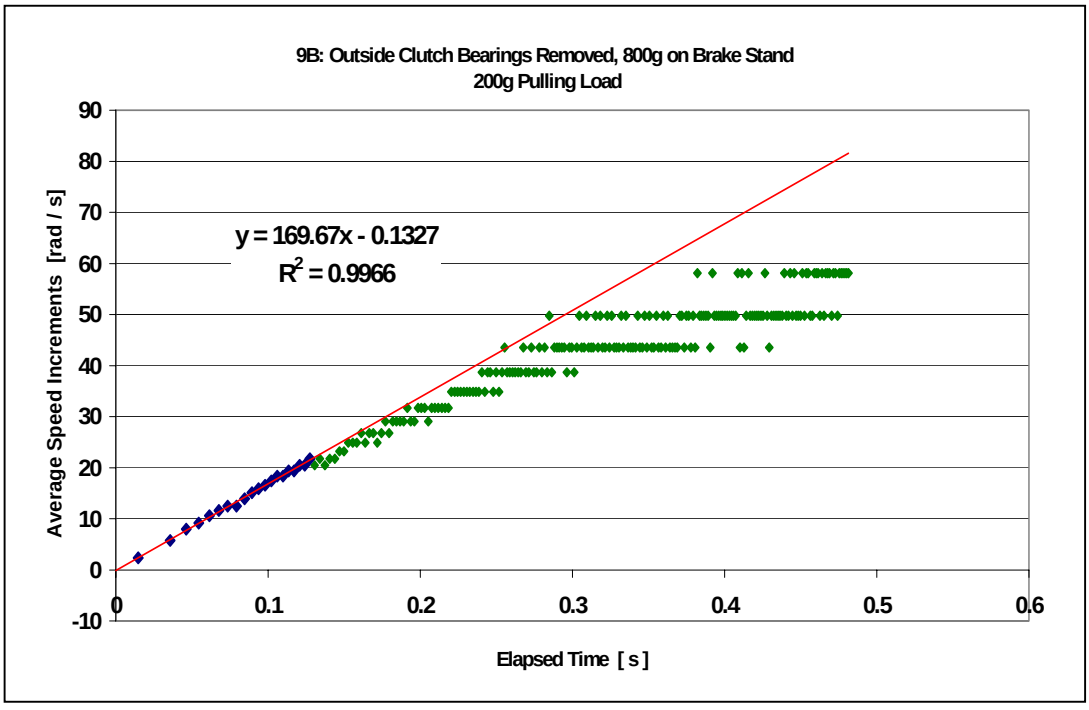

Charts A2.1—9A, 9B. (color) 800g load on brake stand, outside clutch bearings removed, 200g pulling load

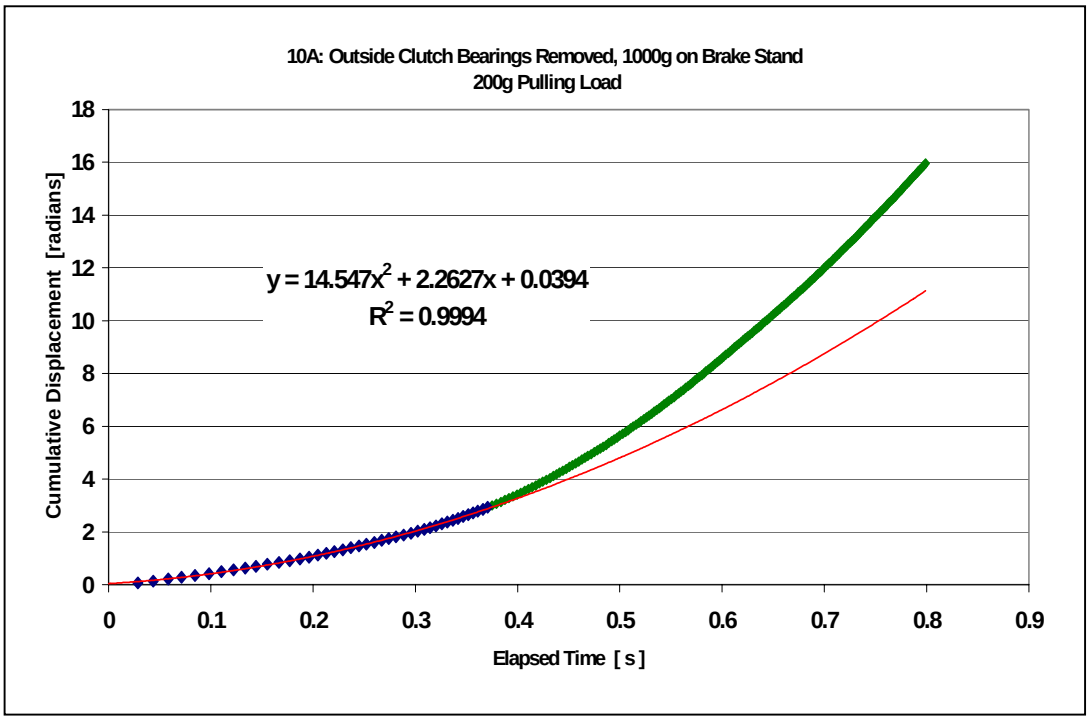

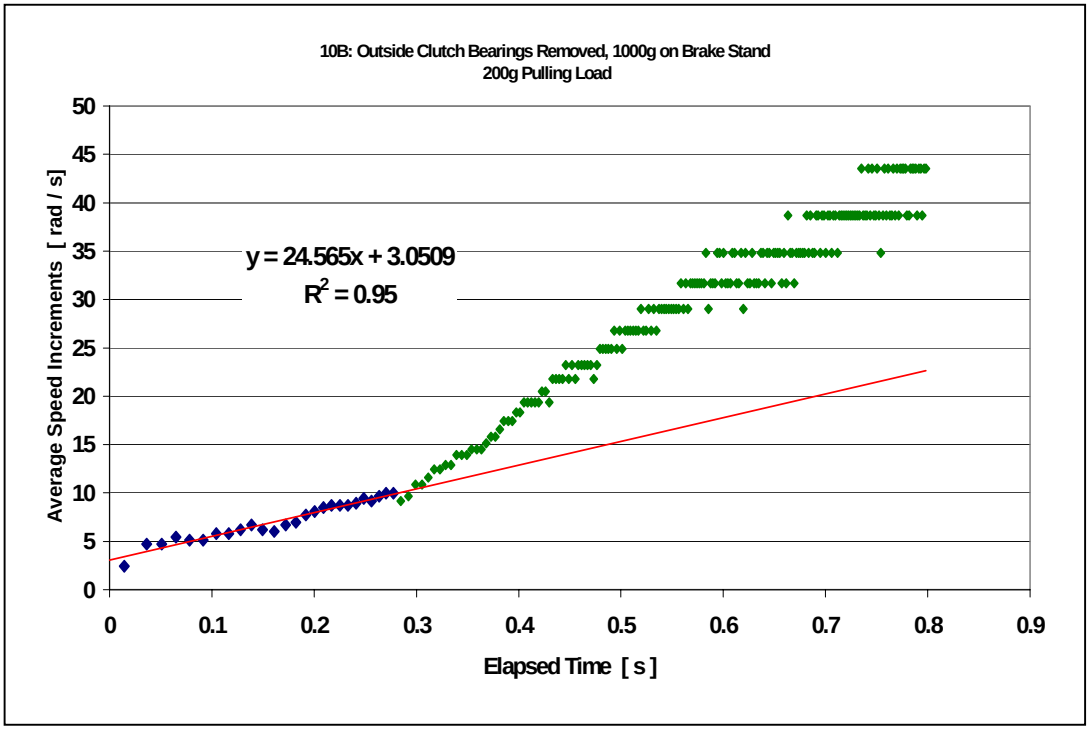

Charts A2.1—10A, 10B. (color) 1000g load on brake stand, outside clutch bearings removed, 200g pulling load

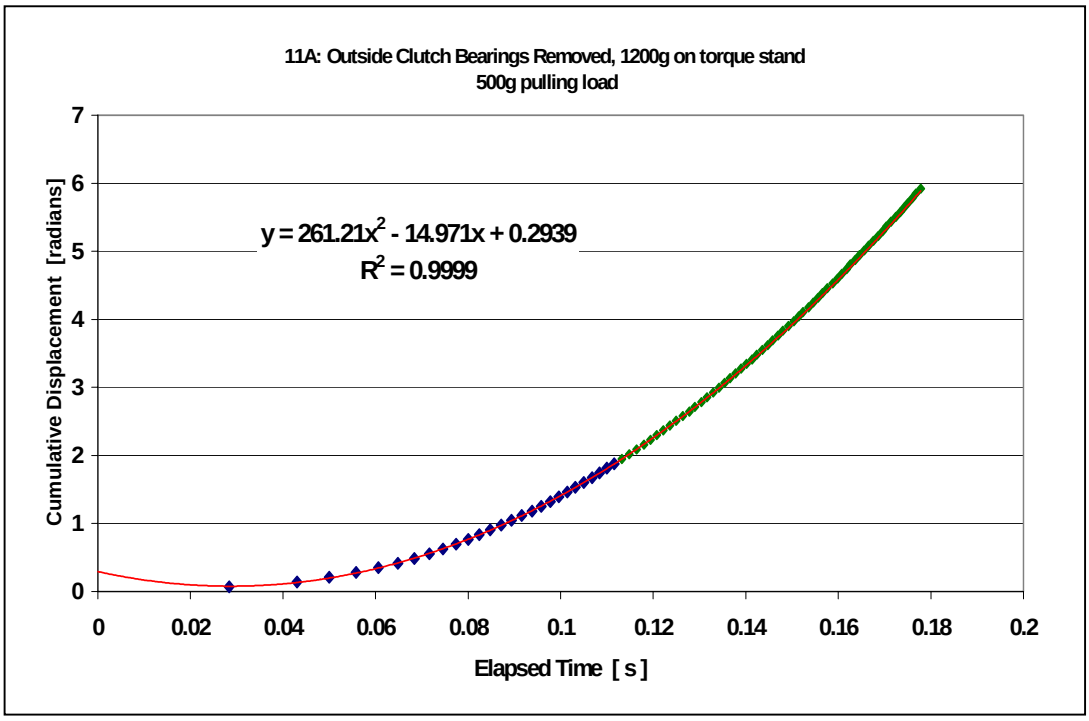

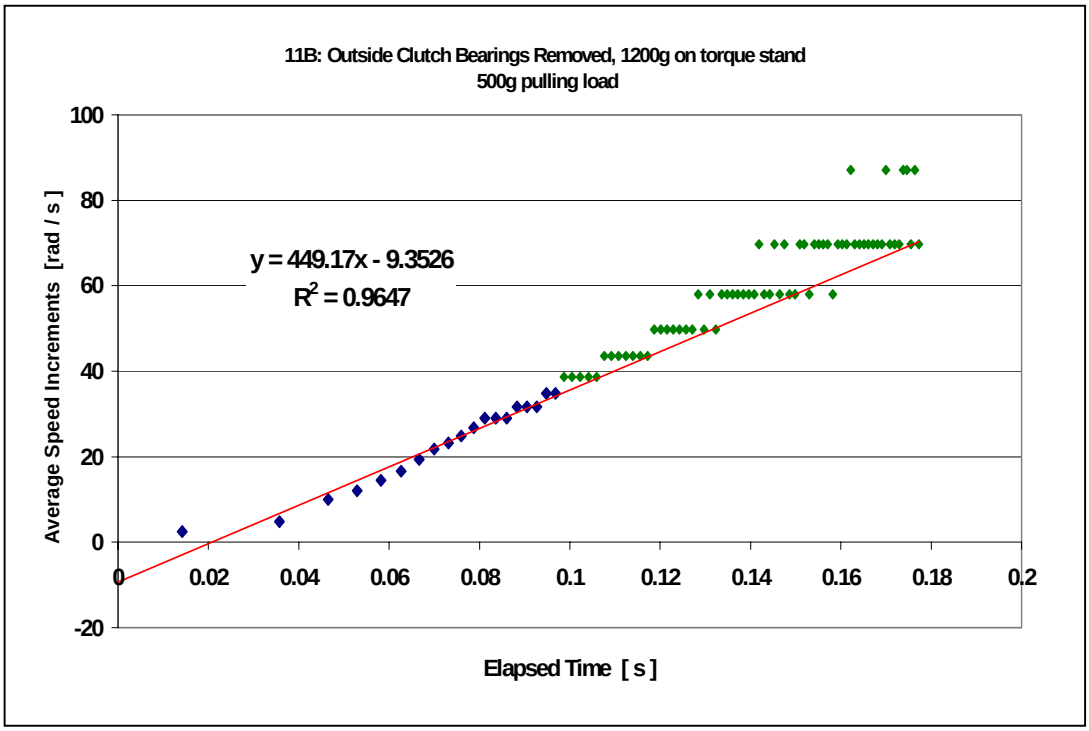

Charts A2.1—11A, 11B. (color) 1200g load on brake stand, outside clutch bearings removed, 500g pulling load

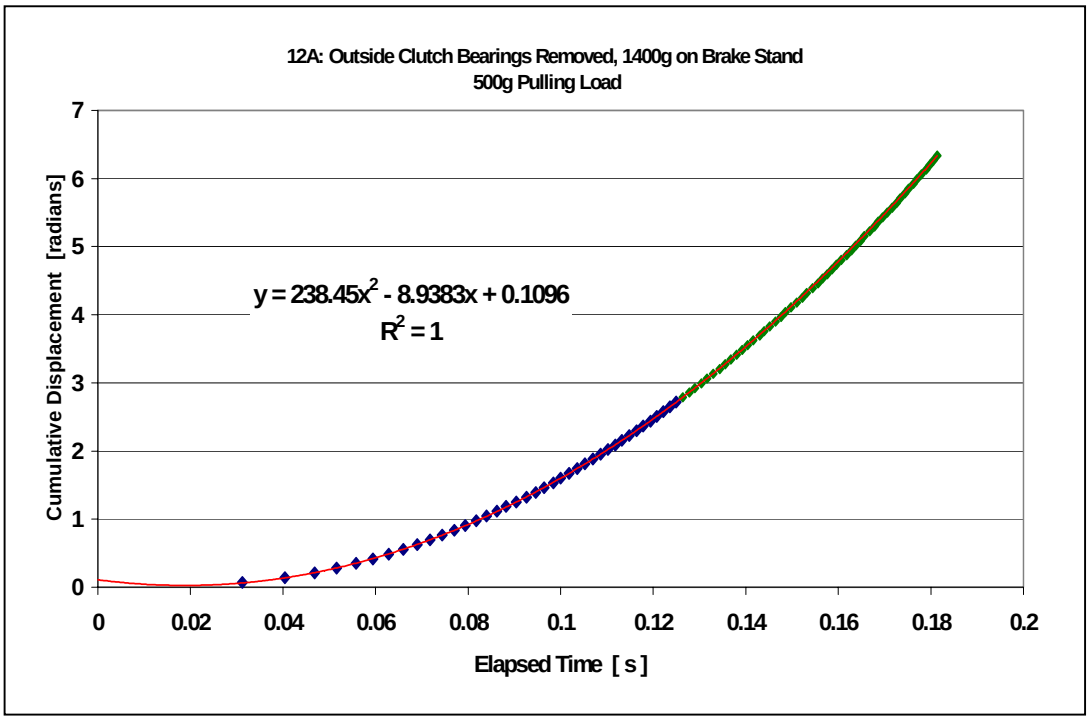

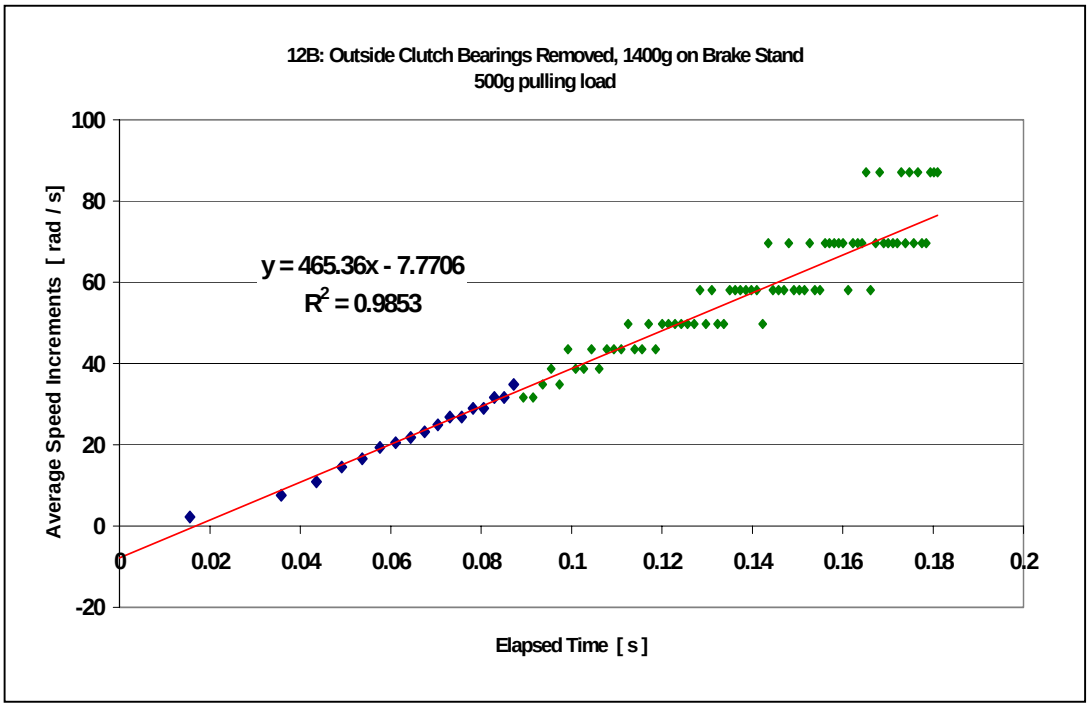

Charts A2.1—12A, 12B. (color) 1400g load on brake stand, outside clutch bearings removed, 500g pulling load

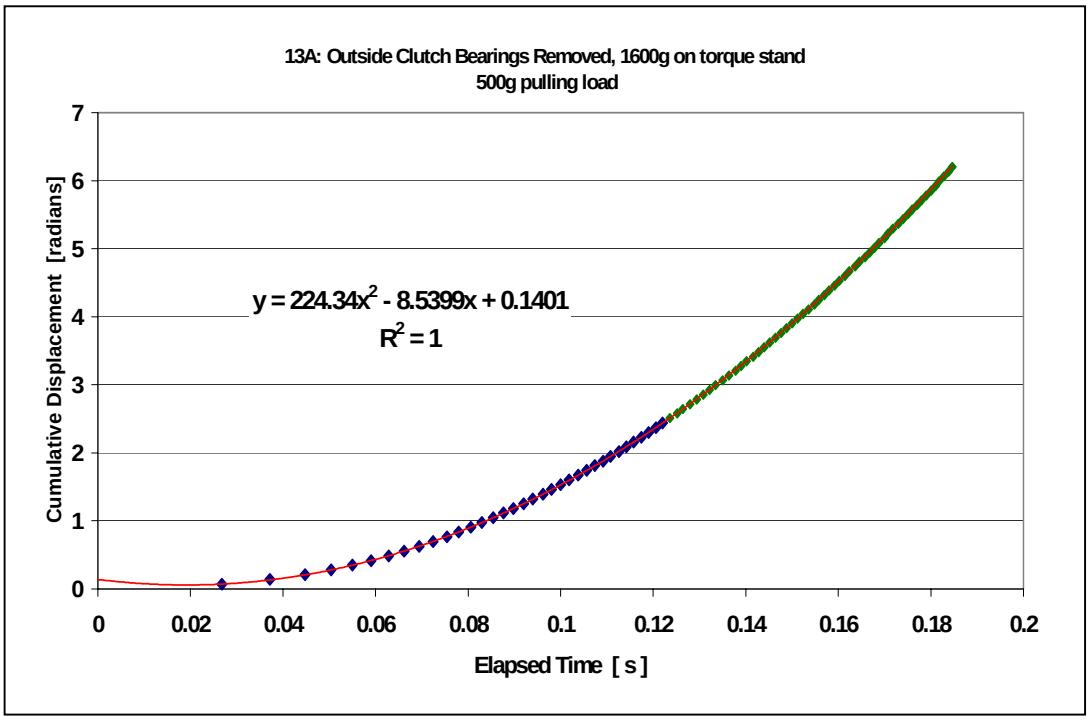

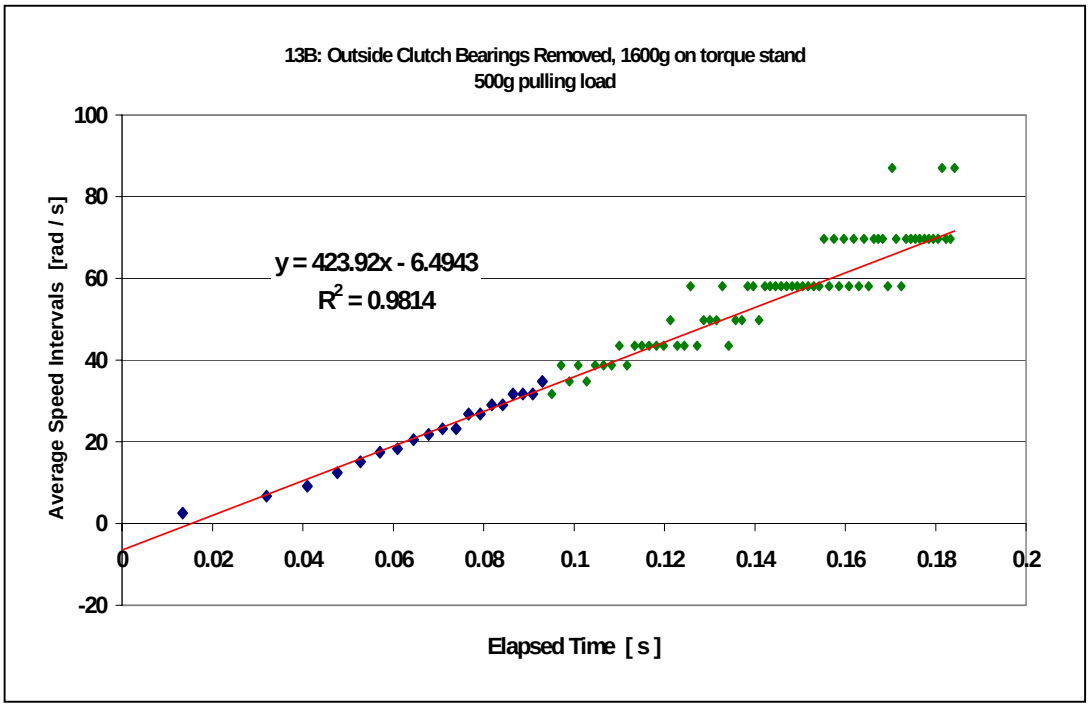

Charts A2.1—13A, 13B. (color) 1600g load on brake stand, outside clutch bearings removed, 500g pulling load

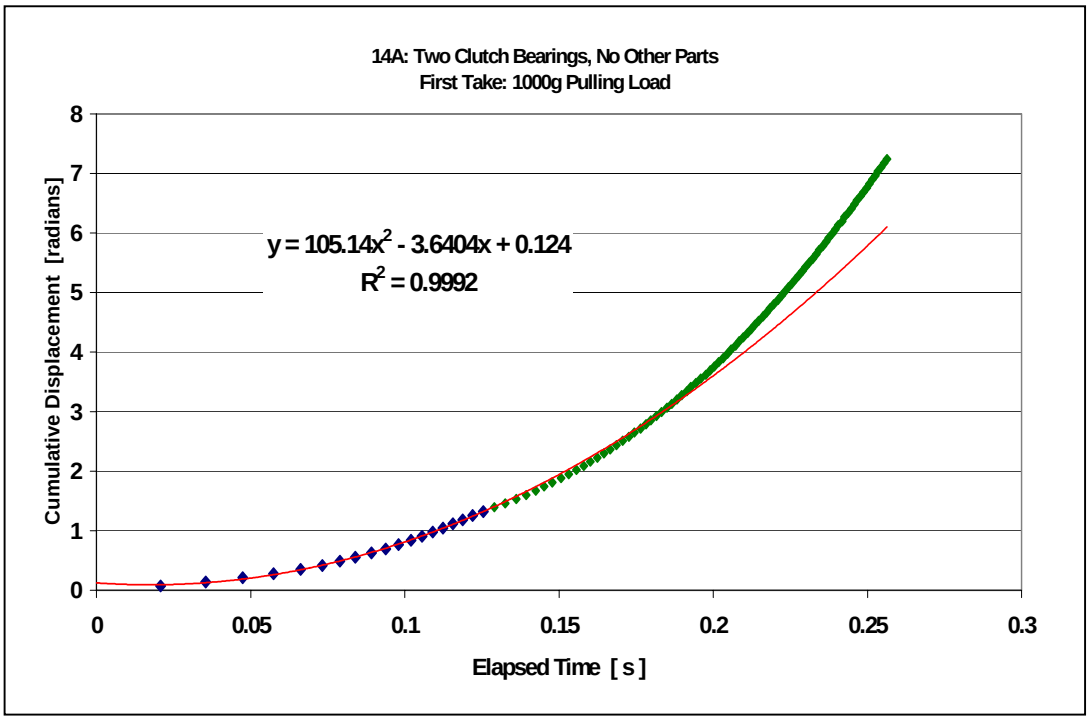

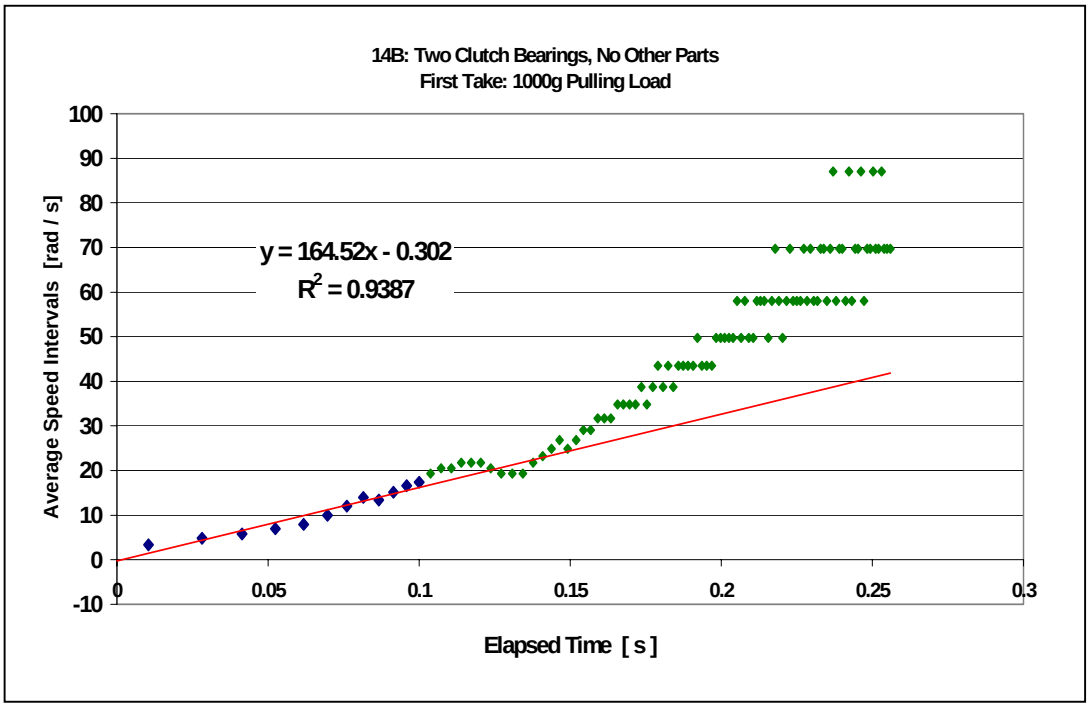

Charts A2.1—14A, 14B. (color) Two clutch bearings, no other parts, 1000g pulling load (First take)

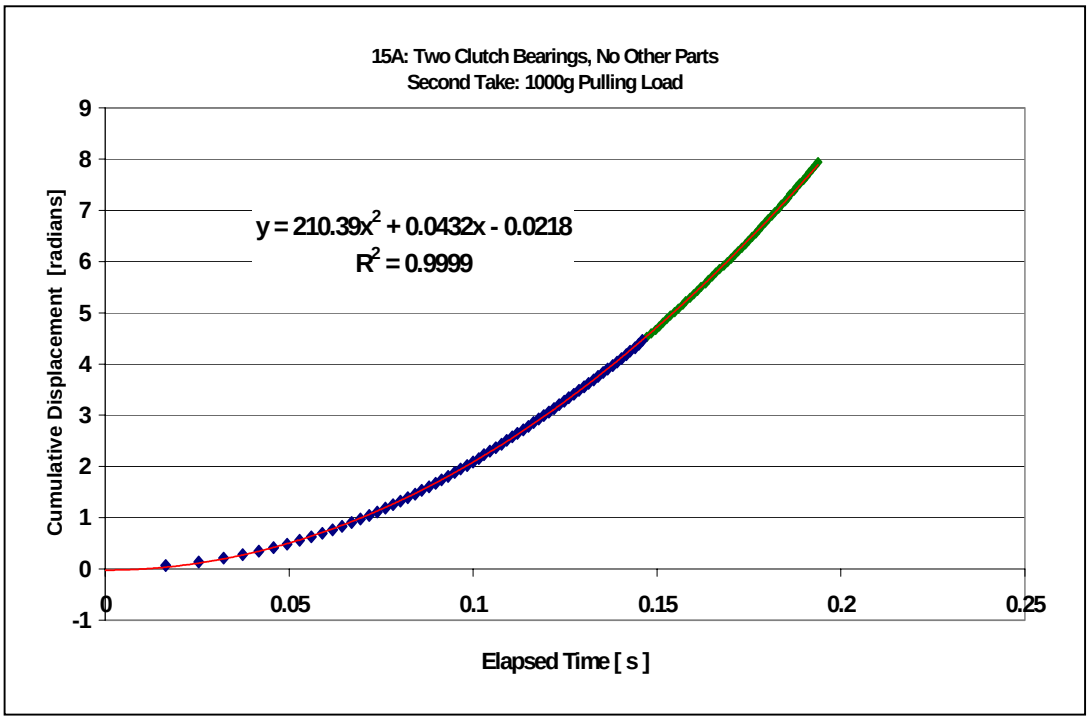

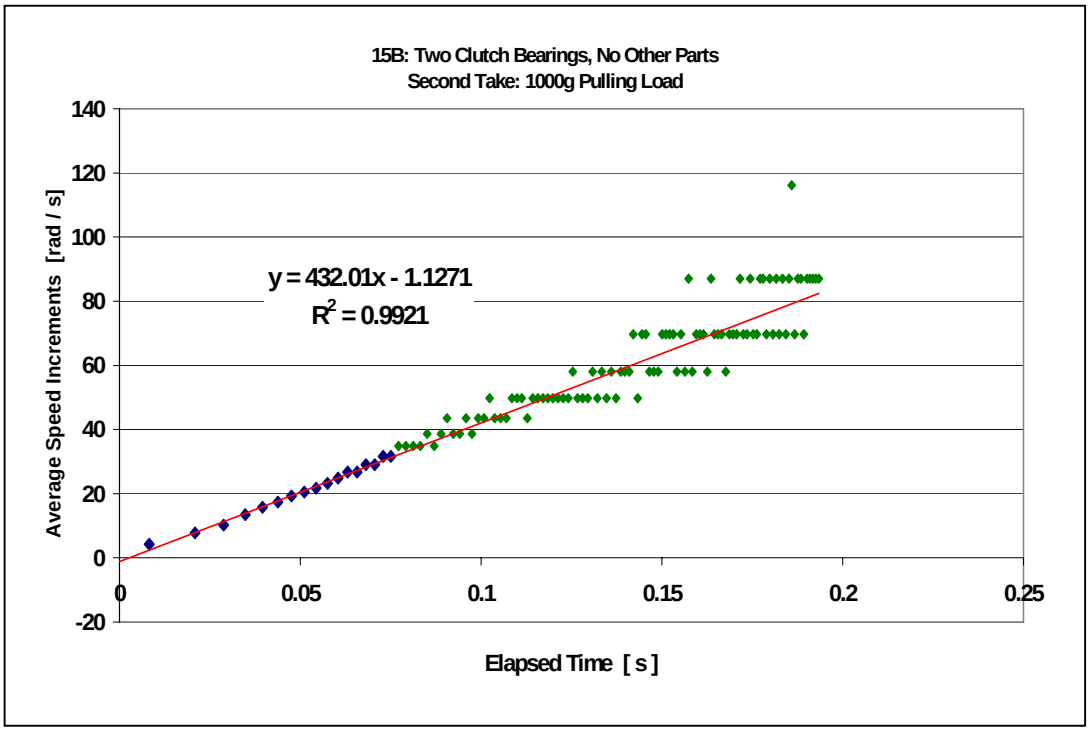

Charts A2.1—15A, 15B. (color) Two clutch bearings, no other parts, 1000g pulling load (Second take)

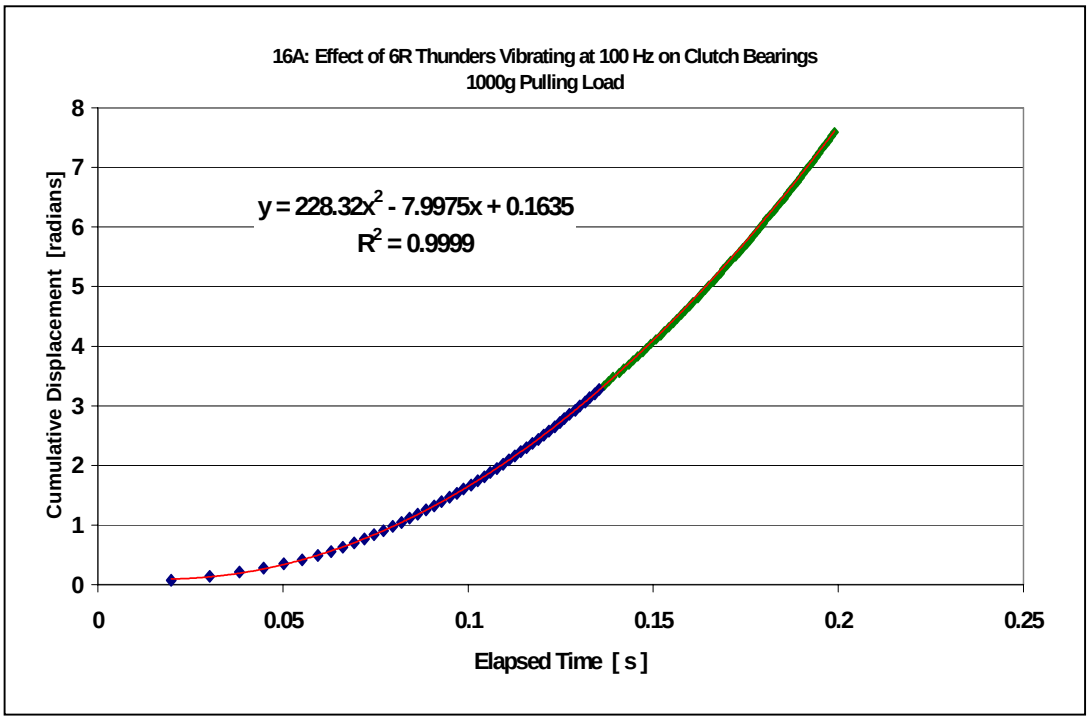

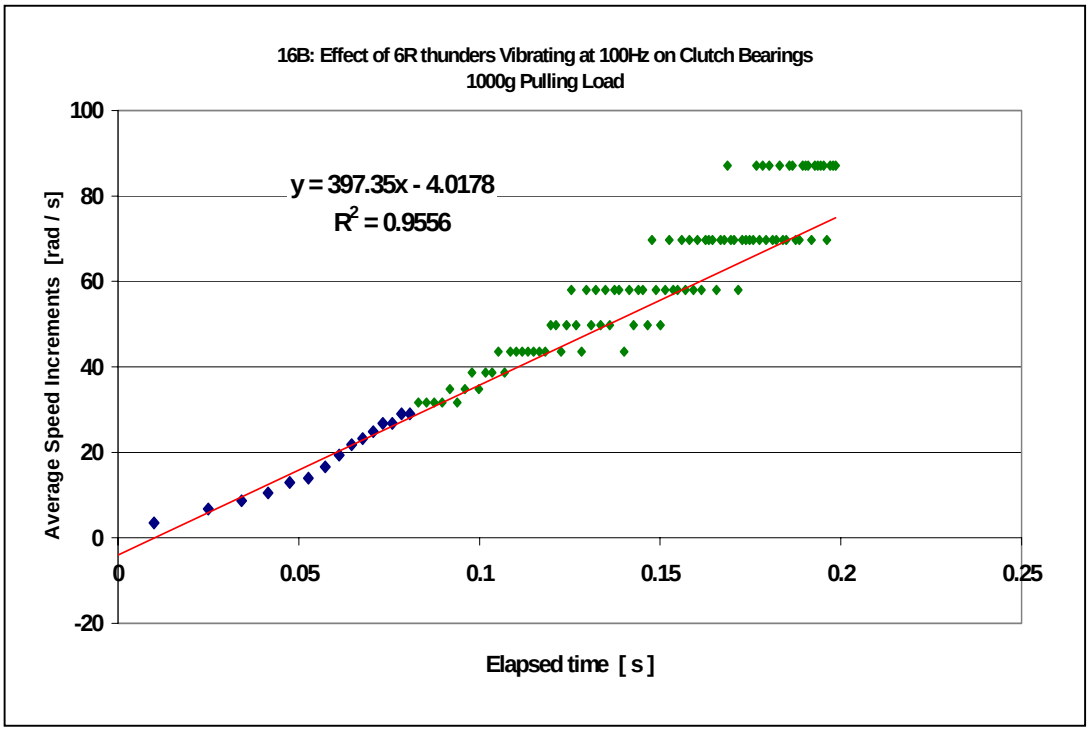

Charts A2.1—16A, 16B. (color) Effect of 6R Thunders vibrating at 100 Hz on clutch bearings, 1000g pulling load

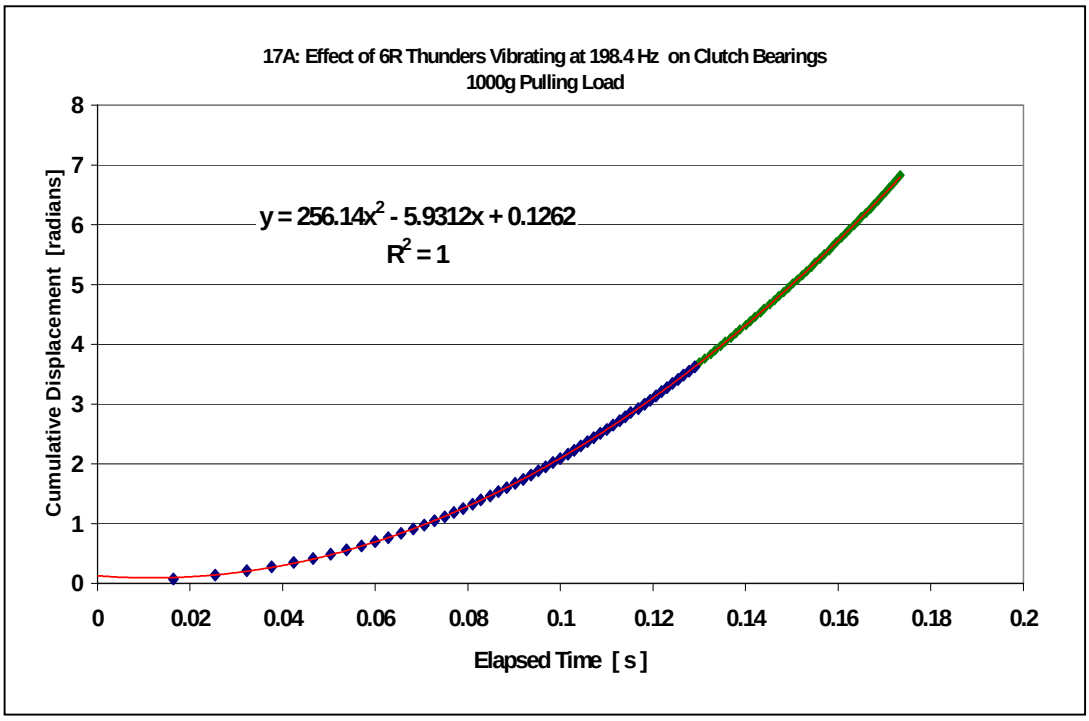

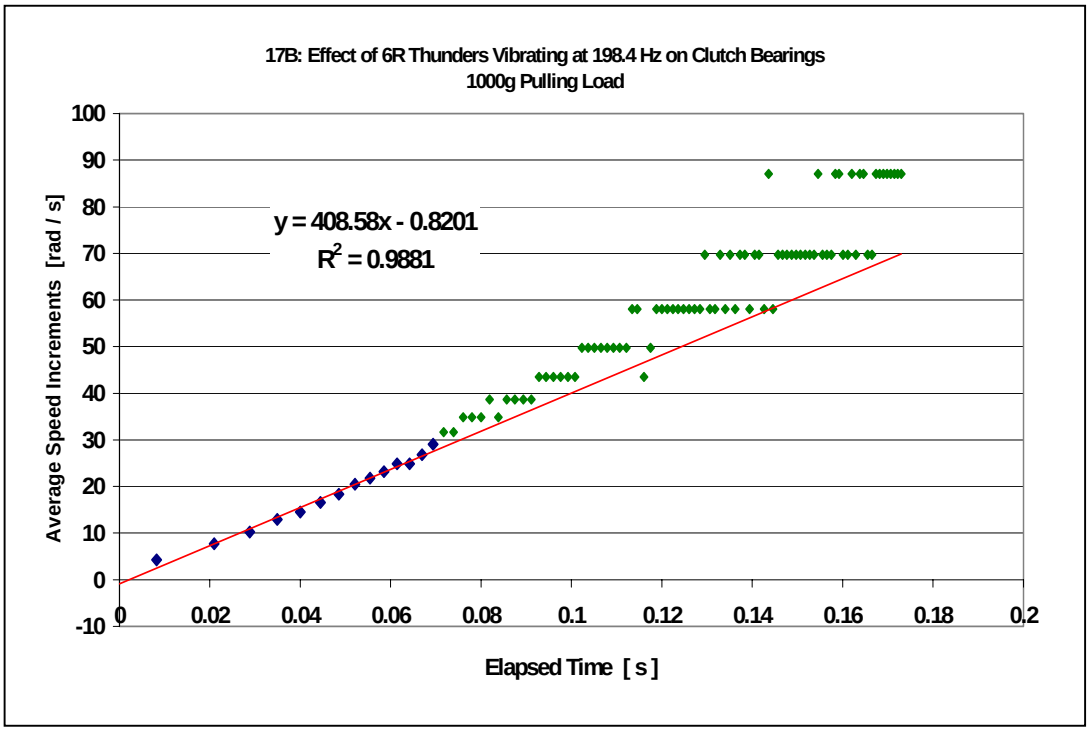

Charts A2.1—17A, 17B. (color) Effect of 6R Thunders vibrating at 198.4 Hz on clutch bearings, 1000g pulling load

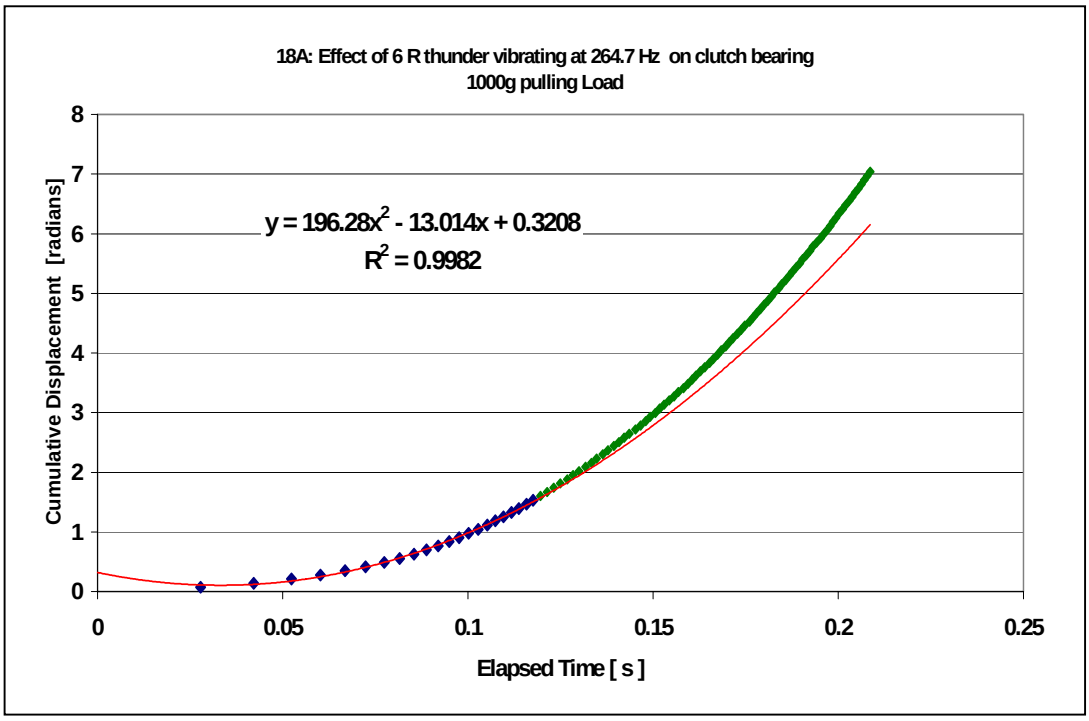

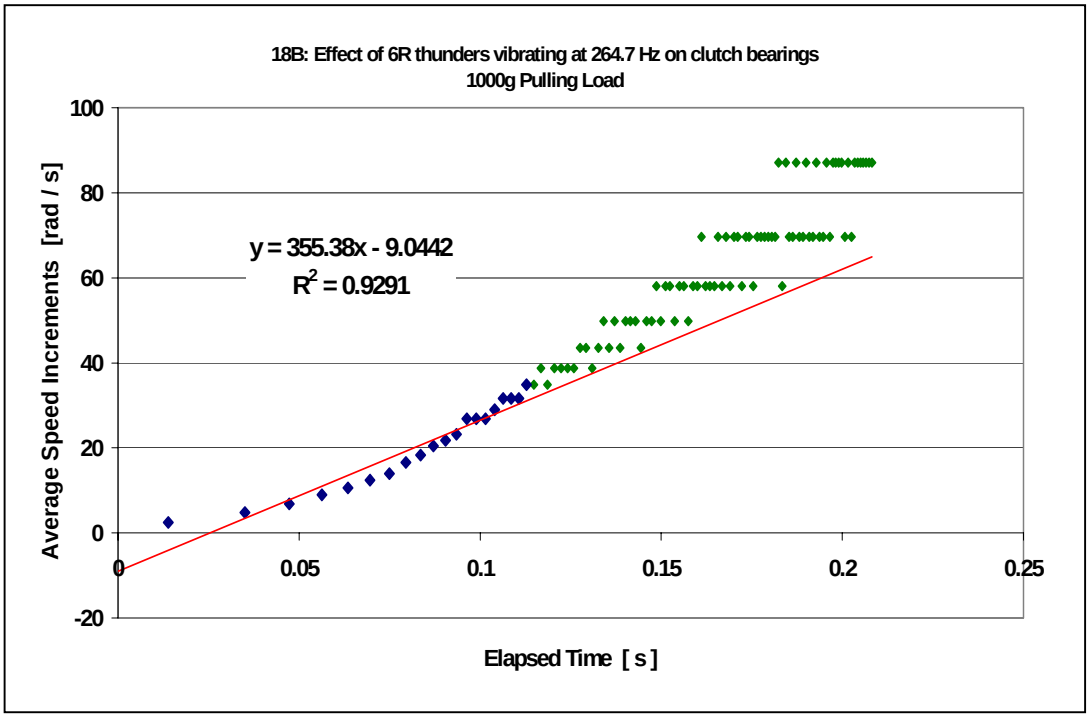

Charts A2.1—18A, 18B. (color) Effect of 6R Thunders vibrating at 264.7 Hz on clutch bearings, 1000g pulling load

From analysis given in Section A2.2, we have the results shown in Table A2.1—3. (Section A2.2 provides theoretical basis for calculating torques provided by falling masses and angular accelerations that would result in a system having no friction. The difference between calculated and measured angular accelerations will indicate resistance in the axle assembly.)

Table A2.1—3. Angular accelerations and torques calculated for frictionless axle

Falling Mass [kg]	α [rad. s^{-2}]	τ [Nm]
1.6328	1330.46370	2.399082E-02
1.2	1206.66221	2.175844E-02
1	1127.50047	2.033100E-02
0.5	809.04247	1.458859E-02
0.2	437.95043	7.897088E-03

If we call the quantities in Table A.2.1—3 "applied torques," in the sense that measured accelerations should be comparable to those calculated if indeed the axle experienced neither bearing friction nor braking friction, then we can analyze measured values as follows. The subscript "RES" indicates "resistance."

(A2.1—1) $\Sigma\tau = \tau_{APPL} + \tau_{RES} = I\alpha_{MEAS} \rightarrow \tau_{RES} = I\alpha_{MEAS} - \tau_{APPL}$

As long as a complex assembly rotates about the same axis, it can be treated as a linear combination of more elemental components. The composite rotational inertia of all rotating parts in the rotary motor discussed in Chapter 7 is determined in Section A2.3 of this appendix. Given the rotational moment, I = 1.803191253E-5 kg m^2, internal resistance in each tested configuration can be calculated. (Use last part of equation A2.1—1: $\tau_{RES} = I\alpha_{MEAS} - \tau_{APPL}$.)

From Chart A2.1—**1A**: Outside clutch bearings in place, actuator collars with inside clutch bearings in place, 1632.8g pulling load:

τ_{RES} = (1.803191253E-5)(89.18) – (2.399082E-02) = -0.022382734 Nm

This is the inherent resistance of the motor since all parts are in place.

From Chart A2.1—**3A**: Outside clutch bearings removed; inside clutch bearings in place, 1200g pulling load:

τ_{RES} = (1.803191253E-5)(105.148) – (2.175844E-02) = -0.01986242 Nm

From Chart A2.1—**15A**: Outside clutch bearings only (i.e., actuator collars removed), 1000 g pulling load:

τ_{RES} = (1.803191253E-5)(420.78) – (2.033100E-02) = -0.012743531 Nm

From Chart A2.1—**16A**: Effect of 100 Hz vibration on clutch bearings, 1000 g pulling load:

τ_{RES} = (1.803191253E-5)(456.64) – (2.033100E-02) = -0.012096907 Nm

From Chart A2.1—**17A**: Effect of 198.4 Hz vibration on clutch bearings, 1000 g pulling load:

τ_{RES} = (1.803191253E-5)(512.28) – (2.033100E-02) = -0.013252392 Nm

From Chart A2.1—***18A***: (For comparison—Chart A2.1—18 results were disqualified.) Effect of 264.7 Hz vibration on clutch bearings, 1000 g pulling load:

τ_{RES} = (1.803191253E-5)(392.56) – (2.033100E-02) = -0.011093611 N m

From Chart A2.1—**5A**: Mass of plunger on torque stand, non-clutch bearings only, 200g pulling load:

τ_{RES} = (1.803191253E-5)(369.04) – (7.897088E-03) = -1.242591E-3 Nm

This is the inherent resistance of non-clutch bearings.

From Chart A2.1—**7A**: 400g on torque stand, non-clutch bearings only, 200g pulling load:

τ_{RES} = (1.803191253E-5)(219.86) – (7.897088E-03) = -3.932591711E-3 Nm

Of this, 1.242591E-3 Nm can be attributed to bearings and plunger, leaving 2.690000711E-3 Nm, equivalent to a force of 0.564829545 N applied tangentially at a radius of 5.2705E-3 m.

(A2.1—2) $$\frac{2.690000711E-3 \quad N\,m}{5.2705E-3 \quad m} = 0.510388143\ N$$

Given 400g on the brake stand, the normal force on the axle was (0.400)(9.8) = 3.92 N. The coefficient of friction is calculated below.

(A2.1—3) $$\frac{0.5103881\ N}{3.92\ N} = 0.130201045 = 0.1302$$

From Chart A2.1—**8A**: 600g on torque stand, non-clutch bearings only, 200g pulling load:

τ_{RES} = (1.803191253E-5)(154.28) – (7.897088E-03) = -5.115124535E-3 Nm

Of this, 1.242591E-3 Nm can be attributed to bearings and plunger, leaving 3.872533535E-3 Nm, equivalent to a force of 0.734756386 N applied tangentially at a radius of 5.2705E-3 m.

Given 600g on the brake stand, the normal force on the axle was (0.600)(9.8) = 5.88 N. The coefficient of friction is 0.124958569 = 0.1250.

From Chart A2.1—**9A**: 800g on torque stand, non-clutch bearings only, 200g pulling load:

τ_{RES} = (1.803191253E-5)(148.776) – (7.897088E-03) = -5.214372181E-3 Nm

Of this, 1.242591E-3 Nm can be attributed to bearings and plunger, leaving 3.971781181E-3 Nm, equivalent to a force of 0.75358717 N applied tangentially at a radius of 5.2705E-3 m.

Given 800g on the brake stand, the normal force on the axle was (0.800)(9.8) = 7.84 N. The coefficient of friction is 0.096120812 = 0.09612

From Chart A2.1—**11A**: 1200g on torque stand, non-clutch bearings only, 500g pulling load:

τ_{RES} = (1.803191253E-5)(522.42) – (1.458859E-02) = -5.168358256E-3 Nm

Of this, 1.242591E-3 Nm can be attributed to bearings and plunger, leaving 3.925767256E-3 Nm, equivalent to a force of 0.744856703 N applied tangentially at a radius of 5.2705E-3 m.

Given 1200g on the brake stand, the normal force on the axle was

(1.200)(9.8) = 11.76 N. The coefficient of friction is 0.063338155 = 0.06334

From Chart A2.1—**12A**: 1400g on torque stand, non-clutch bearings only, 500g pulling load:

τ_{RES} = (1.803191253E-5)(476.9) – (1.458859E-02) = -5.989170914E-3 Nm

Of this, 1.242591E-3 Nm can be attributed to bearings and plunger, leaving 4.746579914E-3 Nm, equivalent to a force of 0.900593855 N applied tangentially at a radius of 5.2705E-3 m.

Given 1400g on the brake stand, the normal force on the axle was (1.400)(9.8) = 13.72 N. The coefficient of friction is 0.065640951 = 0.06564.

From Chart A2.1—**13A**: 1600g on torque stand, non-clutch bearings only, 500g pulling load:

τ_{RES} = (1.803191253E-5)(448.68) – (1.458859E-02) = -6.498031486E-3 Nm

Of this, 1.242591E-3 Nm can be attributed to bearings and plunger, leaving 5.255440486E-3 Nm, equivalent to a force of 0.997142678 N applied tangentially at a radius of 5.2705E-3 m.

Given 1600g on the brake stand, the normal force on the axle was (1.600)(9.8) = 15.68 N. The coefficient of friction is 0.063593283 = 0.06359

The following tables summarize these results and indicate that four conditions were not acceptable due to high variability. These conditions have been indicated by red typeface.

Table A2.1—4. Analytical results derived from plots

Fitted Equations for A-Type Plots	Slope	Fitted Equations for B-Type Plots
Chart 1A: $y = 44.59x^2 - 0.4605x + 0.1066$ $R^2 = 0.9999$	89.18	Chart 1B: $y = 86.184x + 0.2121$ $R^2 = 0.9802$
Notes to 1A,B: No added resistive load--Outside clutch bearings, Actuator collars in place, 1632.8g pulling load		
Chart 2A: $y = 51.311x^2 - 2.3132x + 0.1424$ $R^2 = 0.9996$	102.622	Chart 2B: $y = 89.812x - 0.3268$ $R^2 = 0.9567$
Notes to 2A,B: No added resistive load--Outside clutch bearings removed, 1200g pulling load		
Chart 3A: $y = 52.574x^2 - 0.5874x + 0.0355$ $R^2 = 0.9997$	105.148	Chart 3B: $y = 97.508x + 0.1213$ $R^2 = 0.9756$
Notes to 3A,B: No added resistive load, Outside clutch bearings removed, sample 2, higher resolution		
Chart 4A: $y = 125.1x^2 + 1.2714x + 0.0058$ $R^2 = 0.9999$	250.2	Chart 4B: $y = 250.42x + 1.3176$ $R^2 = 0.987$
Notes to 4A,B: No added resistive load; 200g pulling load		
Chart 5A: $y = 184.52x^2 - 2.8365x + 0.1064$ $R^2 = 1$	369.04	Chart 5B: $y = 339.7x - 0.259$ $R^2 = 0.974$
Notes to 5A,B: Mass of plunger on torque stand; 200g pulling load		
Chart 6A: $y = 74.549x^2 - 2.5776x + 0.0443$ $R^2 = 0.9999$	149.098	Chart 6B: $y = 158.92x - 3.2909$ $R^2 = 0.984$
Notes to 6A,B: 200g load on torque stand; 200g load on torque stand		

Table A2.1—4, Continued.

Fitted Equations for A-Type Plots	Slope	Fitted Equations for B-Type Plots
Chart 7A: $y = 109.93x^2 + 1.9571x + 0.0009$ $R^2 = 1$	219.86	Chart 7B: $y = 211.79x + 2.5347$ $R^2 = 0.9871$
Notes to 7A,B: 400g on torque stand; 200g pulling load		
Chart 8A: $y = 77.14x^2 - 8.2901x + 0.321$ $R^2 = 0.9998$	154.28	Chart 8B: $y = 143.14x - 6.3019$ $R^2 = 0.9812$
Notes to 8A,B: 600g on torque stand; 200g pulling load		
Chart 9A: $y = 74.388x^2 + 1.5695x - 0.0606$ $R^2 = 0.9999$	148.776	Chart 9B: $y = 169.67x - 0.1327$ $R^2 = 0.9966$
Notes to 9A,B: 800g on torque stand; 200g pulling load		
Chart 10A: $y = 14.547x^2 + 2.2627x + 0.0394$ $R^2 = 0.9994$	29.094	Chart 10B: $y = 24.565x + 3.0509$ $R^2 = 0.95$
Notes to 10A,B: 1000g on torque stand; 200g pulling load		
Chart 11A: $y = 261.21x^2 - 14.971x + 0.2939$ $R^2 = 0.9999$	522.42	Chart 11B: $y = 449.17x - 9.3526$ $R^2 = 0.9647$
Notes to 11A, B: Outside clutch bearings removed, 1200g on torque stand, 500g pulling load		
Chart 12A: $y = 238.45x^2 - 8.9383x + 0.1096$ $R^2 = 1$	476.9	Chart 12B: $y = 465.36x - 7.7706$ $R^2 = 0.9853$
Notes to 12A,B: 1400g on torque stand; 500g pulling load		

Table A2.1—4, Continued.

Fitted Equations for A-Type Plots	Slope	Fitted Equations for B-Type Plots
Chart 13A: $y = 224.34x^2 - 8.5399x + 0.1401$ $R^2 = 1$	448.68	Chart 13B: $y = 423.92x - 6.4943$ $R^2 = 0.9814$
Notes to13A,B: 1600g on torque stand; 500g pulling load		
Chart 14A: $y = 105.14x^2 - 3.6404x + 0.124$ $R^2 = 0.9992$	210.28	Chart 14B: $y = 164.52x - 0.302$ $R^2 = 0.9387$
Notes to14A,B: Measuring resistance of clutch bearings		
Chart 15A: $y = 210.39x^2 + 0.0432x - 0.0218$ $R^2 = 0.9999$	420.78	Chart 15B: $y = 432.01x - 1.1271$ $R^2 = 0.9921$
Notes to 15A,B: Repeat measure resistance of clutch bearings		
Chart 16A: $y = 228.32x^2 - 7.9975x + 0.1635$ $R^2 = 0.9999$	456.64	Chart 16B: $y = 397.35x - 4.0178$ $R^2 = 0.9556$
Notes to 16A,B: Effect of 100 Hz vibration on clutch bearings		
Chart 17A: $y = 256.14x^2 - 5.9312x + 0.1262$ $R^2 = 1$	512.28	Chart 17B: $y = 408.58x - 0.8201$ $R^2 = 0.9881$
Notes to17A,B: Effect of 198.4 Hz vibration on clutch bearings		
Chart 18A: $y = 196.28x^2 - 13.014x + 0.3208$ $R^2 = 0.9982$	392.56	Chart 18B: $y = 355.38x - 9.0442$ $R^2 = 0.9291$
Notes to 18A,B: Effect of 264.7 Hz vibration on clutch bearings		

Table A2.1—5. Analytical results derived from plots in condensed form—f” and f ’ are the values for acceleration

Source	f”	R2		Source	f ’	R2
Chart 1A	89.18	0.9999		Chart 1B	86.184	0.9802
1A,B: No added resistive load--Outside clutch bearings, Actuator collars in place, 1632.8g pulling load						
Chart 2A	102.622	0.9996		Chart 2B	89.812	0.9567
2A,B: No added resistive load--Outside clutch bearings removed, 1200g pulling load						
Chart 3A	105.148	0.9997		Chart 3B	97.508	0.9756
3A,B: No added resistive load, Outside clutch bearings removed, 1200g pulling load, sample 2, higher resolution						
Chart 4A	*250.2*	*0.9999*		*Chart 4B*	*250.42*	*0.987*
4A,B: No added resistive load, 200g Pulling Load						
Chart 5A	369.04	1		Chart 5B	339.7	0.974
5A,B: Mass of plunger on torque stand, 200g pulling load						
Chart 6A	*149.098*	*0.9999*		*Chart 6B*	*158.92*	*0.984*
6A,B: 200g on torque stand, 200g pulling load						
Chart 7A	219.86	1		Chart 7B	211.79	0.9871
7A,B: 400g on torque stand; 200g pulling load						
Chart 8A	154.28	0.9998		Chart 8B	143.14	0.9812
8A,B: 600g on torque stand; 200g pulling load						
Chart 9A	148.776	0.9999		Chart 9B	169.67	0.9966
9A,B: 800g on torque stand; 200g pulling load						
Chart 10A	*29.094*	*0.9994*		*Chart 10B*	*24.565*	*0.95*
10A,B: 1000g on torque stand; 200g pulling load						
Chart 11A	522.42	0.9999		Chart 11B	449.17	0.9647
11A,B: 1200g on torque stand; 500g pulling load						

Table A2.1—5, Continued.

Source	f”	R2		Source	f’	R2
Chart 12A	476.9	1		Chart 12B	465.36	0.9853
12A,B: 1400g on torque stand; 500g pulling load						
Chart 13A	448.68	1		Chart 13B	423.92	0.9814
13A,B: 1600g on torque stand; 500g pulling load						
Chart 14A	*210.28*	*0.9992*		*Chart 14B*	*164.52*	*0.9387*
14A,B: Measuring resistance of clutch bearings, 1000g pulling load in this and every case following						
Chart 15A	420.78	0.9999		Chart 15B	432.01	0.9921
15A,B: Repeat measure resistance of clutch bearings						
Chart 16A	456.64	0.9999		Chart 16B	397.35	0.9556
16A,B: Effect of 100 Hz vibration on clutch bearings						
Chart 17A	512.28	1		Chart 17B	408.58	0.9881
17A,B: Effect of 198.4 Hz vibration on clutch bearings						
Chart 18A	*392.56*	*0.9982*		*Chart 18B*	*355.38*	*0.9291*
18A,B: Effect of 264.7 Hz vibration on clutch bearings						

Table A2.1—6. Selection of plots to use and plots to omit

Source	Evaluation
Chart 1A	Okay
Chart 2A	Okay
Chart 3A	Okay
Chart 4A	*Omit. Doesn't fit pattern. 5A&B are better plots.*
Chart 5A	Good
Chart 6A	*Omit. Not good fit.*
Chart 7A	Good
Chart 8A	Okay
Chart 9A	Okay
Chart 10A	*Omit. Bad fit.*
Chart 11A	Not bad.
Chart 12A	Good
Chart 13A	Good
Chart 14A	*Omit. Doesn't fit pattern. Much lower that 16, 17, 18*
Chart 15A	Plot looks better than 14. Repeat of same conditions.
Chart 16A	Good
Chart 17A	Not bad
Chart 18A	*Omit. Bad fit.*

A2.2 Theoretical Basis for Falling Mass Experiment Allowing Calculation of Angular Accelerations and Torques that would be Obtained in a Frictionless System

After Sample Problem 11-11
Halliday, Resnick and Walker, 4th ed.; Fundamentals of Physics, p. 302.

Figure A2.2—1. FBD's for Axle and Cord

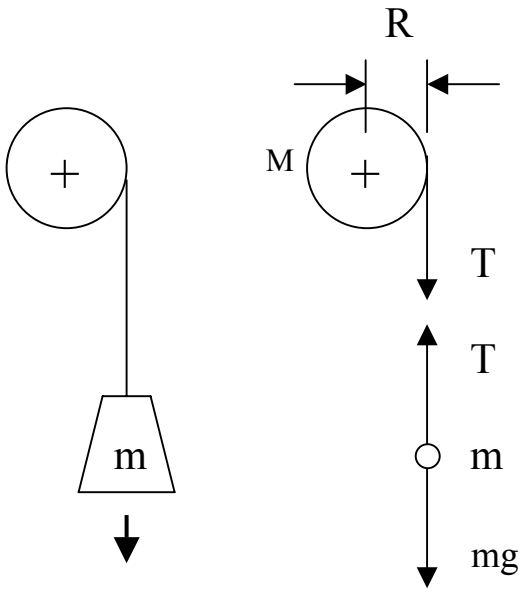

m = mass of hanging block

M = mass of axle

R = radius of axle and length of moment arm perpendicular to line of action of T

T = tension in cord,

Cord has no mass, does not slip.

No friction in axle.

The block of mass m accelerates downward so its weight (mg) must exceed the tension (T) in the cord. By Newton's second law,

(A2.2—1) $T - mg = ma$, where T is the tension in the cord.

Torque (clockwise is negative) acting on axle is –TR, the tangential force multiplied by the moment arm. (Weight of axle and reaction exerted by support act through the axis of the axle and consequently exert no torque.) From Newton's second law in angular form,

(A2.2—2) $\tau = I\alpha$, and

(A2.2—3) $a_T = R\alpha$ (see note on p.2) $\rightarrow$ $\alpha = \frac{a_T}{R}$, where τ is torque, I is

rotational inertia, α is angular acceleration [rad s^{-2}], a_T is tangential linear acceleration, and R is the radius of the body to which the torque is applied. Since $I = \frac{1}{2} MR^2$ for a solid cylinder or disk about central axis, and torque is defined as the vector product of the perpendicular component of force and the moment arm, (A2.2—2) can be expressed as follows.

(A2.2—4) $-TR = \frac{1}{2} MR^2 \frac{a_T}{R} \rightarrow T = -\frac{1}{2} Ma_T$, where M is the mass of the axle.

Replacing α with a_T/R assumes that the cord does not slip and consequently that linear acceleration of the falling mass is equal to the tangential linear acceleration of the circumference of the axle. (Let a also indicate a_T.)

Combine (A2.2—1) and (A2.2—4): $T - mg = ma \rightarrow T = ma + mg$

$ma + mg = -\frac{1}{2} Ma$

$ma + \frac{1}{2} Ma = -mg \rightarrow a(m + \frac{1}{2} M) = -mg \rightarrow a\left(\frac{2m+M}{2}\right) = -mg \rightarrow$

(A2.2—5) $a\left(\frac{2m+M}{2m}\right) = -g \rightarrow a = -g\left(\frac{2m}{2m+M}\right)$

After finding a_T, then $\alpha = \frac{a_T}{R}$, and $\tau = I\alpha$. One can also determine the tension, $T = -\frac{1}{2} Ma_T$. Finally, from (A2.2—5) and (A2.2—4):

(A2.2—6) $\tau = \frac{1}{2} MR^2 \frac{a_T}{R} \rightarrow \tau = -\frac{1}{2} gMR \left(\frac{2m}{2m+M} \right)$

The following observations can be made. From (A2.2—5), we see that the acceleration of the falling block is less than g , since [2m / (2m + M)] < 1 . The tension in the cord is less than the weight of the hanging block, since

$T = ma + mg = -mg \left(\frac{2m}{2m+M} \right) + mg = mg \left[1 - \left(\frac{2m}{2m+M} \right) \right]$, and the

quantity in brackets is positive and less than one, since [2m / (2m + M)] < 1 .
For a massless axle (M = 0), a = – g , and T = 0 , corresponding to a falling block with no resistance to slow it.

The following calculations indicate the accelerations which would result if the axle experienced no bearing friction or braking friction.

The "cord" in the preceding analysis was a wire 0.04 inch in diameter. Thus, the moment arm in the system is the sum of the axle radius and wire radius, R = (0.1875 + 0.02)inch (0.0254 m/inch) = (0.2075)(0.0254) = 5.2705E–3 m.

Combining (A2.2—3) and (A2.2—5) produces an equation which bypasses tangential acceleration, a_T , as an intermediary in calculating angular acceleration, α .

(A2.2—7) $\alpha = \frac{a_T}{R}$ and $a_T = -g \left(\frac{2m}{2m+M} \right)$. Thus, $\alpha = \frac{-g}{R} \left(\frac{2m}{2m+M} \right)$

The derivation of this expression assumed, however, that the rotational inertia belonged to a simple cylinder or disk rotated about its central axis. Since both the axle

radius—the moment arm for the force of falling weights—and the rotational inertia of the entire axle and wheel assembly are known, an "equivalent mass" can be calculated for a cylinder having the same rotational inertia as the entire assembly.

Given the rotational moment, I = 1.803191253E–5 kg m^2, axle radius, R = 5.2705E–3 m, and rotational inertia for a simple cylinder or disk rotated about its central axis given by I = ½ MR^2, the mass of a cylinder having the specified characteristics is calculated as follows.

(A2.2—8) $$M_{EQ} = \frac{2I}{R^2} = \frac{2(1.0803191253E-5)}{(5.2705E-3)^2} = 1.298279359 = 1.29828\ kg$$

The following formula can be derived from (A2.2—7) and (A2.2—8).

(A2.2—9) $$\alpha = \frac{-9.8}{5.2705E-3}\left(\frac{2m}{2m+1.29828}\right) = -1859.406128\left(\frac{2m}{2m+1.29828}\right)$$

The value calculated from (A2.2—9) can be substituted into $\tau = I\alpha$, or the pre-factor in (A2.2—6) can be evaluated to produce another formula as follows.

From (A2—6), $-\frac{1}{2}$ gMR = $-\frac{1}{2}$ (9.8)(1.29828)(5.2705E-3) = -0.033528665 Nm

(A2—10) $$\tau = -\frac{1}{2}\,gMR\left(\frac{2m}{2m+M}\right) = -0.033528665\left(\frac{2m}{2m+1.29828}\right)$$

In the experiment, the masses used to produce acceleration of the axle and wheel assembly while acceleration was measured have the values, m = 1.6328, 1.2, 0.2, 0.5, and 1 kg. Measured accelerations should be compared to those which would result if the axle experienced no bearing friction or braking friction. Table A2.2—1 lists results of calculations using (A2.2—9) and (A2.2—10).

Table A2.2—1. Angular accelerations and torques calculated for frictionless axle

Falling Mass [kg]	α [rad. s^{-2}]	τ [Nm]
1.6328	1330.46370	2.399082E-02
1.2	1206.66221	2.175844E-02
1	1127.50047	2.033100E-02
0.5	809.04247	1.458859E-02
0.2	437.95043	7.897088E-03

Notes on Fundamentals of Rotational Motion.

Differentiate $s = \theta r$ to get $\frac{ds}{dt} = \frac{d\theta}{dt} r$, or $v = \omega r$. The first equation says that the distance traveled along a circular arc by a point in a rotating body is related to the angle of rotation by the radial distance of the point from the center of rotation (and defines radian measure: $\theta = s/r$). For rotation through a given angle, a point farther from the center of rotation will move through a longer circular arc than will a point closer to the center. The second equation relates the linear speed, v, along the circular arc to the angular speed, ω [rad s^{-1}], again by radial distance, r. Since all points within a rigid body have the same angular speed, the greater the radius, the greater the linear speed, which is the magnitude of the velocity vector tangent to the circular path of the point in question.

Now differentiate $v = \omega r$, again regarding r as not changing in time:

$\frac{dv}{dt} = \frac{d\omega}{dt} r$. This presents a complication. The quantity dv/dt represents only the part of the linear acceleration responsible for changes in the magnitude v of the linear velocity **v**. Like **v**, that part of the linear acceleration is tangential to the path of the point in question, and is called the tangential component a_T of the linear acceleration of the point: $a_T = \alpha r$, where $a_T = dv/dt$ and $\alpha = d\omega/dt$.

In addition, a point moving in a circular path has a radial component of linear acceleration, $a_R = v^2/r$, also known as centripetal acceleration, that is responsible for changing the direction of the linear velocity **v**. Thus, when a particle moves along a circular arc of radius r, the vector component of acceleration responsible for constantly changing its direction is directed toward the center of rotation, and has magnitude v^2/r.

Substitute $v = \omega r$ into $a_R = v^2/r$ to get $a_R = \omega^2 r$.

Thus, the linear acceleration of a point on a rotating body has two components. The radial component, $a_R = \omega^2 r$, is always present as long as the angular velocity is not zero, and the tangential component, $a_T = \alpha\, r$, is present as long as the angular acceleration is not zero. Thus, uniform circular motion at constant angular velocity involves only centripetal acceleration.

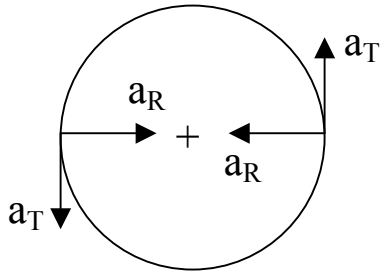

Figure A2.2—2. Applied loads and resulting accelerations

A2.3 Determination of Composite Rotational Inertia of Rotating Assembly in Motor

Halliday, Resnick and Walker. Some Rotational Inertias, p.297:

Solid cylinder (or disk) about central axis: $I = \frac{1}{2} MR^2$

Annular cylinder (or ring) about central axis: $I = \frac{1}{2} M (R_1^2 + R_2^2)$

Hoop about central axis: $I = MR^2$

Data from Supplemental Notebook 3, p.8, 8/16/2003

Axle Rod, Radius = 0.1875 in. (diameter = 0.375 in.)

R = (0.1875 in.)(0.0254 m/in.) = 4.7625E-3 m
M = 85.8213g

$I = \frac{1}{2}(0.0858213)(4.7625E\text{-}3)^2 = 9.732738851E\text{-}7$ kg m^2

Paper Disk:

I.D.:	0.375 in.	O.D.	3.55 in.	M =	5.2839g
	0.385		3.56	From **A**:	0.0012
	0.38		3.525	Total:	5.2851g
	0.385		3.535		
	0.37		3.535		
	0.375		3.53		
	0.39		3.54		
	0.395		3.505		
	0.385		3.52		
	0.395		3.535		
	0.3835 in., n = 10		3.5335 in., n= 10		

$R_1 = (0.19175)(0.0254) = 4.87045E\text{-}3$ m

$R_2 = (1.76675)(0.0254) = 0.04487545$ m

$I = \frac{1}{2} M (R_1^2 + R_2^2) = \frac{1}{2} (0.0052851)[(4.87045E\text{-}3)^2 + (0.04487545)^2]$

$= 5.384267756E\text{-}6$ kg m^2

Compare to rotational inertia of disks ($I = \frac{1}{2} MR^2$) with $R = R_1 = 4.87045E\text{-}3$ m and $R = R_2 = 0.04487545$ m.

First, estimate mass missing from hole at center:

Total volume = $\pi(R_2^2 - R_1^2)h = \pi\,[(1.76675)^2 - (0.19175)^2]\,0.025 = 0.242266862$ in.^{3}

Volume of hole at center = $\pi\,(0.19175)^2\,0.025 = 2.887756876E\text{-}3$ in.^{3}

Estimated amount of mass cut out = (0.002887756876 / 0.242266862) 5.2851 = 0.062996993 g

(1) $I_1 = \frac{1}{2}\,(6.2996993E\text{-}5)(4.87045E\text{-}3)^2 = 7.471847559E\text{-}10$ kg m^2

(2) $I_2 = \frac{1}{2}\,(5.2851E\text{-}3)(0.04487545)^2 = 5.321583079E\text{-}6$ kg m^2

Difference = 5.32084E-6 kg m^2 , compared to 5.38427E-6 kg m^2 from above.

Paper Hoop:

O.D.: 3.6
3.59
3.585
3.585
3.575
3.59
3.575
3.6
3.59
3.6
3.589

Rim after removal: 1.9477g
"Mass that should be added to rim mass": 0.1815
(see **A** and **B**) 2.1292
from **A**: 0.0200
2.1492g

Inside radius:
Outside radius: 1.7945 in.
Thickness: 0.025
Inside radius: 1.7695 in.
(1.7695)(0.0254) = 0.0449453 m

R = (1.7945)(0.0254) = 0.0455803 m (outside radius)

$I = \frac{1}{2}\,M\,(R_1^2 + R_2^2) = \frac{1}{2}\,(2.1492E\text{-}3)[(0.0449453)^2 + (0.0455803)^2]$

$= 4.403327963E\text{-}6$ kg m^2

(Difference between measured radius of hoop, 1.7945 in., and measured radius of disk, 1.76675 in., is 0.02775 in., which is reasonable. If disk radius is used, resulting thickness of hoop would be 0.02775 in. instead of 0.025 in.)

Compare with rotational inertia of hoop with negligible thickness, $I = MR^2$. Use average radius = ½ (0.0449453 + 0.0455803) = 0.0452628 m

$I = (2.1492E\text{-}3)(0.0452628)^2 = 4.403111E\text{-}6$ kg m^2 , compared with 4.403328E-6 kg m^2 from above.

Adjustment **A:**

Center cardboard:	5.2839g
Rim after removal:	1.9477
"Mass that should be added to rim mass":	0.1815
Total:	7.4131g

Cardboard part of wheel before disassembly*:	7.4343g
Total accounted for:	7.4131
Difference to be apportioned:	0.0212g

Add 0.02g to rim; 0.0012g to disk. (subjective assessment of relative proportions of little piles of glue flecks)

* "Some glue may be lost—assign weight to rim" (This is why 0.02g vs. 0.0012g was assigned to rim)

Split Collars (See Figure A2.3—1):

Total Volume of Collar:

Volume of annular simple solid =

$+ (0.3725)\,\pi\,[(0.43)^2 - (0.1875)^2] = 0.175237$

Less volume of splits =

$- 2(0.3725)(0.2425)(0.06) = 0.01083975$

Less volume of screw insets (see below) =

- 0.0109083

Add volume of screw heads =

+ 2(0.135) π (0.11)^2 = 0.0102636

Less volume of screw sockets =

- 2(0.175) π (0.0575)^2 = 0.0036354

Add volume of screws exposed in splits =

+ 2(0.06) π (0.1)^2 = 0.00376991184

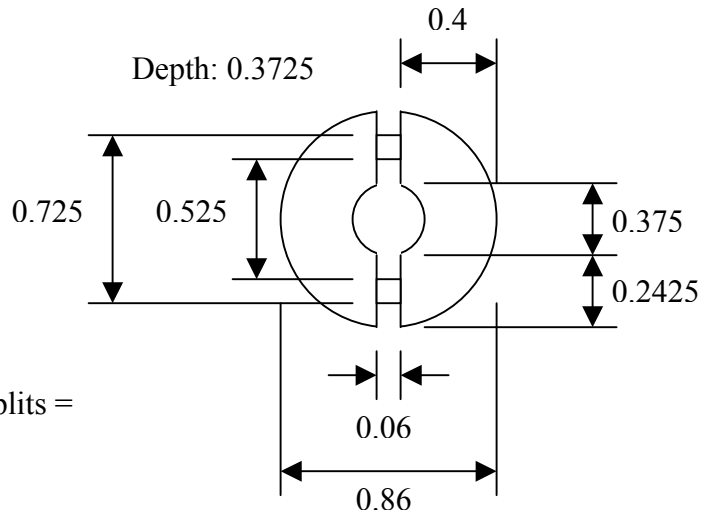

Figure A2.3—1. Split collar dimensions

Sum of items above:

(0.175237 + 0.0102636 + 0.0037700) – (0.010840 + 0.0109083 + 0.0036354) in.^{3}

= 0.1638869 in.^{3}

Total Mass of Collar

Mass of outside collars:	19.5678g
	19.6225
Mass of collar on wheel:	19.5994
Average:	19.5994g (Use 19.6g)

Density: 19.6 / 0.1638869 = 119.59/in.^{3} (7.298 g /cm^3)

However, density of steel of any kind is 7.85 g /cm3 = 128.64 g /in.3. This would suggest a correct volume of 19.6 / 128.64 = 0.152363 in.^{3}. The difference is 0.0115239 in.^{3}. There are fillets and a circular groove on one side.

Use calculated density (128.64 g /in.^{3}) as needed. Mass that would be present if splits were solid (less mass of screws exposed in splits) can be estimated as

(128.64)(0.01083975-3.76991184E-3) = (128.64)(7.069838816E-3) = 0.909464065 g

= 9.09464065E-4 kg

R_1 = (0.1875)(0.0254) = 4.7625E-3 m R_2 = (0.43)(0.0254) = 0.010922

I_{SIMPLE} = ½ (0.0196 + 9.09464065E-4) $[(4.7625E-3)^2 + (0.010922)^2]$

= 1.455879589E-6 kg m^2

Deduct rotational inertia of missing space treated as a "stick" rotated about axis through its centroid perpendicular to its long dimension. The formula is valid for any cross section because differing cross sections are accounted for by the linear density (M/L). The parallel axis theorem $I = I_{CM} + Mh^2$, where h is the perpendicular distance between the two parallel axes, is used to avoid including the space through which axle inserts.

$I_{SPLIT} = {}^1/_{12}\ ML^2 + Mh2$

$= {}^1/_{12}$ (9.09464065E-4)$[(0.2425)(0.0254)]^2$ + (9.09464065E-4)[(0.1875

+0.12125)(0.0254)]^2

$= {}^1/_{12}$ (9.09464065E-4)$(6.1595E-3)^2$ + (9.09464065E-4)$(7.84225E-3)^2$

= 5.880822473E-8 kg m^2.

Two such spaces contribute a missing 1.176164495E-7 kg m^2.

Consider the exposed screw sections to have the rotational inertia of two particles of mass M connected by a rod of length L and negligible mass. I = ½ ML^2. (p.298, Halliday, Resnick and Walker) Average diameter (= L) to screw centers is 0.625 inch.

$I_{SECTIONS}$ = ½ $[(3.76991184E-3)(128.64)(0.001)][(0.625)(0.0254)]^2$

= 6.110893261E-8 kg m^2

$I_{TOTAL} = I_{SIMPLE} - I_{SPLITS} + I_{SECTIONS}$ = 1.455879589E-6 –1.176164495E-7 + 6.110893261E-8

= 1.399372072E-6 kg m^2.

Compare with I = ½ (0.0196) [$(4.7625E-3)^2$ + $(0.010922)^2$] = 1.39132E-6 kg m^2.

Note on calculating volume missing due to screw insets.

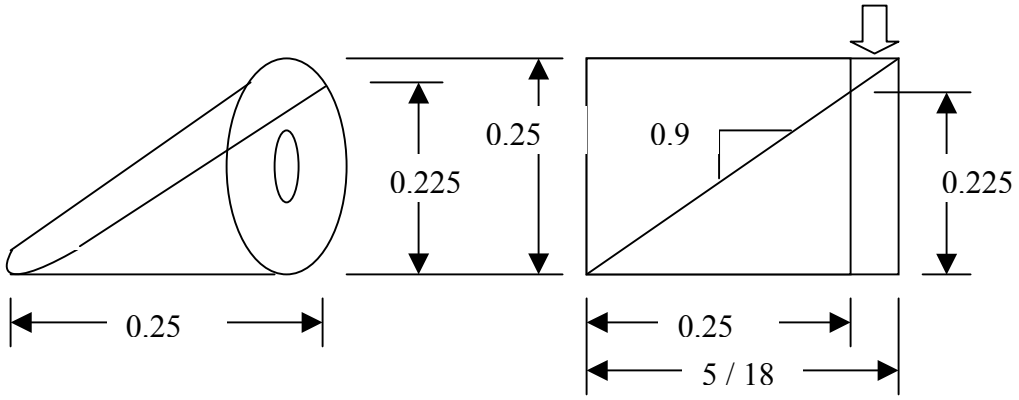

Figure A2.3—2. Schematic shape of screw insets

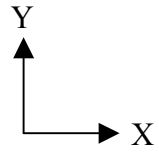

Extension of volume sought would bisect a cylinder just a little longer than 0.25 inch.

$$y = \frac{0.225}{0.25}\, x = 0.9\; x = 0.25 \quad if\; x = \left(\frac{10}{9}\right)\left(\frac{1}{4}\right) = \frac{5}{18} = 0.2777\overline{7}$$

Difference in length = (5/18 – 1/4) = (10/36 – 9/36) = 1/36 = 0.027777…

Half-cylinder of length 5/18 in., less entire extension:

½ (5/18)π$(0.125)^2$ – (1/36)π$(0.125)^2$ = (1/9)π$(0.125)^2$ = 0.005454154 $in.^3$

For two screw insets, this would amount to 0.0109083 $in.^3$. The small amount (block arrow in diagram) which should be added back can be neglected. Even when it is accounted for and doubled (since inserted screws do not quite extend to end of threaded holes on other half of collar, leaving small depressions), the calculated density only changes from 7.298 g /cm^3 to 7.304 g /cm^3.

Washer:

I.D.:	0.441 in.	O.D.	1.02 in.	Mass of glue-free washer:	7.6061 g
	0.438		1.015	From Adjustment B:	0.0812
	0.437		1.025	Total:	7.6873 g
	0.437		1.02		
	0.439		1.018		
	0.431		1.024	I.D. = 0.4373 in. = 0.01110742 m	
	0.438		1.021	O.D. = 1.0207 in. = 0.02592578 m	
	0.436		1.026		
	0.437		1.016		
	0.439		1.022		
	0.4373 in.		1.0207 in.		

$I = \frac{1}{2}\,(0.0076873)[(0.02592578)^2 + (0.01110742)^2] = 3.057703706E\text{-}6$ kg m^2

Adjustment **B**:

Masses after glue scraped off:

Collar:	19.6079 g	"Entire wheel":	35.0016 g
Washer:	7.6061	Total of glue-free parts:	34.6345
Center circle:	5.2839	Glue, etc.:	0.3671g (1)
Paper rim:	1.9477		
Metal tape:	0.1889		
	34.6345 g		

"Paper and glue scraped from washer":	0.0812 g	
"Mass that should be added to rim mass":	0.1815	
"Washer & collar & glue" less glue-free collar and washer:	0.0557	(3)
"Washer & glue" less glue-free washer:	0.0552	
	0.3736 g	(2)

Difference between (1) and (2) = 0.0065 g

Deduct this from (3), leaving 0.0492 g. The small difference suggests that no glue amounts were double-counted. "Mass that should be added to rim mass," was covered in Adjustment **A**. The list above will be parceled out as follows.

0.0812 g → Add to washer mass.

0.0557 g → 0.0492 g → Calculate rotational inertia for a "hoop" ($I = MR^2$) having radius of collar, R = (0.43)(0.0254) = 0.010922 m

0.0552 g → Calculate rotational inertia for a "hoop" ($I = MR^2$) having radius of washer (O.D. = 1.025 inch), R = (0.5125)(0.0254) = 0.0130175 m

For hoop at radius of collar, $I = (4.92E\text{-}5)(0.010922)^2 = 5.869072133E\text{-}9$ kg m^2

For hoop at radius of washer, $I = (5.52E\text{-}5)(0.0130175)^2 = 9.353932905E\text{-}9$ kg m^2

Metal Tape:

Total length of tape: 3.455 + 3.440 = 6.895 in.

Mass of tape: 0.1889 g

Linear density of tape = 0.1889 / 6.895 = 0.0274 g /in.

Of the total length, 1.5 in. is located on an imaginary hoop at the outside of the collar.

Mass = (1.5)(0.0274) = 0.0411 g

$I = (4.11E\text{-}5)[(0.43)(0.0254)]^2$
$= (4.11E\text{-}5)(0.010922)^2$
$= 4.902822452E\text{-}9$ kg m^2

Construct approximate radii from data in figure. The diameter of the paper disk is 3.5355 in. (radius = 1.76775 in.).

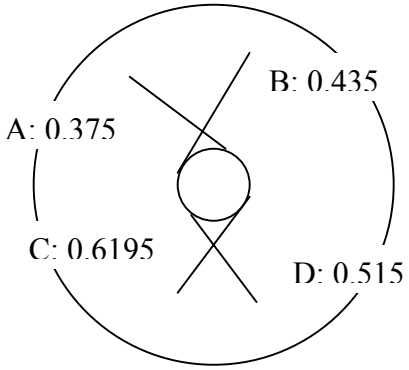

Figure A2.3—3. Approximate placement of metal tape. Inner circle is collar circumference; outer circle is paper disk circumference. Marked values are distance in inches between ends of tape and outer circumference, measured along radii.

(A) 1.76775 – 0.375 = 1.39275 in.
(B) 1.76775 – 0.435 = 1.33275 in.
(C) 1.76775 – 0.6195 = 1.14825 in.
(D) 1.76775 – 0.515 = 1.25275 in.

Total calculated length = 5.1265 in. Actual total (less 1.5 in. around collar) is 5.395 in. If the calculated lengths are considered projected lengths, the average angle relative to a radius was $\cos^{-1}(5.1265 / 5.395) \approx 18^{\circ}$, which is about what was observed.
To estimate actual lengths (to determine mass, divide by the cosine = 0.950231696.

(A) (1.39275 / 0.9502317) = 1.465695162 in.; (1.465695162)(0.0274) = 0.040160047 g
(B) (1.33275 / 0.9502317) = 1.402552668 in.; (1.402552668)(0.0274) = 0.038429943 g
(C) (1.14825 / 0.9502317) = 1.208389496 in.; (1.208389496)(0.0274) = 0.033109872 g
(D) (1.25275 / 0.9502317) = 1.318362674 in.; (1.318362674)(0.0274) = 0.036123137 g
(Cosine = 0.950231696 actually used in calculations above.)

Total calculated mass = 0.14782 g vs. (5.395)(0.0274) = 0.14782 g.
Total calculated length = 5.395 in., equal to (6.895 – 1.5) = 5.395 in.

Convert half lengths (along radial directions) to meters:

(A) ½ (1.465695162)(0.0254) = 0.018614328 m
(B) ½ (1.402552668)(0.0254) = 0.017812418 m
(C) ½ (1.208389496)(0.0254) = 0.015346546 m
(D) ½ (1.318362674)(0.0254) = 0.016743205 m

Calculate rotational inertia of each approximately radial strip of tape as a "stick" rotated about axis through its centroid perpendicular to its long dimension ($I = {}^{1}/_{12}\, ML^2$). The formula is valid for any cross section because differing cross sections are accounted

for by the linear density (M/L). The parallel axis theorem $I = I_{CM} + Mh^2$, where h is the perpendicular distance between the two parallel axes, is again needed. The offset, h, is 0.43 in. = 0.010992 m. L is total length of tape pieces

$I_A = {}^1/_{12}\,(4.0160047E\text{-}5)(2(0.018614328))^2 + (4.0160047E\text{-}5)(0.010992 + 0.018614328)^2$

$= {}^1/_3\,(4.0160047E\text{-}5)(0.018614328)^2 + (4.0160047E\text{-}5)(0.010992 + 0.018614328)^2$

$= 3.984006754E\text{-}8$ kg m^2

$I_B = {}^1/_3\,(3.8429943E\text{-}5)(0.017812418)^2 + (3.8429943E\text{-}5)(0.010992 + 0.017812418)^2$

$= 3.59494916E\text{-}8$ kg m^2

$I_C = {}^1/_3\,(3.3109872E\text{-}5)(0.015346546)^2 + (3.3109872E\text{-}5)(0.010992 + 0.015346546)^2$

$= 2.556825424E\text{-}8$ kg m^2

$I_A = {}^1/_3\,(3.6123137E\text{-}5)(\,0.016743205)^2 + (3.6123137E\text{-}5)(0.010992 + 0.016743205)^2$

$= 3.116294507E\text{-}8$ kg m^2

$I_{TOTAL} = 3.984006754E\text{-}8 + 3.59494916E\text{-}8 + 2.556825424E\text{-}8 + 3.116294507E\text{-}8 + 4.902822452E\text{-}9 = 1.374235809E\text{-}7$ kg m^2

(The fifth term was the I_{HOOP} from 1.5 in. of tape on perimeter of collar.)

Grand Total:

Axle rod :	9.732738851E-7 kg m^2
Paper Disk:	5.384267756E-6
Paper Hoop:	4.403327963E-6
Split Collars:	1.399372072E-6
	1.399372072E-6
	1.399372072E-6
Washer:	3.057703706E-6
Glue, collar hoop:	5.869072133E-9
Glue, washer hoop:	9.353932905E-9
Metal Tape:	1.374235809E-7
Total:	1.803191253E-5 kg m^2